ISSN 0289-842X

The 160 cm Cyclotron
1966–1990

RIKEN Accelerator Progress Report
1990

Supplement

理化学研究所
The Institute of Physical and Chemical Research

The 160 cm Cyclotron

1966—1990

RIKEN Accelerator Progress Report
Supplement 1990

理化学研究所
the Institute of Physical and Chemical Research
Wako-shi, Saitama, 351-01 JAPAN

Editors

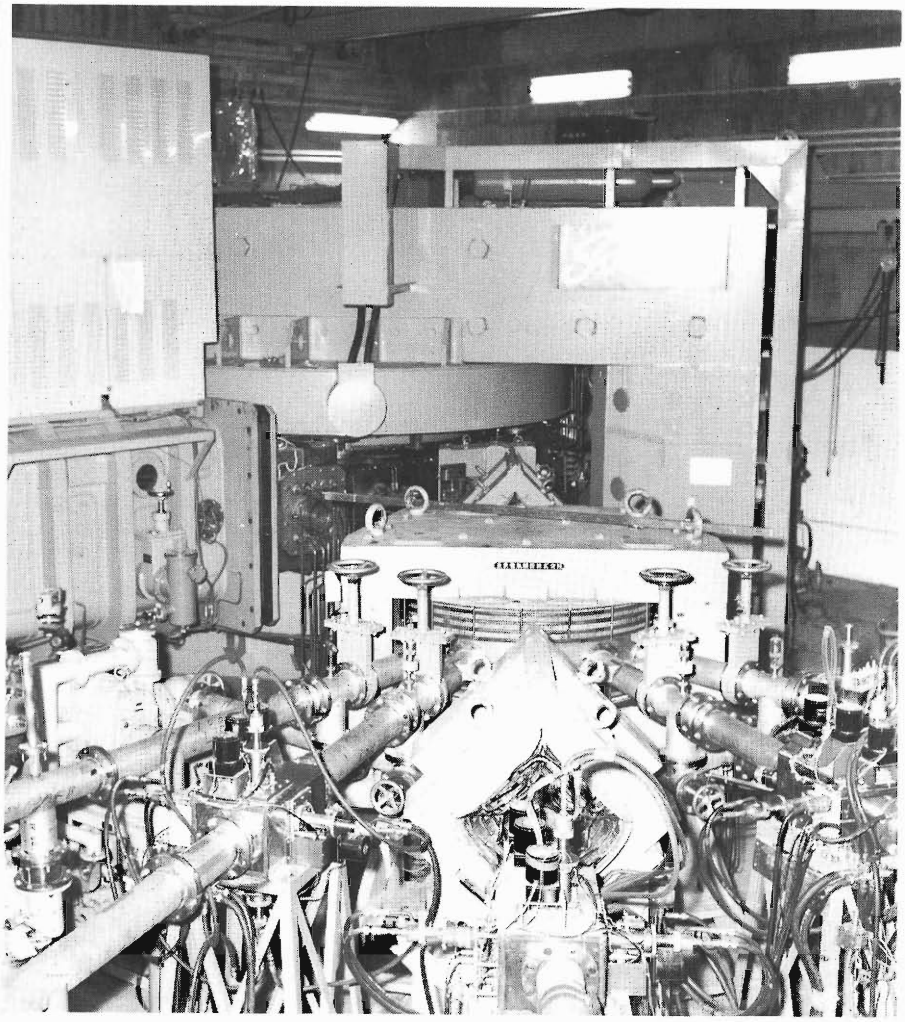

The 160cm Cyclotron

The 160 cm Cyclotron and members of the Cyclotron Laboratory and the Radiation Laboratory who contributed to its construction.

(Photograph : 1966)

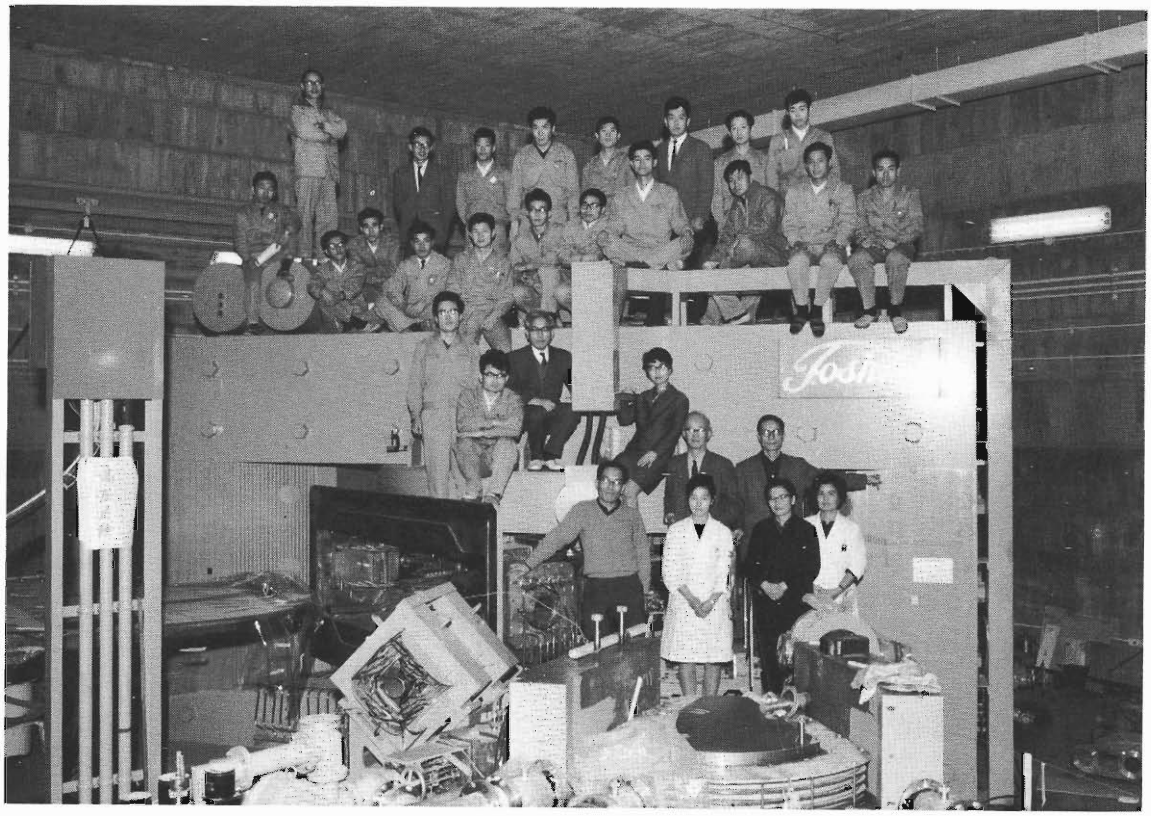

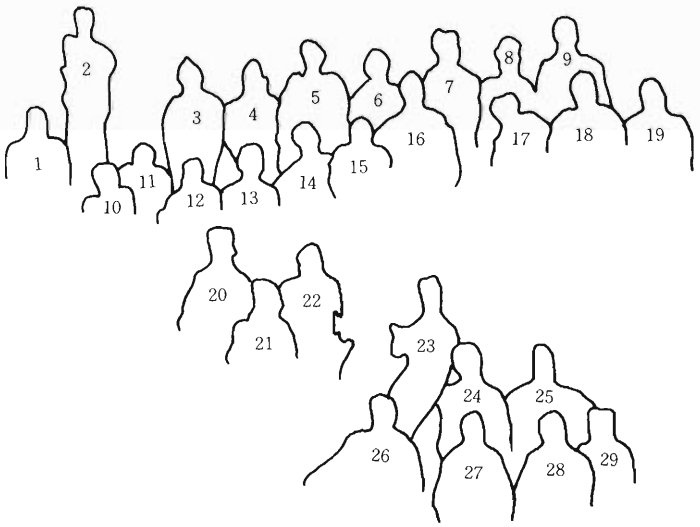

1) Masatoshi Odera(C)
2) Shoshichi Motonaga(C)
3) Akira Hashizume(R)
4) Shin Fujita(C)
5) Hiromichi Kamitsubo(C)
6) Kiyoshi Ogiwara(C)
7) Yoshihiko Tendow(R)
8) Masatake Hemmi(C)
9) Hisao Nakajima(C)
10) Osamu Terashima(C)
11) Shigeru Takeda(C)
12) Toshihiko Inoue(C)
13) Noriyoshi Nakanishi(C)
14) Shunji Nakajima(C)
15) Akira Shimamura(C)
16) Yoshiaki Chiba(C)
17) Isao Kohno(C)
18) Yoshitoshi Miyazawa(C)
19) Kisaku Yoshida(C)
20) Takeshi Wada(C)
21) Takashi Fujisawa(C)
22) Hiroo Kumagai(C)
23) Yohko Awaya(R)
24) Fumio Yamasaki(R)
25) Tatsuji Hamada(R)
26) Takashi Karasawa(C)
27) Kayoko Tatsuta(C)
28) Reiko Sudo(C)
29) Masako Furuyama(C)

(C): Cyclotron Laboratory
(R): Radiation Laboratory

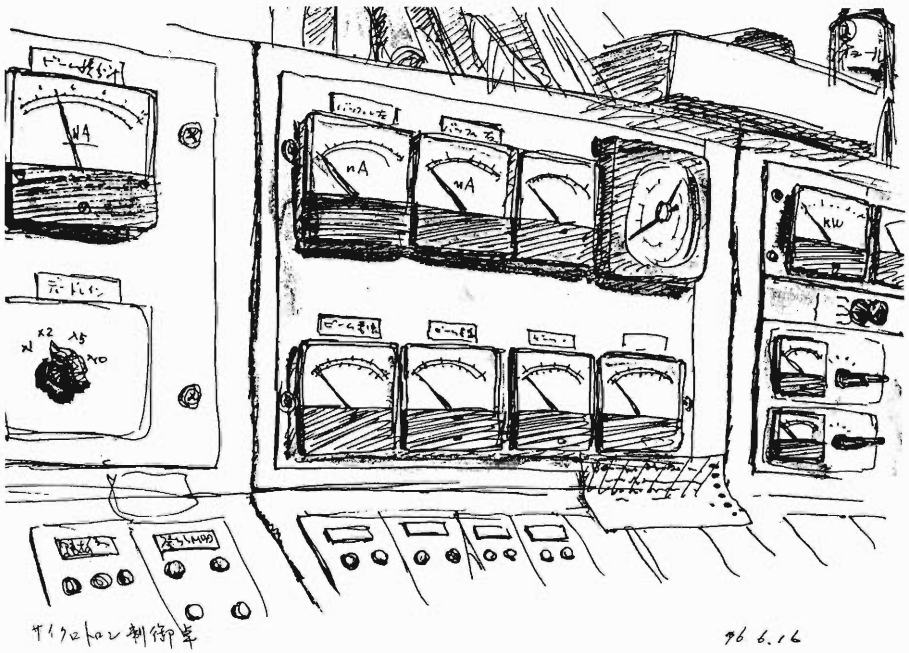

サイクロトロン制御室

96 6.16

Haruo NAGAOKA (1893–1976)
First President of RIKEN (1958–1966)

Fumio YAMASAKI (1907–1981)
Head of Radiation Lab. (1957–1968)

Hiroo KUMAGAI (1911–1977)
Head of Cyclotron Lab. (1962–1971)

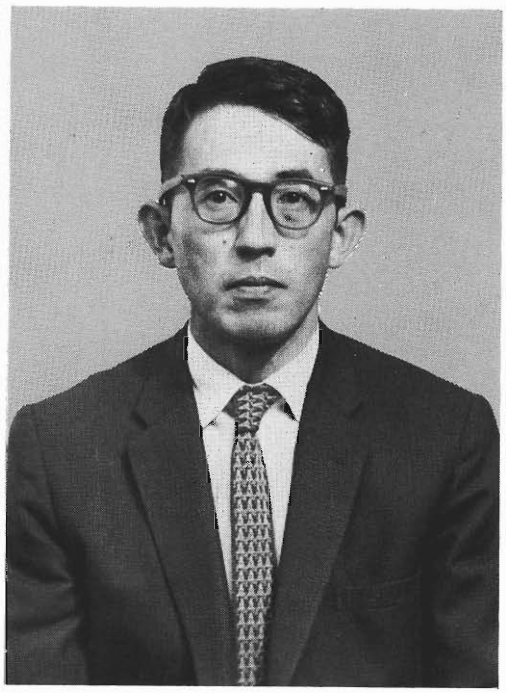

Kazuhisa MATSUDA (1922–1971)
Head of Cyclotron Lab. (1971)

Construction site for the cyclotron facility. (1964)

S. Kikuchi, H. Kumagai

H. Nagaoka, H. Kumagai, S. Kikuchi

J. Sanada, O. Nishimoto, I. Nonaka
① ② ③

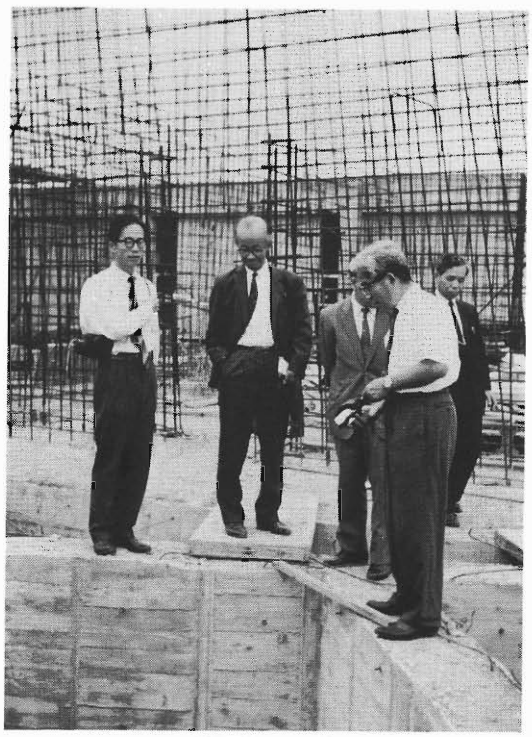

T. Hamada, F. Yamasaki, H. Kumagai

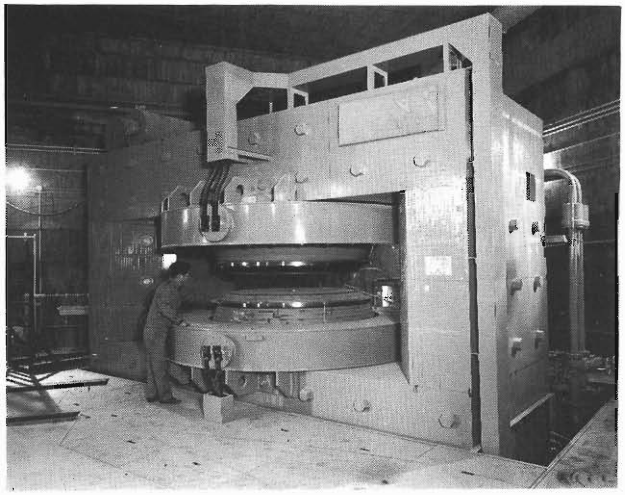

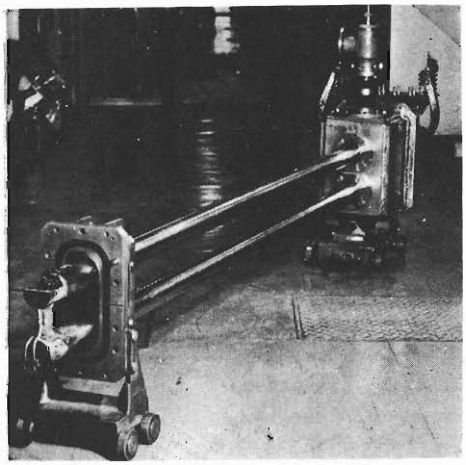

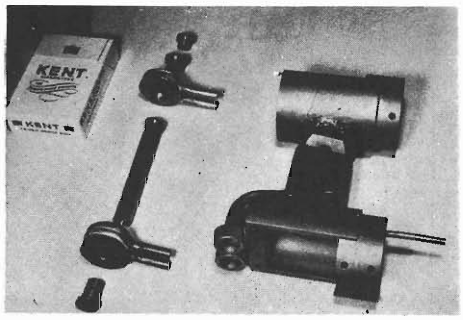

Heavy-ion source.

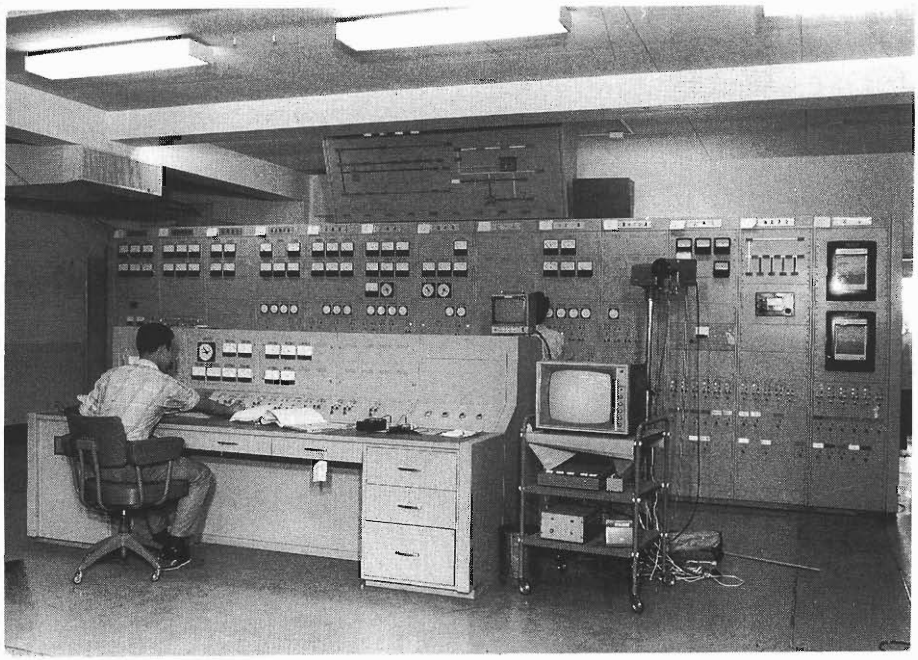

Control system of the cyclotron and operation console.

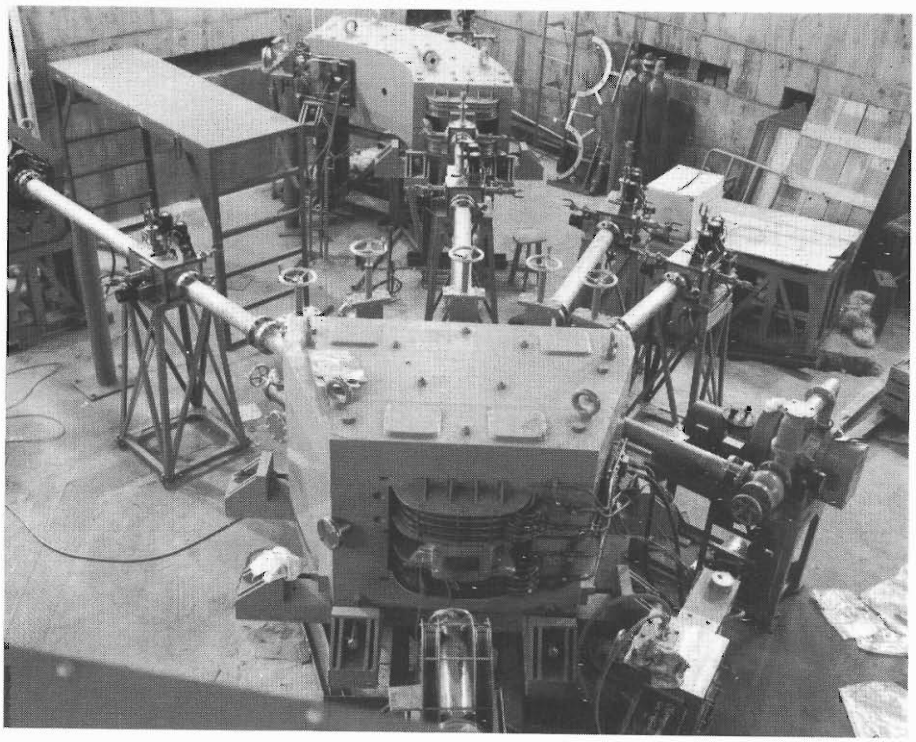

Switching magnet and beam lines.

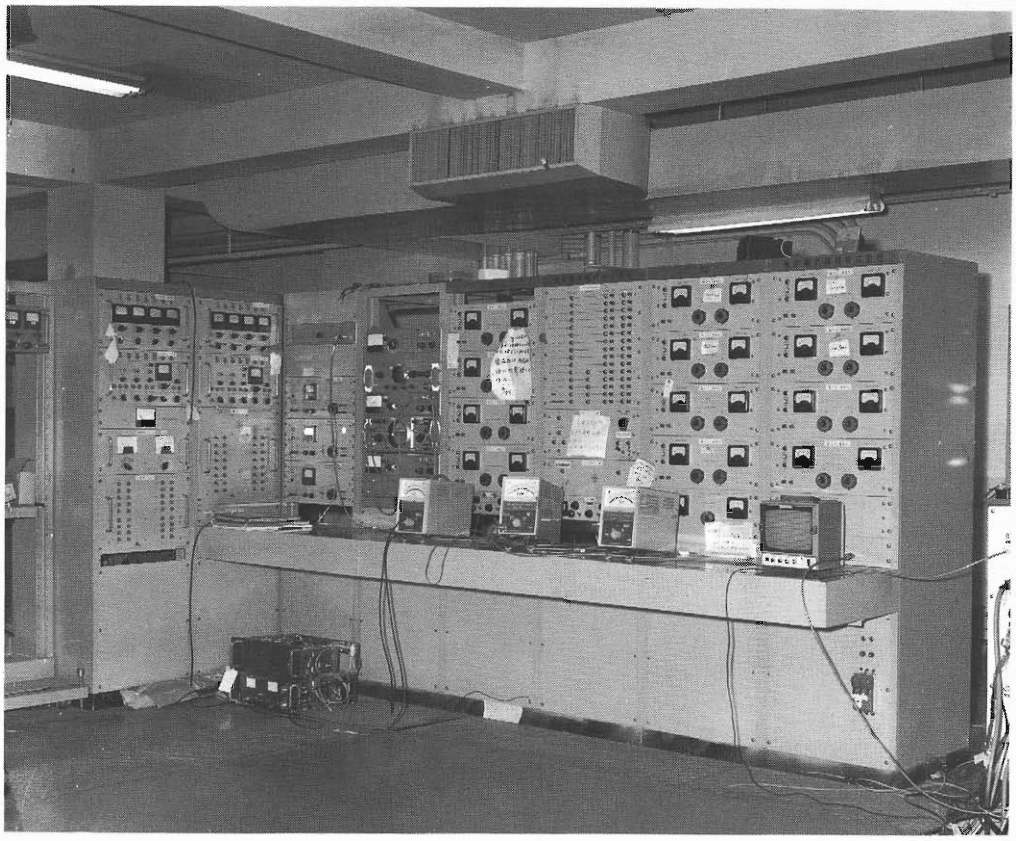

Beam handling system.

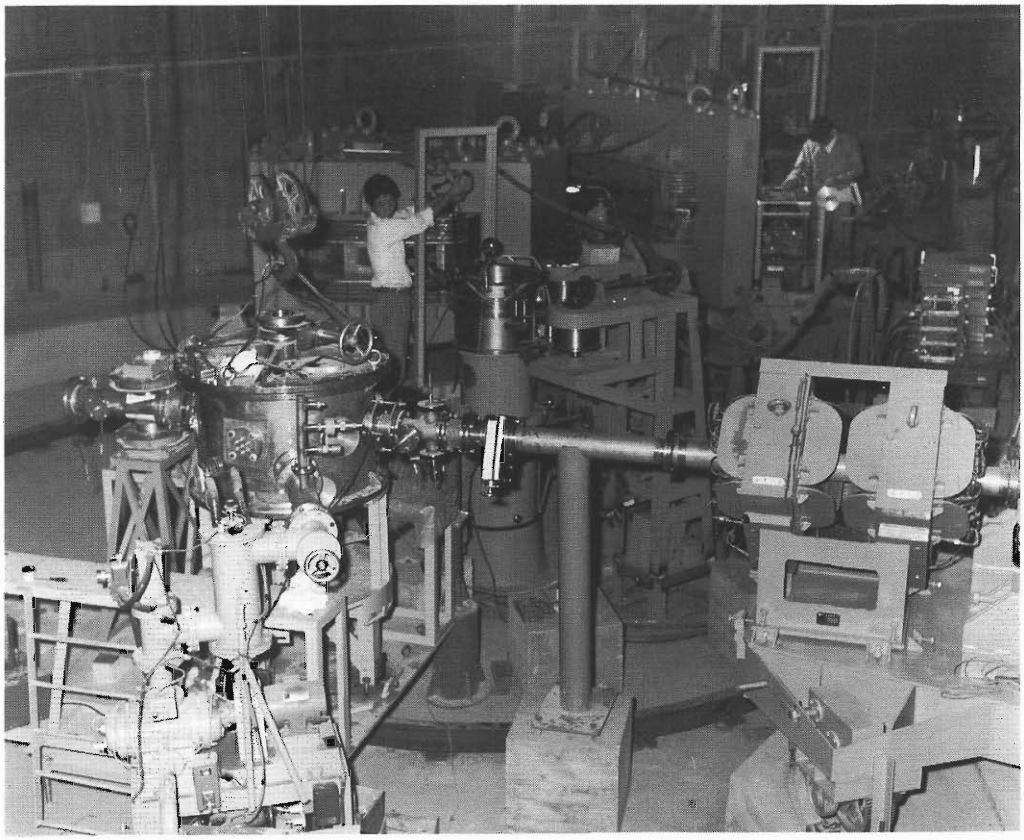

Experimental setup in early days.

Ion-Free beta-ray spectrometer.

100 cm scattering chamber. (1970)

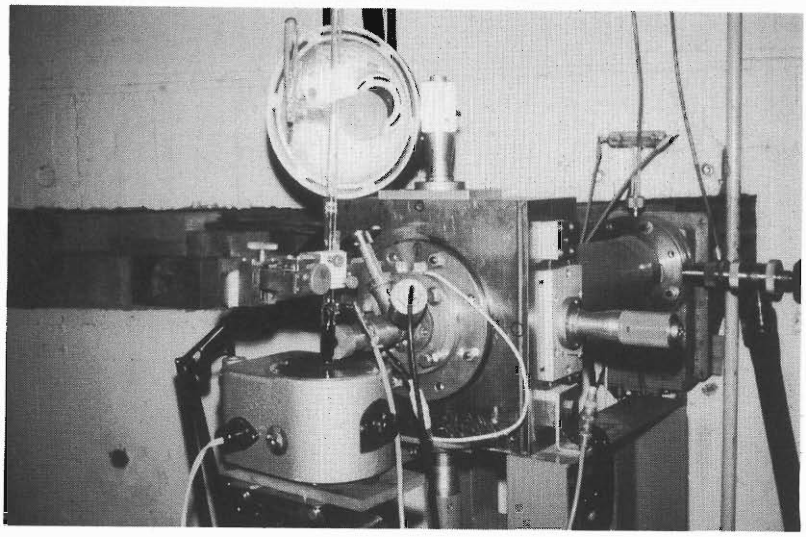

A glass cell, placed at the exit of a beam duct, for irradiation of liquid samples. (1968)

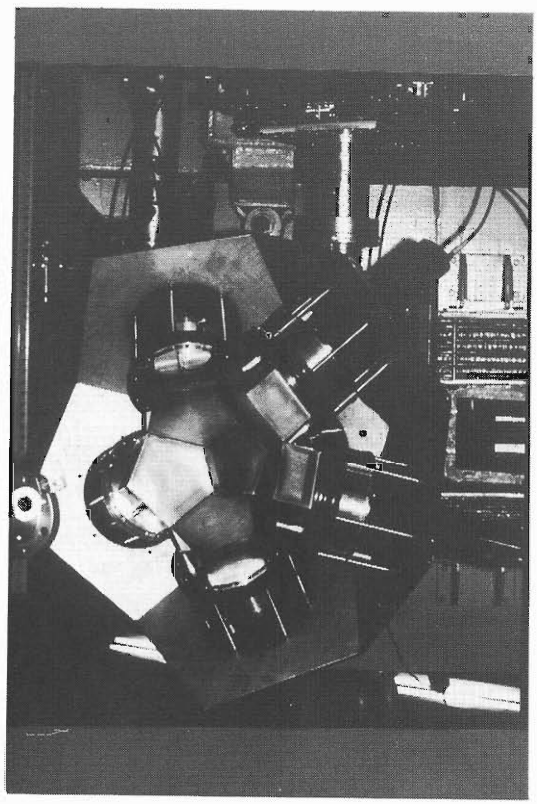

Neutron multiplicity filter composed of six liquid scintillation detectors. (1983)

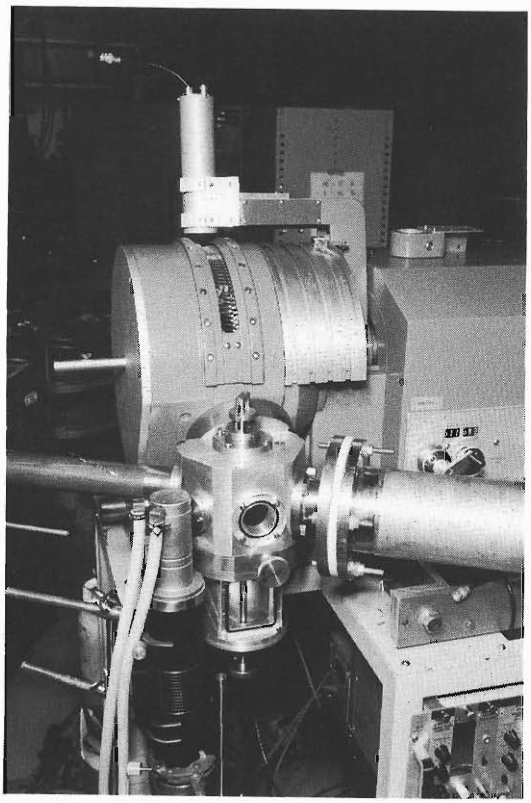

On-line X-ray crystal spectrometer. (1975)

CONTENTS

RIKEN 160 cm Cyclotron
— A Pioneer Facility for Accelerator Science —

1. Historical Overview

The Institute of Physical and Chemical Research, generally known as RIKEN, is originated from the direct ancestor of RIKEN founded in 1917. RIKEN was the first private scientific foundation in Japan and had made great contribution to the scientific and industrial progress in Japan. Emphases were placed on creative and advanced research, on cooperation between research people of different disciplines, and on the harmony among pure science, applied science , and thier industrial applications.

The first cyclotron in Japan was built by Y. Nishina and his collaborators in 1937. It was used for pioneering studies on nuclear physics, nuclear chemistry, and radiation biology. After seven years, in 1944, a large cyclotron with a pole diameter of 60" was also constructed by Nishina. Unfortunately, both of them were destroyed immediately after world war II. In 1952 a small cyclotron was rebuilt by utilizing the magnet of the same type as that of the old cyclotron. This cyclotron was used for RI production and, later , for the study of the functions of lungs in collaboration with Nakano Hospital by using ^{15}O. At that time, RIKEN and the Hammersmith Hospital in London were the only two institutions where ^{15}O was used for medical researches.

In 1958, RIKEN was reorganized to form a nonprofit research institute with the financial support by the Government. First President of new RIKEN, H.Nagaoka (photo in page v) was very enthusiastic for construction of a big cyclotron. In 1961, an advisary committee (IPCR Cyclotron Construction Committee) was formed, composed of prominent specialists in accelerator science. The members are listed in Table 1. The committee recommended the construction of a variable-frequency cyclotron which basically follows the FF cyclotron at the Institute for Nuclear Study (INS), the University of Tokyo. In addition, the committee recommended that the new cyclotron should be designed so as to accelerate heavy ions.

The preliminary design study was carried out in parallel to the discussions in the committee by the staff members of the Radiation Laboratory, headed by F.Yamazaki (photo in page v). To promote the project more efficiently, the Cyclotron Laboratory started in 1962 and H.Kumagai (photo in page v) was invited to be the head of the laboratory. Since then, the Cyclotron Laboratory took a responsibility, together with the Radiation Laboratory, for the cyclotron construction. The project was authorized in 1962 and the construction of the cyclotron started in 1963. At the same time RIKEN invited several cyclotron experts from INS to the IPCR Cyclotron Technical Committee. The members are listed in Table 2.

At the beginning, about ten people joined in the Cyclotron Laboratory and were divided the work in five groups, magnet (headed by S.Motonaga), RF (M. Kodera), vacuum (T.Karasawa), cooling and control (I.Khono), and ion source (I,Khono). Soon after, K.Matsuda (photo in a front page) and others successively jointed in the Laboratory in the

following years. Under the supervision of Kumagai, they worked very hard in the design and R&D work, and the construction of the cyclotron in an atmosphere of freedom.

The cyclotron was ordered to Toshiba Electric Co. Ltd. Total budget was about one billion yen, including model magnets, a test bench for heavy-ion source development, and buildings. RIKEN and Toshiba collaborated with each other very well and solved many technical difficulties. The cyclotron was completed in 1966 and the first beam of 8 MeV protons was obtained on October 4, 1966. Two weeks later, Nagaoka retired as President of RIKEN.

After the machine study and the test experiments carried over four months, the cyclotron was opened to the users in various research fields. From the end of 1969, it was opened also to outside researchers. Matsuda conducted the cooperative use and enthusiastically promoted interdisciplinary studies using the cyclotron. It was our great regret that he suddenly passed away in March 1971 at the age of 49.

The cyclotron was shut down at the end of April 1990 after 23 years of stable operation, having accomplished its glorious mission.

2. The First Heavy-Ion Accelerator in Japan.

The RIKEN 160 cm cyclotron was of a weak focussing type and designed to accelerate ions from hydrogen to neon in a wide range of energies. A plane figure of the cyclotron is shown in Fig. 1 and the cyclotron characteristics are given in Table 3. The operating ranges of the electro-magnet and radio-frequency system were 0.5 to 2.0 tesla and 5.0 to 12.0 MHz, respectively. Figure 2 shows how the cyclotron characteristics were improved chronologically. Soon after the first operation, the working hours of the cyclotron exceeded 5,000 hours per year. The net on-beam hours per year, or beam time, are shown in Fig. 3 over the past 23 years.

The first acceleration of nitrogen ions was succeeded in 1967. This was a distinguished milestone in the history of the heavy-ion science in Japan. Next year, the heavy-ion reaction experiments were performed using nitrogen ions. Figure 4 shows beam times allotted to light and heavy ions during the past 16 years. For 8 years from 1978 to 1985, net beam time of the heavy ions reached 4,000 hours per year and the heavy-ion beam time accounted about 70% of the total beam times. It should be emphasized that enthusiastic development of the heavy-ion sources by Kohno and the ion source group contributed very much to the stable acceleration of heavy ions. These graphs indicate that the efforts of the cyclotron crews for the stable operation were rewarded with good fruits of highly efficient operation of the machine and remarkable research achievements.

In Table 4 are listed the ions , their energy ranges, and extracted currents which are realized with the cyclotron in these 23 years. On the basis of our experiences and acievements in the R&D on accelerator engineering, the construction of new heavy-ion accelerators started in 1974.

3. Achievements in Nuclear Physics

Accelerators have been , in general, developed based on a demand to pursue nuclear and particle physics further and further. In other words, nuclear and particle physics provides strong motivation for the improvement of the accelerator performance. Collaboration between accelerator people and nuclear physicists from both inside and outside of RIKEN worked well to improve the cyclotron, so that many excellent results were obtained in nuclear study. Some of them shall be mentioned in the following.

Extensive measurements of nuclear magnetic moments made by T.Yamazaki (Univ. of Tokyo) and his collaborators revealed for the first time the mesonic effects in the nuclear structure. Light-ion reactions (direct reactions) with ^{3}He particles were also studied extensively by the group headed by Matsuda. In connection with direct reactions, a polarized ion source was developed by the group of Motonaga. This source was installed at the INS cyclotron.

The success in the heavy-ion acceleration encourage the study of nuclear physics. The Cyclotron Laboratory headed, by H.Kamitsubo, extensively carried out studies of heavy-ion reactions and obtained remarkable achievements. Alpha decay from highly excited states with very short lifetimes in translead nuclides was measured by Nomura and his co-workers. His measurement was then extended to the α particles from the preequilibrium nuclear states. He found that a hot spot is formed in the nucleus immediately after the heavy-ion collsions and determined a decay time of the hot spot. Inamura and others studied massive transfer reactions induced by ^{14}N and found that a "window" of transferred angular momentum can be determined from α-γ coincidence measurements. He also measured together with Kasagi (Tokyo Inst. Tech.) neutron multiplicity in heavy-ion fusion reactions. These techniques are of great use for in-beam spectroscopic studies, especially in selecting reaction channels.

Heavy-ion reactions in the energy range of 50 to 100 MeV were thouroughly studied with the cyclotron. Systematic behavior of the optimum Q-values in multi-nucleon transfer reactions were measured and analyzed by Kamitsubo and his collaborators. Angular momentum transfer to residual nuclei was determined for the first time by Ishihara and his colleagues by measuring the multiplicity of gamma rays in strongly damped collisions. This work gave a strong impact to the later studies of heavy-ion reactions.

The most remarkable results in this field were obtained from comprehensive studies of the polarization phenomena in heavy-ion reactions. Sugimoto and his co-workers (Osaka Univ.) together with the RIKEN group measured for the first time the polarization of the emitted particles from ^{14}N induced reactions. Ishihara and his group succeedingly obtained the polarization of residual nuclei from the measurement of circularly polarized gamma rays. Particle-particle correlation measurements can also provide valuable imformation on the reaction mechanism; Ishihara and his collaborators beautifully demonstrated final state interactions through the α-α correlation measurement for ^{14}N induced reactions and got time information concerning the formation and decay of intermediate states.

Nuclear physics on the cyclotron was terminated when a new separated-sector cyclotron

with K=540 MeV (Ring Cyclotron) came close to its completion. The first beam from the Ring Cyclotron was successfully extracted in December 1986.

4. Pioneer Facility for Accelerator Science in Japan

As mentioned above, accelerators were developed mainly for the study of nuclear and particle physics. However, even at the very beginning of the accelerator age, chemical and biological studies using radioactive isotopes attracted much attention of scientists in these research fields. With the progress in accelerator technology, it has been gradually recognized that the accelerator is a very useful tool for the studies in a wide range of disciplines. Here we give a general name of accelerator science to these disciplines.

When a routine operation of the RIKEN 160 cm cyclotron started, almost all the accelerators in Japan had been monopolized by nuclear and particle physicists and there was no room for researchers in other disciplines. The RIKEN 160 cm cyclotron , on the other hand, was opened for users of various resaerch fields from the beginning. At the meeting of the Cyclotron Administration Committee, Kumagai, as Chairman of the Committee, declared that one third of the total beam time should be reserved for RI production and radiochemistry study, and other one third for the studies of condenced matter and biological materials. The remaining one third whould be used for nuclear study. This " one third rule" has been the principal guide line in the use of accelerators at RIKEN.

Actual beam times allotted annually to the different disciplines are shown in Fig. 5, in which curve I indicates the beam time for nuclear physics, curve II for atomic and solid state physics, and curve III for radiochemistry, radiation chemistry, and radiation biology. The beam time for atomic and solid state physics increased rapidly in 1975, due to the start of the studies of atomic physics. In the following is given a brief sketch of activities in these research fields.

4-1 New Approaches to the Study of Atoms and Materials

Energetic heavy ions offered new techniques for studies of ion-atom collision processes. Multiple inner-shell ionization induced by heavy-ions was extensively studied by Y.Awaya and her group by measuring the X-ray spectra of excited target atoms with Si(Li) detectors and crystal spectrometers. Effect of the chemical states was also observed in the X-ray spectrum. Radiative electron capture processes by energetic, highly-charged heavy ions were studied. Secondary electrons were measured to study the surfaces of materials.

The crystalline structure of condensed matter is often thrown into disorder by impurity atoms and external factors such as mechanical, thermal perturbation, and so on. E.Yagi and his collaborators investigated the defects in metals by applying channeling and Rutherford back- scattering techniques with the cyclotron. The exact position of impurity atoms was clearly determined from proton channeling experiments.

High temperature is indispensable in the operation of a fast breeder or a controlled thermo-

nuclear reactor. However, the damage of the inside core and wall materials due to irradiation of fast neutrons precludes such operation. The simulation experiments for embrittlements of materials by helium were carried out by H.Sakairi and the Metal Physics Laboratory for the first time in Japan, using α-particles obtained from the cyclotron.

4-2 New Research Area by RI Production and Activation Analysis

Positron Emission Tomography (PET), or nuclear medicine, is a novel technique for canser diagnosis and for the study of brain functions. In Japan a project team was formed in 1970 under the support of Grant-in-Aid for Scientific Research of the Ministry of Education, Science, and Culture. Several researchers of RIKEN, including T.Nozaki , joined in the team and took a responsibility for providing radio-isotopes to the medical people. At the beginning ^{18}F was produced extensively and then isotopes such as ^{43}K, ^{52}Fe,^{67}Ga, ^{73}Se,^{77}Br, ^{87}Y, and ^{203}Pb were provided to medical people. Nozaki enthusiastically worked in developments of the most efficient method for synthesis of medical-use isotopes and their labeled compounds. Later he engaged in the synthesis of short-lived isotopes, ^{11}C,^{13}N, and ^{15}O. In connection with this, it should be pointed out that a compact cyclotron specialized for RI production was developed by T.Karasawa at RIKEN. In this sense, the RIKEN 160cm cyclotron played a pioneering role in the development of nuclear medicine in Japan.

Nozaki and his collaborators developed a method to determine absolute amounts of light element contaminations such as C,N,and O in high-purity materials, mainly Si and GaAs single crystals, by radio-activation analysis using light ion (p and ^{3}He) beams from the cyclotron. They succeeded in determining the phase diagrams of C,N, and O in Si crystals. These data, together with other important data such as solubility and diffusion constants, are the most reliable ones.

H.Sekizawa and the members of the Magnetic Material Laboratory carried out Mossbauer spectroscopy experiments on magnetic substances containing ^{61}Ni, using the decay of ^{61}Cu, the life-time of which is very short for this type of experiments. Mossbauer spectroscopy of ^{119}Sn using ^{119}Sb as a source nuclide was applied to the study of the chemical structure of a very small quantity of elements contained in solids and on the surfaces by F.Ambe and his collaborators. The perturbed angular correlation of γ-rays was studied by the radiochemistry group using ^{99}Rh and ^{111}Cd.

Positron annihiration experiments were also carried out by N.Shiotani using a short-lived isotope of ^{90}Nb to study the Fermi-surface structure in metals.

4-3 Radiation Chemistry and Biology, Basic Data for Radiation Therapy

Kinetic energy transfer takes place in a localized space along the path of an energetic ion in the matter. This energy transfer (LET) generates transient chemical species such as electronically excited molecules and ions in ground or excited states, which species in high local concentration undergo reactions different from those by low-LET radiations (γ-rays and

electrons). M.Imamura and his collaborators of the Radiation Chemistry Laboratory studied these transient phenomena by measuring absorption and emission spectra, yields of final products, and so on.

The Radiation Biology Laboratory headed by A.Matsuyama conducted the studies on molecular and cellular mechanisms of radiation lesions and their repair by using heavy-ion beams from the cyclotron. Effects of radiation on bacteriophages, living cells and cellular constituents such as DNA or protein were investigated. Heavy ions show very high relative biological effectiveness (RBE) and induce structual changes of cell constituents, which were observed as abnormal metabolism, cell inactivation, or mutation. Collaboration with medical people were conducted by I.Kaneko.

4-4 Collaborative R&D Work with Industry

In the past 23 years many groups came from industry for irradiation tests. The calibration of space radiation monitors was carried out by several groups for a series of satellites. Studies of irradiation effects on a teflon plate coated with silver, a cover glass for a solar cell, and solid fuels for satellites and rockets were carried out by bombarding protons and α particles. Single event upset and latch-up in microprocessors due to heavy cosmic particles were simulated by bombardment of ^{14}N and ^{20}Ne on LSI.

The effect of fast neutron irradiation on insulator materials for electric cable was studied by bombarding them with fast neutrons produced by bombarding a thick Be target with 20MeV deuterons. Proton irradiation was also studied to compare with the effects of neutron irradiation .

The switching characteristics of a thyristor is expected to be improved by proton bombardment. Research groups from industry for R&D on this subjent collaborated with I.Khono and the cyclotron crew .

Outside users from industry are listed in page 27 together with their subjects.

5. Collaboration with other organizations

The cyclotron was also open for use of research groups from universities and national laboratories. From the beginning, groups from the Univ. of Tokyo, Kyoto Univ., Osaka Univ., Kyushu Univ., Tokyo Inst. Tech., Tokyo Metrop. Univ., and others carried out their own experiments or jointly with our experimental groups. In addition to them, research people from Natl. Res. Inst. for Metals, Natl. Inst. for Radiological Sci., Jap. Atomic Energy Res. Inst., and others shared machine times of the cyclotron. We also provided short-lived RI and irradiation services for outside users.

A number of graduate students carried out experiments at the cyclotron for their master or doctor theses. In the past 20 years, 16 students finished their master theses by using the cyclotron and 14 students got doctorates with their work at the cyclotron. They stayed at RIKEN for several years to prepare their theses. It should be pointed out that these figures do

not include the undergraduate students who did experiments at the cyclotron as a part of their theses. In addition to them, 14 staff members also got doctorates with their research works at the cyclotron. The names of graduate students and the subjects of doctor theses are listed in page 23—25.

International collaborations were also flourishing. The study of polarization phenomena in heavy-ion collisions with the Cyclotron Institute of the Texas A&M university. Many visitors from foreign countries came to RIKEN anf joined various experiments at the cyclotron. Several international conferences and symposia were organized by the RIKEN accelerator groups. Their titles are listed in page 35.

6. A Great Stride to the New Heavy Ion Research Facility

In order to promote the cooperative research activities in a wide range of disciplines at the cyclotron, RIKEN started the construction of a next-generation heavy-ion accelerator complex in 1974. A variable-frequency heavy-ion linear accelerator (RILAC) was completed in 1980 and has been in routine operation. A separated-sector cyclotron with K=540 MeV (RIKEN Ring Cyclotron) was then completed in 1986 and has been providing heavy ion beams in the energy range of several tens of million electron volts per nucleon (MeV/n) in combination with the RILAC. A new injector cyclotron, an AVF cyclotron with K=70 MeV, was completed in March 1989 and in July, the maximum energy of 135 MeV/n was achieved for ^{14}N. RIKEN Ring Cyclotron is the cyclotron which can accelerate heavy ions at the highest energy in the world. It can also accelerate light ions such as deuterons and helium 3 at the highest energy in the world. This new accelerator complex succeeds the RIKEN 160 cm cyclotron and will greatly promote the resaerch activities in accelerator science.

Hiromichi KAMITSUBO
Head of Cyclotron Laboratory
(1971—Present)

Table 1. IPCR Cyclotron Construction Committee. (1961)

Chairman	Hiroo KUMAGAI	accelerator
	Toshizo TITANI	analytical chemistry
	Ryukiti R. HASIGUTI	metal physics
	Seishi KIKUCHI	nuclear physics
	Itaru NONAKA	nuclear physics
	Nobufusa SAITO	radiochemistry
	Shoji SETO	material engineering
	Kenichi SHINOHARA	radiation chemistry
	Yoshio SUGE	electric engineering
	Yoshio TSUGE	civil engineering
	Fumio YAMASAKI	radiation physics

Table 2. IPCR Cyclotron Technical Committee. (1963)

Chairman	Kazuhisa MATSUDA
	Jumpei SANADA
	Yoshio SAJI
	Akira BABA
	Izuo HAYASHI

Table 3. Cyclotron characteristics.

Acceleration system	
Number of dees	2
Dee width	180 deg.
Beam aperture	5 cm
Radio frequency	6 to 12.5 MHz
Tuned by	Movable short plus movable panels
Gain max.	400 kV/turn
Dee-gnd. max.	100 kV
RF power input max.	150 kW
Magnet	
Type of magnet	Weak focusing type
Pole tip dia.	162 cm
Extraction radius	73 cm
Gap between pole tips	26 cm
Field at max. excitation	2.0 Wb/m^2
Circular triming coils	4 pairs
Weights Fe (Cu)	310 (20) tons
Magnet excitation	6×10^5 amp-turns
Power max.	400 kW
Ion source	
For light ions (H, He)	Livingston type
For heavy ions (Gas)	Electron bombarded hot cathode PIG type
For heavy ions (Solid)	Same with sputtering electrode

Table 4. Particles, energy ranges, and particle yields.

Particle	Energy (MeV)	Extracted beam current (μA)
p	5–17	30
d	8–26	30
$^{3}He^{++}$	12–50	30
$^{4}He^{++}$	16–52	30
$^{6}Li^{2+}$	25–48	0.2
$^{7}Li^{2+}$	29–48	2.0
$^{7}Li^{3+}$	29–75	0.05
$^{9}Be^{3+}$	45	0.8
$^{10}B^{3+}$	60	0.3
$^{11}B^{3+}$	66	1.3
$^{12}C^{4+}$	55–100	3.0
$^{14}N^{4+}$	65–100	3.0
$^{14}N^{5+}$	60–125	1.0 (3.0)[a)]
$^{16}O^{5+}$	65–125	1.0 (3.0)[a)]
$^{19}F^{5+}$	80–130	0.3
$^{19}F^{6+}$	80–150	0.1
$^{20}Ne^{6+}$	82–160	0.3[a)]

a) Pulsed operation.

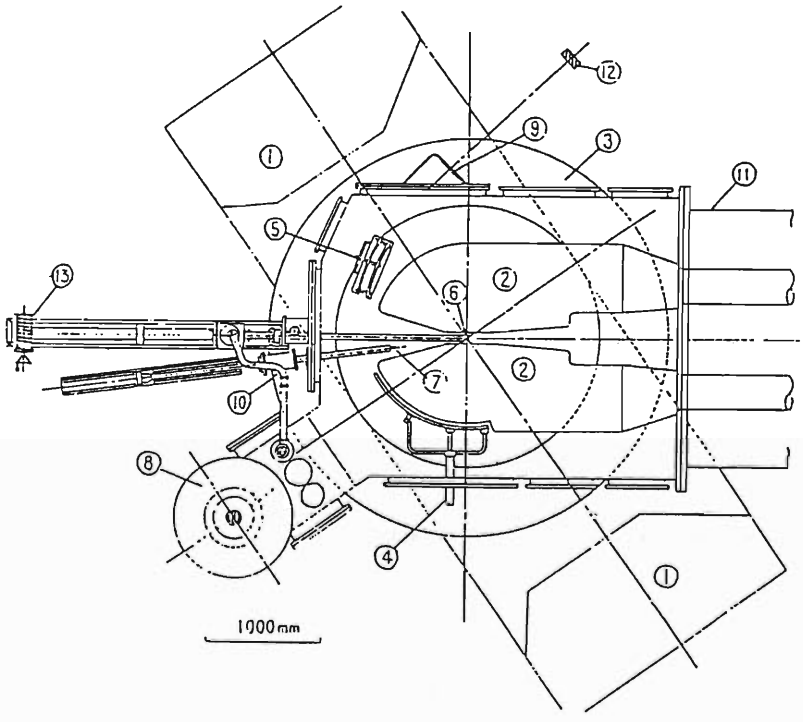

Fig. 1. Schematic view of the accelerating chamber arrangement.
1, Side yoke; 2, Dees; 3, Coil tank; 4, *RF*-deflector; 5, Beam focusing magnetic channel; 6, Ion source; 7, Beam probe; 8, 32″ oil diffusion pump; 9, Beam exit flange; 10, Exhaust pipe for ion source; 11, Oscillator tank; 12, Gate drop probe; 13, Winch

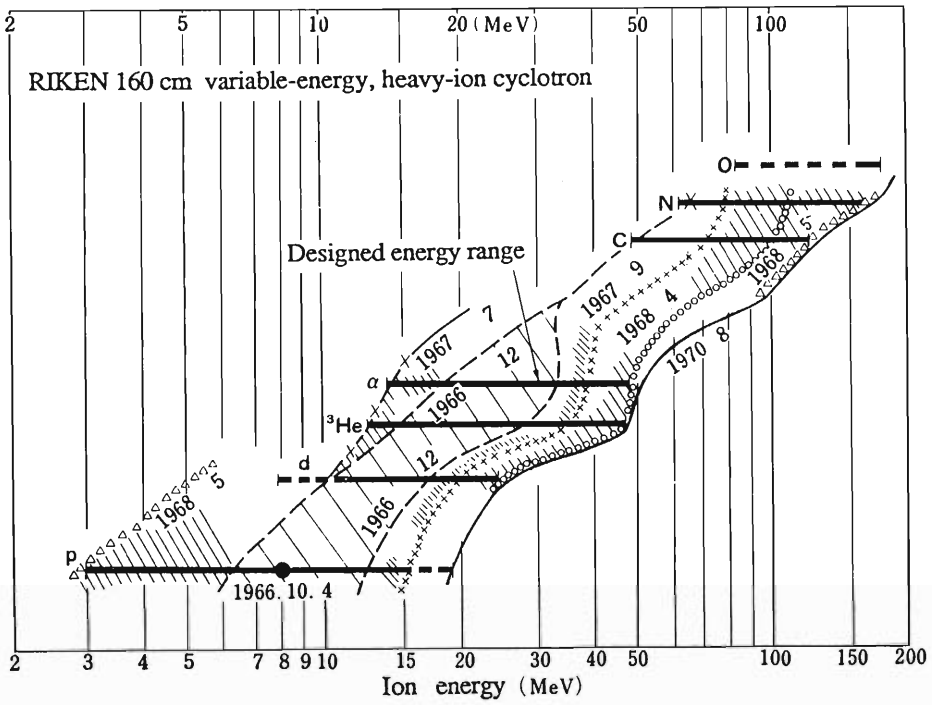

Fig. 2 Record of the characteristics of the RIKEN 160 cm cyclotron.

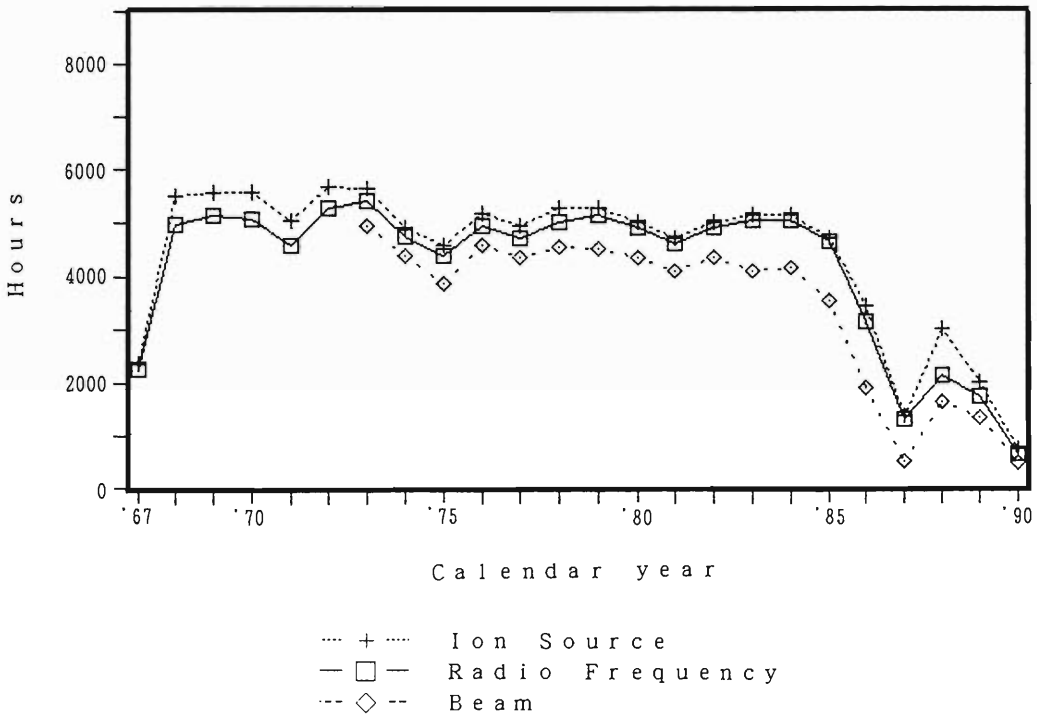

Fig. 3. Net beam time, and net operation times of ion source and radio frequency during the last 23 years.

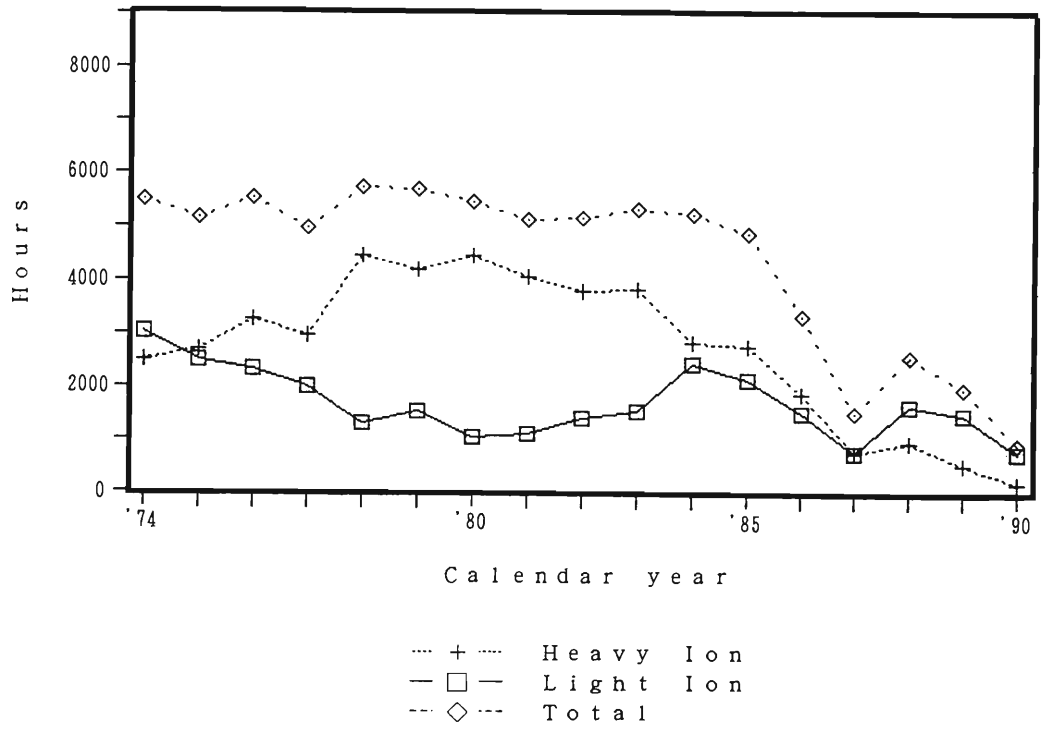

Fig. 4. Beam times allotted to heavy and light ions during the last 16 years.

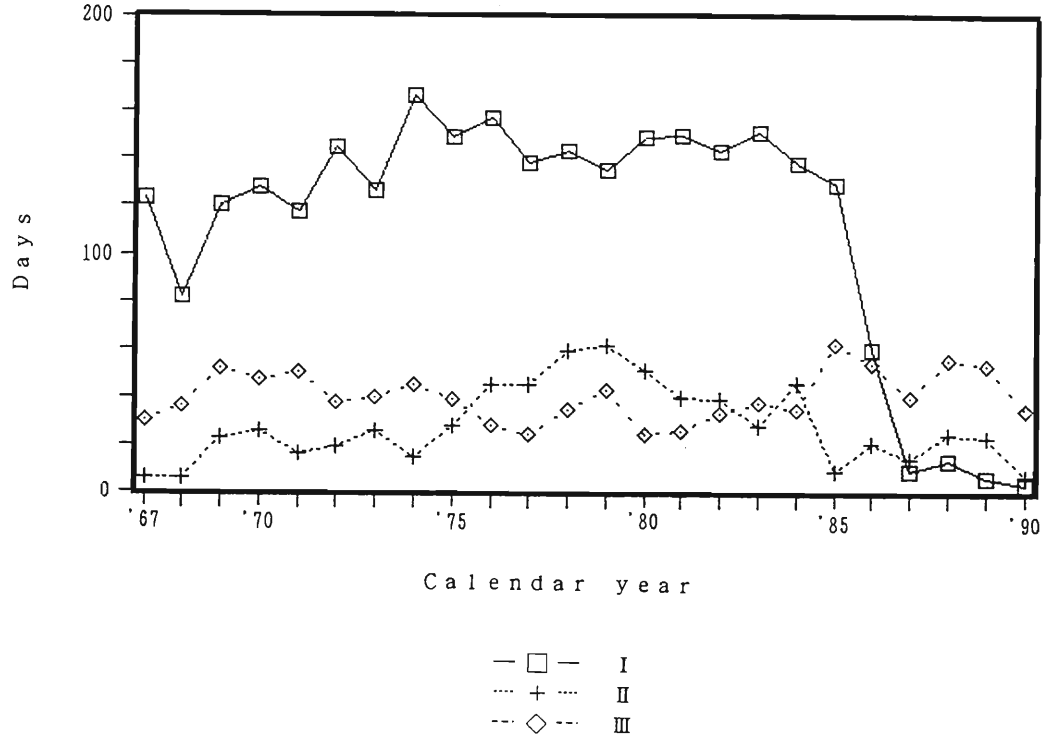

Fig. 5. Research activities on the 160 cm cyclotron during the last 23 years. Total beam times per year are plotted against the calendar year for major disciplines. (I), Nuclear physics; (II), Atomic and solid-state physics; and (III), Radiochemistry, radiation chemistry, and radiation biology.

List of First Personnel Associated with the 160 cm Cyclotron.(1967)

the IPCR Cyclotron Construction Committee

熊谷寛夫	Hiroo KUMAGAI (chairman)
千谷利三	Toshizo TITANI
橋口隆吉	Ryukiti R.·HASIGUTI
菊池正士	Seishi KIKUCHI
野中到	Itaru NONAKA
斉藤信房	Nobufusa SAITO
瀬藤象二	Shoji SETO
篠原健一	Kenichi SHINOHARA
菅義夫	Yoshio SUGE
柘植芳男	Yoshio TSUGE
山崎文男	Fumio YAMASAKI

the IPCR Cyclotron Adminstration Committee

山崎文男	Fumio YAMASAKI (chairman)
橋口隆吉	Ryukiti R. HASIGUTI
熊谷寛夫	Hiroo KUMAGAI
今村昌	Masashi IMAMURA
唐沢孝	Takashi KARASAWA
松田一久	Kazuhisa MATSUDA
松山晃	Akira MATSUYAMA
斉藤信房	Nobufusa SAITO
杉本光男	Mitsuo SUGIMOTO
田中稜	Yutaka G. TANAKA

Managers of Users Group

浜田達二	Tatsuji HAMADA
小寺正俊	Masatoshi ODERA

the IPCR Cyclotron Constructing Personnel

Leader

熊谷寛夫 Hiroo KUMAGAI

Magnet

元永昭七 Shoshichi MOTONAGA, 唐沢孝 Takashi KARASAWA
逸見政武 Masatake HEMMI, 宮沢佳敏 Yoshitoshi MIYAZAWA
中西紀喜 Noriyoshi NAKANISHI

Oscillator

小寺正俊 Masatoshi ODERA, 千葉好明 Yoshiaki CHIBA
藤沢高志 Takashi FUJISAWA, 寺島為 Osamu TERASHIMA

Vacuum System

唐沢孝 Takashi KARASAWA, 宮沢佳敏 Yoshitoshi MIYAZAWA
戸沼正雄 Tadao TONUMA 吉田喜作 Kisaku YOSHIDA

Ion Source

河野功 Isao KOHNO, 中島諄二 Shunji NAKAJIMA
戸沼正雄 Tadao TONUMA

Control

河野功 Isao KOHNO, 井上敏彦 Toshihiko INOUE
竹田繁 Shigeru TAKEDA

Beam Transport

上坪宏道 Hiromichi KAMITSUBO, 逸見政武 Masatake HEMMI
松田一久 Kazuhisa MATSUDA, 元永昭七 Shoshichi MOTONAGA
中西紀喜 Noriyoshi NAKANISHI

RI System

浜田達二 Tatsuji HAMADA, 橋爪朗 Akira HASHIZUME
野崎正 Tadashi NOZAKI, 島村旻 Akira SHIMAMURA

General Management

浜田達二 Tatsuji HAMADA, 松田一久 Kazuhisa MATSUDA

the IPCR Cyclotron Operating Personnel

Management

唐沢孝 Takashi KARASAWA, 小寺正俊 Masatoshi ODERA
元永昭七 Shoshichi MOTONAGA, 河野功 Isao KOHNO
宮沢佳敏 Yoshitoshi MIYAZAWA

Operator

藤田新 Shin FUJITA, 池上九三男 Kumio IKEGAMI
中島尚雄 Hisao NAKAJIMA, 荻原清 Kiyoshi OGIWARA
大沢信道 Nobumichi OSAWA, 寺島為 Osamu TERASHIMA
吉田喜作 Kisaku YOSHIDA

Scientific and Engineering Personnel

Cyclotron Lab.

熊谷寛夫	Hiroo KUMAGAI,	千葉好明	Yoshiaki CHIBA
藤沢高志	Takashi FUJISAWA,	藤田二郎	Jiro FUJITA
逸見政武	Masatake HEMMI,	井上敏彦	Toshihiko INOUE
上坪宏道	Hiromichi KAMITSUBO.	唐沢孝	Takashi KARASAWA
河野功	Isao KOHNO,	松田一久	Kazuhisa MATSUDA
宮沢佳敏	Yoshitoshi MIYAZAWA,	元永昭七	Shoshichi MOTONAGA
中島諄二	Shunji NAKAJIMA,	中西紀喜	Noriyoshi NAKANISHI
小寺正俊	Masatoshi ODERA,	島村昇	Akira SHIMAMURA
竹谷繁	Shigeru TAKEDA,	戸沼正雄	Tadao TONUMA
和田雄	Takeshi WADA		

Radiation Lab.

山崎文男	Fumio YAMASAKI,	粟屋容子	Yohko AWAYA
浜田達二	Tatsuji HAMADA,	橋爪朗	Akira HASHIZUME
稲村卓	Takashi INAMURA,	加藤武雄	Takeo KATO
岡野真治	Masaharu OKANO,	太田光子	Mitsuko OTA
天道芳彦	Yoshihiko TENDOW		

Analytical Chemistry Lab.

斉藤信房	Nobufusa SAITO,	荒谷美智	Michi ARATANI
野崎正	Tadashi NOZAKI		

Nuclear Chemistry Lab.

斉藤信房	Nobufusa SAITO,	安部文敏	Fumitoshi AMBE
安部静子	Shizuko AMBE,	稲荷田万里子	Mariko INARIDA

Geochemistry Lab.

島誠	Makoto SHIMA,	天野貞代	Sadayo AMANO
岡田昭彦	Akihiko OKADA		

Biochemistry I Lab.

田中穣	Yutaka G. TANAKA

Radiobiology Lab.

松山晃	Akira MATSUYAMA,	服部行彦	Yukihiko HATTORI
北山滋	Shigeru KITAYAMA		

Radiation Chemistry Lab.

今村昌	Masashi IMAMURA,	松井正夫	Masao MATSUI
中野和城	Kazushiro NAKANO,	関博之	Hiroshi SEKI

Microbiology Lab.

賀田恒夫　Tsuneo KADA

Metal Physics Lab.

橋口隆吉　Ryukiti HASIGUTI,
坂入英雄　Hideo SAKAIRI,
岩崎邦彦　Kunihiko IWASAKI
塩谷亘弘　Nobuhiro SHIOTANI

Magnetic Materials Lab.

杉本光男　Mitsuo SUGIMOTO,
岡田卓也　Takuya OKADA

Precision Engineering Lab.

水野万亀雄　Makio MIZUNO

Plastic Working Lab.

宮内邦雄　Kunio MIYAUCHI

Radiation Monitors

甲田陸男　Kugao KOODA,
坂本一郎　Ichiro SAKAMOTO

Editors of the Progress Report

松田一久　Kazuhisa MATSUDA,
田中穣　Yutaka G. TANAKA
野崎正　Tadashi NOZAKI

List of Personnel when Linac Laboratory was Born from Cyclotron Laboratory. (1975)

Members of the Board

HAGIHARA Hitosi 萩原 仁 (Chairman)
KAMITSUBO Hiromichi 上坪宏道
NOZAKI Tadashi 野崎 正
HAMADA Tatsuji 浜田達二
NAKANE Ryohei 中根良平
ODERA Masatoshi 小寺正俊

Users Committee

HAMADA Tatsuji 浜田達二 (Chairman)
KAMITSUBO Hiromichi 上坪宏道
MATSUYAMA Akira 松山 晃
ODERA Masatoshi 小寺正俊
SEKIZAWA Hisashi 関沢 尚
IMAMURA Masashi 今村 昌
KOHNO Isao 河野 功
NOZAKI Tadashi 野崎 正
SAKAIRI Hideo 坂入英雄

Operation and Machine Maintenance Group

FUJITA Shin 藤田 新
KAGEYAMA Tadashi 影山 正
KOHNO Isao 河野 功
OGIWARA Kiyoshi 荻原 清
IKEGAMI Kumio 池上九三男
KOHARA Shigeo 小原重夫
NAKAJIMA Hisao 中嶋尚雄
TAKEBE Hideki 武部英樹

Scientific and Engineering Personnel

Cyclotron Laboratory

FUJISAWA Takashi 藤沢高志
INAMURA Takashi 稲村 卓
KAMITSUBO Hiromichi 上坪宏道
KOHNO Isao 河野 功
MOTONAGA Shoshichi 元永昭七
NAKANISHI Noriyoshi 中西紀喜
SUZUKI Toshio 鈴木敏男
YAMAJI Shuhei 山路修平**
FUJITA Jiro 藤田二郎
ISHIHARA Masayasu 石原正泰
KARASAWA Takashi 唐沢 孝
MATSUURA Toshihiko 松浦俊彦
NAKAJIMA Shunji 中島諄二
NOMURA Toru 野村 亨*
WADA Takeshi 和田 雄

Linac Laboratory (Electronics Laboratory)

CHIBA Yoshiaki 千葉好明
INOUE Toshihiko 井上敏彦
ODERA Masatoshi 小寺正俊
TONUMA Tadao 戸沼正雄
HEMMI Masatake 逸見政武
MIYAZAWA Yoshitoshi 宮沢佳敏
SHIMAMURA Akira 島村 晏
YOSHIDA Fusako 吉田房子

* On leave of absence to : DPHNBE, CEN Saclay, B.P. 2, 91190 Gif/Yvette, France
** On leave of absence to : Institut für Theoretische Physik der Universität Frankfurt/M 6 Frankfurt/M.I, Robert-Mayer-Strasse 8-10, West Germany.

Radiation Laboratory

AWAYA Yohko 粟屋容子
HASHIZUME Akira 橋爪 朗
KATOU Takeo 加藤武雄
KUMAGAI Hidekazu 熊谷秀和
TAKAHASHI Tan 高橋 旦
HAMADA Tatsuji 浜田達二
IZUMO Koichi 出雲光一
KONNO Satoshi 金野 智
OKANO Masaharu 岡野真治
TENDOW Yoshihiko 天道芳彦

Nuclear Analytical Chemistry Laboratory

AMBE Fumitoshi 安部文敏
ARATANI Michi 荒谷美智
IWAMOTO Masako 岩本正子
SAITO Nobufusa 斎藤信房
AMBE Shizuko 安部静子
ITO Yoshiko 伊東芳子
NOZAKI Tadashi 野崎 正

Synthetic Organic Chemistry Laboratory

OSAWA Tomihiko 大沢富彦

Radiobiology Laboratory

KITAYAMA Shigeru 北山 滋
YATAGAI Fumio 谷田貝文夫
MATSUYAMA Akira 松山 晃

Radiation Chemistry Laboratory

IMAMURA Masashi 今村 昌
MATSUI Masao 松井正夫
KIMURA Kazuie 木村一宇

Metal Physics Laboratory

KOYAMA Akio 小山昭雄
SHIOTANI Nobuhiro 塩谷亘弘
SAKAIRI Hideo 坂入英雄
YAGI Eiichi 八木栄一

Magnetic Materials Laboratory

OKADA Takuya 岡田卓也
SEKIZAWA Hisashi 関沢 尚

Work Shop

TAKESHITA Isao 竹下勇夫
YOKOYAMA Ichiro 横山一郎

Radiation Monitoring and Safety Office

IGARASHI Kazui 五十嵐一戌
SAKAMOTO Ichiro 坂本一郎
KODA Kugao 甲田陸男
USUBA Isao 薄葉 勲

List of Personnel, as of April 1990

Director of RIKEN Accelerator Ressearch Facility

KAMITSUBO Hiromichi 上坪宏道

Steering Committee

AMBE Fumitoshi 安部文敏
CHIBA Yoshiaki 千葉好明
HASHIZUME Akira 橋爪 朗
ISHIHARA Masayasu 石原正泰*
KATSUMATA Koichi 勝又紘一
KOHNO Isao 河野 功
MIYAZAWA Yoshitoshi 宮沢佳敏
TAKAMI Michio 高見道生
YANO Yasushige 矢野安重
AWAYA Yohko 粟屋容子
HANAOKA Fumio 花岡文雄
INAMURA Takashi 稲村 卓
KAMITSUBO Hiromichi 上坪宏道
KIRA Akira 吉良 爽
MATSUOKA Masaru 松岡 勝
NAGAMINE Kanetada 永嶺謙忠
TANIHATA Isao 谷畑勇夫

* Chairman

Scientific and Engineering Personnel

Cosmic Radiation Laboratory

IMAI Takashi 今井 喬
KOHNO Tsuyoshi 河野 毅

Cyclotron Laboratory

BE Suck Hee 裵 碩喜
FUJISAWA Takashi 藤沢高志
FUJITA Shin 藤田 新
HARA Masahiro 原 雅弘
INAMURA Takashi 稲村 卓
KAMITSUBO Hiromichi 上坪宏道
MORITA Kosuke 森田浩介
NAGASE Makoto 長瀬 誠
NAKAJIMA Shunji 中島諄二
OGIWARA Kiyoshi 荻原 清
SASAKI Shigeki 佐々木茂樹
SOUTOME Kouichi 早乙女光一
WADA Takeshi 和田 雄
YANO Yasushige 矢野安重
DATE Shin 伊達 伸
FUJITA Jiro 藤田二郎
GOTO Akira 後藤 彰
IKEGAMI Kumio 池上九三男
KAGEYAMA Tadashi 影山 正
KOHARA Shigeo 小原重夫
NAGAOKA Ryutaro 長岡隆太郎
NAKAGAWA Takahide 中川孝秀
NAKANISHI Noriyoshi 中西紀喜
SAITO Motozo 斉藤始三
SHIKATA Takashi 四方隆史
TAKEBE Hideki 武部英樹
YAMAJI Shuhei 山路修平
YOKOYAMA Ichiro 横山一郎

Linear Accelerator Laboratory

CHIBA Toshiya 千葉利哉
FUJIMAKI Masaki 藤巻正樹
KASE Masayuki 加瀬昌之
CHIBA Yoshiaki 千葉好明
HEMMI Masatake 逸見政武
KUBO Toshiyuki 久保敏幸

KUMAGAI Hidekazu 熊谷秀和
SUZUKI Takeshi 鈴木 健
TONUMA Tadao 戸沼正雄
YANOKURA Minoru 矢野倉 実
MIYAZAWA Yoshitoshi 宮沢佳敏
TANIHATA Isao 谷畑勇夫
WADA Takahiro 和田隆宏
YOSIDA Koichi 吉田光一

Radiation Laboratory

GONO Yasuyuki 郷農靖之
ICHIHARA Takashi 市原 卓
IZUMO Koichi 出雲光一
NOMURA Izumi 野村和泉
TENDO Yoshihiko 天道芳彦
HASHIZUME Akira 橋爪 朗
ISHIHARA Masayasu 石原正泰
KONNO Satoshi 金野 智
TAKAHASHI Tan 高橋 旦

Atomic Processes Laboratory

ANDO Kozo 安藤剛三
FUKUDA Hiroshi 福田 宏
KAMBARA Tadashi 神原 正
NISHIDA Masami 西田雅美
AWAYA Yohko 粟屋容子
HARSTON Michael
KANAI Yasuyuki 金井保之
SHIMAMURA Isao 島村 勲

Metal Physics Laboratory

ISHIDA Katsuhiko 石田勝彦
MATSUZAKI Teiichiro 松崎禎市郎
SHIOTANI Nobuhiro 塩谷亘弘
KADONO Ryousuke 門野良典
KOYAMA Akio 小山昭雄
NAGAMINE Kanetada 永嶺謙忠
YAGI Eiichi 八木栄一
MATSUSHITA Akira 松下 昭

Magnetic Materials Laboratory

OKADA Takuya 岡田卓也
SAKAI Nobuhiko 坂井信彦

Plasma Physics Laboratory

OYAMA Hitoshi 大山 等
YANO Katsuki 矢野勝喜

Inorganic Chemical Physics Laboratory

AMBE Shizuko 安部静子
MAEDA Kuniko 前田邦子
TAKAMI Michio 高見道生
KAWAI Jun 河合 潤
SASA Yoshihiko 佐々嘉彦

Radiochemistry Laboratory

AMBE Fumitoshi 安部文敏
ITOH Yoshiko 伊東芳子
KOBAYASHI Yoshio 小林義男
ARATANI Michi 荒谷美智
IWAMOTO Masako 岩本正子
OHKUBO Yoshitaka 大久保嘉高

Chemical Dynamics Laboratory

KIMURA Kazuie 木村一宇
KIRA Akira 吉良 爽

Radiation Biology Laboratory

HANAOKA Fumio 花岡文雄
KITAYAMA Shigeru 北山 滋
NAKANO Kazushiro 中野和城
YATAGAI Fumio 谷田貝文夫

Safety Control Affairs Office

KAGAYA Satoru 加賀屋 悟
KATOU Hiroko 加藤博子
KATOU Takeo 加藤武雄
KOHNO Isao 河野 功
MATSUZAWA Yasuhide 松沢安秀
MIYAGAWA Makoto 宮川真言
SAKAMOTO Ichiro 坂本一郎
SHINOHARA Shigemi 篠原茂己
USUBA Isao 薄葉 勲

Surface Characterization Center

IWAKI Masaya 岩木正哉
KOBAYASHI Kenzo 小林健三
KOBAYASHI Takane 小林 峰
SAKAIRI Hideo 坂入英雄
MATTHEWS Andrew

Synchrotron Radiation Facility Design Group

BE Suck Hee 裵 碩喜
HARA Masahiro 原 雅弘
KAMITSUBO Hiromichi 上坪宏道
NAGAOKA Ryutaro 長岡隆太郎
OIKAWA Yosifumi 老川嘉郁
SASAKI Shigeki 佐々木茂樹
TAKEBE Hideki 武部英樹
TANAKA Hitoshi 田中 均
WADA Takeshi 和田 雄

List of the People Who Took Doctorates Using the 160 cm Cyclotron and the Titles of Their Theses

Fumitoshi Ambe: "Chemical Effects of Neutron-Induced Nuclear Reactions in Halates and Related Compounds", The University of Tokyo, 1967.

Shoji Nagamiya*: "Study of the Effective Spin and Orbital Magnetic Moments of Nucleons", Osaka University, 1972.

Kotaro Hiruta*: "Alpha Decay of ^{218}Th, a New Isotope", Tokyo Institute of Technology, 1973.

Shigeru Takeda: The (d,t) reactions on N = 50 Nuclei", Tokyo Institute of Technology, 1973.

Tadao Tonuma: "Charge Changing of Energetic Heavy Ions in Gases", Waseda University, 1973.

Isao Kohno: "Elastic and Inelastic Scattering of ^{14}N and ^{12}C Projectiles by ^{12}C ad ^{28}Si", Osaka University, 1974.

Yoshishige Yamazaki*: "Nuclear Magnetic Moments of High-Spin Isomers and Spin-Relaxation Phenomena", The University of Tokyo, 1974.

Michi Aratani: "Charge Spectrometry and Its Application", The University of Tokyo, 1975.

Nobuhiro Shiotani: "Positron Annihilation in Transition Metals", The University of Tokyo, 1975.

Morio Yoshie*: "Studies of ^{14}N-, ^{12}C-, and ^{11}B-Induced Reactions on ^{90}Zr and $^{92\text{-}100}$Mo at Energies above the Coulomb Barrier", Tokyo University of Education, 1975.

Tomokazu Fukuda*: "Measurement of Heavy-Ion Fusion Cross Section by Beam Attenuation Method", The University of Tokyo, 1977.

Tohru Motobayashi*: "Alpha-Transfer Reactions between 1p or 2s-1d Shell Nuclei", The University of Tokyo, 1977.

Takeshi Wada: "Elastic and Inelastic Scatterings of Deuteron from Even Mass Isotopes of Molybdenum", Tokyo Institute of Technology, 1978.

Koichiro Asahi (Tanaka)*: "Spin Polarization of ^{12}B in the Reactions Induced by ^{14}N, ^{10}B, and ^{12}C on ^{100}Mo Targets", The University of Tokyo, 1980.

---

* Students who performed their studies at Riken.

Hiroaki Utsunomiya*: "Study of Preequilibrium Alpha-Particle Emission in Heavy-Ion Reactions", Kyoto University, 1980.

Minoru Yanokura*: "Isotopic Dependence of Heavy-Ion Reactions in Light Mass System", Tokyo Metropolitan University, 1980.

Yuichiro Nagame*: "Strongly Damped Components of Heavy-Ion Reactions in Relatively Light Mass Region", Tokyo Metropolitan University, 1981.

Tohru Sugitate*: "Polarization Phenomena of Emitted Protons in Heavy-Ion Reactions", Tokyo Institute of Technology, 1981.

Kazuo Ieki*: "Study of Spin Polarization of Residual Nuclei in Heavy-Ion Induced Reactions by Gamma-Ray Circular Polarization Measurement", Kyoto University, 1983.

Akio Koyama: "Fast Ion Interaction with Solids", The University of Tokyo, 1983.

Tadashi Kambara: "Collisional Quenching of np-States of 110 MeV H-Like Ne Ions in Gaseous Targets", Kyoto University, 1984.

Takashi Fujisawa: "Analyzing Power-Polarization Inequality in the Inelastic Scattering of Protons on ^{12}C for Incident Energies from 22.0 to 29.0 MeV", Osaka University, 1985.

Hideo Harada*: "Study of Excited States in ^{110}Sn", Tokyo Institute of Technology, 1985.

Masahiko Sugawara*: "Study of Nuclear Structure of Ra Isotopes", Tohoku University, 1985.

Fumio Yatagai: "Studies on LET Effect on Bacterial Cells", Waseda University, 1985.

Toshifumi Kosaka: "Study on Ionizing Radiation Induced Potentially Lethal Damage and Its Repair", Nihon University, 1988.

Yoshiko Itoh: "Study of Light Element Impurities in Semiconductor by Charged Particle Activation Analysis", Osaka University, 1989.

Yoshio Kobayashi: Mossbauer Spectroscopic Studies of Ruthenium Compounds", Tokyo Metropolitan University, 1989.

List of the People Who Obtained Master Degrees by Completing Their Experimental Studies Using the 160 cm Cyclotron

Masatoshi Kobayashi, The University of Tokyo, 1969.

Hiroshi Teranishi, The University of Tokyo, 1969.

Osamu Hashimoto, The University of Tokyo, 1972.

Hiroshi Ikezoe, The University of Tokyo, 1973.

Tatsuya Kanai, Tokyo University of Education, 1974.

Takao Ooi, Tokyo University of Education, 1975.

Tadashi Shimoda, Kyoto University, 1977.

Sadayuki Uchiyama, Waseda University, 1977.

Sugao Ise, Tokyo Gakugei University, 1978.

Yasuo Miyake, Osaka University, 1978.

Toshiyuki Kojima, Rikkyo University, 1979.

Mitsunori Fukuda, Tokyo Institute of Technology, 1985.

Kenya Kubo, The University of Tokyo, 1986.

Iwao Arai, Science University of Tokyo, 1986.

Makiko Suehiro, The University of Tokyo, 1990.

Kohju Tachi, Shibaura Institute of Technology, 1990.

List of Outside Users Under Contract and Their Themes

M. Nakamura et al. "Production of ^{43}K for Heart Diagnosis"	Med. Dept., Kyushu Univ.
Y. Murakami et al. "Production of ^{52}Fe used for Diagnosis"	Tokyo Metropolitan Univ.
H. Kakehi A. Tsuya H. Murayama "Production of ^{18}F for Tumor Search"	Chiba Univ. Hospital National Cancer Center Res. Inst. Tokyo Medical Univ.
M. Iio and T. Hara "Production of ^{197}Hg for Diagnosis of Lung Tumor"	Nakano National Hospital
T. Katou, S. Kawasaki, and T. Furuta "Study of Effect of Helium Bubbles on the Mechanical Behavior of Stainless Steel, SUS 32"	Japan Atomic Energy Res. Inst.
H. Kamei and M. Terasawa "Simulation Study by Charged particles of Neutron Damage of Reactor Materials"	Electrical and Nuclear Engineering Lab., Toshiba Research and Development Center
H. Kakehi "Production of ^{111}In for Tumor Search"	Chiba Univ. Hospital
Y. Araki and M. Kashima "Study of Potassium Metabolism by ^{43}K"	Med. Dept., Univ. of Tokyo
K. Noguchi et al. "Production of ^{7}Be for Experimental Practice at the Highest Class of Radio-isotope School"	Radio-isotope School, Japan Atomic Energy Res. Inst.
K. Noguchi et al. "Activation Analysis of Impurities in Silicon"	Radio-isotope School, Japan Atomic Energy Res. Inst.
O. Ezawa et al. "Production of ^{52}Fe"	Radio-isotope School, Japan Atomic Energy Res. Inst.
J. Ando "Production of Tl Radio-isotopes for Medical Use"	Med. Dept., Kanazawa Univ.

Y. Wada and K. Tsutsumi "Study of Method for Measurement of Helium in an Activated Stainless Steel SUS 316"	Power Reactor and Nuclear Fuel Development Corporation, Tokai Works
T. Hara and M. Iio "Production of ^{18}F for Bone Tumor Search"	Nakano National Hospital
T. Hara and M. Iio "Production of ^{47}Sc for Cancer Diagnosis"	Nakano National Hospital
Y. Homma "Study of the Production of ^{61}Co, ^{61}Cu, ^{135}La and ^{123}I"	Chem. Dept., Tokyo Metropolitan Univ.
N. Nakazawa "Production of ^{123}I for Diagnostic Use"	First Radioisotopes Co.
K. Shiraishi "Radiation Damage of Stainless Steel"	Japan Atomic Energy Research Inst.
S. Furusawa "Production of ^{130}I for Study of Angular Correlation of the Gamma-Rays of ^{130}Xe"	Dept. Phys., Niigata Univ.
S. Iwata and T. Tamura J. O. Rasmussen "Study of the Decay Chain of ^{156}Er"	Research Reactor Institute, Kyoto Univ. Univ. of California
M. Terasawa, M. Shimada, and M. Iimura "Cyclotron Irradiation for Study of FBR Material Embrittlment"	Toshiba R. & D. Center
K. Komura, M. Sakamoto,* and A. Ando** "Production of ^{167}Tm for Medical Use"	Inst. for Nuclear Study, Tokyo Univ., *Kanazawa Univ., and **Junior College of Medical Technology
T. Furusawa, M. Hishinuma, and K. Fukai "Study of Stainless Steel Swelling by Helium Injection"	Japan Atomic Research Inst.
A. Iida "X-ray Diffraction Study of the Effect of Alpha-Bombardment of Si-Crystal"	Faculty of Engineering, Tokyo Univ.

Y. Murakami and H. Nakahara "Study of Nuclear Reaction Products for the Purpose of Medical Use"	Faculty of Science, Tokyo Metropolitan Univ.
N. Nagashima "Determination of C in Si by Activation Analysis"	Semiconductor Department, Hitachi, Ltd.
Y. Honma and K. Kurata "Production of ^{48}V, ^{48}Cr, ^{51}Cr, ^{81}Rb, and ^{82m}Rb"	Kyoritsu College of Pharmacy
K. Yuita "Production of ^{43}K"	National Inst. of Agricultural Sciences
K. Usami and K. Mukai "Surface Analysis by Charged Particle Activation"	Hitachi R. and D. Center
A. Hishinuma, T. Furuta, H. Kamizuka, K. Fukai, and T. Otomo "Simulation Test on Neutron Irradiation Damage of Stainless Steel for Fast Breeder Reactors by α-Bombardment"	Japan Atomic Energy Research Inst.
Y. Wada, K. Senno, K. Fukuda, M. Suzuki, K. Suzuki, and H. Sakamoto "Study of Irradiation Damage of Transistors by Proton Bombardment"	Musashino Electrical Communication Lab., Nippon Telegraph and Telephone Public Corporation
S. Hayashi, S. Iwata, M. Yanokura*, and A. Murakami** "Calibration of Solid Track Detectors with Heavy Ions"	Research Reactor Inst., Kyoto Univ. *Faculty of Science, Tokyo Metropolitan Univ. **Faculty of Science and Engineering, Saga Univ.
A. Hishinuma, T. Furuta, K. Fukai, and T. Otomo "Helium Implantation Effect on Creep Rupture Properties of Modified 316 Stainless Steel for Fast Reacter Material"	Japan Atomic Energy Research Inst.
K. Suganuma and S. Yajima* "Development of Ferritic Stainless Steel for Atomic Reactor"	Research Inst. for Iron, Steel and Other Metals, Tohoku Univ. *Irradiation Research Lab., in JMTR.

R. Nagura, H. Ono, Y. Narimatsu, and T. Hishiyama "Calibration of Space Environment Monitor Carried on GMS-2 with Protons"	Space Development Div., Nippon Electric Co., Ltd.
F. Yajima "Production of ^{18}F"	Mitsubishi Chemical Industries Ltd.
M. Harada and H. Matsutani* "Study of Effect by Bombarding High Energy Proton on a Solar Cell"	Japan Trust Center for Electronic Parts *Electronic Parts Div., Sharp Co., Ltd.
K. Yuita "Production of ^{77}Br"	National Inst. of Agricultural Sciences
H. Emori "Radiochemical Analysis of ^{16}O in GaAS"	Mitsubishi Metal Co., Ltd.
T. Watanabe "Production of ^{18}F"	Mitsubishi Aluminum Co., Ltd.
T. Abe "Radiochemical Analysis of ^{14}N in Si Crystal"	Shinetsu Semiconductor Co., Ltd.
M. Watanabe and T. Usami "Radiochemical Analysis of B and ^{14}N in Si Crystal"	Toshiba R & D Center
T. Abe "Radiochemical Analysis of C and ^{16}O in Si Crystal"	Shinetsu Semiconductor Co., Ltd.
Y. Higashiguchi "Development of Ferritic Stainless Steel for Reactor"	Research Inst. for Iron, Steel and Other Metals, Tohoku Univ.
T. Matsutani "Study of Effect by Bombarding High Energy Proton on a Solar Cell"	Electronic Parts Div., Sharp Co., Ltd.
T. Fukushima "Study of Effect by Bombarding High Energy Proton on I.C. and Transistor"	Kamakura Factory, Mitsubishi Electric Co., Ltd.
M. Hiranuma "Photograph of Cyclotron Beam"	Nomura Research Inst.

S. Yoshida and K. Mitsui "Study of Effect by Bombarding High Energy Proton on a GaAs Solar Cell"	LSI R & D Lab., Mitsubishi Electric Co., Ltd.
H. Muraoka "Radiochemical Analysis of ^{14}N in Si Crystal"	Semiconductor Div., Toshiba Electric Co., Ltd.
T. Iizuka "Radiochemical Analysis of ^{16}O in Si Crystal"	Japan Electric Industry Developing Association (JEIDA)
M. Koitabashi "Study of Effect by Bombarding High Energy Proton on a Teflon Plate Coated by a Silver"	Central Res. Lab., Mitsubishi Electric Co., Ltd.
S. Suzuki "Study of Effect by Bombarding High Energy Proton on a Solid Fuel for a Rocket"	Space Development Div., Nissan Automobile Co., Ltd.
M. Yatsuhashi and T. Suematsu "Study of Effect by Irradiating Fast Neutron on a Insulator Covering a Cable"	Fujikura Cable Works, Ltd.
A. Morio and M. Harada "Study of Single Event Upset in Microprocessors by Bombarding ^{20}Ne Particles"	Japan Trust Center for Electronic Parts
H. Ueyama "Study of Effect by Bombarding High Energy Proton on a Si Solar Cell"	Sharp Co., Ltd.
S. Orito and S. Nakamura "Test of Sensibility of CR39 Track Detector for High Energy Proton"	Faculty of Science, Univ. of Tokyo
E. Tohji "Radiochemical Analysis of ^{14}N and ^{16}O in Si Crystal"	Toshiba Ceramics Co., Ltd.
H. Yamamoto "Radiation Damage of Cover Glass for a Solar Cell"	R & D Div., Asahi Glass Co., Ltd.
A. Morio and M. Harada "Study of Single Event Upset in Microprocessors by Bombarding ^{14}N and ^{20}Ne Particles"	Japan Trust Center for Electronic Parts

T. Kimura "Radiochemical Analysis of ^{16}O, ^{14}N and ^{11}C in Si Crystal and GaSb"	Japan Chemical Analysis Center
T. Kimura and H. Hukushima "Radiochemical Analysis of ^{16}O, ^{14}N and ^{12}C in Si Crystal and GaAs"	Japan Chemical Analysis Center
Y. Moriguchi "Radiation Damage of Cover Glass for a Solar Cell"	R & D Div., Asahi Glass Co., Ltd.
T. Hayashi "Radiation Damage of Cover Glass for a Solar Cell"	Institute of Space and Astronautical Science
K. Yamamoto "Study of Single Event Upset in Microprocessors by Bombarding ^{14}N and ^{40}Ar Particles"	Semiconductor R & D Lab., Toshiba Co., Ltd.
S. Yoshida and M. Goto "Study of Effect by Bombarding High Energy Proton on a GaAs Solar Cell"	LSI R & D Lab., Kamakura Works, Mitsubishi Electric Co., Ltd.
K. Omura and T. Abe "Calibration of Space Environment Monitor Carried on a Satellite with Variable Particles"	Kamakura Works, Mitsubishi Electric Co., Ltd.
H. Tanaka and Y. Kitamura "Study of Latch-up in Microprocessors by Bombarding ^{14}N and ^{42}Ar Particles"	NEC, Ltd.
M. Watanabe and K. Ueno "Improvement of Thyristors by Proton Irradiation"	Fuji Electric Corporate R & D, Ltd.
T. Abe and K. Tomii "Improvement of Thyristors by Proton Irradiation"	Semiconductor R & D Lab., Matsushita Electric Work Co., Ltd.
H. Akiyama "Improvement of Thyristors by Proton Irradiation"	LSI Lab., Mitsubishi Electric Co., Ltd.

K. Toriyama "Study of Single Event Upset in Microprocessors by Bombarding ^{14}N and ^{12}C Particles"	Mitsubishi Electric Co., Ltd.
T. Kikuchi and K. Yamazaki "Study of Single Event Upset in Microprocessors by Bombarding ^{14}N and ^{12}Ne Particles"	Nippon Electric Co., Ltd.
Y. Fujita "Calibration of Space Environment Monitor Carried on a Satellite with Proton and α-Particles"	Meisei Electric Co., Ltd.
T. Suematsu "Effects of the Proton Irradiation on Cable Materials"	Fujikura Co., Ltd.
H. Okazaki "Radiation Damage of InP Solar Cells"	Nippon Mining Co., Ltd.
T. Ohga "Radiation Damage of Solar Cells"	Nippon Telephone Telegram Co., Ltd.
M. Kitagawa "Improvement of Thyristors by Proton Irradiation"	Toshiba Co., Ltd.
Y. Shimizu "Improvement of Thyristors by Proton Irradiation"	Hitachi Co., Ltd.
K. Ogura "Test of Sensibility of CR39 Track Detector for High Energy Protons"	Faculty of Engineering, Nippon University
H. Arai "Radiation Damage of Solar Cells"	NEC Co., Ltd.
T. Hayashi and A. Ohnishi "Radiation Damage of Cover Glass for a Solar Cells"	Institute of Space and Astronomical Science

List of International Conferences and Symposia on Accelerator Science

1. Symposium on Direct Reactions with ^{3}He (Sept. 1967)
2. Fourth International Hot-Atom Chemistry Symposium (Oct. 1967)
3. Symposium on In-Beam Spectroscopy by Heavy-Ion Reactions (Sept. 1972)
4. Symposium on Cluster Structure of Nuclei and Heavy-Ion Reactions (Mar. 1975)
5. Symposium on Heavy-Ion Reactions and Pre-Equilibrium Processes (Sept. 1977)
6. Symposium on Application of Ion Beams to Material Science (May 1978)
7. 1984 INS-RIKEN International Symposium on Heavy-Ion Physics (Aug. 1984)
8. The First Japan-China Joint Symposium on Accelerator Technology for Nuclear Science and Their Applications (Sept. 1980)
9. U.K.-Japan Seminar on Theoretical Studies of Atomic Collisions (Aug. 1985)
10. Studies of Condensed Matter with Medium- and High-Energy Accelerators (Oct. 1985)
11. International Seminar on Dynamic Processes of Highly Charged Ions (Aug. 1986)
12. International Symposium on Muon-Catalyzed Fusion μCF86 (Sept. 1986)
13. Eleventh International Conference on Cyclotrons and Their Applications (Oct. 1986)
14. U.S. -Japan Joint Seminar on Interactions of Highly Ionized Atoms Produced by Ion-Atom Collisions (Mar. 1987)
15. Symposium on Dynamic Interactions of Charged Particles with Solids (Oct. 1987)
16. RIKEN-IN2P3 Symposium on Heavy-Ion Collisions (Oct. 1987)
17. The Third Japan-China Joint Symposium on Accelerator Technology for Nuclear Science and Their Applications (Nov. 1987)
18. Heavy-Ion Physics and Nuclear Astrophysical Problems (July 1988)
19. The Fifth International Conference on Cluster Aspect of Nucleus and Subnuclear System (July 1988)
20. Symposium on Biological Effects of High LET Radiation (Aug. 1988)
21. Symposium on Topics on Light and Light-Heavy Ion Reactions (Oct. 1989)
22. Symposium of Collective Motion of Nuclei and Nuclear Reaction Mechanism (Dec. 1989)
23. Symposium on High-Energy Ion-Atom Collisions (Mar. 1990)
24. Second IN2P3-RIKEN Symposium on Heavy-Ion Collisions (Apr. 1990)

Selected Papers

Accelerator development and accelerator physics

Reprinted from Proc. Int. Symp. on Magnet Technol., p. 239–247 (1965).

A B-CONSTANT MAGNET POLE DESIGN

Takashi Karasawa, Shoshichi Motonaga, Yoshitoshi Miyazawa, Noriyoshi Nakanishi, Masatake Henmi and Hiroo Kumagai

Cyclotron Lab. The Institute of Physical and Chemical Research
Komagome, Bunkyo-ku, Tokyo

Summary

The shapes of the pole in which the magnetic induction B of iron is constant are presented for a wide range of ratio of diameter to gap. The shapes are derived from a simple equation with a correction factor k as a function of the ratio of the diameter to the gap. The constancy of B was experimentally confirmed.

Introduction

The relative distribution of the magnetic field in the median plane in an electromagnet changes with the variation of the central field. It is because parts of the pole, especially the edge of the pole tip, are saturated. If the proper shape is so constructed that all parts of the pole tip have the same magnetic induction, the relative distribution is constant at every central field.

On the electromagnet which can produce high central field, the ampere turn loss in both pole and yoke must be small. Usually the shape of the pole tip is tapered and the cross-sectional area of the pole tip increases with the distance from the flat surface of the pole tip. The profile of the B-constant pole also supplies the basis of the shape of the pole for design of high-field electromagnet.

Several profiles of B-constant were reported[1,2,3] and we have developed one of the profiles called by us edgeless profile.[4] These profiles are all based on the two-dimensional semi-infinite treatment, and deviation from the B-constant condition may appear at the case when the ratio of diameter to gap is small. The ratios of diameter to gap of the electromagnet widely used are about 6 ~ 10 for the cyclotron and about 3 ~ 5 for the nuclear magnetic resonance or electron spin resonance. We experimentally confirmed that the edgeless profile satisfies the B-constant condition when the ratio of diameter to gap is 6 ~ 7. For the ratio of diameter to gap about 2, we have found experimentally, approximately B-constant profiles by simple modifications on the edgeless profile.

Calculations of the B-Constant Pole Profile

Hyperbolic Cosine Type

This profile has been reported by one of us[1] and we make here a brief explanation. We have calculated the profile of B-constant pole by following simplified assumptions: (1) We treat the problem as a two-dimensional semi-infinite one and select the coordinate as shown in Fig. 1, where the x-axis is the center of the gap and z-axis is at the end of the parallel surface of the gap. (2) We regard the magnetic permeability of iron to be sufficiently large. (3) The z component of B at the surface of the pole tip is inversely proportional to z. The last assumption is expressed in the equation

$$\frac{d\,(z/d)}{d\,(x/d)} = \sqrt{(z/d)^2 - 1} \qquad (2.1)$$

and we get $z/d = \cosh(x/d)$. (2.2)

The profile derived from Eq. (2.2) is shown in Fig. 1.

Edgeless Types

In the cosh type profile, the tangent is continuous at the junction of the parallel plate and tapered part of the pole tip but the charge density of the pole tip surface at that point is somewhat larger than that at the center (see Chap. 3). We have improved this circumstance by alteration of the third assumption used for cosh type profile.

It is well-known that the charge distribution on the parallel plate condenser increases to the edge, and the flux density in the median plane decreases at the outside. It is possible that an equipotential line between the plate and median plane is the profile of the B-constant pole. We use conformal transformation with the following relation

$$Z = W + \exp(W) \qquad (2.3)$$

where $z = x + iy$, $w = u + iv$, the lines u = constant are flux lines and the lines v = constant are equipotential lines. The line element on the equipotential line is $d\ell$ and we derive from (2.3)

$$\frac{\sigma}{\mu}\frac{d\ell}{dx} = \frac{\partial U}{\partial \ell}\frac{d\ell}{dx} = \frac{1}{1 + \cos V \exp(U)} \qquad (2.4)$$

where σ is charge density on the equipotential line and μ is the permeability of free space.

The condition required in the B-constant profile is that charge density on the surface of the pole divided by dx is constant. This means the equation (2.4) has constant value. When $V = \pi/2$ and $-\pi/2$, Eq. (2.4) has a constant value

$$\frac{\sigma}{\mu}\frac{d\ell}{dx} = \frac{1}{1 + \exp(U)} \quad \text{and} \quad \frac{1}{1 - \exp(U)} \qquad (2.5)$$

Then we can decide x and y for the B-constant profile

$$x = U \qquad y = \pi/2 + \exp(U), \quad y = \pi/2 - \exp(U) \qquad (2.6)$$

When the origin of the coordinate is selected on the x-axis, Eqs. (2.6) will give a certain profile. Now we may select a point for $x = 0$ such that the profile derived from (2.6) fits the cosh profile for large values of y. Then the final equation of the edgeless profile is

$$Z/d = 1 + 0.125 \exp(x/d \cdot \pi/2) \qquad (2.7)$$

where z is the distance from the median plane and x is the distance from the point corresponding to the end of the parallel surface of the cosh type and $2d$ is the gap width. We define the distance from the center of the pole tip to the point $x = 0$ as the principal radius. The profile derived from Eq. (2.7) is shown in Fig. 1-b.

Experimental Results

The Case of Large Ratio of Diameter to Gap

The general view of one of the electromagnets used for our study is shown in Fig. 2. The pole tip can be changed within the distance of 65 mm from the median plane and the exciting coils can be moved along the pole axis about 40 mm each way. The carbon content of the iron of the pole and pole tip is about 0.15%.

Several pole tips which have profiles deviating slightly from cosh and edgeless types were examined. We will describe two typical cases· cosh and edgeless profiles. These profiles are derived from Eqs.(2.2) and (2.7) shown in Table 1.

TABLE 1

Cosh and Edgeless Type Pole Profiles
(units in mm)

Cosh Type

h	0	1.8	6.8	16.8	41.8	56.6
d	105	117	125	133	142	150

Edgeless Type

h	0	0.5	1.05	2.3	6.8	9.4	13.1	17.6	33	54.8
d	90	111	108	116	128	131	135	138	145	150

The relative radial distributions in the median plane were measured by the differential usage of Hall generators.[5] Experimental results are shown in Fig. 3-a and 3-b on the cosh type. The change of the relative distribution occurs at high field $B \geq 1.5$ Wb/m^2.

The direct measurement of B along the axis in the pole tip was made by the electronic integrating flux meter with one-turn search coils wound at various parts of the pole. When the local magnetic induction must be precisely measured, the magnetic flux through two coils was subtracted. The schematic diagram of this method is shown in Fig. 4. The experimental results are shown in Fig. 5 on the cosh type. The magnetic induction in the pole, except in the vicinity of the end of the parallel surface of the pole tip, called edge by us, is constant but somewhat larger than the magnetic induction at the center of the air gap B_c. This phenomena suggests the possibility of local saturation near the edge. The experimental result shows that the local magnetic induction B_1 near the edge is about 20% larger than B_c. On the high field, say 2.0 Wb/m^2, the ratio of B/B_c in the pole is slightly reduced and B_1 near the edge is about 15% larger than B_c. When the air gap is reduced, the ratio B/B_c is slightly reduced as shown in Fig. 5 but the local saturation near the edge is not removed.

The experimental results on the edgeless profile, described in Table 1, are shown in Figs. 6 and 7. The magnetic induction in the pole is constant within the experimental error – estimated at 1% – and the relative distributions are constant up to 2.0 Wb/m^2.

Edgeless Profile Above 2.0 Wb/m^2

The magnet whose pole base is 720 mm in diameter with a flat pole tip of 457 mm was used for more precise experiments. The general view of the pole tip is shown in Fig. 8. The gap length $2d$ between flat surfaces is 87 mm and principal radius is 276 mm. The profile is derived from Eq. (2.7).

When the pole tips were set at 87 mm gap, some deviation on the relative distribution appeared above 2.0 Wb/m^2 of the central field. At 75 mm of gap length, the relative distribution is approximately constant and acceptable for B-constant profile. These results are shown in Fig. 9. The magnetic induction in the pole tip along the pole axis was measured locally near the principal radius. The results are shown in Fig. 10. One may see that at 87 mm gap, the magnetic inductions normalized by B_c are somewhat larger than 1.0, but at 75 mm gap they are close to 1.0 or somewhat less than 1.0.

These experimental results mean that the profile shown in Fig. 8 is adequate for B-constant at 75 mm gap rather than 87 mm gap derived from theory. The discrepancy between experiment and theory may be caused by the assumptions in the theory which are the two-dimensional semi-infinite and/or sufficiently large permeability of the iron.

When permeability of iron near the pole tip surface becomes not so sufficiently large, say below 100, the surface of the pole tip is not equipotential. If this circumstance occurs, the edgeless profile which gives the B-constant pole at the magnetic field below 2.0 Wb/m^2, needs some correction at small permeability.

The Case of Small Ratio of Diameter/Gap

The theoretical treatment is based on the two-dimensional semi-infinite model,and discrepancies between experiment and theory may occur at small ratios of diameter to gap. We made an experiment in which the ratio was about 2. The pole tip is so constructed that the principal radius is 25 mm and the air gap is 30 mm. The profile of the pole tip is shown in Fig. 11. The diameters at large z are slightly larger than derived from Eq. (2.7) as shown in the dotted line in Fig. 11. The magnetic induction along the pole axis at various parts on the pole tip was measured. On the small ratio of

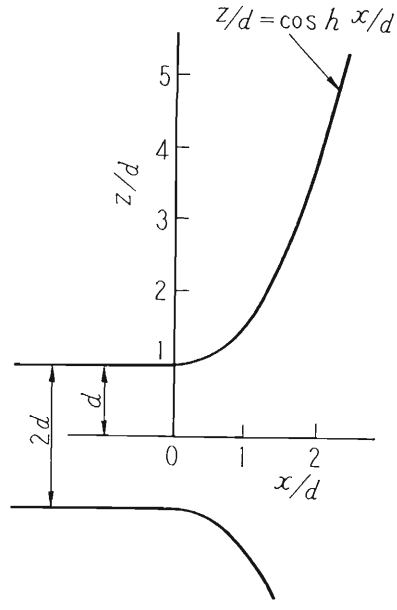

Figure 1a. Hyperbolic cosine type pole profile.

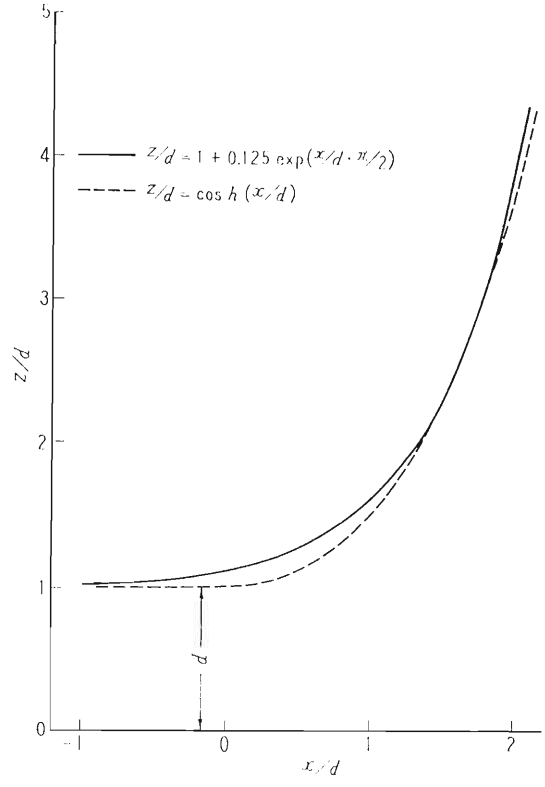

Figure 1b. Hyperbolic and edgeless type pole profiles.

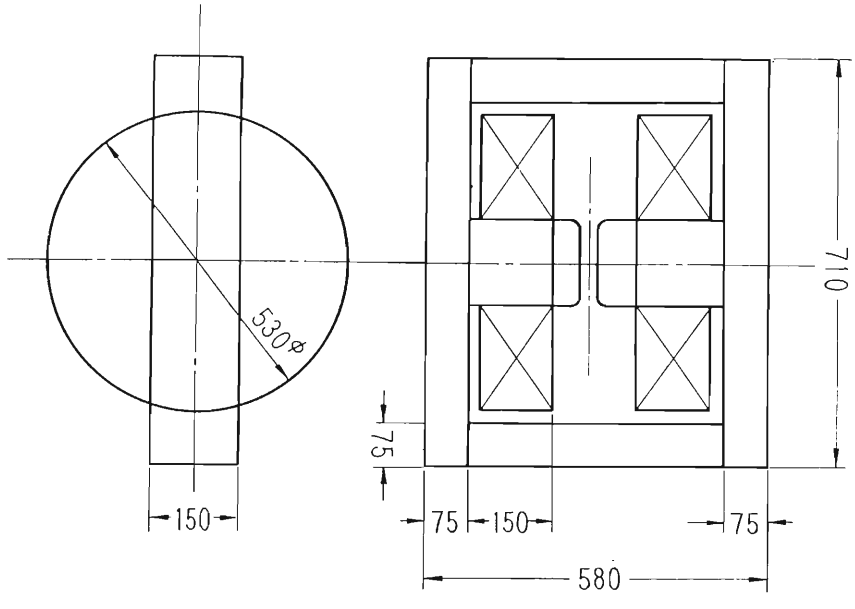

Figure 2. General view of the magnet.

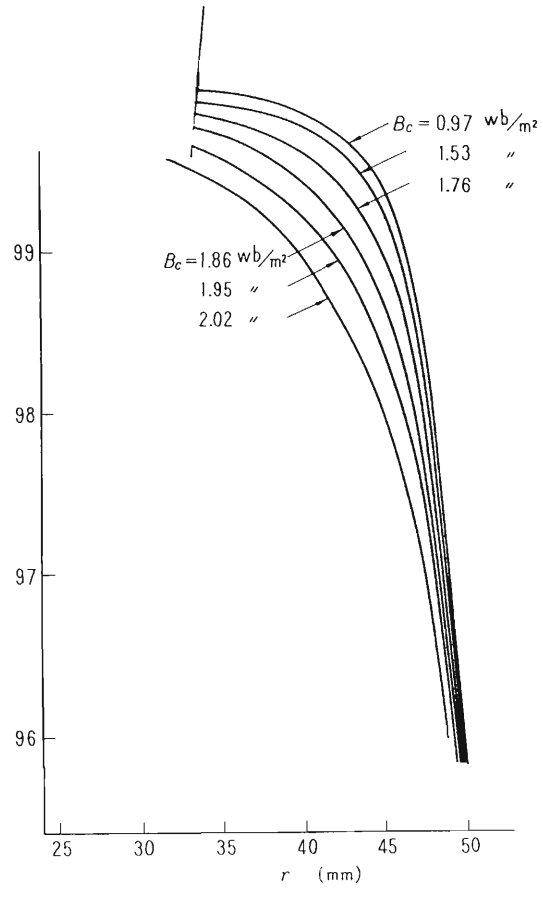

Figure 3a. Relative distributions of cosh type pole.

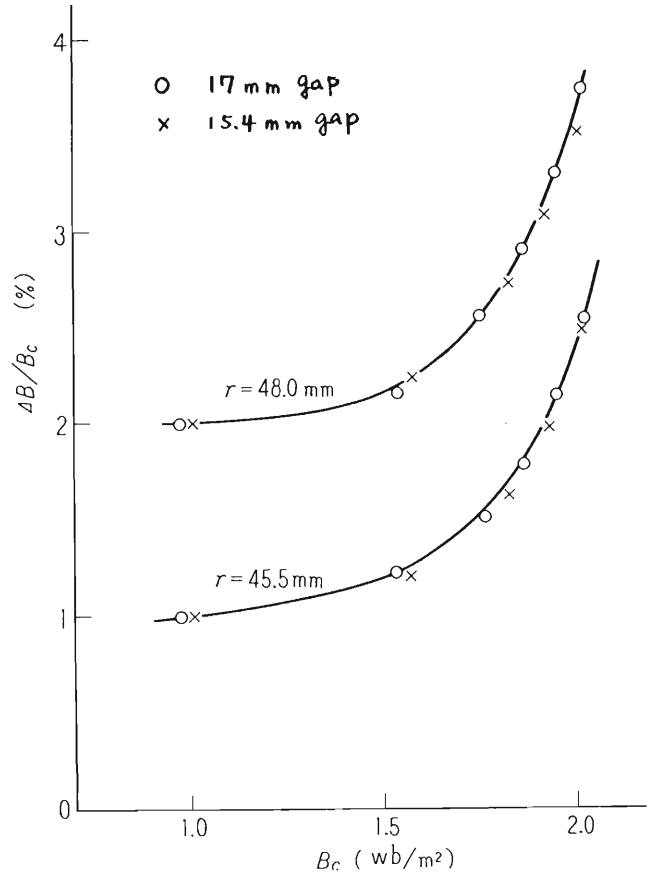

Figure 3b. Relative distributions of cosh type pole.

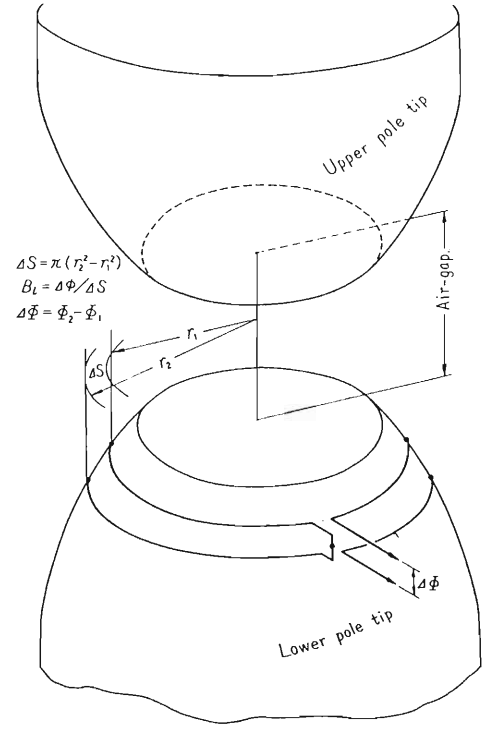

Figure 4. A method of measuring local saturation.

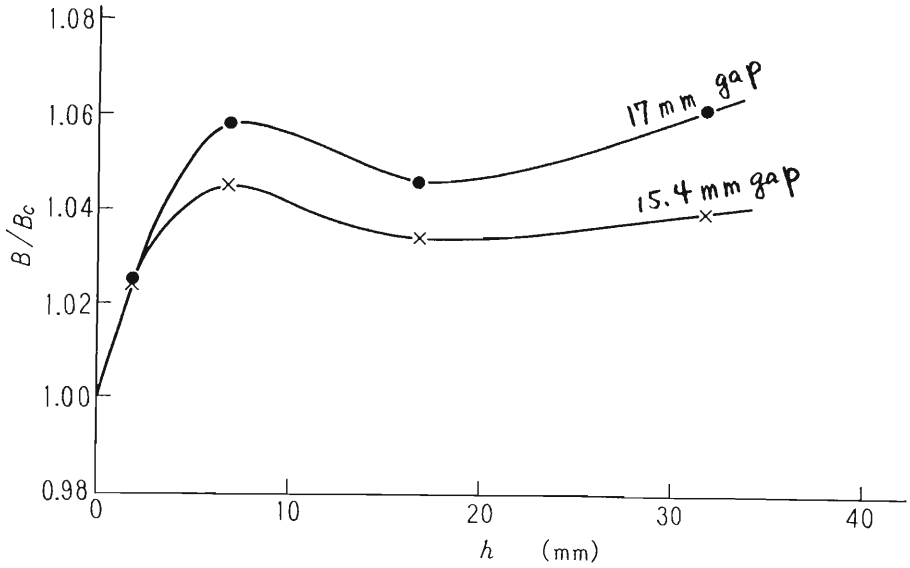

Figure 5. Mean magnetic induction along axis on cosh type pole.

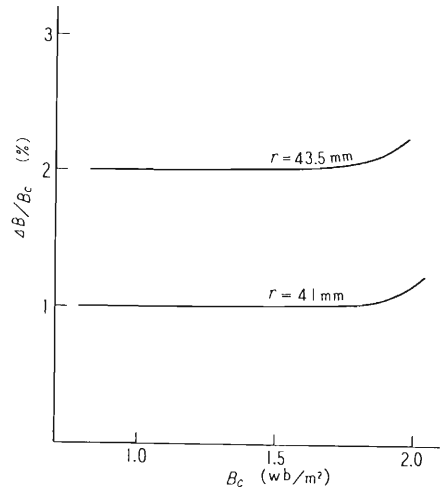

Figure 6. Relative field distribution on the edgeless pole profile.

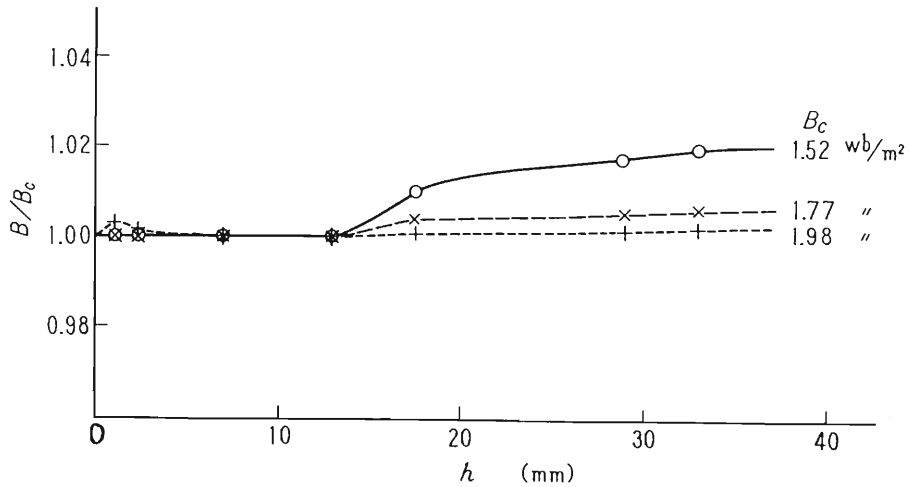

Figure 7. Mean magnetic induction on edgeless pole profile.

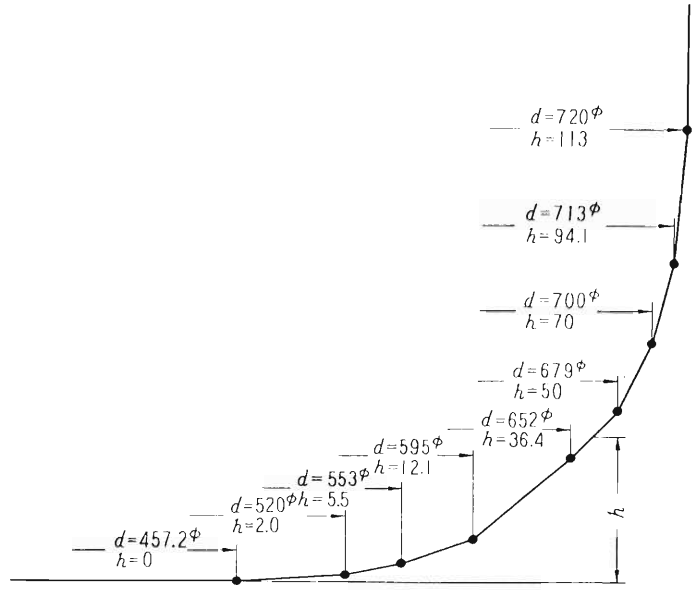

Figure 8. Pole tip shape of the edgeless profile. (Principal radius 276 mm)

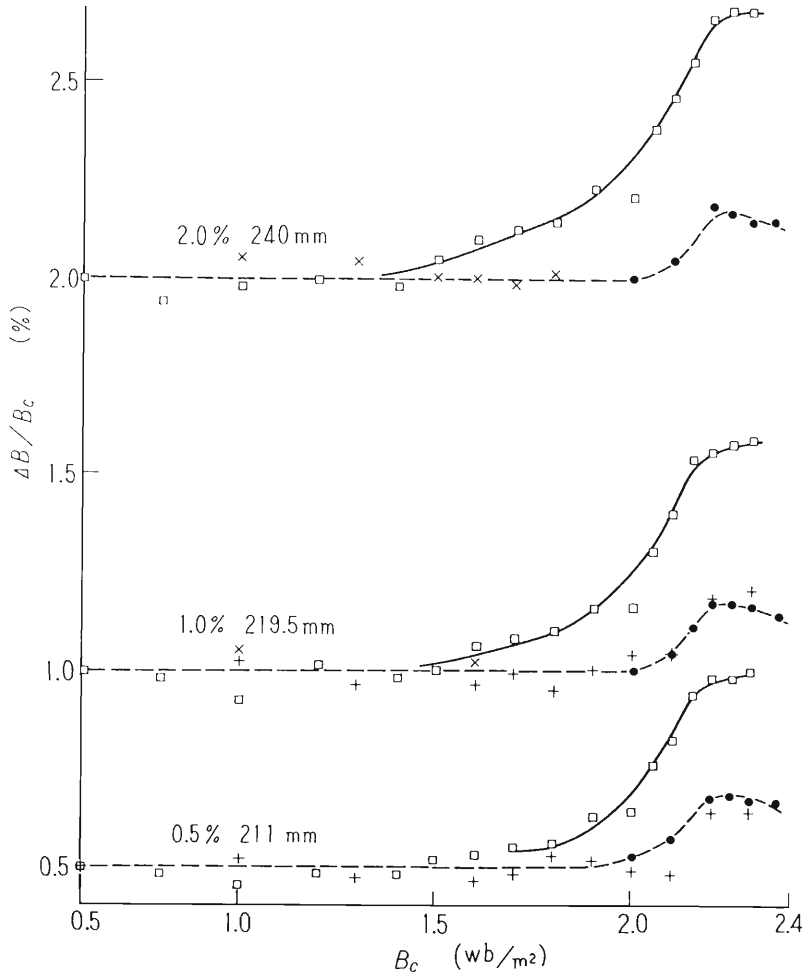

Figure 9. Magnetic field variation at various radii versus B_c.

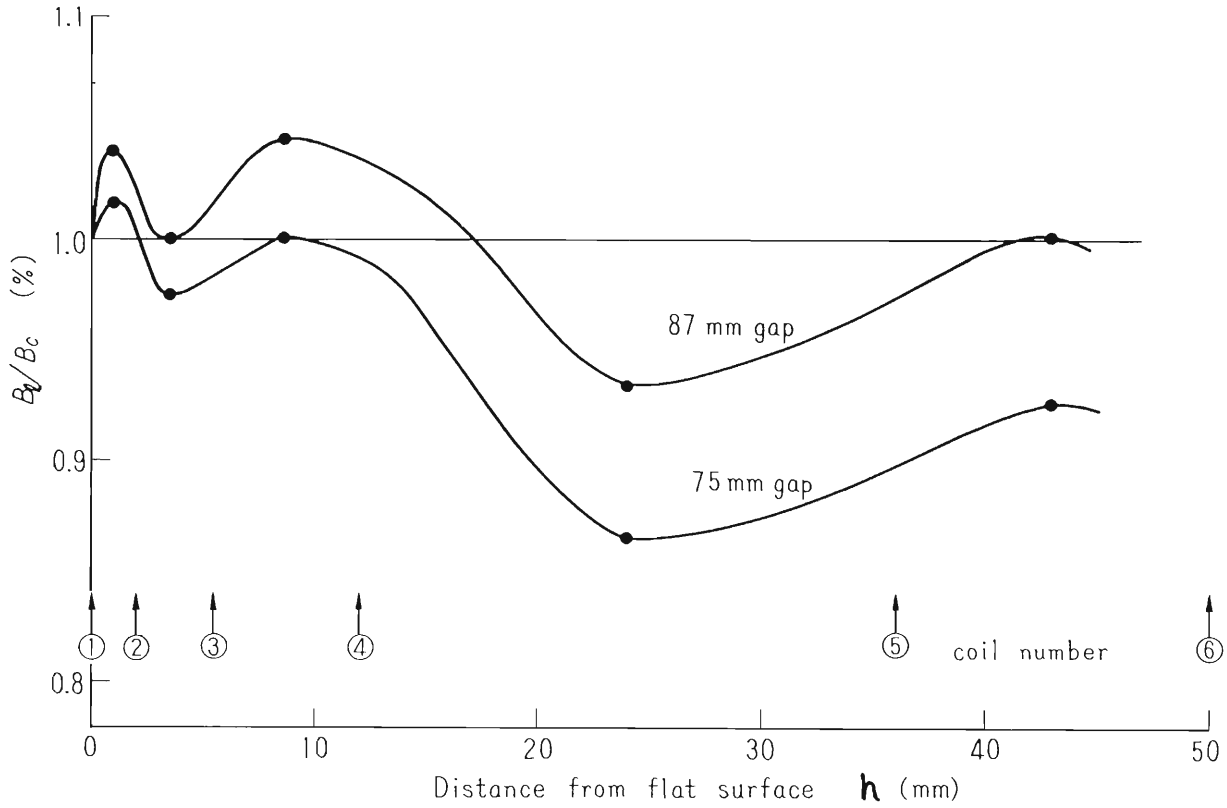

Figure 10. Local magnetic induction near the edge.

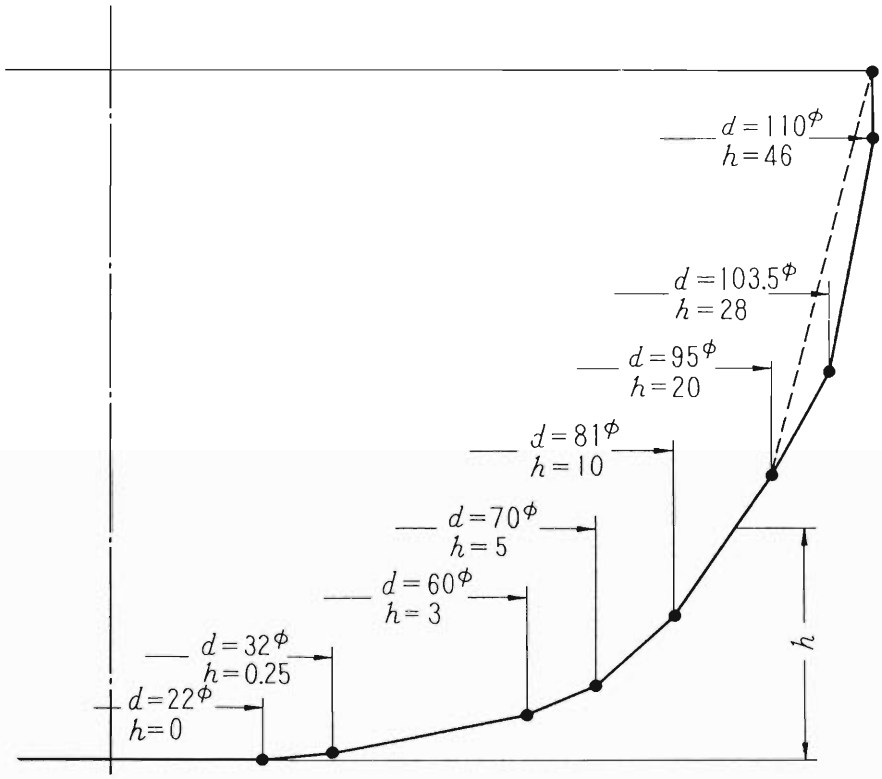

Figure 11. Pole tip shape of the edgeless profile.

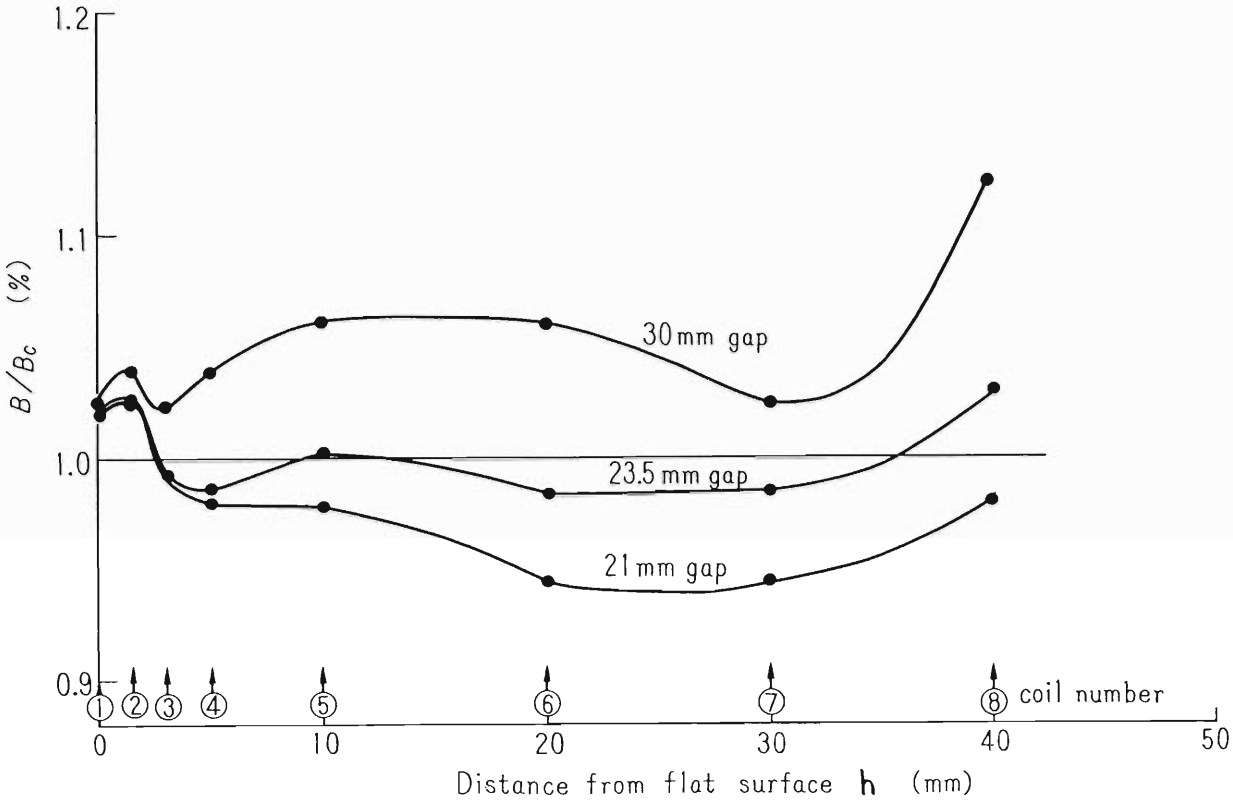

Figure 12. Mean magnetic induction on edgeless type pole profile.

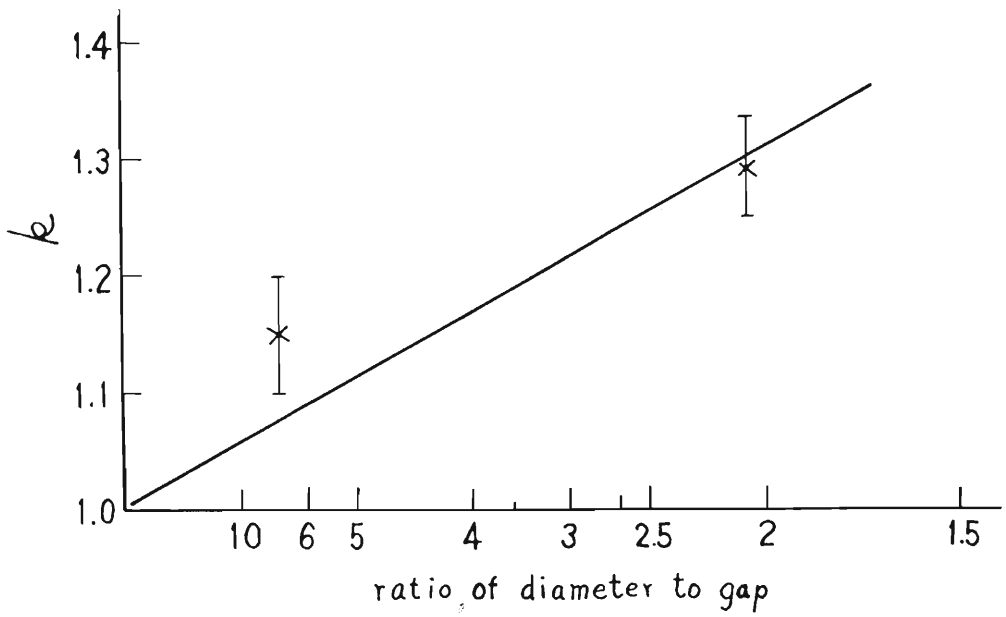

Figure 13. Correction for k as a function of the ratio of pole diameter to gap.

diameter to gap, the magnetic induction B_o at the center of surface of the pole tip is slightly larger than B_c at the center of the median plane; at 30 mm air gap, 5%; at 23.5 mm air gap, 3%; and at 21 mm air gap, 2%. Considering this condition, B along the axis is normalized by B_o rather than B_c in Fig. 12. When the air gap is 30 mm, B is larger than B_o, but when the air gap is 23.5 mm, B is constant at various parts of the pole tip and we determine the modified edgeless profile for B-constant pole in this case. This is expressed in the following equation

$$Z/d = 1 - \frac{k-1}{k} + 0.125 \exp(x/d \cdot \pi/2)$$

$$d = kd_o \qquad k \geq 1.0 \qquad (5.1)$$

Conclusion

The B-constant profile may vary by various factors; the ratio of diameter to gap, the permeability of iron, the location of the exciting coils, and others. We have tried only two cases of the ratio of diameter to gap and experimentally confirmed that edgeless profile and modified edgeless ones satisfy approximately B-constant conditions. We consider that x/d at the same z/d increases monotonically when the ratio of diameter to gap decreases and the correction factor k is not much larger than 1.0. We present the shape of the B-constant profile in Eq. (5.1) and k as shown in Fig. 13 for a wide range of the ratio of diameter to gap. We estimate $K = 1.15$ at ratio of diameter/gap = 7.3. This value of k may be somewhat over-estimated.

Our observations show that the location of the exciting coils does not affect the magnetic induction in the pole more than the experimental error of 1%.

More experimental and theoretical studies may be needed to estimate the effect of decreasing permeability of iron.

The authors wish to express their thanks to Dr. K. Matsuda and other members of the Cyclotron Lab for encouragement during these studies.

References

1. H. Kumagai, N.I.M. 6,213 (1960).
2. C. M. Braams, N.I.M. 26,83 (1964).
3. A. Huber and H. Primas, N.I.M. 33,125 (1965),
4. T. Karasawa, et al., Jap. Jour. Appl. Phys. to be published.
5. F 10 A simple and Convenient Method for Field Mapping by Differential Usage of Hall Generators in this symposium.

Reprinted from Nucl. Instrum. Methods, 65, 247–252 (1968).

DESIGN AND PERFORMANCE OF A FOCUSING MAGNETIC CHANNEL FOR A VARIABLE ENERGY MULTIPARTICLE CYCLOTRON

M. ODERA, Y. MIYAZAWA, T. TONUMA, M. HEMMI and O. TERAJIMA

The Cyclotron Laboratory, Institute of Physical and Chemical Research, Yamato-machi, Saitama-Pref., Japan

Received 24 June 1968

Design of a focusing magnetic channel which is to be used for the compensation of defocusing effect of the fringing field of the cyclotron is described. It can be used in the wide range of magnetic field strength giving essentally the same beam trajectories for the variable energy, multiparticle operation without any readjustment. Practical design and performance in the IPCR cyclotron are given.

1. Introduction

When the accelerated beam is extracted from the accelerating chamber of a cyclotron, it must pass the fringing field of the main magnet. The gradient of the field gives characteristic focusing and defocusing effects on the beam. Usually the beam spreads out radially and converges axially with respect to the magnetic field. A long passage in this fringing field generally results in difficulty in beam handling. Several methods to correct this effect are devised, such as magnetic field shielding channels[1]), magnetic focusing channels[2]), use of coil and iron together to get shielding and focusing effect simultaneously[3]) etc.

Some of those means are not suited to a variable energy, multiparticle cyclotron, where the strength of the magnetic field is varied over a wide range. Most of the other means need some adjusting techniques, to lead the beam in the external focusing system properly when the acceleration energy or particles are changed.

Here is described the design and performance of a focusing magnetic channel, which is now in use in the IPCR variable energy multiparticle cyclotron. The equilibrium orbit inside the channel can be matched with the central orbit of the beam without it. The radial extent of the beam profile shrinks by a large factor at the outside of the accelerating chamber, resulting in much increase of the usable beam. It does not need any adjustment for the entire range of the main magnetic field from 3000 G to 20000 G. The field distribution which it gives, can be calculated easily. The relative distribution, hence focusing property of the channel remains essentially the same and the trajectory of the beam is nearly constant through the entire range of operation of the cyclotron.

2. The field distribution given by an infinitely long triplet of ferromagnetic bars with circular cross section

When an infinitely long straight iron bar of circular cross section is placed in a uniform magnetic field of strength B_0, the magnetization and disturbance it gives to the originally uniform field, can be expressed in a closed analytical form. The magnetization strength in the bar is constant throughout the cross section and the direction is parallel to the original field. This property of constant magnetization assures that local saturation does not occur in the bar. Hence, the patterns of field

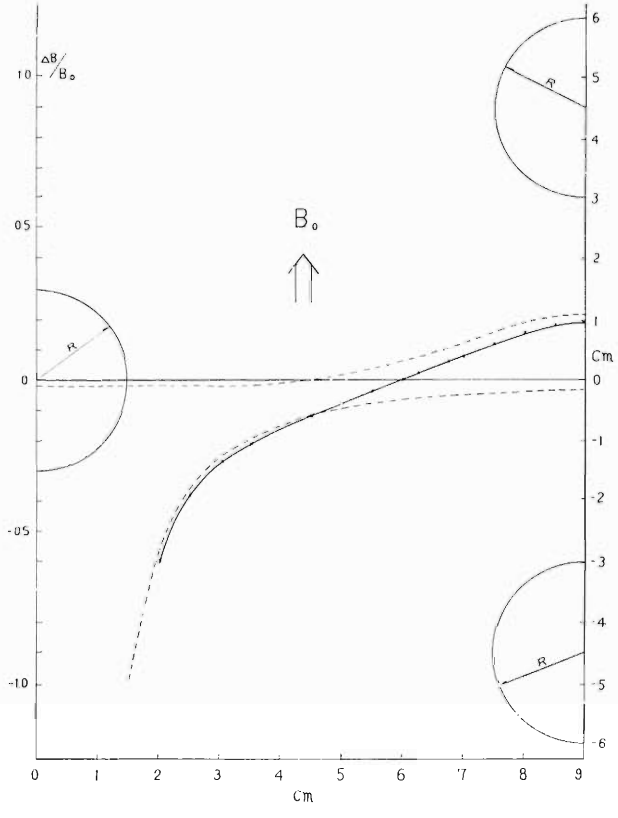

Fig. 1. Magnetic field induced by a magnetized bar triplet in the median plane. Lower and upper dotted lines are distributions induced by left single bar and right pair of bars respectively. The solid curve is synthesized from the two dotted ones. The linear portion has constant gradient of about 8% per cm.

distribution which the bar gives do not change as long as the magnetic induction in it does not become greater than that of the saturation strength of the material[4]). This situation can be realized generally for bars of elliptic cross section.

The magnetic induction at the outside of the bar is represented by

$$B_z = R^2\{(z^2-y^2)/(z^2+y^2)^2\}B_0, \quad (1)$$

$$B_y = R^2\{yz/(z^2+y^2)^2\}B_0. \quad (2)$$

Here, x, y, z are coordinates with direction to the axis of the bar, direction perpendicular both to the bar and original field B_0 and direction of B_0 respectively. R is the radius of the bar. B_y, B_z are the y, z components of magnetic induction induced by magnetization of the bar.

Choosing a mutual geometrical configuration of three such bars, one can calculate and synthesize a convenient magnetic field by these equations. For the special configuration shown in fig. 1, the distribution gives almost constant gradient, the width of which is nearly 6 cm.

3. Practical design

A scale model (1:3) was constructed and measurements were made to know saturation properties and end effects of the channel with finite length. Fig. 2a is the configuration of the measurements and fig. 2b shows the end effect. 40 mm inward from the end was sufficient to obtain a field gradient, coincident with the calculated one. This relation was able to be maintained until B_0 exceeds 10000 G. The magnetic induction in an infinitely long bar is equal to $2B_0$ and in a sphere is $3B_0$. Saturation is expected to set-in from that end,

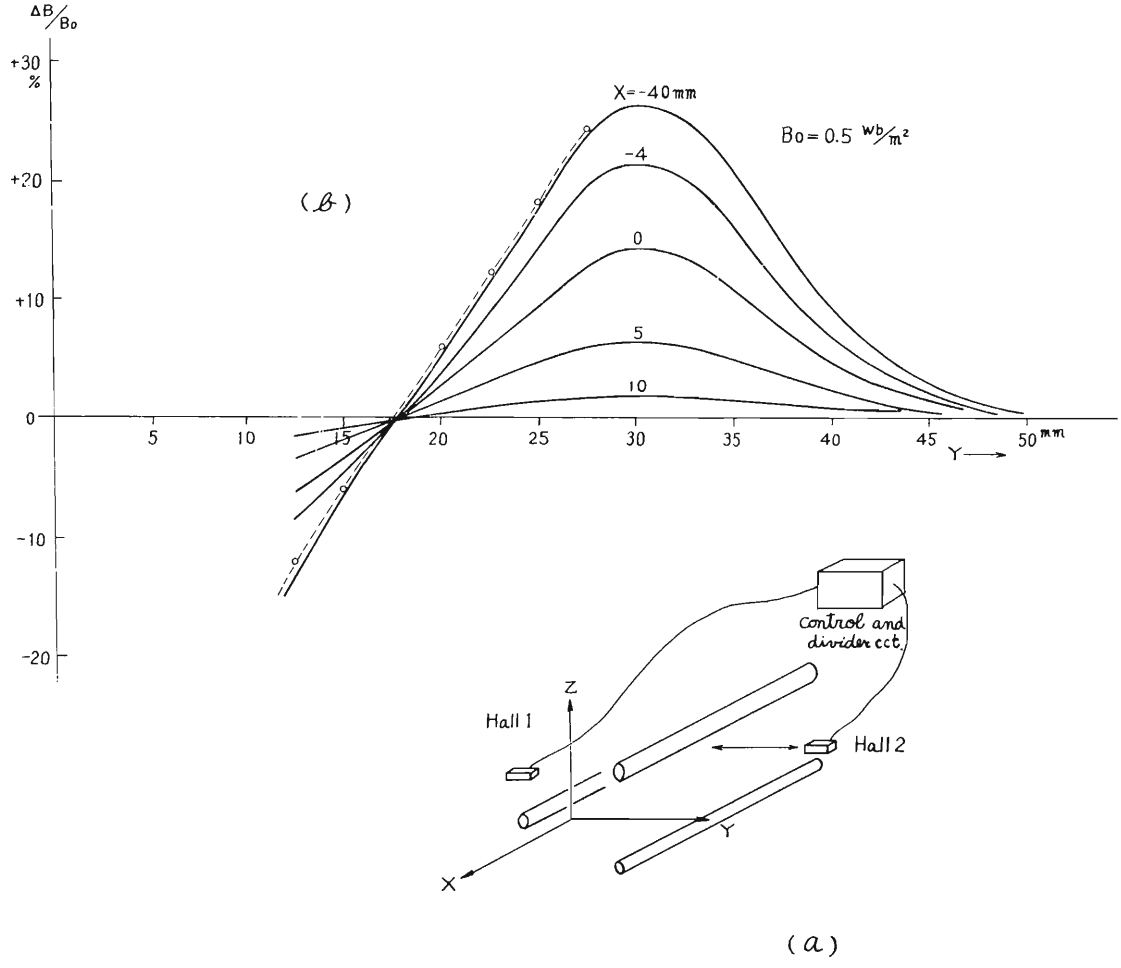

Fig. 2. Results of measurements on an iron channel of finite length. a. Configuration of measurements using two Hall method[5]); b. Field distribution in the median plane. Parameter is the distance inwards from the end. Open circle and dotted curve are the calculated values for an infinitely long channel.

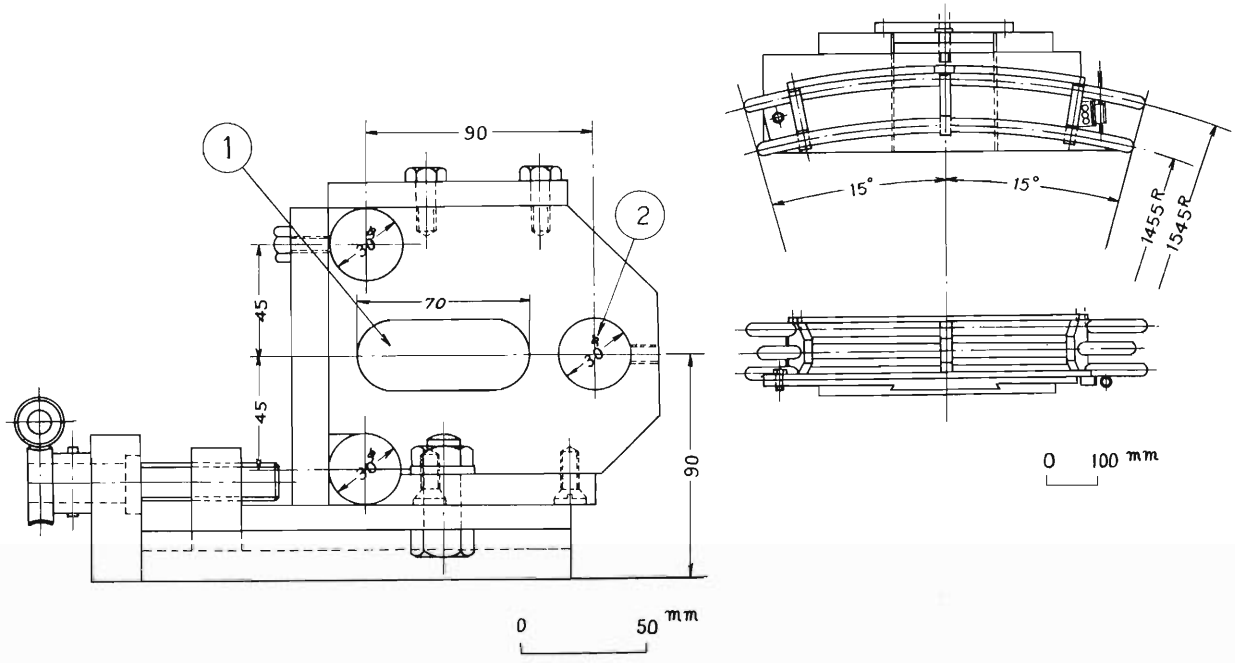

Fig. 3. Practical design. 1. Window for beam path; 2. Soft iron bar, 3.0 cm dia.

where the B-constant condition is not fulfilled perfectly. This result, that the end effect is limited in a small region near the end of a finite bar over a wide range of the field strength is encouraging. The distribution in the middle of the channel agreed well with the calculated one up to a value of B_0 of 13000 G. Since the magnetic field at the site where the channel is scheduled to be installed in the present case does not exceed 10000 G, these results are more than sufficient.

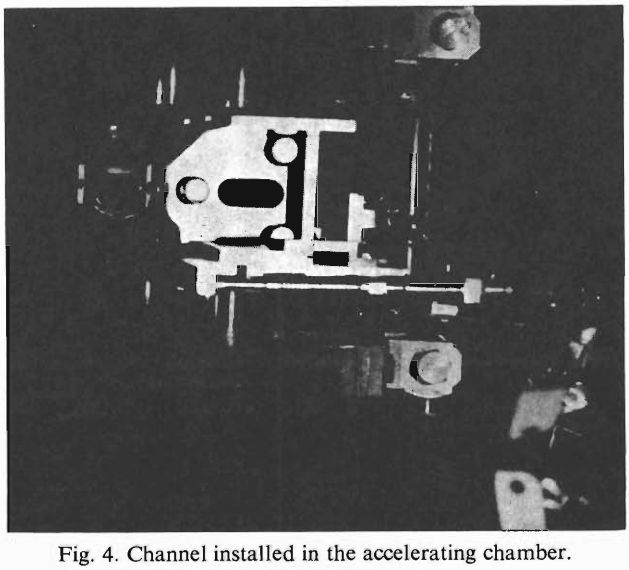

Fig. 4. Channel installed in the accelerating chamber.

The beam trajectories are calculated and the dimensions of the channel are chosen to obtain a slightly divergent beam at the exit of the accelerating chamber. Owing to insufficient knowledge of the beam properties at the entrance of the channel, a somewhat longer channel than needed was constructed and shortened by cut-and-try procedure to get a beam of the desired quality. Figs. 3 and 4 are the design and the photograph of the channel. It can be moved transversely to the beam direction in the median plane of the magnetic field and rotated horizontally around the pivot located at the entrance. All the position adjustments can be made from outside of the vacuum chamber through O-ring seals.

Small graphite plates to pick up beam currents were attached at the entrance and exit of the channel to monitor the behavior of the beam passing through it. No cooling of the channel was required in spite of its proximity to the dee.

4. Performance

The cyclotron was in operation for several months and the beam transport system was already installed and being used at the time of the design of the channel. Therefore, the channel was required not to deflect the beam path, but to converge the diverged beam along the central trajectory to increase the intensity of the beam accepted in the transport system.

Fig. 5 shows the plan view of the accelerating chamber. The position of installation of the channel is inscribed. Also the calculated trajectories of the beam with and without the channel, are drawn.

Undesirable disturbances of the magnetic field induced by the channel in the main field where ions are accelerated was measured. If it gives a large first harmonic component in the azimuthal distribution, the radial oscillation of the beam orbit will build up. As a consequence, the conditions for acceleration of ions in the dees and for clearing the deflector-septum canal will be changed. Fig. 6 indicates the variation of the azimuthal "bumps" as the distance from the center of the main field changes. As can be seen in the figure, the disturbance diminishes rapidly as the radius of the main field becomes smaller. It decreases faster than inverse square of distance from the channel. At $R = 60$ cm the azimuthal variation cannot be distinguished from that, originally existing in the main magnetic field. Even at 70 cm, which is 30 cm apart from the nearest bar of the channel and where the acceleration of ions gets near its end, the first-order harmonic component is not large enough, to cause an appreciable radial oscillation amplitude to the circulating beam. Actually, the beam comes out in the expected trajectory and a good extraction efficiency has been obtained. The disturbances of the magnetic field induced by the channel seem hardly giving bad effects on the acceleration of the ions, and any compensation measures are not necessary.

The beam quality was measured at the exit of the chamber by several methods. The first one was an array of graphite plates, permitting quick centering of the beam. Secondly, light sensitive di-azo papers used ordinarily for the duplication of documents were exposed to the beam and then developed. Its slow sensitivity to room light, ease of development and direct representation of the beam intensity distribution helped us very much to judge directly the quality of the beam. Fig. 7 shows some of the profiles taken in this way; (a), is from H_2^+ without the channel. The beam spreads out in the full width of the window. Shadows are for the sake of measurements of the beam direction. (b), is obtained by He_4^{++} with the channel of initial length. The focusing effect is too strong. (c), is the image of the H^+ beam after the channel is shortened by 20 cm. Thirdly we used several combinations of transversely

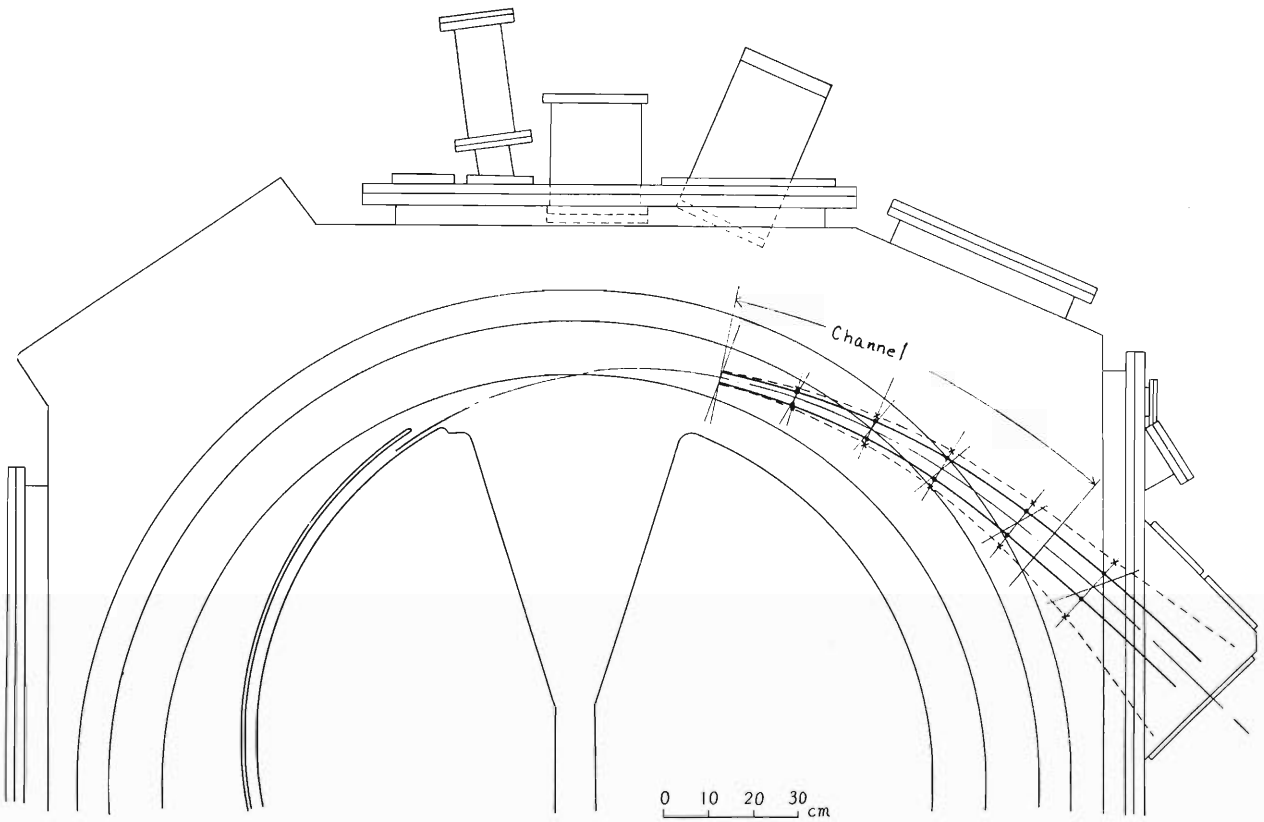

Fig. 5. Plan view of the accelerating chamber. Solid and dotted lines are the calculated trajectories of the beam, with and without the channel. The site of the installation of the channel is indicated.

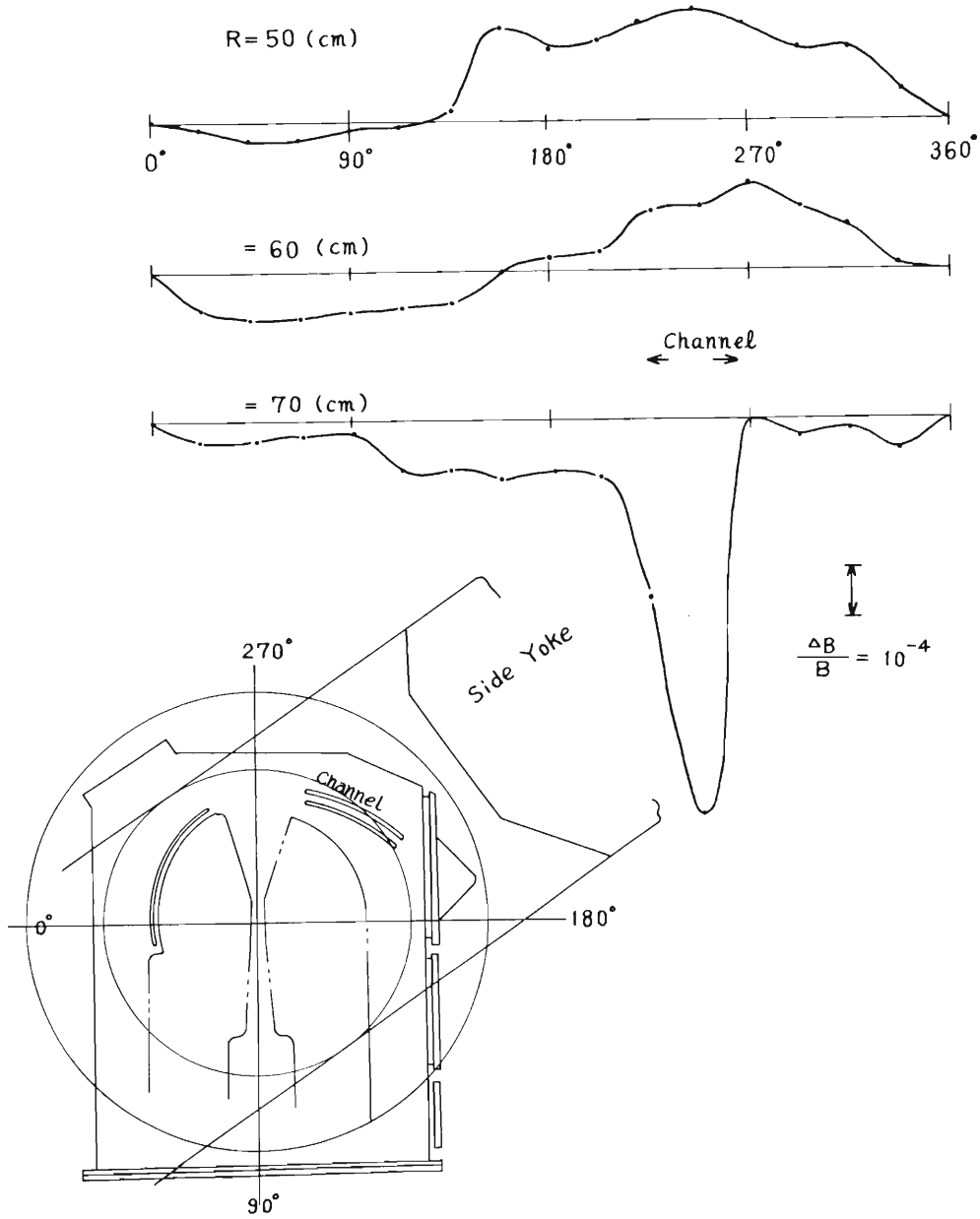

Fig. 6. Disturbance in the field of the main magnet.

travelling needle probes placed apart along the beam pipes.

After these measurements and some adjustments of positions of the channel, the intensity of the beam at the entrance of the beam transport system amounted from 60 to 90% of that emerged from the deflector channel. Thus over ten μA of proton, deuteron, α and ^{3}He beams could be utilized at the outside of the acceleration chamber. Also extraction of multiple-charged heavy ions became efficient. Moreover, activation of the accelerating chamber and beam pipes decreased. The channel itself hardly suffers activation, except the graphite pieces which detect the beam current or protect the iron from beam hitting. Most halflives of activities induced in graphite are generally short except that of ^{7}Be.

The authors express their thanks to H. Kumagai and K. Matsuda for their encouragement and discussions. Also helps of T. Karasawa, S. Motonaga and the cyclotron crew are much acknowledged for stable operation of the cyclotron and detailed measurements. Construc-

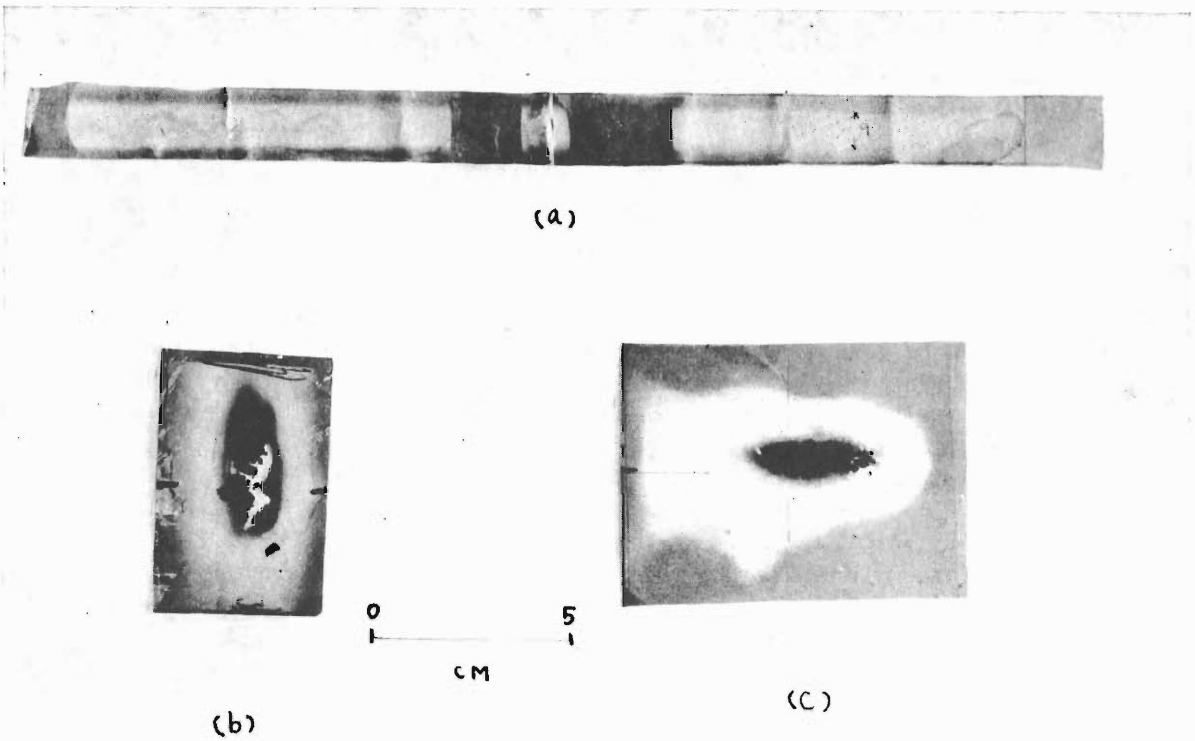

Fig. 7. Images on di-azo paper of beam profiles at the exit port of the accelerating chamber.
a. H_2^+, 18 MeV, before installation of the channel. Shadows are made by the metal plates. Width of the port is 240 mm.
b. $^4He^{++}$, 28 MeV, long channel. Length 80 cm.
c. H_2^+, 14 MeV, short channel. Length 60 cm.

tion of this apparatus was made by the machine shop of this Institute. Installation in the narrow space of the acceleration chamber which was a rather laborious task progressed largely by helps of A. Shimamura and N. Oosawa.

References

[1]) For instance, R. W. Müller and B. Berkes, Nucl. Instr. and Meth. **41** (1966) 151.
[2]) S. Suwa, J. Sanada, T. Karasawa, A. Suzuki, H. Ogawa, H. Yamaguchi, Y. Saji, S. Kikuchi, H. Kumagai, I. Hayashi, K. Matsuda and K. Nishimura, Nucl. Instr. and Meth. **5** (1959) 189.
[3]) R. S. Lord, E. D. Hudson, F. M. Russell and R. J. Jones, CERN 63-19 (1963) 297;
E. D. Hudson and R. S. Lord, Proc. Int. Symp. *Magnet technology* (1965) p. 700.
[4]) H. Kumagai, Nucl. Instr. and Meth. **6** (1960) 213;
H. Kumagai et al., INSJ-2 (1957) Report on the wide-range magnet for a 160 cm synchrocyclotron; Technical Report of Institute for Nuclear Study, Univ. of Tokyo.
[5]) M. Hemmi, T. Karasawa and S. Motonaga, Proc. Int. Symp. *Magnet technology* (1965) p. 472 (U.S. Dept. of Commerce, Virg. U.S.A.).

Reprinted from Jpn. J. Appl. Phys., 9, 532–541 (1970).

Acceleration of Multicharged Heavy Ions in IPCR (Riken) Ordinary 160 cm Cyclotron

Yoshitoshi MIYAZAWA, Tadao TONUMA, Isao KOHNO, Shunji NAKAJIMA, Toshihiko INOUE, Akira SHIMAMURA, Kisaku YOSHIDA and Takashi KARASAWA

The Institue of Physicai and Chemical Research, Yamato-machi, Saitama

(Received December 15, 1969)

In the *IPCR* (*Riken*) 160 cm ordinary cyclotron the operation ranges of electromagnet and radio frequency system are 0.5 to 2.0 wb/m^2 and 5.0 to 12.0 MH$_Z$ respectively, and various particles of different mass to charge ratios from proton to Ne^{5+} ion can be accelerated with variable energy.

Multicharged heavy ion sources of electron bombarded hot cathode type for this cyclotron have been developed to produce C^{4+}, N^{4+}, O^{4+}, N^{5+} and O^{5+} ions. At present these ions are produced in sufficient quantities under arc power of 2.0 to 2.5 kW. The source life is mainly limited by the erosion of tungsten cathode at about 20 hours.

The attenuation of beam current by charge exchange collision with residual molecules and the spectra of various ions accelerated in the cyclotron are discussed.

C^{4+}, N^{4+} and O^{4+} ions are accelerated up to 39 to 120 MeV, 45 to 100 MeV and 52 to 100 MeV respectively and used for several experiments.

§ 1. Introduction

The resonance condition at which a particle is accelerated in the cyclotron is given by

$$\frac{m}{q}=15.2\times\frac{B}{f}.$$

where m and q are the mass and charge of particle used respectively, in which the mass and charge of proton are taken as unity, B is the magnetic field strength in wb/m^2 and f is the oscillator frequency in MH$_Z$ of cyclotron.

In order to accelerate a heavy ion, it is necessary to make the oscillator frequency lower and the magnetic field higher in the design because the ratio of mass to charge (m/q) of a heavy ion is large compared with light ions such as proton and α particle.

The *IPCR* 160 cm ordinary cyclotron was constructed to use a magnetic field strength of 0.5 to 2.0 wb/m^2 corrected with four circular trim coils[1] and an oscillator frequency of 5 to 12 MH$_Z$ satisfied by a shorting plate and movable liners. As resonance conditions at the *IPCR* cyclotron shown in Fig. 1 limit the ratio of m/q of a heavy ion below 5.3, an ion source is required to produce multicharged ions of heavy elements such as carbon, nitrogen and oxygen.

The multicharged heavy ion source had been examined by the bench test since 1965, and in 1968 the first ion source, which had been already reported,[2] was used practically in the *IPCR* cyclotron.

The new ion source is described in this

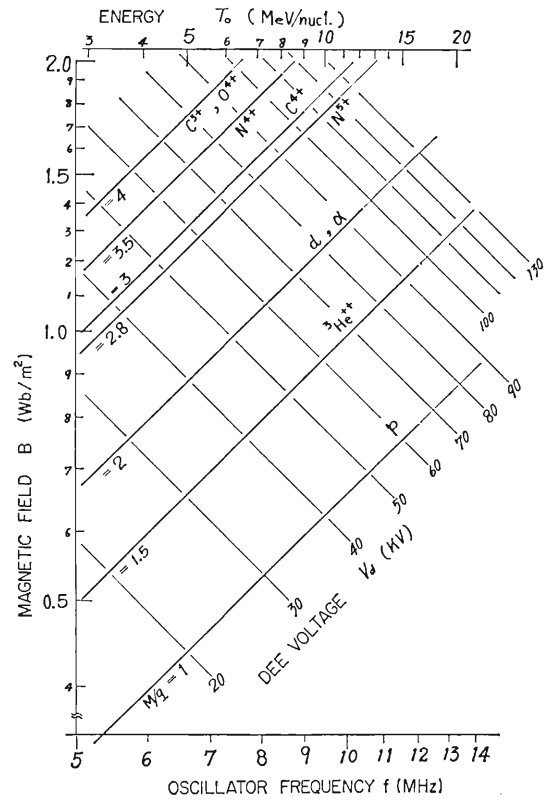

Fig. 1. The resonance condition of *IPCR* 160 cm variable energy cyclotron. Radius of beam exit is 74 cm.

Table I. Projectiles, Energy Range and Particle Yield.

Projectile	C^{3+}	C^{4+}	N^{4+}	N^{5+}	O^{4+}	O^{5+}
Energy (MeV)	39–75	39–120	45–100	45–160	52–100	52–140
Maximum ccrrent(uA)*	5	4	5	1	2	0.4

* Maximum beam current extracted from the cyclotron.

paper and, at present, C^{4+}, N^{4+} and O^{4+} etc. are accelerated at sufficient intensity as shown in Table I. The plane view of the *IPCR* cyclotron is shown in Fig. 2. In § 2 the construction and operation of the heavy ion source are described and in § 3 problems concerning the heavy ion acceleration, charge spectrum, beam attenuation with charge exchange, dee voltage and beam extraction are described.

§ 2. Multicharged Heavy Ion Source

2.1. *Construction of new ion source*

We have improved the first ion source,[2] and the new one is now operating satisfactorily. Most important feature of improvements is that mechanical rigidity and stability are much increased.

Fig. 3 is a cross sectional view of the source which is of electron bombarded hot cathode type similar to Morozov's.[3] The arc plasma is established between both tungsten cathodes K_1 (10 mm diameter, 8 mm length) and K_2 (10 mm diameter, 15 mm length). An arc chamber is constructed of a water cooled copper block and a copper chimney (84 mm length, ID 6 mm, OD 12 mm) which has a source aperture (2 mm × 10 mm). This chimney can be easily exchanged when the aperture has been eroded by ion bombardment. The gas is introduced into the arc chamber through several small holes (3 mm diameter,

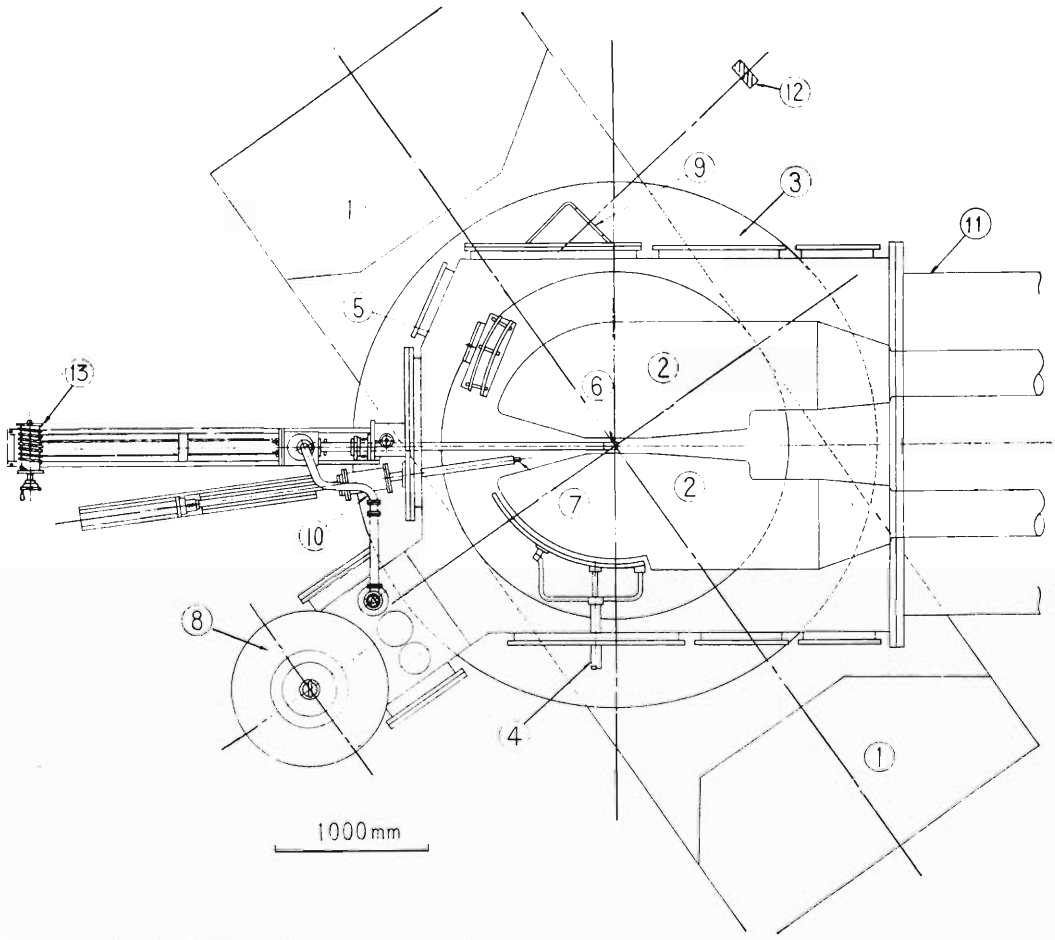

Fig. 2. The schematic view of the accelerating chamber arrangement.

1. Side yoke 2. Dees 3. Coil tank 4. *RF*-deflector 5. Beam focusing magnetic channel 6. Ion source 7. Beam probe 8. 32″ oil diffusion pump 9. Beam exit flange 10. Exhaust pipe for ion source 11. Oscillator tank 12. Gate drop probe 13. Winch

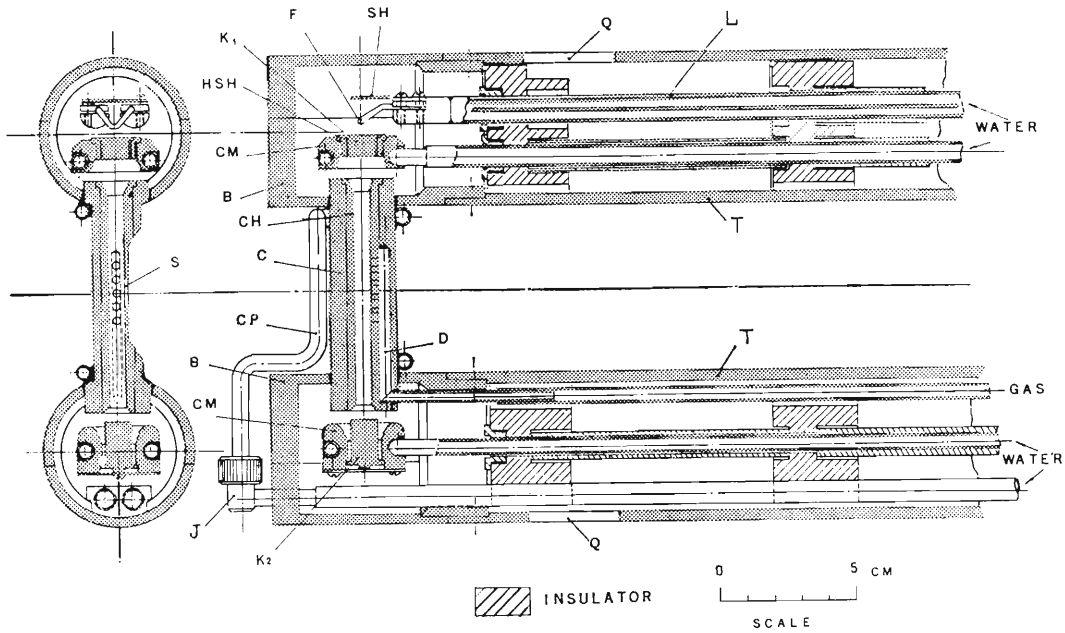

Fig. 3. Schematic view of the ion source.

K_1—Hot cathode (W)
CM—Cathode mount (copper and water cooled)
S—Source aperture
D—Distribution plenum
B—Anode box (copper)
F—Filament (W)
J—Cooling joint
L—Leading tube
K_2—Reflector cathode (W)
SH—Electron shield (M_0)
C—Anode block (copper and water cooled)
CH—Anode chimney (copper)
HSH—Cathode heat shield
Q—Exhaust window
T—Supporting tube

5 mm apart) from the distribution plenum (ID 4 mm) which is provided along the chimney.

The filament and cathode leading tubes are supported at the front top of the supporting tube supporting tube with a steatite space, and this spacer is covered with steatite sleeves to prevent the spacer from being coated with sputtered tungsten.

As the filament for electron bombardment a 2 mm diameter tungsten wire is used and heated by direct current, and this wire is strong enough not to be bent by Lorentz force in the strong magnetic field.

Two copper boxes (*B* in Fig. 3) are welded to the anode block which has a copper cooling tube. These anode system can be easily exchanged by loosening the joint (*J*) and separating the cooling pipe.

To prevent growth of sparks in the supporting tubes, there are exhaust windows (*Q*) (15 mm×30 mm) near the top of the supporting tube and a by-pass vacuum pipe at the end box of the supporting tubes, connected to the oil diffusion pump of the cyclotron. These evacuating devices are provided for making high vacuum in the supporting tube to take away the large out-gassing from the surfaces of the leading tubes, steatite spacer and supporting tubes.

Table II. A comparison between the first ion source and the new one.

	First ion source	New ion source
Anode made material	graphite not cooled	copper-water cooled
Alignment	unreliable	reliable
Life time	10-20 hours	above 20 hours
Exchange of anode	somewhat difficult	easy
Arc stability with CO_2 gas	unstable	stable

Stainless supporting tubes (*T*) in the new ion source are not cooled but there have been no trouble. A comparison between the first ion source and the new one is shown in the following Table II.

2.2. *Source operation*

Heavy ions, C^{4+}, N^{4+}, N^{5+}, O^{4+} and O^{5+},

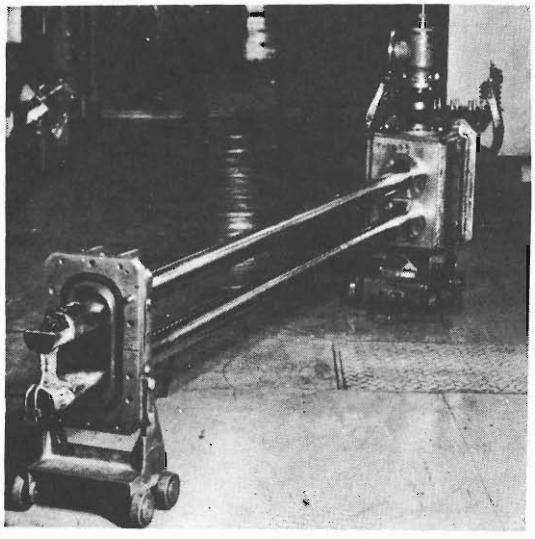

Fig. 4. (a) New heavy ion source.

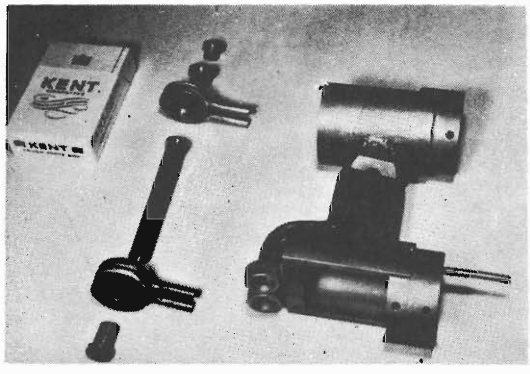

Fig. 4. (b) Disassembled parts from the arc chamber.
Left: upper cathode, heat shield, cathode mount, chimney, cathode mount and lower cathode from up to down, respectively.
Right: anode block.

were accelerated in the cyclotron. For production of nitrogen ions, nitrogen gas was introduced into the ion source, and for carbon and oxygen ions, CO_2 gas and oxygen gas respectively. The electron bombardment power required to burn the arc discharge was about 500 W (1.2 kV × 0.4 A).

The source was continuously operated with arc voltage (V_{arc}) of 250 to 400 V and current (I_{arc}) of 3 to 8 A, and then the arc power ($V_{arc} \times I_{arc}$) was 1.5 to 2.4 kW. The life of source was limited by erosion of the upper cathode. When the source was operated at arc power of about 2.0 kW, the source life was about 20 hours, and the source was restored after one hour by exchanging only the upper cathode. The cathode erosion occured at the ratio of 0.3 grams per hour. The chimney was exchanged after several tens of hours operation. The yield of ion beam extracted from the ion source and accelerated in the cyclotron was measured with an inner beam probe and a gate drop probe (Fig. 2). Fig. 5 shows the variation of yields of N^{4+}, N^{5+} and C^{4+} versus the flow rate for various constant arc voltages and currents. It is shown that the smaller gas flow brings about the higher yield of multicharged ions. For the starting of discharge, somewhat large gas flow has been necessary. After the discharge was started, the gas flow was reduced as small as possible without extinguishing the discharge. Towards the end of the cathode life, the gas flow needed to start the discharge was three or five times larger than that of usual operation. The arc discharge of CO_2 gas was kept at a smaller gas flow rate than that of N_2 gas.

Fig. 6 and 7 show the variation of yields N^{4+}, N^{5+} and C^{4+} versus the arc power and arc voltage at various constant gas flow rates. These arc conditions for the constant gas flow were produced by varying the electron bombardment power. Both N^{4+} and N^{5+} yields increase with the arc power and, especially, N^{5+} yields for the arc voltage of 340 V reaches about four times when the arc power is varied from 1.5 to 2.4 kW. When the arc power is kept constant, both yields increase with increase of the arc current and decrease of the arc voltage to the optimum value. As shown in Fig. 7, the C^{4+} yield becomes maximum at an arc voltage from 260 V to 300 V when the arc power is kept constant. In the case of oxygen ions, yield variations with gas flow rate, arc power and voltage showed almost the same features as nitrogen and carbon ions.

§ 3. Heavy Ion Acceleration

3.1. *Accelerated heavy ion in the cyclotron*

In the source an arc plasma was established stably using N_2, O_2, CO_2 or Ne gas. To know the kinds of multicharged heavy ions in the cyclotron, the m/q spectra of accelerated ion beams were measured with a beam probe fixed at the radius of 65 cm (see Fig. 2) by varying the magnetic field strength from 0.5 to 2.0 wb/m^2 under the conditions of constant oscillator frequency and dee voltage.

The spectrum measured is shown in Fig. 8(a) when CO_2 is fed in the source. In this figure (3), (5) and (7) mean the numbers of harmonics of acceleration mode. In this case,

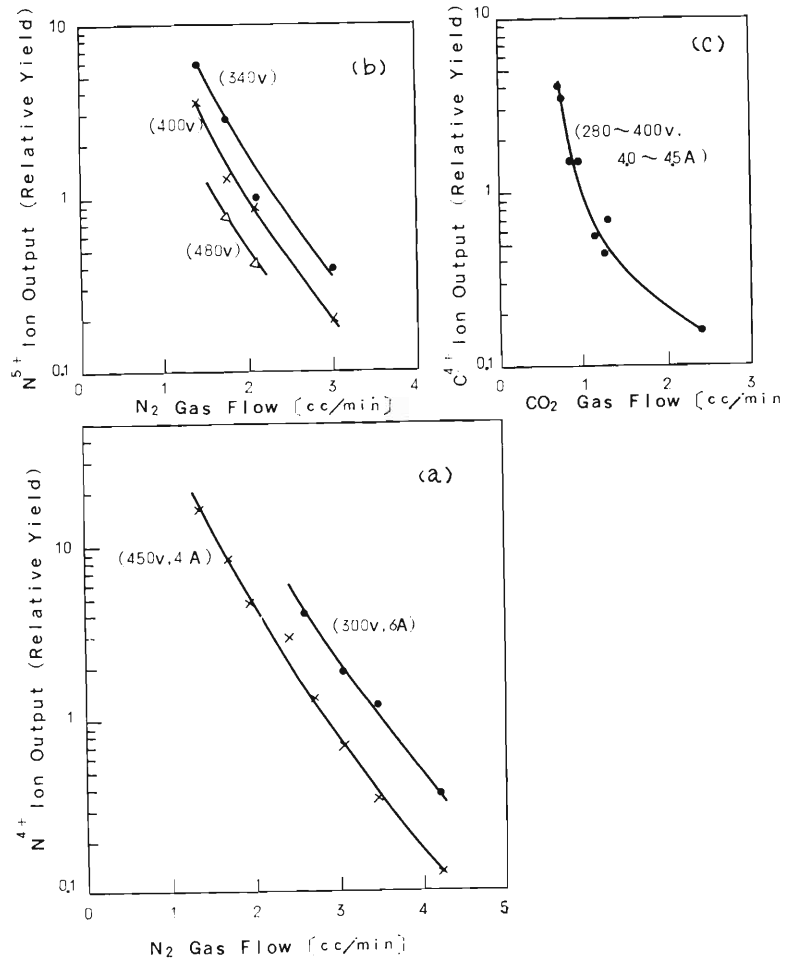

Fig. 5. (a) The N^{4+} ion relative yield *vs* N_2 gas flow rate. ( ) represent arc voltages and currents.
(b) The N^{5+} ion relative yield *vs* N_2 gas flow rate. ( ) represent arc voltages.
(c) The C^{4+} ion relative yield *vs* CO_2 gas flow rate. ( ) represent arc voltages and currents.

four kinds of beams are measured at relatively high intensity. They are C^{2+} and O^{2+} ions accelerated with the 3rd harmonic frequency, C^{4+} ion and mixture of C^{3+} and O^{4+} found at the ratio $m/q=4$.

As shown in Fig. 8(b), it is found that the spectra not only of N ions but also of C and O ions are detected when the N_2 gas is fed in the source. Carbon peaks may come from oil vapour of vacuum pump, vacuum grease, or residual CO_2 gas in the gas supply system, because the anode is made of copper.

Fig. 8(c) shows the spectrum of O_2 gas. The O ions are mainly detected, but small quantities of C and N ions can be detected, too. O^{4+} and C^{3+} ions have the same ratio of m/q and cannot be distinguished. The contamination of C^{3+} ion in O^{4+} ion is estimated to be about 5% by passing the deflected beam through a thin foil. If a pure O ion beam is wanted, it is desirable to accelerate O^{5+} ion although its beam current is small.

When Ne gas is fed in the source, the spectrum is shown in Fig. 8(d). In this case, not only ^{20}Ne ion but also a little amount of its isotope ^{22}Ne ion, are detected. The N ion is also detected, and this is supposed to be due to the fact that the gas feed pipe has not evacuated sufficiently after supply the nitrogen gas. A small peak with $m/q=4$ is assigned to mixture of C^{3+}, $^{20}Ne^{5+}$ and O^{4+} ions. The harmonic accelerated ions cannot be extracted from the cyclotron because in the *RF*-deflector the dee voltage only is employed as the deflector voltage.

3.2. *Beam attenuation during acceleration (in relation to charge exchange effect)*

The beam attenuations for proton, deuteron and α-particle are not remarkable for the radius from 40 cm to 70 cm, as shown by curve (a) in Fig. 9. However it is remarkable in the case of multicharged heavy ion as curve (b) in Fig. 9.

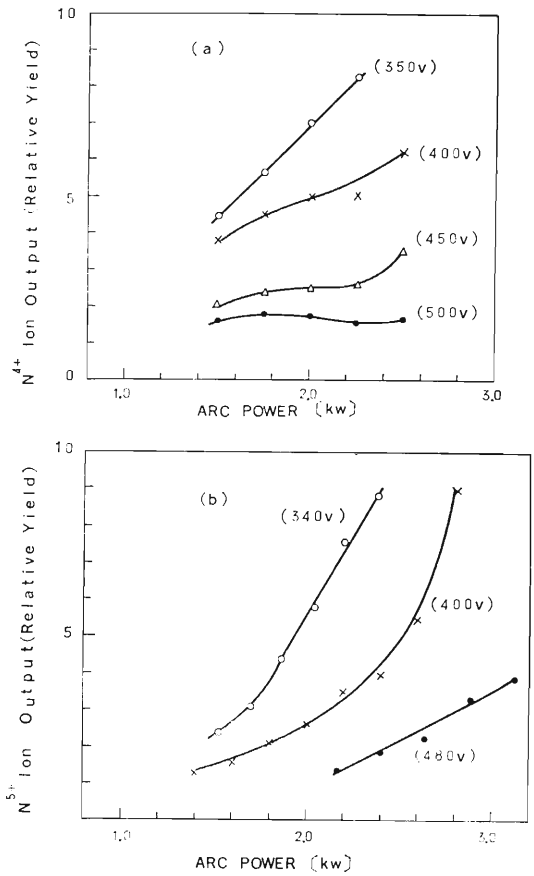

Fig. 6. (a) The N^{4+} ion relative yield *vs* arc power. N_2 gas flow rate are 2.4 cc/min and ( ) represent arc voltage.
(b) The N^{5+} ion relative yield *vs* are power. N_2 gas flow rate are 1.9 cc/min and ( ) represent arc voltage.

Collision with residual gas causes charge exchange which breaks down the resonance condition of particles.

Fig. 10 shows the ratio of N^{4+} beam current measured at 70 cm radius to that at 40 cm radius (maximum radius is 74 cm) versus the pressure of the accelerating chamber of the cyclotron. It is found that the ratio decreases rapidly with the pressure. The pressure of the chamber was varied by adjusting the nitrogen gas flow introduced into the ion source. The pressure of the accelerating chamber near the diffusion pump is shown in Fig. 10, but it is noticed that the pressure in dees, where ions are accelerated, is 3~4 times larger than that in the chamber.

When the cross section for the process which changes the charge state of nitrogen ion from 4+ to 5+, the path length of ions during acceleration and the pressure in the dees are given, the ratio of attenuation caused by charge exchange can be calculated. In Fig. 10 the solid line represents the results of the calculation using the charge exchange cross section data measured by Dmitriev[4] and by the authors, and it agrees well with the measured values.

If the ratio of the beam attenuation should be kept at larger than a half, it is necessary that the pressure is reduced below 4×10^{-6}

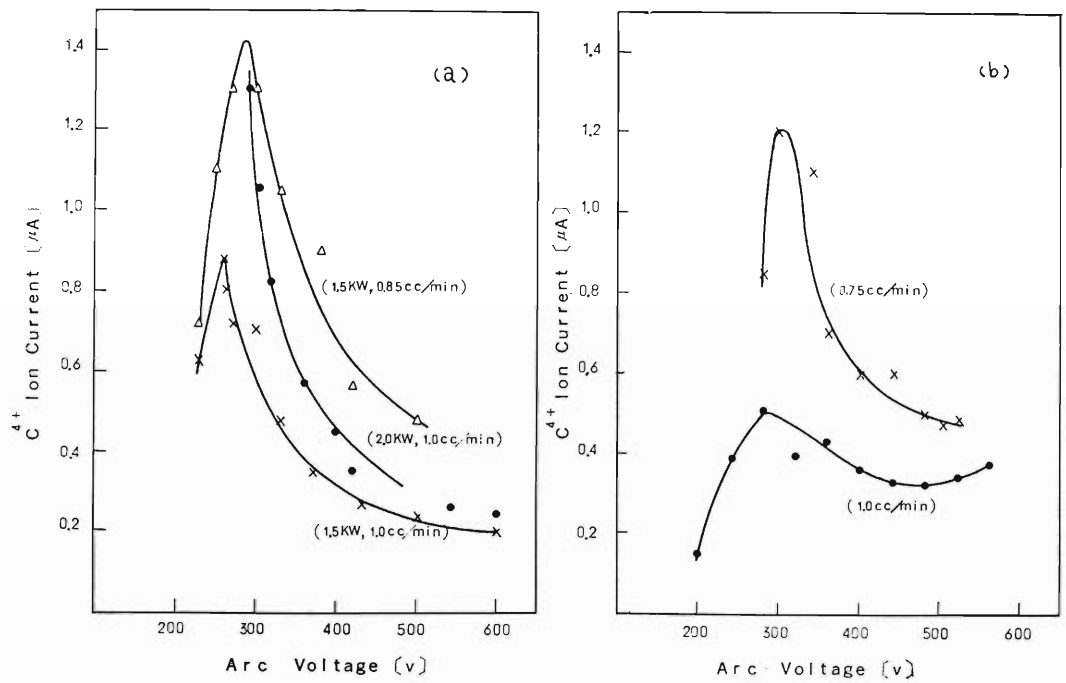

Fig. 7. (a) The C^{4+} ion yield *vs* arc voltage. ( ) represent arc power and CO_2 was flow rate, respectively.
(b) The C^{4+} ion yield *vs* arc voltage when arc current is 5.0 A constant. ( ) represent CO_2 gas flow rate. Radius of beam probe position is 60 cm.

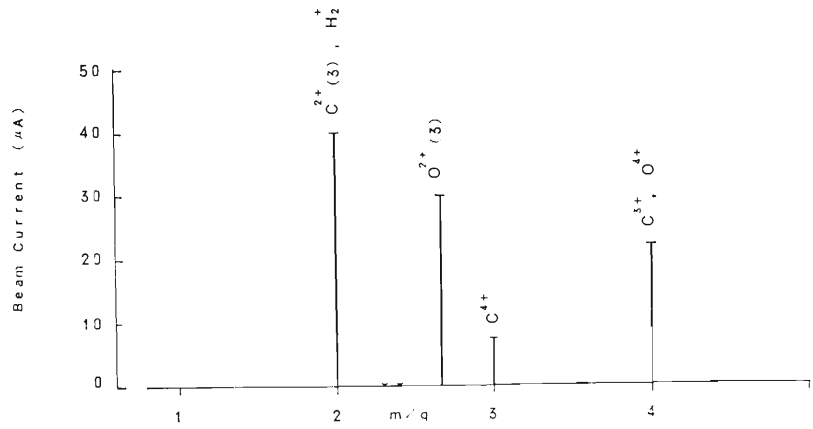

Fig. 8. (a) The m/q spectrum of the ion beam when CO_2 gas was fed in the source. f=7.078MHz, V_d=60 kV, arc power=360^V×3.1^A Radius of beam probe position is 65 cm.

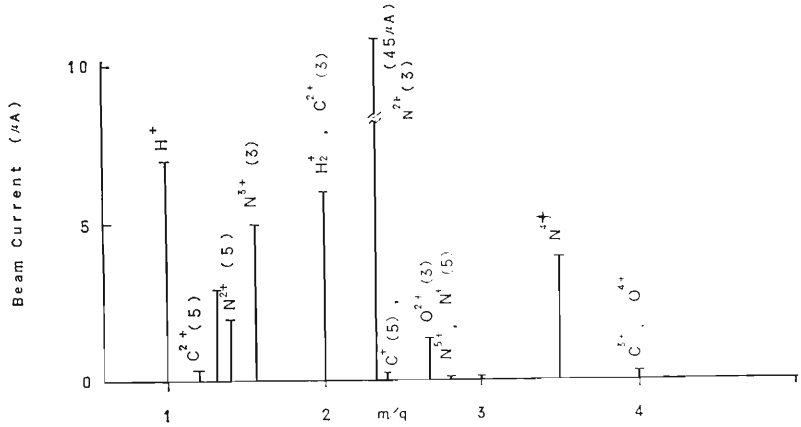

Fig. 8. (b) The m/q spectrum of the ion beam when N_2 gas was fed in the source. f=6.468 MHz, V_d=47 kV, arc power=320^V×3.4^A.

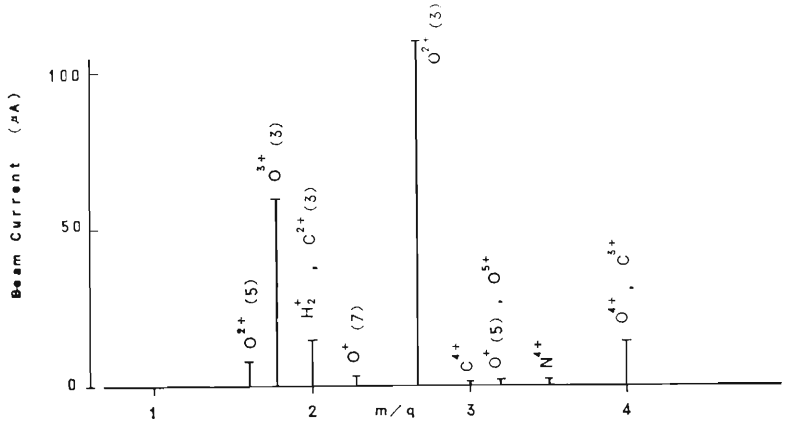

Fig. 8. (c) The m/q specrum of the ion beam when O_2 gas was fed in the source. f=6.48 MHz, V_d =50 kV, arc power=410^V×3.5^A.

Torr. Under the normal condition the pressure of accelerating chamber is $2\sim4\times10^{-6}$ Torr.

3.3. *Dee voltage and beam extraction*

In an ordininary cyclytron the threshold values of dee voltage exists for accelerating the ion to the maximum radius. Usually the cyclotron is operated at the dee voltage somewhat larger than the threshold voltage, and we call this voltage the required dee voltage. The required dee voltage for the energy per nucleon of ion is shown in Fig. 11. At the oscillator frequency below 7 MHz, the gap between the dees and the movable liners is narrow. When the ions are not accelerated, the relation between their gap and

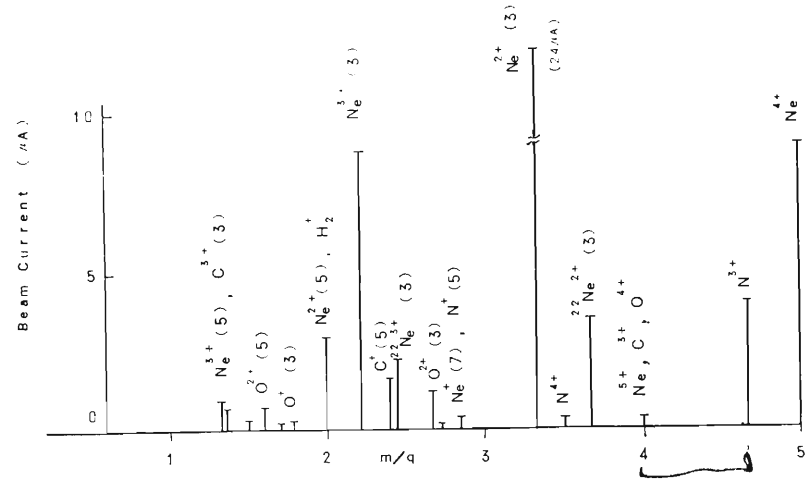

Fig. 8. (d) The m/q spectrum of the ion beam when Ne gas was fed in the source. $f=6.0\,MH_z$, $V_d=45\,kV$, arc power$=410^V\times4^A$.

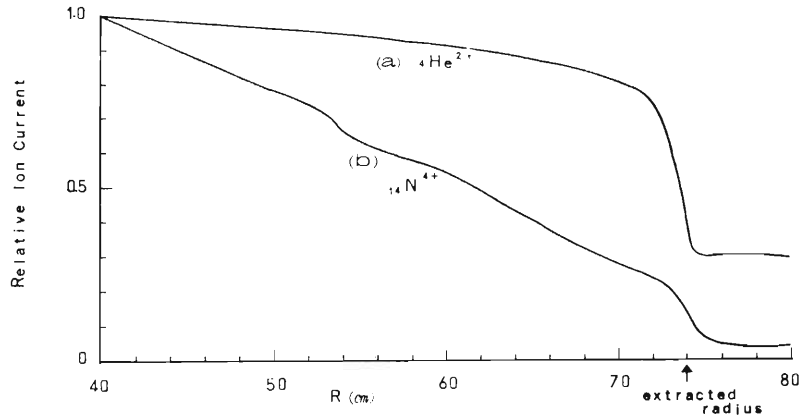

Fig. 9. Beam attenuation *vs* radius.
(a) $^4He^{2+}$ (b) N^{4+}
pressure$=8\times10^{-6}$ Torr, frequency$=6.50\,MH_z$.

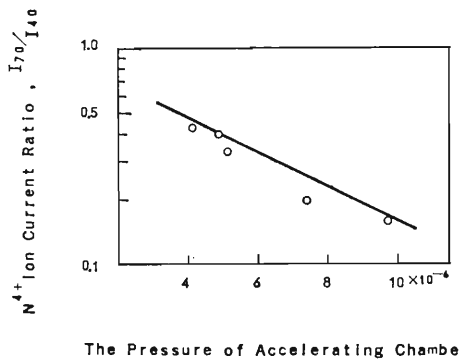

Fig. 10. Beam attenuation *vs* pressure.
○: measured value, solid line: calculation using charge exchange cross section and path length of ion. The pressure in dees is three times larger than the accelerating chamber.

the dee voltage obtained without electric discharge is shown in Fig. 12. For the acceleration of C^{3+} and O^{4+} ions with $m/q=4$ at the energy of 6.5 MeV/nucl., the resonant magnetic field strength is maximum (2.0 wb/m^2) and at the same time the required dee voltage is maximum without the electric discharges. The maximum energies of internal beam which has the ratio of m/q lower than 4 are defined by the dee voltage, and the minimum energies of their ions are limited by the frequency of oscillator. In order to extract the ions from the cyclotron through the deflector channel some electric field (E_{def}) between the deflector and the septum is needed. In the case of our cyclotron the deflector is of a *RF*-typeem ploying a dee voltage only. In this cyclotron the radial distribution of magnetic field is not varied with the change of exciting currents and the relativistic mass increase of accelerated ion is not so large. Therefore, the electric field for the extraction of ions may be expressed as follows:

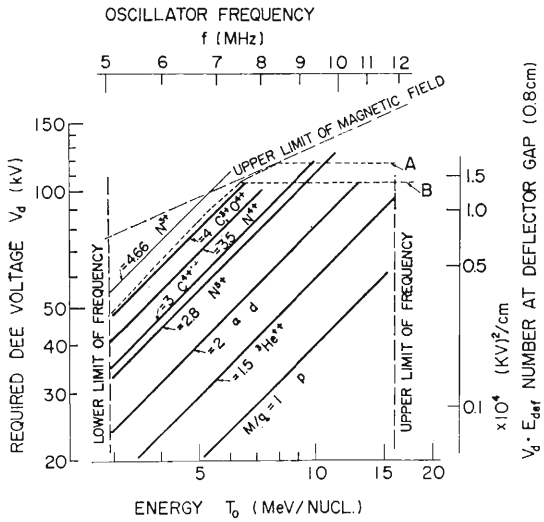

Fig. 11. Required dee voltage for the energy per nucleon of various particles.

A: limit of maximum dee voltage.

B: limit of $V_d \cdot E_{\mathrm{def}}$ at the deflector.

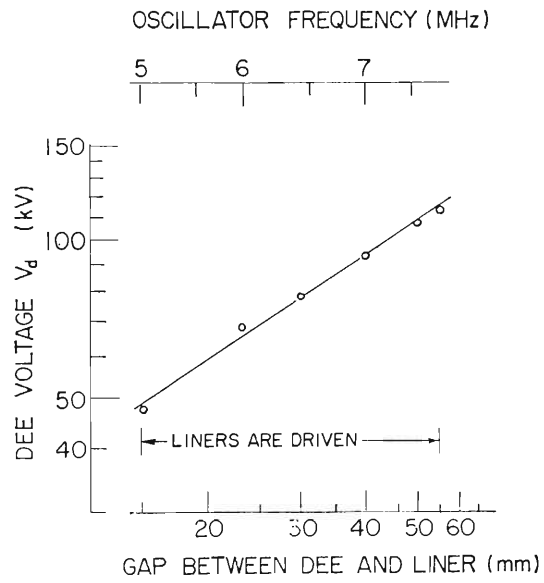

Fig. 12. Relation of the obtained dee voltage and the gap between dee and liner.

$$E_{\mathrm{def}}=\frac{V_d}{g}\propto\frac{m}{g}\cdot T_0,$$

where T_0 is the ion energy per nucleon and g is the gap between deflector and septum. In the normal operation, the 10 MeV proton is accelerated at the dee voltage of 40 kV and the deflector gap is so adjusted that the electric field not less than 40 kV/cm is applied for the extraction. In the frequency region above 8 MHz, the dee voltage was mainly limited by the electric discharges between the deflector and the septum.

The tendendency to spark across a vacuum gas is typified by the product $V \cdot E$. The maximum $V \cdot E$ number at the deflector gap is about 1.7×10^4 (kV)^2/cm without ion beam and about 1.4×10^4 (kV)^2/cm with ion beam. Usually the deflector gap is used at about 6 to 10 mm. Therefore, the maximum energy of external ion beam is limited by the $V \cdot E$ number at the deflector channel as shown in Fig. 11. The N^{5+} ion was accelerated up to 160 MeV using the precession at the dee voltage somewhat lower than that in the normal operation. The ions such as C^{2+}, N^{2+} and O^{2+} accelerated by the third harmonic mode were observed large enough internal ion beam, but they could not be extracted from the cyclotron since the deflector is of a *RF*-type which employs a dee voltage only. If the deflector is modified to that of *DC* type, the harmonic accelerated ions may be extracted from the cyclotron.

§ 4. Conclusion

The ion sources for the multicharged heavy ions developed in this Laboratory are used for studies of nuclear physics, nuclear chemistry, radiation chemistry and biology with good reliability. The special features of the source are mechanical rigidity of the chimney and good vacuum in the supporting tube to prevent growth of discharge. The source is operated continuously for about 20 hours and easy to repair within one hour.

The operating conditions which affect the yield of multicharged ions, such as gas flow, arc voltage and arc current, are examined. When the gas pressure in the chimney is low, the yield of multicharged ions increases.

In the ion source it is supposed that multicharged heavy ions are mainly produced in the process of ionizing step by step, because the quantities of C^{4+} and N^{4+} reach the maximum values at relatively lower arc voltage of 250 to 300 V under constant arc current.

Spectra of the accelerated beams are presented. These spectra show that the beam intensities of low charged ions accelerated by the fundamental mode with the same dee voltage.

The attenuation of the ion beam current caused by the charge exchange is seen. It depends on the pressure in the cyclotron and the path length of the ions. Then, it is necessary for the acceleration of heavy ions that the pressure in the cyclotron is lower

and the dee voltage is higher.

At present, the heavy ions accelerated in the *IPCR* 160 cm cyclotron arc C^{3+}, C^{4+}, N^{4+}, N^{5+}, O^{4+} and O^{5+} ions. The limits of their energies are restricted not only by the region of electromagnetic and oscillator frequency, but also by the dee voltage which is required to accelerate the ion to the maximum radius. The N^{3+} ions cannot be acelerated for the latter reason.

It is more difficult in general to extract heavy ion beam because the ratio of m/q is larger. Though the *RF* deflector of this cyclotron is not always effective for the extraction ion beam, this method enables one to extract several ion beams which reach the maximum radius inside dees. But ions beams of higher energy and ion beams accelerated by a higher harmonic mode cannot be extracted because of the lack of dee voltages and the presence of *RF* deflector, respectively.

It will be necessary in the future to develop an ion source in which other heavy elements are used to produce their ion beam and to investigate a method of extracting ion beam accelerated by a higher harmonic modes.

Acknowledgements

The authors wish to express his cordial thanks to H. Kumagai for his advice and encouragement, and they express their sincere thanks to T. Inamura and the cyclotron operating crew for their helpful cooperation throughout the present work.

References

1) N. Nakanishi, S. Motonaga, Y. Miyazawa and T. Karasawa: Japan. J. app. Phys. **8** (1969) 1226.
2) I. Kohno, T. Tonuma, Y. Miyazawa, S. Nakajima, T. Inoue, A. Shimamura and T. Karasawa: Nuclear Instrum. **66** (1968) 283.
3) P. M. Morozov, B. N. Makov, M. S. Ioffe: Atomyana Energiya **2**, (1957), 272.
4) I. S. Dmitriev, V. S. Nikolaev, L. N. Fateeva Ya. A. Teplova: Soviet Physics-JETP **15** (1962) 11.

Reprinted from Jpn. J. Appl. Phys., 9, 1306–1311 (1970).

Charge Exchange of Carbon and Nitrogen Ions in Nitrogen Gas

Tadao TONUMA, Yoshitoshi MIYAZAWA, Takashi KARASAWA and Isao KOHNO

The Institute of Physical and Chemical Research, Yamato-machi, Saitama

(Received July 20, 1970)

Electron loss and capture cross section of carbon and nitrogen ions were measured at 3.5~7 MeV/nucl., *i.e.* velocities of $2.6\sim3.7\times10^9$ cm/sec in nitrogen gas. Cross sections obtained were σ_{45}, σ_{56}, σ_{65}, for carbon ions and $\sum_{k=5}^{7}\sigma_{4k}$ for nitrogen ions when they passed through the charge exchange (collision) chamber. Cross sections of single electron loss σ_{45} and σ_{56} are nearly proportional to v_0/v and those of single electron capture σ_{65} are proportional to $(v_0/v)^6$, where v_0 is the atomic unit of velocity and v is ion velocity.

This paper reports also on the comparison between the beam attenuation of N^{4+} ions, which were accelerated in the IPCR 160 cm cyclotron, caused by charge exchange at collisions with residual gases, and the attenuation calculated from measured $\sum_{k=5}^{7}\sigma_{4k}$ in nitrogen gas.

§ 1. Introduction

The capture or loss of an electron by a fast ion upon colliding with an atom is one of the most important phenomena accompanying the passage of fast atomic particles through matter. Interest in these phenomena in the range of ion velocity $V > V_0(=e^2/\hbar)$ arises mainly in connection with the problems of obtaining fast multicharged ions in accelerators and also with the topic of energy loss of these ions in matter. For example, uranium accelerators proposed in Oak Ridge[1] and HILAB,[2] which are composed of two stage accelerators, require to produce multicharged ions caused by charge exchange with a stripper provided between the two accelerators for accelerating the particles effectively. The range and energy loss of heavy particles passing through matter depend on effective charge of these ions.[3] Measurements of cross sections of electron loss and capture of ions are required to interpret quantitatively the beam attenuation of ions during acceleration in an accelerator. However, owing to experimental difficulties, the effective cross section of loss or capture of electrons in the high velocity range had been studied until now for the atoms and ions of hydrogen and helium[4] and the electron loss and capture by heavy ions ($Z=2\sim18$) had been investigated mainly at ion energy $E<1$ MeV/nucl.[5,6] Cross sections of electron loss and capture by iodine ions have recently been measured.[7] However, for heavy ions, information existed mainly on the charge composition of ion beams in an equilibrium state after they have passed through a rather thick layer of matter.[8-12]

Now C^{4+} and N^{4+} ions are accelerated in the IPCR (RIKEN) 160 cm cyclotron[13] at energies of 40 to 85 MeV and 50 to 100 MeV, respectively.[14,15] It is able to carry out charge exchange of heavy ions using C^{4+} and N^{4+} ions of 3.5 to 7 MeV/nucl. This paper reports the apparatus of experiments and the experimental results of the cross sections of electron loss and capture by C^{4+} and N^{4+} ions in nitrogen gas and explains quantitatively the beam attenuation of N^{4+} ion in the IPCR cyclotron.

§ 2. Procedure

2.1. *Experimental apparatus*

Cross sections of electron loss and capture were measured, using an apparatus shown in Fig. 1. Multicharged ions of C^{4+} and N^{4+} accelerated in the IPCR cyclotron are deflected at 45 degrees by a deflecting magnet (DM) and arrive at the analyzing magnet (AM) by which the charge states of ions are analyzed after they have traversed the charge exchange (collision) chamber. The

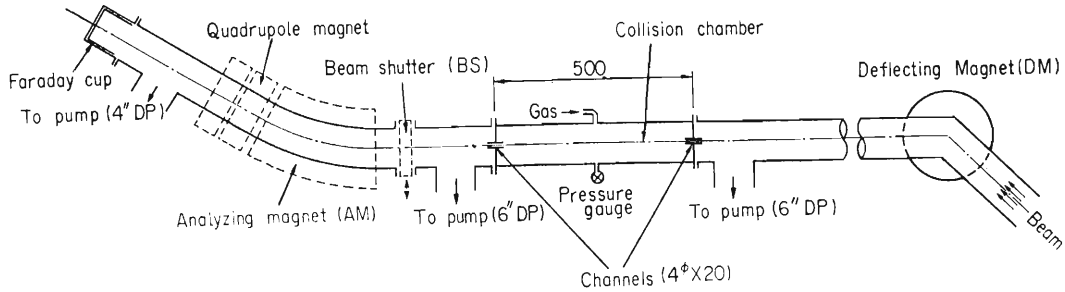

Fig. 1. Diagram of apparatus.

analyzing magnet, of which the field strength varies from zero to $8k$-gauss and the radius of curvature is 1.6 meters, deflects the ions by 35 degrees. Each ion that has been changed into several charge states of ions in the collision chamber and deflected by the analyzing magnet, is focused by a quadrupole magnet and arrives at a Faraday cup with a spot of less than 1 cm in diameter. Both the analyzing magnet and the quadrupole magnet are, therefore, adjusted according to the individual charge states of ions. The collision chamber consists of a cylinder of 2″ in diameter and 50 cm long with inlet and exit channels of 4 mm in diameter and 20 mm long. On both sides of the collision chamber a 6″ oil diffusion pump (400 l/sec) is provided to keep the adjoining vacuum space at sufficiently low pressure. When target gas is admitted to the chamber continuously, the pressure of this vacuum space becomes 10^{-3} times that of the collision chamber. The pressure in the chamber varies from 1×10^{-3} to 4×10^{-1} Torr for nitrogen gas. The final pressure in the chamber is about 5×10^{-4} Torr when no gas is supplied. The pressure gauges used are a high pressure ionization gauge and a Pirani gauge with $\pm10\%$ accuracy calibrated with a MacLead gauge.

The relative amount of ions (F_k) of charge state k is experimentally calculated by the following formula:

$$F_k=\frac{\frac{I_k}{k}\cdot\frac{1}{I_s(k)}}{\sum\limits_k \frac{I_k}{k}\cdot\frac{1}{I_s(k)}}, \qquad (1)$$

where I_k is the current of ions of charge state k measured by the Faraday cup, $I_s(k)$ is the total ion current which traverses the collision chamber. $I_s(k)$ is measured using the beam shutter (BS) as the probe, which moves remotely by air pressure. Measurements of I_k and $I_s(k)$ were repeated alternatively in short time.

2.2. *Mathematical analysis*

The variation of the charge composition of an ion beam while it passes through a matter is given by a system of differential equations:

$$\frac{dF_k}{d\pi}=\sum_j F_j\sigma_{jk}-F_k\sum_j\sigma_{kj} \quad (j\neq k), \qquad (2)$$

where F_k is the relative amount of ions of charge k in the ion beam ($\sum\limits_k F_k=1$), π is the number of gas atoms in a volume with 1 cm^2 cross section along the ion path ($\pi=\int N\,dl$, where N is the number of gas atoms per cm^3 and dl is an ion path element in the gas), σ_{jk} with $j\neq k$ is the cross section for the process which changes the ion charge from the initial value j to k, and $k>j$ and $k<j$ represent electron loss and capture, respectively. The cross sections are, therefore, calculated by solving eq. (2).

As shown by the experiment, even before the collisions with the atoms of the material appreciably alters the velocity of the ions, the charge on the particles undergoes repeated change and an equilibrium charge distribution is established in the ion beam. The latter is independent of the charges of the ions before they enter the material, and is fully determined by the relation between the effective cross sections for loss and capture of electrons, when the equilibrium state is attained, $dF_k/d\pi=0$, so that instead of (2) we have

$$\sum_j F_{j\infty}\sigma_{jk}-F_{k\infty}\sum\sigma_{kj}=0, \qquad (3)$$

where $F_{j\infty}$ and $F_{k\infty}$ are the relative amounts of ions of charge j and k in the equilibrium distribution, and are equal to the limiting values of F_j and F_k as $\pi\to\infty$ by eq. (2).

§ 3. Experimental Results

3.1. *Cross sections of electron loss and capture by carbon ions in nitrogen gas*

Charge exchange experiment was carried out in nitrogen gas using C^{4+} ions at energies of 39, 50 and 78 MeV. Figure 2 shows the relation between charge distribution and gas target thickness (Torr. cm) of nitrogen gas in the collision chamber for carbon ions of 50 MeV. F_4, F_5 and F_6 represent the relative amounts of C^{4+}, C^{5+}, C^{6+} ions respectively determined by the eq. (1). The energy loss of ions by gas of maximum Torr. cm is assumed to be about 20 KeV. As shown in Fig. 2, F_4 decreases exponentially with the gas target thickness, F_5 increases until up to a certain value of gas target thickness and decreases beyond this thickness, and F_6 increases with the thickness. At a higher gas target thickness F_k (k=4, 5, 6) attain an equilibrium state. When no gas is admitted to the collision chamber, F_5 and F_6 are detected at about 0.04 and 0.004 respectively, depending on the residual gas in the system. Therefore, each relative amount of ions is determined with accuracy of about 5% for residual gases and other errors. The relation of charge distribution versus gas target thickness varies with energy of incident particle. This means that the cross sections of electron loss and capture depend on the ion energy.

When C^{4+} ion was an incident particle in the region of 39 to 78 MeV, the relative amounts of $F_k(k\leq 3)$ of C^{3+} and C^{2+} ions etc. could not be observed. It shows that the cross sections of σ_{43}, σ_{42}, σ_{32} are equal to zero.

From the measurements it was found that $F_{4\infty}$ is zero in the region above 39 MeV, or $\sigma_{54}=\sigma_{64}=0$. Thus, the charge composition of ion beam is expressed by the following equation from (2):

$$\begin{pmatrix} \frac{dF_4}{d\pi} \\ \frac{dF_5}{d\pi} \\ \frac{dF_6}{d\pi} \end{pmatrix} = \begin{pmatrix} -(\sigma_{45}+\sigma_{46}) & 0 & 0 \\ \sigma_{45} & -\sigma_{56} & \sigma_{65} \\ \sigma_{46} & \sigma_{56} & -\sigma_{65} \end{pmatrix} \begin{pmatrix} F_4 \\ F_5 \\ F_6 \end{pmatrix} . \quad (4)$$

Cross sections of electron loss and capture can be calculated by eq. (4). Considering the initial condition and the equilibrium state in eq. (4), the solutions of F_k (k=4, 5, 6) are written as

$$\begin{aligned} F_4 &= e^{-(\sigma_{45}+\sigma_{46})\pi} \\ F_5 &= Ae^{-(\sigma_{45}+\sigma_{46})\pi} - (A+F_{5\infty})e^{-(\sigma_{56}+\sigma_{46})\pi} + F_{5\infty} \quad (5) \\ F_6 &= -(A+1)e^{-(\sigma_{45}+\sigma_{46})\pi} \\ &\quad + (A+F_{5\infty})e^{-(\sigma_{56}+\sigma_{65})\pi} + F_{6\infty} , \end{aligned}$$

where $F_{5\infty}$ and $F_{6\infty}$ are observed values and

$$A = \frac{\sigma_{45}-\sigma_{65}}{(\sigma_{56}+\sigma_{65})-(\sigma_{45}+\sigma_{46})} . \quad (6)$$

The equilibrium states give the following relation from eq. (3):

$$F_{6\infty}/F_{5\infty} = \sigma_{56}/\sigma_{65} , \quad (7)$$

and from eq. (5) the relations;

$$\left(\frac{dF_4}{d\pi}\right)_{\pi\to\infty} = -(\sigma_{45}+\sigma_{46}) , \qquad \left(\frac{dF_5}{d\pi}\right)_{\pi\to 0} = \sigma_{45}$$

and

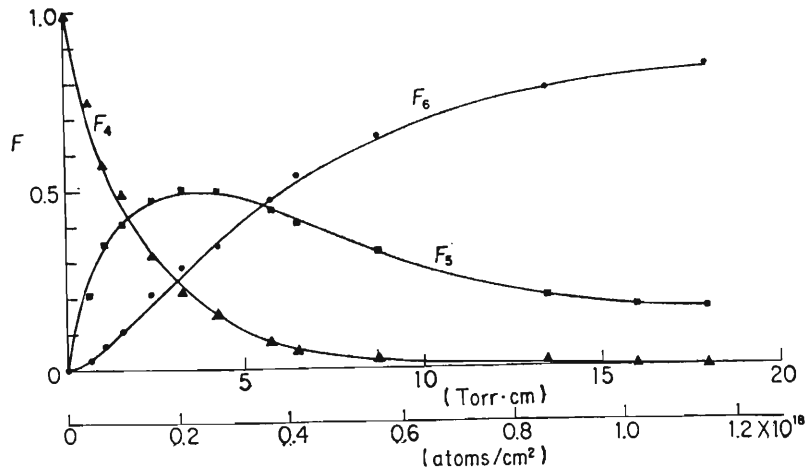

Fig. 2. Charge distribution *vs* target thickness of nitrogen gas for 50 MeV C^{4+} ions. Solid line shows the calculated charge distribution using $\sigma_{45}=7.2\times10^{-18}$, $\sigma_{56}=3.2\times10^{-18}$ and $\sigma_{65}=0.5\times10^{-18}$ in cm²/atom.

Table I. Cross sections of electron loss and capture by carbon ion in nitrogen gas.

σ_{ij} (cm²/atom) \ E_c (MeV)	39	50	78
$\sigma_{45}\times10^{18}$	9.2±0.3	7.2±0.2	5. 4±0.2
$\sigma_{56}\times10^{18}$	4.6±0.3	3.2±0.3	2. 8±0.3
$\sigma_{65}\times10^{18}$	1.7±0.3	0.5±0.2	0.17±0.1

$$\left(\frac{dF_6}{d\pi}\right)_{\pi\to0}=\sigma_{46}\ ,$$

are derived.

The least-square fit was obtained leading to the cross sections for carbon ions in nitrogen gas as shown in Table I. The calculations were carried out with a PDP 124 computer of the IPCR. The cross sections were determined when the measured F_k and the calculated F_k of eq. (5) agreed with the best fit by choosing A and σ_{46} suitably. Then σ_{46} is almost equal to zero by calculation. Cross sections of σ_{45}, σ_{56} and σ_{65} are given from eqs. (5), (7) and the chosen A. In Table I σ_{45} and σ_{56} which represent the cross sections of single electron loss decrease with ion energy and σ_{65} of single electron capture decreases rapidly with ion energy. A solid line in Fig. 2 shows the calculated relative amount of 50 MeV carbon ions in nitrogen gas using the cross sections in Table I.

3.2. *Cross sections of electron loss by nitrogen ions in nitrogen gas*

Cross sections of electron loss by nitrogen ions were measured when N^{4+} ions passed through nitrogen gas at energies of 45 and 85 MeV. Figure 3 shows the relation between charge distribution and gas target thickness when 45 MeV N^{4+} ions traversed the collision chamber. The relative amounts F_k (k=4, 5, 6, 7) of N^{4+}, N^{5+}, N^{6+}, N^{7+} ions were observed. Equation (2) becomes of four-component system so that it is more complicated to determine the cross sections than in the three-component system of C^{4+} incident ions. Apporoximately, the π dependence of F_k and $dF_k/d\pi$ determine σ_{jk}. The experimental uncertainties particularly in $dF_k/d\pi$ prevent obtaining a unique set of values for the cross sections. The value of only $\sum_{k=5}^{7}\sigma_{4k}$ is, however, calculated exactly because F_4 is equal to $\exp\left(-\sum_{k=5}^{7}\sigma_{4k}\pi\right)$ from the intial condition and its equilibrium charge state is zero. Table II shows the values of $\sum_{k=5}^{7}\sigma_{4k}$ which are the cross sections of electron loss only. It is found that $\sum_{k=5}^{7}\sigma_{4k}$ decreases with the energy of nitrogen ions and seems to be nearly equal to $\sigma_{45}(\sigma_{45}\gg\sigma_{46}\gg\sigma_{47})$ from the result of $\sigma_{46}\sim0$ when C^{4+} is an incident particle in nitrogen gas.

Table II. Cross sections of electron loss by nitrogen ion in nitrogen gas.

σ_{ij} (cm²/atom) \ E_N (MeV)	45	85
$\sum_{j=5}^{7}\sigma_{4j}\times10^{17}$	2.1±0.1	1.4±0.1

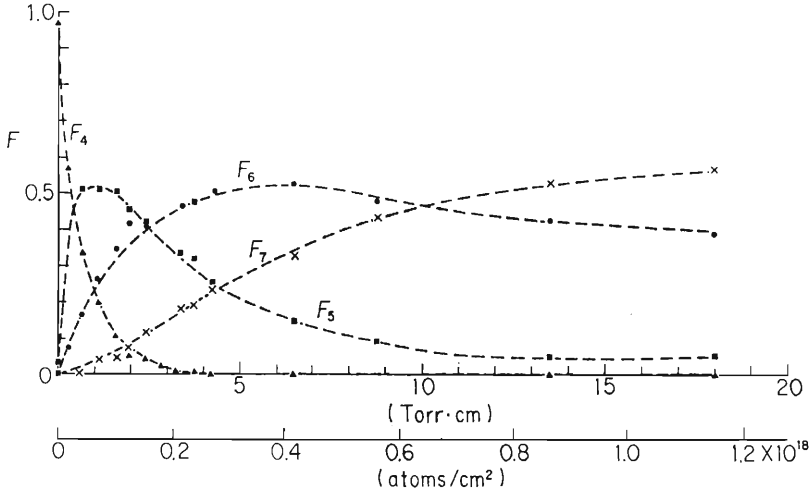

Fig. 3. Charge distribution *vs* target thickness of nitrogen gas for 45 MeV N^{4+} ions.

3.3. *Beam attenuation caused by charge exchange*

Now, the yields of heavy ions in the accelerator are reduced by charge exchange at collisions with residual gas molecules during acceleration. Knowledge of cross sections for electron loss by heavy ions in gas is, therefore, essential to diagnose heavy ion acceleration and to determine the pressure in the accelerating chamber and the focusing system when a heavy ion accelerator is designed.

We apply the cross sections of electron loss $\sum_{k=5}^{7}\sigma_{4k}$ for nitrogen ions given in Table II to beam attenuation of 65 MeV N^{4+} ions, from 40 to 70 cm in radius, accelerated in the IPCR 160 cm cyclotron. Figure 4 shows the relation between the ratio of N^{4+} ion yield measured at 70 cm radius to that at 40 cm radius (maximum radius is 74 cm) and the pressure of the accelerating chamber of cyclotron. The pressure of the chamber was varied by adjusting the nitrogen gas flow introduced into the ion source. It is found that the ratio decreases rapidly with the pressure. Figure 4 shows the pressure of the accelerating chamber near the diffusion pump, but it is noticed that the pressure in dees, where ions are accelerated, is about 3.5 times larger than that of the chamber. When the cross sections of electron loss $\left(\sum_{k=5}^{7}\sigma_{4k}\right)$ caused by charge exchange from N^{4+} to N^{5+}, N^{6+}, N^{7+} ions in nitrogen gas (σ_{43}, σ_{42}, $\sigma_{41} \ll \sigma_{45}$ in this energy region) and the path length of ions during acceleration between ion radius 40 and 70 cm and the pressure in dees (n atoms per cm^3) are given, the ratio of beam attenuations (I_{70}/I_{40}) can be calculated by

$$\frac{I_{70}}{I_{40}} \simeq \exp\left(-n\int_{40}^{70}\sum_{k=5}^{7}\sigma_{4k}\,dl\right).$$

Where $\sum_{k=5}^{7}\sigma_{4k}$ depends on the energy of N^{4+} ions during acceleration. In Fig. 4 a solid line with some errors represents the results of calculation using the cross sections of electron loss in Table II and ref. 5). Errors of the calculation depend mainly on uncertainties of the path length $\left(\int_{40}^{70} dl\right)$ of ions during acceleration.

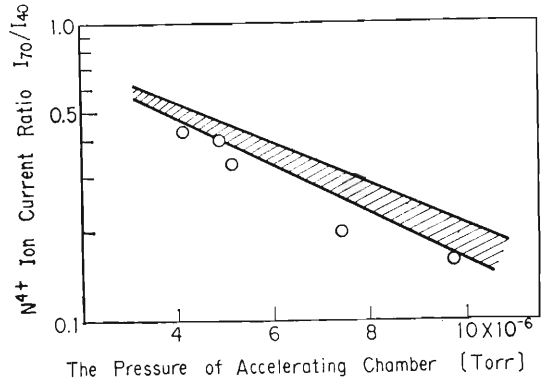

Fig. 4. Circle points give the measured value. Solid line gives the calculated values with errors using the cross sections of electron loss, path length of ions and the pressure. The pressure in dees is about 3.5 times larger than that in the accelerating chamber.

§ 4. Discussion

Below 1 MeV/nucl. of ions the cross sections of electron loss and capture by many kinds of heavy ions except carbon ions have been measured and analyzed by I. S. Dmitriev *et al.*[5,6] H. L. Reynolds[16] has also measured the cross sections of electron loss and capture for 26 MeV nitrogen ions in a Zapon foil. We have measured the cross sections of

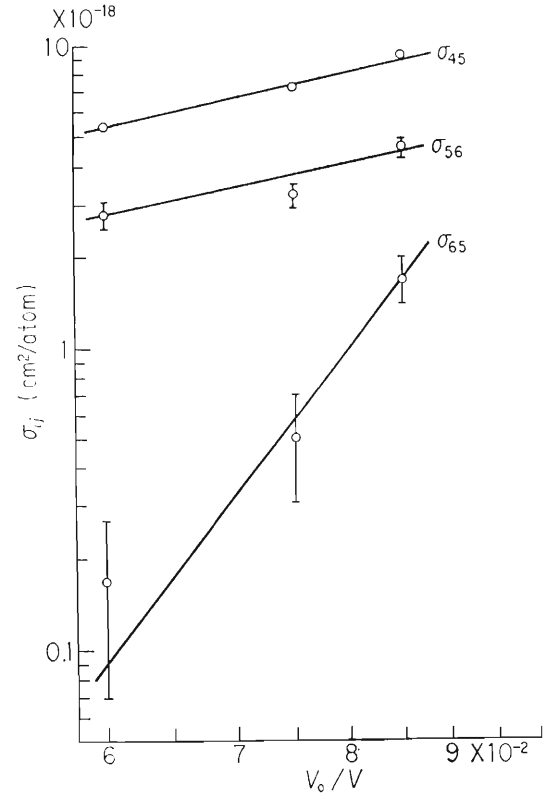

Fig. 5. The relation between cross sections of electron loss and capture by carbon ion in nitrogen gas and v_0/v.

electron loss and capture of C^{4+} and N^{4+} ions traversing nitrogen gas at energies of 3.5 to 7 MeV/nucl., that is, at velocities (V) of 2.6 to 3.7×10^9 cm/sec. In this velocity region the cross sections of single electron loss $\sigma_{j,j+1}$ (σ_{45} and σ_{56} of carbon ions) are proportional to v_0/v (Fig. 5) and generally agree with the Dmitriev's formula.[5] The cross sections of single electron capture σ_{65} of carbon ions are nearly proportional to $(v_0/v)^6$ (Fig. 5), which is equal to the results obtained by Bohr in the case of hidrogen and helium ions at velocities $v \gg v_0$.[17]

It is said, however, that the cross sections of electron loss and capture vary due to gas density with increasing gas pressure in the collision chamber.[18] The density effect may be caused by the collisions, which are repeated not only in the ground state but also in excited state of incident particles. Thus the cross sections of electron loss and capture obtained by us represent the mean values when the collision takes place in a ground state of ions and in excited states of ions repeatedly in the collision chamber. But the density effect seems to be small in this case.

As for the cross sections of nitrogen ions, only $\sum_{k=5}^{7}\sigma_{4k}$ was measured exactly when N^{4+} ions were incident particles. If N^{5+} or N^{6+} ions are introduced into the collision chamber, other cross sections will be given exactly. It is, therefore, intended to provide a thin foil before the deflecting magnet (DM) in Fig. 1 to introduce N^{5+} or N^{6+} ions, which are selected by the magnet. Also, it is intended to measure the cross sections of electron loss and capture by ions of ^{3}He, ^{12}C, ^{14}N, ^{16}O in He and Ar gases, and the equlibrium charge composition of their ions in some solid media.

From the results of beam attenuation in the IPCR 160 cm cyclotron, it is found that the pressure of the cyclotron must be below 4×10^{-6} Torr if the ratio of beam attenuations from 40 cm to 70 cm in radius should be kept larger than a half.

The authors wish to express their cordial thanks to H. Kumagai and M. Odera for their advice and encouragement, and also to F. Yoshida for making the programming and operating the computer.

References

1) A Proposal of APACHE in Oak Ridge (1969).
2) A Proposal of HILAB (1968).
3) W. Bath and I. S. Grant: Nuclear Phys. **63** (1965) 481.
4) S. K. Allison: Rev. mod. Phys. **30** (1958) 1137.
5) I. S. Dmitriev, V. S. Nikolaev, L. N. Fateeva and Ya. A. Teplova: Soviet Physics-JETP **15** (1962) 11.
6) V. S. Nikolaev, I. S. Dmitriev, L. N. Fateeva and Ya. A. Teplova: Soviet Physics-JETP **13** (1961) 695.
7) G. Ryding, A. Wittkower and P. H. Rose: Phy. Rev. **184** (1969) 93.
8) L. C. Northcliffe: Phy. Rev. **120** (1960) 1744.
9) Reynolds, Wyly and Zucker: Phy. Rev. **84** (1955) 474.
10) V. S. Nikolaev, L. N. Fateeva, I. S. Dmitriev and Ya. A. Teplova: Soviet Physics-JETP **5** (1957) 789.
11) V. S. Nikolaev, L. N. Fateeva, I. S. Dmitriev and Ya. A. Teplova: Soviet Physics-JETP **6** (1958) 1019.
12) C. D. Moak, H. O. Lutz, L. B. Bridwell, L. C. Northcliffe and S. Datz: Phy. Rev. **2** (1968) 427.
13) IPCR Cycl. Prog. Pep. Vol. 1 (1967).
14) I. Kohno, T. Tonuma, Y. Miyazawa, S. Nakajima, T. Inoue, A. Shimamura and T. Karasawa: Nuclear Instrum. and Methods **66** (1968) 283.
15) Y. Miyazawa, T. Tonuma, I. Kohno, S. Nakajima, T. Inoue, A. Shimamura and T. Karasawa: Japan. J. appl. Phys. **9** (1970) 532.
16) H. L. Reynolds, L. D. Wyly and A. Zucker: Phy. Rev. **98** (1955) 1825.
17) N. Bohr: The passage of Atomic Particles through Matter, Kgl. Danske Vindinskab. Selskab: Mat.-fys. Medd. **18** No. 8 (1948)
18) V. S. Nikolaev: Soviet Physics-USPEKHI **8** (1965) 269.

Reprinted from Sci. Papers of I.P.C.R., 67, 99–113 (1973).

The Radiofrequency System of the IPCR (RIKEN) Variable Energy Multi-Particle Cyclotron

By Masatoshi ODERA, Yoshiaki CHIBA, Takashi FUJISAWA, Yoshitoshi MIYAZAWA, and Osamu TERAJIMA*

The Riken (IPCR) Cyclotron is a variable-energy multi-particle machine which is capable of accelerating proton, deuteron, helium−3, alpha-particle and also heavy ions such as of carbon, nitrogen and oxygen in a wide range of energy. This report describes the design and performance of its radiofrequency system. The system is required to work in a frequency range from 5 to 13.5 MHz and estimated to consume maximum power of 150 kW including beam load. Use of a pair of movable liners, a moving shorting plane and an additional fixture to change the shape of the shorting plane makes coverage of the required frequency range possible without excessive power dissipation. All adjustment of the parameters necessary for operation can be made at the control panel remotely, except the addition of a small capacitor to the anode of the oscillator tube at some low frequency region. The need to enter the cyclotron vault is not frequent. No special precaution necessary for operation has been felt for six years by virtue of the conservative design. A testing method devised to measure the characteristics of a resonator having a large Q value is described. Some mechanical features of the Rf system are also given.

I. INTRODUCTION

The IPCR 160 cm cyclotron was intended to be used as a general purpose accelerator in various fields of research such as chemistry, biology, and solid state physics, as well as nuclear physics. Easy operation is required in spite of large variety of particles to be accelerated and wide range of energy change. The whole system was designed conservatively to make the possibility of machine failure minimum.

A shielded Lecher type resonating system was chosen as an accelerating electrode having two dees. It also acts as a plate tank circuit of a self-excited grounded-grid oscillator. Frequency change is made by means of a pair of movable liners above and below the dees and a traveling shorting plane. The range of frequency is 5~12.5 MHz by these means. By attaching a deforming fixture to the shorting plane, resonant frequency up to 13.5 MHz can be obtained. Energies of ions are 3~20 MeV for proton, 3~12.5 MeV per nucleon for d and α, 3~16.5 MeV per nucleon for ^{3}He, and 3~9 MeV per nucleon for heavy ions. A half-scale model of resonator was constructed to ascertain the results of calculation and to test the measuring instrumentation. Following is an account of the principle of design, details of manufacture, characteristics of the radiofrequency system

* 小寺正俊, 千葉好明, 藤沢高志, 宮沢佳敏, 寺嶋 為 (Cyclotron Laboratory of this Institute)

completed and its performance.

II. SHIELDED LECHER RESONATOR

Merits of the shielded Lecher type resonator as a resonant cavity of a variable energy cyclotron were described by I. Hayashi[1] in detail. Here, a few brief description will suffice.

As shown schematically in FIG. 1, there are two fundamental resonant modes of oscillation in this type of cavity. By shaping the shorting plane as shown in the figure to form a capacitor against the shield wall instead of a simple plane shorting the outer conductor and the stems, it is possible to make the two modes have very different resonant frequencies. This makes it easy to suppress the unwanted mode. This is the largest advantage of and the reason for the use of this type as a resonator. Next, in the wanted push-pull mode (FIG. 1 (a)) leakage of the radiofrequency field behind the shorting plane is very small by virtue of the narrow and long gap between shorting device and wall. The gap plays a role of a wave guide for frequencies below cut-off. The current flowing at the end of the tank is so small that the capacitors attached between the stems and ground at its end is able to make the Rf potential developed between the stems and walls negligible while they are insulated electrically. In consequence, biasing of the stems becomes possible to suppress multipactoring phenomena. Easy building-up and stable operation of the accelerating field are helped by this dee bias provision.

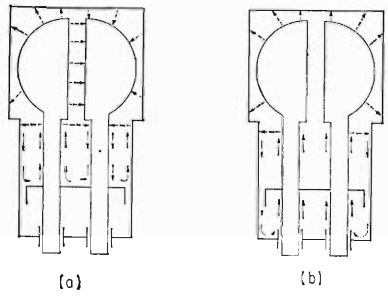

(a) Fundamental push-pull mode, (b) Push-push mode.

FIG. 1. Modes of resonace of a shielded Lecher pair. Arrows with solid line denote current, dotted line electric field.

(1) I. HAYASHI: *Nucl. Instr. Methods*, **17**, 261 (1962).

III. RESONANT FREQUENCY AND Q VALUE

Estimation of resonant frequency of the cavity was made by usual transmission line calculation. Figure 2 shows the distribution of characteristic impedance used in the calculation. The impedance was determined from the value of capacity per unit length of each cross section. The capacity was obtained by resistance measurement between the inner and outer conductors of the cross section drawn with silver paint on a conducting paper. The method was simple and gave quickly the impedance of any complex figure having a two-dimensional pattern of lines of force. Since the error was not small in this method (~5%) owing to insufficient uniformity of resistance distribution of the paper used, measurements by an electrolytic tank were made again for the final cross section adopted.

Relatively large radiofrequency voltage is required in the low frequency range to accelerate heavy ions. Hence, a large characteristic impedance is desirable to maintain high Q values. On the other hand, the highest resonant frequency is lowered by a large value of the impedance, so that some compromise must be made. Trial calculations were done for several

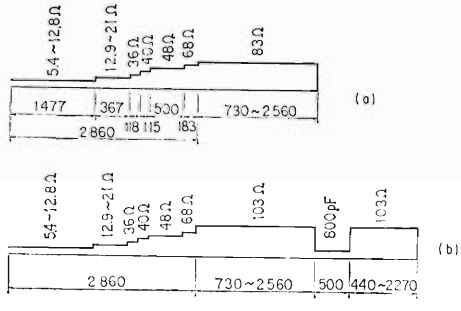

(a) Push-pull mode, (b) Push-push mode.

FIG. 2. Parameters of the resonator as a two-conductor transmission line. (Length is in mm)

combinations of impedance, resulting in a final choice as shown in FIG. 2. The resonant frequency and Q value calculations were done by a code given by one of the authors, T. F. The code was also used to investigate the coupling circuit characteristics. Figure 3 (a) shows a comparison of the calculated and measured frequencies and FIG. 3 (b) that of Q values.

In estimating the load of the oscillator, two-thirds of calculated Q values were assumed. Measured Q was nearly of a value supposed at the early tuning period. After modifying the connection method of the movable liner to the floor of the accelerating chamber this value has been improved, and now it is about 90% of the calculated value.

Figure 3 also shows frequencies and Q values of the unwanted mode. In the push-push mode, the radiofrequency voltage of the two dees is in phase and no accelerating field exists between the dee-to-dee gap. A large separation of the frequencies of push-push and push-pull modes seen in the figure contributes greatly to easiness and stability of operation of the cyclotron as stated earlier.

At the outset, operation at frequencies higher than 12 MHz was scheduled to be made by removing the movable liners. But, since the use of the liners as the fine frequency tuning elements was found to be convenient, and especially vital to the acceleration of the heavy ions, the plan was changed. A pair of new liners was manufactured, by which the dee-liner capacitance was reduced and the high frequency limit increased from 12.0 to 12.5 MHz. The highest energy of proton increased from 16 to 17.3 MeV. Further, a deformation attachment of the shorting plane was devised. Increase of the resonant frequency by this attachment was calculated to be 8%. Although it lowered the Q value considerably, the oscillator was powerful enough to compensate the loss. Figure 4 shows the change of frequency measured when the new liners and the shorting plane deforming attachment were installed. The highest frequency, 13.5 MHz, corresponds

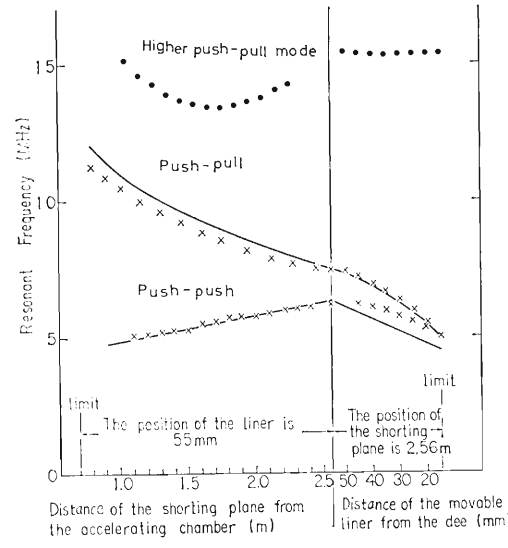

(a)

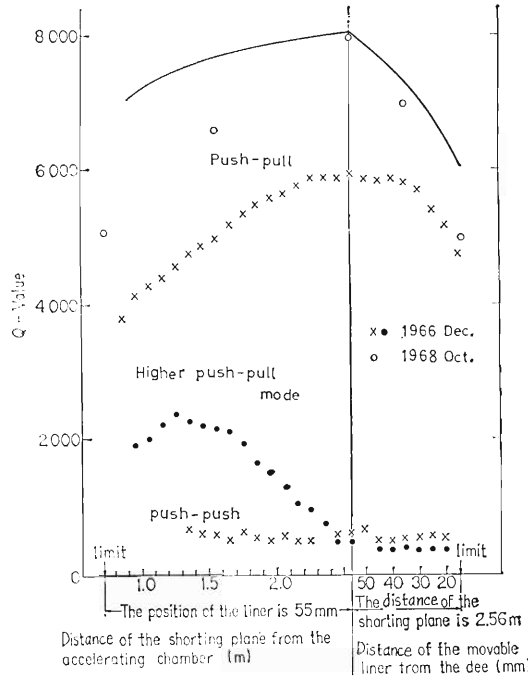

(b)

FIG. 3. Calculated and measured resonant frequencies and Q values. Solid lines show calcurated values.

to the energy of proton of 20 MeV. The attachment is used only when the energy higher

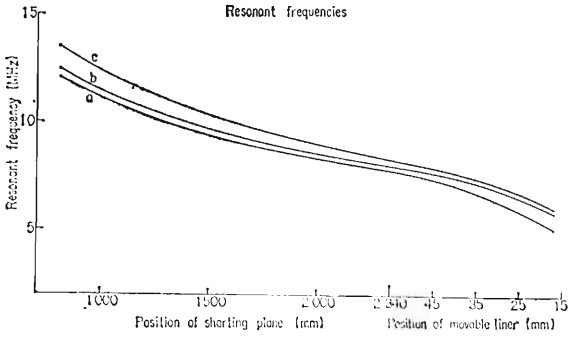

a : initial values, b : use of new movable liners,
c : use of a shorting plane deforming attachment.

FIG. 4. Change of push-pull resonant frequency by modification of the resonator.

than 17.3 MeV is desired.

IV. COUPLING CIRCUITS

As shown schematically in FIG. 5, the features of the radiofrequency magnetic flux of push-pull and push-push modes are very different. The flux generated by currents flowing the two stems is added in the former mode and subtracted in the latter. Then, the coupling strength or mutual inductance of a loop suitably placed between the stems is very different for each mode. This, together with the feedback circuit adjustment to make grid exciting phase suitable only to the wanted mode, is effective to suppress the unwanted mode of oscillation.

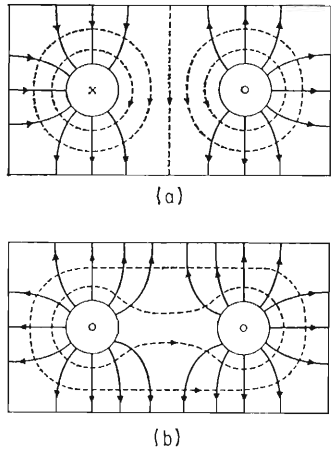

FIG. 5. Comparison of the radiofrequency magnetic flux for two modes, (a) push-pull and (b) push-push.

General arrangement of the power tube, the plate loop and the feedback loop is shown in FIG. 6 and the oscillator circuit is schematically shown in FIG. 7. Each feed line was made as short as possible to minimize the phase displacement in them and to avoid the feed line resonance.

However, the plate line resonates around 15 MHz owing to the plate grid capacitance of the power tube and the self-inductance of the

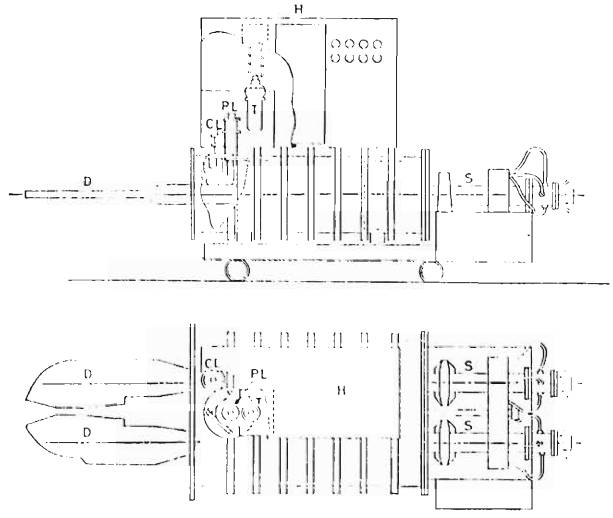

D : dees, PL : plate loop, CL : cathode loop, T : tube,
S : stems, H : oscillator house.

FIG. 6. General layout of the resonator and oscillator system.

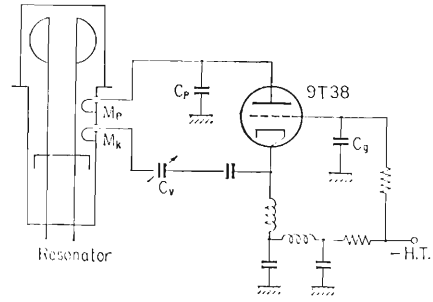

M_p : plate loop, M_k : cathode loop, C_p : capacitance between plate and grid electrode, at low frequency 100 pF is added, C_v : variable vacuum condenser, C_g : capacitance between grid and cathode.

FIG. 7. Oscillator circuit.

plate loop which has a large area in order to supply power at the lowest frequency. Exact resonance frequency of the line varies according to the position of the plate loop which is made movable between the stems up and down to adjust the load of the oscillator tube. This is the only parasitic mode remained troublesome though it has not brought about any serious damage. At about 7.5 MHz, that is nearly half of the resonant frequency, the oscillation becomes unstable at times and a small capacity added to the anode of the tube eliminates the instability. At a high frequency near 12 MHz the parasitics sometimes occur but not so strong, and adjustment of the feedback elements such as variable capacitor or rotatable cathode loop can suppress them. If the time schedule of experiments permits to break the vacuum and attach a cover to the plate coupling loop to lower the self-inductance, the instability near 12 MHz can be removed completely.

It is interesting to note that when the shorting plane attachment that was stated in Introduction and will be described in detail in Chap. V is used to obtain higher frequencies, no such a parasitic oscillation would be observed. This is because the attachment cuts off the direct coupling of magnetic flux of the plate and cathode loop as will be seen in FIG. 15 of Chap. IV.

The calculation of the feedback line characteristics shows that the range of value necessary for the coupling capacitor is within 50 to 1000 pF. A single vacuum variable capacitor is found to be sufficient, and it is remotely adjustable.

The main loop can be moved up and down when the Rf power is "on". Mutual inductance between the loop and the Lecher system varies from 0.02 to 0.066 μH while the position changes by 37 cm. By this means the most suitable oscillation condition can be established. Although the optimum load for maximum power output of the oscillator tube is around 300 ohm, usually a higher value of around 500 ohm is used for tenacity of oscillation against the abrupt change of load such as sparking in the resonator.

The minimum value of the mutual inductance is still too large above 12.5 MHz to obtain the suitable oscillation condition. A copper plate cover to reduce the effective area of the loop is in provision. However, use of the shorting plane deforming fixture that surrounds the loop seems to decrease the mutual inductance. There is no difficulty in obtaining a good oscillation condition above 12.5 MHz by the loop without cover in that case.

The feedback loop is also rotatable remotely. Mutual inductance varies from 0 to 0.033 μH.

The power tube is a high power triode of type 9T38 designed by the Technical Research Laboratory of the Japan Broadcasting Corporation (NHK).* Some characteristics are indicated in TABLE I. The original specifications were given for the medium wave service. But there seems no difficulty to use the tube in the frequency range of our cyclotron with power

TABLE I. *Characteristics of 9T38*

Electrical		
Mutual conductance (at Ib=5A)	80	m℧
Amplification Factor	40	
Interelectrode Capacitance		
Grid-Plate	97	PF
Grid-Filament	180	PF
Plate-Filament	3	PF

Maximum Rating (R-F Power Amplifier, Class C)		
	30 MHz	2 MHz
D-C Plate Voltage	12	15 kV
D-C Grid Voltage	−1500	−1500 V
D-C Plate Current	20	20 A
D-C Grid Current	3	3 A
Plate Input	200	300 kW
Plate Dissipation	120	120 kW
Grid Dissipation	2	2.5 kW

* The authors are grateful to the designer Mr. Ohta and other members of the NHK laboratory and Mr. Uchimaru of Nippon Electric Co. for supplying the test data of the tube under development.

output less than 150 kW. It has been used over 30.000 h without failure. The anode of the tube is connected to the main loop by a sliding contact to let the latter move freely. The contact surface seems not to require cooling though its provision has been made.

V. MECHANICAL FEATURE OF THE SYSTEM

1. Stem tank

The tank is made of copper-clad steel by welding.* Thickness of copper is 3 mm and that of steel is 12 mm. Sanding is made only on the seam of copper welding. Inner surface is sufficiently smooth to let the wheels of shorting device travel on it. Stainless steel tubing for cooling water is welded on the outer surface in the atmosphere.

2. Stems

Figure 8 shows the cross section of the stem. It is made by inserting a steel pipe of 270 mm in diameter engraved with a water path into a heated copper pipe and by drawing it through a die to secure firm contact of iron and copper. Its length is 5 m. When the dee is mounted, the length is 8 m in total. The stems are insulated from the tank so as to be biased negatively to suppress multipactoring. It is found that 750 V is sufficient for this purpose. They get out of vacuum through the end plate of the tank and each can be moved remotely independently of the tank by means of stainless steel bellows and gimbal mechanisms. The radiofrequency voltage appears on the stems which are out of vacuum when the capacities of the two dees are considerably different. The voltage is picked up and indicated at the meter panel of the control room. A large capacity compensator at the side of west dee enables the adjustment of balance.

An auxiliary beam probe is provided inside of the west stem. It is used for the diagnosis of beam. It can be moved remotely and its position is indicated on the meter panel.

3. Shorting device

The device is not of a simple "plane" but has a depth of 50 cm. It is constructed from an aluminum frame and the copper plates. It is cooled with deionized water. This depth is

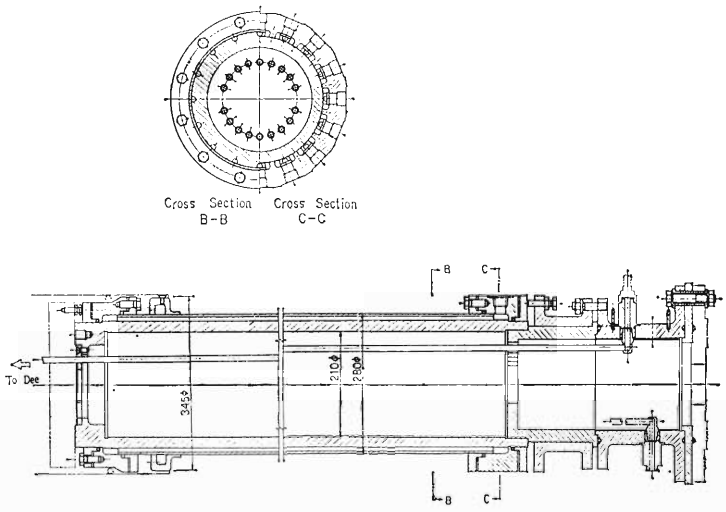

FIG. 8. Structure of stems.

* We acknowledge the effort of Messrs of Toshiba Electric Co. for careful welding of the copper clad steel that was a new material for their technical experience.

effective in suppressing the leakage of high frequency field behind the device as stated in Chap. II. It also works as a capacitive load in the push-push mode oscillation and lowers the frequency of the mode drastically. Structure of the device is shown in FIG. 9.

The weight of the device is supported by the wheels on the floor of the resonator tank lest the movement of the device does affect the position of dee. The wheels are provided with an aluminum tyre and fixed to and insulated from the device by the bolts with ceramic insulating rings.

Maximum current at the shorting plane amounts to 6000 A or nearly 70 A/cm at the shorting contacts. The contact must endure this high current density and also slide smoothly on the surface of the stem frequently in vacuum to change frequency.

Figure 10 is a schematic drawing of the contact. The sliding contact is made of silver rods hard-soldered to copper blocks which are pressed to the stem surface by pneumatic pressure of 4 kg/cm². The number of the contacts is 60 for each stem. The blocks are connected to a cooling pipe by short thin copper ribbons to accommodate small unevenness of surface of the stem and unequal

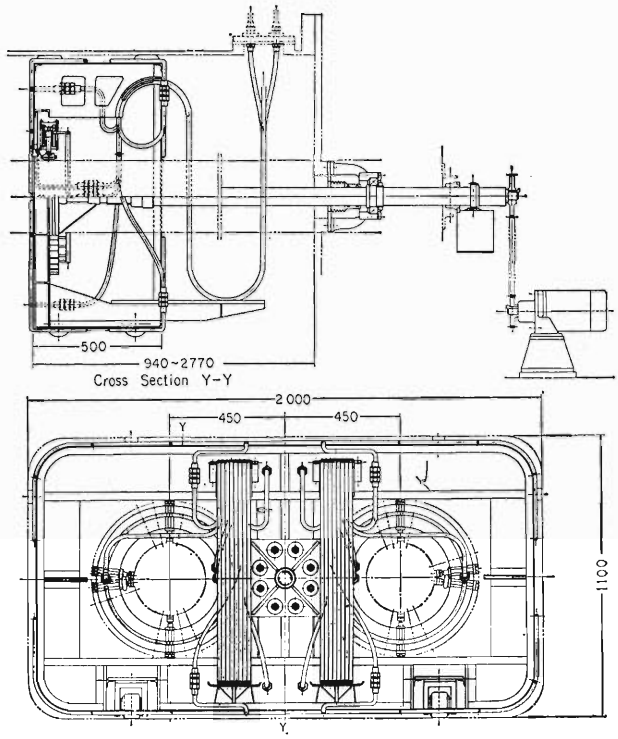

FIG. 9. Structure of shorting device. Deionized water is supplied by flexible stainless steel tubes.

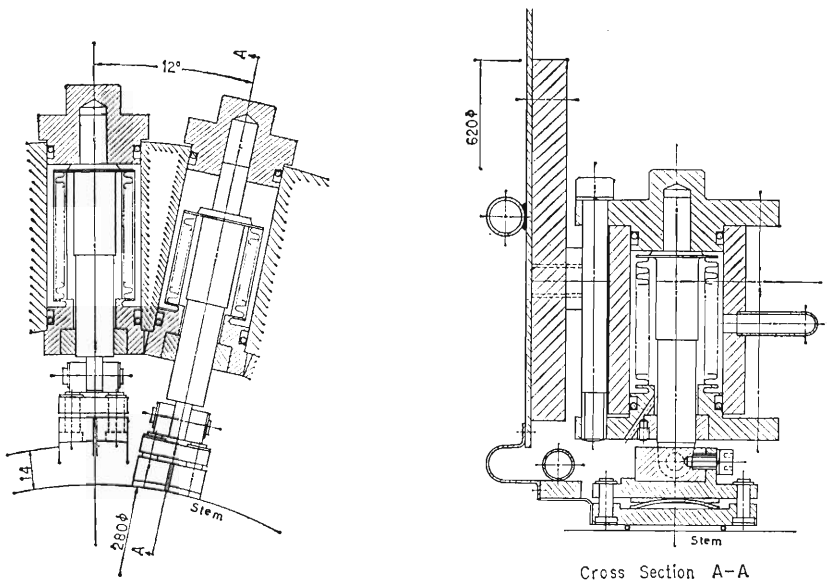

FIG. 10. Details of shorting contact. Silver lines soldered to copper blocks are pressed against the surface of stems by pneumatic pressure.

wear of the silver contact. The cooling pipe in turn is connected with longer and thicker ribbons to the shorting pland body at a larger radius where the current density considerably decreases. The long ribbons permit independent movement of the stem against the shorting device. The contact device works well and no trouble has been experienced since the beginning of the operation 7 years ago.

4. Dee

The dee is made from a high tensile cast aluminum frame and two copper plate covers with cooling pipes hard-soldered. Figure 11 shows the structure of the east dee. The east dee has a beam outlet and a septum mount. Beam is deflected by the radiofrequency field between the septum and a deflector that is grounded. Capacity of the east dee against ground thus depends sensitively on the deflector septum distance. Unbalance of capacities of east and west dees however does not cause any serious difficulty in this Lecher type resonator. Too much unbalance causes some Rf voltage to appear at the end of the stem under atmospheric pressure. It can be compensated easily as stated in 2. of this chapter.

5. Movable liner

The movable liners above and below the dees are constructed from stainless steel frames and covers made of copper plates 4 mm thick. Copper cooling tubings are hard-soldered to the covers with the distribution proportional to the radiofrequency ohmic loss.*

Originally, the tubings are soldered on the sides facing to the magnetic poles so that the dees see only the smooth surface of the cover. When a higher frequency is desired a new liner having cooling pipes on the dee side is constructed. Contrary to the previous misgivings, vacuum sparking decreases and operation

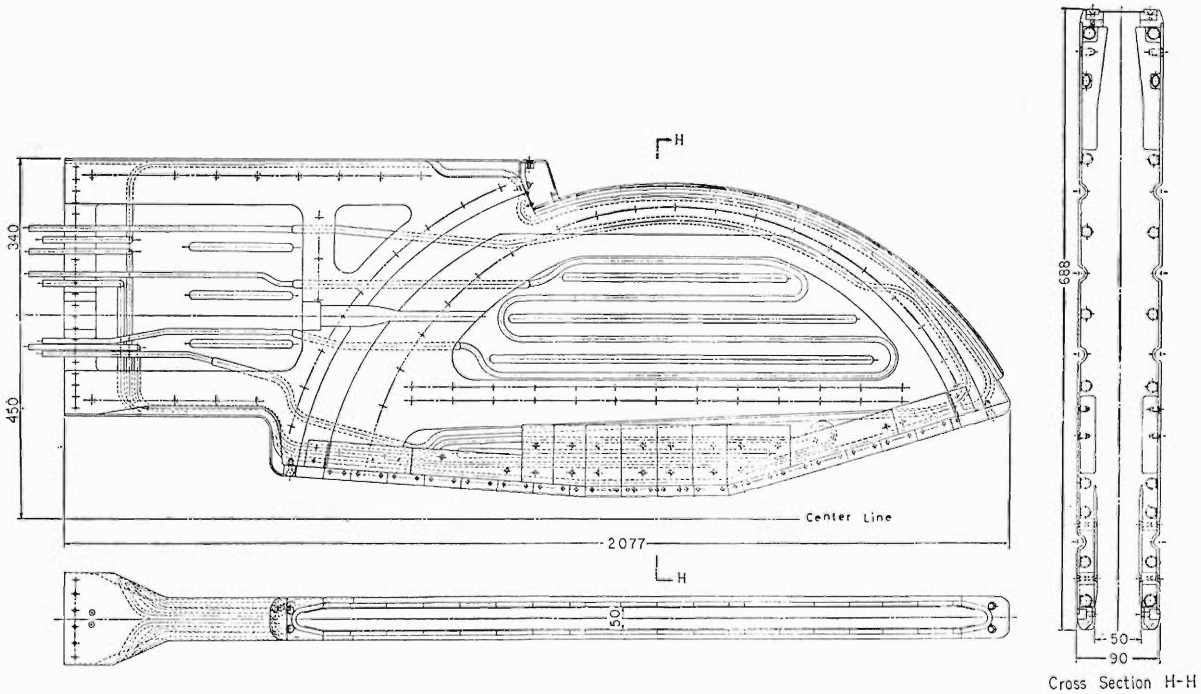

FIG. 11. Construction of east dee.

* We are grateful to Dr. T. Karasawa of this Institute and Messrs of Tsurumi Works of Toshiba Electric Co. for careful model testing of this cooling pipe distribution.

becomes improved at high frequency, though sparking increases at the lowest frequency. This interesting phenomenon will be explained by a curing hypothesis of sparking. In that theory, strong electric field concentration by dusts or sharp scratches on the conductor surface becomes a cause of breakdown. Curing process is the gradual removal of these dusts or defects by sparking itself. When the electrode surface is flat, the dusts kicked or generated by sparking have to settle on somewhere of the surface of the same flat conductor and become a source of sparking again. When the conductor is uneven, those dusts sent back into a recess where the field is weak will not become a sparking source anymore.

Figure 12 compares the cross sections of the old and new liners. Figure 13 is a photograph of the new liner. Both old and new liners have worked well. They are positioned remotely and frequency setting by them can be made as fine as 100 Hz. After warming-up for about 30 min. the frequency is stablized to this order.

Figure 14 shows the structure of stems supporting the liner from outside of the accelerating chamber. Number of stems is four for each liner. They are driven simultaneously by a chain and gear mechanism. The full stroke is

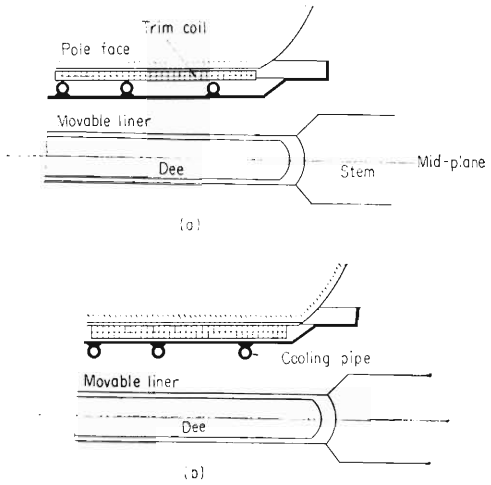

(a) Initial liner, (b) new liner.

FIG. 12. Cross section of movable liners.

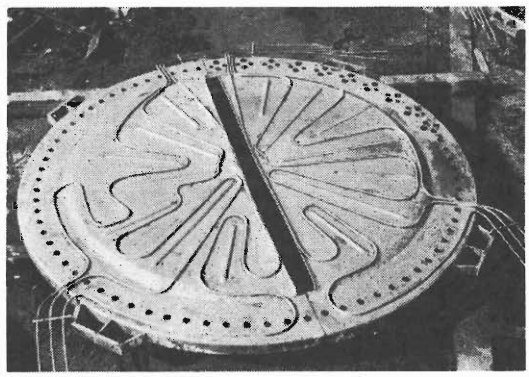

FIG. 13. Photograph of new liner. Slot is cut to allow space for ion source stems.

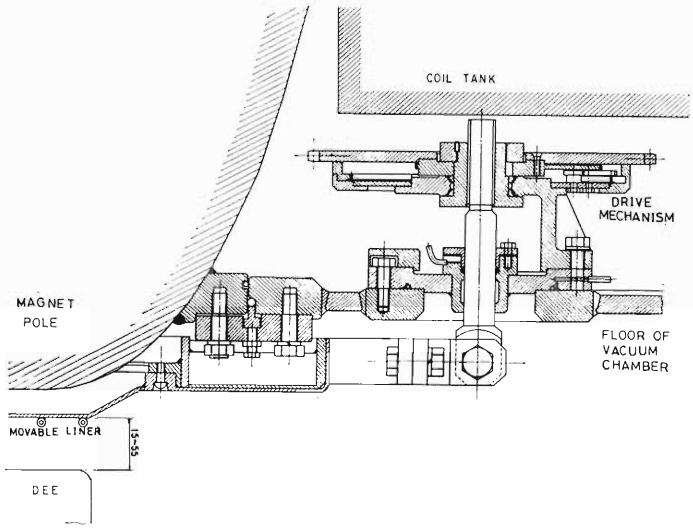

FIG. 14. Movable liner, supporting stem and driving gears.

40 mm through the vacuum seal.

6. Shorting plane deforming attachment

Figure 15 is an outline of the attachment and FIG. 16 shows the manner it is fixed on the shorting device. Frequency shift by perturbation of the boundary of a resonator can be calculated by the equation:

$$\omega^2 = \omega_a{}^2(1 + \int(H_a{}^2 - E_a{}^2)dV)$$

where ω_a, H_a and E_a are frequency, magnetic and electric field strength before the boundary is purturbed respectively. Integration is to be made over the volume removed. H_a or E_a is normalized to give unity when squared and integrated over the total volume of the cavity. Measurements of resonant frequency agreed well with the prediction of about 8% shift. Considerable decrease of the Q value is seen as was expected. The cooling water can remove the increased loss.

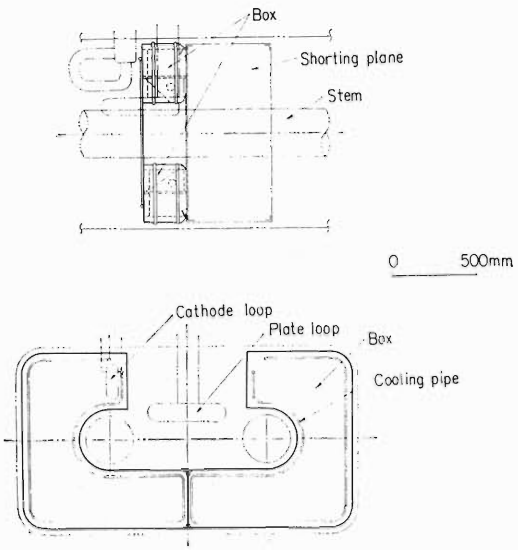

FIG. 15. Shorting plane deforming attachment.

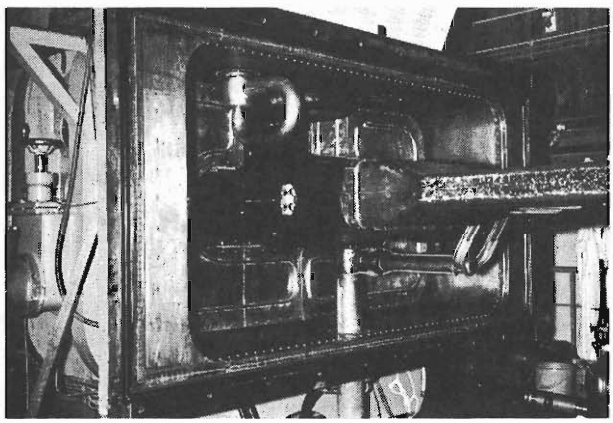

FIG. 16. Photograph of deforming attachment installed.

7. Coupling loops

The power transmitting conductors to the coupling loops form coaxial lines where they pass vacuum seals. The outer surface of the outer conductor of the coaxial line is covered with a thick stainless steel tube electro-plated with chromium so as not to suffer wear from friction when the loop is moved. The material of inner surface of the outer conductor where high frequency current flows is copper. The cooling water flows between this copper cylinder and the outer stainless steel tube. Figure 17 shows the structure of the plate coupling loop. As can be seen, the cooling water comes in at the radiofrequency ground potential into the outer conductor shell, goes down into the loop, comes up to the center conductor, returns through the same path in the reverse order and flows out of the outer conductor again to the ground. Thus, there is no need of insulation for water tubings. The plate loop is moved up and down rather frequently. Range of stroke is 37 cm. The cathode loop is rotatable at 90 deg. They are positioned remotely. It passed four years before a pair of O-rings of the plate loop had worn out. There is no sign of wear yet for the vacuum seal of the cathode loop. The surfaces of stainless steel cylinders have worn out a little but there appears no need of replacement. The positioning mechanism of the loops is wholesome yet, in spite of daily frequent usage for 6 years.*

* We appreciate the effort of Messrs T. Masuda and T. Tsuji of the Toshiba Electric Co. for the excellent engineering work of this structure as well as of the other mechanical parts of the resonating system.

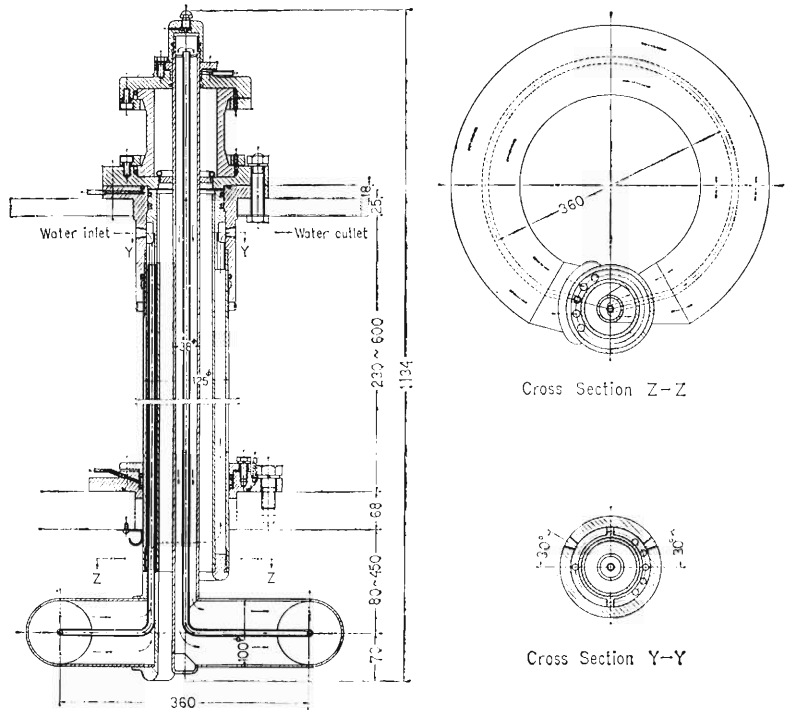

FIG. 17. Structure of plate coupling loop. Arrows indicate water flow.

VI. RESONANT FRERUENCY AND Q MEASUREMENT

The usual method of frequency and Q value measurements of a cavity with large Q requires a well-padded and stabilized oscillator and a detector system that affects the cavity Q value negligibly. There is another method of Q measurement by impulse excitation of cavity by a large pulse. The pulse width must be narrow enough to contain the resonant frequency component. Determination of the decay constant of the excited oscillation gives the Q value. This method is simpler and easier to perform than the usual frequency response measurement when a high power narrow pulse generator is available. However, the resonant frequency must be determined by other method separately and it cannot be discriminated which mode is being excited by this method alone. We designed a measuring device that makes possible the measurements of the resonant frequency and Q of a cavity at a time.

Figure 18 is a block diagram of the device. An ordinary pulse generator of width variable from 30 to 200 μ sec is sufficient for this purpose. Fast rise time is not required. A pulse enables an electronic switch to feed the radiofrequency power to the exciting loop and begins to charge an exponential decay curve generator. At the end of the pulse the switch is turned off and

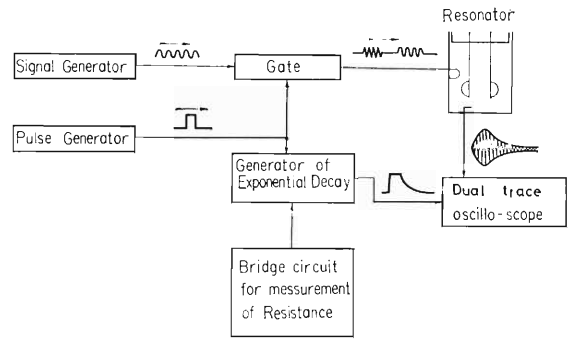

FIG. 18. Block diagram showing the method of *Q* measurement by pulse modulation of radio-frequency signal.

the signal source is cut off from the cavity. At the same time, an exponentially decaying signal is supplied to a measuring CRT. A standard C. W. signal generator of very low harmonic component is desirable as a radio-frequency source to avoid excitation by harmonics. High Q cavity is very sensitive to the weak harmonic component of the exciter when the harmonic frequency matches to some mode.

We used a pentode as an electronic switch and an amplifier because of its low plate to grid capacitance, hence little signal feed through is probable at the time of cut-off. Excitation of the cavity can be observed by a signal picked up by a small loop attached to the resonator and displayed on a CRT screen. Resonance in the feeding or pick-up line must be carefully eliminated.

By varying the frequency of the signal generator, the resonance frequency can be quickly found. Degree of excitation can be easily controlled by adjustment of pulse width. In FIG. 19 a change of oscilogram figure near resonance is seen. Small undulation on the envelope indicates the small difference in frequency of the free oscillation of the cavity and of the exciter.

A decay curve generator comprising an RC network simulates the exponential decay of oscillation of the cavity after cut-off. The envelope and RC decay curve are compared on the oscilloscope screen and the values of RC are determined by measurement with a bridge. The reproducibility of measurement is good and a value within 3% can be obtained by different observers. Any defect in the cavity like cooling pipe resonance is detected by a sharp depression in the Q value at a certain frequency and the effects of modification to remedy the defect can be quickly evaluated.

VII. PERFORMANCE

Figure 20 shows the shunt resistance between dee and ground. The radiofrequency power

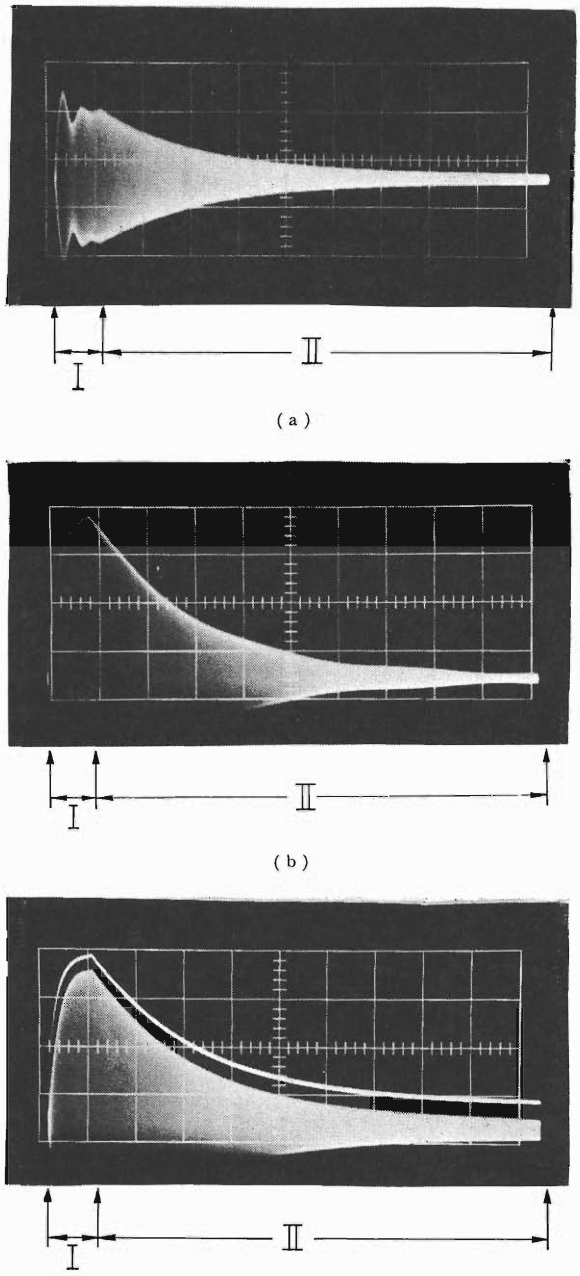

(a) Excitation near resonance, (b) small undulation can be seen in the decaying envelope. It indicates existence of small leakage of exciter frequency through opened switch, (c) comparison of decaying envelope and exponential curve made by RC network.

FIG. 19. Oscillograms of excitation and decay of cavity resonance. Period I is the interval where switch is closed and in Period II switch is opened and electromagnetic oscillation decay with time constants determined by Q values.

required to obtain a desired dee voltage at each frequency is known by this graph. Figure 21 shows the power output and plate dissipation of the power tube. Multipactoring phenomenon seldom causes difficulty except occasionally after a prolonged exposure of the accelerating chamber to the atmosphere in summer. Usually, by virtue of the dee-bias and if the vacuum is kept below 2×10^{-5} torr, no difficulty in operation has been experienced. The working vacuum can be obtained within 2 to 4 h after roughing has begun, depending on the

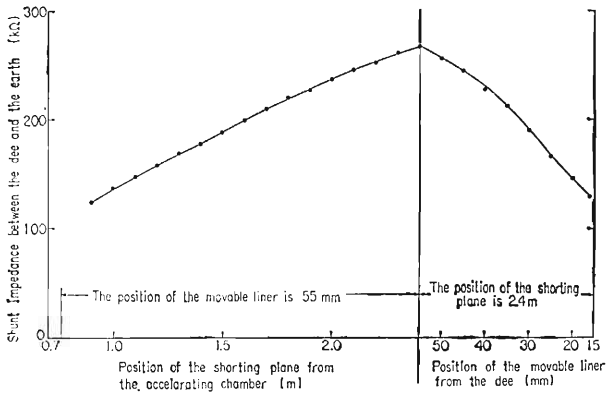

FIG. 20. Shunt resistance calculated by measured Q values.

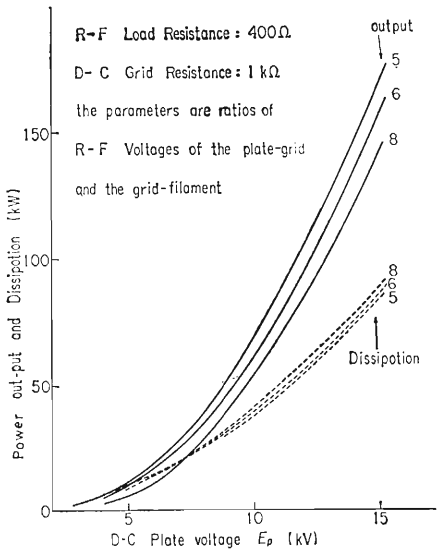

FIG. 21. Power output of oscillator as a function of plate supply voltage.

interval at which the vacuum system is kept at atmospheric pressure.

Usually the movable liner is used as an tuning element during power is on. The shorting plane is moved only when a large frequency change is desired and power is off. Suitable plate load of the oscillator can be judged from the ratio of DC-plate voltage to current and is adjusted by the plate loop positioning mechanism. All the operation can be made from the control panel except insertion of a small capacity between plate and earth in operation near 7.5 MHz as noted above. Frequency drift is rather swift for the first 10 min. of operation amounting to $5\sim15$ kHz. After warm-up of about 20 min, the drift becomes smaller by an order of magnitude.

Voltage holding capability depends on the vacuum pressure and perhaps on the state of surface of the accelerating chamber. It increases with time rather speedily for several hours of operation of the oscillator after the workable pressure has been attained. Then it slows down in spite of vacuum pressure of $2\sim3\times10^{-6}$ torr, which is usually obtained in a half day after roughing has begun from the atmospheric pressure. The highest voltage of 120 kV between the dee and liner wall can be obtained only after two or three days of continued operation.

Change of material of the thin plate of the septum from carbon to tungsten seems to have increased voltage limit.

Also, by extending the initial portion of the septum into the dee where the radiofrequency field is not present, increase of extractable beam current is observed. Figure 22 shows the relative positions of the septum, dee and deflector. Perhaps the thermal electrons generated by beam at the septum where the electric field is present are accelerated along the direction of the magnetic field and by locally heating the liners other electrons are emitted. The process will be multiplicative above some threshold value of the power dissipated by the initial thermal electrons. Local melting and evapora-

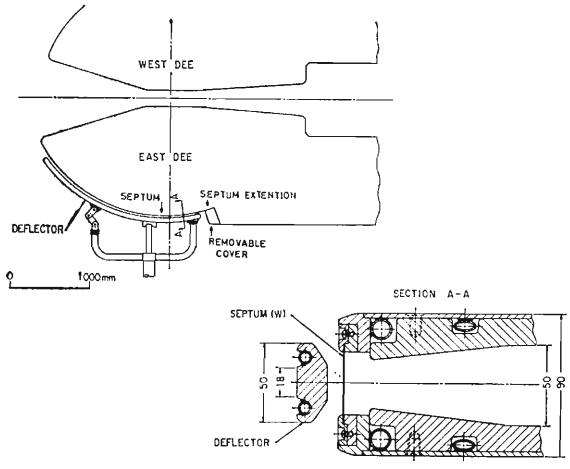

FIG. 22. Structure of the beam deflecting channel.

tion of the part of the liner just above and below the initial part of the septum seem to justify the supposition. The copper plates of the corresponding small area that has been punctured are now replaced by tungsten plates. The latter material seems to endure the bombardment by electron better. That the extension of the septum into the dee is effective in suppressing the local heating of the liner can be seen by the decrease of damage of the liner and dee. Also chance of observation of a fire ball on the liner at the corresponding places becomes less. Of course, the extension changes the initial condition for deflection of beam. Relative merits of the position of the initial part of septum are now being evaluated by the machine operating personnel.

The heavy ions of A/q up to 4 are now accelerated. The maximum magnetic field of 2.0 Wb/m^2 and 74 cm in radius would permit the maximum energy obtainable to more than 10 MeV per nucleon for ions of $A/q=3$. But the maximum dee-to-wall voltage of 120 kV does not allow to obtain energies higher than 9 MeV for heavy ions. More careful tuning of the frequency and voltage is required than in case of lighter ions to extract beam properly through the septum deflector canal. Larger number of turns required to reach the final orbit or smaller separation of the orbit at extraction radius must be the reason for the above fact. Fine tuning feasibility of the movable liner was found very convenient in this respect. In TABLE II, kind of ions, range of energy and current extracted outside of the accelerating chamber are indicated. A 3-to 5-fold current intensity and other kind of ions like Ar, Kr or Xe are available for irradiation within the dee.

TABLE II. *Energy and current of ions being accelerated*

Particle	Energy (MeV)	Extracted current† (μA)
p	4~17	60
d	8~24	50
$^3He^{++}$	12~45	30
$^4He^{++}$	16~45	30
C^{4+}	50~95	4
N^{4+}	60~95	4
N^{5+}	50~120	1
O^{5+}	60~120	0.5

† The current list was obtained from the operation diary over the last two years.

VIII. CONCLUSION

The resonating system of the IPCR 160 cm variable-energy multi-particle cyclotron resonates at frequencies from 5 MHz to 13.5 MHz. Use of the shielded Lecher line resonator together with the movable liners and the self-excited oscillator having the shortest feed lines has yielded a flexible system easy to operate. Frequency is changed by a traveling shorting plane in a rough step and by the movable liners in fine. The frequency higher than 12.5 MHz is obtained by attaching the shorting plane deforming boxes. The load seen by the oscillator can be adjusted by moving the plate coupling loop when power is on. Several protection measures are provided for mis-operation of the machine and radiation hazard to cut off the high voltage source of the oscillator. During more than seven years of operation no serious difficulty was encountered in the

TABLE III. *An example of operation of cyclotron in June, 1973*

Date	Time	Hours	Theme	Team	Particle	Energy (MeV)	Frequency (MHz)
14	02~14	12	Nuclear fuel material irradiation	Power Reactor and Nuclear Fuel Development Corporation	α	34	8.69
//	14~22	8	Production of K-43 for medical use	Kyushu Univ.	//	29	8.03
//	22~01	3	Production of I-123 for medical use	Tokyo Municipal Univ.	//	42	9.67
15	01~04	3	Production of Hg-197 for medical use	Nakano Hospital	h	32	9.90
//	04~08	4	Reserved for cooling down of activity				
//	08~24	16	He-3 induced nuclear reaction	Nuclear Phys. Group B	//	29.3	9.40
16 (Sat)	00~24	24	//	//	//	//	//
17 (Sun)	00~24	24	//	//	//	//	//
18 (Mon)	00~09	9	//	//	//	//	//
	09~17	8	Reserved for periodical inspection and repair of the cyclotron				
19	09~13	4	Production of Po-210	Univ. of Tokyo	α	40	9.43
	13~23	10	Irradiation of bacterial spores	Radiation Biology Laboratory	//	16	5.96
	23~11	12	Particle analyser study	Particle Analyzer Instrumentation Group	p	15	11.6

use of the radiofrequency system. TABLE III shows an example of the time schedule of the cyclotron. Time arailable for the experiments is about 5000 h a year.

The authors are grateful to Dr. H. Kumagai, former chief, and the members of this laboratory for their encouragement and discussion given in design, construction and adjustment. Special regard is due to the cyclotron crew for compilation of the operation data and for cooperation to improve the machine. They took important part in various modification works.

This paper is dedicated to late chief Dr. K. Matsuda who has been a leader of machine physics and nuclear physics of this laboratory. He worked hard in the construction of this cyclotron and gave invaluable criticism to this work.

Reprinted from J. Phys. Soc. Jpn., 25, 1207–1213 (1968).

Cross Sections of the $^{12}C(^3He, p)^{14}N$ Reaction

Kazuhisa MATSUDA, Noriyoshi NAKANISHI,
Sigeru TAKEDA and Takeshi WADA
The Institute of Physical and Chemical Research, Yamato-machi, Saitama

(Received July 24, 1968)

Differentical cross sections of the $^{12}C(^3He, p)^{14}N$ reaction were measured at the incident energy of 25.3 MeV. Angular distributions for individual levels showed patterns of the direct surface reaction. Contributions from overlapping peaks were resolved with a computer code. Strong peaks were found at the excitation energies of 9.0 MeV and near 13.0 MeV. These facts are in agreement with other cases of the proton-neutron transfer to ^{12}C. Comparisons between the reactions of $(^3He, p)$ and of (α, d) are discussed.

§ 1. Introduction

Two-nucleon transfer reactions seem to be an open problem, even at the present stage of the nuclear reaction analysis. At present, special interests are given on the two like-nucleon transfer reaction for the reason of collective enhancement,[1] while, the proton-neutron transfer reaction involves another kind of interests, *i.e.*, the proton-neutron correlation in the nucleus. A similar reaction mechanism[2~4] will be encountered in both types of two-nucleon transfer reactions: of like nucleons and of different nucleons. To test the reaction model, it is preferable that the shell model structure of involved states is established as well as possible.[5] Along this line, the experiment of $^{12}C(\alpha, d)^{14}N$ at Berkeley[6~8] and the analysis of Glendening[3] were published. Many experimental studies for the direct reaction from ^{12}C to ^{14}N,[9] including (h, p) reaction[10,11,17] have been done.* A precise study of angular distributions for the reaction of $^{12}C(h, p)^{14}N$ at a high incident energy seems to be valuable.** In this article, the scattering system for the newly built cyclotron and the experiments are described briefly. Experimental results of the $^{12}C(h, p)^{14}N$ are presented along with a description of data-processing method. A preliminary result of ^3He elastic scatterings from ^{12}C is analyzed by the optical model. Some discussions are given on the difference between the reactions of $^{12}C(h, p)^{14}N$ and of $^{12}C(\alpha, d)^{14}N$. An attempt for the analysis of the present result is now in progress.

* In the following, ^3He in a bracket will be abbreviated as "h".

** After the completion of this article, the authors knew the work of Mongelson and Harvey[17] at an incident energy of 20 MeV. The second column in Table II was added according to their result. The energy resolution of experiment was higher than the present work, while the result of the data analysis in this article is in a general agreement with theirs, *i.e.* as shown in Table II.

§ 2. Experimental

The ^3He beam of 25.3 MeV was obtained from the IPCR (the Institute of Physical and Chemical Research) variable energy cyclotron, which is able to accelerate ^3He ions to the energies between 10 MeV and 45 MeV. The outline of the beam handling system is shown in Fig. 1. For this experiment, the extracted beam was passed through the beam analyzing magnet ($\phi=80°$, $\rho=160$ cm), which analyzed the beam energy within 0.2%. A combination lens of a sector magnet and a quadrupole-pair magnet, focused again the analyzed beam to a spot on the target at the center of a 75 cm scattering chamber without a beam collimator. The size of the spot was about 3 mm wide and 6 mm high. The horizontal divergence of the beam was limited within 1.5 degrees. The beam energy was determined by measuring the proton N.M.R. frequency in comparison with the case of Th C' alpha particles. The average intensity of the beam on the target was 0.3 μA. Details of the cyclotron, the beam handling system and the scattering chamber were described elesewhere.[12]

A telescope of semiconductor detectors was mounted on the turning table in the scattering chamber, whose precision of angular position was 0.1 degrees. Beam axis was determined by measuring the left-right asymmetry of the elastic scattering yield within an accuracy of ± 0.1 degrees. A defining slit of detector of 3 mm width and of 5 mm height was placed at the position of 20 cm apart from the center. The counter telescope consisted of three transmission type silicon detectors. The first detector was of a surface-barrier type with a depth of 200 μ, which gave ΔE signals. The

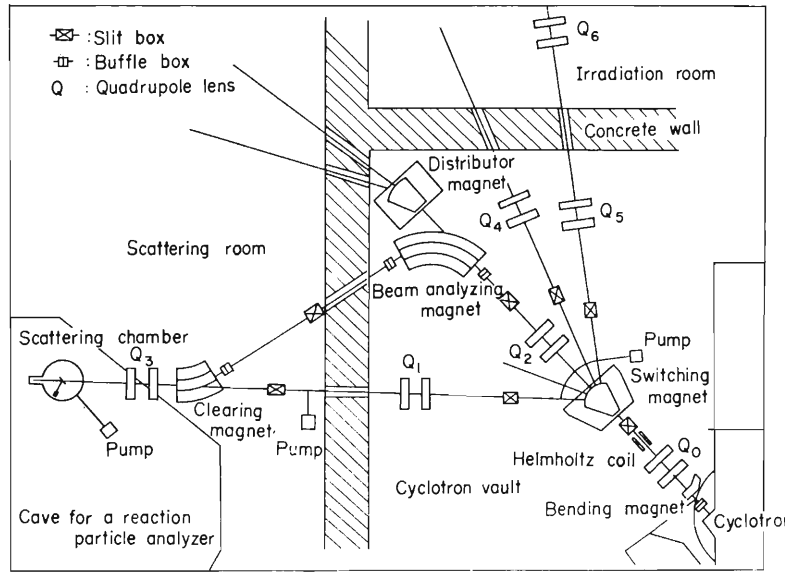

Fig. 1. The out-line of the beam handling system.

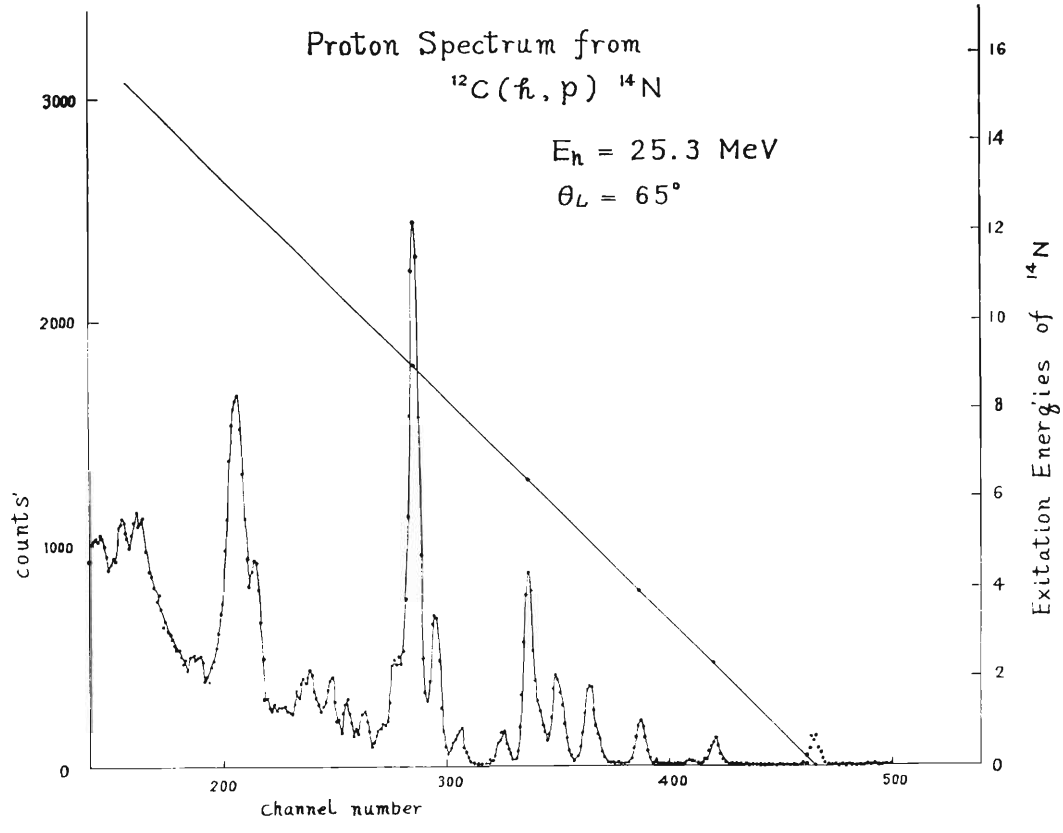

Fig. 2. An example of the proton spectrum.

other two, which gave E signals, were the detectors of Li-drift type with depths of 3 mm and mounted in series so as to stop protons with energies as high as 35 MeV. The energy resolution of the system was 250 KeV. The reason for the poor resolution was not clear but may be attributed to the reaction kinematics and to defects of pulse handling system. Both signals of ΔE and E were amplified and fed to a summing circuit and to a particle-identifier with squaring tubes (Raytheon QK-329). Both the proton spectrum and the spectrum of heavier ionizing particles were recorded on a 1600 channel pulse height analyzer (Victoreen SCIPP-1600) at the same time. An example of proton spectrum is shown in Fig. 2.

Carbon films of 0.6 mg/cm² (run *A*) and 0.4 mg/cm² (run *B*) were used. They were made from colloidal solution of "dag", according to the tech-

nique described by Pehl *et al.*[7] The thickness was estimated from the energy loss of Th-C' alpha particles. Differential cross sections were determined by the usual method of measuring yields to individual peaks and of integrating charges collected in a Faraday cup. Two independent runs: *A* and *B*, were made with different targets and with an interval of half a month (*A*: October, 1967 and *B*: November, 1967). As described later, the two runs gave a good agreement in relative differential cross sections, but a somewhat large difference (35%) in absolute normalization. The reason was not made clear, but perhaps it might be due to errors of target thickness. Considering general accuracy of these data, the absolute scale of the run *A* was adopted, which also gave a fairly good behaviour of elastic cross sections in comparison with optical model analysis.

§ 3. Results

A. Angular distributions for isolated peaks

Previously reported level energies[13,16] of ^{14}N below 9.41 MeV are listed on Table I, with their spin-parity assignments in the literatures. Four peaks in the spectrum are certainly attributed to individual levels of ^{14}N. These correspond to the ground state and to the levels at 2.31, 3.95 and 7.03 MeV.

A strong peak at about 9.0 MeV does not correspond to a single level but this group is prominent. The angular distributions of these five groups were obtained directly and the results are shown in Fig. 3. In this figure, the dotted points represent experimental values of run *A* and the cross points those of run *B*. A normalization factor 1.35 was multiplied to the data of run *B* as mentioned in § 1. The agreement between the results of both runs is satisfactory.

B. Levels from 4.91 MeV to 6.44 MeV and the method of data-analysis

According to the Table I and to ref. 7), there are seven levels in this energy interval, *i.e.* at 4.91, 5.10, 5.69, 5.83, 6.05, 6.21 and 6.44 MeV. At first sight of the overlapping of peaks in the spectrum, it seemed impossible to discriminate the individual contributions of these levels. The spectrum, however, is undoubtedly giving an information about them. To solve this complexity, a spectrum-fitting code was used. The code* searches the parameter values to make standard deviations σ minimum between the experimental spectrum and the calculated one. To avoid unexpected ambiguities, the following assumptions were made on the calculated spectrum. (1) the spectrum is composed of seven gaussian peaks with the same width and constant background

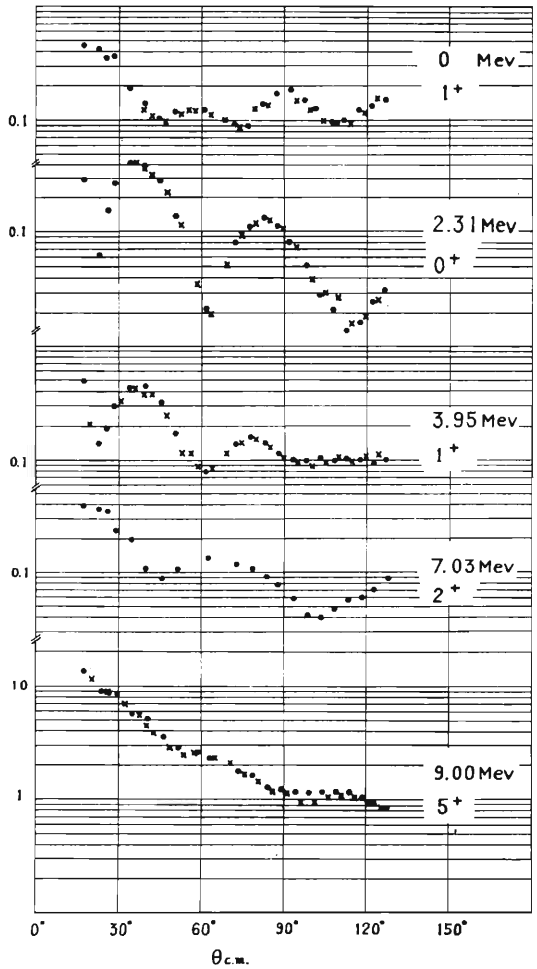

Fig. 3. Angular distributions for isolated peaks. Points represent results of the run *A* and crosses represent those of the run *B* (normalized).

counts. (2) the level energies coincide exactly with the seven reported values of 4.91, 5.10, 5.69, 5.83, 6.05, 6.21 and 6.44 MeV. (3) the pulse height ($E+\Delta E$) is assumed to be linear with the level energy between 3.95 MeV and 6.44 MeV. To obtain results for one detection angle, following procedures were performed. By assuming the gaussian width and the channel positions for 3.95 MeV and 6.44 MeV, the peak height of seven gaussian distribution were searched as parameters and minimum σ^2-value was obtained. By changing the width and the channel-energy relation by 0.1 channel steps, the process was repeated. When the smallest value of σ^2 was obtained, the corresponding area under each gaussian peak was considered as the resolved yield for level. Figure 4 gives an example of fitting. Though an apparent

* This code was made by one of the authors (T.W.).

agreement between the calculation (the solid curve) and the observation (dotted points) ensure a general certainty, it is difficult to give any numerical error estimate to the processed result. For the case of overlapping peaks the process gives a more confident result for the larger peak and a less certain one for the smaller peak. The result for the small peak between large peaks is most doubtful. Thus for three peaks at 5.10, 5.83 and 6.44 MeV, the errors may be small (about 5%) and for three peaks at 4.91, 5.69 and 6.21 MeV, the results include considerable errors (10%~30%, depending on detection angles). The result for 6.0 MeV is out of confidence and a precise experiment of Holbrow *et at.*[11,14] showed no evidence of levels near 6.0 MeV. In the present spectrum analysis, however, the existence of the peak is preferable as shown in Fig. 4. The six angular distributions thus obtained are shown in Fig. 5.

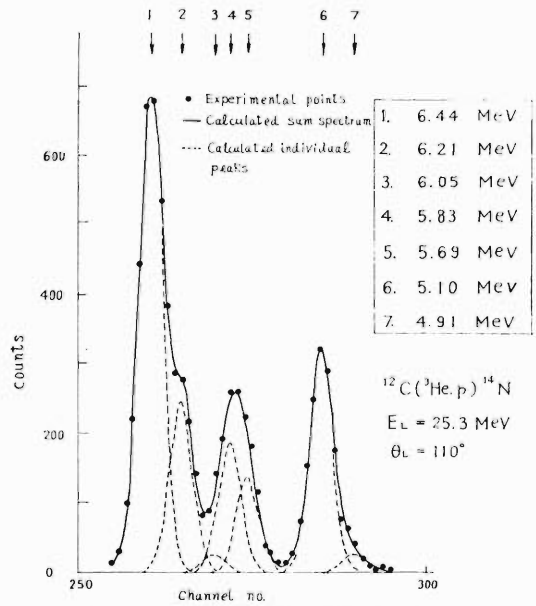

Fig. 4. An example of the spectrum analysis between the excitations of 4.91 MeV and of 6.44 MeV. Points are the experimental values and the solid curve is the calcutated spectrum. The dashed lines represent the contributions of analyzed peaks.

C. *Other levels*

Fifteen levels are reported between 7.40 MeV and 9.41 MeV, of which the most certain ones are shown in Table I. Of these, the $^{12}C(\alpha, d)^{14}N$ experiment of Pehl *et al.*[7] showed detectable yields for the four $T=0$ levels at 7.97, 8.47, 9.00 and 9.41 MeV. The present $^{12}C(h, p)^{14}N$ experiment revealed detectable proton groups for the three $T=1$ levels at 8.06, 8.63 and 9.17 MeV, in addition. Moreover, according to the data analysis as described in the previous sub-section, the yields for the 8.91 MeV levels is considerably large. Contributions from the level at 8.71 MeV was too small to be recognized. The contributions of the 8.98 and 9.129 MeV levels cannot be resolved from that of the 8.963 MeV level. The precise measurement with a magnetic analyzer by Holbrow *et al.*[11] also showed contributions from the above

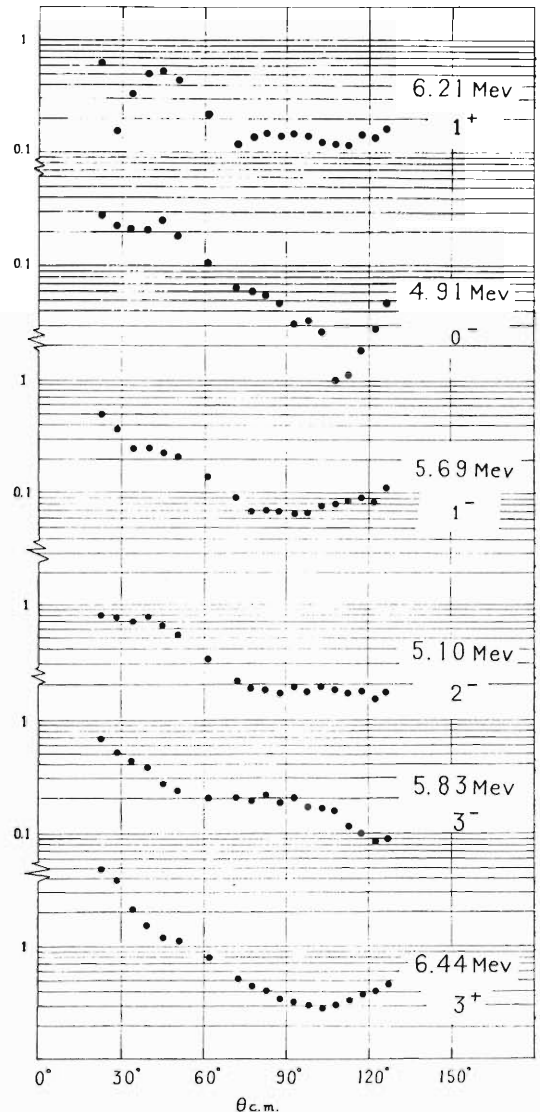

Fig. 5. Angular distributions for peaks between the excitation energies of 4.91 and of 6.44 MeV.

nine levels. Differential cross sections for these levels were obtained by the similar analysis as described in the sub-section *B*, and angular distributions are shown in Fig. 6. Because no method was found to ensure their reliability, these curves are to be considered as rough indications of angular distributions. The magnitudes of the integrated cross sections from 30° to 130° are, however, more certain and given in Table I and in Fig. 9.

In the energy range above the 9.41 MeV excitation, the spectra showed many overlapping peaks,

Table I. Cross sections of $^{12}C(h, p)\,^{14}N$ at E_h=25.3 MeV and comparison with those of $^{12}C(\alpha, d)\,^{14}N$

Level identified (MeV)	Previously reported level energies[10] (MeV)	Integrated cross sections (mb)	Spin-parity (reported)	Dominant configuration	$\sigma_{in}/21+1$	$\sigma(h, p)/\sigma(\alpha, d)$	
						Reference12) (relative)**	Reference 5)
0	0	1.37	1^+	$(p_{1/2})^2$	0.46	0.28	1.4
2.31	2.311	1.04	$0^+(T=1)$	$(p_{1/2})^2$	1.04	>360	
3.945	3.945	1.51	1^+	$(p_{3/2})^{-1}(p_{1/2})^{-1}$	0.50	1	4.9
4.91	4.91	0.84	(0^-)	$p_{1/2}\,s_{1/2}$	(0.84)	1.06	
5.10	5.10	3.04	2^-	$p_{1/2}\,d_{5/2}$	0.61	0.47	2.5
5.67	5.69	1.22	1^-	$p_{1/2}\,s_{1/2}$	0.41	2.2	
5.83	5.83	2.09	3^-	$p_{1/2}\,d_{5/2}$	0.30	0.44	2.0
	6.05						
6.21	6.21	2.24	1^+	$(s_{1/2})^2$	0.75	1.90	5.9
6.44	6.44	7.75	3^+	$s_{1/2}\,d_{5/2}$	1.11	1.28	
7.03	7.03	1.05	2^+	$(p_{3/2})^{-1}(p_{1/2})^{-1}$	0.21	1.19	3.3
7.97	7.97	0.7*	2^-	$p_{2/1}\,d_{3/2}$	0.14*	0.9*	2.3*
8.06	8.06	0.7*	$1^-(T=1)$	$p_{2/1}\,s_{1/2}$	0.23*	>26*	
8.47	8.489	2.6*	(4^-)	$(p^{3/2})^{-1}(p^{1/2})^2 d_{5/2}(?)$	(0.32)*	1.00*	2.4*
8.63	8.63	0.9*	$0^+(T=1)$	$(s_{1/2})^2$		50*	
8.71	8.71		$0^-(T=1)$	$p_{1/2}\,s_{1/2}$			
8.91	8.91	5.7*	$3^-(T=1)$	$p_{1/2}\,d_{5/2}$	0.57*		
	8.963		(5^+)	$(d_{5/2})^2$			
9.00	group 8.98	12.3* 24.8	2^+	?	av (0.6)*	0.64	2.2*
	9.129		(2^-)	$p_{3/2}\,p_{1/2}\,s_{1/2}$ or $(p_{3/2})^{-1}(p_{1/2})^2 d_{5/2}$			
9.17	9.17	2.6*	$2^+(T=1)$	Core excited	0.52*		
9.41	9.41	3.3*	$2^-, 3^-$	?	0.66*, 0.47*	2.2*	4.1*
13.0	group						8.4*

*: Values specified by asterisk are obtained from $\int_{30°}^{130°} \sigma(h, p)\,d\Omega$, and others from $\int_{15°}^{130°} \sigma(h, p)\,d\Omega$.

**: Reference gives no absolute cross section, these ratios are relative values, normalized to that of 3.945 MeV level.

of which several peaks corresponding to the excitation energies at 9.7, 10.2, 10.6-10-7, 11.4 MeV can be recognized over the angles. A strong group around 13.0 MeV seems to consist of more than four peaks, which surely include not only the 12.76 MeV, peak of $T=0$ found in ref. 7), but also some other strong contributions from the $T=1$ levels in the neighbourhood. A tentative assignment of level energies for these peaks gives the values of 12.6–12.7, 12.95, 13.1 and 13.2 MeV. The sum cross sections for this group of peaks were shown in Fig. 7. The angular distribution is very similar to that for the 9.0 MeV group.

D. Elastic scattering

Differential cross sections for the elastic scattering of ^{3}He from carbon were measured. Because the ^{3}He group was not discriminated from groups of deuterons and alpha particles, the data were not satisfactory and the angular range was limited. The results are shown in Fig. 9, together with the calculated curve. The optical model analysis was done with the automatic search code "SEARCH"* with six parameters. The values of parameters are given in the figure. The starting points of the automatic search was selected as the values of Kellog and Zurmühle[15] for the scattering from ^{13}C as shown in Fig. 8.

§ 4. Discussion

The integrated cross sections for individual levels are given in Table I and Fig. 9. The range of integration is from 15° to 130° except for the

* This code was written by one of the authors (T.W.).

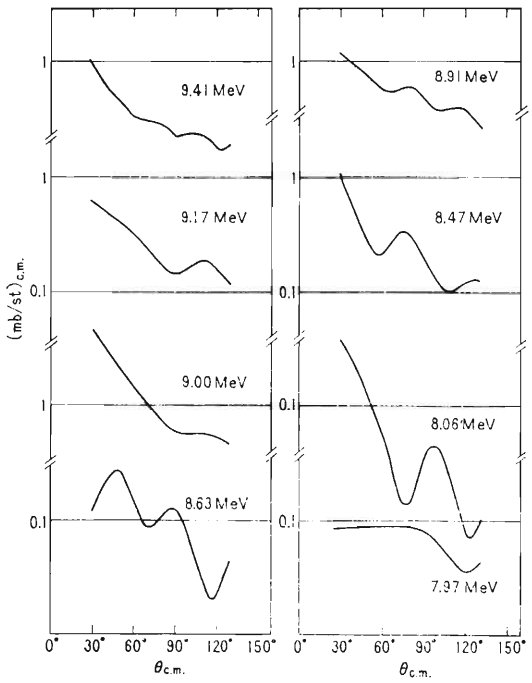

Fig. 6. Tentative angular distributions for peaks between 7.97 MeV and 9.41 MeV, which are used for tne estimation of integrated cross sections.

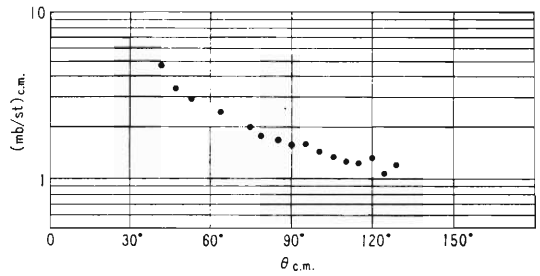

Fig. 7. The angular distribution of the group of peaks around the 13.0 MeV excitation.

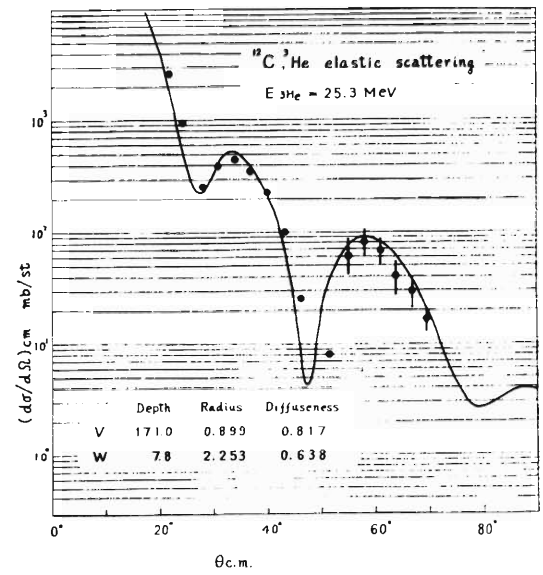

Fig. 8. The angular distribution of the elastic scattering of ^{3}He from carbon. Points represent the result of measurement and the solid curve is the result of automatic search. The optical model parameters are given on the figure.

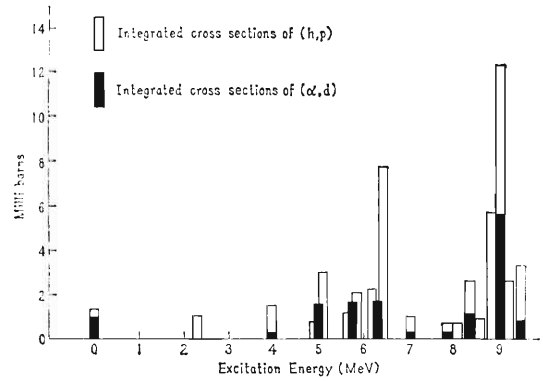

Fig. 9. The integrated cross sections of (h, p) and (α, d)[7] for individual levels of ^{14}N.

cases as specified. The reported values for the $^{12}C(\alpha, d)^{14}N$ reaction at 53 MeV[7] and at 42 MeV[16] are also included. In general, the yield of (h, p) is larger than that of (α, d) by a factor of two or three. The DWBA analysis will elucidate this difference.

Some levels of $T=1$ were excited considerably by the (h, p) reaction, which are not excited by the (α, d) reaction. The groups corresponding to the energies of 9.0 MeV and of 13.0 MeV are excited strongly in both types of reactions; (h, p) and (α, d). For the 9.0 MeV group the integrated cross section of (h, p) is about four times as large as that of (α, d). The contributions from the $T=1$ levels at 8.91 MeV and 9.17 MeV will explain this large factor. The large cross section of (h, p) for the 13.0 MeV also may be explained by the contributions from the neighbouring $T=1$ levels. Shell model calculations[5] suggest the existences of $T=1$ levels, which will be excited by the two-nucleon transfer reaction in this energy region. Thus the present work suggests the existence of levels of $T=1$ near the 13.0 MeV excitation, probably with large spin value. Generally, high spin states are excited strongly; such as 6.44 MeV (3^+), 8.91 MeV (3^-) and 9.00 MeV (5^+). The fluctuation of cross sections among individual levels are smoothed out considerably if they are divided by $(2I+1)$, which are shown in Table I. This fact had already been pointed out by Glendenning.[3]

The simple theory of two-nucleon transfer reaction tells that the difference between the (h, p) reaction and the (α, d) reaction leading to a $T=0$ state comes from the distortion effect and the overlapping integral between light particles. The very interesting fact is related with the excitations of the ground state (1^+) and of the 3.945 MeV state

Table II. Comparison between $\sigma(h, p)$ and $\sigma(\alpha, d)$. Integrated cross sections for the 3.945 MeV state of ^{14}N are normalized to unit in all cases.

^{14}N levels (MeV)	$\sigma(h, p)^a$ 25.3 MeV	$\sigma(h, p)^b$ 20 MeV	$\sigma(\alpha, d)^c$ 42 MeV	$\sigma(\alpha, d)^d$ 53 MeV
0	0.91	0.71	3.2	3.2
3.945	1	1	1	1
4.91	0.56	0.73	0.52	5.1
5.10	2.0	2.14	4.3	
5.67	0.81	1.22	0.36	5.3
5.83	1.48	1.36	3.1	
6.21	1.38	2.04	0.77	5.5
6.44	5.1	6.1	3.7	
7.03	0.70	0.69	0.58	1.03
7.97	0.5*	0.76	0.52	1.00
8.47	1.72*	1.53	1.71	3.5

a: Present work. Integration from 15° to 130° without asterisk and from 30° to 130° with asterisk.
b: Reference 17).
c: Reference 16). Integration from 10° to 90°.
d: Reference 7).

(1^+). According to shell model calculations,[12] the ground state of ^{14}N contains a large component of $(P_{1/2})^2$ and a small component of $P_{3/2}^{-1} P_{1/2}^{-1}$, while the 3.945 MeV state is in the alternative situation. The cross section of (α, d) is larger for the ground state than for the 3.945 MeV state. On the contrary, the (h, p) reaction excites the 3.945 MeV level stronger than the ground state and their angular distributions are apparently different. Because of the facts of the same spin-parity and of the small energy difference compared with outgoing proton energy, neither the distortion effect nor the spectroscopic component can easily explain this difference between (h, p) and (α, d). It seems that a deep consideration of reaction mechanism is necessary on this point. To show this point and the differences between σ_{in} (h, p) and σ_{in} (α, d) to many individual levels, Table II is added to Table I and Fig. 9.

Concerning the angular distribution, the following prominent features should be mentioned. The pattern for the 2.31 MeV level (0^+) corresponds to the $\Delta L=0$ transfer reaction, while that for the 7.03 MeV level (2^+) is related to the $\Delta L=2$. Then, the angular distributions for the 3.95 MeV (1^+), for the 6.21 MeV (1^+) and for 8.63 MeV (0^+) have dominant features of $\Delta L=0$. The angular distribution for the ground state (1^+), however, may be a mixture of $\Delta L=0$ and $\Delta L=2$. For further discussions on the angular distribution, a detailed analysis seems to be necessary.

Acknowledgements

The authors are obliged to T. Karasawa and the cyclotron operating crew and also indebted to S. Motonaga, I. Kohno and other colleagues for the beam handling system and the ^3He acceleration. They should like to express their thanks for many valuable discussions with S. Yamaji, H. Kamitsubo, Y. Awaya and other colleagues.

References

1) S. Yoshida: Nuclear Phys. **33** (1962) 685.
2) C.L. Lin and S. Yoshida: Progr. theor. Phys. **32** (1964) 885.
3) N.K. Glendenning: Phys. Rev. **137** (1964) B102.
4) E. M. Henley and D. U. L. Yu: Phys. Rev. **133** (1964) B1445.
5) W.W. True: Phys. Rev. **130** (1963) 1530.
6) B.G. Harvey and J. Cerny: Phys. Rev. **120** (1960) 2162.
7) R. H. Pehl, E. Rivet, J. Cerny and B. G. Harvy: Phys. Rev. **137** (1964) B114.
8) E. Rivet, R.H. Pehl, J. Cerny and B. G. Harvy: Phys. Rev. **141** (1966) 1021.
9) D.A. Bromely: ANL-6878 (1964) p. 353; K. Nagatani and D.A. Bromely: *ibid.* p. 423.
10) S. Hinds and R. Middleton: Proc. Phys. Soc. **75** (1960) 745.
11) C. H. Holbrow, R. Middleton, J. Parkes and J. Bishop: *Nuclear Spin-Parity Assignment* ed. N.R. Gove and R. L. Robinson (Academic Press 1966) p. 354.
12) IPCR Cyclotron Progress Report 1967. This report will be delivered upon request.
13) Ajzenberg-Selove and Lauritsen: Nuclear Phys. **11** (1959) 1; K. Kunz and J. Schintlmeister: *Nuclear Tables* (Pergamon Press, 1964).
14) C. H. Holbrow, R. Middleton and B. Rosner: Phys. Rev. **152** (1965) 970.
15) E. M. Kellog and R. W. Zurmüle: Phys. Rev. **152** (1966) 890.
16) C.D. Zafiratos, L.S. Lilley and F.W. Slee: Phys. Rev. **154** (1967) 887.
17) N. Mongelson and B.G. Harvey: UCRL-17299, Annual Progress Report-1966.

Reprinted from Phys. Rev. Lett., 25, 547–550 (1970).

ANOMALOUS ORBITAL MAGNETISM OF PROTON DEDUCED FROM THE MAGNETIC MOMENT OF THE 11^- STATE OF ^{210}Po†

T. Yamazaki and T. Nomura
Department of Physics, University of Tokyo, Bunkyo-ku, Tokyo, Japan,
The Institute of Physical and Chemical Research, Yamato-machi, Saitama-Ken, Japan

and

S. Nagamiya* and T. Katou
The Institute of Physical and Chemical Research, Yamato-machi, Saitama-Ken, Japan
(Received 1 June 1970)

The g factor of the 24-nsec $(h_{9/2}i_{13/2})$ 11^- state of ^{210}Po has been determined to be 1.090 ± 0.016 by the spin-rotation method in the reaction ^{208}Pb$(\alpha, 2n)$. The anomalous g_l^{eff} factor of 1.09 ± 0.02 has been deduced from this value and the known g factor of $h_{9/2}$ under the assumption of the renormalized single particle operator $\vec{\mu} = g_l^{\text{eff}}\vec{l} + g_s^{\text{eff}}\vec{s}$.

In a previous Letter[1] we reported on a measurement of the g factor of the $(h_{9/2}^2)$ 8^+ state of ^{210}Po, which turned out to be equal to that of the $h_{9/2}$ state of ^{209}Bi within 1% error. We discussed a possible blocking effect of the occupying particles on the $(h_{11/2}^{-1}h_{9/2})$ 1^+ type spin polarization and concluded from the observed additivity that such spin polarization mechanism is only a partial contributor to the large deviation from the Schmidt value. A question was then raised as to whether the g_l factor is 1 or not.

So far many theories[2-7] have predicted such corrections that can be renormalized into the orbital magnetism $g_l\vec{l}$, but no clear experimental evidence has yet been found mainly because a larger anomaly in the spin part $g_s\vec{s}$ exists. In order to elucidate this point we tried to measure the g factor of the $(h_{9/2}i_{13/2})$ 11^- state of ^{210}Po in which the spin contributions are nearly cancelled out so that the g factor should be nearly equal to g_l. A preliminary result ($g = 1.05 \pm 0.20$) was reported three years ago by one of the authors,[8] but the present result has an accuracy sufficient to demonstrate for the first time that the effective orbital g factor in question is really anomalous. In the following we present the experimental result and discussions.

A metallic ^{208}Pb target of 30 mg/cm^2 thickness was bombarded with 30-MeV α particles from the Institute of Physical and Chemical Research cyclotron to populate the 11^- isomeric state[9,10] of 24-nsec half-life of ^{210}Po in the reaction ^{208}Pb$(\alpha, 2n)^{210}$Po. A relevant level scheme is given in Fig. 1(a). A 30-cm^3 Ge(Li) detector was placed at 135° to the beam to measure the time-differential perturbed angular distribution of delayed γ rays between the natural beam bursts of 120.0 nsec interval. The total counting rate in the detector was around 3×10^4 cps without appreciable loss of energy resolution. An external magnetic field of 19.05 kG was applied up and down perpendicularly to the beam-detector plane. The experimental procedures were similar to those described earlier.[1,11]

Energy and time spectra were taken by a 4096-channel two-parameter pulse-height analyzer (256 time channels × 16 energy channels). The energy channels covered both the 1180-keV $2^+ \rightarrow 0^+$ and the 1292-keV $11^- \rightarrow 8^+$ γ rays. Time differential patterns $R(t) = \{N^\downarrow(t) - N^\uparrow(t)\}/\{N^\downarrow(t) + N^\uparrow(t)\}$ as shown in Fig. 1(b) yielded $\omega_L(\gamma 1292) = 101.0 \pm 1.5$ MHz and $\omega_L(\gamma 1180) = 82.5 \pm 1.3$ MHz. The latter is predominantly the Larmor frequency at the 110-nsec 8^+ state with small correction due to partial feeding from the 11^- state, which turned out to be compatible with the previous measurement[1] within the experimental error. The former is the Larmor frequency of interest at the 24-nsec 11^- state. There is a long-lived tail in the time distribution of the 1292-keV γ rays, which is supposedly due to another isomeric state of 78 nsec half-life,[10] but the Larmor frequency obtained above was free from disturbance of this tail. After the correction for the Knight shift of 1.47%[12] we obtain

$$g(11^-) = 1.090 \pm 0.016. \tag{1}$$

The wave function of the 11^- state of ^{210}Po is expressed as

$$|11^-\rangle = (1-\alpha^2)^{1/2}|h_{9/2}i_{13/2}; 11^-\rangle + \alpha|(h_{9/2}^2)8^+, (\hbar\omega_3)3^-; 11^-\rangle. \tag{2}$$

The second term is important especially for the $11^- \rightarrow 8^+$ $E3$ transition and its squared amplitude was estimated to be 0.05 from the analysis[8,10] of the experimental $B(E3)$. The magnetic moment due to the second term can be estimated using

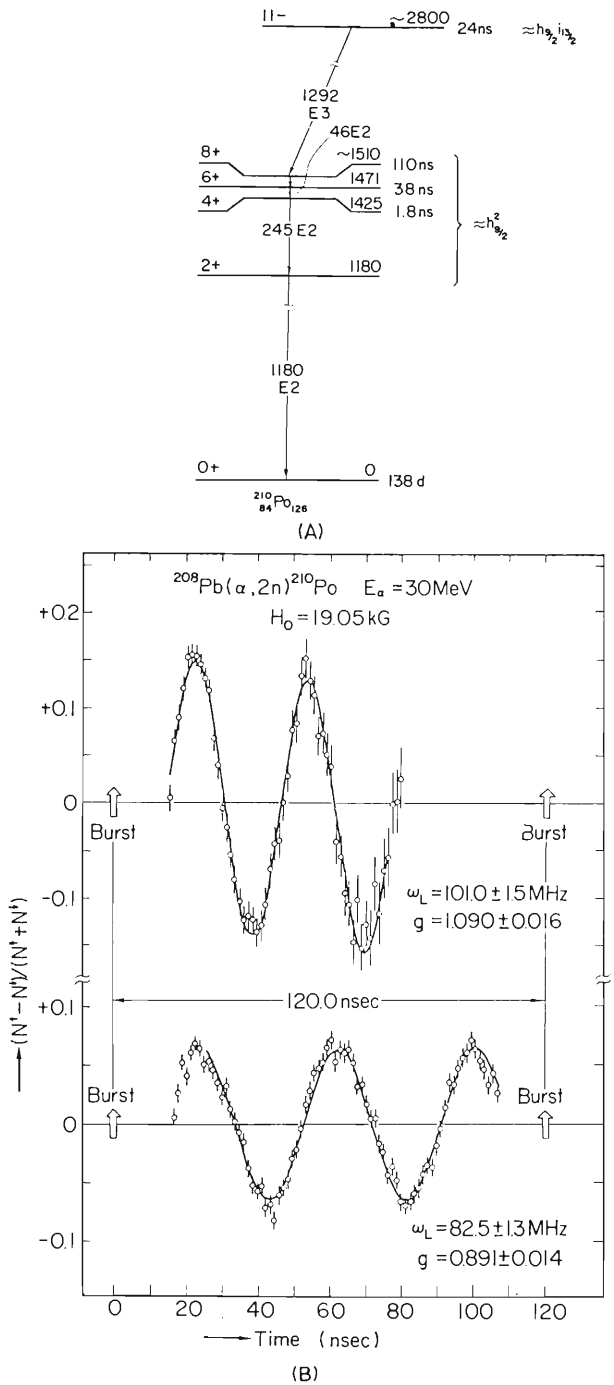

FIG. 1. (a) Level scheme of ^{210}Po associated with the high-spin isomeric states, populated in the reaction ^{208}Pb $(\alpha, 2n)^{210}$Po, as proposed by Yamazaki (Ref. 10). (b) Time-differential spin-rotation patterns for the 24-nsec 11^- state of ^{210}Po (upper) and for the 110-nsec 8^+ state of ^{210}Po (lower). Counts $N^\uparrow$ and $N^\downarrow$ correspond to the external magnetic field up and down, respectively. Because of the long-lived tail in the time spectrum the quantity $N^\uparrow + N^\downarrow$ is replaced by a decay function of 24 nsec half-life in the upper case. The solid curves are best-fitted ones. Various types of normalization and functions yielded the same Larmor frequency.

the g factors of the 8^+ state of ^{210}Po[1] and the 3^- state of ^{208}Pb.[13] Hence, we have for the first term

$$g((h_{9/2}\, i_{13/2})11^-) = 1.104 \pm 0.017. \tag{3}$$

Because this state is of the unique configuration, we can deduce $g(i_{13/2})$ by use of the known value[14] of $g(h_{9/2})$. The results are shown in Table I together with the Schmidt estimate.

It is seen that the deviation from the Schmidt value (Δg or $\Delta\mu$) for the $i_{13/2}$ orbital is rather small in contrast to the case of the $h_{9/2}$ moment. The contribution of the core polarization calculated by Arima and Horie[15] is presented in column 6 of the table. While $\Delta\mu_{\mathrm{calc}}(h_{9/2})$ is too small to be compared with $\Delta\mu_{\mathrm{exp}}(h_{9/2})$, $|\Delta\mu_{\mathrm{calc}} \times (i_{13/2})|$ is rather too large to be compared with $|\Delta\mu_{\mathrm{exp}}(i_{13/2})|$. This fact readily suggests that g_l might be anomalous.

Let us classify all possible corrections to magnetic moments into two parts, one proportional to spin $\vec{s}$ and the other independent of spin direction. Phenomenologically, we can express a renormalized single-particle moment as

$$g(jl) = g_l^{\mathrm{eff}} \pm \frac{1}{2l+1}(g_s^{\mathrm{eff}} - g_l^{\mathrm{eff}})$$

for

$$j = l \pm \tfrac{1}{2}. \tag{4}$$

An experimental value of $g(jl)$ gives a linear relation between g_l^{eff} and g_s^{eff}. In Fig. 2 are shown two lines corresponding to the experimental values, $g^{\mathrm{exp}}(h_{9/2})$ and $g^{\mathrm{exp}}(i_{13/2})$, presented in Table I.

If we assume that g_s^{eff} as well as g_l^{eff} is the same for the two orbitals $h_{9/2}$ and $i_{13/2}$, then the cross point of the two lines determines a unique set:

$$g_l^{\mathrm{eff}} = 1.09 \pm 0.02, \tag{5}$$

$$g_s^{\mathrm{eff}} = 3.1 \pm 0.2. \tag{6}$$

Under this assumption the g factor of the two-particle state is shown to be nearly equal to g_l^{eff} as follows:

$$g(j_1 = l_1 + \tfrac{1}{2}, j_2 = l_2 - \tfrac{1}{2};\ J = j_1 + j_2) = g_l^{\mathrm{eff}} + \frac{1}{J(2l_2+1)}(g_s^{\mathrm{eff}} - g_l^{\mathrm{eff}}). \tag{7}$$

As far as the spin polarization of the core is concerned, the two-body interaction of the δ-function type leads to g_s^{eff}s that are nearly independent of the orbitals (except for the $p_{1/2}$ orbital), as shown by Arima and Horie.[15] Column 7 of Table I presents $g_s^{\mathrm{eff}}(i_{13/2})$ and $g_s^{\mathrm{eff}}(h_{9/2})$

Table I. The experimental g factors of the $h_{9/2}$ and $i_{13/2}$ protons in comparison with the Schmidt estimate. The calculation of the core polarization following the framework of Arima and Horie (Ref. 15) is shown in columns 6 and 7.

Proton orbital	g^{exp}	g^{sp}	$\Delta g^{exp} \equiv g^{exp} - g^{sp}$	$\Delta\mu^{exp}$	Calculation $\Delta\mu$	Calculation g_s^{eff} [c]
$h_{9/2}$	0.9067[a]	0.583	0.324	1.46	0.81	3.62
$i_{13/2}$	1.241 ± 0.029[b]	1.353	-0.112 ± 0.029	-0.73 ± 0.19	−1.06	3.49

[a] From Ref. 14.

[b] Present value deduced from $g(11^-, {}^{210}\mathrm{Po})$.

[c] Deduced under the assumption of $g_l = 1$.

calculated within the framework of Arima and Horie. These values are also shown in Fig. 2[(a) and (b), respectively].

Since a refined calculation of Blomqvist et al.[16] including a realistic force gave almost the same result for the $h_{9/2}$ orbital as that of Arima and Horie, we may expect that $g_s^{eff}(i_{13/2})$ is unchanged as well with the realistic two-body interaction. Corrections to g_s from other origins[2-7] may also be nearly independent of the orbitals. Just for the sake of a support to this conjecture the g factor of the $s_{1/2}^{-1}$ state of ^{205}Tl,[14] which should be g_s^{eff} itself, is shown in Fig. 2. This value is very close to the cross point. Even if we allow an orbital dependence of $|g_s^{eff}(h_{9/2}) - g_s^{eff}(i_{13/2})| = 0.5$, this causes an ambiguity of only 0.02 in g_l^{eff}, being comparable with the quoted error in (5).

The present experiment has thus shown clearly an anomalous value, 1.09 ± 0.02, of g_l^{eff}. The shell-model calculation of the core polarization[15,16] accounted for about half of the deviation of the $h_{9/2}$ magnetic moment of ^{209}Bi from the Schmidt value. Based on the present analysis the remainder is now ascribed to the anomalous g_l^{eff} factor, whatever it originates from. An analysis[17] of the magnetic hyperfine coupling in the muonic atom of Bi indicated that g_l should not be too far from 1.0, but the present value is certainly within this allowance.

The mesonic effect[2,3] is believed to be the main source of such an anomaly. The meson-exchange current renormalizes not only the g_s factor but also the g_l factor. A recent calculation of Chemtob[3] gives $\delta g_l = 0.10$ for odd-proton heavy nuclei, which is just compatible with the present ex-

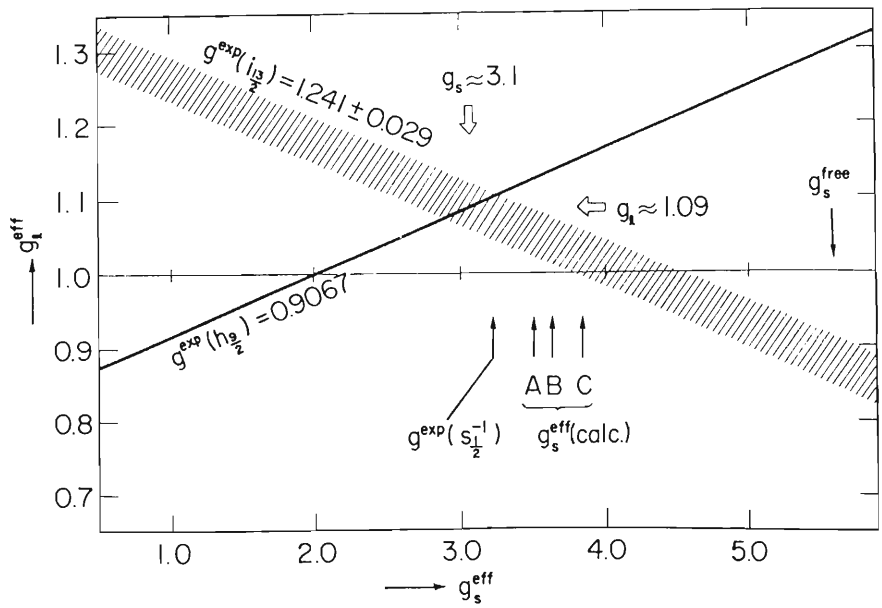

FIG. 2. Relation between g_s^{eff} and g_l^{exp} when g^{exp} is given. The two lines correspond to $g^{exp}(h_{9/2})$ and $g^{exp}(i_{13/2})$. The cross point determines a unique set of $g^{eff} = 1.09 \pm 0.02$ and $g_s^{eff} = 3.1 \pm 0.2$ under the assumption of the orbital independence of g_l^{eff} and g_s^{eff}. The $g^{exp}(s_{1/2}^{-1}, Tl)$ is also given for comparison. The g_s^{eff}'s from the calculation of the core polarization are indicated; A: $g_s^{eff}(i_{13/2})$, B: $g_s^{eff}(h_{9/2})$ both by Arima and Horie (Ref. 15), and C: $g_s^{eff}(h_{9/2})$ by Blomqvist *et al.* (Ref. 16).

periment. For protons, a velocity-dependent potential also leads to a correction. The case of a spin-orbit interaction was calculated by Jensen and Mayer[4] and later by Zaretskii.[5] Since this correction changes sign as the spin direction, it is classified into g_s^{eff} in our phenomenological analysis. This effect results in $\delta g_s^{\text{eff}} = -(0.5 \sim 1)$. Bhaduri and Van Leuven[6] derived an expression for g_l^{eff} assuming a momentum-dependent internucleon force. This effect amounts to $g_l^{\text{eff}} = 1.114$, which is in good agreement with the present observation.

The present data themselves cannot discriminate among these theories. A characteristic feature of the mesonic effect and also the effect of Bhaduri and Van Leuven is that δg_l is isovector so that we expect $g_l^{\text{eff}} - 0.10$ for neutron, while the one-body velocity-dependent effect applies only to proton. Because of the lack of more experimental data of good precision in the closed-shell region this point is open to further experimental investigation.

We would like to thank Professor H. Kumagai and Professor K. Matsuda for their interest and encouragement. We are indebted to Professor A. Arima and Professor H. Miyazawa for valuable discussions. The help of the cyclotron crew of the Institute of Physical and Chemical Research is gratefully acknowledged.

---

†Work partially supported by the Nishina Memorial Foundation.

*On leave of absence from Department of Physics, Osaka University.

[1]T. Yamazaki, T. Nomura, T. Katou, T. Inamura, A. Hashizume, and Y. Tendou, Phys. Rev. Lett. 24, 317 (1970).

[2]H. Miyazawa, Prog. Theor. Phys. 6, 801 (1951); Y. Hara and E. Kuroboshi, Prog. Theor. Phys. 20, 163 (1958), and 21, 768 (1959).

[3]M. Chemtob, Nucl. Phys. A123, 449 (1969).

[4]J. H. D. Jensen and M. G. Mayer, Phys. Rev. 85, 1040 (1951).

[5]D. F. Zaretskii, Zh, Eksp. Teor. Fiz. 36, 869 (1959) [Sov. Phys.-JETP 9, 612 (1959)].

[6]R. K. Bhaduri and P. Van Leuven, Phys. Lett. 20, 182 (1966).

[7]A. B. Migdal, Zh. Eksp. Teor. Fiz. 46, 1680 (1964) [Sov. Phys.-JETP 19, 1136 (1964)].

[8]T. Yamazaki, in *Nuclear Structure and Nuclear Reaction, Proceedings of the International School of Physics "Enrico Fermi," Course XL,* edited by M. Jean (Academic, New York, 1969), p. 791.

[9]T. Yamazaki and G. T. Ewan, Phys. Lett. 24B, 278 (1957).

[10]T. Yamazaki, Phys. Rev. C 1, 290 (1970).

[11]T. Yamazaki and E. Matthias, Phys. Rev. 175, 1476 (1968).

[12]See the compilation by L. E. Drain, Met. Rev. 12, 195 (1967). The Knight shift of Po produced in the metallic Pb target is assumed to be that of Pb in Pb.

[13]J. D. Bowman, F. C. Zawislak, and E. N. Kaufmann, Phys. Lett. 29B, 226 (1969).

[14]I. Lindgren, in *Perturbed Angular Correlations,* edited by E. Karlsson, E. Matthias, and K. Siegbahn (North-Holland, Amsterdam, 1964), p. 379.

[15]A. Arima and H. Horie, Progr. Theoret. Phys. 12, 623 (1954).

[16]J. Blomqvist, N. Freed, and H. O. Zetterstrom, Phys. Lett. 18, 47 (1965).

[17]J. Johnson and R. A. Sorensen, Phys. Lett. 26B, 700 (1968).

Reprinted from Nucl. Phys., A159, 653–660 (1970).

STROBOSCOPIC DETERMINATION OF THE MAGNETIC MOMENT OF THE 8^+ ISOMERIC STATE OF ^{208}Po

S. NAGAMIYA †

Cyclotron Laboratory, The Institute of Physical and Chemical Research, Wako-shi Saitama-ken, Japan

and

T. NOMURA and T. YAMAZAKI

Department of Physics, University of Tokyo, Bunkyo-ku, Tokyo, Japan, and the Institute of Physical and Chemical Research, Wako-shi, Saitama-ken, Japan ††

Received 20 July 1970

Abstract: The g-factor of the $[h_{\frac{9}{2}}(p)^2\ p_{\frac{1}{2}}(n)^{-2}]8^+$ isomeric state of ^{208}Po has been determined to be 0.902 ± 0.006 by the stroboscopic resonance method, in which the aligned isomeric state of 380 ns half-life was generated by the reaction ^{206}Pb(α, 2n)^{208}Po in microscopic beam bursts of a cyclotron. The observed g-factor agrees with that of the $[h_{\frac{9}{2}}(p)^2]8^+$ state of ^{210}Po within an accuracy of 1 %, indicating that the effect of the $[p_{\frac{1}{2}}(n)^{-1}\ p_{\frac{1}{2}}(n)]1^+$ type spin polarization on the magnetic moment is negligibly small, as expected from the theoretical predictions.

E | NUCLEAR REACTIONS ^{206}Pb(α, 2nγ), $E = 29$ MeV; measured $\alpha\gamma(\theta, H, t)$. ^{208}Po level deduced μ stroboscopic method.

1. Introduction

It is well known that the magnetic moment of the $h_{\frac{9}{2}}(p)$ ground state of ^{209}Bi deviates largely from the single-particle estimate. The theoretical calculations based on the M1 spin polarization mechanism given by Arima and Horie [1]), Blin-Stoyle and Perks [2]), and recently by Blomqvist *et al.* [3]), could account for only a half of its deviation and the remainder has been left as a question.

Yamazaki *et al.* [4]) recently reported on a g-factor measurement of the $[h_{\frac{9}{2}}(p)^2]8^+$ state of ^{210}Po and discussed a blocking effect of the presence of particles in the $h_{\frac{9}{2}}$ orbit on the $[h_{\frac{11}{2}}(p)^{-1}\ h_{\frac{9}{2}}(p)]1^+$ type spin polarization. From a good agreement of the observed magnetic moment with that of the ground state of ^{209}Bi they concluded that the $[h_{\frac{11}{2}}{}^{-1}\ h_{\frac{9}{2}}]1^+$ type spin polarization is not the sole contributor to the anomalous magnetic moment of ^{209}Bi.

The following questions were raised from this conclusion. (i) Is there an anomalous orbital magnetism? This problem has recently been answered experimentally [5]) with the observation of the magnetic moment of the $[h_{\frac{9}{2}}(p)\ i_{\frac{13}{2}}(p)]11^-$ state of ^{210}Po, which indicated that the effective g_l factor is 1.09.

† On leave from Department of Physics, Osaka University.

†† Work partially supported by the Nishina Memorial Foundation.

(ii) What is the structure of the spin polarization mechanism? This problem can be studied by observing the blocking effect of polarizing particles on the M1 spin polarization.

Measuring the g-factors of the $[h_{\frac{9}{2}}(p)^2]8^+$ isomeric state of ^{204}Po, ^{206}Po and ^{208}Po, which were systematically identified by Yamazaki *et al.* [6-8]), will give information on the second point described above and especially on the effects of neutrons on the M1 spin polarization mechanism, since these states are ones analogous to the $[h_{\frac{9}{2}}(p)^2]8^+$ state of ^{210}Po except that the neutron numbers are different.

In this paper we report the g-factor measurement of the $[h_{\frac{9}{2}}(p)^2\ p_{\frac{1}{2}}(n)^{-2}]8^+$ isomeric state of ^{208}Po and discuss the effects of neutrons on the M1 spin polarization.

2. Experimental details

The method we employed in measuring the g-factor was the stroboscopic resonance method. This method has recently been developed [9,10]) in the field of pulsed beam γ-ray spectroscopy, and proved to be a very convenient method of accurately determining the g-factor of an excited state if the lifetime of the latter is longer than the period of the applied pulsed beam. The principle of this method is simple. Since an anisotropy of γ-rays from excited aligned nuclei in a magnetic field is destroyed unless the period of a pulsed beam coincides with an integral multiple of half the Larmor period of the excited nuclei, a search for a maximum of the anisotropy as a function of the strength of an applied magnetic field (or as a function of the period of an applied pulsed beam) should determine the Larmor period.

The stroboscopic resonance occurs when

$$n\frac{\pi}{\omega_L} = T_B, \tag{1}$$

where ω_L is the Larmor frequency, T_B is the period of a pulsed beam and n is an arbitrary integer. If we define the half width ΔH to be the interval between the two field strengths at which the anisotropy of γ-rays is reduced to half the value of its maximum, then

$$\frac{\Delta H}{H_0} = \frac{T_B}{n\pi\tau}, \tag{2}$$

where τ is the mean life of excited nuclei and H_0 is the resonant magnetic field given by

$$H_0 = \frac{\hbar\omega_L^{(0)}}{g\mu_N} = n\frac{\hbar(\pi/T_B)}{g\mu_N}, \qquad \omega_L^{(0)}; \text{ resonant Larmor frequency.} \tag{3}$$

The accuracy of the determination of the g-factor can be estimated from eq. (2). The inverse proportionality of an expected accuracy to the mean life τ is a natural consequence when no competing relaxation process exists. For details of this method see refs. [9,10]).

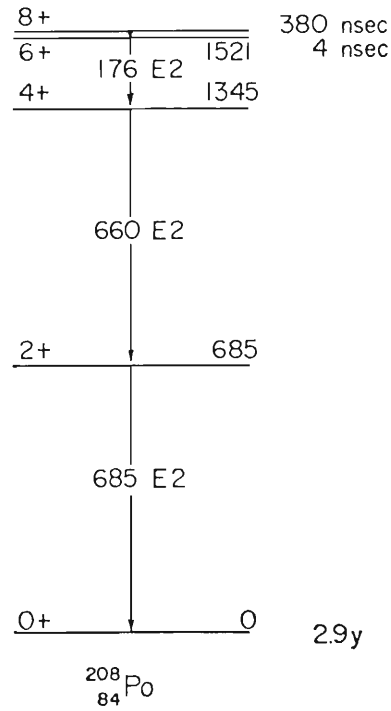

Fig. 1. Levels of ^{208}Po strongly populated in the reaction ^{206}Pb(α, 2n)^{208}Po, as proposed by Treytl, Hyde and Yamazaki [7]).

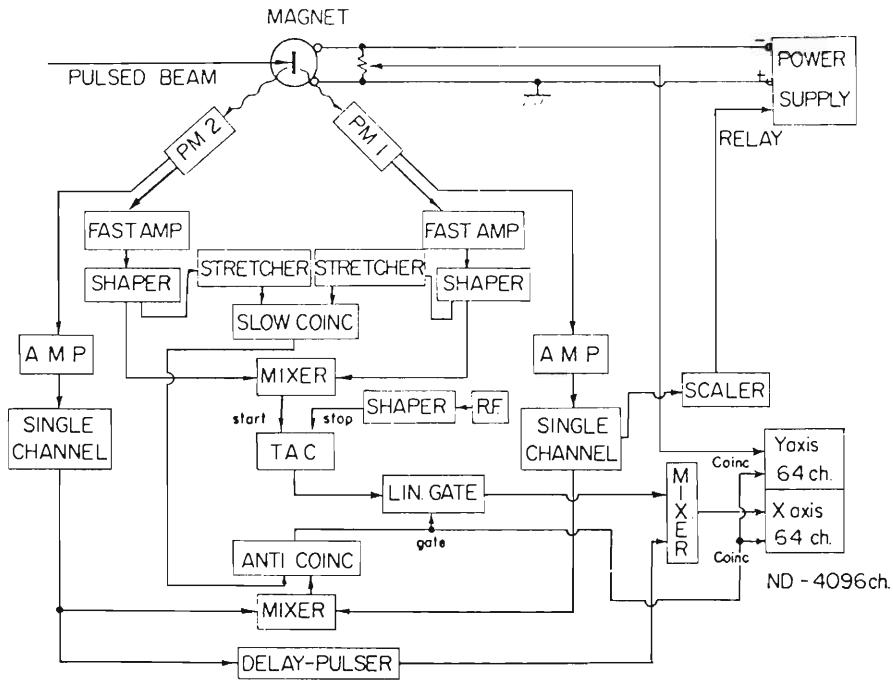

Fig. 2. A block diagram of the electronics arrangement used in the stroboscopic resonance method. The systems are essentially the same as those used in the ordinary time-differential PAD method except that the magnetic field is varied. When both the two counters simultaneously detect γ-rays (within the 2 μsec interval), the output of the TAC is rejected in the linear gate circuit by the slow-coincidence → anti-coincidence → linear gate system. In order that the x-channels represent the time distribution patterns of γ-rays detected by both the counter 1 (PM1) and 2(PM2) the constant pulse ($\approx$ 5V, 2 μsec) is added to the TAC output only when the counter 2 detects the γ-rays.

A 50 mg/cm^2 thick metallic foil of ^{206}Pb was bombarded with 29 MeV α-particles from the Institute of Physical and Chemical Research Cyclotron. The time interval T_B of the natural beam bursts of a cyclotron at this energy was 123.43 nsec, which is suitably shorter than the mean life τ ($\approx$ 550 nsec) of the isomeric state of interest. Gamma-rays following the ^{206}Pb(α, 2n) ^{208}Po reaction were detected with two 4.5 cm × 4.5 cm diam. NaI(Tl) counters placed at 60° and 150° with respect to the beam direction. An external magnetic field was applied perpendicularly to the beam-detector plane.

Energy spectra of delayed γ-rays exhibited two remarkable peaks corresponding to 176 keV ($6^+ \rightarrow 4^+$) and unresolved 660 keV ($4^+ \rightarrow 2^+$) and 685 keV ($2^+ \rightarrow 0^+$) transitions in ^{208}Po. A relevant level scheme is shown in fig. 1. We used these two peaks to analyze the perturbing effect of the external magnetic field on the 8^+ isomeric state, since the angular distributions of these γ-rays, which were generated through the 8^+ isomeric state [6, 7], are not affected by the short-lived 6^+ state ($t_{\frac{1}{2}}$ = 4 nsec) but are determined by the perturbation of the long-lived 8^+ state ($t_{\frac{1}{2}}$ = 380 nsec).

The electronics arrangement is shown in fig. 2. In order to observe the anisotropy of γ-rays as a function of the strength of the applied magnetic field the 4096-channel pulse-height analyzer was used with two dimensions (64 channels × 64 channels). The x-channels were used to analyze the time distributions of energetically selected γ-rays and the y-channels to identify the strength of the applied magnetic field. The x-channels were furthermore divided into two sections for the two NaI(Tl) counters placed at 60° and 150°, respectively. The strength of the magnetic field was varied automatically by the signal produced in the γ-ray scaler.

Magnetic field measurements were carried out by means of a Hall effect probe, which was calibrated by the NMR systems. The reliability of the field strength thus determined was about to 0.2 %.

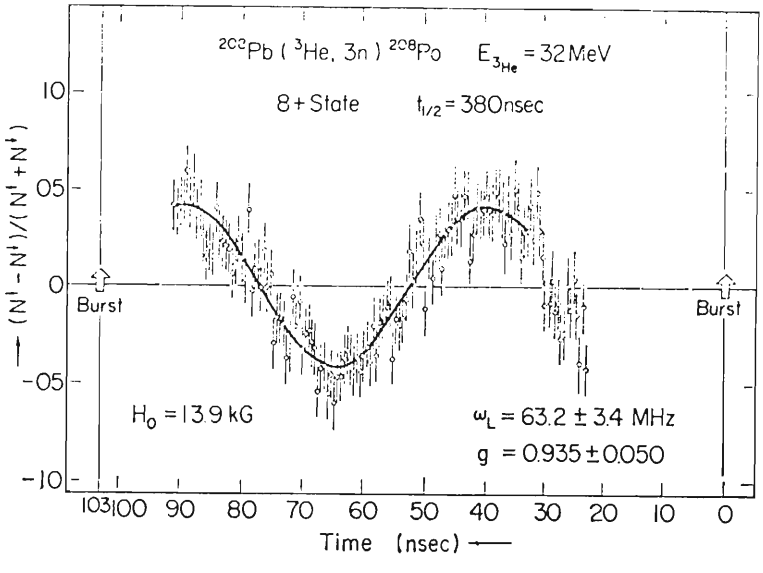

Fig. 3. Time-differential patterns of the γ-ray angular distribution. Counts $N\uparrow$ and $N\downarrow$ correspond to the external magnetic field up and down, respectively. The solid curve is the best fit.

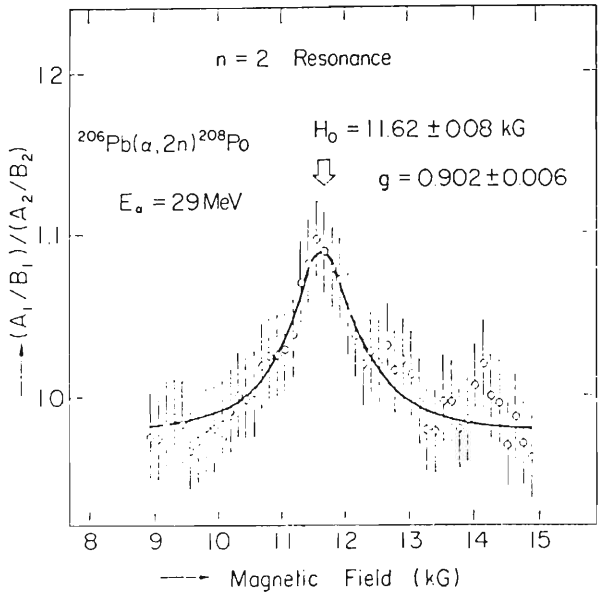

Fig. 4. The $n = 2$ stroboscopic resonance. The solid curve is one fitted by a Lorenzian curve. A theoretically expected lineshape is more complicated, but is known to be a symmetric function having its center at the resonant field H_0 [ref. [10]]. Thus it is permitted to use a Lorenzian curve to determine the position of H_0.

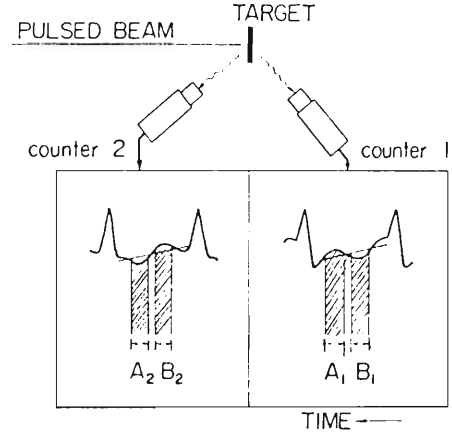

Fig. 5. A measure of the anisotropy of the γ-ray angular distribution. Suppose the angular distribution of γ-rays is given by $W(\theta) = N_0(1+B_2\cos(2\theta))$ and the value B_2 is positive, then, at the resonant field H_0, the counts A_1 and B_2 have maximum values and the A_2 and B_1 have minimum values. Hence, the double ratio $(A_1/B_1)/(A_2/B_2)$ can be considered as a measure of the anisotropy of γ-rays.

3. Results and discussions

3.1. g-FACTOR OF THE $[h_{\frac{9}{2}}(p)^2\, p_{\frac{1}{2}}(n)^{-2}]8^+$ STATE

Prior to the stroboscopic measurements we had roughly determined the g-factor of the 8^+ isomeric state of ^{208}Po by the ordinary method of the time-differential perturbed angular distribution. In this measurement the ^{208}Pb(^{3}He, 3n)^{208}Po reaction was used. Fig. 3 shows the result from which we obtain $g = 0.935 \pm 0.050$.

Fig. 4 shows the $n = 2$ stroboscopic resonance. As a measure of the anisotropy of γ-rays we used such a quantity as $(A_1/B_1)/(A_2/B_2)$ schematically illustrated in fig. 5.

By sweeping the external field we searched for the resonant magnetic field at which the Larmor period of the 8^+ isomeric state coincides with the period of the excitation with a pulsed beam from the cyclotron. The resonant magnetic field has been determined to be

$$H_0 = 11.62 \pm 0.08 \text{ kG}. \tag{4}$$

Since the period of a pulsed beam was 123.43 nsec, the resonant Larmor frequency becomes, from eq. (1),

$$\omega_L^{(0)} = 50.905 \text{ MHz}. \tag{5}$$

Assuming that the Knight shift of ^{208}Po in the metallic ^{206}Pb is 1.47 % [this value is for Pb in the metallic Pb (ref. [11])], and combining the value (4) with (5), we can deduce from eq. (3) that the g-factor of the 8^+ isomeric state of ^{208}Po is

$$g(8^+) = 0.902 \pm 0.006. \tag{6}$$

It was pointed out by Treytl, Hyde and Yamazaki [7]) that the $[h_{\frac{9}{2}}^2]I^+$ states of ^{208}Po are described as the two-particle states weakly coupled to a surface vibration of the ^{206}Pb core, since the observed values of $B(E2)$ are large compared with those in ^{210}Po. They expressed the wave functions of the $[h_{\frac{9}{2}}^2]I^+$ members as

$$\begin{aligned} |I^+) = {} & a_1^I|[h_{\frac{9}{2}}^2]I, (0\hbar\omega)0; I^+) + a_2^I|[h_{\frac{9}{2}}^2]I-2, (1\hbar\omega)2; I^+) \\ & + a_3^I|[h_{\frac{9}{2}}^2]I, (1\hbar\omega)2; I^+) + a_4^I|[h_{\frac{9}{2}}^2]I+2, (1\hbar\omega)2; I^+), \end{aligned} \tag{7}$$

by assuming the following interaction

$$H_{\text{int}} = -k\sqrt{\frac{\hbar\omega}{2C}} \sum_\mu \{b_\mu + (-)^\mu b^\dagger_{-\mu}\}\{Y_{2\mu}(\theta_1, \phi_1) + Y_{2\mu}(\theta_2, \phi_2)\}. \tag{8}$$

The correction for the g-factor caused by the second, third and fourth terms in eq. (7) is very small in magnitude because the E2 collective terms affect the correction by the squares of their amplitudes. By using the coupling constant $k\sqrt{\hbar\omega/2C} \approx 0.6$ MeV adopted by Yamazaki [6]) and putting the collective g-factor $g_R \approx Z/A \approx 0.4$ we obtain [12]) for the first term in eq. (7)

$$g([h_{\frac{9}{2}}(p)^2 p_{\frac{1}{2}}(n)^{-2}]8^+) = 0.905 \pm 0.006. \tag{9}$$

3.2. COMPARISON WITH OTHER STATES AND WITH THEORY

The present result is listed in table 1 together with the g-factors of the 8^+ state of ^{210}Po, the $\frac{17}{2}^-$ state of ^{209}Po, and of the ground state of ^{209}Bi. The second value in the last column, 0.85 ± 0.05, is deduced from the g-factor determined by Yamazaki and Matthias [13]) by using the Lande formula. This value is considered to be the g-factor of the $h_{\frac{9}{2}}(p)^2$ state with one neutron hole in the ^{208}Pb core. The third value in the last column is the present result of the g-factor of the $h_{\frac{9}{2}}(p)^2$ state with two neutron holes in the ^{208}Pb core.

TABLE 1

The g-factors of the $[h_{\frac{9}{2}}^2]$ proton states

		Configuration	$t_{\frac{1}{2}}$	g-factor	g-factor of $h_{\frac{9}{2}}^2$
^{210}Po	8^+	$h_{\frac{9}{2}}(p)^2$	110 nsec	0.911±0.01 [a])	0.911±0.010
^{209}Po	$\frac{17}{2}^-$	$h_{\frac{9}{2}}(p)^2\ p_{\frac{1}{2}}(n)^{-1}$	100 nsec	0.867±0.05 [b])	0.85 ±0.05
^{208}Po	8^+	$h_{\frac{9}{2}}(p)^2\ p_{\frac{1}{2}}(n)^{-2}$	380 nsec	0.902±0.006 [c])	0.905±0.006
^{209}Bi	$\frac{9}{2}^-$	$h_{\frac{9}{2}}(p)$		0.9067	

[a]) From ref. [4]).
[b]) Obtained from ref. [13]) after the Knight shift correction.
[c]) Present result.

Yamazaki *et al.* [4]) found that the following additivity for the magnetic moments holds well:

$$g(^{210}\mathrm{Po}[h_{\frac{9}{2}}^2]8^+) = g(^{209}\mathrm{Bi}[h_{\frac{9}{2}}]\tfrac{9}{2}^-). \tag{10}$$

The present result shows that this additivity can be extended to ^{208}Po.

Concerning the M1 spin polarization due to neutrons this fact implies that the contribution of the $[p_{\frac{3}{2}}^{-1}p_{\frac{1}{2}}]1^+$ neutron particle-hole to the magnetic moment is negligibly small. This is supported theoretically, since the deviation δg due to the $[p_{\frac{3}{2}}^{-1}p_{\frac{1}{2}}]1^+$ type spin polarization is estimated to be

$$\delta g_{\mathrm{calc}} \approx 0.01, \tag{11}$$

under the assumption of the δ-function type interaction applied by Arima and Horie [1]).

The order of magnitude of the M1 core polarization due to the $[i_{\frac{13}{2}}(n)^{-1}i_{\frac{11}{2}}(n)]1^+$ excitation cannot be evaluated from the present measurement, because the contribution of such a particle-hole to the magnetic moment is proportional to $(U_{j_p}V_{j_h})^2$ where $j_p = i_{\frac{11}{2}}$ and $j_h = i_{\frac{13}{2}}$ and the change of $(U_{j_p}V_{j_h})^2$ from ^{210}Po to ^{208}Po is at most 0.7 % [ref. [14])]. Further information on the g-factors of the states that are deficient of more neutrons will be necessary in order to deduce the magnitude of such spin polarizations.

The authors are grateful to Professors H. Kumagai and K. Matsuda for their interest and encouragement and to Professor A. Arima for the helpful discussions. One of them (S.N.) would like to thank Professor K. Sugimoto for his encouragement and discussions. We are also indebted to the crew of the Institute of Physical and Chemical Research Cyclotron for their operation of the machine.

References

1) A. Arima and H. Horie, Prog. Theor. Phys. **12** (1954) 623
2) R. J. Blin-Stoyle and M. A. Perks, Proc. Phys. Soc. **A67** (1954) 885
3) J. Blomqvist, N. Freed and H.-O. Zetterström, Phys. Lett. **18** (1965) 47

4) T. Yamazaki, T. Nomura, T. Katou, T. Inamura, A. Hashizume and Y. Tendou, Phys. Rev. Lett. **24** (1970) 317
5) T. Yamazaki, T. Nomura, S. Nagamiya and T. Katou, Phys. Rev. Lett. **25** (1970) 547
6) T. Yamazaki, Phys. Rev. **C1** (1970) 290
7) W. J. Treytl, E. K. Hyde and T. Yamazaki, Nucl. Phys. **A117** (1968) 481
8) T. Yamazaki and G. T. Ewan, Phys. Lett. **24B** (1967) 278
9) J. Christiansen, H.-E. Mahnke, E. Recknagel, D. Riegel, G. Weyer and W. Witthuhn, Phys. Rev. Lett. **21** (1968) 554; Phys. Rev. **C1** (1970) 613
10) S. Nagamiya and K. Sugimoto, Osaka University Laboratory of Nuclear Studies report OULNS 69–3 (1969)
11) L. E. Drain, Met. Rev. **12** (1967) 195
12) A. Bohr and B. R. Mottelson, Mat. Fys. Medd. Dan. Vid. Selsk. **27**, No. 16 (1953)
13) T. Yamazaki and E. Matthias, Phys. Rev. **175** (1968) 1476
14) L. S. Kisslinger and R. A. Sorensen, Mat. Fys. Medd. Dan Vid. Selsk. **32** , No. 9 (1960)

Reprinted from J. Phys. Soc. Jpn., 33, 881–889 (1972).

Inelastic Scattering of Protons from ^{100}Mo and ^{98}Mo

Yohko AWAYA, Kazuhisa MATSUDA,* Takeshi WADA,
Noriyoshi NAKANISHI, Shigeru TAKEDA
and
Shuhei YAMAJI

The Insitute of Physical and Chemical Research, Wako, Saitama

(Received December 6, 1971)

Angular distributions of elastically and inelastically scattered protons from ^{100}Mo and ^{98}Mo were measured at $E_p=14.7$ MeV. Results were analysed in terms of the optical model and the distorted wave Born approximation theory. In addition, the differential cross sections for the first 2^+ and 3^- states and those for the possible members of two-quadrupole-phonon triplet were compared with coupled channel calculations. Reasonable agreements between the experiment and the theory were obtained except for the second 0^+ state of ^{100}Mo. Admixture of one-phonon component was required for the second 2^+ state.

§ 1. Introduction

The inelastic scattering of protons from nuclei has been considered to be a powerful tool to investigate the collective character of nuclei. The analysis of the obtained data has been made usually by two methods: one being the distorted wave Born approximation (DWBA)[1] and the other the coupled channel (CC) calculation.[2] As the former usually involves the one-step excitation, its usefulness has been shown mainly for the one-quadrupole-phonon and one-octupole-phonon states. The latter is required for the multi-step excitation, such as the excitation of two-phonon states of vibrational nuclei. Since the experimental data of excitation of two-phonon states by the inelastic proton scattering were limited, the analysis by the CC calculation has not been made for many cases. The extensive study of the CC calculation has been done by Tamura.[2]

The properties of the even-mass molybdenum nuclei seem to change with the mass number: the ^{92}Mo nucleus is considered to be explained by the shell model, but the collective character becomes more apparent as the mass increases. According to a recent report,[3] the ^{104}Mo and ^{106}Mo nuclei can be regarded as deformed. In order to investigate this mass number dependence, a systematic study of inelastic proton scattering from all the stable even-mass molybdenum nuclei has been made. The preliminary results of this work have been reported.[4] Since the data obtained for the ^{100}Mo and ^{98}Mo nuclei show that they have a vibrational character and the angular distributions for the two-phonon states have been obtained as well as for others, these nuclei are considered to be good subjects for CC calculations. The main aim of this article is to show the experimental data of the ^{100}Mo(p,p') and ^{98}Mo(p,p') reactions and the results of analysis by the CC calculations. The experimental results of the ^{92,94,96}Mo(p,p') reactions and the systematic analysis of elastic scattering data and of angular distributions for the one-phonon states will be reported elsewhere.

Prior knowledge about the inelastic scattering of nuclear particles from ^{100}Mo and ^{98}Mo is limited, and we could not find any data other than those of the ^{98,100}Mo(d,d') reactions.[5]* The excited states of ^{98}Mo have been studied by the ^{97}Mo(d,p) reaction,[6] the decay of ^{98,98m}Nb,[7–9] the ^{97}Mo(n,γ) reaction,[10] the in-beam spectroscopy[11] and the ^{100}Mo(p,t) reaction.[12] Only a few states are known[13] in ^{100}Mo.

§ 2. Experimental Procedures and Results

The proton beam was obtained from the cyclotron of the Institute of Physical and Chemical Research. The beam handling system was previously reported.[14] The bombarding energies were 14.67 and 14.69 MeV for ^{100}Mo and ^{98}Mo, respectively. The targets were self-supporting metallic foils obtained from Oak Ridge National Laboratory. The isotopic composition of the target material specified by the maker is shown in Table I. The

* Deceased.

* After the completion of this article, the work done by Lutz *et al.*[22] came to our knowledge. Their results are added to Table III and IV, and the comparison of their results with the present work is also added at the end of § 4.

thickness of each target was estimated from the energy loss of alpha-particles emitted from Th-C′, and from Rutherford scattering of 16 MeV alpha-particles at forward angles. The values obtained by these two methods agreed within about 5%,[15] and were 1.08 mg/cm² for ^{100}Mo and 0.80 mg/cm² for ^{98}Mo. The spectra of scattered protons were measured by two 2 mm thick surface-barrier silicon detectors. They were placed about 20 cm away from the target, and the solid angle was 3.75×10^{-4} sr for the detector at forward angle and 4.50×10^{-4} sr for the backward one. The overall energy resolution was about 60 keV FWHM on the average and 50 keV FWHM under the best condition.

Table I. Isotopic abundance of targets.

	^{100}Mo	^{98}Mo
^{92}Mo	0.6 ±0.02	0.14±0.05
^{94}Mo	0.23±0.02	0.1 ±0.05
^{95}Mo	0.4 ±0.02	0.22±0.05
^{96}Mo	0.81±0.02	0.34±0.05
^{97}Mo	0.36±0.02	0.58±0.05
^{98}Mo	1.69±0.05	98.3 ±0.1
^{100}Mo	95.9 ±0.1	0.31±0.05

Examples of spectra of scattered protons from ^{100}Mo and ^{98}Mo are shown in Figs. 1 and 2, respectively. Twenty two states were assigned to ^{100}Mo and fifteen to ^{98}Mo, and angular distributions of inelastically scattered protons were obtained for sixteen states and thirteen states for ^{100}Mo and ^{98}Mo, respectively. The energies of the excited states are listed in Table III with deformation parameters. The 0.80-MeV peak was observed in the ^{100}Mo spectra, and its angular distribution

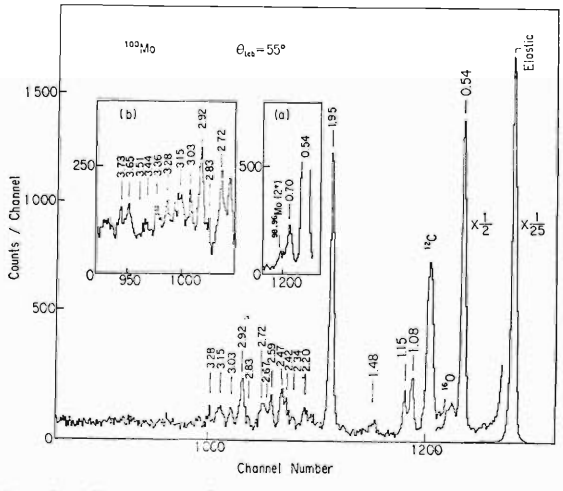

Fig. 1. Spectra of scattered protons from ^{100}Mo obtained at $\theta_{lab}=55°$, at $\theta_{lab}=90°$ (a), and at $\theta_{lab}=95°$ (b).

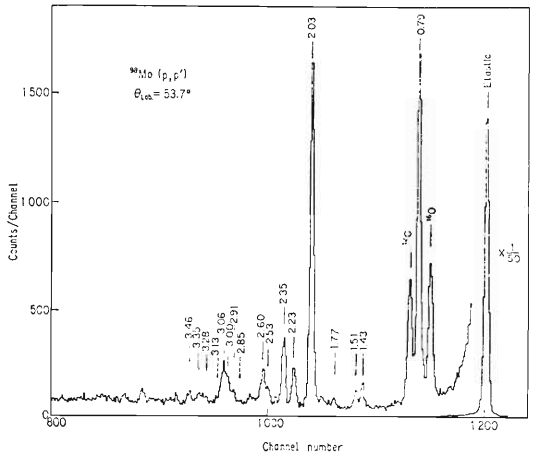

Fig. 2. Spectrum of scattered protons from ^{98}Mo.

showed an $L=2$ pattern. However the yield for this peak was almost the same as that expected from the amount of impurities of ^{96}Mo and ^{98}Mo, whose first 2^+ states lie at about 0.8 MeV, so the 0.80-MeV peak was considered to belong to these impurities and omitted from Table III. About one tenth of the yield for the 1.48-MeV state of ^{100}Mo comes from the impurity of ^{98}Mo in the ^{100}Mo target. Errors in the excitation energies are about 5 keV for well defined peaks and about 10 keV for small ones. Unresolved peaks were separeted, if

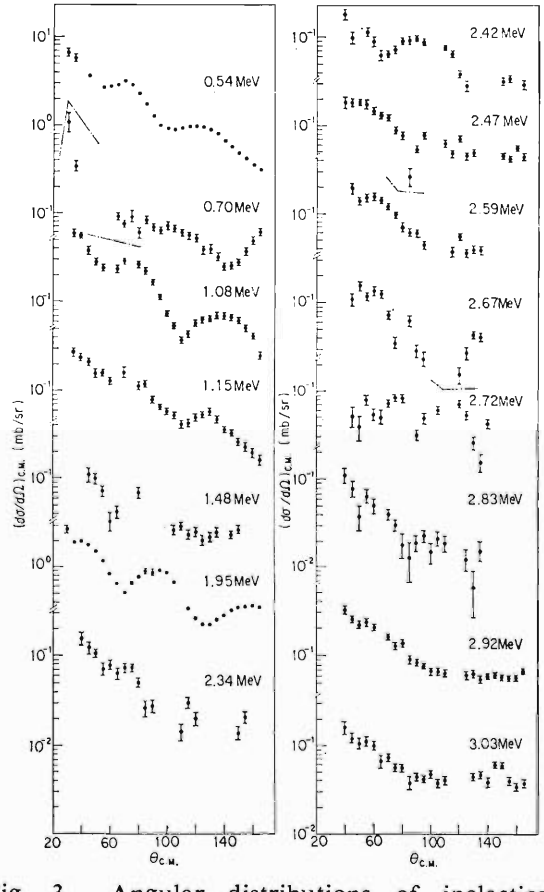

Fig. 3. Angular distributions of inelastically scattered protons from ^{100}Mo.

necessary, by using a χ^2-fit code written by one of the authors (T. W.).

The differential cross sections for the excited states of ^{100}Mo and ^{98}Mo are shown in Figs. 3 and 4, respectively. Those for the elastic scattering are shown in Fig. 5 together with the optical model calculations. The error bars in the figures show the statistical uncertainty. The systematic error is estimated to be less than 10%.

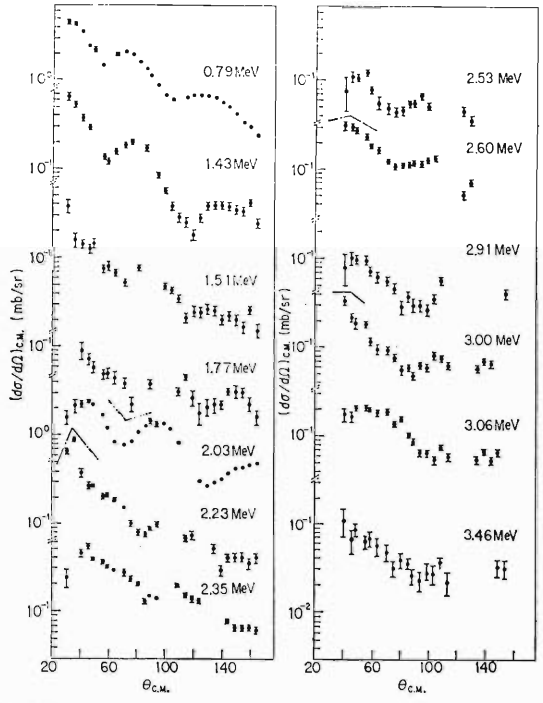

Fig. 4. Angular distributions of inelastically scattered protons from ^{98}Mo.

Up to the excitation energy of 2 MeV, the level structures of ^{100}Mo and ^{98}Mo observed in this work resemble each other. Two strongly excited states, which are considered to be the one-phonon 2^+ and 3^- states, are observed in both nuclei. They are the 0.54-MeV and the 1.95-MeV states of ^{100}Mo and the 0.79-MeV and 2.03-MeV states of ^{98}Mo.

There are two excited states at the excitation energy of almost twice as high as the first 2^+ state in each nucleus. They are the 1.08-MeV and the 1.15-MeV states of ^{100}Mo and the 1.43-MeV and the 1.51-MeV states of ^{98}Mo. There is a similarity between the angular distributions for the 1.08-MeV state of ^{100}Mo and the 1.43-MeV state of ^{98}Mo, while the angular distribution for the 1.15-MeV state of ^{100}Mo shows resemblance to that for the 1.51-MeV state of ^{98}Mo. The spins and parities of the 1.43-MeV and the 1.51-MeV states of ^{98}Mo have been assigned to be 2^+ and 4^+, respectively.[8] From the excitation strength and energy, they are regarded as the members of the two-phonon triplet. Then it would be natural to assume that the 1.08-MeV and 1.15-MeV states of ^{100}Mo are two-phonon 2^+ and 4^+ states, respectively.

Weakly excited states were observed in both nuclei in about the middle between the two-phonon states and the first 3^- states. These might be a member of the three-phonon states. No analysis was tried for them because of their small cross sections.

A peak was observed at 0.70 MeV in ^{100}Mo, whereas to our regret the 0.735-MeV state of ^{98}Mo was not resolved from the strongly excited 2^+ state at 0.79 MeV. However the 0^+ assignment for the 0.735-MeV state is established in the studies of the decay of ^{98}Nb, the ^{100}Mo(p, t) reaction[12] and the ^{97}Mo(n, γ) reaction.[10] Considering the overall similarity between the level structures of ^{100}Mo and ^{98}Mo, as well as the forward peaked angular distribution for the 0.70-MeV state of ^{100}Mo, the spin and parity of the 0.70-MeV state of ^{100}Mo are most likely to be 0^+. This assignment was recently confirmed by the ^{98}Mo(t, p) reaction.[16]

Taking into account all together, the ^{100}Mo and ^{98}Mo nuclei are considered to have typical vibrational structures aside from the fact that the excited 0^+ states are pulled down in energy. Therefore we have tried the CC calculations as well as DWBA.

§ 3. Comparison with the Calculations

Optical model analysis

The elastic scattering data were fitted by an optical model calculation. The form of the optical potential is

Table II. Optical parameters.

		V	W_D	V_{ls}	r_0, r_{ls}	r_I	a_0, a_{ls}	a_I	r_c	σ_R	χ^2
^{100}Mo		55.16	9.50	7.68	1.18	1.28	0.740	0.702	1.25	1272	0.44
^{98}Mo	A	55.14	5.48	8.23	1.18	1.43	0.650	0.813	1.25	1412	0.49
	B	55.16	9.50	7.68	1.18	1.28	0.740	0.702	1.25	1256	1.31

V, W_D, V_{ls}; in MeV. r_0, r_I, r_{ls}, a_0, a_I, a_{ls}; in fm. σ_R; in mb.

$$U=-Vf(r,r_0,a_0)+4ia_I W_D\frac{\mathrm{d}}{\mathrm{d}r}f(r,r_I,a_I)$$
$$+2\left(\frac{\hbar}{m_\pi c}\right)^2 V_{ls}\frac{1}{r}\frac{\mathrm{d}}{\mathrm{d}r}f(r,r_{ls},a_{ls})(\boldsymbol{l}\cdot\boldsymbol{s})+V_c\,,$$

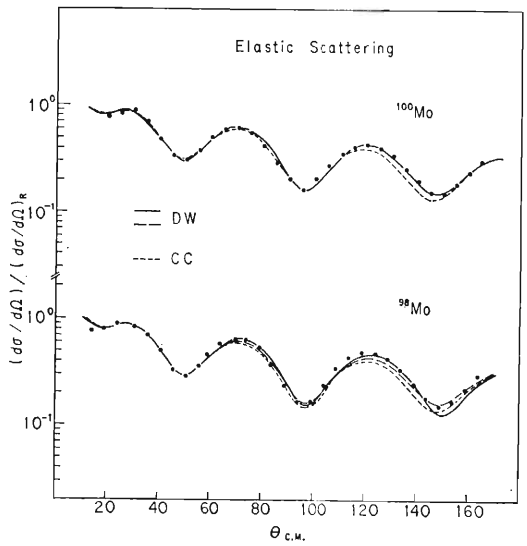

Fig. 5. Differential cross sections divided by Rutherford cross sections for elastically scattered protons from ^{100}Mo and ^{98}Mo. The solid and long-dashed curves are optical model calculations obtained by using parameters shown in Table II. The solid curve for ^{98}Mo is obtained for parameters of set A and long-dashed curve for set B. The short-dashed curves are predictions of CC calculations.

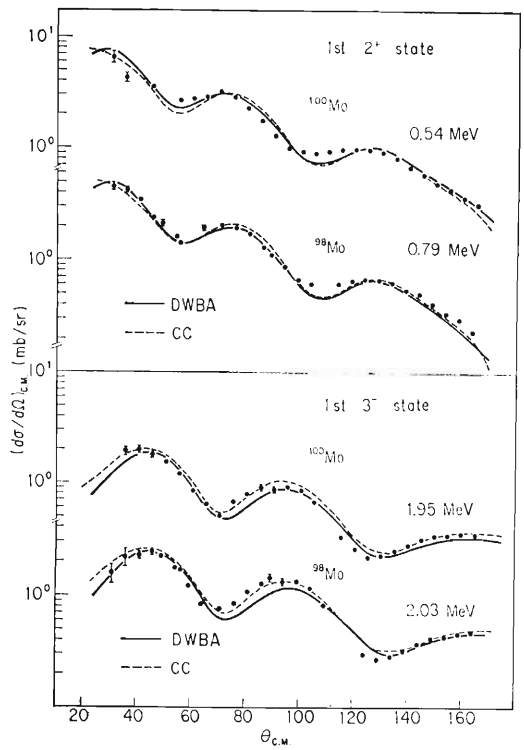

Fig. 6. Comparison of the differential cross sections for the first 2+ and 3− states of ^{100}Mo and ^{98}Mo with calculated curves. The DWBA and CC results are shown by solid and dashed curves, respectively.

$$f(r,r',a')=[1+\exp\{(r-r'A^{1/3})/a'\}]^{-1}\,,$$

where V_c is Coulomb potential for an uniformly charged sphere with a radius of $r_cA^{1/3}$. The best fit parameters were searched by using the code "SEARCH".* Obtained parameters are shown in Table II, and the calculated curves are compared with the experimental data in Fig. 5. In spite of the good fit to the experimental data, the depth of the imaginary potential of set A for ^{98}Mo seems to be too small as compared with Perey's systematics, and the reaction cross section is considerably larger than those for other nuclei in this mass region. Moreover, when the parameter set A is used, the fits of the DWBA curves to the one-phonon 2+ and 3− states are not so good as those obtained with the parameter set B. Therefore the parameter set B is used for ^{98}Mo in the following calculations.

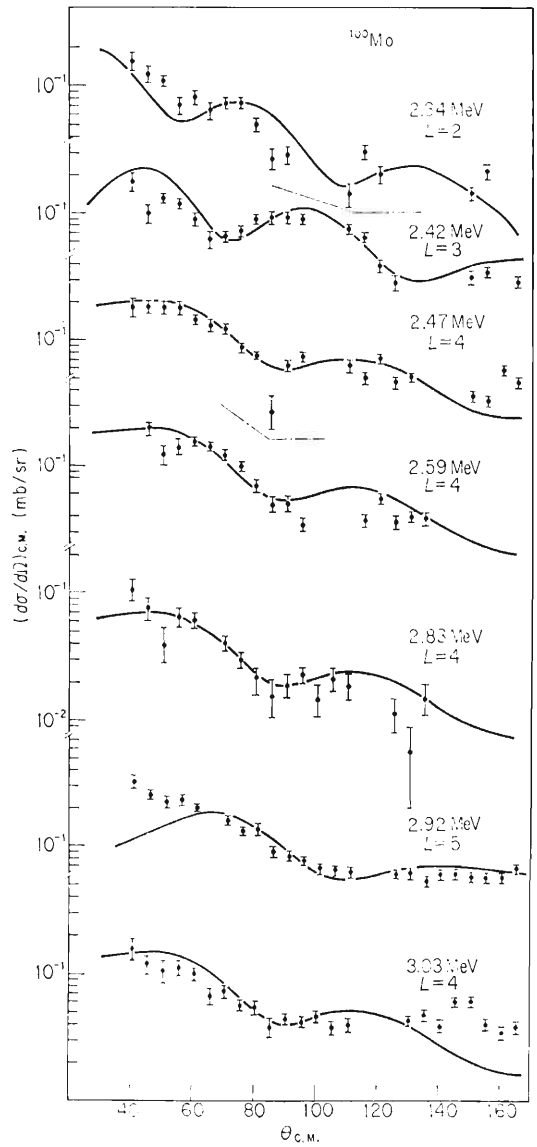

Fig. 7. The DWBA fits to the states of ^{100}Mo.

* Coded by T. Wada. Calculations were made on a FACOM 270-30 computer.

DWBA calculations

The DWBA calculations were made by using the revised code of "INS-DWBA 2".* Complex form factors for the one-phonon-excitation process were used. An effect of Coulomb excitation was included.

The angular distributions for the first 2^+ and 3^- states are fitted well by the DWBA calculated curves with $L=2$ and $L=3$, where L is the transferred angular momentum, as shown in Fig. 6.

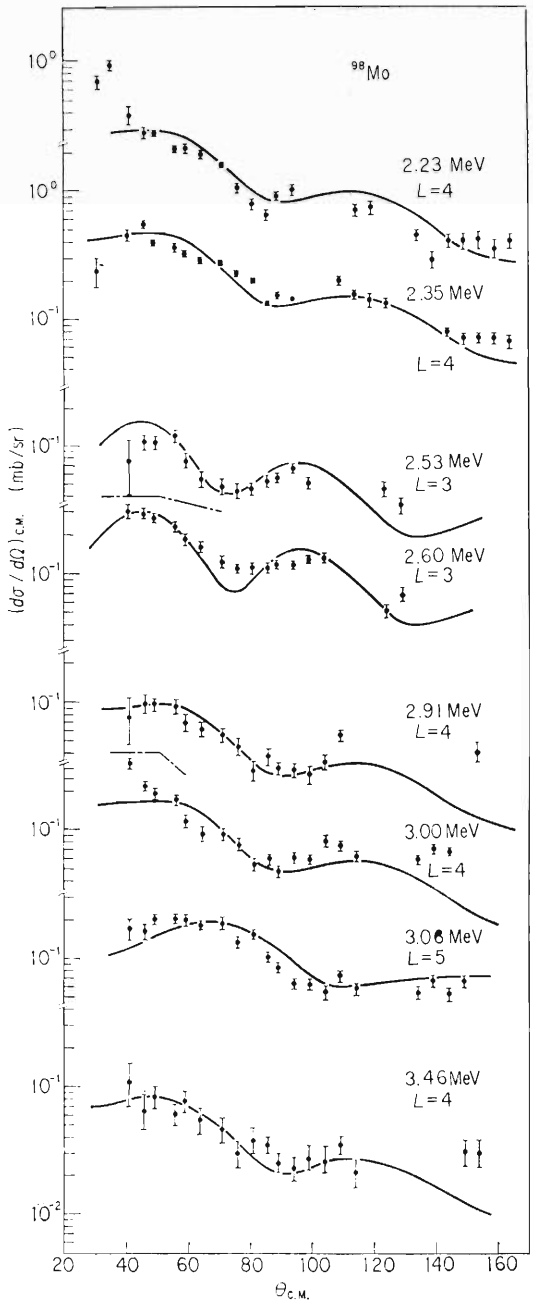

Fig. 8. The DWBA fits to the states of ^{98}Mo.

Besides the one-phonon 2^+ and 3^- states, some differential cross sections are well fitted by the DWBA curves. The results are shown in Figs. 7 and 8, and the deformation parameters, β_L, obtained from these calculations are listed in Table III.

Coupled channel calculations

Details of the formalism of the CC calculation have been described by Tamura.[2] The DWBA theory treats the one-step excitation process as it contains only the first-order perturbation term. It cannot predict the differential cross sections caused by the two-step process such as the two-phonon excitation. In such cases, however, one can employ CC calculations in which the elastic scattering and the inelastic scattering processes are treated simultaneously. The present calculations have been made by using Tamura's code "JUPITOR 1"** on FACOM 230-60 and FACOM 270-30 computers. A detailed study of the parameters was made for the case of ^{100}Mo only, and calculations for ^{98}Mo were done using the parameters chosen after ^{100}Mo. A complex coupling including Coulomb excitation effect was used.

Extensive studies of the parameters used in CC calculations for the one-phonon and two-quadrupole-phonon states have been made by Tamura,[2] Sakai and Tamura[17] and Oak Ridge groups[18,19] on the inelastic proton scattering. In these works, searches were made on parameters W, β_{0I}, β_{2I}, β_{0I}' and β_{0I}'' to find best fits to the experimental data. Here W is the depth of the imaginary potential, β_{0I} is proportional to the transition matrix between the ground state and the one-phonon (I^π) state, and β_{2I} to the one between the one-phonon (2^+) state and the two-phonon (I^+) state. The parameter β_{0I}' is proportional to the matrix between the ground state and the two-phonon (I^+) state and chosen to be $(\beta_{02}\beta_{2I})^{1/2}$. β_{0I}'' represents the relative amplitude of the one-phonon state wave function in the predominant two-phonon state wave function, that is, $|I\rangle=(\beta_{0I}''/\beta_{02})|I\rangle_{1ph}+(1-\beta_{0I}''^2/\beta_{02}^2)^{1/2}|I\rangle_{2ph}$.[20]

Tamura and others have chosen[2,17-19] the value of W to be smaller than that for the optical potential. Since the origin of the imaginary potential is partly taken into account directly in the CC calculation, the reduction of value of W is considered to be reasonable. They used

* Coded by Drs. M. Kawai, K. Kubo and H. Yamaura, and revised by Drs. S. Igarashi, K. Kubo, M. Kawai and S. Okai. Calculations were performed on a HITAC 5020E computer.

** The code has been rewritten for a FACOM 230-60 computer by Drs. M. Wakai, S. Igarashi, O. Mikoshiba and S. Yamaji, and for a FACOM 270-30 computer by S. Yamaji.

Table III. Excited states of ^{100}Mo and ^{98}Mo.

^{100}Mo							^{98}Mo						
Present work				Ref. 22			Present work				Ref. 22		
E_x(MeV)	L	I^π	β_L	E_x(keV)	I^π	β_{0I}	E_x(MeV)	L	I^π	β_L	E_x(keV)	I^π	β_{0I}
0.54	2	2+	0.19	534	2+	0.23					736	0+	
0.70		(0+)		694	0+		0.79	2	2+	0.16	788	2+	0.17
				800	2+	0.03	1.43		2+		1433	2+	
1.08		2+		1063	2+		1.51		4+		1510	4+	
1.15		4+		1140	4+		1.77				1760	2+	0.03
1.48				1463	2+	0.03	2.03	3	3−	0.20	2024	3−	0.20
				1500			2.23	4	(4+)	0.07	2208	4+	0.06
				1768			2.35	4	(4+)	0.09	2343	6+	0.11
1.95	3	3−	0.17	1910	3−	0.21					2450	4+	0.04
(2.20)							2.53	3	(3−)	0.05	2500	3−	0.06
2.34	2	(2+)	0.03				2.60	3	(3−)	0.07			
2.42	3	(3−)	0.06				(2.69)						
2.47	4	(4+)	0.06				(2.85)						
2.59	4	(4+)	0.05				2.91	4	(4+)	0.04			
2.67							3.00	4	(4+)	0.05			
2.72							3.06	5	(5−)	0.08			
2.83	4	(4+)	0.04				(3.13)						
2.92	5	(5−)	0.08				3.28						
3.03	(4)	(4+)	0.06				3.35						
3.15*							3.46	4	(4+)	0.04			
3.28													
3.36													
3.44													
3.51													
3.65													
3.72													

* Unresolved peak.

β_L is obtained from the DWBA calculations.

β_{0I} is obtained from the CC calculations with $0^+-2^+-3^-$ coupling for the first 2^+ and 3^- states and with 0^+-I^π coupling for the others.

$W_{el}=0.80W_{opt}$ for the elastic channel, $W=1.2W_{el}$ for the one-quadrupole-phonon channel, $W=1.1W_{el}$ for the one-octupole-phonon channel, and $W=(1.0\sim1.2)W_{el}$ for the two-phonon channel.[17-19] The β_{02} and β_{03} values obtained by them were the same as or not so different from $(\beta_2)_{DWBA}$ and $(\beta_3)_{DWBA}$. The β_{2I} value was usually a little larger than $\beta_2/2$. As to the 2_2^+ state, the admixture of the one-phonon state was required to get better fits.[18,19]

The present calculations were made referring to the previous (p, p') works on Pd and Cd isotopes[17-19,21] and the results are shown in Figs. 5, 6, 9 and 10.

The calculated curves for the elastic scattering (Fig. 5) and for the inelastic scattering to the first 2^+ (Fig. 6) and the second 2^+ states (Figs. 9 and 10) are obtained from the $0_1^+-2_1^+-2_2^+$ coupling, and the curves for the first 3^- states (Fig. 6) are obtained from the $0_1^+-3_1^-$ coupling. Calculations for the first 4^+ states (Figs. 9 and 10) and for the second 0^+ state (Fig. 9) are made assuming $0_1^+-2_1^+-4_1^+$ and $0_1^+-2_1^+-0_2^+$ coupling, respectively.

In our calculations, optical parameters are the same as shown in Table II (set B for ^{98}Mo) except for W. The value of W is $0.88W_D$ for all channels.* The parameters β_{02} and β_{03} are taken to be the same as β_2 and β_3 for DWBA. They are

* In the code "JUPITOR 1", the value of W is common for a set of coupled channels.

0.19 and 0.17 for ^{100}Mo, and 0.16 and 0.20 for ^{93}Mo (see Table III). The reasonable fits are obtained for $\beta_{22}=\beta_{02}'=\beta_{24}=\beta_{04}'=\beta_2$. The other parameters will be discussed separately below.

For the possible 2^+ and 4^+ members of the two-phonon triplet in ^{100}Mo, $\beta_{02}''=0.050$ and $\beta_{04}''=-0.01$ are used. However, the calculation with $\beta_{04}''=0.0$ also gives a good fit and is also shown in Fig. 9 with a dashed curve. In the case of ^{98}Mo, β_{02}'' was taken at first same as that for ^{100}Mo, but it gave the calculated differential cross section for the second 2^+ state about 30% larger than the experimental value. Therefore it was reduced to 0.043, which gave the same value of β_{02}''/β_{02} as for ^{100}Mo, and a good fit was obtained. The same values of β_{04}'' as for ^{100}Mo, -0.01 and 0.0, are used for ^{98}Mo. The curve for $\beta_{04}''=0.0$ seems to give a slightly better fit in this case (Fig. 10).

The CC calculation for the 0.70-MeV state in ^{100}Mo has been made for the $0_1^+-2_1^+-0_2^+$ coupling under condition of $\beta_{20}=\beta_{00}'=\beta_{02}$ and $\beta_{00}''=0.0$, and is compared with the experimental

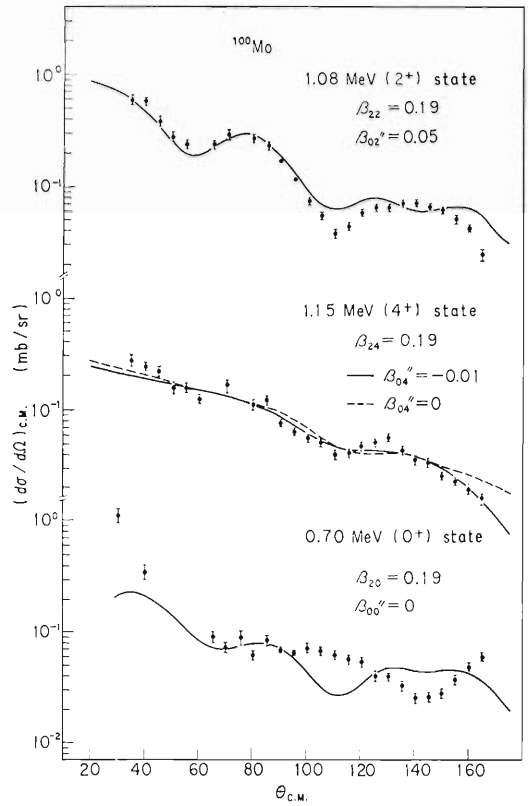

Fig. 9. The CC fits to the possible members of the two-quadrupole-phonon triplet of ^{100}Mo.

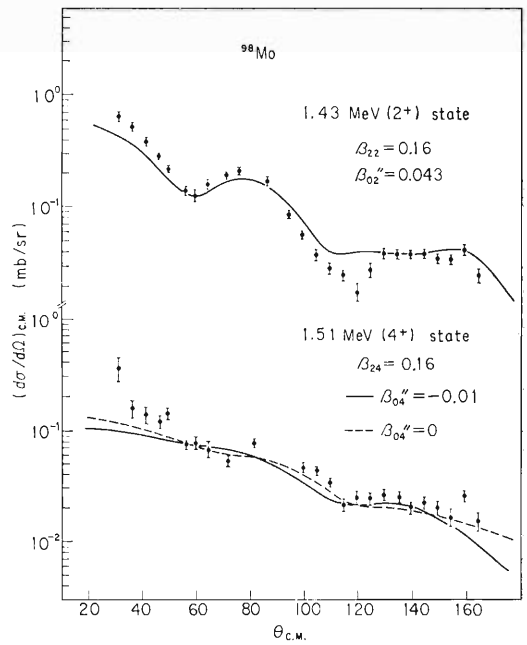

Fig. 10. The CC fits to the possible members of the two-quadrupole-phonon triplet of ^{98}Mo.

Table IV. Summary of β-parameters in CC calculations for the one-phonon and two-quadrupole-phonon states of ^{100}Mo and ^{98}Mo.

Nucleus	Present work						ref. 22					
	E_x (MeV)	I^π	β_{0I}	β_{2I}	β_{0I}'	β_{0I}''	E_x (keV)	I^π	β_{0I}	β_{2I}	β_{0I}'	β_{0I}''
^{100}Mo	0.54	2+	0.19				534	2+	0.226			
	0.70	0+	0.19	0.19	0.19	0.0	694	0+	0.226	0.226	0.226	0.0
	1.08	2+	0.19	0.19	0.19	0.05	1063	2+	0.226	0.226	0.226	0.06
	1.15	4+	0.19	0.19	0.19	−0.01	1140	4+	0.226	0.170	0.170	0.02
	1.95	3−	0.17				1910	3−	0.210			
^{98}Mo							736	0+	0.168	0.168	0.168	0.0
	0.79	2+	0.16				788	2+	0.168			
	1.43	2+	0.16	0.16	0.16	0.043	1433	2+	0.168	0.168	0.168	0.04
	1.15	4+	0.16	0.16	0.16	0.0	1510	4+	0.168	0.100	0.100	0.03
	2.03	3−	0.20				2024	3−	0.195			

data in Fig. 9. The absolute value of differential cross section is reproduced well but the pattern is not. It was difficult to get a fit for this state although some trials were made.

The β-parameters obtained from the CC fits are summarized in Table IV.

§ 4. Discussions

The experimental angular distributions for the one-phonon states and possible members of two-phonon triplet of ^{100}Mo and ^{98}Mo are well fitted by the CC calculations except for the 0_2^+ state of ^{100}Mo. The 2^+ and 4^+ assignments for the 1.08-MeV and 1.15-MeV states of ^{100}Mo are plausible from this analysis. The good fits of the calculated curves to the experimental data are obtained with $W=0.88W_D$ for all channels.

If a target nucleus is a typical harmonic vibrational one, the relations $\beta_{02}=\beta_{2I}=\beta_{0I}'$ and $\beta_{0I}''=0$ hold for the two-quadruporle-phonon states. The second 2^+ and the first 4^+ states of ^{100}Mo and ^{98}Mo, especially the 4^+ states, seem to satisfy these harmonic relations. The admixture of the one-phonon component is required, however, for the 2_2^+ states. It is interesting that the same value of β_{02}''/β_{02} gives good fits for both nuclei. This means the ratio of the admixture of one-phonon component to the two-phonon wave function is the same in both nuclei. The fact that fitted curves for the states of ^{98}Mo have been obtained with the parameters chosen after those for ^{100}Mo may suggest that the level structure of ^{100}Mo and ^{98}Mo are similar to each other. Since the parameters used here are searched after the Cd and Pd cases,[17-19,21] it might be worth listing here the β-parameters for ^{112}Cd [19] as an example to compare with those obtained in the present analysis. They are: $\beta_{02}=0.20=(\beta_2)_{DWBA}$, $\beta_{22}=0.10$ and $\beta_{02}''=0.054$ for the 1.311-MeV 2^+ state, $\beta_{24}=0.12$ and $\beta_{04}''=0.01$ for the 1.413-MeV 4^+ state and $\beta_{22}=0.104$ and $\beta_{00}''=-0.0108$ for the 1.220-MeV 0^+ state.

Heck *et al.* obtained the value of $b=B(E2,2_2^+\to 2_1^+)/B(E2,2_2^+\to 0_1^+)$ for the 1.432-MeV 2^+ and 1.759-MeV 2^+ state of ^{98}Mo as 16.0 ± 2.1 and 177 ± 60, respectively.[10] From these results, they preferred the 1.759-MeV state as the candidate for the member of the two-phonon state to the 1.432-MeV state. The b-value for the 1.43-MeV state can be estimated from the present CC calculation using the relation,[18]

$$\frac{5\alpha^2}{2(1-2\alpha^2)^2}=\frac{B(E2,0_1^+\to 2_2^+)}{B(E2,2_1^+\to 2_2^+)}=\frac{5}{b},$$

where $\alpha=\beta_{02}''/\beta_{02}$. When α is taken to be 0.043/0.16, the value of b is 20.3 in agreement with that obtained by Heck *et al.* The large b-value for the 1.759-MeV state cannot be explained within the framework of the present experiment. The cross section for exciting this state is much smaller than that predicted by the CC calculation. The 2^+ member of the two-phonon state is most likely the 1.43-MeV state according to the present data, and this interpretation does not contradict the result obtained by Heck *et al.* when the admixture of the one-phonon component is taken into account.

The angular distribution for the 0_2^+ (0.70-MeV) state of ^{100}Mo has not been fitted by the CC calculation although the absolute cross section is reproduced. This would mean that this state might not be of pure vibrational character. Taketani *et al.* have suggested[12] that the wave function of the second 0^+ state of ^{98}Mo has a deformed component. This could also be the case for the 0_2^+ state of ^{100}Mo. The ^{98}Mo$(t,p)^{100}$Mo and ^{100}Mo$(t,p)^{102}$Mo reactions have been studied recently, and it is found that the second 0^+ states have been strongly excited in both cases.[16] The analysis of these results is now in progress, and further information on the 0_2^+ state of ^{100}Mo will be obtained in near future.

The angular distributions for the higher excited states than the first 3^- state have been analysed in terms of DWBA theory. So many states of ^{98}Mo have been observed above the first 3^- state in the ^{97}Mo(d,p) and ^{97}Mo(n,γ) reactions,[6,10] and it is difficult to identify the states observed in the present work with those in the previous experiments to discuss their properties. Some of these excited states could be arising from the three-quadrupole-phonon or one-quadrupole-one-octupole-phonon coupling. In such a case, L-assignments based on DWBA would be questionable and the β_L-values would only give a measure of the excitation strength. The CC calculations for the three-quadrupole-phonon and the one-quadrupole-one-octupole-phonon coupling might have been worth while, but were not made because a large amount of computer time was required.

Comparison with the results obtained by Lutz et al.[22]

The main results of the present experiment and analysis for the ^{100}Mo and ^{98}Mo have been found to be almost the same as those by Lutz *et al.* The incident energy of protons in their experiment

was 15 MeV, which was almost the same as ours, and the energy resolution of their measurement was a little better. They obtained the angular distribution for the second 0^+ state of ^{98}Mo. They observed states up to 1.91 MeV in ^{100}Mo and up to 2.5 MeV in ^{98}Mo (Table III). They also analysed the angular distributions with CC calculation by $0_1^+-2_1^+-3_1^-$ coupling for the first 2^+ and 3^- states and ~~$0_1^+-2_1^+-0_2^+-2_2^+-4_1^+$~~ $0_1^+-2_1^+-0_2^+-2_2^+-4_1^+$ coupling for the second 0^+ and 2^+ states and the first 4^+ state. Comparison of the β-parameters is shown in Table IV. The results for the 2_2^+states agree with ours in so far as $\beta_{02}=\beta_{22}=\beta_{02}'$ and the admixture of the one-phonon component is required. Probably the main difference between their results and ours exists in β-parameters for the 4^+ state. Their results show that β_{24} is equal to β_{04}', but β_{24} and β_{04}' are smaller than β_{02}. More admixture of the one-phonon component is required than in the present analysis. However, detailed discussion about the difference of the values of β-parameters might be meaningless since they are sensitive to other parameters, especially to W. The calculated curves for the 0_2^+ and 4_1^+ states in their work are slightly different from ours at large angles. They made CC calculations for other states than those mentioned above by assuming 0^+-I^π coupling and assigned the spins and parities. Their assignments are shown in Table III in comparison with our L-assignments.

Acknowledgements

The authors wish to express their appreciation to Dr. T. Tamura for the use of his CC code, and to Drs. Kouichi Izumo and H. Kamitsubo for discussions. They are also indebted to the cyclotron crew for their operation of the cyclotron, to Mrs. F. Yoshida for her assistance in processing data, and to the members of the computer room for their help in the calculations. One of the authors (Y. A.) is grateful to Dr. T. Hamada for his encouragement.

This paper is written as a memorial to one of the authors (K. M.), who died after the completion of this experiment.

References

1) There are many references, for example, G. R. Satchler: Nuclear Phys. **55** (1964) 1, and references therein.
2) Taro Camura: Rev. mod. Phys. **37** (1965) 679.
3) E. Cheifez, R. C. Jared, S. G. Thompson and J. B. Wilhmey: Phys. Rev. Letters **25** (1970) 38.
4) T. Wada, K. Matsuda, Y. Awaya, N. Nakanishi and S. Takeda: ICPR Cyclotron Progr. Rep. 3 (1969) 36 (unpublished); Y. Awaya, T. Wada, K. Matsuda, N. Nakanishi and S. Takeda: ibid. **3** (1969) 38 (unpublished).
5) Y. S. Kim and B. L. Cohen: Phys. Rev. **142** (1966) 788.
6) K. R. Evans, F. Ajzenberg-Selove and Baruch Rosner: Phys. Rev. **165** (1968) 1327.
7) K. Hübenthal, E. Monnand and A. Moussa: Nuclear Phys. **A128** (1969) 577.
8) K. Hübenthal, E. Berthier, J. C. Hocquenghem and A. Moussa: Compt. Rend. **265B** (1967) 162.
9) S. C. Gujrathi and S. K. Mukherjee: Nuclear Phys. **85** (1966) 288.
10) D. Heck, U. Fanger, W. Michaelis, H. Ottmar ane H. Schmidt: Nuclear Phys. **A165** (1971) 327.
11) C. M. Lederer, J. M. Jaklevic and J. M. Hollander: Nuclear Phys. **A169** (1971) 449.
12) H. Taketani, M. Adachi, M. Ogata, K. Ashibe and T. Hattori: Phys. Rev. Letters **27** (1971) 520.
13) C. M. Lederer *et al.*: *Table of Isotopes* (John Willey and Sons, 1967) p. 236; *Nuclear Data Sheets* (compiled by Nuclear Data Group, Academic Press, New York and London).
14) K. Matsuda, N. Nakanishi, S. Takeda and T. Wada: J. Phys. Soc. Japan **25** (1968) 1207.
15) K. Matsuda, Y. Awaya, N. Nakanishi and S. Takeda: ICPR Cyclotron Progr. Rep. **4** (1970) 38 (unpublished).
16) K. Matsuda, S. Takeda, N. Nakanishi, I. Kohno, Y. Awaya, S. Yamaji and S. Kusuno: in preparation.
17) M. Sakai and T. Tamura: Phys. Letters **10** (1964) 323.
18) R. L. Robinson, J. L. C. Ford, Jr., P. H. Stelson and G. R. Satchler: Phys. Rev. **146** (1966) 816.
19) P. H. Stelson, J. L. C. Ford, Jr., R. L. Robinson, C. Y. Wong and T. Tamura: Nuclear Phys. **A119** (1968) 14.
20) T. Tamura: Progr. theor. Phys. suppl. No. **37** and **38** (1966) 383.
21) R. L. Robinson, J. L. C. Ford, Jr., P. H. Stelson, Taro Tamura and C. Y. Wong: Phys. Rev. **187** (1969) 1609.
22) H. F. Lutz, D. W. Heikkinen and W. Bartolini: Phys. Rev. **C4** (1971) 934.

Reprinted from Phys. Lett., 40B, 543–545 (1972).

IN-BEAM ALPHA SPECTROSCOPY OF N=128 ISOTONES. LIFETIMES OF ^{216}Ra AND A NEW ISOTOPE ^{217}Ac

T. NOMURA, K. HIRUTA*, T. INAMURA and M. ODERA

Cyclotron Laboratory, The Institute of Physical and Chemical Research, Wako-shi, Saitama, 351, Japan

Received 14 June 1972

By means of the pulsed-beam technique a new isotope ^{217}Ac has been found to decay with E_α = 9.65 ± 0.02 MeV and $\tau_{1/2}$ = 0.10 ± 0.01 μs. The half-life of ^{216}Ra has been determined to be 0.18 ± 0.03 μs.

Many neutron-deficient translead elements are known to be high-energy α-particle emitters with short half-lives. In particular the nuclides with 128 neutrons are expected to have the largest α-decay energies due to the extra stability of the N=126 neutron shell, and lifetimes of these nuclei will fall in the submicrosecond region. It is almost impossible to measure such short lifetimes by the usual preparation of α-particle activities. Even the rapid helium-jet collection system [1] needs much longer transportation time (usually more than 1 ms), and thus lifetime measurements so far performed have been limited to cases where activities of interest are provided from the decay of parent nuclei having sufficiently long half-lives. In this note we report a simple pulsed-beam technique of observing such short-lived α-particle decay and some experimental results obtained by its application to the N=128 isotones – the discovery of a new isotope ^{217}Ac and lifetime measurements of ^{216}Ra and ^{217}Ac.

The present method is based on the direct observation of delayed α-particles emitted from final nuclei produced in a target by nuclear reactions. Alpha particles were detected with a thin (about 200 μm) Si-detector of surface barrier type and time distributions of α-particle spectra were taken between natural beam bursts of the cyclotron in the same way as employed by Yamazaki and Ewan [2] in the study of the γ-ray decay from nanosecond isomers. The beam spread of the IPCR cyclotron is around 2 ns and its repition period ranges from 100 to 150 ns depending on beam energy. A thin target is desirable, but the lower limit of the target thickness is set by the condition that recoiling α-particle emitters formed by reactions must be stopped within the target. This practically determines the energy resolution of the α-particle spectrum. The Si-detector was placed at 135° with respect to the beam to avoid strong Coulomb scattering of incident particles.

In the present experiment heavy- ion reactions of the (HI,xn) type were used for the production of ^{216}Ra and ^{217}Ac. Fig. 1(a) shows a delayed α-particle spectrum from 91 MeV ^{14}N bombardment on a ^{208}Pb (95% enriched) target of about 1 mg/cm^2 thickness. A prominent 9.65 MeV peak is attributed to the ground-state decay of a new isotope ^{217}Ac produced in the (^{14}N,5n) reaction. The assignment is based on the following facts.

a) The measured excitation function for this peak is just of (^{14}N,5n) type as shown in fig. 1(b). It is to be noted here that this excitation curve is very similar to the one for the ^{208}Pb(^{12}C,5n)^{215}Ra reaction (see the lower part of this figure) when both curves are given versus excitation energies of their compound nuclei.

b) From its energy and measured half-life ($\tau_{1/2} \approx 35$ s) another prominent peak at 6.77 MeV can be assigned to the known ground-state decay of ^{213}Fr, a daughter nucleus of ^{217}Ac. The yield of this peak is almost equal to that of the 9.65 MeV peak at every incident energy, leading to the conclusion that the 9.65 MeV peak must result from the ground-state decay of ^{217}Ac.

A more precise measurement of the decay energy with a relatively thin target (300 μg/cm^2) yielded E_α = 9.65 ± 0.02 MeV for ^{127}Ac, where the energy calibration was performed with the known α-particle

* On leave of absence from Department of Physics, Tokyo Institute of Technology.

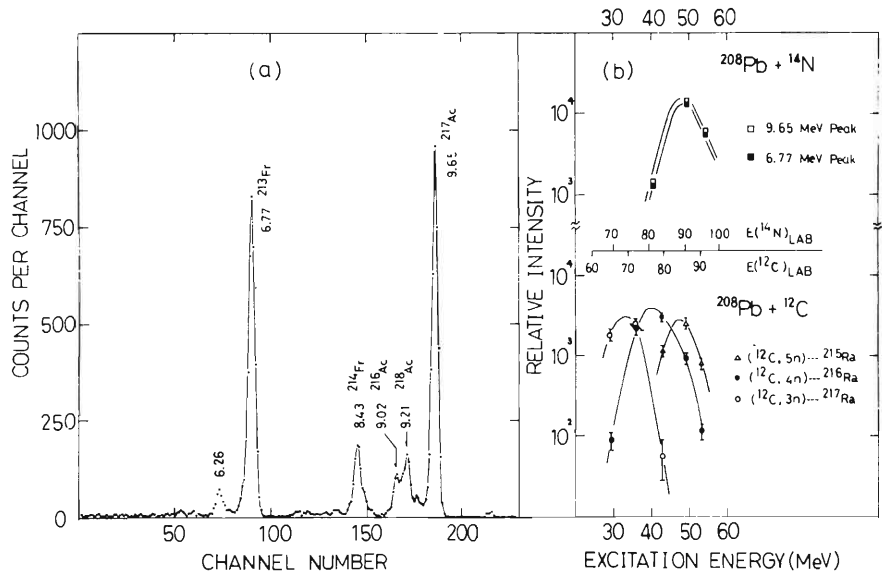

Fig. 1(a). A delayed α-particle spectrum from 91 MeV ^{14}N bombardment on a ^{208}Pb target of about 1 mg/cm^2 thickness. The spectrum was taken about 10 ns after the cyclotron beam bursts. Energies are given in MeV. (b) Excitation functions for the 9.65 MeV and 6.77 MeV peaks from the ^{208}Pb + ^{14}N reaction (upper part) and those for the previously known α-particle decay of ^{215}Ra, ^{216}Ra and ^{217}Ra populated by the ^{208}Pb(^{12}C,5n), ^{208}Pb(^{12}C,4n) and ^{208}Pb(^{12}C,3n) reactions, respectively (lower part).

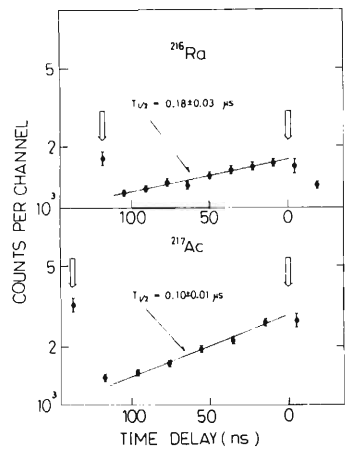

Fig. 2. Decay curves of ^{216}Ra and ^{217}Ac taken by the use of a time-to-amplitude converter, for which start and stop pulses were provided from fast outputs of the Si-detector and rf-signals of the cyclotron, respectively. Delay time is given from the front edge of beam bursts indicated by arrows.

groups of ^{213}Fr (6.773 MeV), ^{214}Fr (8.427 MeV) and ^{218}Ac (9.205 MeV) produced in the same target. Taking into account the recoil energy given to the daughter nucleus the Q_α-value for ^{217}Ac was determined to be 9.83 ± 0.02 MeV, which agrees well with a calculated value of 9.80 MeV by Wapstra and Gove [3].

The earliest information on ^{216}Ra came from unpublished work of Griffioen and Macfarlane [4], who reported a α-particle decay energy of 9.304 MeV. In the present work a 9.31 ± 0.02 MeV peak appeared strongly by irradiation of the ^{208}Pb target with a 79 MeV ^{12}C beam. The measured excitation function for this peak is of (^{12}C,4n) type as shown in fig. 1(b), which thus confirms the previous mass assignment.

Time distributions of the ground-state decay of ^{216}Ra and ^{217}Ac are shown in fig. 2, from which half-lives of ^{216}Ra and ^{217}Ac have been determined of 0.18 ± 0.03 μs and 0.10 ± 0.01 μs, respectively. In order to search for possible long-lived γ-decaying isomers which would affect the half-life determination for α-particle decay by the present method, delayed γ-ray spectra were taken under the same conditions except that the Si-detector was replaced by a Ge(Li)-counter. For the ^{208}Pb + ^{12}C reaction several delayed γ-transitions were found to originate from isomeric states in ^{216}Ra, but their lifetimes were so short (less than 20 ns) that no significant effect on the above mentioned half-life for α-particle decay was expected. Possibilities of other decay modes of ^{216}Ra and ^{217}Ac such as electron capture were checked by noting the α-particle decay intensity of their daughter nuclei. These decay modes contribute less than 1% in both nuclei.

Table 1
Experimental and theoretical α-particle reduced widths for the ground-state decay of N=128 isotones

	E_α (MeV)	$\tau_{1/2}$ (μs)	$\gamma^2_{\alpha(\text{exp.})}$ (keV)	$\gamma^2_{\alpha(\text{calc.})}$ (keV)	Ref. for experiments
^{212}Po	8.785	0.304	1.49	1.49[a)]	[6]
^{213}At	9.080	0.11 ± 0.02	2.02	1.19	[7]
^{214}Rn	9.035	0.27 ± 0.02	1.79	2.38	[8]
^{215}Fr	9.365	< 0.5		1.79	[4]
^{216}Ra	9.304[b)]	0.18 ± 0.03	2.32	2.68	present work
^{217}Ac	9.65 ± 0.02	0.10 ± 0.01	1.60	1.79	present work

a) The reduced width for ^{212}Po is taken as a standard and set equal to the experimental reduced width.
b) Taken from tef. [4].

Table 1 summarizes the present results together with the previous data for other N=128 isotones having $Z \geqq 84$. The experimental reduced α-particle width was deduced from

$$\gamma_\alpha^2 = \frac{\hbar\lambda}{2} \cdot \frac{1}{P}$$

where λ is the α-decay constant and P the barrier penetrability calculated for S-wave α-particles using a pure Coulombic potential at a radius of $R_0 = 1.57\ A^{1/3}$ fm. Because absolute values of γ_α^2 are very sensitive to the choice of R_0 and moreover the nuclear potential was neglected to define the barrier, only relative values of γ_α^2 should be considered as significant.

Since the experimental values of γ_α^2 for odd nuclei are very close to the ones for the even-even nuclei, all the decays of the odd nuclei given in the table must be "unhindered" transitions. We can therefore conclude that all pairs of parent and daughter nuclei have the same spin and parity. The most probable spin-parity assignment for the odd nuclei is $J^\pi = 9/2^-$ on the basis of the shell model, which predicts $[(\pi h^n_{9/2})_{9/2^-}(\nu g^2_{9/2})_{0^+}]\,9/2^-$ for the odd parents and $[(\pi h^n_{9/2})_{0^+}(\nu g^2_{9/2})_{0^+}]\,0^+$ for the even-even parents. Assuming the above configuration for the parents and $\pi h^{n-2}_{9/2}$ (closed shell for neutrons) for the daughters we have calculated theoretical values of γ_α^2 after Mang [5], which are given in the last column of the table. The agreement with experiment is quite satisfactory.

The present method has been proven very powerful for the investigation of short-lived α-particle activities. This method also makes it possible to search for long-range α-particles emitted from isomeric states in the nanosecond region. In fact, some long-range α-particle decays have been found during the present experiment and are now under study. Another interesting feature is that the nuclear alignment formed in the reaction may be preserved during the short decay time and thus an anisotropic angular distribution is expected for α-particles having non-zero angular momenta. This fact will enlarge the applicability to many other problems.

We wish to thank Dr. H. Kamitsubo for his continuous interest in this work and valuable discussions. One of us (KH) thanks Prof. S. Kageyama for enlightening conversations. The excellent machine operation by the IPCR cyclotron crew is also gratefully appreciated.

References

[1] R.D. Macfarlane and R.D. Griffioen, Nucl. Instr. 24 (1963) 461.
[2] T. Yamazaki and G.T. Ewan, Phys. Lett. 24B (1967) 278.
[3] A.H. Wapstra and N.B. Gove, Nucl. Data Tables A9 (1971) Parts I and III.
[4] R.D. Griffioen and R.D. Macfarlane, Lawrence Radiation Laboratory Report, UCRL-10023 (1961).
[5] H.J. Mang, Phys. Rev. 119 (1960) 1069.
[6] Table of Isotopes, 6th ed., eds. C.M. Lederer, J.M. Hollander and I. Perlman (John Wiley and Sons, 1966).
[7] J. Borggreen, K. Valli and E.K. Hyde, Lawrence Radiation Laboratory Report, UCRL-19539 (1970).
[8] K. Valli, E.K. Hyde and J. Borggreen, Phys. Rev. C1 (1970) 2115.

Reprinted from Phys. Rev. C, 14, 1458–1470 (1976).

Systematics of optimum Q values in multinucleon transfer reactions induced by heavy ions

T. Mikumo,* I. Kohno, K. Katori,* T. Motobayashi,† S. Nakajima, M. Yoshie,* and H. Kamitsubo
Institute of Physical and Chemical Research, Wako-shi, Saitama, Japan
(Received 15 April 1976)

The most probable effective Q values, $Q^m_{\rm eff}$, for multinucleon transfer reactions $A(a,b)B$ ($M_b < M_a$) have been systematically studied on fp-shell nuclei and Zr-Mo isotopes induced by ^{14}N and ^{12}C, in the energy range between 60 and 100 MeV. As regards the "quasielastic" part of the bump in the energy spectrum, the dependence of $Q^m_{\rm eff}$ on the incident and outgoing channel variables, i.e., A, a, E_i, θ, and n, the number of transferred nucleons, has been extensively investigated. The present data, together with those obtained at higher energies by the Dubna group, show systematic behaviors of $Q^m_{\rm eff}$: (i) for a given $A(a,b)B$ and E_i, $Q^m_{\rm eff}$ changes little with $\theta_{\rm lab}$, (ii) at a given E_i, $Q^m_{\rm eff}$ of (a,b) is nearly the same for adjacent A and is not sensitive to their individual nuclear structure, and (iii) the linear relation $Q_{\rm eff} = \alpha_{\rm eff} n + \beta_{\rm eff}$ holds for $n \leq 4-5$, whereas the linearity breaks down for larger n. The relation $\alpha_{\rm eff} = -0.1\ (E_i - V^i_c) - 0.9$ MeV holds for a wide range of reactions. The ratio of the most probable effective velocity to the incident velocity v^m_f/v_i at the transfer region decreases from about unity to $0.4-0.5$ as n increases. The differences in reaction mechanisms for smaller n and larger n have been discussed.

[NUCLEAR REACTIONS ^{52,53}Cr(^{14}N,x), $x = ^{13,12}$C, ^{12,11,10}B, ^{10,9,7}Be, ^{7,6}Li, ^{4}He; $E = 64$, 70, 80, 90, 95 MeV, $\theta = 10-33°$; ^{90}Zr(^{14}N; ^{13,12}C, ^{11}B), $E = 75$ MeV, $\theta = 30.5°$; ^{A}Mo(^{14}N,x), $A = 92$, 94, 95, 96, 97, 98, 100, $E = 97$ MeV, $x = ^{13,12}$C, ^{12,11,10}B, ^{10,9,7}Be, ^{7,6}Li, ^{4}He, $\theta = 25, 30°$; ^{92}Mo(^{12}C;x), $x = ^{10}$B, ^{10,9,7}Be, ^{7,6}Li, $E = 90$ MeV, $\theta = 20°$; measured energy spectra of x and optimum Q values.]

I. INTRODUCTION

In multinucleon transfer reactions $A(a,b)B$ induced by heavy ions at energy much higher than the Coulomb barrier, the shape of the spectrum of the reaction products is mainly characterized by a continuous bell-shaped form (bump). The systematics of the most probable or optimum Q values, Q^m, of the reactions, and their dependence on the incident and exit channel variables have been one of the main subjects in the investigation of multinucleon transfer reactions with heavy ions from a macroscopic point of view.[1-3]

For sub-Coulomb reactions, the behavior of Q^m has been explained by models assuming Rutherford trajectories for the scattering particles. Somewhat different assumptions lead to different "optimum" Q values.[4-6]

For reactions in an energy region well above the Coulomb barrier, several different models have been proposed[7-9] to reproduce the experimental Q^m values, which are as yet limited to reactions at fairly high bombarding energies and/or to very heavy target nuclei.[1] The models proposed in Refs. 7–9 have been able to fit the available data, but the implications of these models are somewhat contradictory. Wilczyński,[9] for instance, claims that Q^m is determined mainly by the mass balance of the nuclei involved in the reaction; Siemens *et al.*[8] point out the essential role of recoil effects and a strong dependence on reaction kinematics, while Brink[7] suggests that the key factor determining Q^m or the most probable "effective" Q values, $Q^m_{\rm eff}$ (see Sec. III), is the velocity of the scattering particles.

In an earlier survey of the systematics of Q^m using ^{14}N and ^{12}C beams of 60–90 MeV and targets of fp-shell nuclei (^{52,53}Cr, ^{50}Ti, and ^{54}Fe) and of heavy nuclei (^{208}Pb and ^{209}Bi),[3] the present authors observed that Q^m does not reflect sharply the structure of individual target nuclei and that, for a given incident beam and target, Q^m is proportional to the number of transferred nucleons, n, for $n \leq 4-5$.

It is important to identify not only the atomic numbers of the emitted particles, b, but also of their mass numbers. Very little data has been reported on the systematics of the Q^m values of individual outgoing nuclides, except for the results of Dubna group for the reactions ^{232}Th + ^{15}N [Ref. 1(a)] and ^{232}Th + ^{22}Ne [Ref. 1(b)] at fixed energies and at fixed angles and the results previously reported by the present authors.[3] In other studies, including those of ^{232}Th + ^{40}Ar,[2] the Q^m values of the products either were classified only according to atomic number or were not as extensive.

The present work aims at a more systematic study of the most probable Q values for a wide range of incident and outgoing variables, i.e., incident beam (^{14}N and ^{12}C), energy (64–97 MeV),

target mass (^{52,53}Cr, ^{90}Zr, and all the stable isotopes of molybdenum) and the mass, charge, energy, and angle of emission of emitted particles. The energy and mass region of this study covers the gap of previous data between the sub-Coulomb and high-energy regions. The present authors thus attempt a unified view of the global behavior of multinucleon transfer reactions and the systematics of the most probable Q values.

Data and detailed discussions on reaction cross sections and angular distributions of reaction products are given in separate papers.[3,12,13]

II. EXPERIMENTAL PROCEDURE

The present work was performed with $^{14}N^{4+}$ beams from the IPCR cyclotron. The experimental facilities and details are described elsewhere.[10-13]

The experimental conditions and measured particles are tabulated in Table I, together with those of previous data.[3] Table I shows the incident channel $A+a$ of reaction $A(a,b)B$, the incident laboratory and c.m. energies, E_{lab} and E_i, the Coulomb barrier of the incident channel, V_C^i, and the products b measured at the laboratory angle $\theta_{lab}(b)$. We chose the radius parameter r_0 to be 1.4 fm.

All targets used in the present work were self-supporting foils, 0.45 to 1 mg/cm^2 thick, of isotopes enriched to more than 90%.

The beam was focused onto the target to a size of 1×6 mm^2 and an intensity of 50 to 200 nA.

The reaction products b were detected with two sets of silicon detector telescopes. The ΔE detectors were 30 μm thick and the E detectors were 200 to 2000 μm thick. All the data were stored on a magnetic tape with the aid of a DDP 124 computer used as in the on-line mode and were later analyzed. The energy spectra of individual Z and A were obtained using the program "MTSORT."[13] Thus, using the incident beam of ^{14}N, isotopes of O, N, C, B, Be, Li, and He were identified by their mass spectra, with a resolution of 3–6%. The overall energy resolution was between 500 and 800 keV.

TABLE I. Multinucleon transfer reactions $A(a,b)B$ investigated. E_{lab} is the incident laboratory energy, E_i the incident c.m. energy, V_C^i the Coulomb barrier in the incident channel with the radius parameter r_0 fixed at 1.4 fm, and $\theta_{lab}(b)$ the laboratory emission angle of b.

$A+a$	E_{lab} (MeV)	E_i (MeV)	E_i/V_C^i (r_0=1.4 fm)	$E_i-V_C^i$ (r_0=1.4 fm)	b measured	$\theta_{lab}(b)$ (deg)
^{52}Cr + ^{14}N	95	74.9	2.7	46.7	^{13}C, ^{12}C, ^{12}B, ^{11}B, ^{10}B, ^{10}Be ^{9}Be, ^{7}Be, ^{7}Li, ^{6}Li, ^{4}He	16, 20, 25
	90	70.9	2.5	42.7	^{13}C, ^{12}C, ^{12}B, ^{11}B, ^{10}B, ^{10}Be ^{9}Be, ^{7}Be, ^{7}Li, ^{6}Li, ^{4}He	16, 25 18, 22, 26
	80	63.0	2.2	34.8	^{13}C, ^{12}C, ^{12}B, ^{11}B, ^{10}B, ^{10}Be ^{9}Be, ^{7}Be, ^{7}Li, ^{6}Li, ^{4}He	18, 22, 27
	70	55.2	2.0	27.0	^{13}C, ^{12}C, ^{12}B, ^{11}B, ^{10}B, ^{10}Be ^{9}Be, ^{7}Be, ^{7}Li, ^{6}Li, ^{4}He	22, 27
	64	50.4	1.8	22.2	^{13}C, ^{12}C, ^{12}B, ^{11}B, ^{10}B, ^{10}Be ^{9}Be, ^{7}Be, ^{7}Li, ^{6}Li, ^{4}He	20, 27
^{53}Cr + ^{14}N	90	71.2	2.5	43.2	^{16}O, ^{15}O ^{15}N, ^{13}C, ^{12}C, ^{11}B, ^{10}B, ^{10}Be, ^{9}Be, ^{7}Be, ^{7}Li, ^{6}Li, ^{4}He	16
^{50}Ti + ^{14}N	70	54.7	2.1	28.7	^{13}C, ^{12}C, ^{11}B, ^{10}B	25
^{54}Fe + ^{14}N	70	55.6	1.8	25.3	^{13}C, ^{12}C, ^{11}B, ^{10}B	26
^{52}Cr + ^{12}C	90	73.1	3.0	48.5	^{10}B, ^{10}Be, ^{9}Be, ^{7}Be	18
	70	56.9	2.3	32.3	^{10}B, ^{10}Be, ^{9}Be	18, 22
	60	48.8	2.0	24.2	^{10}B, ^{10}Be, ^{9}Be	17, 19, 22 25, 27
^{50}Ti + ^{12}C	60	48.4	2.1	25.7	^{10}B, ^{10}Be, ^{9}Be	25
^{54}Fe + ^{12}C	60	49.1	1.9	22.7	^{10}B, ^{10}Be, ^{9}Be	25
^{208}Pb + ^{14}N	90	84.3	1.2	13.4	^{13}C, ^{12}C	60, 65, 70, 75 80, 85
^{209}Bi + ^{14}N	91	85.3	1.2	13.6	^{13}C, ^{12}C	60
^{208}Pb + ^{12}C	78	73.8	1.2	12.2	^{11}B, ^{10}Be, ^{9}Be	75
^{209}Bi + ^{12}C	78	73.8	1.2	11.5	^{11}B, ^{10}Be, ^{9}Be	70
^{A}Mo + ^{14}N	97 (A = 92, 94, 95, 96, 97, 98, 100)	84.7	2.0	41.4	^{16}O, ^{15}O, ^{15}N, ^{13}C, ^{12}C, ^{12}B, ^{11}B, ^{10}B, ^{10}Be, ^{9}Be, ^{7}Be, ^{7}Li, ^{6}Li, ^{4}He	25, 30
^{90}Zr + ^{14}N	75	64.9	1.6	23.0	^{13}C, ^{12}C, ^{11}B	30, 45
^{92}Mo + ^{12}C	90	79.6	2.1	41.5	^{10}B, ^{10}Be, ^{9}Be, ^{7}Be, ^{7}Li, ^{6}Li	20

III. RESULTS AND DISCUSSION

A. Experimental results

In Fig. 1, the energy spectra of emitted particles b from the reaction $^{96}Mo + ^{14}N$ at $E_{lab} = 97$ MeV and $\theta_{lab} = 25°$ are shown. They are dominated by a continuous bump except for the spectrum of ^{15}O. The arrows with notations g.s. and V_C^f indicate the positions of the ground state and the Coulomb barrier in the final channel, respectively. The spectra of the Be and Li isotopes are of a symmetric form, whereas those of the heavier particles are asymmetric and have a tail on the low-energy side. The spectrum of ^4He is asymmetric but has a tail on the high-energy side.

In order to obtain the angular dependence of Q^m, the energy spectra of the various emitted particles were measured at the angles listed in Table I.

Figure 2 shows the energy spectra of ^{12}C from the reaction $^{53}Cr + ^{14}N$ at $E_{lab} = 90$ MeV and $\theta_{lab} = 15$, 24, and 27°. We see that the bump of the energy spectrum consists of two parts with respect to the energy of emitted particles for $n \leq 4$. The higher-energy part has larger cross sections at small angles, while the yield of the lower-energy part is relatively larger at large angles. The following discussion of Q^m concerns the higher-energy part

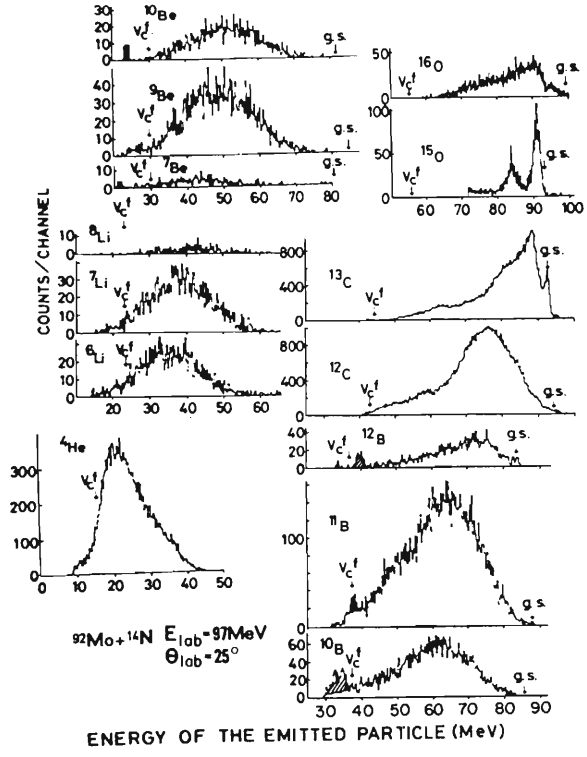

FIG. 1. Energy spectra of emitted particles $^{16,15}O$, $^{13,12}C$, $^{12,11,10}B$, $^{10,9,7}Be$, $^{8,7,6}Li$, and ^4He from the reactions $^{96}Mo + ^{14}N$ at $E_{lab} = 97$ MeV, $\theta_{lab} = 25°$. The notations g.s. and V_C^f denote the position of the ground state and the Coulomb barrier in the final channel.

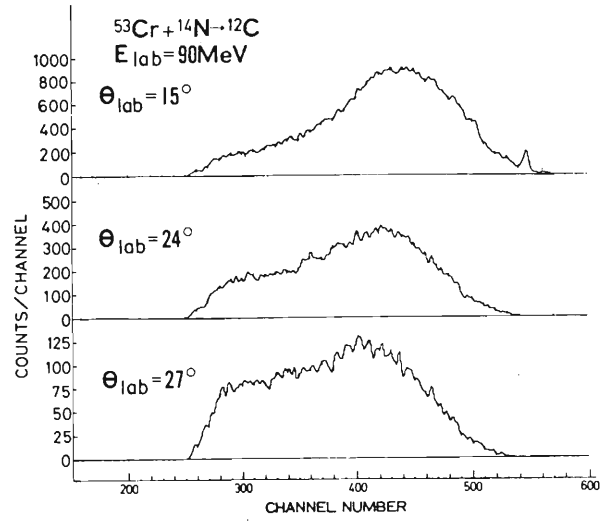

FIG. 2. Energy spectra of ^{12}C from the reaction $^{53}Cr + ^{14}N$ at $E_{lab} = 90$ MeV, $\theta_{lab} = 15°$, 24°, and 27°.

of reactions with $M_b < M_a$, when two peaks are present.

Figure 1 also shows that the full width at half maximum (FWHM) of the bump, Γ, for a given set of incident variables increases with n up to ~ 4 and then decreases for larger n (see Sec. III B and Tables II and III). This general trend in the spectrum shape and width are partly due to the existence of two components in the energy spectra for $n \leq 4$. For a given reaction, $A(a, b)$, Γ increases as the increase of E_i (see Fig. 3).

The shape of the energy spectrum depends also on the bombarding energy. The variation of the energy spectrum of ^9Be from the reaction $^{52}Cr + ^{12}C$ at $E_{lab} = 60$, 70, and 90 MeV is shown in Fig. 3. It is clearly seen that for an increase in E_{lab}, (i) the selective peaks disappear, (ii) the bump shifts toward higher excitation energies, and (iii) the bump broadens.

In order to determine the dependence of the spectrum shape on the target mass, the ^{14}N-induced reactions were studied for all stable isotopes of molybdenum $^A Mo$ ($A = 92$, 94, 95, 96, 97, 98, and 100) at $E_{lab} = 97$ MeV and $\theta_{lab} = 25°$. The spectra of the emitted ^{13}C are shown in Fig. 4. It is seen that gross features of the spectra are very similar.

B. Systematics of the most probable Q values Q^m

Let us first define some useful Q values. Q^m is the Q value corresponding to the peak position of the bump of the spectrum. The values Q_1 and Q_2 denote the Q values for which the yields are one-half of the value at Q^m, corresponding, respectively, to the higher and lower energies of the outgoing particles. Thus, $\Gamma = Q_1 - Q_2$ gives the

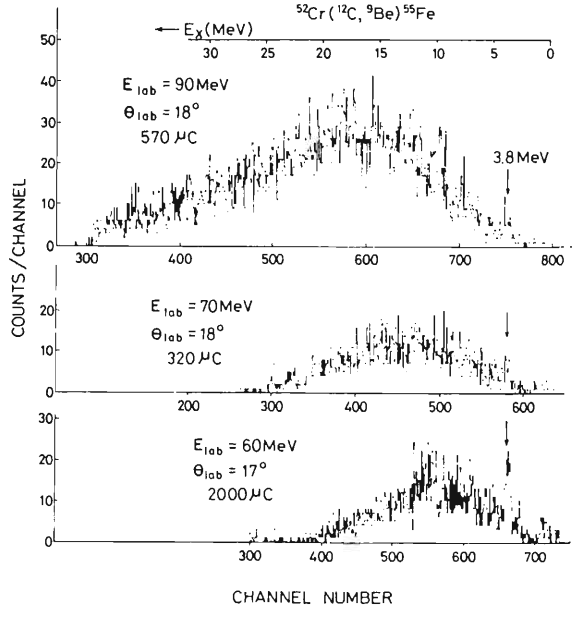

FIG. 3. Energy spectra of ^{9}Be from ^{52}Cr + ^{12}C at E_{lab} = 60, 70, and 90 MeV.

FWHM of the bump. The Q_{gg} is the ground state Q value.

It is often argued[9,14] that in the "stripping-type" transfer reaction, i.e., $M_b < M_a$, the weakly bound lighter product nucleus b is not excited, so that the high excitation energy E_x is concentrated in the primary heavy product B. In such a situation, the relation

$$Q^m = Q_{gg} - E_x^m \tag{1}$$

is obtained, where E_x^m corresponds to the most probable excitation energy of the heavier product B. Therefore, the most probable Q value, Q^m, the ambiguity of which is estimated to within ±2 MeV in most cases, can be obtained.

Table II indicates the Q values of the reactions ^{52,53}Cr + ^{14}N. It shows the E_{lab}, identified particle b, and laboratory angle of emission θ_{lab}. The values of Q^m, Q_{gg}, Q_1, Q_2, and E_x^m for each reaction are arranged according to the order of the values of θ_{lab}. When two components in the bump are present, $Q^m(1)$ and $Q^m(2)$ denote the Q^m values corresponding to the higher- and the lower-energy parts, respectively. The $\overline{Q}_{eff}^m$ are the "effective" Q^m values (see Sec. III C) of the higher-energy part averaged over the observed angles. At 90 MeV, the $\overline{Q}_{eff}^m$ are averaged over the ^{52}Cr + ^{14}N and ^{53}Cr + ^{14}N reactions. The table shows that E_x^m increases with an increase in n, the number of transferred particles; it is about 10 MeV for $n = 1$ and about 70 MeV for $n = 10$.

Table III compiles the Q values for the reactions ^{A}Mo + ^{14}N (A = 92, 94, 95, 96, 97, 98, and 100), ^{92}Mo + ^{12}C and ^{90}Zr + ^{14}N at E_{lab} = 97, 90, and 90 MeV, respectively.

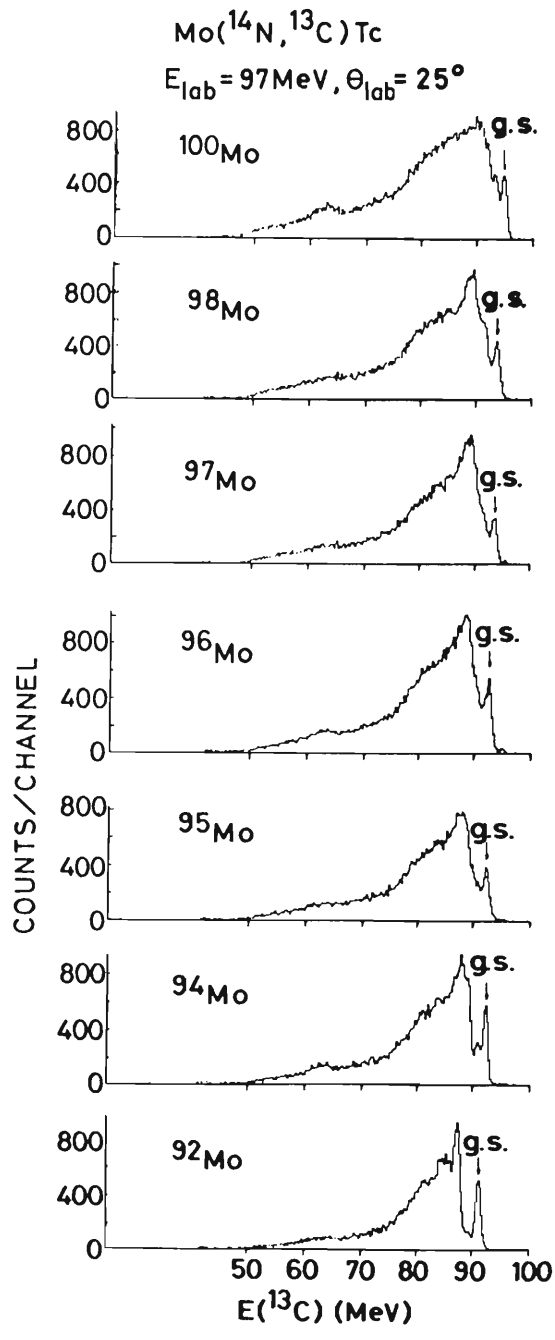

FIG. 4. Energy spectra of ^{13}C from the reactions ^{A}Mo + ^{14}N (A = 92, 94, 95, 96, 97, 98, and 100) at E_{lab} = 97 MeV, θ_{lab} = 25°.

1. Dependence of Q^m on θ_{lab}

As is shown in Tables II and III, the Q^m for specific reactions do not depend sensitively on the emission angles θ_{lab} of the products. In Fig. 5, the Q^m of several products in the reaction ^{53}Cr

TABLE II. Q values of the reactions $^{52,53}Cr + ^{14}N$. Q^m, Q_1, Q_2, and E_x^m are arranged according to the order of the θ_{lab}. $\bar{Q}_{eff}^m$ is the value averaged over data for different θ_{lab}. The $\bar{Q}_{eff}^m$ preceded by an asterisk and listed as $^{52}Cr + ^{14}N$ denote those values averaged over reactions $^{52}Cr + ^{14}N$ and $^{53}Cr + ^{14}N$. For the $^{53}Cr + ^{14}N$ reactions, $Q^m(1)$ and $Q_{eff}^m(1)$ correspond to the higher-energy parts, while $Q^m(2)$ and $Q_{eff}^m(2)$ correspond to the lower-energy parts of the continuous spectra.

$A+a$	E_{lab} (MeV)	b	θ_{lab} (deg)	Q_{gs} (MeV)	Q^m (MeV)	Q_1 (MeV)	Q_2 (MeV)	$\bar{Q}_{eff}^m$ (MeV)	E_x^m (MeV)
$^{52}Cr + ^{14}N$	95	^{13}C	16, 20, 25	− 1.0	−10.5, −11, −12	−5, −5, −5	−25, −31, −33	− 8.3	9.5, 10, 11
		^{12}C		+ 3.0	−18, −18.5, −18.5	−9.5, −10, −10	−30, −31, −50	−15.4	21, 21, 21.5
		^{11}B		− 3.7	−28, −30, −32	−16, −16, −18.5	−43, −41, −46	−23.8	24, 26, 28
		^{10}B		− 4.0	−36, −36.5, −40	−20, −24, −27	−49, −59, −56	−29.3	32, 32.5, 36
		^{10}Be		− 9.1	−, −, −39	−, −, −29	−, −, −49	−29.2	−, −, −30
		^{9}Be		− 4.3	−42, −44, −43	−28, −33, −29	−54, −47, −57	−33.4	38, 40, 39
		^{7}Be		− 6.1	−47, −49, −51	−36, −38, −40	−56, −59, −61	−39.2	41, 43, 45
		^{7}Li		− 6.3	−48, −48, −48	−37, −38, −39	−60, −60, −59	−34.3	42, 42, 42
		^{6}Li		− 2.2	−52, −54, −55	−43, −46, −44	−63, −65, −68	−39.6	50, 52, 53
		^{4}He		+ 7.8	−, −64, −66	−, −61, −	−, −69, −	−46.0	−, 72, 74
$^{52}Cr + ^{14}N$	90	^{13}C	16, 25	− 1.0	−10.5, −10.5	−4, −3	−18, −18.5	*− 7.1	9.5, 10.5
		^{12}C		+ 3.0	−17, −17	−9, −7	−35, −32	−13.9	20, 22
		^{12}B		− 9.7	−20, −19	−12, −	−33, −	−13.1	10, 11
		^{11}B		− 3.7	−27, −30	−15, −24	−40, −47	−21.8	23, 27
		^{10}B		− 4.0	−32, −29	−20, −21	−48, −47	−23.5	28, 24
		^{10}Be		− 9.1	−33.5, −	−23, −	−48, −	−23.6	23.5, −
		^{9}Be		− 4.3	−37, −	−27, −	−49, −	−27.2	33, −
		^{7}Be		− 6.1	−43.5, −	−27, −	−49, −	−34.0	37.5, −
		^{7}Li		− 6.3	−44	−34, −35	−59, −56	−31.3	38, 43
		^{6}Li		− 2.2	−50, −47	−40, −39	−60, −61	−33.6	48, 45
		^{4}He		+ 7.8	−58, −57	−52, −52	−65, −62	−40.1	66, 68
$^{53}Cr + ^{14}N$	90	^{13}C	16	+ 0.0	−9	−4.5	−16		9
		^{12}C		+ 5.3	−16.5	−8	−27		22
		^{12}B		− 8.4	−19	−12	−31		9
		^{11}B		− 0.5	−26	−12	−39		25
		^{10}B		− 4.3	−28	−20	−41		24
		^{10}Be		− 5.7	−32	−26	−49		26
		^{9}Be		− 3.9	−37	−28	−49		33
		^{7}Be		− 6.5	−44	−	−		37.5
		^{7}Li		− 2.9	−45	−35	−55		42
		^{6}Li		− 2.3	−45	−40	−48		43
		^{4}He		+10.7	−59	−40	−65		70
$^{52}Cr + ^{14}N$	80	^{13}C	18, 22, 27	− 1.0	−10, −11.5, −10.5	−5, −6, −4.5	−18, −20, −20	− 7.8	9, 10.5, 9.5
		^{12}C		+ 3.0	−17, −18, −22	−7, −7.5, −8	−30, −29.5, −44	−16.1	20, 21, 25
		^{12}B		− 9.7	−19, −20, −23	−13, −13, −	−25, −27, −	−13.3	9, 10, 19.5
		^{11}B		− 3.7	−26, −25, −28	−15, −17, −15	−34, −34, −34	−18.5	22, 21.5, 24
		^{10}B		− 4.0	−31, −31, −32.5	−18, −19, −21	−41, −41, −45	−23.8	27, 27, 28.5
		^{10}Be		− 9.1	−, −30, −			−20.2	−, 21, −
		^{9}Be		− 4.3	−32, −34, −32.5	−23, −, −27	−42, −, −42	−23.0	28, 30, 28.5
		^{7}Be		− 6.1	−38, −36, −39	−31, −, −	−46, −, −	−28.0	32, 30, 33
		^{7}Li		− 6.3	−38.5, −39, −39	−30, −32, −31	−48, −51, −48	−25.1	32, 33, 33
		^{6}Li		− 2.2	−43, −43.5, −45	−33, −34, −36	−51, −53, −54	−30.3	41, 41.5, 43
		^{4}He		+ 7.8	−52, −51, −53	−49, −48, −47	−57, −56, −59	−34.3	60, 59, 60.5
$^{52}Cr + ^{14}N$	70	^{13}C	22, 27	− 1.0	−10, −8.5	−4.5, −4	−14.5, −15	− 6.4	9, 7.5
		^{12}C		+ 3.0	−14, −13	−6, −5	−25, −26	−10.6	17, 16
		^{12}B		− 9.7	−16, −	−11, −	−21, −	− 9.8	6.5, −
		^{11}B		− 3.7	−19, −19	−12, −11	−25.5, −26	−12.8	15, 15.5
		^{10}B		− 4.0	−27, −28.5	−17, −18	−34, 37	−21.6	23, 24.5
		^{9}Be		− 4.3	−28, −28	−21, −22	−36, −33	−18.2	24, 24
		^{7}Be		− 6.1	−32, −33	−21, −	−36, −	−22.7	25, 27
		^{7}Li		− 6.3	−32, −34	−24, −	−41, −	−19.3	26, 28
		^{6}Li		− 2.2	−36, −35	−29, −28	−45, −45	−21.8	34, 33
		^{4}He		+ 7.8	−44, −44	−41, −38	−48, −48	−26.1	51.5, 51.5

TABLE II. (*Continued*)

$A+a$	E (MeV)	b	θ_{lab} (deg)	Q_{gg} (MeV)	Q^m (MeV)	Q_1 (MeV)	Q_2 (MeV)	$\bar{Q}^m_{eff}$ (MeV)	E_x^m (MeV)
$^{52}Cr+^{14}N$	64	^{13}C	20, 27	− 1.0	−8, −7	−2, −2	−13, −12	− 4.6	7, 6
		^{12}C		+ 3.0	−12.5, −14	−4, −4	−20.5, −21	−10.4	15.5, 17
		^{12}B		− 9.7	−14, −			− 7.6	4, −
		^{11}B		− 3.7	−16, −17	−9, −9	−23, −23.5	−10.3	12, 13
		^{10}B		− 4.0	−22, −23	−15, −14	−29, 5, −30	−16.3	18, 19
		^{9}Be		− 4.3	−24, −25	−18, −	−30, −	−14.5	20, 21
		^{7}Be		− 6.1	−27, −29			−18.0	21, 23
		^{7}Li		− 6.3	−30, −31	−24, −25	−35, −36	−16.8	24, 25
		^{6}Li		− 2.2	−32, −33.5	−23, −23	−41, −41	−19.1	30, 31.5
		^{4}He		+ 7.8	−38, −39	−35, −33	−43, −44	−20.6	46, 46.5

$A+a$	E_{lab} (MeV)	b	θ_{lab} (deg)	Q_{gg} (MeV)	$Q^m(1)$ (MeV)	$Q^m_{eff}(1)$ (MeV)	$Q^m(2)$ (MeV)	$Q^m_{eff}(2)$ (MeV)
$^{53}Cr+^{14}N$	90	^{13}C	15	+0.0	− 8.5	− 5.5	−23	−20
			18		−10	− 7	−24	−21
			21		−11	− 8	−26	−23
			24		−11.5	− 8.5	−26.5	−23.5
			27		−12	− 9	−28	−25
			30		−14	−11	−30.5	−27.5
		^{12}C	10	+5.3	−16.5	−13.5		
			12		−16	−13	−33	−30
			15		−17	−14	−34	−31
			18		−17	−14	−36	−33
			21		−18	−15	−35	−32
			24		−18	−15	−35	−32
			27		−18	−15	−34	−31
			30		−19	−16	−34	−31
			33		−18.5	−15.5	−34	−31
		^{11}B	10	−0.5	−26	−20	−38.5	−32
			12		−25	−19	−37	−31
			15		−26.5	−20		
			18		−26.5	−20	−40	−34
			21		−28.5	−22	−40	−34
			24		−30	−24	−42	−36
			27		−30.5	−24		
			30		−32.5	−26		
			33		−33.5	−27		
		^{10}B	10	−4.3	−29	−23	−42	−36
			12		−29	−23	−40	−34
			15		−29	−23	−41	−35
			18		−30	−24		
			21		−32	−26		
			24		−33	−27		
			27		−33	−27		
			30		−34	−28	−41.5	−35
			33		−36	−30		
		^{9}Be	12	−3.9	−37.5	−28		
			15		−38	−28		
			18		−38	−28		
			21		−39	−28		
			24		−38.5	−29		
			27		−39	−29		
			30		−39.5	−30		
			33		−40	−30		

TABLE III. Q values of the reactions ^{A}Mo+^{14}N, ^{92}Mo+^{12}C, ^{90}Zr+^{14}N. Q^m, Q_1, Q_2, and Q^m_{eff} are arranged according to the order of the θ_{lab}.

			^{A}Mo+^{14}N, E_{lab} = 97 MeV, θ_{lab} = 25°, 30°			
A	b	Q_{gg} (MeV)	Q^m (MeV)	Q_1 (MeV)	Q_2 (MeV)	Q^m_{eff} (MeV)
92	^{13}C	− 3.5	− 7.5, − 9.7	− 7, − 7	−14, −16	− 2.4, − 4.6
94		− 2.7	− 6.5, − 8.4	− 6, − 6	−15, −18	− 1.4, − 3.3
95		− 2.1	− 6.6, − 8.5	− 5, − 6	−16, −18	− 1.5, − 3.4
96		− 1.9	− 6.3, − 8.0	− 4, − 4	−16, −18	− 1.2, − 2.9
97		− 1.3	− 6.1, − 8.4	− 3, − 4	−14, −19	− 1.0, − 3.3
98		− 1.0	− 5.5, − 8.4	− 3, − 3	−16, −20	− 0.4, − 3.3
100		− 0.1	− 6.3, − 8.9	− 1, − 3	−18, −19	− 1.2, − 3.7
Mean			− 7.5	− 4	−17	− 2.5
92	^{12}C	+ 0.2	−18.4, −18.1	−10, −10	−26, −27	−13.3, −13.0
94		+ 0.3	−18.4, −17.8	−10, −10	−28, −27	−13.3, −12.7
95		+ 2.4	−18.3, −18.1	−10, −10	−27, −28	−13.2, −13.0
96		+ 0.6	−18.2, −17.6	−10, − 9	−27, −27	−13.1, −12.5
97		+ 2.7	−18.3, −18.1	−10, −10	−27, −28	−13.2, −13.0
98		+ 0.6	−18.1, −17.5	−10, − 9	−27, −27	−13.0, −12.4
100		+ 1.3	−18.1, −17.5	− 9, − 9	−27, −27	−13.0, −12.4
Mean			−18.1	−9.5	−27	−13.0
92	^{12}B	−14.8	−22.2, −24.1	−18, −19	−34, −35	−13.5, −11.6
94		−12.8	−23.0, −24.3	−16, −17	−35, −34	−13.7, −12.4
95		−12.2	−21.6, −23.2	−16, −18	−35, −32	−12.6, −11.0
96		−11.1	−21.4, −23.5	−16, −17	−35, −35	−12.9, −10.8
97		−10.4	−21.2, −22.9	−15, −17	−36, −36	−12.3, −10.6
98		− 9.4	−20.6, −23.0	−14, −15	−37, −35	−12.4, −10.0
100		− 7.6	−20.4, −23.1	−13, −15	−38, −37	−12.5, − 9.8
Mean			−22.7	−16	−35	−12.1
92	^{11}B	− 9.2	−28.4, −29.6	−18, −20	−42, −42	−17.8, −19.0
94		− 8.2	−29.2, −28.5	−19, −21	−43, −41	−18.6, −17.9
95		− 5.3	−29.3, −28.9	−19, −20	−43, −43	−18.7, −18.3
96		− 7.0	−29.4, −28.8	−19, −20	−43, −43	−18.8, −18.2
97		− 4.1	−28.6, −28.9	−19, −20	−43, −44	−18.2, −18.3
98		− 6.0	−29.1, −28.0	−18, −19	−45, −45	−18.5, −17.2
100		− 4.7	−27.8, −27.9	−18, −19	−45, −44	−17.2, −17.3
Mean			−28.8	−19	−43	−18.2
92	^{10}B	− 9.9	−31.6, −31.8	−22, −22	−44, −46	−21.0, −21.2
94		− 9.4	−31.7, −32.5	−22, −25	−48, −42	−21.1, −21.9
95		− 9.3	−31.3, −30.8	−22, −22	−45, −47	−20.7, −20.2
96		− 8.8	−31.8, −31.0	−22, −22	−45, −45	−21.2, −20.4
97		− 8.8	−31.1, −31.6	−22, −23	−45, −46	−20.5, −21.0
98		− 8.2	−32.0, −32.0	−22, −23	−49, −50	−21.4, −21.4
100		− 7.3	−32.0, −31.8	−21, −22	−48, −47	−21.4, −21.2
Mean			−31.6	−22	−46	−21.0
92	^{10}Be	−16.9	−38.8, −42.6	−33, −34	−48, −51	−22.5, −26.3
94		−15.0	−41.7, −42.2	−32, −32	−53, −52	−25.4, −25.9
95		−11.9	−41.2, −42.0	−31, −33	−52, −53	−24.9, −25.7
96		− 8.8	−41.3, −42.2	−32, −33	−53, −53	−25.0, −25.9
97		− 8.8	−41.8, −43.7	−30, −33	−55, −54	−25.5, −27.4
98		−11.1	−41.9, −43.3	−30, −32	−53, −54	−25.6, −27.0
100		− 9.0	−41.5, −42.8	−30, −32	−54, −55	−25.2, −26.5
Mean			−42.0	−32	−53	−25.6

TABLE III. (*Continued*)

A	b	Q_{gg} (MeV)	Q^m (MeV)	Q_1 (MeV)	Q_2 (MeV)	Q^m_{eff} (MeV)
92	^{9}Be	−12.7	−43.2, −44.6	−32, −35	−54, −56	−26.9, −28.3
94		−11.3	−43.9, −45.1	−32, −34	−55, −56	−27.6, −28.8
95		−10.6	−43.6, −44.8	−33, −34	−55, −57	−27.3, −28.5
96		− 9.9	−43.7, −44.1	−33, −34	−56, −56	−27.4, −27.8
97		− 9.3	−44.8, −45.1	−33, −34	−56, −56	−28.5, −28.8
98		− 8.6	−44.6, −45.5	−34, −35	−56, −57	−28.3, −29.2
100		− 6.8	−45.2, −45.5	−34, −34	−56, −57	−28.9, −29.2
Mean			−44.5	−33	−56	−28.3
92	^{7}Be	−14.2	−50.0, −50.7	−42, −42	−59, −60	−33.7, −34.4
94		−13.9	−50.1, −51.0	−43, −43	−59, −61	−33.8, −34.7
95		−13.8	−49.0, −51.0	−40, −42	−60, −61	−32.7, −34.7
96		−13.7	−48.0, −50.9	−41, −41	−59, −61	−31.7, −33.8
97		−13.5	−51.2, −51.1	−42, −43	−59, −62	−34.9, −34.8
98		−13.2	−52.3, −52.5	−45, −42	−64, −	−36.0, −36.2
100		−12.2	−51.6, −50.4	−43, −42	−63, −	−35.3, −34.1
Mean			−50.7	−42	−61	−34.4
92	^{7}Li	−16.7	−53.5, −55.6	−44, −45	−62, −65	−30.1, −33.2
94		−15.0	−53.9, −55.7	−45, −45	−64, −66	−31.5, −33.3
95		−11.8	−54.0, −55.0	−44, −45	−64, −65	−31.6, −33.1
96		−13.4	−54.0, −55.6	−44, −45	−64, −64	−31.6, −33.2
97		−10.2	−54.1, −55.7	−44, −46	−64, −65	−31.3, −33.3
98		−11.7	−54.5, −55.3	−44, −45	−64, −65	−32.1, −32.9
100		− 9.9	−54.6, −55.7	−45, −45	−64, −65	−32.2, −33.3
Mean			−54.8	−45	−64	−32.3
92	^{6}Li	−12.8	−57.0, −57.8	−48, −48	−67, −68	−34.7, −35.5
94		−11.7	−58.3, −58.3	−48, −48	−68, −70	−36.0, −36.0
95		−11.5	−56.7, −57.6	−47, −48	−67, −67	−34.4, −35.3
96		−13.4	−56.1, −56.6	−47, −47	−66, −66	−33.8, −34.3
97		−10.4	−56.5, −58.1	−48, −49	−67, −68	−34.1, −35.8
98		− 9.4	−57.5, −59.3	−48, −49	−69, −72	−35.2, −37.0
100		− 7.9	−57.7, −59.5	−48, −49	−69, −71	−35.4, −37.2
Mean			−57.6	−48	−68	−35.3
92	^{4}He	− 4.0	−68.2, −69.1	−60, −62	−73, −73	−39.5, −40.4
94		− 2.7	−68.6, −69.3	−59, −62	−74, −74	−39.9, −40.6
95		− 0.2	−68.4, −69.0	−60, −62	−73, −73	−39.7, −40.3
96		− 1.4	−68.4, −68.9	−60, −62	−73, −74	−39.7, −40.2
97		+ 1.3	−68.3, −69.0	−60, −61	−73, −73	−39.6, −40.3
98		− 0.1	−68.6, −69.1	−60, −62	−74, −74	−39.9, −40.4
100		+ 1.7	−68.4, −68.2	−59, −60	−74, −74	−39.7, −40.1
Mean			−68.7	−60.5	−73	−46.0
			^{92}Mo + ^{12}C, E_{lab} = 90 MeV, θ_{lab} = 20°			
	^{10}B	−14.7	−22	−17	−32	−16
	^{10}Be	−16.9	−25	−20	−34	−13
	^{9}Be	−14.7	−29	−22	−38	−17
	^{7}Be	−16.5	−44	−34	−53	−32
	^{7}Li	−19.2	−46	−36	−56	−29
	^{6}Li	−17.7	−51	−42	−60	−34
			^{90}Zr + ^{14}N, E_{lab} = 75 MeV, θ_{lab} = 30.5°			
	^{13}C	− 2.4	− 8.0	− 5.5	−12.8	− 3.3
	^{12}C	+ 0.6	−12.4	− 7.2	−20.4	− 7.3
	^{11}B	− 7.8	−20.5	−13.8	−28.4	−10.3

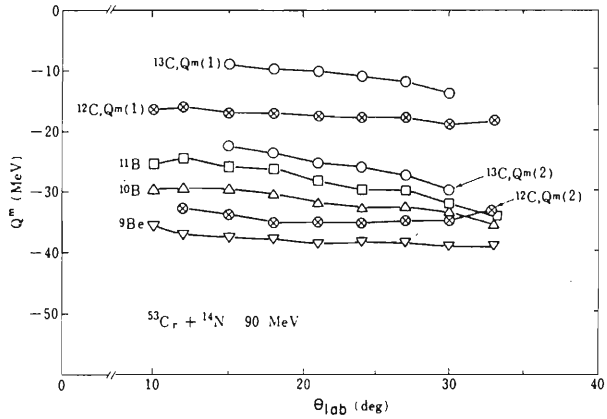

FIG. 5. The most probable Q values Q^m of the reactions ^{53}Cr + ^{14}N at E_{lab} = 90 MeV as function of the angle of emission θ_{lab}. For ^{13}C and ^{12}C, the Q^m values of higher- and lower-energy components are shown.

+ ^{14}N at 90 MeV are plotted against θ_{lab}. This shows more clearly the weak dependence of Q^m on θ_{lab} over a wide range of θ_{lab}.

For ^{A}Mo + ^{14}N reactions, the largest differences in the Q^m at 25° and 30° are for ^{13}C and ^{12}B and about 2 MeV, which is still small compared with the width, Γ, of the bump. For other b, the Q^m are almost the same at the two angles. This can be clearly seen in Fig. 6 in which the four Q values Q^m, Q_1, Q_2, and Q_{gg} of the reactions ^{A}Mo + ^{14}N at θ_{lab} = 25° and 30° are shown. This situation is in contrast with the case for sub-Coulomb or near-Coulomb reactions, where the "optimum" Q values are strongly dependent on the emission angles.[5] The Q^m values of the present study coincide with none of the optimum Q values cited above[4,5,6] (see Ref. 12). In the study of the reactions Ag + ^{14}N at E_{lab} = 100, 160, and 250 MeV, Moretto *et al.*,[15] found Q^m to be independent of θ_{lab}. In research on the ^{58}Ni(^{16}O, ^{12}C) reaction above the Coulomb barrier (E_{lab} = 60, 72, and 81 MeV), Wilczyński *et al.*[16] found that Q^m changes with angle $\theta_{c.m.}$ when $\theta_{c.m.}$ is larger than θ_{gr}, grazing angle, while Q^m remains unchanged at smaller angles, which is consistent with the results of the present study.

2. *Dependence of Q^m on adjacent A*

Another aim of this study is to determine the dependence of Q^m on A. It was confirmed that the difference of the Q^m for specific reactions (a, b) at the same E_t is very small compared with that of the Q_{gg} for A = ^{52}Cr, ^{53}Cr, ^{50}Ti, and ^{54}Fe (Ref. 3(a) and Table II). For all the stable isotopes of molybdenum, the Q^m are almost constant for all individual $A(a, b)$, as is shown in Fig. 6 and Table

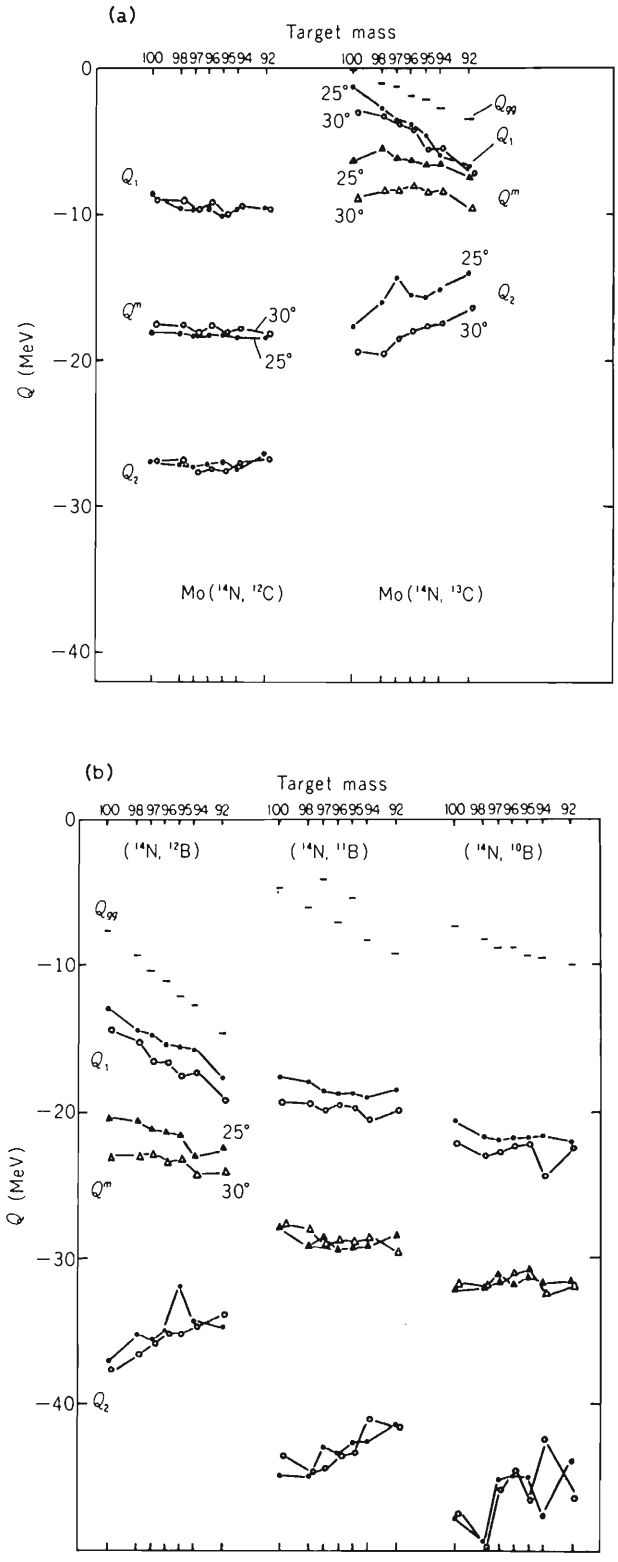

FIG. 6. The most probable and half-maximum Q values Q^m, Q_1, and Q_2 in the reaction (a) (^{14}N, ^{13}C), (^{14}N, ^{12}C); (b) (^{14}N, ^{12}B), (^{14}N, ^{11}B), and (^{14}N, ^{10}B) on Mo isotopes vs mass number of target. The ground state Q values Q_{gg} are also shown.

III, despite the large differences in Q_{gg}. That Q^m is independent of adjacent A has been reported for the reactions ^{A}Ni(^{18}O, ^{16}O) (A = 58, 60, 62, and 64) at E_{lab} = 63 MeV and θ_{lab} = 30°.[17]

3. Dependence of Q^m on E_i and n

Figure 7 shows the variation of Q^m in the reaction ^{52}Cr + ^{14}N with incident laboratory energy E_{lab}. For small n, Q^m is almost constant throughout the entire energy range, while with an increase in n, the absolute value Q^m and the gradient of $|Q^m|$ vs E_{lab} increase.

Figure 8 is a plot of Q^m vs n for the reactions ^{52,53}Cr + ^{14}N. A linear relation,

$$Q^m = \alpha n + \beta , \qquad (2)$$

is obtained up to a given number of transferred nucleons: $n \leq 4$–5. The values of α and β are given in the inset in the upper-right-hand corner of Fig. 8. For the reactions studied here α is linear in the incident energy E_i and lies between −5 and −8 MeV/nucleon, whereas β is independent of E_i and has a value of about −3 MeV. Note that these relations hold irrespective of proton or neutron transfer, although the Q_{gg} are quite different for isobaric product pairs, such as ^{12}C and ^{12}B, ^{10}B and ^{10}Be, and ^{7}Be and ^{7}Li.

This variation of Q^m with E_i is not compatible with the prediction of Wilczyński[9] based on the determination of Q^m from known quantities, i.e., the separation energies of the transferred nucleons from the projectile in "stripping-type" reactions.

A plot similar to that in Fig. 8 for the reactions ^{92,100}Mo + ^{14}N at E_{lab} = 97 MeV [see, e.g., Fig. 2 of Ref. 3(c)] shows a splitting for isobars and a grouping according to the atomic number of b. This suggests the increasing importance of Coulomb effects which leads us to the following discussion of the effective Q values.

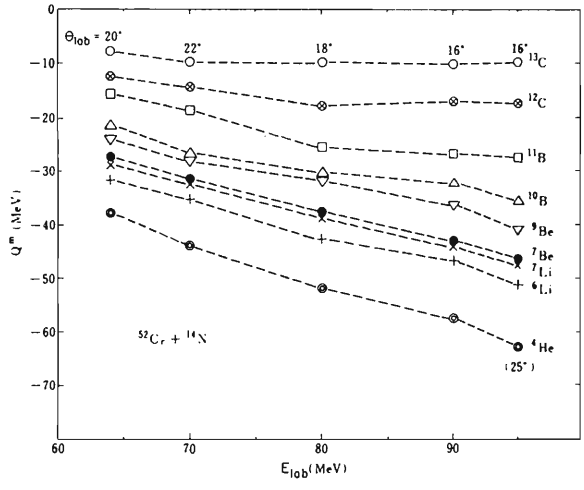

FIG. 7. The most probable Q values Q^m of the reactions ^{52}Cr + ^{14}N as a function of the bombarding energy E_{lab}.

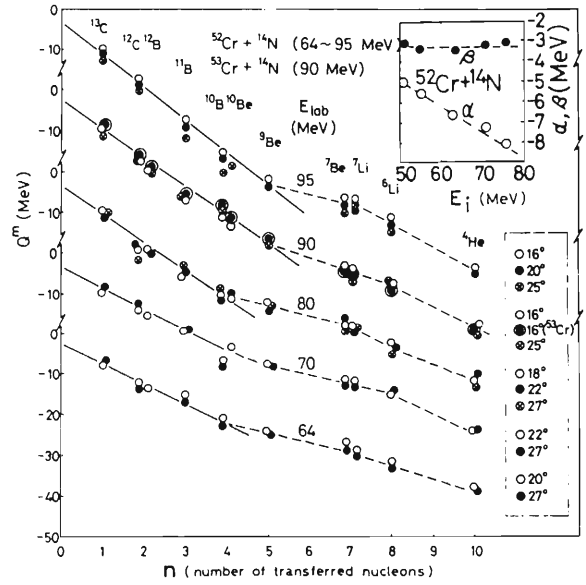

FIG. 8. The most probable Q values Q^m of the reactions ^{52,53}Cr + ^{14}N as function of the number of transferred nucleons n. In the upper right part the values of α of Eq. (2) are plotted vs incident c.m. energy E_i.

C. Systematics of most probable effective Q values Q^m_{eff}

In heavy-ion reactions, because of large difference between the Coulomb barriers of the incident and exit channels, Buttle and Goldfarb[4] and Brink[7] have introduced the concept of "effective Q values" Q_{eff}. It is defined as the Q value corrected for the difference $\Delta V = V_C^i - V_C^f$ in the Coulomb barriers between incident and outgoing channels.

1. Dependence of Q^m_{eff} on n and E_i

Figure 9 is a plot of the most probable effective Q values, Q^m_{eff} vs n for the reactions ^{52}Cr + ^{14}N and ^{A}Mo + ^{14}N, A = 92–100. The Q^m_{eff} are averaged over the angles θ_{lab} and the target isotopes and are compiled in Tables II and III. Figure 9 also shows similar plots for the data of the Dubana group[1,9] for the reactions ^{232}Th + ^{15}N at E_{lab} = 145 MeV and ^{232}Th + ^{22}Ne at E_{lab} = 174 MeV. The data for ^{232}Th(^{15}N, ^{14}N) at E_{lab} = 98.5 MeV[18] is also shown for reference. Except for some discrepancies between ^{12}C and ^{12}Be, and ^{11}B and ^{11}Li in the reaction ^{232}Th + ^{15}N, all the data follow the linear relation

$$Q^m_{eff} = \alpha_{eff} n + \beta_{eff} \qquad (3)$$

for $n \leq 4$–5. The radius parameter r_0 was chosen to be 1.4 fm. (For reactions with lower V_C^i and

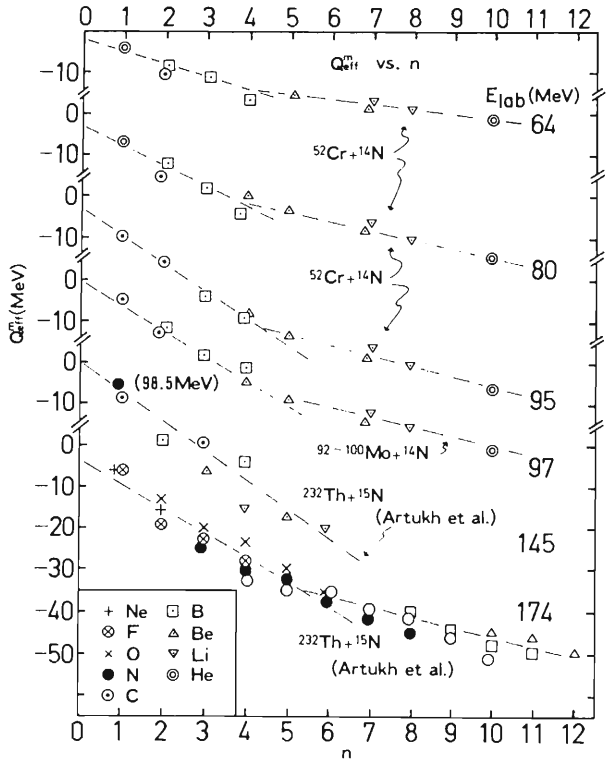

FIG. 9. The most probable effective Q values Q^m_{eff} of the reactions $^{52}Cr+^{14}N$ and $^{92-100}Mo+^{14}N$ as function of transferred nucleons n. The data are averaged over angles and target isotopes. The Q^m_{eff} values of the reactions $^{232}Th+^{15}N$ and $^{232}Th+^{22}Ne$ of Dubna data are also plotted vs n.

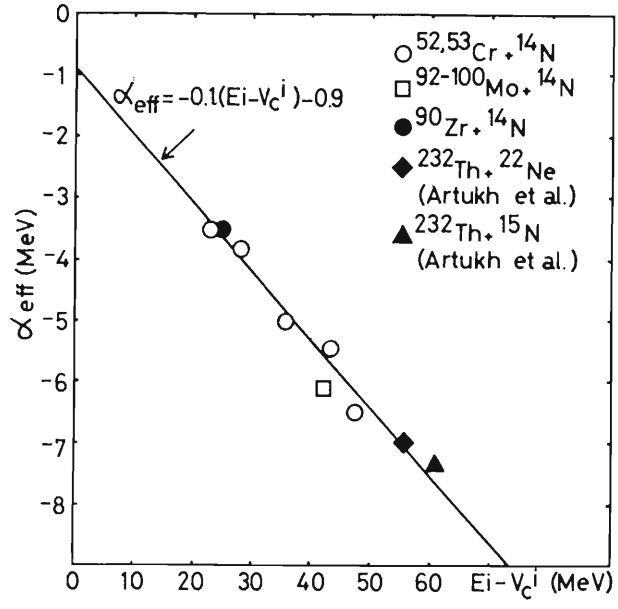

FIG. 10. The α_{eff} values of Eq. (2) plotted vs effective incident energy $E_i - V_C^i$.

E_{lab}, i.e., $^{52}Cr+^{14}N$ at $E_{lab}=64$ and 70 MeV, the linear relation (2) holds rather better than that of relation (3). In these cases, r_0 should be large, e.g., $r_0 \approx 2$ fm. On the other hand, for reactions with high V_C^i, i.e., $^{232}Th+^{22}Ne$, r_0 should be small, e.g., $r_0 \approx 1.2$ fm. As a compromise, $r_0 = 1.4$ fm was employed throughout.) The gradient of linear relation (3), α_{eff}, is plotted against $E_i - V_C^i$ in Fig. 10. This figure also includes the data for $^{90}Zr+^{14}N$ at $E_{lab}=75$ MeV. This plot gives a linear relation

$$\alpha_{\text{eff}} = -0.1(E_i - V_C^i) - 0.9(\text{MeV}). \quad (4)$$

The data for the segment β_{eff} of the linear relations (3) are scattered between 0 and −5 MeV but are around −3 MeV for $^{52,53}Cr+^{14}N$ reactions.

It is possible to rewrite Q^m_{eff} as

$$\begin{aligned} Q^m_{\text{eff}} &= (E_f^m - V_C^f) - (E_i - V_C^i) \\ &= Q^m + \Delta V_C = Q_{gg} - E_x^m + \Delta V_C = E_f^m - E_i + \Delta V_C \\ &= \Delta E^m + \Delta V_C , \end{aligned} \quad (5)$$

where E_f^m and ΔE^m are the most probable kinetic energies in the exit channel and the most probable energy loss of the scattering particle, respectively. Relation (3) reflects the fact that, as long as n is not too large, i.e., $n \lesssim 4-5$, a constant amount of kinetic energy per nucleon is transferred during the "stripping" and this constant rate, α_{eff}, is proportional to the energy available at the barrier, $E_i - V_C^i$. This situation holds throughout a wide range of incident variables when E_i is large compared with V_C^i. The segment β^m_{eff} may correspond to the energy loss of the projectile in the nuclear matter due to inelastic processes,[8] although it is still difficult to form a systematic view on this point.

The simple dependence for Q^m_{eff} with respect to E_i, A, n, and θ_{lab} were obtained without introduction of the difference in the nuclear potentials at the initial and the final channels as proposed by Siemens *et al.*[8] The systematics of Q^m are qualitatively understood with the recent interpretation of Wilczyński *et al.*[16] in terms of nuclear friction, with the radial component being much more important than the tangential component.

As is shown in Fig. 1, the cross sections for the production of b for a given incident channel and energy are very different from one product to another. The most important factor which governs the reaction mechanism, and hence the Q^m, is the energy loss of the scattering particle in the nuclear matter. The key factors which determine the cross section σ are the Γ, the Q_{gg} and the level density of the residual nucleus around excitation E_x^m; the spectral form is qualitatively reproduced.[3,13,14]

2. Most probable effective outgoing velocity v_f^m

In the transfer region, the initial velocity v_i and the most probable outgoing velocity v_f^m, at the barrier corresponding to Q_{eff}^m, are obtained from the relations

$$\begin{aligned}
&\tfrac{1}{2}\mu_i v_i^2 = E_i - V_C^i \,, \\
&\tfrac{1}{2}\mu_f (v_f^m)^2 = E_f^m - V_C^f \\
&\qquad = E_i - V_C^i + Q_{\text{eff}}^m \\
&\qquad = \tfrac{1}{2}\mu_i v_i^2 + Q_{\text{eff}}^m \,, \qquad (6)
\end{aligned}$$

where μ_i and μ_f are the reduced masses in each channels.

Figure 11 shows the ratios v_f^m/v_i plotted against n for various reactions. The values of v_f^m are averaged over the emission angles. The general trend is very similar for a wide range of reactions listed in the figure: The ratio v_f^m/v_i decreases from about unity for $n = 1$ to 0.4–0.5 for $n = 10$. This is in contrast with the simple theories (e.g., Ref. 7) which assume that the reaction be direct and that $v_f \approx v_i$.

The possibility of contributions from the sequential particle decay of excited primary fragments, as proposed by Bondorf and Nörenberg,[19] would result in a constant average velocity v_f^m, which is not the case in the present experiment.

Since the pioneer work of the Orsay[20] and Dubna groups,[2] it is well known that the spectrum of b consists of two parts which are called "quasi-elastic" and "deep inelastic" processes. The present authors have also observed the existence of two parts in the spectrum as mentioned above. The higher energy part of this spectrum corresponds to a "quasielastic" process; however, Fig. 11 throws some doubt on the term "quasi-elastic" at least for larger n.

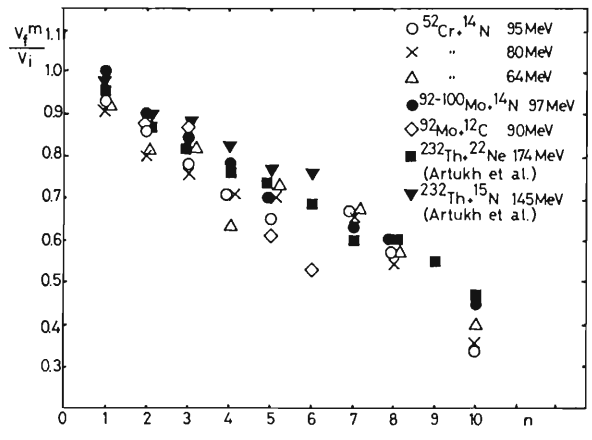

FIG. 11. The ratio of the most probable final velocity v_f^m to the incident velocity v_i in the transfer region plotted against the number of transferred nucleons n.

3. Reactions for larger number of transferred particles

The variation of the Q^m with the E_{lab} and n was discussed above (Fig. 7).

For reactions involving n larger than 4–5, the residual energy of the particle traveling in the nuclear matter, probably at its diffuse rim, will become insufficient to dissipate energy at the same rate α_{eff}, hence the linearity (3) breaks down and Q_{eff}^m saturates with respect to n (Figs. 8 and 9). However, this saturation may be due to different reaction mechanisms such as transfer in cluster, breakup of the projectile, sequential decay and/or a compound nuclear reaction. For the largest n, i.e., $n = 10$ with $b = {}^4$He in the present case, $Q_{\text{eff}}^m \approx V_C^i - E_i$, irrespective of the incident variables. This is a necessary but not a sufficient condition that the reaction proceed via a compound nucleus.[21] The angular distribution of the emitted α particles are peaked in the forward direction. The possibility of breakup of the projectile, $a \to b + c$, where c is an unobserved particle, cannot be ruled out, merely on the basis of kinematic consideration for $n \geq 4$.[12]

IV. CONCLUSION

The spectrum of outgoing particles, b, for multinucleon transfer reactions $A(a, b)$, induced by heavy ions of energy much higher than the Coulomb barrier were investigated. The discussion has been limited to the higher-energy part of the spectrum for $M_b < M_a$, when two components were observed.

Throughout a wide range of E_i and $A + a$, the simple linear relation (3) between the most probable effective Q value, Q_{eff}^m, vs n, the number of transferred nucleons, was obtained for $n \leq 4$–5. It was found that a constant amount of energy α_{eff}, which is about one-tenth of the energy available at the barrier $E_i - V_C^i$, is lost per nucleon transferred.

The key factors which govern the reaction are the energy loss of the scattering particle in the diffuse rim of the nuclear matter and the level density of the residual nucleus. The occurrence of reactions at the very diffuse rim is deduced, in ^{52,53}Cr + ^{14}N reactions, from the very weak dependence of Q^m and θ_{lab} and a constant value of β in Eq. (2). The values of Q_{eff}^m are independent of the N and Z of individual adjacent target nuclei and hence of their nuclear structure. For reactions of ^{14}N + Cr, even Q^m depends only on n [Eq. (2)], irrespective of neutron and proton transfer.

The ratio of the most probable final velocity to the incident velocity v_f^m/v_i is about unity for $n = 1$ and decreases as n increases.

For $n > 4-5$, the linear relation breaks down and the role of other reaction mechanisms becomes more important.

The energy and mass regions studied here play the role of a "bridge" between the reactions of very heavy nuclei, dominated by deep inelastic processes[2,22] and those between lighter heavy ions, which reveal many selective peaks.[23]

ACKNOWLEDGMENT

The authors would like to express their thanks to the cyclotron crew of IPCR. They wish to thank Dr. D. M. Brink, Dr. D. K. Scott, Dr. R. H. Siemssen, Dr. P. J. Siemens, Dr. M. Lefort, Dr. M. Ishihara, and Dr. T. Kohmura for their valuable discussions.

---

*Institute of Physics, University of Tsukuba, Ibaraki, Japan and Department of Physics, Tokyo University of Education, Otsuka, Bunkyo-ku, Tokyo.

†Department of Physics, University of Tokyo, Bunkyo-ku, Tokyo.

[1](a) A. G. Artukh, G. F. Gridnev, V. L. Mekheev, V. V. Volkov and J. Wilczyński, Nucl. Phys. A168, 321 (1971); (b) A211, 299 (1973).

[2]A. G. Artukh, G. F. Grindnev, V. L. Mikheev, V. V. Volkov and J. Wilczyński, Nucl. Phys. A215, 91 (1973).

[3](a) T. Mikumo, I. Kohno, K. Katori, T. Motobayashi, S. Nakajima, M. Yoshie, and H. Kamitsubo, in *Proceedings of the International Conference on Reactions between Complex Nuclei, Nashville, 1974* (North-Holland, Amsterdam, 1974), Vol. 1, p. 64; (b) Proceedings of the INS-IPCR Symposium on Cluster Structure of Nuclei and Transfer Reactions Induced by Heavy Ions, Tokyo [IPCR Cyclotron Progress Report Suppl. 4, 1975, p. 617]; (c) H. Kamitsubo, *ibid.*, p. 623; (d) H. Kamitsubo, M. Yoshie, I. Kohno, S. Nakajima, I. Yamane, and T. Mikumo, Symposium on Heavy-Ion Transfer Reactions [Argonne Physics Division Informal Report No. PHY-1973 B, March 1973 (unpublished), Vol. II, pp. 549, 573].

[4]P. J. A. Buttle and L. J. B. Goldfarb, Nucl. Phys. A176, 299 (1972).

[5]J. P. Schiffer, H. F. Körner, R. H. Siemssen, K. W. Jones and A. Shwarzschild, Phys. Lett. 44B, 47 (1973).

[6]W. von Oertzen, in Symposium on Heavy-Ion Transfer Reactions [Argonne Physics Division Informal Report No. PHY-1973 B, March 1973 (unpublished), Vol. II., p. 675]; *Lecture Notes in Physics* (Springer-Verlag, Berlin, 1973), Vol. 23, p. 267.

[7]D. M. Brink, Phys. Lett. 40B, 37 (1972).

[8]P. J. Siemens, J. P. Bondof, D. H. E. Gross, and F. Dickmann, Phys. Lett. 36B, 24 (1971).

[9]J. Wilczyński, Phys. Lett. 47B, 124 (1973).

[10]Y. Miyazawa, T. Tonuma, and I. Kohno, Jpn. J. Appl. Phys. 9, 532 (1970).

[11]I. Kohno, S. Nakajima, T. Tonuma, and M. Odera, J. Phys. Soc. Jpn. 30, 910 (1970).

[12]I. Kohno, K. Katori, T. Mikumo, T. Motobayashi, S. Nakajima, M. Yoshie, and H. Kamitsubo (unpublished).

[13]M. Yoshie and I. Kohno, Sci. Papers Inst. Phys. Chem. Res. 69, No. 3 (1975); (unpublished).

[14]J. P. Bondorf, F. Dickmann, D. H. E. Gross, and P. J. Siemens, J. Phys. (Paris) 32, C6-145 (1971).

[15]L. G. Moretto, S. K. Kataria, R. C. Jared, R. Schmitt, and S. G. Thompson, Nucl. Phys. A255, 491 (1975).

[16]J. Wilczyński, K. Siwek-Wilczyńska, J. S. Larsen, J. C. Acquadro, and P. R. Christensen, Nucl. Phys. 244, 147 (1975).

[17]W. Henning *et al.*, Heidelberg Spring Meeting Verhandl. DPG (VI) 8, 23 (1973), cited by H. Körner, Symposium on Heavy-Ion Transfer Reactions [Argonne Physics Division Informal Report No. PHY-1973 B, March 1973 (unpublished), Vol. I, p. 9].

[18]V. V. Volkov, F. Gridnev, G. N. Zorin, and L. P. Chelnokov, Nucl. Phys. A126, 1 (1969).

[19]J. P. Bondorf and W. Nörenberg, Phys. Lett. 44B, 487 (1973).

[20]J. Galin, D. Guerreau, M. Lefort, J. Péter, X. Tarrago, and R. Basile, Nucl. Phys. A159, 461 (1970).

[21]D. M. Brink (private communications).

[22]F. Hanappe, M. Lefort, C. Ngo, J. Pêter, and B. Tamin, Phys. Rev. Lett. 32, 738 (1974).

[23]N. Anyas-Weiss, J. Cornell, P. Fisher, P. N. Hudson, A. Mecha-Rocha, D. J. Millener, A. D. Panagiotou, D. K. Scott, D. Strottman, D. K. Brink, B. Buck, P. J. Ellis, and T. England, Phys. Rep. 12C, 201 (1974).

Reprinted from IPCR-Cyclotron Report, 35, 1–8 (1976).

ANGULAR MOMENTUM TRANSFER OF THE QUASI-ELASTIC AND DEEPLY INELASTIC PROCESSES IN THE $^{14}N + ^{93}Nb$ REACTION AT E=120 MeV

M. Ishihara, T. Numao, T. Fukuda, K. Tanaka, T. Inamura

The Institute of Physical and Chemical Research
Wako-shi, Saitama, 351 Japan

Gamma ray multiplicities have been measured for the inelastic and multi-nucleon transfer reactions in $^{14}N + ^{93}Nb$ at bombarding energy E_{lab}=120 MeV to deduce the transferred angular momenta for quasi-elastic and deeply inelastic processes. The results indicate, in agreement with models of frictioning nuclei in collision, that the ℓ waves at the grazing collision is relevant to the former process while the latter is due to relatively low ℓ waves in the vicinity of the fusion critical angular momentum. The γ-ray multiplicities and the optimum Q values obtained for the DI humps are consistent with the prediction for stuck nuclei.

It has been shown[1] that processes called quasi-elastic (QE) and deeply inelastic (DI) collisions generally exist in the reactions induced by heavy ions of N to Kr with energies well above the Coulomb barriers. These processes, characterized by gross humps in the energy spectrum, involve considerable amounts of energy transfer. Hence, several authors have attempted to describe such mechanism in terms of frictioning nuclei.[2,3] In these models of collisions, a role of tangential friction is stressed. Experimentally, this would be best tested by the measurement of angular momentum transfer. In the present work, we therefore measured multiplicities of γ rays emitted by reaction products so that angular momentum I transferred to the fragments may be deduced. The $^{14}N + ^{93}Nb$ reaction at E_{lab}=120 MeV was chosen, in which both QE and DI processes were observed.

A 4.0-mg/cm^2 metallic foil target of ^{93}Nb was irradiated by ^{14}N ions accelerated at the IPCR cyclotron. The light reaction products ranging from He to F were detected and identified by a telescope system composed of two Si detectors of 15 and 2000 μm thicknesses. The thin ΔE detector was used to avoid the low-energy cutoff for the DI humps. The solid angle subtended by the telescope was taken as large as 4.6 msr to obtain a sufficient counting rate in the coincidence measurement. Gamma rays from the fragments were measured by a 7.5 cm x 7.5 cm NaI(Tℓ) detector usually mounted 6.0 cm from the target and at 90^o in the scattering plane. A 4.5-mm Cu absorber was placed in front of the detector to flatten the energy dependence of the total efficiency. The overall efficiency Ω_γ averaged over the observed γ-ray spectrum with a threshold at E_γ=200 keV was calibrated to be 2.2 % for the above detector geometry. The energy and identified particle spectra were recorded event by event in singles as well as in coincidence with γ rays. The spectra of γ energy and particle-γ time correlation were also recorded simultaneously.

The γ-ray multiplicity M_γ was then determined by the relation, $M_\gamma(E_f)=N_{coinc}(E_f)/\Omega_\gamma N_{sing}(E_f)$, where N_{sing} and N_{coinc} represent singles and coincident counting rates, respectively, for the identified light products with energy E_f. An additive correction for the multiple counting of the γ detector was made according to Ref. 4. Contributions from chance coincidences were subtracted using the time spectrum. The rate of neutron events in the NaI detector was determined to be less than 10 % of that of γ events from the measurements of N_{coinc} with and without a thick Pb absorber

inserted in front of the detector. The effect of anisotropic particle-angular correlation was examined for the particle detector angle $\theta_{lab}=40^{o}$ by placing the γ detector at two angles of $\theta_{\gamma}=45^{o}$ and 90^{o} in the scattering plane as well as at the angle normal to the plane. The N_{coinc} value deduced by averaging over these three angles agreed within 5 % with that for $\theta_{\gamma}=90^{o}$ in plane. For this average value of N_{coinc} and after correcting for the other factors above, a systematical error for M_{γ} was estimated to be about 15 %.

The measurement of M_{γ} was made for several laboratory scattering angles between $\theta_{lab}=23^{o}$ and 50^{o}. In Fig. 1 we compare energy and M_{γ} spectra for carbon obtained at $\theta_{lab}=23^{o}$, 30^{o} and 40^{o}. It is seen that the QE hump gradually diminishes while the DI hump becomes dominant towards backward angles. For the lighter particle, these two humps become less distinguishable because of smaller energy separations. In spite of such an apparent difference in the energy spectra, the pattern of the M_{γ} spectrum looks similar to each other, showing a general trend of increase with decreasing E_f until it reaches the maximum of $M_{\gamma}=9\sim11$ at lowest E_f. The size of M_{γ}, however, seems to vary systematically, increasing with θ_{lab}. Since the angle dependence of M_{γ} may partly be due to the incomplete correction for the particle-γ angular correlation, we shall only consider, in the following, the results of $\theta_{lab}=40^{o}$, where the effect of the angular correlation was examined.

To relate the measured value of M_{γ} to the fragment spin I, we assume a simple relation of $I=fM_{\gamma}$ as a first order approximation. For the dissipation of I by γ cascades alone, the value of $f\approx1.7\ \hbar$ may be used.[4] However, additional dissipation $(\Delta I)_p$ by particle evaporations may not be ignored for the excited nuclei in the Nb region, for which an appreciable alpha-particle evaporation rate is expected.[5] Using statistical model formulas[5] on spin change and evaporation rate, a calculation on $(\Delta I)_p$ was performed for the excited nuclei relevant to the carbon product with $E_f\approx V_f$, the Coulomb barrier. It showed that an effective f value of about $2.4\ \hbar$ was needed to account for the total spin dissipation by γ rays and particles. We tentatively use this value of f in the following analyses, though it may be a little too large for the region of QE humps.

In Fig. 2, the results of $M_{\gamma}(E_f)$ obtained for various light reaction products of Z=2 to 8 are plotted together. The M_{γ} value averaged over the isotopes with the weight of N_{sing} is used. Instead of E_f, the abscissa is

chosen to be the angular momentum ℓ_f of relative motion determined as $\ell_f=R_f[2\mu_f(E_f - V_f)]^{1/2}$, where μ_f is the reduced mass. The reaction radius R_f and the Coulomb barrier V_f are taken as $R_f=1.4(A_{1f}^{1/3}+ A_{2f}^{1/3})$ fm and $V_f=Z_{1f}Z_{2f}e^2/1.5(A_{1f}^{1/3}+ A_{2f}^{1/3})$, respectively. The values of μ_f, A_{1f} and A_{2f} are deduced by averaging in the same way as for M_γ. This expression given for ℓ_f corresponds to the condition that the direction of motion of the light product is tangential just after the reaction.

Two solid lines shown for comparison represent the relation, $I=\ell_i-\ell_f$, which is relevant to a classical description of collisions that the fragment spin I and the orbital angular momenta ℓ_i and ℓ_f are all oriented in parallel. The upper line corresponds to the choice of $\ell_i=\ell_{gr}$ and the lower line to that of $\ell_i=\ell_{cr}$. The values of grazing and critical angular momenta ℓ_{gr} and ℓ_{cr} are taken to be 60 and 44 based on an optical model calculation and the observed fusion cross section[6], respectively.

It is noted that most of the experimental points plotted are confined in the region between the two theoretical lines, irrespectively of type of particles except alphas. It should also be noted that the data points tend to shift gradually from the upper to the lower line as ℓ_f becomes smaller and, hence, transfer of energy and/or mass becomes larger. This is typically seen for the carbon data, which lies close to the line of $\ell_i=\ell_{gr}$ for the center of the QE hump and moves towards the line of $\ell_i=\ell_{cr}$ as the excitation goes up for the DI hump. These results well comply with the description[2] of colliding ions that the QE and DI processes are initiated by incident waves between ℓ_{gr} and ℓ_{cr} and that the reaction due to the smaller ℓ_i suffers the more of tangential friction, finally arriving at the DI process. Though the choice of the f value is a little uncertain, the arguments above are hardly altered by a change of f by ± 10 %.

Fig. 3 shows the plot of M_γ measured at the centers of QE and DI humps versus mass A_{1f} of the light reaction product. A dotted line is due to the prediction for the sticking mode[2,3] of motion, which may be formed by full exertion of tangential friction and is proposed to interpret the DI process; $I=\ell_i\mathcal{J}/(\mathcal{J} + \mu_f R_f^2)$, where the moment of inertia $\mathcal{J}$ for the internal freedom of motion is taken as a sum of the rigid moments of inertia $\mathcal{J}_{rig}$ of the heavy and light products. The expressions of $\ell_i=\ell_{cr}$ and $\mathcal{J}_{rig}= \frac{2}{5} M(1.2A^{1/3})^2$ are also assumed. The agreement with experiment is fairly good. The same model predicts that the energy excess $E_f - V_f$ is given

by $\hbar^2(\ell_i-I)^2/2\mu_f R_f^2$. This amounts to 8.5 MeV for carbon, which is again in agreement with the value of 8.0 ± 2.0 MeV observed for the center of the DI hump.

A solid line of V-like shape represents an expression, $I=m\ell_{gr}/M_{li}$, where m is the transferred mass and M_{li} is the projectile mass. This relation is obtained for the model[7] of grazing collisions that the relative velocity v_t of transferred nucleons tends to be the same as that of the projectile (v_i) in the region of transfer if the initial angular momentum of the transferred nucleion about the center of mass of the projectile (or alternatively the target) is ignored. The behaviour of the QE data seems to be reproduced qualitatively by the theoretical line. A recent study[8] on systematics of QE humps showed that the observed optimum Q values effectively correspond to v_t larger than v_i by 20~30 %. The agreement may be improved if this is taken into account.

The authors wish to thank Profs. H. Kamitsubo and M. Lefort for many stimulating discussions.

REFERENCES

1. A.G. Artukh, G.F. Gridnev, V.L. Mikheev, V.V. Volkov and J. Wilczynski, Nucl. Phys. A215, 91(1973); F. Hanappe, M. Lefort, C. Ngo, J. Peter and B. Tamain, Phys. Rev. Lett. 32, 738(1974); L.G. Moretto, S.K. Kataria, R.C. Jared, R. Schmitt and S.G. Thompson, Nucl. Phys. A255, 491(1975).
2. J. Wilczynski, Phys. Lett. 47B, 484(1973).
3. J.P. Bondorf, M.I. Sobel and D. Sperber, Phys. Rep. 15C, 83(1974); J.P. Bondorf, J.R. Huizenga, M.I. Sobel and D. Sperber, Phys. Rev. 11c, 1265(1975).
4. G.B. Hagemann, R. Broda, B. Herskind, M. Ishihara, S. Ogaza and H. Ryde, Nucl. Phys. A245, 166(1975).
5. D.C. Williams and T.D. Thomas, Nucl. Phys. A92, 1(1967).
6. T. Fukuda and M. Ishihara, private communication.
7. D.M. Brink, Phys. Lett. 40B, 37(1972).
8. H. Kamitsubo, in Proceedings of Symposium on Macro Features of Heavy-Ion Collisions, Argonne, Illinois, 1976.

FIGURE CAPTIONS

Fig. 1 Energy(a) and M_γ(b) spectra of carbon obtained at $\theta_{lab}=23^o$, 30^o and 40^o. The abscissa is the center of mass energy of the carbon product. Error bars are due to statistics. The lines drawn are for a guide to eyes.

Fig. 2 Plot of M_γ vs ℓ_f of the light product. The two solid lines represent the relation, $I=\ell_i-\ell_f$, for $\ell_i=\ell_{gr}$(upper) and for $\ell_i=\ell_{cr}$(lower).

Fig. 3 Plot of M_γ for the centers of DI and QE humps vs the light product mass A_{lf}. The dotted line is due to the model[2,3] of sticking motion and to be compared with the DI results. The solid line is due to the model[7] of grazing collision and for the QE results.

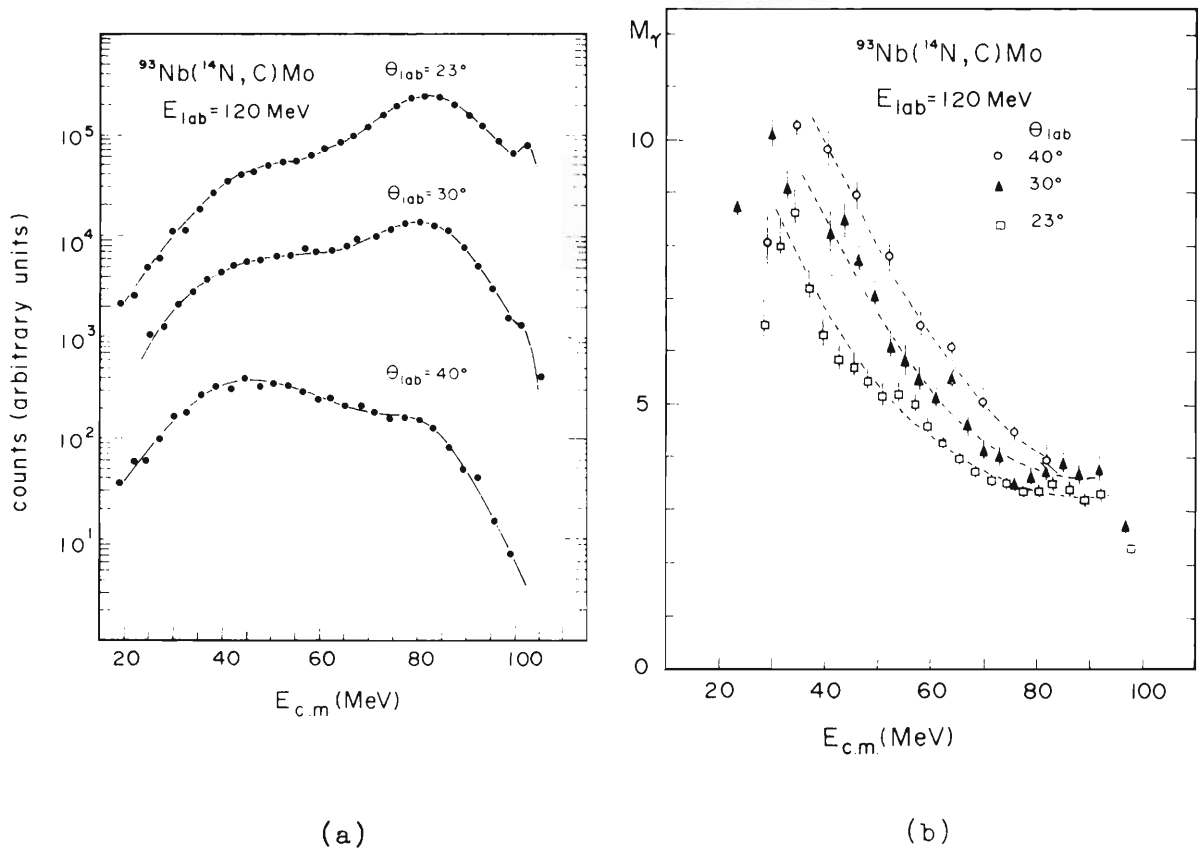

(a) (b)

Fig. 1

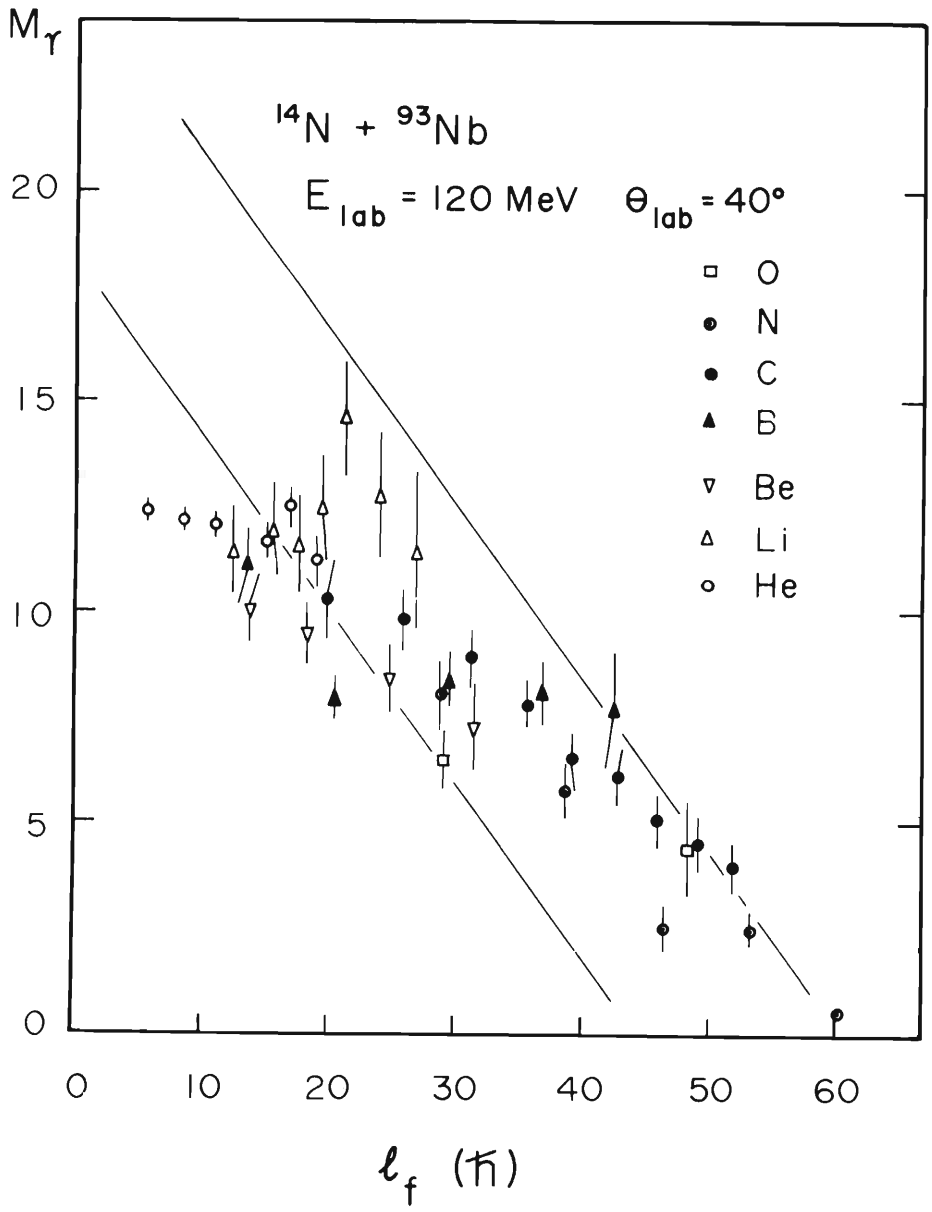
M_γ
$^{14}N + ^{93}Nb$
E_{lab} = 120 MeV θ_{lab} = 40°
O
N
C
B
Be
Li
He
20
15
10
5
0
0
10
20
30
40
50
60
ℓ_f ($\hbar$)

Fig. 2

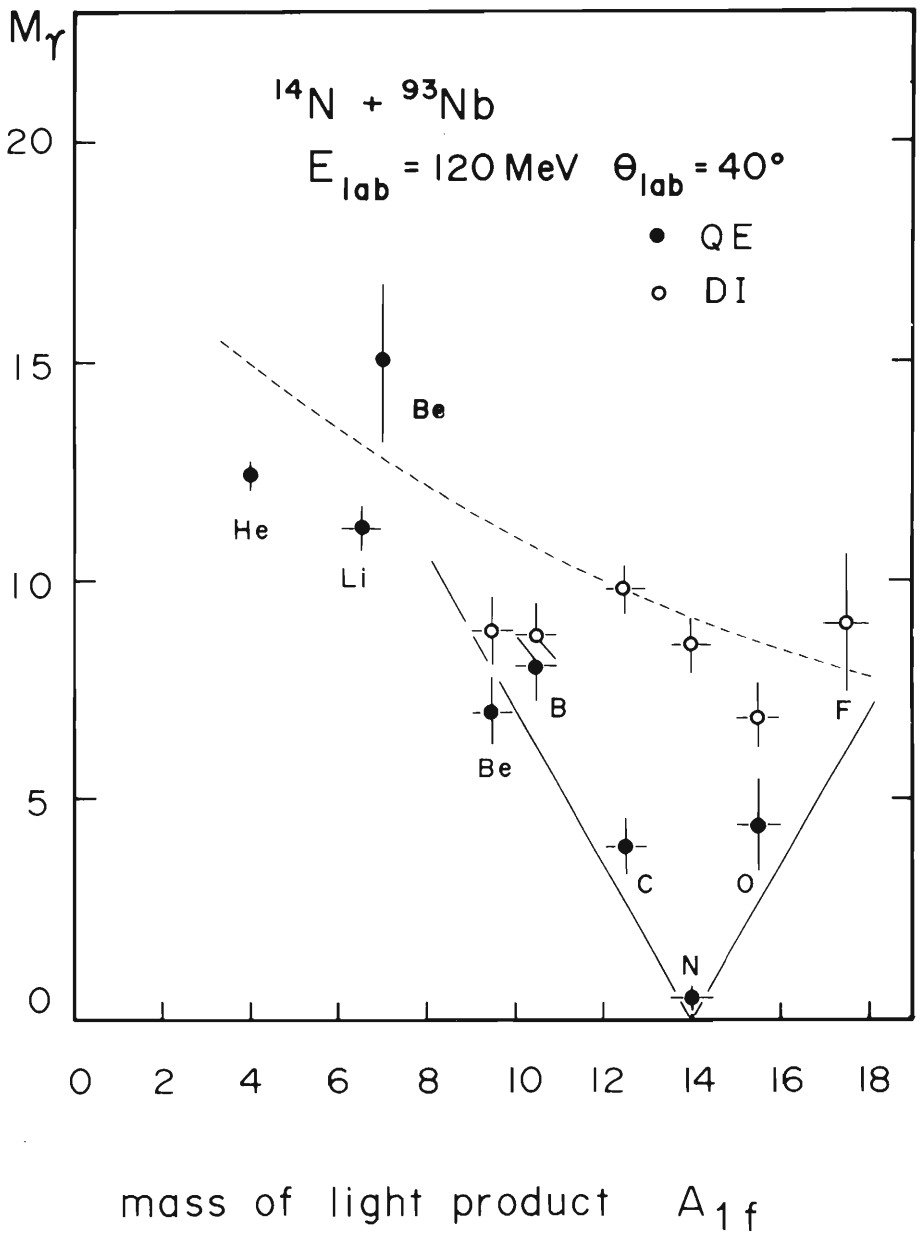
M_γ
$^{14}N + ^{93}Nb$
E_{lab} = 120 MeV θ_{lab} = 40°
● QE
○ DI
He
Li
Be
Be
B
C
N
O
F
0
5
10
15
20
0 2 4 6 8 10 12 14 16 18
mass of light product A_{1f}

Fig. 3

Reprinted from Phys. Lett., 68B, 51–54 (1977).

GAMMA-RAYS FROM AN INCOMPLETE FUSION REACTION INDUCED BY 95 MeV ^{14}N

T. INAMURA, M. ISHIHARA, T. FUKUDA[1] and T. SHIMODA[2]

Cyclotron Laboratory, The Institute of Physical and Chemical Research, Wako-shi, Saitama 351, Japan

and

H. HIRUTA

Department of Physics, Tokyo Gakugei University, Koganei-shi, Tokyo 184, Japan

Received 18 March 1977

Gamma-rays from the ^{159}Tb(^{14}N, αxn)$^{169-x}$Yb reaction, in which non-evaporation α-particles are emitted, have been identified. Yields of E2 cascade transitions suggest that the angular momentum distribution of the entrance channel leading to this reaction is localized just above the critical angular momentum for complete fusion.

It was first pointed out by Quinton et al. [1] that in the bombardment of Ni, Au and Bi with ^{12}C, ^{14}N and ^{16}O, high-energy α-particles were emitted predominantly in the forward direction. Recently, Galin et al. [2] have reported a similar phenomenon for the ^{103}Rh + ^{14}N reaction. Their results indicate that the process, in which high-energy α-particles are emitted in the forward direction only, exists generally in ^{12}C, ^{14}N and ^{16}O-induced reactions, and competes with the evaporation following compound-nucleus formation. Observation of γ-rays, following such forward-peaked high-energy α-particle emission, would be interesting because the starting population for γ-emission might be different from that in the compound nucleus.

Here, following Britt and Quinton [1], we shall refer to the forward-peaked high-energy α-particles as "direct" α-particles.

^{159}Tb was bombarded with 95 MeV ^{14}N beams from the IPCR cyclotron, this combination being chosen because the likely reaction products are well-known rotational nuclei. The ^{159}Tb target was a self-supporting metallic foil 2.1 mg/cm^2 thick. The "direct" α-particles were detected with a Si surface-barrier annular detector at 0° to the beam, the solid angle subtended being 0.73 sr (θ = 16.7°–32.6°). In order to make the contribution from the evaporation process negligible, α-particles with energies below 33 MeV were cut off by placing a 400 μm thick annular aluminum foil in front of the Si detector. Gamma-rays were observed in coincidence with the α-particles thus detected, the γ-detector being a 60 cm^3 Ge(Li) counter placed at 90° to the beam and at a distance of 4 cm from the target.

Protons and α-particles were separated by operating the Si detector with a depletion depth which was thin to protons. The yields of d, t and ^{3}He were shown to be negligible by using a $\Delta E - E$ counter telescope. The energy spectrum of α-particles, observed at 25° to the beam, was found to peak at about 25 MeV, the highest energy being at about 60 MeV.

For comparison, we also observed γ-rays in coincidence with "compound" α-particles emitted in the backward direction. The same annular detector was placed at 180° to the beam, the detection angle being 147.4°–163.3°, but the 400 μm foil was replaced by one of 100 μm.

Fig. 1 shows γ-ray spectra observed in coincidence with (a) "direct" α-particles and (b) "compound" α-particles, together with a singles spectrum (c) for comparison. Accidental coincidences have been subtracted. Energies of the γ-rays identified agree with those reported already [3–5] within 0.5 keV.

As is seen in fig. 1a, the strongest γ-rays coincident with "direct" α-particles are from the ^{159}Tb(^{14}N, α3n)^{166}Yb reaction. This suggests that the "direct" α-particle is emitted first and in most cases

[1] Present address: Department of Physics, Osaka University, Osaka, Japan.

[2] On leave from Department of Physics, Kyoto University, Kyoto, Japan.

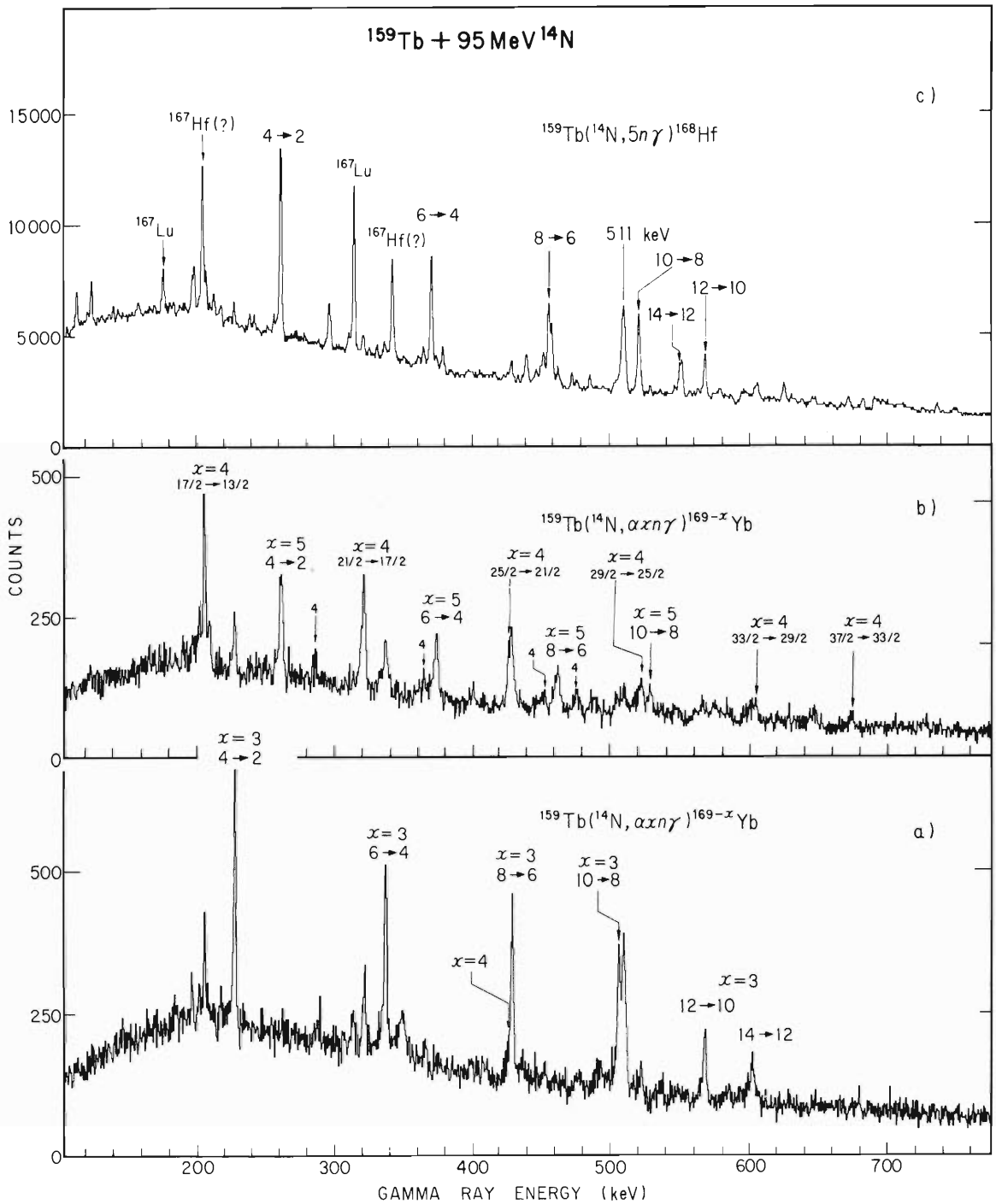

Fig. 1. Gamma-ray spectra observed in coincidence with (a) "direct" α-particles emitted in the forward direction ($E_\alpha \gtrsim 33$ MeV) and (b) "compound" α-particles emitted in the backward direction ($E_\alpha \gtrsim 15$ MeV) in the bombardment of ^{159}Tb with 95 MeV ^{14}N. A singles spectrum (c) is also shown for comparison. The indication $x = 4$ relates to γ-rays from the other bands of ^{165}Yb.

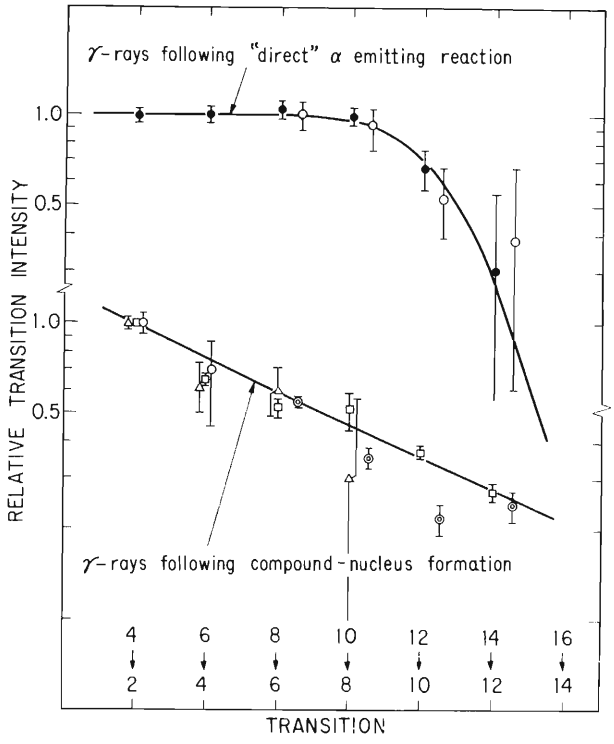

Fig. 2. Gamma-transition intensities relative to the $4^+ \rightarrow 2^+$ ($17/2^+ \rightarrow 13/2^+$ for ^{165}Yb) transition in de-excitation of the ^{159}Tb + 95 MeV ^{14}N reaction products. The upper drawing shows the data obtained in coincidence with "direct" α-particles: • for ^{166}Yb and ○ for ^{165}Yb; the solid line was obtained for ^{166}Yb (see text). The lower drawing shows the data on the residues of compound-nucleus formation: □ for ^{168}Hf, ○ for ^{166}Yb, ◎ for ^{165}Yb, and △ for ^{164}Yb; for ^{165}Yb the normalization was made at 0.54 on account of the spin concerned, and a line is drawn just to guide the eye.

is followed by three neutrons. This reaction can be regarded as incomplete fusion. It is interesting to note that γ-rays from the ^{159}Tb(^{14}N, α5n)^{164}Yb reaction are hardly seen in fig. 1a.

Fig. 2 shows intensities of E2 cascade transitions relative to the $4^+ \rightarrow 2^+$ transition of the residual nuclei, ^{164}Yb, ^{166}Yb and ^{168}Hf; for ^{165}Yb, the intensities are given relative to the $17/2^+ \rightarrow 13/2^+$ transition which is associated with the $i_{13/2}$ decoupled band [4]. For ^{166}Yb produced by the incomplete fusion reaction (fig. 1a), intensities of the cascade transitions have been found equal up to the $10^+ \rightarrow 8^+$ member, and then the yield decreases considerably. This indicates that the starting population for γ-emission was localized somewhat larger than $J = 10$ and only the ground-state band members were fed. This tendency also seems to hold for ^{165}Yb. For the residual nuclei associated with compound-nucleus formation (fig. 1b, c), however, the yields of successively higher cascades showed a near exponential fall, conforming to the general trend reported so far on γ-deexcitation of compound-nuclear reaction products in this mass region.

It seems possible to reproduce the γ-transition yields recorded in coincidence with the "direct" α-particles by assuming a Gaussian shape for the spin distribution of the starting population for γ-emission. The upper solid line in fig. 2 shows a fit to the data on ^{166}Yb corresponding to Gaussian distribution with a half-width of $2\hbar$ and a mean of $13\hbar$. Here, we have tentatively assumed four statistical dipole transitions prior the entry point into the ground state band.

The change in angular momenta during the particle emission can be approximately estimated as follows: the angular momentum removed by the "direct" α-particle emission is on average $21\hbar$, this being a semi-classical value determined from the average kinetic energy (40 MeV in lab) of the recorded α-particles; and according to the prescription given by Alexander and Simonoff [6], three neutron evaporation will remove $6\hbar$. Thus we have a mean value $\langle I \rangle = 40\hbar$ for the angular momentum distribution of the entrance channel of this reaction. This seems quite a reasonable result because the ^{14}N projectile probably just grazes the ^{159}Tb nucleus in order to transfer as many as ten nucleons and the impact parameter should be rather close to the value corresponding to the critical angular momentum I_{cr} for compound-nucleus formation, which is estimated to be $37\hbar$ on the basis of cross-section measurements [7].

In conclusion, we have indicated that for the ^{159}Tb + 95 MeV ^{14}N reaction, unlike compound-nucleus formation, the "direct" α-particle emitting reaction involves incoming partial waves with angular momenta restricted to values just above I_{cr}. Because of this, high-spin states in the residual nuclei can be populated selectively. This is probably true for other heavy ions, such as ^{12}C, ^{16}O and ^{20}Ne. Therefore, measurements of γ-rays coincident with "direct" α-particles appear to be a promising technique to study properties of the yrast region, for example band intersection in deformed nuclei. A detailed study of the angular momentum

distribution of "direct" α-particles would provide important additional information.

We would like to thank Prof. H. Kamitsubo and Dr. T. Nomura for valuable discussion in connection with this study. Comments on the presentation of the manuscript by Dr. J.C. Lisle are gratefully acknowledged.

References

[1] W.J. Kox, A.R. Quinton and C.E. Anderson, Phys. Rev. 120 (1960) 2120;
H.C. Britt and A.R. Quinton, Phys. Rev. 124 (1961) 877.
[2] J. Galin et al., Phys. Rev. C9 (1974) 1126.
[3] O. Saethre et al., Nucl. Phys. A207 (1971) 486.
[4] L.L. Riedinger et al., Phys. Rev. Lett. 33 (1974) 1346.
[5] Nucl. Data Sheets 17, no. 1 (1976).
[6] J.M. Alexander and G.N. Simonoff, Phys. Rev. 133 (1964) 93.
[7] T. Fukuda et al., Contributions INS International Symposium on Collectivity of medium and heavy nuclei, and the Colloque Franco-Japonais, Tokyo (1976) p. 31.

Reprinted from Phys. Rev. Lett., 39, 323–325 (1977).

Spin Polarization of ^{12}B in the Heavy-Ion Reaction $^{100}Mo(^{14}N, ^{12}B)^{102}Ru$

K. Sugimoto, N. Takahashi, A. Mizobuchi, Y. Nojiri, and T. Minamisono
Laboratory of Nuclear Studies, Faculty of Science, Osaka University, Toyonaka, Osaka, 560 Japan

and

M. Ishihara, K. Tanaka, and H. Kamitsubo
Institute of Physical and Chemical Research, Wako-shi, Saitama, 351 Japan

(Received 16 June 1977)

Polarization of product ^{12}B in the reaction $^{100}Mo(^{14}N, ^{12}B)^{102}Ru$ at 90 MeV was measured as a function of product kinetic energy at the reaction angle of 20°. The polarization was found antiparallel to the vector $\vec{k}_f \times \vec{k}_i$ for higher-energy ^{12}B, while parallel for those with lower energy. The zero crossing occurred at around maximum in the energy spectrum.

Spin polarization of products in a transfer reaction induced by heavy ions, specifically the polarization of ^{12}B in the reaction $^{100}Mo(^{14}N, ^{12}B)^{102}Ru$, was measured for the first time. The use of the β-decay asymmetry enabled us to measure the polarization of product $^{12}B_{g.s.}$ ($J^\pi = 1^+$; $E_{\beta max} = 13.37$ MeV; $t_{1/2} = 20.3$ ms). Investigations of such polarization phenomena are useful to elucidate the heavy-ion reaction mechanism. Main interests in the present experiment are (1) whether lighter products show a sizable polarization, (2) how the polarization depends on the reaction Q value, and (3) what kind of model can explain the result.

A pulsed beam of 95-MeV ^{14}N (unpolarized) from the cyclotron at the Institute of Physical and Chemical Research was used to irradiate a ^{100}Mo-(enrichment 95.5%) foil target of 4.8 mg/cm^2 in thickness. The irradiation was cyclic with an on-beam period of 10 ms followed by an off-beam period of 30 ms. The effective incident energy was 90 MeV, since the beam energy loss in the target (tilted) was about 10 MeV. The experimental setup is schematically shown in Fig. 1. Lighter products, emerging from the target chamber in the reaction angle of 20°, impinged into an evacuated stopper chamber through a collimator with an angular spread of ± 3.7°. An aluminum foil with various thickness was inserted between these chambers and used as a degrader of the kinetic energy. Products ^{12}B in a specified range of initial kinetic energy were implanted into a thin platinum stopper, by properly choosing thicknesses of the degrader and the stopper.

β rays from the stopper were detected during the off-beam period by a pair of counter telescopes consisting of two ΔE and one E plastic counters. These telescopes were located above and below the stopper in the direction of expected polarization, i.e., perpendicular to the reaction plane. β rays with energies higher than 3 MeV were detected and the time spectrum was consistent with ^{12}B lifetime. Possible background β emitters with similar lifetime were ^{13}B and ^{12}N, but their yields were known to be insignificant.[1]

The polarization of ^{12}B can be determined from the asymmetry in the β decay. The angular distribution $W(\theta)$ of β rays with respect to the polarization $\vec{P}$ is given as

$$W(\theta) \cong 1 - P\cos\theta,$$

for $^{12}B_{g.s.} \rightarrow {}^{12}C_{g.s.}$ transition. In order to determine the asymmetry free from spurious effects, the direction of ^{12}B spin was controlled by adopting the adiabatic-fast-passage method in NMR during the off-beam period.[2,3] A static magnetic field $\vec{B}_0 = 1.42$ kG was applied normal to the reac-

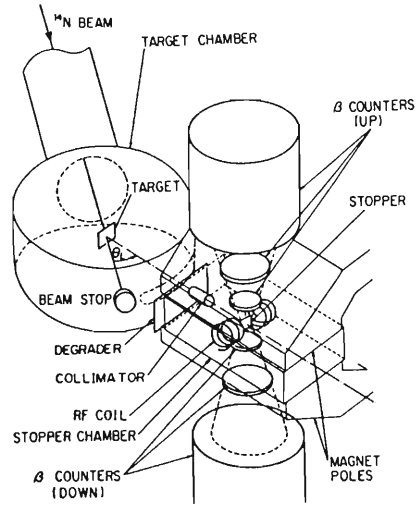

FIG. 1. Schematic drawing of the experimental setup.

tion plane around the stopper, and the NMR was induced by an rf field crossed to $\vec{B}_0$. After every other on-beam period, the rf swept once across the resonance in 5 ms; thus the direction of ^{12}B spin was reversed. At the end of the counting period of 20 ms, the spin was again reversed by applying the rf. In the next period, the rf was applied at off-resonance and the spin direction was unaltered. From the up-down ratio of β-ray counting rates N_{up}/N_{down} at on- and off-resonance periods, the polarization was obtained as $P = (\sqrt{R}-1)/(\sqrt{R}+1)$, where $R = (N_{up}/N_{down})_{off}/(N_{up}/N_{down})_{on}$.

The polarization was essentially preserved during and after the implantation process in the stopper, since the decoupling field $\vec{B}_0$ was present[4] and the spin-lattice relaxation time was known to be much longer than the ^{12}B lifetime in platinum at room temperature.[3,5] It was important to prepare against possible depolarization effects due to hyperfine interactions in ions during flight *in vacuo*. No appreciable depolarization was expected for ^{12}B leaving the target because of predominance in the fully stripped state. After passing through the energy degrader, slower ions captured electrons and depolarization became appreciable for few-electron configurations. In order to eliminate such ambiguous contributions from lower-energy ^{12}B ions, a pair of R measurements were performed by using a thin and a thick platinum stopper. The thin stopper was 5 μm in thickness and stopped ^{12}B ions up to 11 MeV. From the pair of R values, the polarization P was deduced for ^{12}B entering the stopper with energies higher than 11 MeV.

In order to see the adequacy of the present range-energy method, the ^{12}B energy spectrum was measured by detecting β rays. A single broad peak is observed ranging from 40 to 80 MeV as shown in Fig. 2(a). The spectral shape is in good agreement with that obtained by using the silicon-detector telescope.[1]

The polarization obtained is shown in Fig. 2(b) as a function of ^{12}B kinetic energy. The polarization is defined as positive, when it is parallel to $\vec{k}_f \times \vec{k}_i$, where $\vec{k}_f$ and $\vec{k}_i$ are the outgoing and incoming wave vectors, respectively. The measured polarization includes contributions of ^{12}B produced in excited states, through γ de-excitation. The yield of ^{12}B through particle decay of other reaction products, e.g., $^{13}B - n + {}^{12}B$, $^{13}C - p + {}^{12}B$, was estimated to be negligible, based on the recent observation of particle-particle correlation.[6]

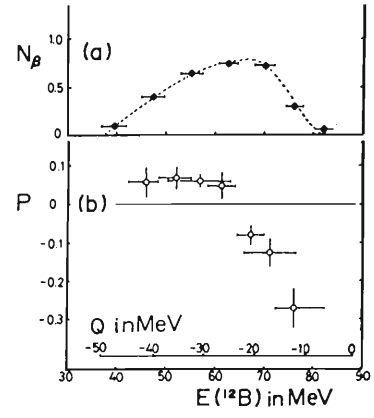

FIG. 2. Energy spectrum (a) in arbitrary scale and polarization (b) of ^{12}B in the reaction $^{100}Mo(^{14}N, {}^{12}B)^{102}Ru$ induced by 90 MeV ^{14}N at 20°, as functions of ^{12}B kinetic energy E and Q value. Horizontal bars indicate energy range pertinent to the measurement. Errors in (b) include those from (1) counting statistics, (2) background subtraction, and (3) correction for depolarization in free ions.

A sizable polarization up to $|P| \simeq 0.3$ is found in the present experiment. For the most energetic part of the spectrum, P is negative and largest. As the energy of ^{12}B decreases, P tends to zero and becomes positive for the lower half of the spectrum. The zero crossing takes place at $Q \sim -23$ MeV, which corresponds roughly to the maximum of the energy spectrum.

According to a macroscopic model introduced by Wilczynski,[7] the polarization of products is expected to be parallel to the incoming orbital angular momentum, and to be parallel to $\vec{k}_f \times \vec{k}_i$ for lighter products along approximately grazing trajectories with small energy dissipation. The experimental result is difficult to explain with this model; the higher-energy part of the spectrum shows the polarization antiparallel to $\vec{k}_f \times \vec{k}_i$.

It is interesting to consider the polarization in terms of a naive microscopic model, following the scheme introduced by Brink.[8] When the (^{14}N, ^{12}B) reaction is assumed to proceed through a simple two-proton transfer, the Q value can be related to the component $\lambda_1\hbar$, normal to the reaction plane, of the angular momentum carried by the transferred pair in the projectile: $Q \simeq \lambda_1\hbar v/R_1 - \frac{1}{2}mv^2 + \Delta V_C$, where v is the speed of the incoming projectile at the instant of collision, R_1 is the radius of the projectile, m is the mass of the transferred pair, and ΔV_C is the difference in the Coulomb barrier between the incoming and outgoing channels. Since the lighter product re-

mains in a hole state of the transferred pair, the sign of polarization should be opposite to that of λ_1. Vanishing polarization is predicted at the Q value, $-(\frac{1}{2}mv^2 - \Delta V_C) \equiv Q_0$, with $\lambda_1 = 0$. As Q increases passing through Q_0, λ_1 changes sign from negative to positive, i.e., positive polarization is expected for $Q < Q_0$, and negative polarization for $Q > Q_0$. The prediction agrees qualitatively with the result of the present experiment. It is interesting to note that the optimum Q value in the energy spectrum roughly coincides with the Q value for $P = 0$. This indicates that the maximum in the cross section occurs for $\lambda_1 = 0$ in accordance with the argument[9] on the optimum Q value.

[1]T. Mikumo, I. Kohno, K. Katori, T. Motobayashi, S. Nakajima, M. Yoshie, and H. Kamitsubo, Phys. Rev. C 14, 1458 (1976); M. Yoshie and I. Kohno, Sci. Pap. Inst. Phys. Chem. Res. (Jpn.) 69, 63 (1975).

[2]K. Sugimoto, K. Nakai, K. Matsuda, and T. Minamisono, J. Phys. Soc. Jpn. 25, 1258 (1968).

[3]T. Minamisono, Y. Nogiri, A. Mizobuchi, and K. Sugimoto, J. Phys. Soc. Jpn., Suppl. 34, 156 (1973).

[4]K. Sugimoto, I. Tanihata, S. Kogo, and M. Tanaka, Hyperfine Interact. 2, 401 (1976).

[5]K. Terakura, N. Yokoyama, S. Kohzuki, and K. Asayama, J. Phys. Soc. Jpn. 36, 130 (1974).

[6]M. Ishihara, H. Kamitsubo, T. Shimoda, T. Fukuda, T. Motobayashi, T. Ohi, and I. Kohno, in *Proceedings of the European Conference on Nuclear Physics with Heavy Ions, Caen, France, 6–10 September 1976*, edited by B. Fernandez *et al.* (Service de Documentation du CEN, Saclay, France, 1976), Vol. 1, p. 157.

[7]J. Wilczynski, Phys. Lett. 47B, 484 (1973).

[8]D. M. Brink, Phys. Lett. 40B, 37 (1972).

[9]P. J. Siemens, J. P. Bondorf, D. H. E. Gross, and F. Dickmann, Phys. Lett. 36B, 24 (1971).

Reprinted from Phys. Rev. Lett., 40, 694–697 (1978).

Statistical Analysis of Preequilibrium α-Particle Spectra and Possible Local Heating

T. Nomura, H. Utsunomiya, T. Motobayashi, T. Inamura, and M. Yanokura
Cyclotron Laboratory, The Institute of Physical and Chemical Research, Wako-shi, Saitama 351, Japan
(Received 29 November 1977)

It is shown that energy spectra of preequilibrium α-particle emission in $^{209}Bi + ^{14}N$ reactions are reproduced well by the statistical formula of Ericson when nuclear temperature is treated as a parameter depending on the emission angle. The resultant temperature shows monotonical decrease with increasing angles, indicating the cooling-down process of the associated composite system.

In reactions induced by heavy ions such as ^{12}C, ^{14}N, and ^{16}O at bombarding energies well above the Coulomb barrier, α particles are known to be emitted with large probability. The α-particle emission occurs predominantly in the forward direction with strong enhancement of the high-energy part when compared to an evaporation spectrum observed in compound reactions.[1,2] As a possible origin of such α-particle emission, Britt and Quinton[1] suggested the breakup of an incident projectile in an interaction with the surface of a target nucleus. A recent work of Inamura *et al.*[3] indicated that this reaction originates from initial channel spins localized just above the critical angular momentum for complete fusion. In other words, the relevant entrance angular momenta lie between those of the grazing collision and those of close collisions leading to rapid formation of a compound nucleus. This is a feature similar to deeply inelastic reactions, in which relaxation phenomena become important because of long interaction times.[4] This suggests the possibility of attributing the above α-particle emission to evaporation from a locally excited nuclear system recently proposed for preequilibrium phenomena by Weiner and Weström.[5]

In this Letter, the same phenomenon is shown to be significant even at low incident energies in the $^{209}Bi + ^{14}N$ reaction. We further present simple statistical analysis for the energy spectra following the idea of Ref. 5 and discuss possible energy relaxation process of a composite system in heavy-ion reactions.

A self-supporting ^{209}Bi target of about 1 mg/cm^2 thickness was bombarded with 85- and 95-MeV ^{14}N ions from the cyclotron at the Institute

of Physical and Chemical Research. The following measurements were carried out. (i) Charged particles with $Z \lesssim 8$ detected with conventional counter telescopes were measured between 20° and 170°. (ii) Angular distributions of fission fragments were taken between 10° and 170° by detecting high-energy particles stopped within a thin (30 μm Si) ΔE counter. (iii) Cross sections for the production of heavy residual nuclei following fusion or fusionlike reactions such as (^{14}N, xn) and (^{14}N, αxn) were measured by detecting α decays of their ground states in-beam in the same way as described in Nomura *et al.*[6] More details will be described elsewhere.

The measured cross sections are summarized in Table I. The following points should be noted. (i) Fission is the almost exclusive mode of the deexcitation of the compound nucleus, neutron evaporation being unimportant. Since α-particle evaporation is far less probable than neutron in this mass region, we expect no significant contribution from the compound reaction to the observed α particles. (ii) The cross section for the emitted α particles is roughly equal to the sum of cross sections for heavy residual nuclei produced by (^{14}N, αxn) and (^{14}N, $2\alpha xn$) reactions, indicating that a possible composite system formed in this projectile-target combination fuses after emitting α particles and decays by neutron emission without fissioning.

The measured angular and energy distributions of α particles were transformed into those in the c.m. system under the assumption of a binary reaction, i.e., $^{209}\mathrm{Bi} + {}^{14}\mathrm{N} \rightarrow \alpha + {}^{219}\mathrm{Ra}$, which seems reasonable from the above-mentioned facts. The present angular distributions are similar to those reported by Britt and Quinton[1] in similar reactions at higher bombarding energies. The yield decreases rapidly with increasing angles up to around 70°, and still continues to decrease slowly at more backward angles; in particular, there is no such rise near 180° as expected from the compound reaction. A main difference between the present results and those reported in Ref. 1 is that we observed a small bump or shoulder near grazing angles at both incident energies, i.e., at around 100° (85 MeV) and 80° (95 MeV), where heavier ejectiles like B and C isotopes had clear peaks in their angular distributions. This suggests that the above bumps are due to direct α particle and/or ^{8}Be emission corresponding to ^{10}B and/or ^{6}Li transfer reactions. More details will be described elsewhere.

TABLE I. Summary of experimental cross sections.

	Cross section (mb)	
	85 MeV	95 MeV
α particles	42 ± 6	(63) [a]
Other charged particles with $3 \leq Z \leq 8$	80 ± 10	Not measured
Fission	890 ± 65	1350 ± 100
(^{14}N, xn)	5 ± 1	3 ± 1
(^{14}N, αxn)	31 ± 3	49 ± 8
(^{14}N, $2\alpha xn$)	3 ± 1	3 ± 1

[a]The given value has a large error due to lack of statistics at forward angles.

The energy spectra at backward angles are peaked around 19–19.5 MeV and have nearly exponential tails toward high energies. They are similar to a spectrum expected from the evaporation process in the compound reaction. The forward spectra are very broad and apparently quite different from the evaporation spectrum. However, there still exist high-energy tails which also fall almost exponentially but very slowly, indicating high "nuclear temperature" of the associated system. It should be noted that the nuclear temperature is not necessarily independent of observed angles in the case of the preequilibrium emission.[5] We shall therefore analyze the experimental spectra $N(E_\alpha)$ by the following simple statistical formula of Ericson[7]:

$$N(E_\alpha) \propto E_\alpha \sigma_c(E_\alpha) \exp(-E_\alpha/T). \quad (1)$$

Here, E_α is the kinetic energy of an α particle, σ_c the inverse cross section, and T the nuclear temperature of the residual nucleus which is related to the usual level density parameter a and the averaged excitation energy U_{av} of the residual nucleus with $T^2 \simeq U_{\mathrm{av}}/a$. When the initial kinetic energy is fully converted to the excitation energy of the relevant system, U_{av} roughly amounts to 30 and 40 MeV in cases of 85 and 95 MeV incident energies, respectively. This is assumed throughout the present analysis.

Equation (1) assumes the spin-independent constant temperature. This may be justified because we are treating high excitation energies and relatively low angular momenta [the maximum spin estimated from the sharp cutoff approximation is 39$\hbar$ (85 MeV) and 52$\hbar$ (95 MeV)]. In fact, the spin-dependent temperature T_j defined by Williams and Thomas[8] as $T_j \simeq T[1 - E_{\mathrm{rot}}(j)/U_{\mathrm{av}}]^{1/2}$ is close to T provided the rotational energy $E_{\mathrm{rot}}(j)$ is calculated by the rigid-body mo-

ment of inertia.

As for $\sigma_c(E_\alpha)$, we used reaction cross sections calculated by Igo,[9] who showed the results as a function of E_α/B_α, where B_α is the barrier height of the optical potential used. A spherical nucleus is assumed in Ref. 9, in which $B_\alpha \simeq 21.5$ MeV. Equation (1) turned out to reproduce well the spectral shape at backward angles when T is taken to be a "compound-nucleus value" described later, but the calculated peak position is by 2–3 MeV higher than the experimental one. A similar discrepancy has been pointed out by Knox, Quniton, and Anderson[10] and was attributed to the nuclear distortion resulting in a smaller Coulomb barrier in average. In order to take this effect into account in the calculation of σ_c, we treat B_α as a parameter and assume, for simplicity, the same dependence of σ_c on E_α/B_α as in the case of a spherical nucleus. It turned out that all the observed spectra could be fitted excellently by Eq. (1) when we assume $B_\alpha = 19.5$ MeV and treat T as another fitting parameter. To show this, we plotted the quantity $N(E_\alpha)/E_\alpha\sigma_c(E_\alpha)$ vs E_α on a semi-log scale, where $N(E_\alpha)$ were taken from experimental spectra. If Eq. (1) can reproduce the experiment, the resultant plot must be a straight line. This is indeed the case at all angles as seen in Fig. 1. The slope of a straight line at each angle gives the best value of nuclear temperature. The values of T thus obtained are shown in Fig. 2. The temperature decreases monotonically with increasing angles and almost reaches a compound-nucleus value expected from an energetically equilibrated system, which is calculated from $T^2 \simeq U_{av}/a$ and $a = A/9$ MeV^{-1} with $A = 219$. This value of a is rather arbitrarily chosen here but is believed to be close to the empirical value in this mass region.[11]

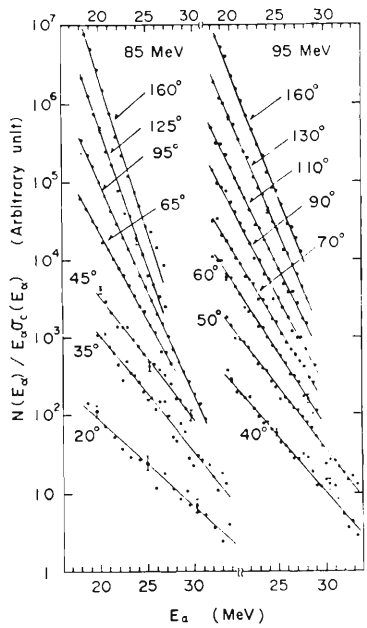

FIG. 1. Plot of $N(E_\alpha)/E_\alpha\sigma_c(E_\alpha)$ vs E_α, where $N(E_\alpha)$ are taken from experimental spectra in ^{209}Bi + ^{14}N reactions. The meaning of the relevant quantities is given in the text. The observed lab angles are indicated.

Weiner and Weström[5] have recently attempted to describe preequilibrium phenomena in terms of diffusion of heat in nuclear matter, starting from a "hot spot" created by a reaction at the nuclear surface. They have shown that evaporated particles from such a locally excited system are expected to show enhancement of high-energy parts in spectra and a large asymmetry in angular distributions. The present result seems to be consistent with this interpretation. Following the above idea, let us consider a possible local heating in the present case. Suppose a projectile captured by a shallow potential between projectile and target. It seems reasonable to assume that such a composite system is quickly heated at the contact point (hot spot) due to large radical frictional forces, but the relative angular momenta are transformed mainly to the rotation of the heavier nucleus (^{209}Bi in our case) due to its large moment of inertia. α particles are supposed to be emitted from this hot spot sitting on the surface of the rotating nucleus, but not from the other cold part of the system. This is consistent with the small effective Coulomb barrier deduced from the energy spectra. The emission occurs in the direction of the tangential velocity at the surface in average. Then, the emission angle can be related to the reaction time in the similar manner as suggested in deeply inelastic phenomena (the concept of negative deflection angle, for instance).[12] It seems therefore that

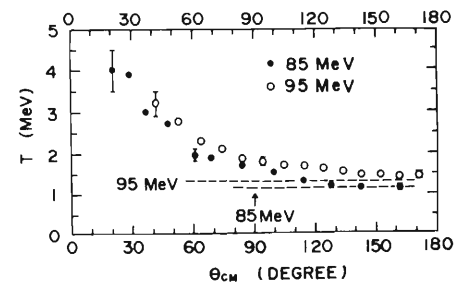

FIG. 2. Nuclear temperature T of the hot spot plotted vs the emission angles. The compound-nucleus values (see text) are given by dashed lines.

the nuclear temperature deduced from the present analysis can be interpreted to have physical significance, i.e., to show the degree of energy relaxation of a composite system versus the reaction time. The lowering of temperature is considered to be a consequence of nucleon-nucleon multiple scatterings.[5] The nuclear relaxation time estimated in Ref. 5 becomes about 5×10^{-21} sec in the present case when the temperature-averaged heat conductivity and specific heat are used. This is roughly equal to half a period of the rotational motion mentioned above, provided that the maximum angular momentum is transferred and a rigid-body moment of inertia is assumed, indicating the importance of the energy relaxation during rotation.

The above interpretation should be considered as a preliminary one. An essential point deduced from our analysis is that energy spectra of pre-equilibrium α particles are determined by penetrabilities and the level density of the residual nucleus. In other words, α particles are mainly emitted from an energetically relaxed composite system except the possible emission occurring at the grazing angle. A similar feature is known in deeply inelastic reactions.[13]

[1]H. C. Britt and A. R. Quinton, Phys. Rev. 124, 877 (1961).
[2]J. Galin, B. Gatty, D. Guerreau, C. Rouusset, U. C. Schlotthauer-Voos, and X. Tarrago, Phys. Rev. C 9, 1126 (1974).
[3]T. Inamura, M. Ishihara, T. Fukuda, T. Shimoda, and K. Hiruta, Phys. Lett. 68B, 51 (1977).
[4]For instance, see W. Nörenberg, J. Phys. C 5, 141 (1976).
[5]R. Weiner and M. Weström, Phys. Rev. Lett. 34, 1523 (1975), and Nucl. Phys. A286, 282 (1977).
[6]T. Nomura, K. Hiruta, T. Inamura, and M. Odera, Nucl. Phys. A217, 253 (1973).
[7]T. Ericson, Adv. Phys. 9, 425 (1960).
[8]D. C. Williams and T. D. Thomas, Nucl. Phys. 53, 577 (1964).
[9]G. Igo, Phys. Rev. 115, 1665 (1959).
[10]W. J. Knox, A. R. Quinton, and C. E. Anderson, Phys. Rev. 120, 2120 (1960).
[11]T. D. Thomas, Annu. Rev. Nucl. Sci. 18, 343 (1968), and references therein.
[12]J. Wilczynski, Phys. Lett. 40B, 37 (1972).
[13]J. Galin, J. Phys. C 5, 83 (1976).

Reprinted from Phys. Lett., 114B, 107–110 (1982).

FINAL-STATE INTERACTION AND TIME INFORMATION IN ^{14}N-INDUCED REACTIONS STUDIED BY α–α CORRELATIONS

S. KOHMOTO, M. ISHIHARA, H. KAMITSUBO, T. NOMURA, Y. GONO [1], H. UTSUNOMIYA, T. SUGITATE [2] and K. IEKI [3]

Cyclotron Laboratory, the Institute of Physical and Chemical Research, Wako-shi, Saitama, 351, Japan

Received 30 April 1982

Angular correlation measurements were performed for the reactions ^{27}Al(^{14}N, $\alpha\alpha$) and ^{93}Nb(^{14}N, $\alpha\alpha$) with 115 MeV incident energy at $\theta = 50°$ with different $\Delta\phi$. Strong evidence for a final-state interaction between two α-particles was obtained. The decay time constant was estimated analysing the result with a proximity rescattering approximation.

Since the early work of Britt and Quinton [1], the emission of energetic light particles has attracted much attention in heavy-ion (HI) reactions. Although knowledge of the time scale for light-particle emission seems to be essentially important for the understanding of the underlying reaction mechanism, little information is available experimentally.

It was pointed out some years ago [2] that a correlation measurement of two identical and non-interacting particles with a small relative momentum is useful to determine the temporal and spatial sizes of the emitter of nuclear dimension, which is originally known as the Hanbury-Brown–Twiss method [3]. Koonin has shown [4], taking the p–p pair in high-energy reactions as an example, that the existance of the final-state interaction (FSI) comprising the Coulomb and nuclear interactions enhances the sensitivity of the method in the determination of these parameters instead of obscuring the effect. In low-energy HI reactions, α-particles associated with a preequilibrium process are abundantly emitted forming continuum spectra. In an attempt for a time-scale determination of these emissions, we have measured correlations between two α-particles emitted from ^{14}N-induced reactions at an incident energy ~8 MeV/A. In this Letter, we report, first, on the evidence of the strong participation of the FSI in α-particle emissions, and then apply to the data a simplified treatment of the FSI, proximity rescattering approximation, to examine the aspect of the time scale of the emissions.

Measurements were performed for the reactions ^{27}Al(^{14}N, $\alpha\alpha$) and ^{93}Nb(^{14}N, $\alpha\alpha$) using the 115 MeV N^{5+} beam from the cyclotron at the Institute of Physical and Chemical Research. The targets were self-supporting metalic foils of 2.7 and 13.4 mg/cm^2 thickness, respectively. Four identical sets of counter telescopes, each of which consisted of 30 and 200 μm Si detectors, were arrayed at different azimuthal angles ϕ but with the same polar angle $\theta = 50°$ with respect to the beam direction. Correlations of α-particles detected between any two sets of telescopes were recorded simultaneously. In this way, correlations for 24 and 30 azimuthal angle differences $\Delta\phi$ from 22° to 180° were obtained for the Al + N and Nb + N reactions, respectively. The data were recorded event-by-event on magnetic tapes and analysed off-line. We additionally measured inclusive spectra of various ejectiles from the reactions ^{27}Al(^{14}N, χ) and ^{93}Nb(^{14}N, χ) as a function of θ at the same incident energy.

In the special case of $E_1 = E_2 = E$ for the coincident particles, where E_1 and E_2 are the kinetic energies of

[1] Linac Laboratory, IPCR, Wako-shi, Saitama, 351, Japan.
[2] Present address: Physics Department, Hiroshima University, Hiroshima, Japan.
[3] On leave from Physics Department, Kyoto University, Kyoto, Japan.

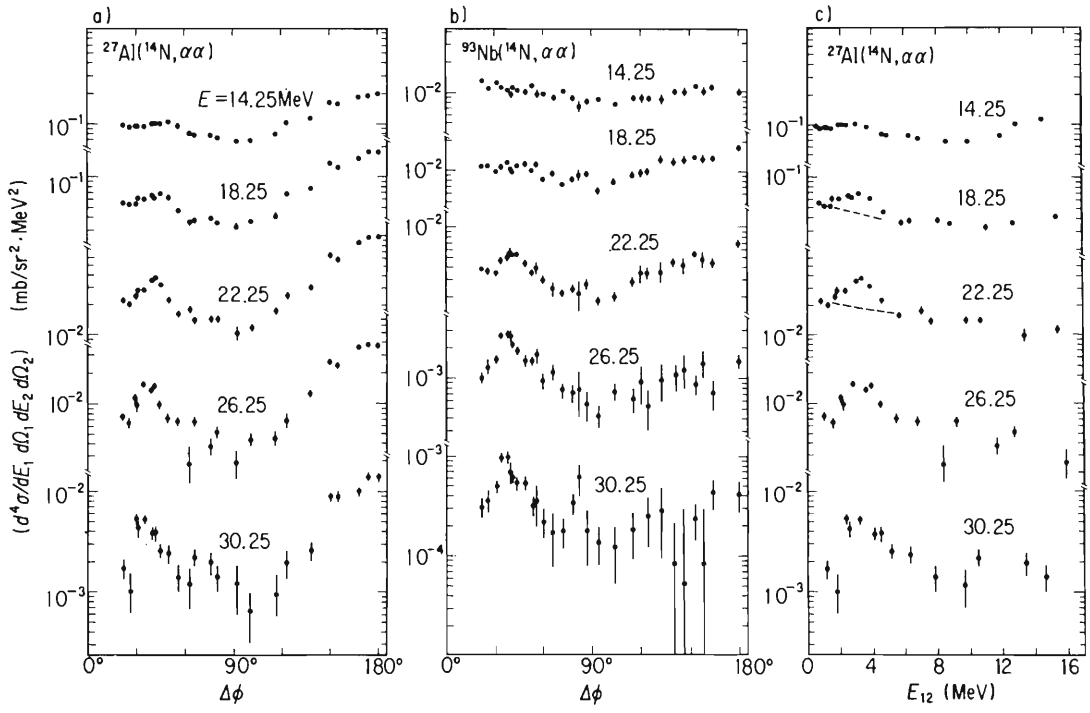

Fig. 1. Laboratory coincidence cross sections for the reactions ^{27}Al(^{14}N, αα) ... (a), (c) and ^{93}Nb(^{14}N, αα) ... (b), measured at θ = 50° and evaluated for the condition $E_1 = E_2 = E$. Cross sections are plotted again the azimuthal angle difference $\Delta\phi$ in (a), (b) and against the relative energy E_{12} between two α-particles in (c).

the two α-particles in the laboratory system, the relative energy E_{12} is given by

$$E_{12} = E \sin^2\theta\,(1 - \cos\Delta\phi)\,.$$

The cross sections of the α–α correlation under this condition are plotted against $\Delta\phi$ and E_{12} in fig. 1 for different values of E. There, we observe increases toward $\Delta\phi = 0°$ and 180° in each curve. This may be attributed to a general phenomenon that two quanta from a high-spin state tend to be favourably emitted in the same plane. A remarkable aspect of primary interest is the enhancement which appeared with a bump structure peaked at $E_{12} \simeq 3$ MeV in all curves (see fig. 1c). This energy corresponds to the resonance energy of the first 2^+ state of the ^{8}Be nucleus, indicating an important role of this state in the intermediate stage of the reaction. We denote the enhanced portion as $(d^4\sigma/dE_1\, d\Omega_1\, dE_2\, d\Omega_2)_{en}$, which is evaluated by subtracting a smooth component underlying the peak from the coincidence cross section. Examples of estimated background component are shown in fig. 1c. We plot in fig. 2, by dots with error bars, the experimental enhanced cross section $(d^4\sigma/dE_1\, d\Omega_1 ...)_{en}$ of the Al + N system obtained at its maximum near E_{12} = 3 MeV for the condition $E_1 = E_2 = E$, taking E as abscissa.

The following two processes are considered as the possible origin of this enhancement: (a) Break-up into two α-particles of excited ^{8}Be nuclei produced in the primary reaction, and (b) FSI between two α-particles independently emitted from the primary reaction. Here we consider, for the primary reaction, the usual quasi-elastic and deep-inelastic reactions or preequilibrium emissions of lighter ejectiles. We first examine the process (a). The break-up cross section of ^{8}Be(2^+) may be estimated on the basis of the Q_{gg} rule [5] and with use of the measured inclusive yields of ^{7,9}Be and other ejectiles. Then, the cross section of coincident α-particles due to the ^{8}Be(2^+) break-up can be calculated by assuming, for simplicity, an isotropic distribution of α-particle emissions in the rest frame of ^{8}Be. Here, it is also assumed that the spectral shape of ^{8}Be(2^+) is given by those of ^{7,9}Be which are analogous to each other. The calculated enhanced cross section (dashed

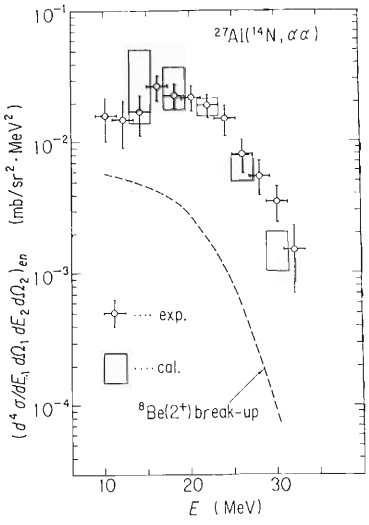

Fig. 2. The experimental enhanced cross section $(d^4\sigma/dE_1\, d\Omega_1\, dE_2\, d\Omega_2)_{en}$ of the reaction $^{27}Al(^{14}N, \alpha\alpha)$, obtained for the condition $E_1 = E_2 = E$ at the maximum near $E_{12} = 3$ MeV, is plotted by dots. The calculated cross section using eq. (1) with $\tau/g = 2 \times 10^{-21}$ s is indicated by rectangles. The vertical length associated with those cross sections indicates the statistical error and also the ambiguities in subtraction of the background. The horizontal length represents the width of energy bin taken to extract the enhanced and primary cross sections. The estimated cross section due to the break-up process of $^{8}Be(2^{+})$ nuclei is shown by the dashed line.

line in fig. 2) was found to be 1/5 to 1/10, depending on E, of the observed enhanced cross section. In view of the significant difference in cross section, the break-up process can hardly be important. The E dependence of calculated cross section is neither consistent with the observed one, again indicating the irrelevance of the process (a). Based on these arguments, we conclude that the dominant process for the observed enhancement is not the break-up process but the FSI.

By taking it for granted that the FSI is the major mechanism, the present data may be related to the space–time structure of the colliding system. Among several theories now available [6–8], we take a simple model using the proximity rescattering approximation [7]. This model may be primitive but provides an intuitive picture of the underlying reaction scheme so that the potential feature of the phenomenon may be better seen.

In this model, the FSI is assumed to act between two α-particles emitted successively in the primary reaction under the following proximity condition: an α-particle 1 is emitted in a direction ω_1 with an energy ω_1, and after a time delay Δt, a second α-particle 2 is emitted with an energy ω_2, greater that ω_1, in the direction ω_2 which coincides with that of the first in the center-of-mass system. Here, the kinematical values ω_1, ϵ_1 ... are expressed in the laboratory system. Under this geometry, the second particle catches up the first at a distance $D(\Delta t)$ from the residual nucleus. If the relative energy is around 3 MeV, the two particles experience resonance-like rescattering which results in the observed cross section.

In this approximation the enhanced cross section measured at the direction Ω_1 and Ω_2 is written by the following relation:

$$(d^4\sigma/dE_1\, d\Omega_1\, dE_2\, d\Omega_2)_{en}$$

$$= (d^4\sigma/d\epsilon_1\, d\omega_1\, d\epsilon_2\, d\omega_2)_{12}(d\sigma/d\Omega)^{2^+}_{\alpha-\alpha}\langle 1/D^2\rangle J\,. \quad (1)$$

The second term in the right-hand side is the cross section for free α–α elastic scattering in the center-of-mass of the two α particles. The choice $E_1 = E_2$ corresponds to the 90° scattering of the two α-particles in their center-of-mass. The cross section relevant is then 620 mb/sr at the 2^+ resonance [9]. The third term expresses the time average of $1/D(\Delta t)^2$, and is associated with the "target" density of the particle 1 "bombarded" by the particle 2. The inverse of this average is proportional to a time constant τ, to the first approximation, if the time delay Δt is distributed as $\exp(-\Delta t/\tau)$ [7]. The last term is the jacobian for the transformation of the coordinate systems involved therein.

In treating the first term of eq. (1), we introduce the temporally-ordered cross sections $(d^4\sigma/dE_1\, d\Omega_1\, dE_2\, d\Omega_1)_{12}$ and $(d^4\sigma/dE_1\, d\Omega_1 ...)_{21}$ of the emissions of the two primary α-particles. By designating the particles 1 and 2 by the condition $E_1 < E_2$, we attribute the first (second) cross section to the successive emissions in which particles are emitted in the time order 1–2 (2–1). Then, the total emission cross section of the two primary α-particles (primary cross section) is expressed by the sum of the two cross sections:

$$(d^4\sigma/dE_1\, d\Omega_1 ...)_{pr}$$

$$= (d^4\sigma/dE_1\, d\Omega_1 ...)_{12} + (d^4\sigma/dE_1\, d\Omega_1 ...)_{21}\,.$$

The first term of eq. (1) can be then rewritten as

$(d^4\sigma/d\epsilon_1\, d\omega_1\, ...)_{12} = g\,(d^4\sigma/d\epsilon_1\, d\omega_1\, d\omega_2\, d\omega_2)_{pr}$,

with $0 < g < 1$, where $(\epsilon_1\omega_1\epsilon_2\omega_2)$ is used instead of $(E_1\Omega_1E_2\Omega_2)$ to distinguish the cross section of the primary emissions which satisfy the proximity geometry and resonance rescattering conditions. Since we have no means to evaluate the temporally-ordered cross sections separately, only the cross section $(d^4\sigma/d\epsilon_1\, d\omega_1 ...)_{pr}$ was estimated, leaving g as undetermined parameter.

Because the primary cross section is that which ought to be observed in the absence of the FSI, the experimental coincidence cross section obtained over the $E_1 - E_2$ planes versus $\Delta\phi$ outside of the region $E_{13} \simeq 3$ MeV can be attributed to $(d^4\sigma/dE_1\, d\Omega_1 ...)_{pr}$. It was found that, in both the Al + N and Nb + N systems, the primary cross section is given by the form

$$(d^4\sigma/dE_1\, d\Omega_1 ...)_{pr} \simeq K(\Delta\phi)\, f(E_1, E_2)\,,$$

i.e. the spectral shape is nearly independent of $\Delta\phi$ for $\Delta\phi \lesssim 100°$ and only the magnitude depends on $\Delta\phi$. It should be noted that the kinematical values used are expressed in the laboratory system. Then, only the azimuthal angles of the particles 1 and 2 involved in $(\epsilon_1\omega_1\epsilon_2\omega_2)$ coincide, but not the polar angles because of the movement of the center-of-mass. In the actual case, however, we ignored the small deviation of the polar angles from 50° and used the data taken at θ = 50°. The primary cross section at a set $(\epsilon_1\omega_1\epsilon_2\omega_2)$ was then deduced by extrapolating the primary cross sections evaluated at the energy set $(\epsilon_1\epsilon_2)$ for $22° \leqslant \Delta\phi \lesssim 100°$ to $\Delta\phi \to 0°$.

In fig. 2 the observed enhanced cross sections of the Al + N system are compared with those calculated by eq. (1) using $(d^4\sigma/d\epsilon_1\, d\omega_1 ...)_{pr}$ thus deduced. By choosing a constant value of $\tau/g = 2 \times 10^{-21}$ s, a fairly good agreement is obtained over the entire energy range, indicating the qualitative adequacy of the present analysis. In the case of the Nb + N system (not shown) also, a single value of $\tau/g = 8 \times 10^{-22}$ s fits well the experimental enhanced cross section. The value of τ/g obtained corresponds to the upper limit of the time constant τ, and if the cross section $(d^4\sigma/d\epsilon_1 d\omega_1 ...)_{pr}$ is shared by the two temporally-ordered cross sections equally (i.e. $g = 1/2$) the constants τ take the values 1×10^{-21} s and 4×10^{-22} s, respectively.

Because of the simple model assumed, the present analysis may be only qualitative rather than quantitative. For instance, the model ignores a finite spatial size of the source for α-particle emission. This may be a ventured assumption because, in both the reactions, the diameter $2R$ of the residual nucleus, which is the size of the source in its maximum extension is only slightly smaller than the averaged distance $\langle D\rangle$ deduced. From this point of view, it is desirable to employ more advanced theories [8] which take into account both the spatial and temporal parameters. But even using these theories, only the upper limit of τ could be discussed because of the lack of knowledge of g. In the reaction with large multiplicity of particle emissions, as is the case in high-energy reactions, it may be reasonable to assume $g = 1/2$, whereas in low-energy reactions the multiplicity is relatively low and the determination of g is left as an open question.

In summary, we have shown a strong evidence of FSI in low-energy ^{14}N-induced reactions. In our case, the FSI acts between two α-particles, which are produced in the primary reaction, on the outside of the residual nucleus, causing an enhancement in the coincidence cross section. This contrasts with the case of the coalescence of nucleons, observed in higher incident energies from a few tens to a few hundreds of MeV/A, where the manifestation of the FSI effect necessitates the presence of the mean field of the nucleus acting as a third body [10]. The enhancement in cross section, by help of the rescattering approximation availed out tentative but direct estimation of the upper limit of the time scale of α-particle emission. It would be interesting to put forward this type of studies to other HI–α exit channels which are known also to have non-negligible coincidence cross sections.

[1] H.C. Britt and A.R. Quinton, Phys. Rev. 124 (1961) 877.
[2] V.G. Grishin et al., Yad. Fiz. 13 (1971) 1116 [Sov. J. Nucl. Phys. 13 (1971) 638].
[3] R. Hanbury-Brown and R.Q. Twiss, Phil. Mag. 45 (1954) 633; Nature (London) 178 (1956) 1046.
[4] S. Koonin, Phys. Lett. 70B (1977) 43.
[5] V.V. Volkov, Proc. Intern. Conf. on Reactions between complex nuclei (Nashville, 1974) Vol. II, eds. R.L. Robinson et al. p. 363.
[6] R. Fox, Phys. Rev. 125 (1962) 311.
[7] S. Kato et al., Nucl. Phys. A195 (1972) 534.
[8] H. Sato and K. Yazaki, lecture notes 1980 INS Kikuchi Summer School on Nuclear physics at high energies (Fuji-Yoshida, 1980) ed. F. Sakata (Institute for Nuclear Study, University of Tokyo), p. 313, and to be published.
[9] T.A. Tombrello et al., Phys. Rev. 129 (1963) 2252.
[10] A. Kekjian, Phys. Lett. 89B (1980) 177.

Reprinted from Phys. Lett., 150B, 83–86 (1985).

SPIN POLARIZATION OF RESIDUAL NUCLEI IN (^{14}N, α) REACTIONS AT 115 MeV

K. IEKI[1], M. ISHIHARA, T. INAMURA, S. KOHMOTO, H. UTSUNOMIYA[2], K. SUEKI[3] and H. KUDO[4]

Cyclotron Laboratory, Institute of Physical and Chemical Research (RIKEN), Wako, Saitama 351, Japan

Received 28 June 1984

Spin polarization of residual nuclei was studied in (^{14}N, α) reactions by means of a γ-ray circular polarization measurement. Variations with target nucleus, scattering angle and Q-value were systematically investigated. The ^{197}Au(^{6}Li, α) reaction was investigated for comparison also. We argue the existence of competition between slow multi-step and fast direct-type processes in the (^{14}N, α) reactions on the basis of the observed polarization.

In recent years several measurements [1,2] of spin polarization have been made in heavy-ion dissipative reactions, revealing large polarizations of residual nuclei. These studies have provided unique information about reaction mechanisms by exploiting the particular sensitivity of polarization to trajectories of scattering ions. Most studies made so far treated reactions with a fairly small number of transferred nucleons. In contrast, the purpose of this work was to investigate many-nucleon transfer reactions associated with fast light-particle emissions. The spin polarization of heavy residues was studied primarily in (^{14}N, α) reactions at 115 MeV by measuring γ-ray circular polarization. The dependence on target, scattering angle and Q-value was systematically investigated. The (^{6}Li, α) reaction on ^{197}Au was studied for comparison also.

Several models have been proposed to describe fast light-particle emission, e.g., a thermal emission model in terms of moving hot spot [3], nonequilibrium models in terms of exciton description [4] or promptly emitted particles [5]. While multi-step (MS) mechanisms are implicit in many cases, there also exists a DWBA approach in terms of the breakup–fusion mechanism [6], which emphasizes an aspect of the simple direct-type reaction (DR). The present results may add new constraints in deciding the relative importance among these different mechanisms, particularly, between slow MS and fast DR processes.

Self-supporting foils of ^{159}Tb, ^{181}Ta, ^{93}Nb, and ^{nat}Ni, whose thicknesses were 3.4, 4.2, 4.2, and 2.7 mg/cm^2, respectively, were bombarded with a 115 MeV ^{14}N beam from the RIKEN cyclotron. An ^{197}Au foil of 1.9 mg/cm^2 was also bombarded with a 49 MeV ^{6}Li beam. Typical beam intensity was 5nA and the beam spot was smaller than 4 mm × 4 mm.

The experimental method used was essentially the same as that of Trautmann et al. [7]. The γ-ray circular polarization was measured using two identical sets of forward-scattering-type polarimeters, in which γ rays were Compton-scattered on a surface of an iron magnet and recorded in 6″Φ × 6″ NaI detectors. The polarimeters were placed at both sides of the normal direction ($\boldsymbol{k}_i \times \boldsymbol{k}_f$) to the reaction plane. The analyzing power A_p of the polarimeter was calculated with a Monte Carlo code which treats the scattering probability of polarized γ rays with electrons in the magnetized iron and surrounding materials. A_p was nearly constant over a wide range of incident γ-ray energy E_γ. When electron spins were polarized at 70% of the saturation value, A_p was around 1.65% for E_γ = 400–4000 keV, and was about 0.8% at E_γ = 200 keV, at which the threshold was effectively set in most experimental runs.

[1] Present address: Department of Physics, Tokyo Institute of Technology, Ohokayama, Meguro, Tokyo, Japan.
[2] Present address: Cyclotron Laboratory, Michigan State University, East Lansing, MI, USA.
[3] Permanent address: Department of Chemistry, Tokyo Metropolitan University, Tokyo, Japan.
[4] Present address: Department of Chemistry, Niigata University, Niigata, Japan.

0370-2693/85/$ 03.30

The calculated analyzing power was found to be reasonable when the circular polarization of 4.4 MeV γ rays measured in the $^{12}C(\alpha, \alpha')\ ^{12}C(2^+)$ reaction at 22.75 MeV and at $\theta_{lab} = 160°$ was compared with a previous result by Hayward and Schmidt [8].

Ejected particles were detected with two sets of counter telescopes consisting of 50 μm and 1500 μm Si solid-state detectors. They were placed at symmetric angles $\pm\theta$ ($\theta = 30°$ for ^{nat}Ni, ^{93}Nb, ^{181}Ta targets, $\theta = 20°, 30°, 40°, 50°$ for ^{159}Tb, and $\theta = 40°$ for ^{197}Au) with respect to the beam axis. The solid angle subtended was typically 40 msr. An aluminum absorber of 140 μm thickness was placed in front of the telescopes to cut off intense elastically scattered ^{14}N particles. This limited the range of detected ejectiles to be lighter than alpha particles and the range of alpha-particle energy to be above 15 MeV. For the measurement in the ^{159}Tb(^{14}N, α) reaction at 50° the absorber was removed so that heavier ejectiles ($Z \leqslant 7$) could also be recorded.

The asymmetry A_s was obtained from coincident rates N_{ij} in pairs of particle detector i ($i = 1, 2$) and NaI detector j ($j = 1, 2$) for Q-bins of 8 MeV width, using relation, $A_s = (x-1)/(x+1)$, with $x = (N_{11}N_{22}/N_{12}N_{21})^{1/2}$. The circular polarization P_γ is related to A_s as $P_\gamma = A_s/A_p$. In relating P_γ to the polarization P_z of the residual nucleus as $P_\gamma = fP_z$, two main effects were considered. First, we assumed that the cascade consists of four statistical dipole transitions and ($M_\gamma - 4$) of E2 stretched transitions [9]: multiplicity M_γ, i.e., the average number of cascade γ rays was determined by comparing γ-ray intensities in singles and coincidences. Secondly, neutrons accompanying the reaction which were recorded in the NaI detector reduced the value of A_s and hence effectively modified f. By considering gamma and neutron multiplicities, f was estimated to be almost constant (~0.5) versus alpha-particle energy E_{cm} for the (^{14}N, α) reactions. This near constancy arises from the fact that M_γ and M_n vary almost in parallel with E_{cm}, while the factor f varies with M_γ and M_n oppositely.

Experimental data obtained are summarized in figs. 1–3. The sign of P_z is defined to be positive when the polarization vector is in the direction of $\boldsymbol{k}_i \times \boldsymbol{k}_f$. An energy spectrum in the (^{14}N, α) reaction as shown in fig. 2a exhibits a smooth continuum shape extending to high energy. Nonequilibrium components of interest constitute a major portion of the spectrum, while the fraction of the equilibrium component was very small in the region of $E_{cm} \geqslant 20$ MeV. Because of the coincidence method used, the spectrum is modified by the weight of M_γ, which results in a reduction of the contribution from three-body final channels [10] such as the sequential breakup process (e.g. $^8\text{Be} \rightarrow 2\alpha$) in the polarization spectrum.

A general feature of polarization in the ^{14}N + ^{159}Tb reaction was observed by measuring the dependence of P_z on an ejectile at $\theta = 50°$. It was found that energy-averaged P_z values differ significantly between ejectiles of larger and smaller Z. P_z for $Z = 4$–6 was largely negative (−0.5 to −0.7) where P_z for lighter ejectiles ($Z = 2$–3) became much smaller (−0.1 to −0.2) and P_z was even positive (~0.1) for $Z = 1$. This trend towards positive P_z in (^{14}N, α) and (^{14}N, p) channels was found to be a prevailing feature in the various reaction systems studied, The P_z spectra for the (^{14}N, α) reactions on ^{nat}Ni and ^{93}Nb (figs. 1a and 1b) typically exhibit such a property, being characterized by a fairly flat shape with vanishing or slightly positive P_z.

In a classical description of dissipative heavy-ion collisions, a large fraction of orbital angular momentum l_i will be converted into intrinsic spin of the resid-

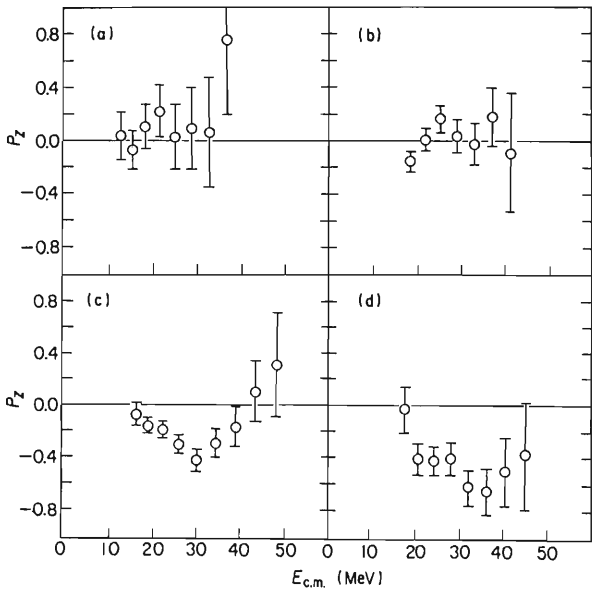

Fig. 1. Spin polarization versus emitted α-particle energy for ^{14}N-induced reactions at $\theta_{lab} = 30°$ on various targets: (a) ^{nat}Ni, (b) ^{93}Nb, (c) ^{159}Tb, (d) ^{181}Ta. Flags indicate statistical errors.

ual nucleus. Hence the polarization vector tends to point to the direction of I_i and the sign of P_z varies according to that of the scattering angle. There also exists a trend that, because of the attractive nuclear interaction, the trajectory will be more deflected towards negative angles as the contact (reaction) time in the collision becomes longer. The results on P_z discussed above may then be interpreted as an indication that fairly slow reaction mechanisms are responsible for channels of light-particle emissions. This observation supports such nonequilibrium description as moving hot spot [3] and exciton [4] models which presume relatively slow processes of multi-step nature.

The polarization spectra in the (^{14}N, α) reactions on heavier targets (^{159}Tb and ^{181}Ta) show a remarkable behaviour (figs. 1c and 1d), exhibiting a local structure of negative dip which is not clearly seen in the cases of the lighter targets. It appears that the structure is superimposed on such a monotonic spectrum with small $|p_z|$ as observed for lighter targets. Characteristics of the structure in the ^{159}Tb(^{14}N, α) reaction are better depicted in a contour plot of P_z in the plane of E_{cm} versus θ_{cm} (fig. 2b). The large negative P_z is prominent in a region centered at around 30 MeV and at around $\theta_{cm} = 40°$, which nearly correspond to the kinetic energy E_b of the beam and the grazing angle θ_{gr}, respectively.

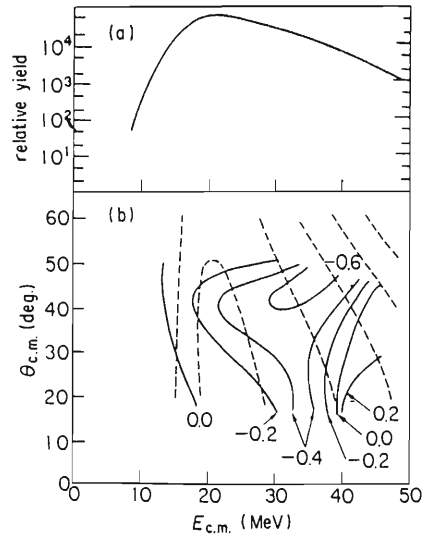

Fig. 2. (a) Energy spectrum for the ^{159}Tb(^{14}N, α) reaction at $\theta_{lab} = 30°$. It is corrected for energy loss in an Al absorber. (b) Contour plots of the spin polarization P_z (solid line) and the differential cross section $d^2\sigma/d\Omega\, dE$ (dashed line) for the ^{159}Tb(^{14}N, α) reaction. The contour lines were obtained from smooth interpolation between experimental data. For the P_z data used, the sizes of statistical errors are similar for $\theta_{lab} \leq 30°$ (see fig. 1c for $\theta_{lab} = 30°$) but are larger by a factor of about 1.5 and 2.0 for $\theta_{lab} = 40°$ and 50°, respectively.

This observation indicates that some extra process contributes to the (^{14}N, α) reactions on ^{159}Tb and ^{181}Ta targets in addition to the major MS process. The location of the dip in the E_{cm} versus θ_{cm} plane suggests a peripheral process of DR nature. As a matter of fact, a recent DWBA calculation in terms of the break-up–fusion formalism [6] reveals that a DR-type process can participate strongly in (^{14}N, α) reactions particularly at energies close to E_b. While the calculation has not given a definite prediction on the polarization, positive angle deflection is expected for such a grazing process, being in favour of the negative polarization observed.

In order to have supporting evidence for the relation between the large negative P_z and the DR-type process, we studied the ^{197}Au(^{6}Li, α) reaction at an incident energy of 49 MeV (fig. 3). This reaction was chosen because it is well described with DWBA theories by assuming the (d + α) cluster configuration of ^{6}Li [11]. The energy spectrum obtained shows a gaussian shape centered at E_b. This is typical of direct-type reactions, exhibiting the effect of kinematical matching conditions [12,6]. The polarization indeed shows a negative value comparable in magnitude with those at the dip in the (^{14}N, α) reaction.

In summary we studied the polarization of the resid-

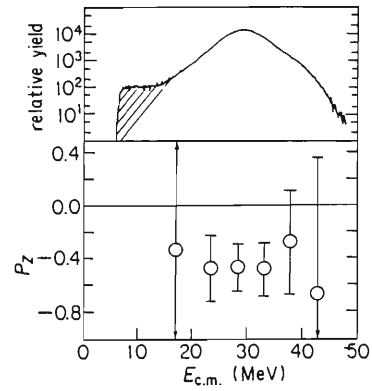

Fig. 3. Differential cross section and spin polarization observed for the ^{197}Au(^{6}Li, α) reaction at $\theta_{lab} = 40°$. The shaded area indicates contributions from target contamination.

ual nuclei in several (^{14}N, α) reactions at 115 MeV. While the energy spectra show smooth uncharacteristic shapes, P_z spectra suggest a competition of two main components of different natures. The major component is accompanied with positive or small negative P_z and indicates its relevance to slow reactions of non-equilibrium nature. The other component is characterized by a dip structure of negative P_z which is significant in a particular region of the E_{cm} versus θ_{cm} plane centered at E_b and θ_{gr}. This feature indicates relevance to such a DR-type process as is clearly seen in the (^{6}Li, α) reaction. The absence of the dip structure for the lighter targets may partly be related to the difference in θ_{gr}. The detection angle (30°) was fairly more backward than θ_{gr} for the lighter targets while it was closer to θ_{gr} for the heavier targets. It is also probable that the relative strengths of the competing processes vary considerably with the reaction systems.

Finally, the present results have shown that appreciable polarization is produced even in residual nuclei in reactions involving fast light-particle emissions and, moreover, that detailed study of polarization can provide a clue to distinguish competing processes in such reactions. These features of polarization are inherently related to the angular momentum transfer mechanisms. Theoretical descriptions incorporating such degrees of freedom explicitly would thus be desirable to refine understanding of light-particle emission mechanisms.

Two of the authors (K.I,K.S) wish to thank Professor H. Kamitsubo for his kindest hospitality during their stay at RIKEN.

References

[1] K. Sugimoto, N. Takahashi, A. Mizobuchi, Y. Nojiri, T. Minamisono, M. Ishihara, K. Tanaka and H. Kamitsubo, Phys. Rev. Lett. 39 (1977) 323.
[2] W. Trautmann, J. de Boer, W. Dünnweber, G. Graw, R. Kopp, C. Lauterbach, H. Puchta and U. Lynen, Phys. Rev. Lett. 39 (1977) 1062.
[3] T.J.M. Symons, P. Doll, M. Bini, D.L. Hendrie, J. Mahoney, G. Mantzouranis, D.K. Scott, K. Van Bibber, Y.P. Viyogi, H.H. Wieman and C.K. Gelbke, Phys. Lett. 94B (1980) 131.
[4] T. Otsuka and K. Harada, Phys. Lett. 121B (1983) 106.
[5] J.P. Bondorf, J.N. De, G. Fai, A.O.T. Karvinen, B. Jakobsson and J. Randrup, Nucl. Phys. A333 (1980) 285.
[6] T. Udagawa and T. Tamura, Phys. Rev. Lett. 45 (1980) 1311.
[7] W. Trautmann, C. Lauterbach, J. de Boer, W. Dünnweber, G. Graw, W. Hamann, W. Hering and H. Puchta, Nucl. Instrum. Methods 184 (1981) 449.
[8] T.D. Hayward and F.H. Schmidt, Phys. Rev. C1 (1970) 923.
[9] D.G. Sarantites, L. Westerberg, M.L. Halbert, R.A. Dayras, D.C. Hensley and J.H. Barker, Phys. Rev. C18 (1978) 774.
[10] H. Utsunomiya, thesis, Kyoto university (1981), unpublished.
[11] F.D. Becchetti, in: Clustering aspects of nuclear structure and nuclear reactions, eds. W.T.H. Van Oers, J.P. Svenne, J.S.C. McKee and W.R. Falk (AIP, New York, 1978).
[12] M. Ichimura, E. Takada, T. Yamaya and K. Nagatani, Phys. Lett. 101B (1981) 31.

Reprinted from Phys. Lett., B, 176, 307–311 (1986).

ENHANCED E2 TRANSITIONS BETWEEN 9^- AND 8^- STATES IN ^{110}Sn AND ^{112}Sn

J. KASAGI, H. HARADA, T. MURAKAMI, K. YOSHIDA, H. TACHIBANAKI

Department of Physics, Tokyo Institute of Technology, 2-12-1 Oh-okayama, Meguro, Tokyo 152, Japan

and

T. INAMURA

Cyclotron Laboratory, RIKEN (The Institute of Physical and Chemical Research), Wako-shi, Saitama 351-01, Japan

Received 11 February 1986; revised manuscript received 27 May 1986

Lifetimes of $J^\pi = 8^-$ and 9^- states in ^{110}Sn and ^{112}Sn have been measured. Large B(E2) values of about 170 e^2 fm^4 have been observed for the $9^- - 8^-$ transitions in both nuclei. The enhanced E2 transitions can be explained as the effect of the generalized-seniority mixing predicted recently by Bonsignori et al.

The low-lying states of Sn isotopes with a closed Z = 50 proton shell have provided the opportunity to investigate the validity of the neutron quasiparticle or generalized-seniority (v_g) concept. In fact the excitation energies of the yrast states (up to 9^- or 10^+) are well reproduced by neutron two-quasiparticle or v_g = 2 model calculations [1,2]. Recently, the influence of the generalized-seniority mixing on the low-lying states of even-A Sn nuclei has been investigated theoretically by Bonsignori et al. [3]. They showed that most of the low-lying states have 10–30% of v_g = 4 admixtures in predominant v_g = 2 configurations, except for the 0_1^+, 2_1^+ and 3_1^- states. Of particular interest is the main source of the generalized-seniority mixing which they claimed to be a kind of particle-phonon coupling mechanism. Hence the effect of v_g = 4 admixtures will result in enhanced E2 transition probabilities. This enhancement is predicted to be seen for the transitions between high-spin states with simple configurations in the v_g = 2 space. Calculations with the V_g = 2 space connot predict the presence of enhanced E2 transitions. The experimental B(E2) values of the $10^+ - 8^+$ transitions in ^{116}Sn and ^{118}Sn [2] are slightly enhanced with respect to the calculated values with $(h_{11/2}h_{11/2})^{J=8,10}$ configurations. They are reproduced by the calculations with $v_g \leqslant 4$ configurations [3]. In this case, however, the effect of the admixtures of deformed states lying at similar excitation energies [4] should also be considered.

The $9^- - 8^-$ transition is a more favourable case. Within the v_g = 2 configurations the 9^- state can consist only of the $(h_{11/2}g_{7/2})$ configuration, and the 8^- state is predicted to consist mainly of the same configuration [2,3]. In addition, no deformed negative-parity bands have been observed. The predicted B(E2) values with $v_g \leqslant 4$ configurations for the $9^- - 8^-$ transitions are about 200 e^2 fm^4 [3], more than 7 times larger than those of the calculation with the v_g = 2 configurations. In ^{110,112}Sn, the 9^- and 8^- states are well established and values of the E2/M1 mixing ratio for the transition between them are also known [2]. Therefore, we have measured the lifetimes of the 8^- and 9^- states in ^{110}Sn and ^{112}Sn.

Levels in ^{110}Sn and ^{112}Sn were populated via the ^{98,100}Mo(^{16}O, 4n)^{110,112}Sn reactions with 72–76 MeV ^{16}O beams from the RIKEN 160 cm cyclotron. In addition to n–γ–γ coincidence and n–γ angular correlation measurements with a neutron multiplicity

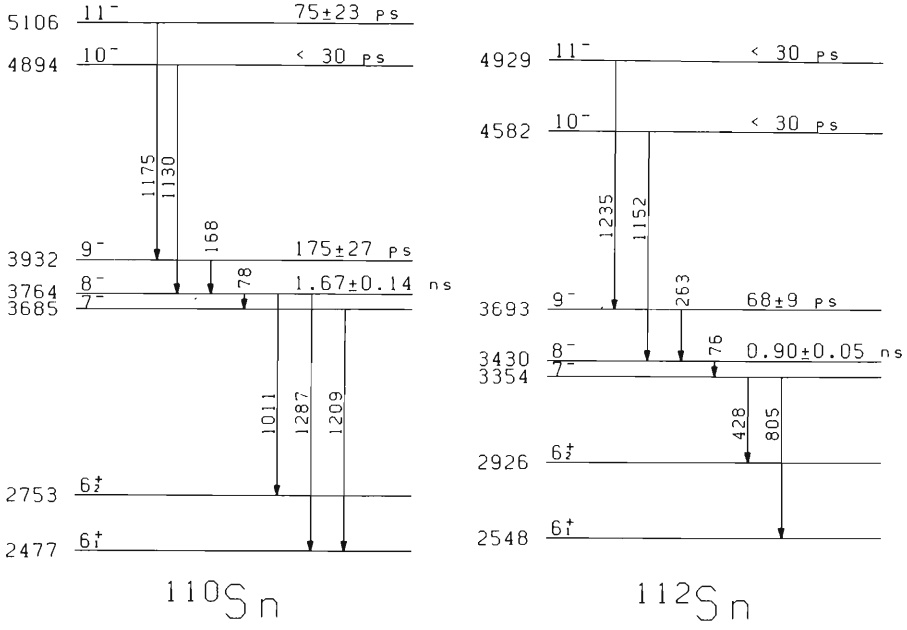

Fig. 1. Decay schemes of negative-parity states in ^{110}Sn and ^{112}Sn observed with the ^{98,100}Mo(^{16}O, 4nγ)^{110,112}Sn reactions.

filter [5], recoil-distance measurements were carried out. Stretched foils of ^{98}Mo (98.3% enriched and 950 μg/cm^2 in thickness) and ^{100}Mo (94.5% enriched and 677 μg/cm^2 in thickness) supported with thin gold foils were used as targets and a thick Ta foil served as a recoil stopper. Gamma rays were measured with a Ge(Li) detector placed at 140° to the beam direction in coincidence with neutrons detected in the neutron multiplicity filter. The usefulness of the neutron multiplicity filter to reduce unwanted events is fully described in ref. [5].

Decay schemes of the negative-parity states in ^{110}Sn and ^{112}Sn presented in fig. 1 are based on the n–γ–γ coincidence data. They agree well with the previous investigation [2] except for the existence of the $8^- - 6_1^+$ transition in ^{110}Sn. Spin and parity assignments given in ref. [2] are consistent with the results of the angular distribution measurements in the present work.

The results of the recoil-distance measurements for the 9^- and 8^- states in ^{110}Sn and ^{112}Sn are shown in fig. 2. Relative yields of non-shifted γ-ray peaks corrected for the change in detector efficiency due to the Doppler shifts are plotted against the target-stopper distance. In order to express the relative yields in terms of the nuclear lifetime, knowledge of the distribution of the recoil velocities is required. We have estimated the spread in the recoil velocities and directions due to the kinematics by using the code "CASCADE" [6] with the assumption of isotropic distributions of the evaporated neutrons in the center-of-mass system. The energy spread in the target has then been evaluated by a Monte Carlo program which was used to analyse the Doppler shift attenuation data [7]. With the estimated velocity distribution of the recoil nuclei the shape of the shifted peak of 1175 keV γ rays observed at the large target-stopper distance was reproduced. The effect of the lifetime of the preceding transition and the correction for the change in the detector solid angle due to different stopper positions have been included in the calculations. The effect of decays from unobserved levels was taken into account as direct-side feeding. The feeding time was assumed to be less than 30 ps. The lifetime was determined together with the feeding time so as to obtain the best fit to the data. The results of the fits are shown in fig. 2 as solid lines. The effect of the attenuation of the angular distribution during recoil in vacuum is found to be negligible from the estimation for a worst case [8]. The change of the yield of the $7^- - 6^+$ transition

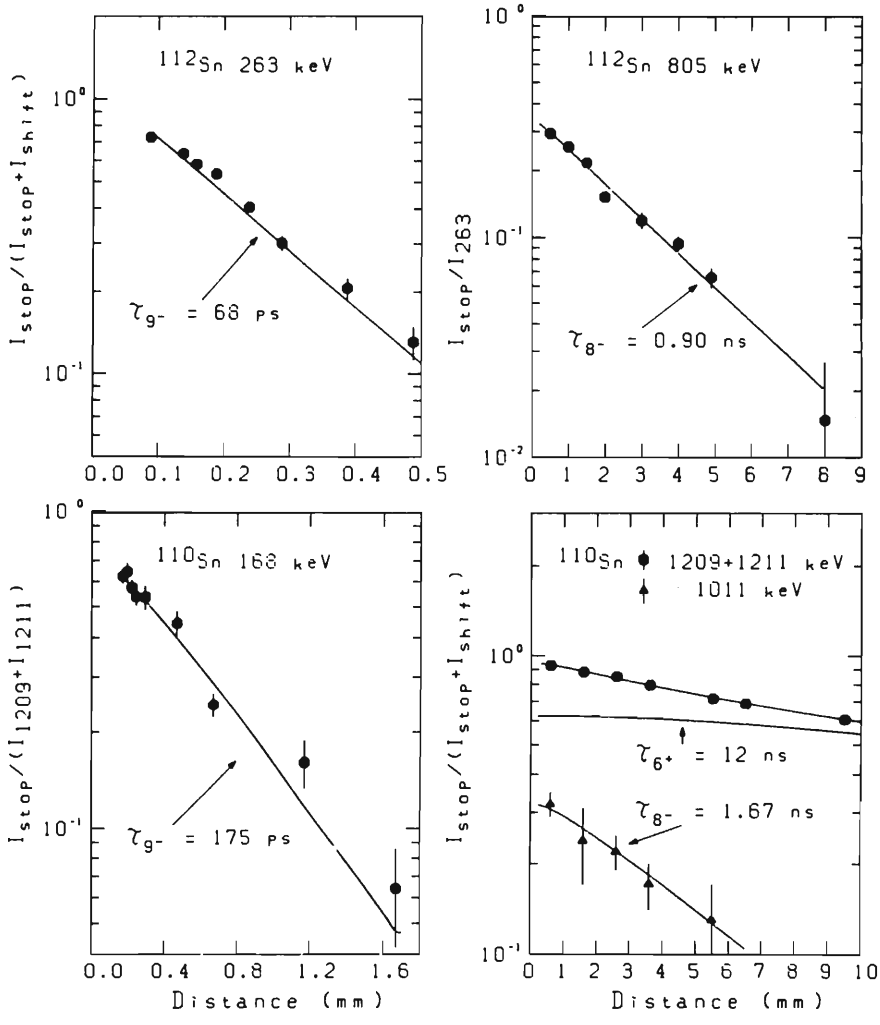

Fig. 2. Plots of relative yields of the stopped peaks against the target-stopper distance for 168, 1011 and 1209 keV γ rays from ^{110}Sn, and 263 and 805 keV γ rays from ^{112}Sn. Solid curves show the results of the fits with the lifetimes indicated in the figure. The fitted curve for the 1209 keV γ rays includes the effect of the 1211 keV (2_1^+) state whose decay time is determined by the 6_1^+ state (τ = 12 ns).

Table 1
Electromagnetic properties of negative-parity levels in ^{110}Sn and ^{112}Sn.

Nuclide	E_X (keV)	τ (ps)	E_γ (keV)	J_i^π	J_f^π	δ	B(M1)(0.01 μ_n^2)	B(E2)(e^{2}fm^4)
^{110}Sn	5106	75 ± 23	1175	11^-	9^-			4.8 ± 1.5
	4894	< 30	1130	10^-	8^-			
	3932	175 ± 27	168	9^-	8^-	0.07 ± 0.02 a)	$6.0\,^{+1.1}_{-0.8}$	$150\,^{+100}_{-80}$
	3764	1.67 ± 0.14 b)	78	8^-	7^-	0.05 ± 0.03 c)	2.7 ± 0.3	$160\,^{+240}_{-100}$
			1011	8^-	6^+			6.5 ± 0.8 d)
			1287	8^-	6^+			0.6 ± 0.1 d)
^{112}Sn	4929	< 30	1235	11^-	9^-			
	4582	< 30	1152	10^-	8^-			
	3693	68 ± 9	263	9^-	8^-	0.14 ± 0.01 a)	$4.3\,^{+0.7}_{-0.5}$	175 ± 35
	3430	0.90 ± 0.05 b)	76	8^-	7^-	0.04 ± 0.03 c)	6.5 ± 0.4	$260\,^{+530}_{-250}$

a) Weighted-average of the present work and the values of ref. [2].
b) ns. c) From ref. [2]. d) B(M2) value in units of μ_n^2fm^2.

in ^{112}Sn observed at 140° is less than 1.5%. The errors of the lifetime listed in table 1 are mainly due to statistics. Those due to the velocity distribution of the recoil nuclei are much less than the statistical errors. Since the transition energies of the $8^- - 7^-$ transitions are very small, the lifetime of the 8^- states have been obtained from the $7^- - 6_1^+$ transitions. In this analysis, we have assumed that the effect of the lifetimes of the 7^- states is negligible. This assumption is justified by the fact that the decay curve of the weak $8^- - 6_2^+$ transition (1011 keV) in ^{110}Sn is reproduced well by the obtained lifetime as shown in fig. 2. The obtained lifetime of the 8^- state in ^{112}Sn is in good agreement with the previously reported one deduced from the centroid shift of a delayed coincidence measurement [2].

The mixing ratios of the $9^- - 8^-$ transitions obtained in the present work ($\delta = 0.06 \pm 0.03$ for ^{110}Sn and $\delta = 0.16 \pm 0.02$ for ^{112}Sn) are in good agreement with those in ref. [2]. Therefore the weighted-average values of the mixing ratios are used to deduce the transition probabilities for the $9^- - 8^-$ transitions.

The electromagnetic properties of the negative-parity states are presented in table 1. As can be seen from table 1, the properties of the negative-parity states in ^{110}Sn are very similar to those in ^{112}Sn. The B(M1) values of the $9^- - 8^-$ and the $8^- - 7^-$ transitions are about $5 \times 10^{-2}\ \mu_n^2$ in both nuclei. No M1 transitions between 10^- and 9^- states have been observed. The upper limit of the branching ratio of the decay of the 10^- state to the 9^- state gives a B(M1) value of less than $2 \times 10^{-4}\ \mu_n^2$. The 7^-, 8^- and 9^- states can be regarded as the $\upsilon_g = 2$ states, while the 10^- state should be the $\upsilon_g = 4$ state. Thus the hindered M1 transition between the 10^- and 9^- states is naturally interpreted as the result of small admixtures of $\upsilon_g = 4$ configurations in the 9^- state. The B(E2) values of the transitions between the $\upsilon_g = 2$ states are very large, although the values of the $8^- - 7^-$ transitions have large experimental uncertainties. It should be noticed that the $9^- - 8^-$ transition shows the largest B(E2) value among the known transitions between the negative-parity levels in even Sn isotopes.

The obtained transition probabilities between the 9^- and 8^- states are compared in table 2 with the calculations performed by Bonsignori et al. [3]. The values of the calculation in table 2 are those with the effective interaction of the finite-range force. As seen from table 2, the calculation without seniority mixing ($\upsilon_g \leqslant 2$) cannot explain the experimental values. The calculated B(M1) values are about two times larger than the experimental ones, whereas the B(E2) values are less than one quarter of the experimental ones. Within the $\upsilon_g = 2$ space, the maximum B(E2) values for the $9^- - 8^-$ transition is obtained when the 8^- state consists of the pure $(h_{11/2}g_{7/2})_8$-configuration. The 8^- state calculated with the $\upsilon_g \leqslant 2$ configurations is predominantly the $(h_{11/2}g_{7/2})_8$-configuration [3]. Thus changing the amount of the admixture of the $(h_{11/2}d_{5/2})_8$-configuration does not explain the observed large B(E2) values.

Table 2
B(M1) and B(E2) values of the $9^- - 8^-$ transitions compared with the calculations [a].

Nuclide	Configurations	B(M1)$(0.01\ \mu_n^2)$	B(E2)$(e^2\mathrm{fm}^4)$
^{110}Sn	experiment	$6.0\ ^{+1.1}_{-0.8}$	$150\ ^{+100}_{-\ 80}$
	$\upsilon_g \leqslant 2$	12.7	23
	$\upsilon_g \leqslant 4$	9.6	169
^{112}Sn	experiment	$4.3\ ^{+0.7}_{-0.5}$	175 ± 35
	$\upsilon_g \leqslant 2$	12.6	36
	$\upsilon_g \leqslant 4$	9.8	206

[a] Ref. [3].

On the other hand, the B(E2) values are surprisingly well reproduced by the calculation with the $\upsilon_g \leqslant 4$ configurations, although the calculated B(M1) values are still larger than the experimental ones. As predicted in ref. [3], the enhanced E2 transitions due to the $\upsilon_g = 4$ admixtures can be seen only for the transitions between the states with simple configurations in the $\upsilon_g = 2$ space, since the transition amplitudes do not contribute coherently to the transitions between the states with several configurations. Thus the observed enhanced B(E2) values of the $9^- - 8^-$ transitions, together with the hindered B(E2) values of the $7^- - 5^-$ transitions in $^{114-122}$Sn [2,9], serve as a salient illustration of the effect of the generalized seniority mixing. For the $8^- - 7^-$ transition, a more precise measurement of the mixing ratio is desirable to conclude whether the E2 transition is enhanced or not. The fact that the observed B(M1) values of the $9^- - 8^-$ transitions are less than those of the calculation might require larger amounts of the $(h_{11/2}d_{5/2})_8$-configuration of the 8^- state than the calculation.

In summary, the present experiment established the lifetimes of the 8^- and 9^- states in ^{110}Sn and ^{112}Sn. Large B(E2) values of about 170 e^2 fm^4 have been observed for the $9^- - 8^-$ transitions in both nuclei. Such large B(E2) values cannot be reproduced by the calculation with the $\upsilon_g \leqslant 2$ configurations but can be reproduced by the calculation with $\upsilon_g \leqslant 4$ configurations [3]. The small $\upsilon_g = 4$ admixtures of about 10–25% enhance the E2 transition rates between the high-spin negative-parity states with simple $\upsilon_g = 2$ configurations in ^{110}Sn and ^{112}Sn.

References

[1] W.F. van Gunsteren, E. Boeker and K. Allaart, Z. Phys. 267 (1974) 87.
[2] A. van Poelgeest, J. Bron, W.H.A. Hesselink, K. Allaart, J.J.A. Zalmstra, M.J. Uitzinger and H. Verheul, Nucl. Phys. A346 (1980) 70.
[3] G. Bonsignori, M. Savoia, K. Allaart, A. van Egmond and G. Te Velde, Nucl. Phys. A432 (1985) 389.
[4] J. Bron, W.H.A. Hesselink, A. van Poelgeest, J.J.A. Zalmstra, M.J. Uitzinger, H. Verheul, K. Heyde, M. Waroquier, H. Vincx and P. van Isacker, Nucl. Phys. A318 (1979) 335.
[5] T. Murakami, J. Kasagi, H. Harada and T. Inamura, Nucl. Instrum. and Methods A241 (1985) 172.
[6] F. Puhlhofer, Nucl. Phys. A280 (1977) 267.
[7] J. Kasagi, S. Nakagawa, N. Kishida, Y. Iritani and H. Ohnuma, J. Phys. Soc. Jpn. 43 (1977) 741.
[8] G. Goldring, in: Heavy ion collisions, Vol. 3, ed. R. Bock (North-Holland, Amsterdam, 1982).
[9] G.H. Carlson, W.L. Talbert Jr. and S. Raman, Nucl. Data Sheets 14 (1975) 247.

Reprinted from J. de Phys., 32, C1-326–C1-327 (1971).

MÖSSBAUER EFFECT OF ^{61}Ni IN SPINEL TYPE MAGNETIC OXIDES

H. SEKIZAWA, T. OKADA, S. OKAMOTO and F. AMBE
The Institute of Physical and Chemical Research, Yamato-Machi, Saitama, 351 Japan

Résumé. — La spectroscopie Mössbauer appliquée au ^{61}Ni a été utilisée pour étudier les champs magnétiques internes d'oxydes contenant du Nickel, de structure spinelle ou spinelle déformée. Les champs magnétiques internes dans des oxydes contenant des ions de Nickel en site octaédrique, ont été trouvés de l'ordre de 70 à 100 kOe. Dans $NiCr_2O_4$, où les ions de Nickel se trouvent sur des sites tétraédriques, nous avons mesuré un champ magnétique interne voisin de 450 kOe à la température de l'Hélium liquide. Cette valeur semble être la plus élevée jamais trouvée pour le ^{61}Ni.

Abstract. — The Mössbauer spectroscopy of ^{61}Ni was effectively utilized to investigate the internal magnetic fields in Ni-containing oxides with spinel or distorted spinel structure. The internal magnetic fields in oxides with the nickel ions in octahedral site were observed to be 70-100 kOe. In $NiCr_2O_4$, in which nickel ions are in tetrahedral site, an internal magnetic field amounting to 450 kOe was observed at liquid He temperature. This value seems to be the largest one ever observed for ^{61}Ni.

I. **Introduction.** — In spite of many experimentally undesirable nuclear properties, ^{61}Ni can be a powerful probe in solid state physics as the only Mössbauer nuclide other than ^{57}Fe in the iron group transition elements [1, 2, 3, 4], especially in the studies of internal magnetic fields.

The purpose of the present paper is to discuss the Mössbauer effect of ^{61}Ni in various Ni-containing oxides with spinel (or distorted spinel) structure.

II. **Experimental.** — The nuclear reactions,

$$^{58}\text{Ni}(\alpha, p)\,^{61}\text{Cu}$$

and ^{58}Ni(α, n) ^{61}Zn $\xrightarrow{\beta^+,\ EC}$ ^{61}Cu were utilized to produce the source nuclide ^{61}Cu. A thin Ni-V (84-16) alloy disc of about 20 mm in diameter was irradiated for several hours with 21 MeV α-particles from the 160 cm IPCR Cyclotron of this Institute, and was used as the source without annealing. The Ni-V (84-16) alloy crystallizes in f. c. c. structure and paramagnetic in nature. The specimens of various oxides were prepared by the convenient ceramic method, using nickel enriched with ^{61}Ni up to 80-90 %. An NaI(Tl) scintillation counter was employed to detect the transmitted radiation. The Mössbauer spectrometer made by Elron or the one by Hitachi was operated in constant acceleration mode with a 400 channel pulse height analyzer.

Because of the low resolution of the ^{61}Ni Mössbauer spectra, computer fitting of them to theoretical curves was an indispensable procedure to extract various parameters from the obtained spectra. Concerning the quadrupole moment of the excited state of ^{61}Ni, the rough estimation of -2 for the ratio Q_{ex}/Q_{gr} due to Erich [3], had been adopted tentatively in the analysis. Fortunately, the quadrupolar interactions in the spinels investigated turned out to be almost negligible compared with the magnetic interactions, except for a few cases mentioned in the text. The values of the isomer shift of the obtained spectra were also found to be of the order of the experimental uncertainty. Consequently, only the internal field is discussed in this paper, and the numerical values of the quadrupolar interaction and the isomer shift will not be presented.

III. **Results and discussion.** — The two groups of oxides with spinel (or distorted spinel) structure were investigated : the first group with the nickel ions in the octahedral site ($NiFe_2O_4$, $NiCo_2O_4$, $NiMn_2O_4$ and $GeNi_2O_4$), and the second group with the nickel ions in the tetrahedral site ($NiCr_2O_4$ and $NiRh_2O_4$).

1. THE SPINELS WITH NICKEL IONS IN THE OCTAHEDRAL SITE. — $NiFe_2O_4$: The Mössbauer spectrum at 80 °K is shown in figure 1. It is an almost symmetric pattern

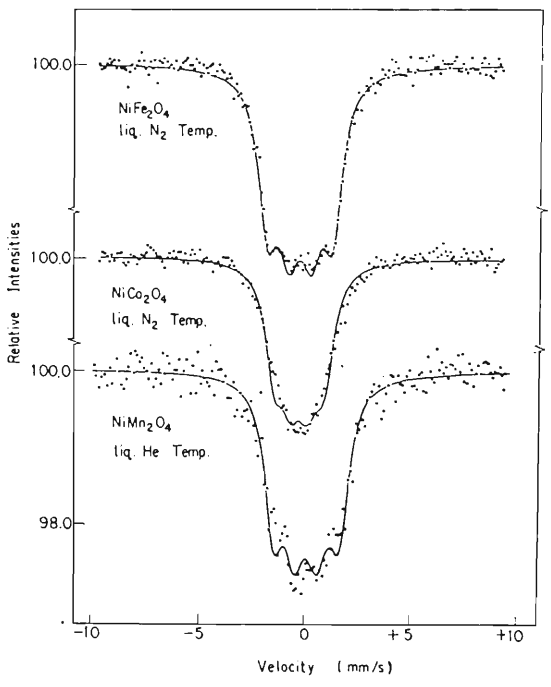

FIG. 1. — The ^{61}Ni-Mössbauer spectra of $NiFe_2O_4$, $NiCo_2O_4$, and $NiMn_2O_4$.

with noticeable peaks on the top, characteristic to a case with appreciable internal magnetic field H_i and negligible electric field gradient (EFG) effect. The value of H_i was found to be 94 kOe. This coincided with the value reported in [1], but the appreciable EFG effect reported therein had not been observed.

$NiCo_2O_4$: The absorption pattern at 80 °K is shown in figure 1. The values of H_i were 73 kOe and 87 kOe at 80 °K and at liquid He temperature, respectively.

$NiMn_2O_4$: According to the recent report by Boucher et al. [5], this spinel is incompletely inverse depending on the heat treatment. The fitting was made under the assumption of completely inverted ionic distribution, but the fitting at liquid He temperature was not very unsatisfactory with H_i of 97 kOe as can be seen in figure 1, and at 80 °K the best fit was obtained with H_i of 72 kOe.

$GeNi_2O_4$: The pattern at 80 °K, which is far above its reported Néel temperature of 16 °K, was slightly asymmetric suggesting that the EFG effect is working.

2. THE SPINELS WITH NICKEL IONS IN TETRAHEDRAL SITE. — $NiCr_2O_4$: As is well known, this oxide has cubic spinel structure at temperatures higher than 310 °K, below which it becomes tetragonal due to the Jahn-Teller effect of the Ni^{2+} ions in the tetrahedral sites. The ferrimagnetic Curie temperature is reported to be about 80 °K. According to Prince [6], the spin structure investigated by neutron diffraction is very complicated but the detailed spin structure is still unknown. At 80 °K, the spectrum seems to be slightly asymmetric with a width wider than the single line cases, as can be seen in the upper part of figure 2.

The most remarkable feature of this spinel is the widening of the pattern on cooling down to the liquid He temperature, as shown in the lower part of the same figure. The value of the internal magnetic field determined by the fitting amounted to 450 kOe, which seems to be the largest one ever reported for ^{61}Ni. Without data with an applied external magnetic field, detailed discussion of the possible origin of such a large field should be premature. However, contribution from the only incompletely quenched orbital moment of the Jahn-Teller distorted Ni^{2+} ions might be a possible mechanism to explain it.

$NiRh_2O_4$: The transition temperature from cubic to tetragonal symmetry is 380 °K, and the antiferromagnetic Néel temperature is reported to be 18 °K. The spectrum taken at 80 °K showed a noticeable asymmetry.

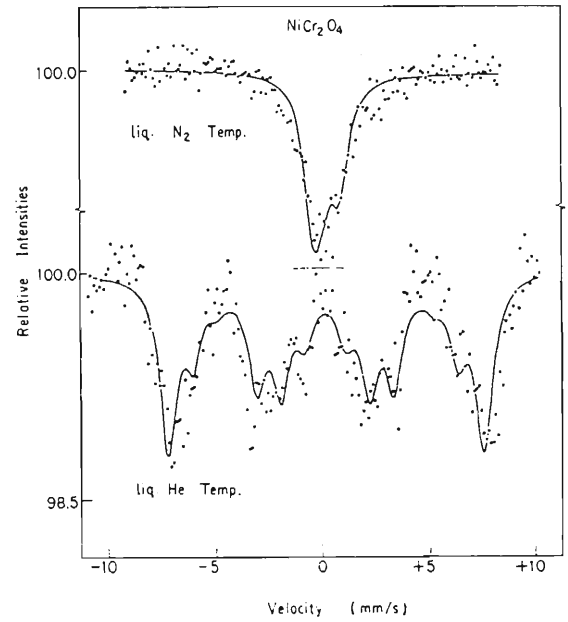

FIG. 2. — The ^{61}Ni-Mössbauer spectra of $NiCr_2O_4$.

IV. **Conclusion.** — A striking difference in magnitude of the internal magnetic field at ^{61}Ni nuclei has been observed between the spinel oxides with nickel ions in the octahedral site and $NiCr_2O_4$ with its nickel ions in the tetrahedral site. The former shows an internal magnetic field of the order of 70-100 kOe and a negligible EFG effect. The latter shows an internal magnetic field as high as 450 kOe, the origin of which is not yet established.

Acknowledgment. — The authors wish to express their sincere gratitude to the members of the Cyclotron Laboratory of this Institute for their earnest support given to this work. They are grateful also to Professors H. Watanabe and N. Saito for their continuing interest and encouragement.

References

[1] TRAVIS (J. C.) and SPIJKERMAN (J. J.), Mössbauer Effect Methodology, Vol. 4, Plenum Press (New York, 1968), 237.
[2] ERICH (U.), KANKELEIT (E.), PRANGE (H.) and HÜFNER (S.), *J. Appl. Phys.*, 1969, **40**, 1391.
[3] ERICH (U.), *Z. Phys.*, 1969, **227**, 25.
[4] OBENSHAIN (F. E.), LOVE (J. C.) and CZJZEK (G.), Proceedings of the 11th International Conference on Low Temperature Physics, Vol. 1, Univ. of St. Andrews (1968), 532.
[5] BOUCHER (B.), BUHL (R.) and PERRIN (M.), *J. Phys. Chem. Solids*, 1970, **31**, 363.
[6] PRINCE (E.), *J. Appl. Phys.*, 1961, **32**, 68 S.

Reprinted from J. Phys. Soc. Jpn., 35, 456–460 (1973).

Positron Annihilation in Ferromagnetic Nickel

Nobuhiro SHIOTANI, Takuya OKADA, Hisashi SEKIZAWA, Tadashi MIZOGUCHI†
and
Takashi KARASAWA

The Institute of Physical and Chemical Research, Wako-shi, Saitama 351
†Gakushuin University, Mejiro, Tokyo 171

(Received March 14, 1973)

The angular correlation of annihilation radiation in ferromagnetic nickel single crystals has been measured by using standard parallel-slit system with a newly developed ^{90}Nb positron source. The crystals were oriented in the [100] and [110] directions. The observed angular distribution curves were anisotropic with appreciable structures. Interpretation of the angular distribution in terms of the shapes of the Fermi surfaces alone were not successful, indicating that consideration of the Bloch character of the electrons in 3d bands is important.

§ 1. Introduction

The study of the properties of nickel has been of considerable importance for the theory of ferromagnetism, since it appears to be the simplest of the 3d elemental ferromagnets. The experimental results for transport properties, optical properties and the de Haas-Van Alphen effect in nickel have been successfully explained on the basis of the energy-band model, and the itinerant theory of magnetism has been found to be valid in principle.[1] There have been many calculations of energy bands in ferromagnetic nickel[2] using the APW method, the Green's function method, the combined interpolation method or the tight binding method. The general characters of the Fermi surfaces predicted by these calculations are qualitatively quite similar to each other. The de Haas-van Alphen data confirmed the existence of the hole pockets at the X points in the third highest band of the minority spin bands and the necks at the L points in the highest majority band. However, no experimental information about shape and size of the large electron surfaces in the highest majority and minority spin bands has been reported. The experiments reported in this paper were undertaken with an aim of studying the above mentioned electron surfaces in ferromagnetic nickel by means of positron annihilation.[3]

When the positrons annihilate in metals, two-quantum annihilation, which is known to be the overwhelmingly dominant process, takes place only from the singlet state of the positron-electron pair and two annihilation radiations are emitted into nearly opposite directions. From the conservation of momentum, the angular correlation of two annihilation radiations reflects the momentum distribution of annihilating positron-electron pairs. Since in metals the positrons are mostly thermalized before annihilation, the angular correlation measurement can be used to investigate the momentum distribution of the electrons and thus the shape of the Fermi surfaces in metals. Detailed experiments have been made on single crystals of various metals and alloys, including copper,[4-6] copper-zinc[7-9] and iron,[10] which are neighbors of nickel in the periodic system of elements. The calculations of the angular correlation curves based on the independent-particle model have also been undertaken and fairly good agreements with the experiments are achieved.

As a consequence of the non-conservation of parity in beta decay, the positron spin is partially polarized along their direction of motion. Using this property, the angular correlation experiment can also be used to study the spin dependent momentum distribution of electrons in ferromagnetic metals. Such investigations have been reported on single crystals of Fe,[10,11] Ni,[12,13] and Gd.[14] These experiments have been mainly concerned with measurement of the quantity $p(\theta)=(N_{\downarrow}(\theta)-N_{\uparrow}(\theta))/(N_{\downarrow}(\theta)+N_{\uparrow}(\theta))$, where $N_{\downarrow}(\theta)$ and $N_{\uparrow}(\theta)$ are the two photon counting rates at an angle θ corresponding to the specimen magnetization being parallel and antiparallel to the spin polarization of the positron beam, respectively.

In an independent particle approximation, the probability that an annihilation will yield two photons of total momentum $\hbar\boldsymbol{p}$ is proportional

to[15]

$$F(\boldsymbol{p})=\sum_{\boldsymbol{k},\sigma} n_{\boldsymbol{k},\sigma}|V(\boldsymbol{p},\boldsymbol{k},\sigma)|^2 , \qquad (1)$$

$$V(\boldsymbol{p},\boldsymbol{k},\sigma)\equiv\int \mathrm{d}\boldsymbol{r}\, \mathrm{e}^{-i\boldsymbol{p}\cdot\boldsymbol{r}}\, \Psi_{\mathrm{pos},-\sigma}(\boldsymbol{r})\Psi(\boldsymbol{k},\sigma,\boldsymbol{r}) . \qquad (2)$$

Here $\Psi(\boldsymbol{k},\sigma,\boldsymbol{r})$ is the electron wave function corresponding to wave number $\boldsymbol{k}$ and spin state σ, and $n_{\boldsymbol{k},\sigma}$ is the occupation number for the state $\boldsymbol{k}$ and σ. Ψ_{pos} is the positron wave function. Then the counting rate measured by the standard parallel-slit apparatus is proportional to

$$F(p_z)=\iint \mathrm{d}p_x\,\mathrm{d}p_y F(p_x,p_y,p_z) , \qquad (3)$$

where $p_z=mc\theta/\hbar$. In the simplest approximation that the electrons are in the plane wave state and the positron wave function is constant throughout the crystal, it is well known that the counting rate $N(\theta)$ is proportional to the cross sectional area of the Fermi sea. However, when the Bloch character is taken into account, a photon pair of total momentum p is resulted from annihilation of not only an electron in state $\boldsymbol{p}$ but also electrons in state $(\boldsymbol{p}+\boldsymbol{G})$'s the higher momentum components, where $\boldsymbol{G}$ is any reciprocal lattice vector.[16] For the transition metals, the s- and d-band electrons are far from free, and thus the physical interpretation of the quantity $p(\theta)$ is by no means straightforward. In the works on nickel oriented crystals cited above, the angular correlation was measured at an interval of about one milliradian with angular resolution of 2.5 milliradian and thus the shape of the angular correlation curves which may exhibit the structure of the Fermi surfaces could not be seen.

In § 2 of this paper, the experimental procedures to obtain angular correlation curves are briefly described. In § 3 the detailed angular correlation curves will be shown and qualitative discussion in connection with the Fermi surfaces will be given.

§ 2. Experimental

The angular correlation curves were taken by using a standard parallel-slit system and an external positron source. About 500 mCi ^{90}Nb positron sources were obtained by irradiation of Zr targets in the IPCR (Institute of Physical and Chemical Research) cyclotron. The reasons why ^{90}Nb was chosen as a source are as follows; the fraction of β^+ decay is over fifty percent, the maximum energy of β^+ is 1.5 MeV and thus the average degree of spin polarization of positron beam is higher than ^{58}Co, ^{22}Na or ^{64}Cu which are

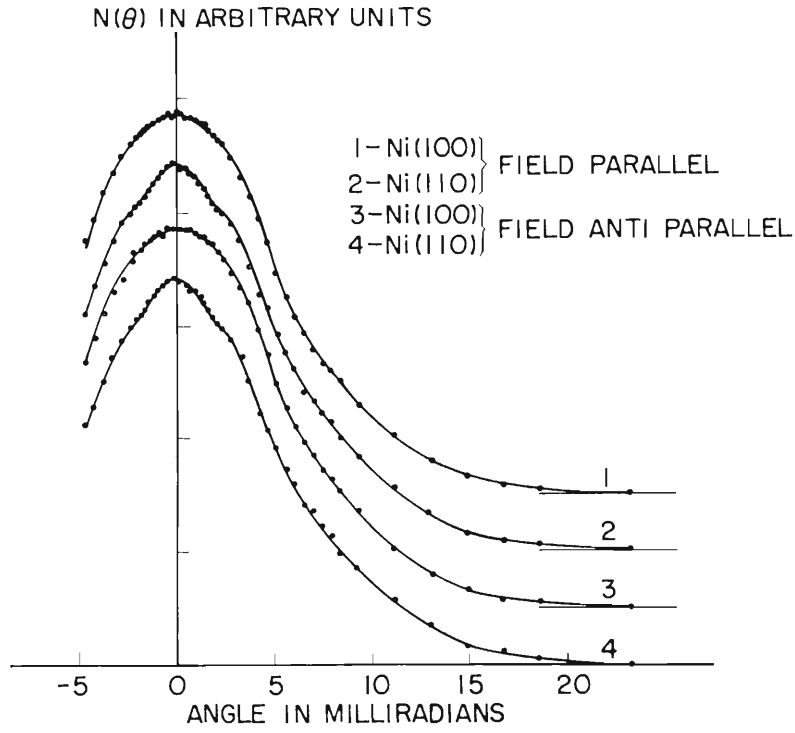

Fig. 1. The angular correlation curves for two crystal directions of nickel. The points are the experimental data and the solid curves are drawn through the experimental data by the procedure described in the text. Field-Parallel (Antiparallel) denotes that the direction of the magnetization of the specimen is parallel (antiparallel) to that of the polarization of positron spins. The curves are normalized to equal area.

commonly used, and the half-life (14.7 h) is suitable for actual production with the IPCR cyclotron. The detailed procedure to obtain carrier-free ^{90}Nb sources was described elsewhere by the authors.[17] A single crystal of 99.999 % purity was oriented and cut into (110) and (100) plates. The surface was first chemically etched to remove distortion introduced during mechanical cutting, then finished by electropolishing. Since the penetration depth of positrons from the source in the specimen is less than 0.5 mm, the surface of the specimen must be reasonably flat and free from distortion. The angular resolution defined by the slit system was measured to be 0.70 milliradian. The source was set to face the specimen. Both the source and the specimen were in a uniform magnetic field, the intensity of which was strong enough to align the net moment of the electron spins in the specimen either parallel or antiparallel to the direction of the positron beam.

The electronic circuit is a standard one with a resolving time of 200 nsec. The coincidence counting rate $N(\theta, t)$ was measured at an angle θ and the time t, which was defined to be the midpoint of the time interval of each counting. Due corrections were made on $N(\theta, t)$ for the decay of the source and the accidental coincidence. The final counting rate was obtained by summing up the counting rates of several runs with proper weights.

§ 3. Results and Discussion

Figure 1 shows the observed angular correlation curves for the [100] orientation and for the [110] orientation. The curves marked Field-Parallel were obtained under the condition that the direction of the magnetization of the specimen was parallel to the direction of the polarization of the positron spins. The curves marked Field-Antiparallel were obtained by reversing the direction of the magnetization of the specimen. The curves are normalized to give an equal area. The smoothed curves drawn through the experimental points were obtained by a procedure equivalent to evaluating at θ_i the least-squares polynomial of degree 3 relevant to the five successive points $(N(\theta_{i+k}), \theta_{i+k})$, $(k=-2, -1, \cdots, 2)$. No correction was made for the finite angular resolution of the apparatus.

It can be seen that the observed angular distribution is anisotropic. The (110) curves show a hump around $\theta=0$ milliradian, the shape of which depends on the direction of the magnetization of the specimen. The (100) curves show no hump around $\theta=0$ milliradian. On the slope of the angular correlation curves of both orientations no sharp cutoff was observed. Extending beyond the Brillouin zone boundaries, a pronounced bell-shaped component of angular distribution was found in both orientations.

According to the energy band calculations by Connolly,[18] the Fermi surface consists of four sheets for the minority spin bands and one in the majority spin bands. The minority spin sheets consist of small hole surfaces at the X points in the 3rd and the 4th bands, and a closed surface, called *d-s* surface, with protrusions along the [110] directions in the 5th band, and a closed surface, called *s-d* surface, of polyhedron-like shape with protrusions along the [100] and the [111] directions in the 6th band. The majority spin sheet, called *s* surface, is a multiply-connected surface with necks at the L points. The minority spin surface on the 6th band cuts the [110] axes at $\theta=3.1$ milliradian, and the [100] axes at $\theta=5.1$ milliradian. The majority spin surface in the 6th band cuts the [110] axes at $\theta=3.9$ milliradian, and the [100] axes at $\theta=5.2$ milliradian. The (110)-Brillouin zone boundaries and the (100)-Brillouin zone boundaries occur at $\theta=7.3$ and 6.9 milliradian, respectively.

The observed remarkable bell-shaped component of angular distribution extending beyond the zone boundaries is mainly due to annihilation with the electrons in the filled 3d bands. In annihilation with electrons in a filled band, due to the higher momentum components which stem from the Bloch character of the electrons, the angular distribution has no sharp cutoff and extends beyond the zone boundaries.[16] The annihilations with the electrons in the ion core below the *d* bands are much less important, since the positron is excluded from the inner core region by its Coulomb repulsion from the positively charged nuclei.

In order to evaluate the part of the angular distribution due to the electrons in the bands with Fermi surfaces, the bell-shaped component was subtracted from each angular correlation curve by fitting a Gaussian function in the region from about 8 to 20 milliradian. The resultant curves are shown in Fig. 2. To discuss the shapes of these curves, the cross sectional area of the three Fermi surfaces, the *s* surface in the majority spin band and the *s-d* and the *d-s* surfaces in the minority bands, was graphically derived along [100] and

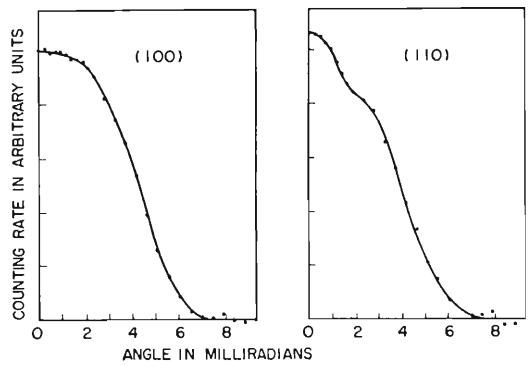

Fig. 2. The angular correlation curves with the bell-shaped filled band component being subtracted from each angular correlation curves in Fig. 1.

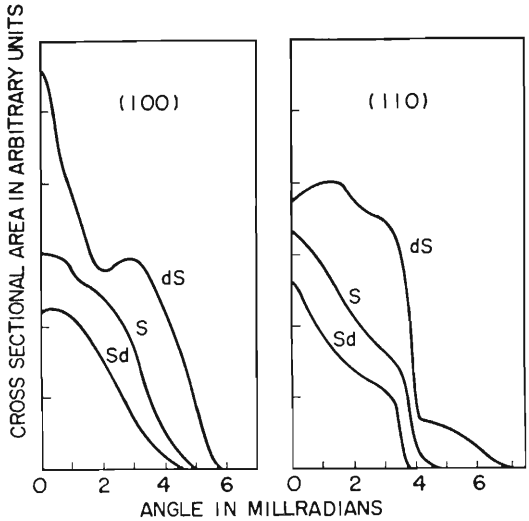

Fig. 3. The area of cross-sections of *s*, *s-d* and *d-s* Fermi surfaces perpendicular to [110] and [100] directions. The dimensions of the Fermi surfaces are taken from ref. 18.

[110] directions from the figures of the Fermi surfaces given by Connolly. From these, three angular distribution curves in terms of the shape of the Fermi surfaces alone were obtained and shown in Fig. 3. On comparing the experimental curves with them, admixture of angular distributions due to *s* and *s-d* surfaces seems to resemble general shapes of the observed curves. For a little more quantitative discussion, the observed angular correlation curves were tried to be fitted with above obtained curves by assigning appropriate weighting factors for the three Fermi surfaces. This roughly corresponds to a procedure in which the character and the $\boldsymbol{k}$-dependence of the electron wave function in the matrix elements of eq. (2) are neglected in evaluation of $F(p_z)$ of eq. (3), and only the averaged values of the matrix elements are taken into account by treating them as the weighting factors for the Fermi surfaces. Thus the weighting factor carries a rough estimation on the degree of contribution to the angular distribution from the electrons in the states below the *s*, *s-d* and *d-s* surfaces. The agreement turned out to be quite poor. This fact strongly indicates that the observed angular distribution can not be interpreted in terms of the shape of the Fermi surfaces alone and that the character and the $\boldsymbol{k}$-dependence of the wave function in the matrix elements in eq. (1) plays an important role for interpretation of the angular distribution in nickel. However, from the shape of the angular distribution due to the *s* surface, the hump around $\theta=0$ milliradian on the (110) curves may be interpreted as due to the existence of the protrusions of the Fermi surfaces for both spins of the 6th band. The necks at the *L* points are too small to be detected.

The statistical error of each point on the smoothed curves is about 0.7 % and is not small enough to be used to see the effect of reversing the direction of magnetization of the specimen. Therefore, the sectional area under the smoothed curve is calculated at an interval of about one milliradian and from this area an averaged value of $N(\theta)$, θ being taken as the middle point of the interval, is obtained. The differences at each point by reversing the direction of magnetization are plotted in Fig. 4. The fact that there exists net negative region at low angles and net positive region at high angles in the (110) difference curve agrees with the results obtained by Mihalisin.[13] However, in our curve the sharp dip exists between 4 and 5 milliradian.

In the (100) difference curve, no clear effect of reversing the magnetization could be detected. This is mainly due to the poor statistics.

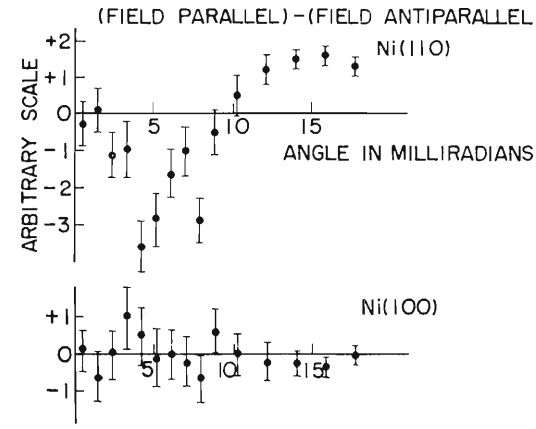

Fig. 4. The difference of the angular correlation curve with "parallel" magnetic field and that with "antiparallel" field, after the smoothing procedure described in the text.

Mihalisin[13] reported the effect but failed to determine the absolute sign of the differences. Later, Berko[11] reported the effect definitely. The difference curve by Berko showed a flat negative region at low angles (less than 8 milliradian) and the positive region at high angles. The negative sign must be critically examined by quantitative calculations of the angular correlation curves based on the band calculation such as the very recent work on iron by Mijnarends.[10]

Acknowledgements

We are grateful to Dr. S. Okano and the members of the Radiation Laboratory of our Institute for valuable suggestions and kind permission to use their electronic facilities. We would like to thank S. Tanaka, M. Iwasaki, and H. Masuda for technical assistance. Continued interests of Professors R. R. Hasiguti and H. Watanabe are gratefully appreciated.

References

1) A. P. Cracknell: *The Fermi Surface of Metals* (Taylor and Francis, London, 1971).
2) A review of the subject is given by J. O. Dimmock, in Solid State Phys. **26** (1971) 167.
3) A review of the subject is given by A.T. Stewart and by S. Berko, *Positron Annihilation*, ed. A. T. Stewart and L. O. Roellig (Academic Press Inc., New York, 1967).
4) K. Fujiwara and O. Sueoka: J. Phys. Soc. Japan **21** (1966) 1947.
5) O. Sueoka: J. Phys. Soc. Japan **23** (1967) 1246.
6) P. E. Mijnarends: Phys. Rev. **178** (1969) 622.
7) W. Triftshauser, A. T. Stewart and R. Taylor: J. Phys. Chem. Solids **35** (1971) 2711.
8) W. Triftshauser and A. T. Stewart: J. Phys. Chem. Solids **32** (1971) 2717.
9) S. Tanigawa, S. Nanao, K. Kuribayashi and M. Doyama: J. Phys. Soc. Japan **31** (1971) 1689.
10) P. E. Mijnarends: Physica **63** (1973) 235, 248.
11) S. Berko and A. P. Mills: J. phys. **32** (1971) C1-287.
12) T. W. Mihalisin and R. D. Parks: Phys. Rev. Letters **18** (1967) 210.
13) T. W. Mihalisin and R. D. Parks: Solid State Commun. **7** (1969) 33.
14) C. Hohenemser, J. M. Weingart and S. Berko: Phys. Letters **28 A** (1968) 41.
15) S. DeBenedetti, C. E. Cowan, W. R. Konneker and H. Primakoff: Phys. Rev. **77** (1950) 205.
16) S. Berko and J. S. Plaskett: Phys. Rev. **112** (1958) 1877.
17) N. Shiotani, S. Ambe, T. Okada and T. Karasawa: Japan. J. appl. Phys. **11** (1972) 412.
18) J. W. Connolly: Phys. Rev. **159** (1967) 415.

Reprinted from Phys. Rev. A, 13, 992–999 (1976).

K and L x rays induced by 5-MeV/amu α-particle and nitrogen-ion bombardment of ten target elements ranging from Cr to Bi

Yohko Awaya, Koichi Izumo, Tatsuji Hamada, Masaharu Okano, Tan Takahashi, A. Hashizume, Yoshihiko Tendow, and Takeo Katou

The Institute of Physical and Chemical Research, Wako-shi, Saitama, 351 Japan

(Received 14 May 1975)

The K and L x rays from ten target elements from Cr to Bi bombarded by 5-MeV/amu α particles and N ions were measured by a Si(Li) detector. Energy shifts of K x rays and intensity ratios of $K\beta/K\alpha$, $L\alpha/Ll$, $L\alpha/L\beta$, $L\alpha/L\gamma$, and L/K were determined by analyzing the experimental results. The ratio of the reduced K-shell ionization cross sections, R_{2K}, showed a systematic deviation from the Z_1^2 dependence.

I. INTRODUCTION

In recent years, many studies have been made of the x rays induced by heavy-ion bombardments. Two kinds of excitation mechanisms of the inner-shell electrons have been discussed and applied to interpret experimental results. One is the electron promotion caused by the formation of quasi-molecular orbitals during the collision time, and the other is the direct Coulomb excitation between the projectile and the bound electron.

The former prevails for the case of $Z_1 \simeq Z_2$ and $v_1 < v_2$ where Z_1 and Z_2 are the atomic numbers of the projectile and the target atom and v_1 and v_2 are the velocities of the projectile and of the bound electron to be excited, respectively. The electron promotion model[1] has explained the large cross section for creating the inner-shell vacancy under these conditions. Many experimentally observed phenomena, such as the level-matching effect and molecular-orbital x rays, have been interpreted with this mechanism.

The latter dominates when v_1 is so high that the projectile is deemed to be a bare nucleus or when the condition of $Z_1 \ll Z_2$ holds even though v_1 is not so high. The plane-wave Born approximation[2] (PWBA) and the binary-encounter approximation[3] (BEA) have been applied mainly for this case, in which the cross section for creating the K-shell vacancy is represented universally by using reduced parameters. Both approximation methods predict a Z_1^2 dependence of the cross section; the prediction has been compared with extensive experimental work done with light projectiles ($Z_1 \leq 2$).[4] Detailed studies,[5-8] however, have shown deviation of the cross section from the Z_1^2 dependence, which can be attributed to a Z_1^3-dependent term in addition to the Z_1^2-dependent part.

In the case where the swift heavy ions are used as projectiles and $Z_1 \ll Z_2$, however, experimental data are not so abundant. Saltmarsh *et al.*[9] have studied the energy shift of K x rays and $K\beta/K\alpha$ intensity ratios by bombarding Ti, Fe, Co, Zr, and Sn targets with 5-MeV/amu He, C, O, and Ne and 10-MeV/amu C ions and suggested that the Coulomb excitation mechanism is applicable to the explanation of experimental results. Van der Woude *et al.*[10] and Cue *et al.*[11] have deduced the existence of a Z_1^3 dependence for 5- and 7.1-MeV/amu heavy ions, respectively. Li and Watson[12] have measured the $K\beta/K\alpha$ intensity ratios of K x rays emitted from targets of $19 \leq Z_2 \leq 47$ following ionization by deuterons, α particles, and C ions.

The aim of the present work is twofold. The first is to obtain more systematic information about the mechanism of vacancy formation in inner shells by bombarding ten target elements ranging from Cr to Bi with 5-MeV/amu α particles and N ions. The energy shift of K x rays and the deviation from the Z_1^2 dependence of the cross section have been studied for this purpose. The amount of deviation from the Z_1^2 dependence has been plotted against a reduced parameter that includes characteristic quantities of projectiles and target atoms. The second is to provide additional K- and L-x-ray data induced by heavy-ion impact, especially for the elements heavier than $Z_2 \simeq 50$, since in this mass region data are less available than in lighter elements. The preliminary results of this work have been reported.[13]

II. EXPERIMENTAL METHOD

Beams of α particles and N^{4+} ions accelerated by the cyclotron of the Institute of Physical and Chemical Research were led to a target chamber whose section perpendicular to the beams was square. The frame of the target chamber and the target holder were made of aluminum and the four walls parallel to the beams were made of Lucite plates to reduce the x-ray background at a detector. The incident energy of both projectiles was 5 MeV/amu. A target was placed at an inclination

of 45° with respect to the beam and the detector. The x rays from the target induced by the beam bombardment were detected by a Si(Li) x-ray detector which was placed perpendicular to the beam direction. The energy resolution of the detector was 270 eV (full width at half-maximum) at 6.4 keV. Between the target and the detector, there were two 50-μm Be foils, i.e., the windows of the target chamber and the detector, in addition to an air space of about 7 mm.

The relative efficiency of the detector was determined with the same source-detector arrangement by using x and γ rays from radioisotopes ^{54}Mn, ^{57}Co, ^{65}Zn, ^{109}Cd, ^{137}Cs, ^{203}Hg, and ^{241}Am. The effects on the efficiency of the experimental conditions were thus taken into account.

Target elements studied were $_{24}$Cr, $_{26}$Fe, $_{29}$Cu, $_{38}$Sr, $_{47}$Ag, $_{56}$Ba, $^{142}_{60}$Nd, $_{71}$Lu, $_{82}$Pb, and $_{83}$Bi. These target elements were chosen from the following three points of view: (i) They were appropriately distributed in the periodic table. (ii) Each of them has a corresponding, easily available radionuclide which emits the same characteristic x rays for use as the energy standard for measuring the energy shift. (iii) We have paid attention to the existence of excited state in the target nuclei, which decays with a large conversion coefficient because the energy of the projectile was high enough to induce nuclear events. Such an excited state can be fed not only through the Coulomb excitation but also through the decay chain of produced radioactivities by (α,xn) or (N,xn) reactions. This contribution becomes important for the targets with higher atomic number as the K-vacancy production cross section decreases with target atomic number. For this sake, it is desirable that the energy of the first excited state of the target nucleus is high and the lifes of the induced radioactivities are as long as possible. The isotopically enriched target of Nd was used for this reason. To check the contribution of the nuclear Coulomb excitation and nuclear transition, γ-ray spectra were measured by using a Ge(Li) detector but their contribution could be neglected except for Lu. The energy of the first excited state of ^{175}Lu is so low that the γ transition from this to the ground state was observed as well as x rays. The contribution of this nuclear transition was subtracted from the yield of K x rays.

The targets of Cr, Fe, Cu, Ag, Pb, and Bi were prepared by evaporating these metallic elements on the backing, while the others were made by sedimentation of their insoluble compounds. Mylar films of 4-μm thickness were used as the backing except for Ag. A thinner Formvar film was used for Ag, since the x-ray spectrum obtained by bombarding a Mylar film had a hump in the vicinity of the position of Ag L x rays which would originate in the impurity elements in the film. Thickness of the target materials ranged from about 20 μg/cm^2 for Cr to 350 μg/cm^2 for Bi.

During the measurement of x rays, the counting rate was kept below 300 sec^{-1} in order to reduce the pileup effect. The number of projectiles was determined from a measurement of the integrated beam current by a combination of a picoammeter and a current integrator and a value for an effective charge of projectiles. By referring to the work on the charge exchange for N^{4+} ions[14] and considering the target thickness, the charge distribution was considered to be in equilibrium. Thus the value[15] of 6.9 was taken for the effective charge of N ions at the Faraday cup.

For N ions, the energy shift of x rays was observed and, for some target elements, the energy of some $K\beta_2$ satellites became higher than the K absorption edge. For L x rays, the energies of some components are larger than the L_3 or L_2 absorption edge in nature. In order to estimate the amount of absorption in the target, the yield of x rays was measured with and without inserting between the two Be windows a spare target whose thickness was almost the same as the target to be bombarded. As the amount of the absorption was found to be smaller than 2%, the correction for this effect was omitted. For measurements of K x rays from elements heavier than Ag, some absorbers were inserted between the two Be windows to reduce the L x rays. A correction was made for the absorption of K x rays by these absorbers.

III. RESULTS AND DISCUSSION

A. Spectrum

In the low-energy region of x-ray spectra a continuous energy distribution of photons was always observed as a background. From the pattern of the spectra and the dependence on the incident energy, this was found to be due to the bremsstrahlung from recoil electrons (δ rays) created by the projectiles within the target.[16] For protons, a precise study has been made by Folkmann *et al.*[17] Examples of this spectrum are shown in Fig. 1 together with the calculated curve fit to the experimental data. The position of the estimated end-point energy, $\sim 2.2E_0$ keV, is shown by an arrow, where E_0 (in MeV) is the incident-particle energy per nucleon.

The peak position and the peak area of the characteristic x rays were determined by using a χ^2 fit, assuming the shape of a peak to be Gaussian. The pattern of the background under the peak was usually assumed to be linear with the channel

number. An exponential background, however, was assumed for some L x rays, since their background was attributed to the bremsstrahlung described above and was estimated from background counts in two energy regions several keV apart. Unresolved peaks were also separated by the same method. In the case of L x rays, which consist of many components, the peak separation was made by referring to transition probabilities[18] and tables of x-ray energies.[19]

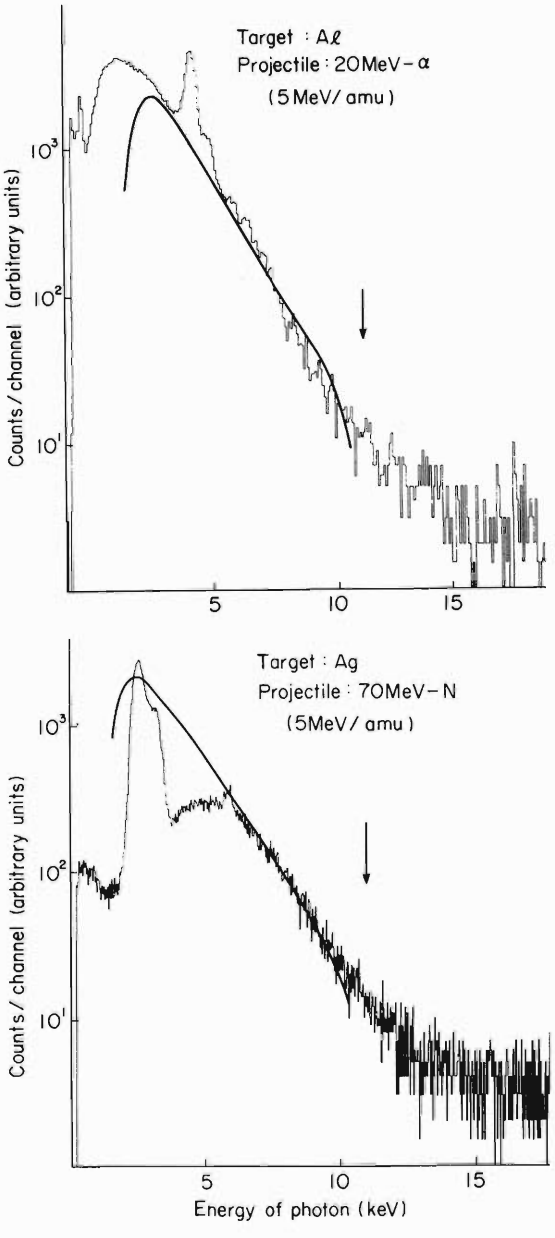

FIG. 1. X-ray spectra obtained for α-particle and N-ion bombardment, showing the continuous background in the low-energy region. Experimental conditions are indicated in each figure. The arrows mark the position of end-point energy by our estimation.

Typical spectra of K and L x rays observed for α-particle and N-ion bombardments and those from the corresponding radioisotopes are shown in Figs. 2 and 3.

Error bars in Figs. 2–9 and errors in Tables I and II include errors in the counting statistics, in the background subtraction, in the relative counting efficiency and energy calibration of the detector, and in fitting the peak to a Gaussian curve.

B. Energy shift

The energy shift of characteristic x rays induced by heavy-ion impact has been reported by many authors since Richard *et al.*[20] studied the energy shift of the $K\beta$ lines of Cu and Ni. The origin of the shift has been attributed to the multiple excitation of inner-shell electrons.[21,22] The amount of the K-x-ray energy shift seems to depend on the cross section for the creation of L vacancies. By the prediction of the PWBA or BEA, this cross section will take a maximum value under the condition $E/\lambda u_L \simeq 1$, where E is the energy

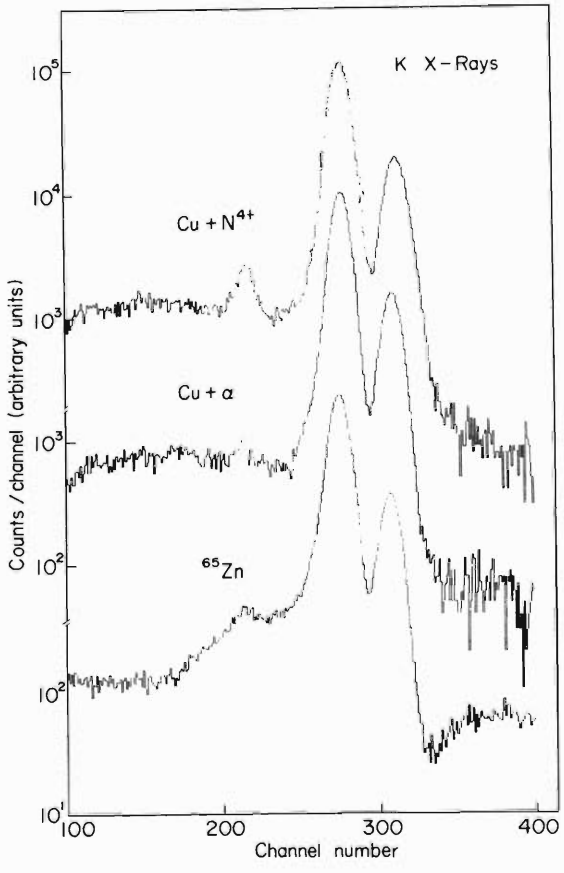

FIG. 2. Spectra of K x rays obtained by N-ion and α-particle bombardment of the Cu target and by the decay of ^{65}Zn.

of the projectile, λ is the ratio of projectile mass (m_1) to the electron mass (m_e), and u_L is the average binding energy of target L electrons. Saltmarsh *et al.*[9] have studied this effect by measuring the Ti and Fe K-x-ray energy shift as a function of the bombarding energy of O ions. They plotted the $K\alpha$ and $K\beta$ energy shift against $E/\lambda u_L$ for Fe and Ti targets, respectively, and found that the maximum occurs at $E/\lambda u_L \simeq 1.3$.

Similar plots were made for the present data and the results are shown in Fig. 4. In the present case, u_L was varied while E was kept constant. The amount of the energy shift of x rays was estimated by comparing the peak position in the spectra obtained for the particle-excited target with that for the corresponding radioisotopes of ^{54}Mn, ^{57}Co, ^{65}Zn, ^{88}Y, ^{109}Cd, ^{137}Cs, ^{143,144}Pm, ^{175}Hf, and ^{207}Bi. When they decay by the electron-capture process or when the excited states of their daughter nuclei decay by the internal conversion process, they emit the same characteristic x rays as those from the corresponding target elements.

The amount of $K\alpha$ energy shift increases until $E/\lambda u_L$ rises to about 1.3 and after that becomes almost constant. When the $K\alpha_1$ and $K\alpha_2$ lines could be separated, their shifts were found to be almost the same. The shift of $K\beta_1$ x rays has a maximum at $E/\lambda u_L \simeq 1.2$. The value of $E/\lambda u_L$ where the amount of $K\alpha$ and $K\beta_1$ energy shifts has a maximum in the present result agrees very well with that of Saltmarsh *et al.* even though the variable quantity in the parameter $E/\lambda u_L$ is different in these two works.

The amount of the energy shift of $K\beta_2$ x rays was plotted as a function of $E/\lambda u_M$, where u_M is the average binding energy of M-shell electrons, instead of a function of $E/\lambda u_L$. If one wants to plot this value against $E/\lambda u_L$ one should refer to the element symbol shown in the figures. Then the maximum of the shift of $K\beta_2$ line, which is found at $E/\lambda u_M \simeq 3$, is displaced to $E/\lambda u_L \simeq 0.5$. On the contrary, when the values of $K\beta_1$ energy shift are plotted as a function of $E/\lambda u_M$ the maximum will be found at $E/\lambda u_M \simeq 13$.

These effects may be explained qualitatively as follows: When we consider an electron in a specified shell, its binding energy is affected more

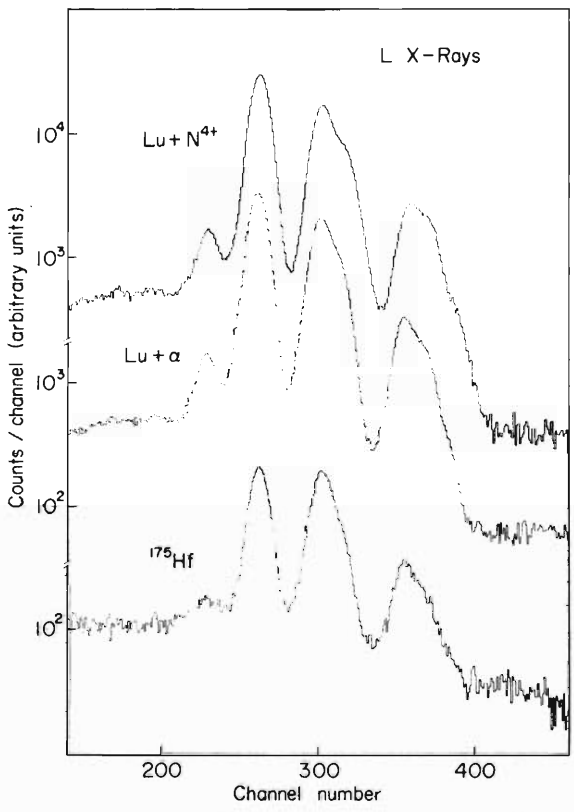

FIG. 3. Spectra of L x rays obtained N-ion and α-particle bombardment of the Lu target and by the decay of ^{175}Hf.

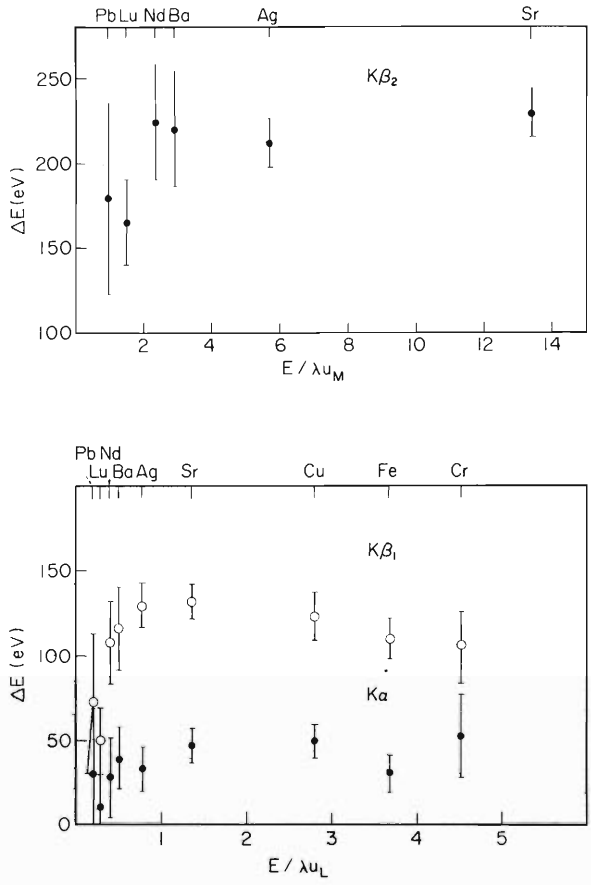

FIG. 4. Energy shift of $K\alpha$, $K\beta_1$, and $K\beta_2$ x rays for N-ion bombardment. The name of the target element corresponding to each experimental point is also shown. The transformation of the abscissa from $E/\lambda u_L$ to $E/\lambda u_M$, or vice versa, can be made by referring to the element symbols.

strongly by the vacancies in inner shells than by those in outer shells. Hence the vacancies in the L shell show a more marked effect on the shift of $K\beta_1$ lines than on that of $K\alpha$ lines and the definite maximum is seen in the $K\beta_1$ energy shift. The vacancies in the M shell also contribute to the shift of these x rays, but their contribution is rather masked by the effect of L vacancies.

For the shift of $K\beta_2$ x rays, the vacancies in the M shell play a more important role than for those of $K\beta_1$ and $K\alpha$ x rays, since $K\beta_2$ x rays are emitted by the transition from the N shell to the K shell. The amount of the energy shift which originates in the M-shell vacancies would have a maximum at $E/\lambda u_M \simeq 1$. The maximum, however, is seen at $E/\lambda u_M \simeq 3$, and this difference is considered to be caused mainly by the additive vacancies in the L shell.

C. Intensity ratios of x-ray components

It has been found that the $K\beta/K\alpha$ intensity ratios observed for heavy-ion bombardments were different from those for photoionization, electron bombardment, and radioisotope decay. The cause of this difference has been attributed to the multiple ionization.[21-23] Recently, Li and Watson[12] measured the $K\beta/K\alpha$ intensity ratio for the elements between K and Ag using 2.35–12.5-MeV/amu deuterons, α particles, and N ions. They also studied the variation of $K\beta/K\alpha$ with electronic configurations of L and M shells.

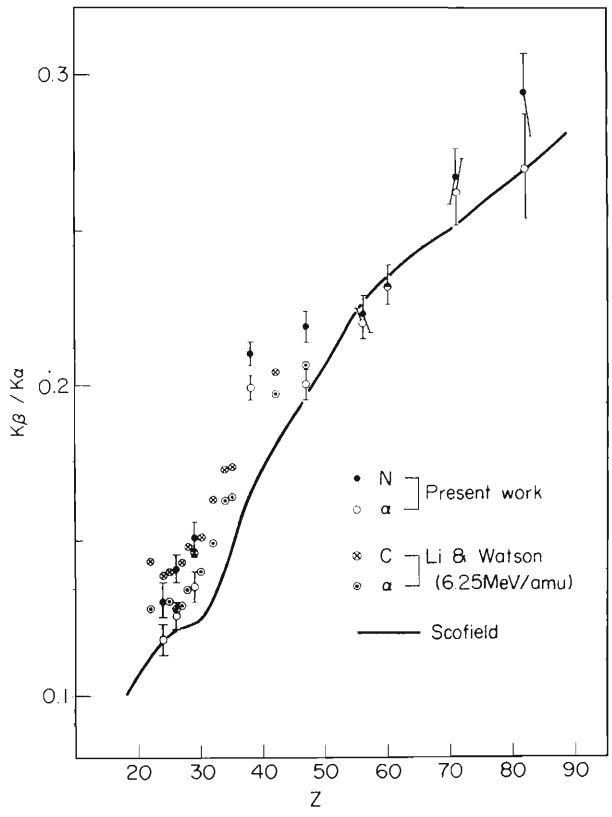

FIG. 5. $K\beta/K\alpha$ values obtained by N-ion and α-particle bombardment. The data for 6.25-MeV/amu α-particle and C-ion impact (Ref. 12) and the calculated curve by Scofield (Ref. 18) are also shown for comparison.

TABLE I. $K\alpha/K\beta$ intensity ratios for K x rays induced by 5-MeV/amu α particles and N ions.

Target element	α particles	N ions
$_{24}$Cr	0.118 ± 0.004	0.131 ± 0.005
$_{26}$Fe	0.126 ± 0.003	0.141 ± 0.004
$_{29}$Cu	0.135 ± 0.005	0.151 ± 0.005
$_{38}$Sr	0.199 ± 0.004	0.210 ± 0.004
$_{47}$Ag	0.200 ± 0.005	0.223 ± 0.005
$_{56}$Ba	0.220 ± 0.004	0.223 ± 0.006
$_{60}$Nd	0.232 ± 0.006	0.232 ± 0.007
$_{71}$Lu	0.262 ± 0.011	0.267 ± 0.009
$_{82}$Pb	0.270 ± 0.017	0.294 ± 0.013

The $K\beta/K\alpha$ ratio obtained in this work is shown in Fig. 5, and the values are listed in Table I. For comparison the figure includes the data obtained by Li and Watson for 6.25-MeV/amu α particles and C ions and the curve calculated by Scofield.[18] The present data seem to agree well with the data obtained by Li and Watson, within the limit of error. The ratio of $K\beta/K\alpha$ for N ions and α particles, $(K\beta/K\alpha)_N/(K\beta/K\alpha)_\alpha$, is larger than unity, as shown in Fig. 6, and this also agrees with the results obtained by Li and Watson.

It was difficult to obtain precise intensity ratios of L-x-ray components, such as $L\alpha_1/L\alpha_2$ or $L\beta_{2+15}/L\alpha_1$, because of the insufficient energy resolution. We obtained the values of $L\alpha/Ll$, $L\alpha/L\beta$, and $L\alpha/L\gamma$ ratios. When the intensities of $L\beta$ and $L\gamma$ x rays were estimated, the $L\beta$ and $L\gamma$ lines were separated into a few main components by the χ^2-fitting method as described above and each peak area was corrected by using the detection efficiency for each peak energy. The

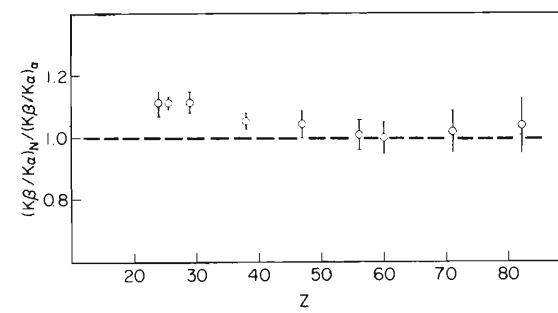

FIG. 6. Ratio of $K\beta/K\alpha$ for N-ion and α-particle bombardment.

results are shown in Fig. 7 in comparison with calculated curves. The solid curve for the $L\alpha/Ll$ ratio is the value calculated by Scofield.[18] The dashed curves for the $L\alpha/L\beta$ and $L\alpha/L\gamma$ ratios were obtained in the following way: Intensity ratio of two x rays is expressed as (intensity ratio) = (ratio of vacancy-production probabilities) × (ratio of transition probabilities) × (ratio of fluorescence yields). The term of the ratio of transition probabilities is calculated using the results by Scofield. In calculating the ratios, the same fluorescence yield and ionization cross section of an orbital electron were taken for each transition contributing to a given line intensity. Then the term for the ratio of fluorescence yields can be eliminated and the term for the vacancy-production probabilities can be represented by the ratio of the numbers of electrons in the lower orbits where vacancies will be produced.

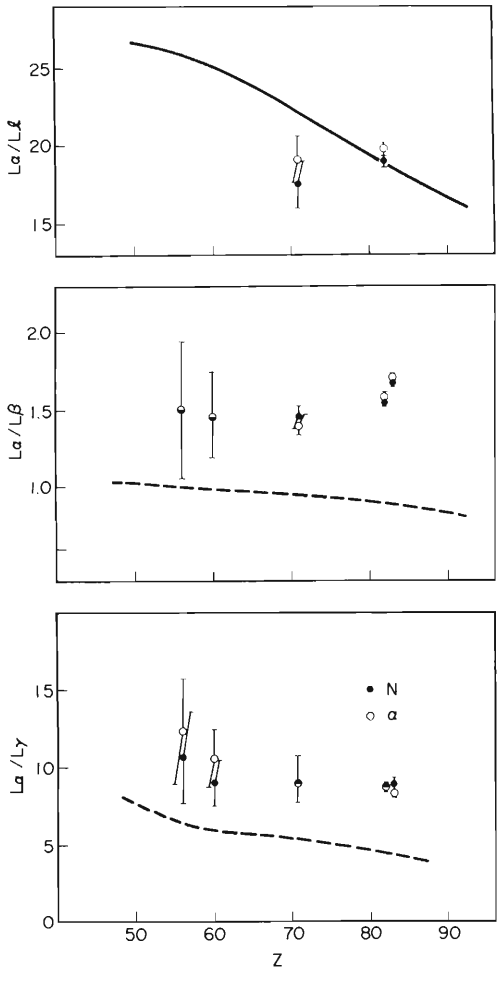

FIG. 7. $L\alpha/Ll$, $L\alpha/L\beta$, and $L\alpha/L\gamma$ values obtained by α-particle and N-ion bombardment. The solid curve for $L\alpha/Ll$ calculated by Scofield (Ref. 18) is also shown. The dashed curves for $L\alpha/L\beta$ and $L\alpha/L\gamma$ are those estimated on the basis of the calculation done by Scofield.

As is seen in Fig. 7, the experimental values for α-particle and N-ion impact are the same for all target elements within the limits of uncertainty. From this fact it might be deduced that in the outer shells α particles and N ions give similar effects on ionization. The calculated values for $L\alpha/L\beta$ and $L\alpha/L\gamma$, on the other hand, are about one-half of the experimental values for both ratios throughout the region of atomic numbers of the targets employed. But the variations with atomic number are systematically parallel for the calculated and experimental ratios. Therefore the discrepancy between the two values of the ratio could be attributed to the difference between the ionization cross section of L_3 electrons ($L\alpha$ x rays originate from the transition to the L_3 hole) and that of L_2 electrons (main components of $L\beta$ and $L\gamma$ x rays originate in the transition to the L_2 hole).

The ratios of K- and L-x-ray yields for α-particle and N-ion bombardment are shown in Fig. 8. The difference between the two ratios increases as the atomic number of the target atom decreases. The L-x-ray yield relative to that of K x rays for N-ion bombardment is about a factor of 2 larger than that for α-particle bombardment. This may be due to the change of the fluorescence yield and the effect of polarization of orbital electrons.

D. Z_1^2 dependence

The PWBA predicts the Z_1^2 dependence of ionization cross section, that is, in the case of K-shell ionization

$$R_{2K} \equiv \frac{\sigma_{2K}(Z_1')/Z_1'^2}{\sigma_{2K}(Z_1)/Z_1^2} = 1$$

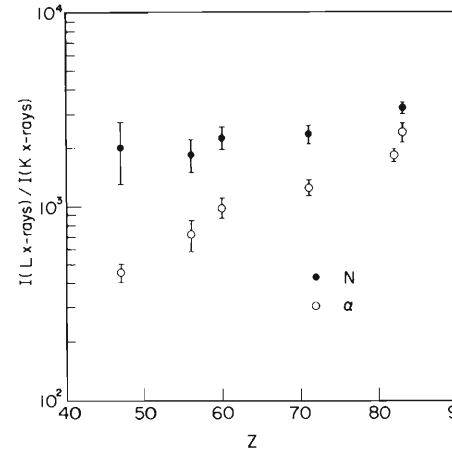

FIG. 8. Intensity ratio of K and L x rays obtained by N-ion and α-particle bombardment.

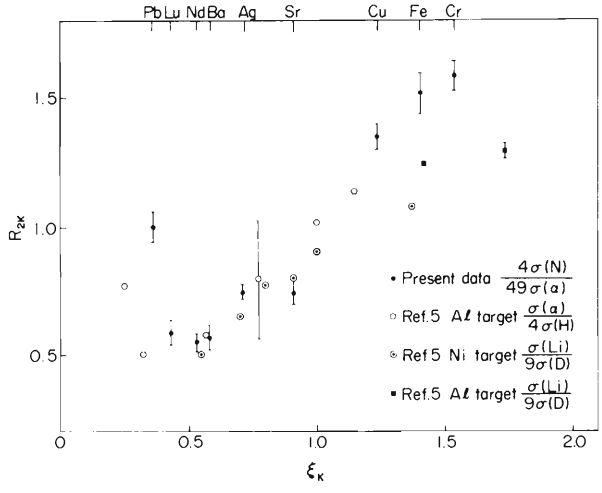

FIG. 9. Ratios R_{2K} of K-shell ionization cross sections as a function of ξ_K. The name of the target element corresponding to each experimental point in the present work is also shown. The results obtained by Basbas *et al.* (Ref. 5) are shown for comparison. Though their data have many more points, some of them are neglected as the points show a smooth curve. The abscissa of their data is converted from v_1/v_{2K} to ξ_K by reading the values of $\frac{1}{2}\theta$ from their figure.

if the incident projectile energies per nucleon are the same, where $\sigma_{2K}(Z_1)$ is the K-shell ionization cross section of the target atom of atomic number Z_2 for the incident charged particle of atomic number Z_1. Some experimental studies, however, showed the deviation from the Z_1^2 dependence in the K-shell ionization cross sections.[5-8,10,11] The cause of this deviation would be twofold, i.e., the increase of binding energy of target electrons (prevailing at $v_1 < v_{2K}$) and the polarization of them (prevailing at $v_1 \gtrsim v_{2K}$), where v_{2K} is the velocity of a K electron of a target atom ($v_{2K} = Z_{2\text{eff}} e^2/\hbar$, $Z_{2\text{eff}} = Z_2 - 0.3$). These two effects show a Z_1^3 dependence and give contributions with opposite signs to the cross section. They cancel each other, giving a ratio R_{2K} of unity, at $v_1/v_{2K} = \frac{1}{2}\theta_K$, or $\xi_K = v_1/(\frac{1}{2}\theta_K v_{2K}) = 1$, where $\theta_K = 2I_{2K}/Z_{2\text{eff}}^2$ and I_{2K} (in a.u.) is the ionization energy of a K-shell electron.

The Z_1^3 dependence has been studied precisely for light-particle impact. As to heavy-ion impact, Van der Woude *et al.*[10] have suggested this dependence in their experiments with 5-MeV/amu α-particle and C-, O-, and Ne-ion bombardment. Cue *et al.*[11] studied this contribution for 7.1-MeV/amu α-particle and B-, C-, N-, O-, F-, and Ne-ion bombardment on Cd, Y, Fe, and Ca. The former plotted R_{2K} vs $E/\lambda u_K$ and found that R_{2K} crosses unity at $E/\lambda u_K \simeq 0.25$. The latter analyzed their results for R_{2K} for each target element and concluded that their results are explicit

TABLE II. Values of ξ_K and R_{2K}. $\xi_K = v_1/\frac{1}{2}\theta_K v_{2K}$, $\theta_K = 2I_{2K}/Z_{2\text{eff}}^2$, $v_{2K} = Z_{2\text{eff}} e^2/\hbar$, $Z_{2\text{eff}} = Z_2 - 0.3$, and $R_{2K} = 4\sigma(N)/49\sigma(\alpha)$.

Target element	ξ_K	R_{2K}
$_{24}$Cr	1.56	1.59 ± 0.05
$_{26}$Fe	1.42	1.52 ± 0.08
$_{29}$Cu	1.26	1.35 ± 0.05
$_{38}$Sr	0.92	0.74 ± 0.04
$_{47}$Ag	0.71	0.75 ± 0.03
$_{56}$Ba	0.58	0.57 ± 0.05
$_{60}$Nd	0.53	0.55 ± 0.03
$_{71}$Lu	0.43	0.61 ± 0.05
$_{82}$Pb	0.36	1.03 ± 0.06

evidence for the existence of a Z_1^3-dependent term and that the two competing effects mentioned above cancel each other at $\xi_K = 1.04$, i.e., for the Y target.

The result of the present work is shown in Fig. 9. The data of Basbas *et al.*[5] for protons, deuterons, and Li ions as projectiles have been adapted to Fig. 9 for comparison by converting the parameter v_1/v_{2K} to ξ_K by graphical reading. Their data include many more points than plotted in Fig. 9, where only typical points are referred to. Numerical values of the present data are listed in Table II.

Values of R_{2K} are plotted as a function of ξ_K because contributions of the two above-mentioned effects on R_{2K} depends on the parameter ξ_K as a whole, not individually on Z_2, v_{2K}, and v_1. The fluorescence yield ω_K for N-ion impact is assumed to be the same as for α-particle bombardment. The ω_K increases in the case where multiple excitation occurs, but this effect is not considered to be very large in the present case. The dependence of R_{2K} on ξ_K is very similar for both data, especially for $\xi_K < 1$, and shows a clear deviation from Z_1^2 dependence of the ionization cross section. As is seen in Fig. 9, the two effects cancel at $\xi_K \simeq 1$, which is consistent with the results of Cue *et al.* and Van der Woude *et al.* cited above, where the value of $E/\lambda u_L \simeq 0.25$ corresponds to the value of $\xi_K \simeq 1.2$. For the elements corresponding to $\xi_K > 1$, that is, Cr, Fe, and Cu, the change of ω_K for N-ion impact may be greater than that for the heavier elements. In addition to the effect of polarization, some amount of the deviation might be due to this factor.

The points at $\xi_K < 0.5$ deviate from the line which means the existence of the Z_1^3-dependent term. This deviation has been explained by the deflection of the projectile by the target nuclei. For the target elements with large Z_2, relativistic effects on the bound electron may be included in the present

data but this effect cannot be separated from others.

IV. SUMMARY

The energy-shift measurements for $K\alpha$, $K\beta_1$, and $K\beta_2$ x rays have shown the effect of the L- and M-shell vacancies predicted by the BEA. The deviation from the Z_1^2 dependence observed for light projectiles, which shows the existence of the Z_1^3-dependent term, has been obtained in the present work. On the basis of these results, the inner-shell ionization caused by N-ion bombardment under the present experimental conditions (incident energy and target elements) is considered to be caused mainly by direct Coulomb excitation.

Our data are concerned with targets with higher atomic number and rather-high-energy projectiles. As such data have not been abundant, they would contribute to the systematics of the inner-shell ionization process by heavy ions.

[1]U. Fano and W. Lichten, Phys. Rev. Lett. 14, 627 (1965); W. Lichten, Phys. Rev. 164, 131 (1967).

[2]E. Merzbacher and H. W. Lewis, Handb. Phys. 34, 166 (1958).

[3]J. D. Garcia, Phys. Rev. A 1, 280 (1970); 4, 955 (1971).

[4]J. D. Garcia, R. J. Fortner, and T. M. Kavanagh, Rev. Mod. Phys. 45, 111 (1973), and references cited therein.

[5]G. Basbas, W. Brandt, R. Laubert, A. Ratkowski, and A. Schwarzschild, Phys. Rev. Lett. 27, 171 (1971).

[6]C. W. Lewis, J. B. Natowitz, and R. L. Watson, Phys. Rev. Lett. 26, 481 (1971); Phys. Rev. A 5, 1773 (1972).

[7]G. Basbas, W. Brandt, and R. Laubert, Phys. Rev. A 7, 983 (1973).

[8]N. Stolterfoht, D. Schneider, and K. G. Harrison, Phys. Rev. A 8, 2363 (1973); N. Stolterfoht and D. Schneider, Phys. Rev. A 11, 721 (1975).

[9]M. J. Saltmarsh, A. van der Woude, and C. A. Ludemann, Phys. Rev. Lett. 29, 329 (1972).

[10]A. van der Woude, M. J. Saltmarsh, C. A. Ludemann, R. L. Hahn, and E. Eichler, in *Proceedings of the International Conference on Inner Shell Ionization Phenomena and Future Applications, Atlanta, Georgia, 1972,* edited by R. W. Fink, S. T. Manson, J. M. Palms, and P. V. Rao, CONF-720 404 (U. S. Atomic Energy Commission, Oak Ridge, Tenn., 1973), p. 1388.

[11]N. Cue, V. Dutkiewicz, P. Sen, and H. Bakhru, Phys. Rev. Lett. 32, 1155 (1974).

[12]T. K. Li and R. L. Watson, Phys. Rev. A 9, 1574 (1974).

[13]Y. Awaya, T. Hamada, M. Okano, A. Hashizume, T. Takahashi, K. Izumo, Y. Tendow, and T. Katou, IPCR Cyclotron Progress Report 7, 87 (1973) (unpublished).

[14]Tadao Tonuma, Isao Kohno, Yoshitoshi Miyazawa, Fusako Yoshida, Takashi Karasawa, Tan Takahashi, and Satoru Konno, J. Phys. Soc. Jpn. 34, 148 (1973).

[15]A. B. Wittkower and H. D. Betz, At. Data 5, 113 (1973).

[16]K. Izumo, Y. Tendow, Y. Awaya, T. Katou, M. Okano, A. Hashizume, T. Takahashi, and T. Hamada, in Ref. 13, p. 93.

[17]F. Folkmann, C. Garrde, T. Huus and K. Kemp, Nucl. Instrum. Meth. 116, 487 (1974).

[18]J. H. Scofield, Phys. Rev. 179, 9 (1969); Phys. Rev. A 10, 1507 (1974); At. Data Nucl. Tables 14, 121 (1974).

[19]J. A. Bearden, Rev. Mod. Phys. 39, 78 (1967).

[20]P. Richard, I. L. Morgan, T. Furuta, and D. Burch, Phys. Rev. Lett. 23, 1009 (1969).

[21]D. Burch and P. Richard, Phys. Rev. Lett. 25, 983 (1970).

[22]A. R. Kundson, D. J. Nagel, P. G. Burkhalter, and K. L. Dunning, Phys. Rev. Lett. 26, 1149 (1971).

[23]R. L. Watson and T. K. Li, Phys. Rev. A 4, 132 (1971).

Reprinted from J. Phys. Soc. Jpn., 42, 939–946 (1977).

Investigation of Ti Interstitials in Slightly Reduced Rutile (TiO_2) by Means of Channeling Method

Eiichi YAGI, Akio KOYAMA, Hideo SAKAIRI and Ryukiti R. HASIGUTI†

The Institute of Physical and Chemical Research, Wako-shi, Saitama 351
†*The Faculty of Engineering, Science University of Tokyo, Kagurazaka, Shinjuku-ku, Tokyo 162*

(Received September 1, 1976)

To investigate the defect structures of slightly reduced rutile (TiO_2) channeling experiments were performed on a slightly reduced specimen and a stoichiometric one with about 6 MeV protons accelerated by a cyclotron. In an angular scan of the backscattering yield of protons from Ti ions with respect to the [001] axial channel, a peak along the [001] direction was observed only in the reduced specimen. By the analysis of the angular scan it was confirmed that main defects in a slightly reduced rutile are Ti interstitial ions. They are located within about 0.4 Å of the [001] mid-channel axis. This result supports the interpretation of EPR experiments that a so-called *C*-center is a Ti interstitial ion.

§1. Introduction

Stoichiometric rutile, TiO_2, is an insulator. Upon slight reduction it becomes an oxygen-deficient nonstoichiometric rutile, TiO_{2-x}, which is an *n*-type semiconductor. It is well established that some kinds of defects introduced into rutile crystals by slight reduction give rise to the *n*-type semiconductivity. But as to the identification of these defects there still remain a number of unresolved problems.

There have been numerous rather indirect investigations of lattice defects in the slightly reduced rutile which make use of such measurements as electrical conductivity, weight change, and so on. The results of these investigations have been interpreted in terms of various proposed defects, among which two main conflicting proposals are an oxygen ion vacancy and a titanium ion interstitial.[1–3] In all but the simplest cases more than one kind of defects are involved. Therefore these experiments, which are based on measuring the combined effects of several defects, cannot easily give unambiguous conclusion about the individual defect types involved.

Since the early 1960s more direct investigations, which make use of such experimental method as electron paramagnetic resonance (EPR), dielectric relaxation, internal friction, and so on, have been advanced to identify the defects. They have given very important information.[4] But the problem of whether the dominant defects introduced by slight reduction are oxygen vacancies or titanium interstitials is not completely solved, although the evidence is somewhat in favour of the latter.

If titanium interstitials are dominant defects, it is to be expected that channeling experiments would give decisive information about the defect structures in slightly reduced rutile as described below. Figure 1(a) shows a crystal structure of rutile. It has an open channel along the [001] axis (*c*-axis). It is illustrated by dotted parallelepiped in Fig. 1(b). The end view of atomic arrangement for the [001] axial direction is shown in Fig. 2 so that the open channel is seen clearly. It has been proposed that a Ti interstitial is at the (1/2, 0, 1/2) type site. If this is the case, the Ti interstitial is situated at the center of the [001] channel. Therefore the channeling method is directly sensitive to such interstitials.

The objectives of the present study are to make channeling experiments on a slightly vacuum reduced rutile crystal and to discuss about its defect structures on the basis of the results of channeling experiments and those of EPR experiments performed previously by Hasiguti group.[4]

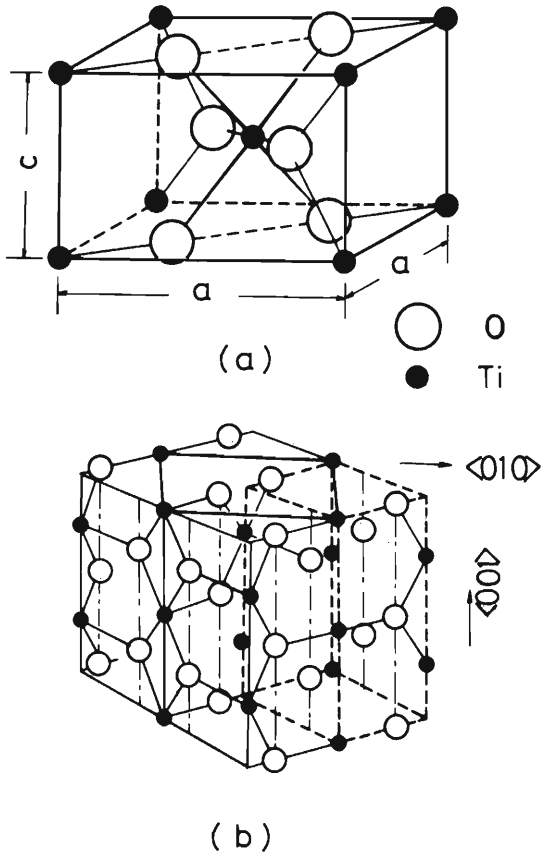

Fig. 1. (a) A unit cell of rutile crystal. Lattice constants: $a=4.594$ Å and $c=2.959$ Å. (b) Atomic arrangement in a rutile crystal. An open channel is indicated by a dotted parallelepiped.

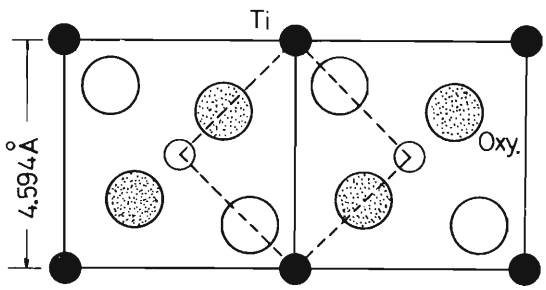

Fig. 2. The end view of atomic arrangement for the [001] axial direction. An open channel is indicated by a dotted square.

§2. Experimental Procedure

The specimen was a stoichiometric rutile single crystal with nominal purity of 99.99%, and a parallelepiped specimen with thickness 0.8 mm was cut from a large boule so that the crystallographic c-axis is parallel to the direction of thickness. The specimen was reduced at 1100°C in vacuum of 10^{-6} mmHg for 240 h and submitted to channeling experiments. Such long time is required for homogeneous reduction according to our previous experiences.[4] Oxygen deficiency (O_d), which is related to x in TiO_{2-x} as $O_d=3.2\times10^{22}x$, was estimated to be about $2\times10^{20}/cm^3$. After the experiments were over, the specimen was oxidized at 1100°C in air for 240 h. Such a stoichiometric specimen was also submitted to channeling analysis.

Channeling effects were investigated by means of backscattering with 5.77 MeV protons obtained from the cyclotron of the Institute of Physical and Chemical Research. The beam was collimated less than 0.025°. The crystal orientation of the target could be changed with respect to the incident beam by varying the angle θ and ϕ which could be set within the accuracy of $\pm0.005°$. The bombardment zone was 0.8 mm^2 and the beam currents were about 1 nA. Irradiation for backscattering measurements was carried out at room temperature. The backscattered protons were measured by a surface-barrier solid state detector (FWHM$\simeq$ 15 keV) placed at a scattering angle of about 150° and at 5 cm from the crystal surface. They were energy-analyzed by the 1024 channel pulse-height analyzer.

§3. Experimental Results

Figure 3 illustrates the energy spectra of backscattered protons with the beam incident parallel to the [001] direction of either TiO_2 or TiO_{2-x} (aligned spectrum) and with the beam along a random direction (random spectrum). Each spectrum consists of superposition of that of protons backscattered from titanium ions (Ti-spectrum) and that from oxygen ions (O-spectrum). Each of two spectra consists of a sharp edge followed by a slowly changing yields at lower energies. The sharp edges are around 5.3 MeV (Ti-spectrum) and 4.5 MeV (O-spectrum), which are due to scattering from titanium ions and from oxygen ions in the surface region respectively. In the aligned spectrum the large attenuation was observed and it amounts to about 70 fold near the surface in the Ti-spectrum. A backscattering yield for aligned incidence is larger in case of TiO_{2-x} than in TiO_2.

In order to investigate the effect of non-stoichiometric defects an angular scan was performed through the [001] crystal axis. Figure 4(a) and (b) indicate the normalized scattering yields from titanium ions in the vicinity of 4000 Å depth as a function of the

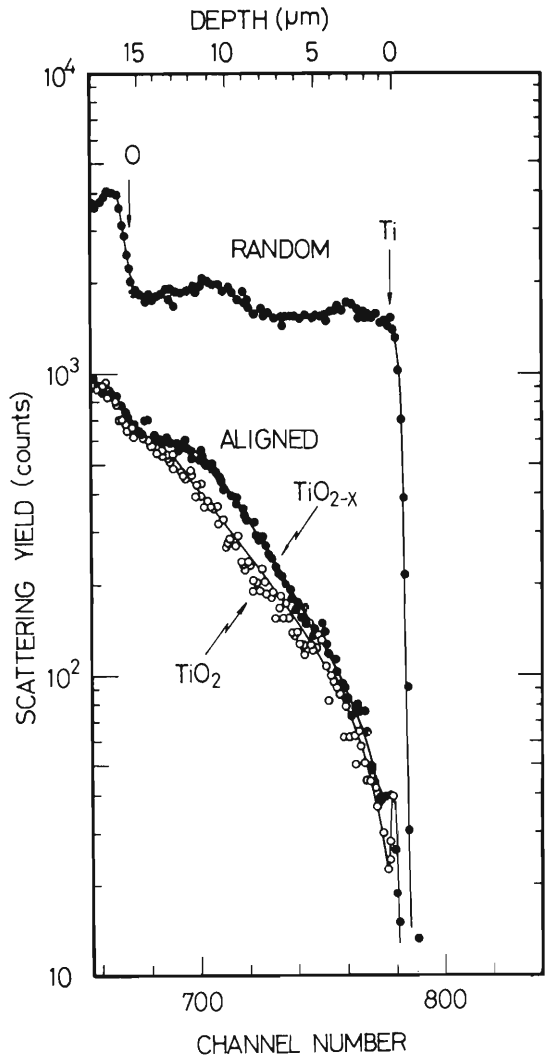

Fig. 3. Energy spectra of backscattered protons with the beam incident parallel to the [001] direction of either TiO_2 or TiO_{2-x} (aligned spectrum) and with the beam along a random direction (random spectrum).

angle θ between the incident beam direction and the [001] crystal axis (Ti-dip) in case of TiO_2 and TiO_{2-x} respectively. The results of an angular scan of the scattering yields from oxygen ions (O-dip) are shown in Fig. 5(a) and (b). In this case the scattering yield from oxygen ions was estimated by subtracting an average value of the yields over 10 channels just above the sharp edge of the O-spectrum from the observed yield.

In case of TiO_{2-x} (Figs. 4(b) and 5(b)) the measurements of backscattering yields were made first at $\theta = -0.03°$ (closed circle) subsequently at various positive values of θ in increasing order and then at various negative values of θ up to $-0.03°$ in increasing order. The yields measured at the last two angles in the sequence of the angular scan are indicated by open circles. The yields indicated by open circles are larger than those by closed ones at the same values of θ around the center of the dip. This is due to the effect of radiation damage. In case of TiO_2 the sequence of the angular scan is a little different from that in case of TiO_{2-x}. The measurements were made first at $\theta = -0.02°$ and then made nearly symmetrically with respect to θ in order of $-0.07°$, $-0.10°$, $0°$, $0.03°$ and $0.08°$. Therefore in case of TiO_2 such damage effect was not observed around the center of the dip.

As to the O-dip the normalized minimum yield χ_{min} and the half-angular width at half-minimum $\psi_{1/2}$ have the same values 0.065 and $0.22°$ respectively in both cases of TiO_2 and TiO_{2-x}. As to the Ti-dip the half-angle $\psi_{1/2}$ has the same value $0.29°$ in both cases. The striking feature is that the very sharp peak with the half-angle ψ_p of $0.05°$ and the maximum yield of 0.027 is observed at the center of the dip in case of TiO_{2-x} and not in TiO_2. The normalized minimum yield is 0.014 in the latter case. By the comparison between Figs. 4(b) and 5(b) taking account of the sequence of an angular scan and by the measurements on the dose dependence of the increase of χ_{min} it was confirmed that the effect of radiation damage during backscattering measurements is not responsible for that sharp peak. That sharp peak is particular to the reduced specimen and its origin is attributed to a flux-peaking effect as described later.

The depth dependence of $\psi_{1/2}$ and ψ_p in the Ti-dip is shown in Fig. 6. The depth of scattering was estimated from the stopping power according to the so-called Aarhus convention, in which it is assumed that the random stopping power applies to both the ingoing and the outgoing trajectories. In this estimation the values of stopping power were taken from the table given by Northcliffe and Schilling.[5] The half-angle $\psi_{1/2}$ has almost same values in both TiO_2 and TiO_{2-x} over the depth of 10 μm and decreases gradually with increasing depth. The half-angle ψ_p decreases rapidly with increasing depth. In this paper such depth dependence will not be further discussed in detail.

In Fig. 7 the quantity $1-\chi_{min}$ measured for backscattering yield from titanium ions, which

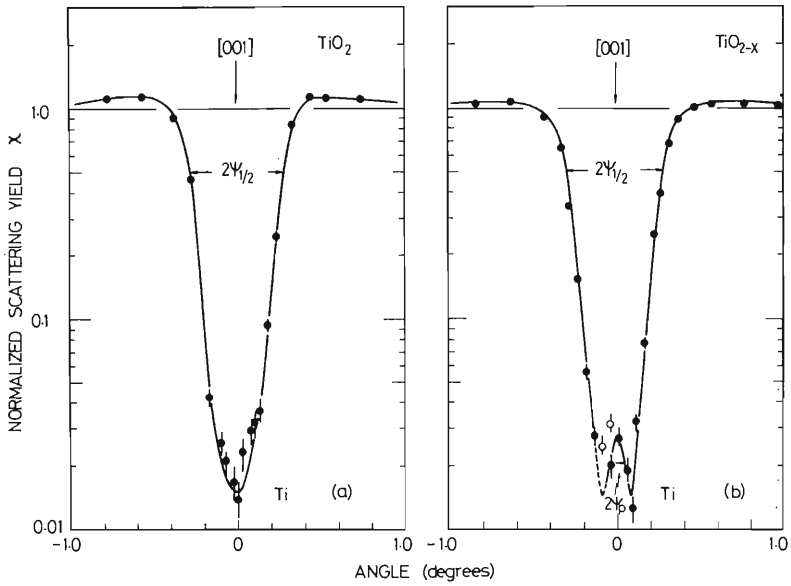

Fig. 4. Backscattering yield from titanium in TiO_2 (a), and in TiO_{2-x} (b) as a function of the angle θ between the incident beam direction and the [001] axial direction.

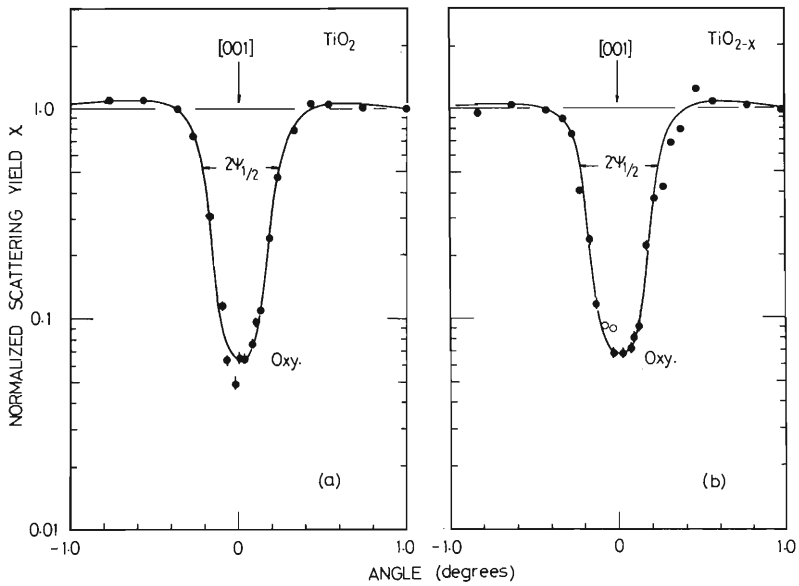

Fig. 5. Backscattering yield from oxygen in TiO_2 (a), and in TiO_{2-x} (b) as a function of angle θ between the incident beam direction and the [001] axial direction.

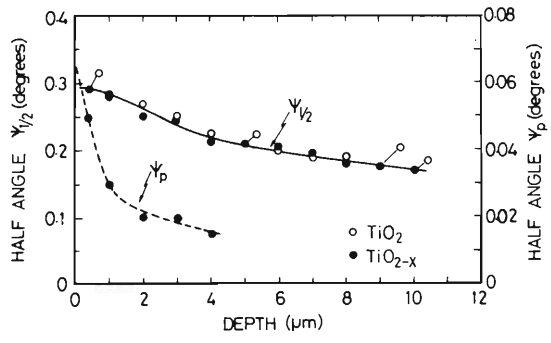

Fig. 6. The depth dependence of the half-angle $\psi_{1/2}$ of the Ti-dip in TiO_2 (○) and in TiO_{2-x} (●) and of the half-angle ψ_p of the sharp peak observed around the center of the Ti-dip in TiO_{2-x}.

may be interpreted to be the measure of the channeled fraction of the incident beam, is plotted on a logarithmic scale as a function of depth. In case of TiO_{2-x} the maximum value of the sharp peak in χ observed around the center of the Ti-dip was taken as the value of χ_{min} in the quantity $1-\chi_{min}$. For depths greater than 4 μm the channeled fraction appears to decrease in an approximately exponential fashion. In TiO_{2-x} it decreases more rapidly with increasing depth than in TiO_2.

All experimental results described above suggest the presence of titanium interstitials in

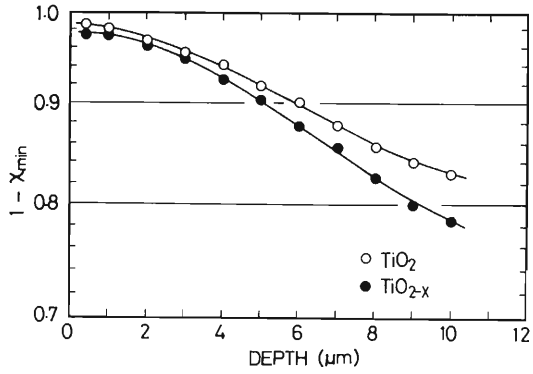

Fig. 7. The depth dependence of the quantity $1-\chi_{min}$ measured for backscattering yield from titanium ions in TiO_2 (○) and in TiO_{2-x} (●).

a slightly reduced rutile TiO_{2-x}.

§4. Discussion

4.1 *Comparison of experimental results on $\psi_{1/2}$ and χ_{min} with calculated ones*

The observed values of χ_{min} and $\psi_{1/2}$ for backscattered protons from titanium ions and oxygen ions in TiO_2 are summarized in Table I. The values for titanium ions are those found by extrapolation to zero target thickness, while the values for oxygen ions are those obtained from scattering in the vicinity of 4000 Å depth because in the latter case the extrapolation to zero target thickness is not easy. The calculated values were determined by taking the formulas developed by Gemmell and Mikkelson[6] by generalizing Barrett's empirical formulas[7] to the case of a polyatomic crystal. Barrett's formulas fitted well a great variety of experimental values. In such generalization, they interpreted the $1.2u_1$ appeared in Barrett's formula as the minimum distance of closest approach to an atomic row for the trajectories of channeled particles, where u_1 is the rms value of one spatial component of the thermal vibration amplitude. They further assumed that a single critical angle exists for each type of row and that the critical angle for any particular row j is determined by the distance of closest approach to this row. This distance is $1.2u^j_{1\max}$, where $u^j_{1\max}$ is the largest of the u_1 values for atomic species in that row. With these assumptions the expression for the half-angle $\psi^j_{1/2}$ for the jth type of row in a given axial direction was given by

$$\psi^j_{1/2}=0.80\{[\sum_i V^{ij}_{rs}(1.2u^j_{1\max})-V_0/E\}^{1/2}, \quad (4.1)$$

where $V^{ij}_{rs}(r)$ is the continuum potential energy due to the ith atomic species in the jth type of row. The term V_0 represents the minimum potential in the open channels between rows.

As to the minimum yield they interpreted, according to Barrett's expression, that beam ions which are incident parallel to the row and which have impact parameter less than $r_{min}=\sqrt{3}u_2$ with respect to the row will not be channeled and therefore will contribute to the minimum yield. The magnitude of u_2 is given by $\sqrt{2}u_1$, which represents the rms displacement of the atoms due to thermal vibrations in the plane normal to the axis. The axial minimum yield in backscattering from the ith atomic species, χ^i_{min}, in the crystal was given by

$$\chi^i_{min}=\sum_j \chi^{ij}_{min}=\sum_j (f_{ij}\sum_k n_k\pi r^2_{jk}). \quad (4.2)$$

The quantities χ^{ij}_{min}, f_{ij} and n_k represent the contribution to χ^i_{min} from rows of type j, the fraction of the ith atomic species in rows of type j, so $\sum_j f_{ij}=1$, and the areal density of the type k rows in a plane normal to the beam direction respectively. The radii r_{jk} are defined by

$$\sum_i V^{ik}_{rs}(r_{jk})=\sum_i V^{ij}_{rs}(\sqrt{3}u^j_{2\max}), \quad (4.3)$$

where $u^j_{2\max}$ is the largest of the u_2 values for elements in the jth row.

In the [001] direction of TiO_2, there are two types of rows, that is to say, titanium row and oxygen row, which contain only one species of either titanium or oxygen. The half-angles $\psi_{1/2}$ for the titanium row and the oxygen row, and the axial minimum yields in backscattering from titanium ions and from oxygen ions, χ^{Ti}_{min} and χ^{O}_{min}, were derived from eqs. (4.1) and (4.2) using Molière's approximation[8] to Thomas-Fermi potential function for $V_{rs}(r)$. The values of thermal vibration amplitude of titanium and oxygen ions in TiO_2 were esti-

Table I. Observed and calculated half-angles $\psi_{1/2}$ and normalized minimum yields χ_{min}.

	$\psi_{1/2}$		χ_{min}	
	obs.	calc.	obs.	calc.
Ti	0.29°	0.27° (0.28°)	0.014	0.015 (0.013)
Oxy.	0.22°	0.16° (0.20°)	0.065	0.089 (0.086)

mated from the experimental data on the Debye-Waller factors obtained by Cromer and Herrington,[9] that is, $u_1(\mathrm{O})=0.100$ Å and $u_1(\mathrm{Ti})=0.081$ Å.

The calculated values are listed in Table I together with the observed ones. For comparison the values obtained using the total potential energy $V_{rs}(r)$, in which the contribution of other atomic rows is taken into account, in place of $\sum_i V_{rs}^{ij}(r)$ in eqs. (4.1) and (4.3) are also listed in parentheses. The agreement between the calculated and the observed values is fairly good, although the calculated one of $\chi_{\min}^{\mathrm{O}}$ tends to be a little higher than the observed one. As to $\psi_{1/2}$ for the oxygen row the latter calculation gives better agreement than the former one. The values of $\chi_{\min}$ for oxygen is higher than that for titanium by factor about 5. This large difference can be explained as follows. Potential contours calculated by use of the static continuum form of Molière function are plotted in Fig. 8. The value of $r_{\min}$ with respect to oxygen rows, which contain only oxygen ions, is 0.24 Å. For it the potential $[V_{rs}^{\mathrm{oxy}}(r_{\min})-V_0]$ is found to be about 52 eV. The radius r corresponding to this potential is about 0.41 Å with respect to titanium rows. This is about twice as large as $r_{\min}=0.24$ Å since titanium rows exert stronger potential than do oxygen rows. As seen from eq. (4.2), the titanium row causes larger contribution to the $\chi_{\min}^{\mathrm{O}}$ for oxygen than does the oxygen row,

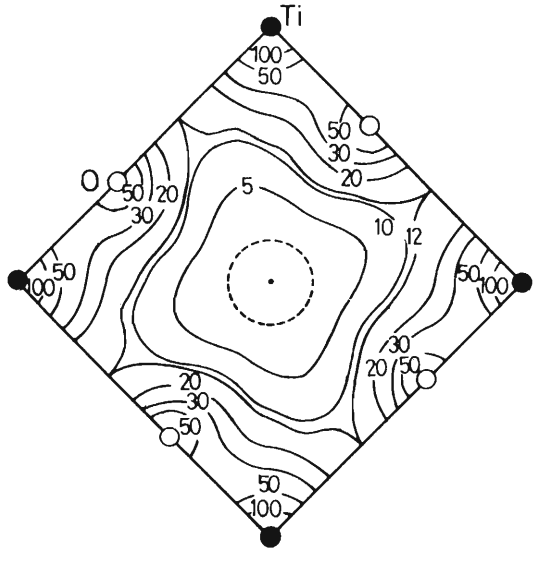

Fig. 8. Potential energy contour diagram for the [001] direction in the unit of eV calculated by use of the static continuum form of the Molière function.

though the large portion of beam with impact parameter less than 0.41 Å may be possibly channeled with respect to titanium rows because the value of $r_{\min}$ with respect to titanium rows is about 0.20 Å. According to the calculation about 58% of $\chi_{\min}^{\mathrm{O}}$ is attributed to the contribution of titanium rows containing no oxygen ions. On the other hand oxygen rows cause little contribution to $\chi_{\min}^{\mathrm{Ti}}$.

4.2 *Flux-peaking effect*

It is known as a flux-peaking effect that for incidence parallel to a major axis, the probability density of channeled beam flux attains higher values than those for a random beam in the allowed area for such a channeled beam.[10] As a result the backscattering yield of channeled particles from interstitials in the center of a channel can be several times greater than the random yield. In TiO_{2-x} if Ti interstitials occupy the proposed sites, they are located at the center of the [001] channel and none of them are shadowed by the ions at normal lattice sites when looking along the [001] crystal direction. Therefore the Ti interstitials are anticipated to give rise to a peak with the higher scattering yield than the random yield in an angular scan of the backscattering yield. The result of the angular scan shown in Fig. 4(b) can be interpreted as the superposition of a dip obtained with respect to Ti ions at normal lattice sites and a peak obtained with respect to interstitial Ti ions.

As to an analytical expression for the flux distribution across an axial channel in case of parallel incidence, the normalized flux F_i at the ith transverse equipotential contour in the channel is given by

$$F_i=\ln(A_0/A_i), \tag{4.4}$$

where A_0 and A_i represent the total area of the channel and the central area surrounded by ith contour respectively.[10] In the limit of $A_i\to 0$, i.e., near the center of the channel, the magnitude of F_i goes logarithmically towards infinity. But, taking account that at such large distances from a string of atoms the transverse potential becomes sufficiently small and flat, it is considered that the flux is flattened out at a finite level in the central region. Then the flux distribution expressed by eq. (4.4) is modified by assuming that the flux is constant in the

central area A_1. The flux in this area, F_{max}, is estimated to be[10]

$$F_{max} = 1 + \ln (A_0/A_1). \quad (4.5)$$

The above estimation is valid at such large depth as the statistical equilibrium in the spatial distribution of flux to be established.[10] A particle incident close to a string of atoms cannot pass through the center of the channel before it penetrates a distance of an order of λ_s

$$\lambda_s = d/\psi_{1/2} \simeq 650 \text{ Å}, \quad (4.6)$$

where for the [001] channel d is the planar spacing for {110} planes. Since most particles are deflected by less than $\psi_{1/2}$ in the first encounter with the string, the statistical equilibrium will not be established until the beam has penetrated the distance several times as large as λ_s. At the depth of about 4000 Å, where Ti-dips and O-dips shown in Figs. 4 to 5 were measured, the above condition is considered to be fulfilled.

The reduction treatment introduced the excess Ti ions of $10^{20}/\text{cm}^3$ into a reduced rutile specimen. As shown in Fig. 4(b) the flux-peaking effect increases the normalized minimum yield in the Ti-dip by the amount of about 0.013. If it is assumed that all of the excess Ti ions become interstitials and are situated within the area of maximum flux A_1 in the center of the [001] channel, the magnitudes of F_{max} and A_1 are estimated to be about 4.2 and 0.45 Å^2 respectively. Some experiments[10,11] and calculations[12–14] on various kinds of crystals showed that the backscattering yield of channeled particles from interstitials in the center of the channel can be a factor of 2 to 10 greater than the random yield, as a result of the flux-peaking effect. Then the value of F_{max} obtained here is of reasonable magnitude. The result on A_1 indicates that Ti interstitials are situated within 0.38 Å of the mid-channel axis, i.e., within the dotted circle shown in Fig. 8.

Next we estimate the angular half-width ψ_p of the flux-peaking effect. This is the value of ψ at which the scattering yield from Ti interstitials falls to a level midway between the well-aligned and the random yield, i.e., 2.6. The scattering yield is determined by the magnitude of the normalized flux F in the mid-channel region. As the first approximation to estimate the magnitude of F it is assumed that for a number of channeled particles their incident transverse energy $E\psi_p^2$ is larger than the transverse potential energy and the latter may be neglected. This is equivalent to assuming that all particles in the beam enter the crystal at the center of the channel and then the beam flux is distributed uniformly across the channel except for a forbidden area Δ around the atomic rows involved.[10] Then the magnitude of F in the mid-channel region is given by

$$F = A_0/(A_0 - \Delta). \quad (4.7)$$

For $F = 2.6$ the region with area of Δ corresponds to that outside the potential contour of 10 eV shown in Fig. 8. Using this value the half-angle ψ_p can be estimated to be 0.060° by eq. (4.1). This is the same order of magnitude as 0.05° found experimentally.

Then the observed small peak in Ti-dip was explained well on the assumption that all of excess Ti ions occupy interstitial sites. Therefore we can say that most excess Ti ions left in the reduced rutile as a result of vacuum reduction occupy the interstitial sites, which are within 0.38 Å of the [001] mid-channel axis.

4.3 Defect structure

According to EPR experiments made by Hasiguti group,[4] defect centers called as *C*-center are main defects in the region of oxygen deficiency O_d less than $10^{19}/\text{cm}^3$ and their concentration increases with increasing O_d, while it decreases with increasing O_d in the region of $O_d > 10^{19}/\text{cm}^3$. Electrical resistivity decreases with increasing O_d in the region of $O_d < 1.2 \times 10^{19}/\text{cm}^3$ and increases with O_d in the region of $O_d > 1.2 \times 10^{19}/\text{cm}^3$.[15] Plane defects come to be observed for $O_d > 5 \times 10^{19}/\text{cm}^3$.[16] From these experimental results, we interpreted that the decrease of the concentration of *C*-centers observed for $O_d > 10^{19}/\text{cm}^3$ is due to clustering of *C*-centers.[4] Therefore it is considered that main defects in the reduced specimen TiO_{2-x} used in the present experiments are *C*-centers and their clusters, though other types of EPR centers are observed with small concentrations. On the other hand the results of the channeling experiments suggest that defects are almost Ti interstitials as described in the previous section. Then it leads to the conclusion that a *C*-center is a Ti interstitial ion.

According to the results of electron micro-

scopic observation,[17] the reduced specimen used in the present work contains {312} and/or {725} planar faults which are related to the *W*-centers observed in EPR experiments. Around the fault the adjacent parts of crystal bounded by a {312} or a {725} fault plane are displaced by the amount of R to each other. The displacement vector $\boldsymbol{R}$ is approximately $\frac{1}{2}[10\bar{1}]$, which corresponds to the vector to displace Ti ions from normal lattice sites to interstitial sites. By these faults a [001] axial channel is displaced so that the [001] titanium row replaces the [001] mid-channel axis beyond the fault plane. Therefore in channeling experiments these faults have an effect on the backscattering yield around the fault plane. But this effect was neglected in the analysis of flux-peaking effect, because by the electron microscopic observation[17] and by the EPR experiments[21] the contribution of interstitials produced around the planar fault to the backscattering yield is estimated to be at most 10% of that of total excess Ti ions.

EPR experiments on *C*-centers were made by Date,[18] Chester,[19] Kingsbury, Ohlsen and Johnson[20] and Hasiguti, Iguchi and Takahashi.[21] *C*-centers were interpreted to be Ti interstitials at (1/2, 0, 1/2) type sites. Chester suggested such possibility in his previous work,[19] but discarded the Ti interstitial model in his later work (reviewed in ref. 4). The results of channeling experiments performed in the present work support the former interpretation of EPR experiments that a *C*-center is a Ti interstitial ion and indicates that main defects in a slightly reduced rutile are Ti interstitial ions.

§5. Summary

The experiments of proton channeling were performed with respect to [001] axial channel of a slightly reduced rutile and of a stoichiometric rutile. In an angular scan of the backscattering yield of protons from Ti ions a sharp peak was observed only in the reduced specimen. By the analysis of this result of an angular scan it was concluded that main defects in a slightly reduced rutile are Ti interstitial ions. They are located within about 0.4 Å of the [001] mid-channel axis. The interpretation of EPR experiments that a *C*-center is a Ti interstitial ion was supported.

Acknowledgements

The authors would like to express their appreciation to the members of the cyclotron laboratory of the Institute of Physical and Chemical Research. They are also indebted to the members of the work shop of their institute for their contribution in making the experimental apparatus. This research was supported in part by the Grant-in-Aid for Scientific Research from the Ministry of Education.

References

1) F. A. Grant: Rev. mod. Phys. **31** (1959) 646.
2) T. Hurlen: Acta Chem. Scand. **13** (1959) 365.
3) R. R. Hasiguti: Kinzoku Buturi (Metal Physics) **9** (1963) 95, 159 [in Japanese].
4) R. R. Hasiguti: Ann. Rev. Mater. Sci. **2** (1972) 69.
5) L. C. Northcliffe and R. F. Schilling: Nuclear Data Tables **A7** (1970) 233.
6) D. S. Gemmell and R. C. Mikkelson: Phys. Rev. **B6** (1972) 1613.
7) J. H. Barrett: Phys. Rev. **B3** (1971) 1527.
8) G. Molière: Z. Naturforsch. **A2** (1947) 133.
9) D. T. Cromer and K. Herrington: J. Amer. Chem. Soc. **77** (1955) 4708.
10) J. U. Andersen, O. Andreasen, J. A. Davies and E. Uggerhøj: Rad. Effects **7** (1971) 25.
11) F. H. Eisen and E. Uggerhøj: Rad. Effects **12** (1972) 233.
12) D. V. Morgan and D. van Vliet: Rad. Effects **12** (1972) 203.
13) R. B. Alexander and J. M. Poate: Rad. Effects **12** (1972) 211.
14) H. D. Carstanjen and R. Sizmann: Rad. Effects **12** (1972) 225.
15) R. R. Hasiguti, E. Yagi and M. Aono: Rad. Effects **4** (1970) 137.
16) E. Yagi, M. Aono and R. R. Hasiguti: in preparation.
17) E. Yagi and R. R. Hasiguti: *Lattice Defects in Semiconductors 1974* (Institute of Physics, London 1975) p. 359.
18) M. Date: Bussei **1** (1960) 22 [in Japanese].
19) P. F. Chester: J. appl. Phys. **32** (1961) 2233.
20) P. I. Kingsbury Jr., W. D. Ohlsen and O. W. Johnson: Phys. Rev. **175** (1968) 1091.
21) R. R. Hasiguti, E. Iguchi and S. Takahashi: *Proc. 9th Int. Conf. Phys. Semiconductors, Moscow, 1968* (Nauka, Leningrad, 1969) p. 1142.

Reprinted from Phys. Lett., 61A, 111–113 (1977).

THE Kα AND Kβ X-RAY SPECTRA OF Al, Ti, Cr, Fe AND Ni INDUCED BY 84 MeV NITROGEN IONS

Y. AWAYA, M. AKIBA, T. KATOU, Hidekazu KUMAGAI, Y. TENDOW, K. IZUMO, T. TAKAHASHI, A. HASHIZUME, M. OKANO and T. HAMADA

The Institute of Physical and Chemical Research, Wako-shi, Saitama 351, Japan

Received 15 October 1976

The K X-rays from the target elements due to N-ion bombardment are measured with a crystal spectrometer. Some aspects owing to high incident energy are discussed. The Kα satellite, Kα hypersatellite and Kβ satellite peak spacings are obtained.

The inner shell ionization cross section has been explained by the plane wave Born approximation (PWBA) or the binary encounter approximation (BEA) with some corrections in certain cases under the condition of $v_1 \geqslant v_{2I}$ or $Z_1 \ll Z_2$, where v_1 and v_{2I} are the velocity of the projectile and that of the I-shell electron to be excited and Z_1 and Z_2 are the atomic number of the projectile and the target element. Then the cross section is proportional to Z_1^2 and takes the maximum value at $Em_e/Mu_I = 1$, where E is the incident energy of the projectile, m_e and M are the mass of the electron and the projectile, and u_I is the binding energy of I-shell electron to be excited. On the other hand, the degree of multiple ionization of K- and L-shells is enhanced drastically with increasing Z_1 for fixed values of v_1, v_{2I} and Z_2 [1, 2].

The study of heavy-ion induced K X-ray spectra with high energy resolution has been made by many authors. In these studies, the incident energy of heavy ions is lower than 4 MeV/amu. Here we will report the Kα and Kβ X-ray spectra of Al, Ti, Cr, Fe and Ni induced by 6-MeV/amu N-ions. As the incident energy is higher than in any other works of this kind, some new features have been observed.

The 6 MeV/amu N^{4+} ions were accelerated by the cyclotron of the Institute of Physical and Chemical Research. An on-line Bragg crystal spectrometer with a flat crystal and Soller slits was prepared for the measurement. The Al K X rays were measured by using the combination of an EDDT(010) crystal and a side-window gas-flow proportional counter placed in the vacuum chamber. The X rays of heavier elements than Ti were measured by the combination of a LiF(200) crystal and a NaI(Tl) scintillation counter which was placed outside the vacuum chamber separated by a 25 μm Mylar film. The targets, ranging in thickness from 0.8 mg/cm^2 to 1.4 mg/cm^2, were placed with an inclination of 60° with respect to ion beams.

The K X-ray spectra of Al, Ti and Ni are shown in fig. 1. The peak is labelled by a symbol of $K^m L^n$ which denotes the corresponding initial configuration having m K-shell vacancies and n L-shell vacancies. α or β means the peak belongs to Kα or Kβ transition. By comparing to previous works with heavy ions, a prominent difference in the pattern of Kα spectra is observed concerning the relative intensity of the diagram and satellite lines. The present data shows that the number of L-shell vacancy n corresponding to the highest peak is one for Al, Ti and Cr and zero for Ni. As to the Fe target, the $K\alpha_{1,2}$ peak and the KLα peak have almost the same intensity. The values of n described above are smaller by about two for Al and by one for Ti, Cr and Fe than those obtained by 30 MeV O-ion impact on each target element [1,3–6]. The n value of Ti obtained in present work is also rather smaller than the value obtained for 36 MeV C-ion impact [5].

This difference means, the incident heavy ions act more proton-like in multiple ionization process as the incident energy increases or the value of Z_1/Z_2 decreases. This means also, from another point of view, that the L-shell ionization cross section is smaller in our experimental condition than in O- or C-ion cases as is expected by the PWBA or BEA. We found that the spectral pattern of Al $K\alpha_{1,2}$ and Kα satellite lines obtained by the present work resembles as a whole to that obtained by 1-MeV α-particle impact [7]. This

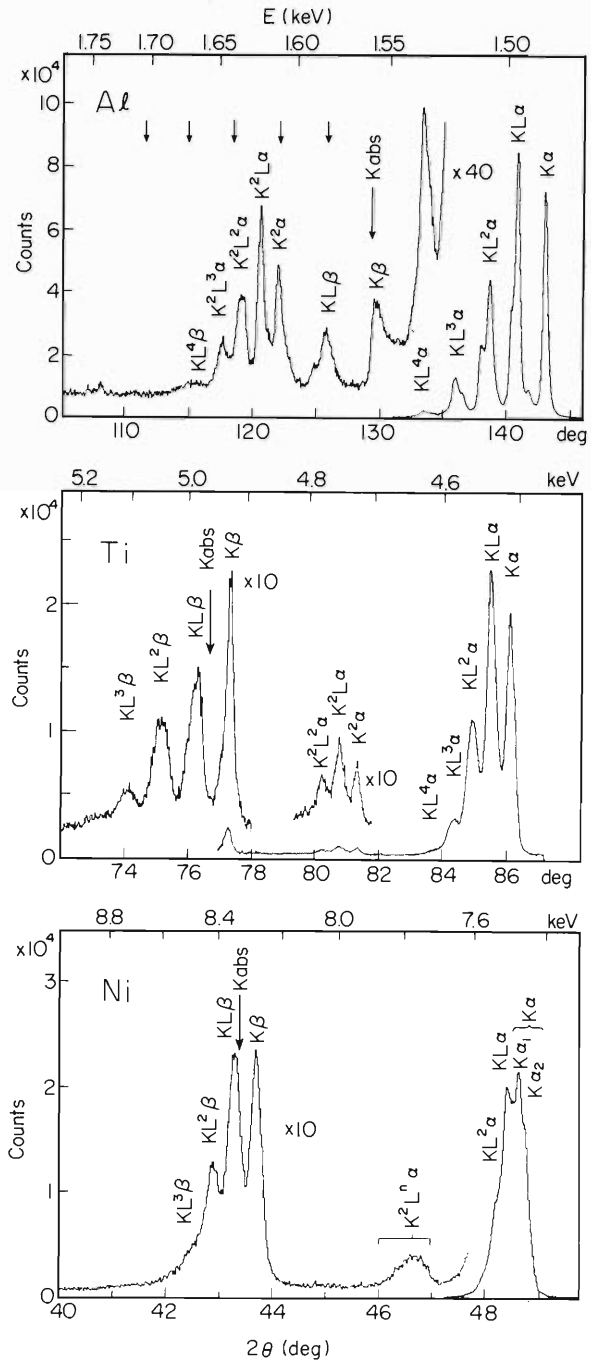

Fig. 1. The K X-ray spectra of Al, Ti and Ni induced by 84 MeV N-ions. The symbol of K^mL^n denotes the initial configurations of m K-shell and n L-shell vacancies. The K_{abs} denotes the K-absorption edge of target element. The arrows indicate the position of $KL^n\beta$ (n = 2–5) line of Al observed by Knudson et al. [8].

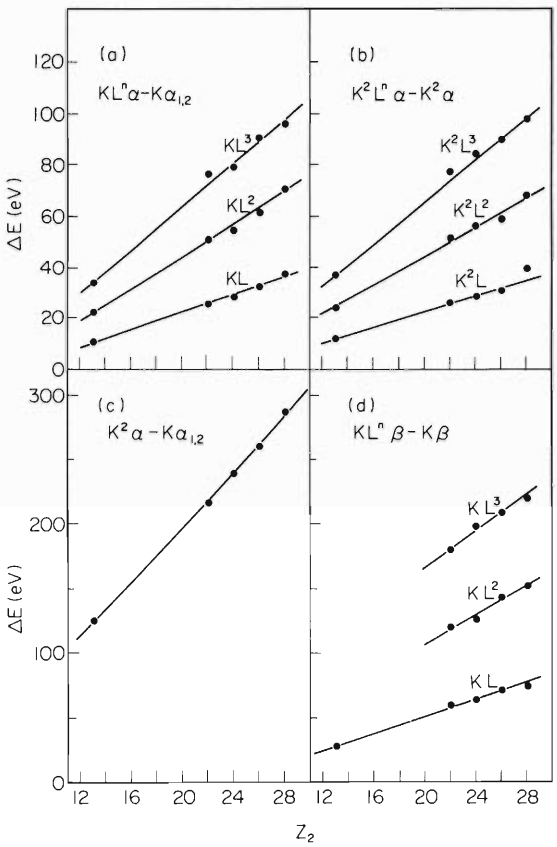

Fig. 2. Plot of $KL^n\alpha$ satellite energies relative to $K\alpha_{1,2}$ (a), of $K^2L^n\alpha$ relative to $K^2\alpha$ (b), of $K^2\alpha$ relative to $K\alpha_{1,2}$ (c) and of $KL^n\beta$ relative to $K\beta$ (d). The curves are drawn for visual aid.

calls the speculation that one of the ways to study the mechanism of multiple ionization may be to find a generalised parameter, which consists of such quantities as Z_1, Z_2, v_1 and v_{21}, and by whose value the gross structure of the spectrum of the diagram and satellite lines is determined.

In the Al spectrum, each of the $KL^n\alpha$ lines (n = 1–4) and the $KL\beta$ line have a structure which may originate in the multiplet splitting, for example, in such a way as the $KL\alpha$ peak may be resolved to the $K\alpha'$, $K\alpha_3$ and $K\alpha_4$ peaks. The $K\alpha$ hypersatellites are excited more strongly than $K\beta$ satellites in the present work whereas only the $K\beta$ satellites have been observed in the case of 5 MeV N-ion impact [8]. This difference in excitation may be attributed to the incident energy difference. The position of $KL^n\beta$ lines (n = 2–5) observed by Knudson et al. [8] is shown by arrows.

The width of the satellites is always larger than that of the diagram line. Hill et al. [5] have studied the variation of the centroid energy and of the width of the Kα diagram and satellite peaks. They found that the centroid position of the Ti $K\alpha_{1,2}$ X rays induced by C and O ions (maximum energy was 3.7 MeV/amu) is about 5 eV and 6 eV higher than that corresponding fluorescent X rays, respectively, and the peak width increases with n. They discussed the energy shift and peak-width variation in terms of the M-shell ionization, the multiplet splitting and variations in distribution of L-shell vacancies among the subshells. In the present work, fluorescent Ti $K\alpha_{1,2}$ X rays are also measured. By comparing to Ti $K\alpha_{1,2}$ X rays induced by N ions, the difference of their centroid position was less than 2 eV. This may be explained by the fact that as the incident energy increases, the M-shell ionization cross section decreases. The variation of peak width observed in the present work may be caused by the same effects discussed by Hill et al. [5], but as the number of M-shell vacancies has a trend to decrease with increase of incident energy, the last two effects become more dominant in the present case.

The values of energy difference between the $K\alpha_{1,2}$ and $KL^n\alpha$ lines, the $K^2\alpha$ and $K^2L^n\alpha$ lines, the $K\alpha_{1,2}$ and $K^2\alpha$ lines, and the Kβ and $KL^n\beta$ lines are shown in fig. 2 as a function of Z_2. The peak position was determined by the least-squares fitting of multiple Gaussian curves to the overlapping peaks. Regarding to each target element, the value of energy spacing between $K\alpha_{1,2}$ and $KL^n\alpha$ lines and that between $K^2\alpha$ and $K^2L^n\alpha$ lines are almost equal for each values of n as is seen in fig. 2. The values of energy spacing between $K\alpha_{1,2}$ and $KL^n\alpha$ lines for Al to Fe agree with the previous data [9] as well as with the calculated values by Jundt and Nagel [10]. The present data for Ni also agree with their calculated value but disagree with the experimental one obtained by them. This disagreement may be due to uncertainty in the position assignment of Ni $K\alpha_{1,2}$ line in their work as pointed out by themselves. Since the data of the Kα hypersatellites and of Kβ satellites induced by heavy ions are not so abundant, the present data will be useful to check the accuracy of the calculations.

References

[1] C.F. Moore, M. Senglaub, B. Johnson and P. Richard, Phys. Lett. 40A (1972) 107.

[2] R.L. Watson, F.E. Jenson and T. Chiao, Phys. Rev. A 10 (1974) 1230.

[3] D.K. Olsen, C.F. Moore and R.L. Kauffman, Phys. Lett, 44A (1973) 109;
F. Hopkins, D.O. Elliot, C.P. Bhalla and P. Richard, Phys. Rev. A 8 (1973) 2952;
P. Richard, C.F. Moore and D.K. Olsen, Phys. Lett. 43A (1973) 519.

[4] R.L. Kauffman, J.H. McGuire and P. Richard, Phys. Rev. A (1973) 1233.

[5] K.W. Hill et al., Phys. Rev. A 13 (1976) 1334.

[6] D. Burch, P. Richard and R.L. Blake, Phys. Rev. Lett. 26 (1971) 1355.

[7] P. Richard et al., Phys. Rev. A 8 (1973) 1369.

[8] A.R. Knudson, D.J. Nagel, P.G. Burkhalter and K.L. Duning, Phys. Rev. Lett. 26 (1971) 1149.

[9] The referenced papers in the figure caption of fig. 2 of ref. [10].

[10] F.C. Jundt and D.J. Nagel, Phys. Lett. 50A (1974) 179.

Reprinted from Phys. Rev. Lett., 42, 1257–1260 (1979).

Bonding Effect on F $K\alpha$ Satellite Structure Produced by 84-MeV N^{4+}

M. Uda, H. Endo, K. Maeda, Y. Awaya, M. Kobayashi, Y. Sasa, H. Kumagai, and T. Tonuma
The Institute of Physical and Chemical Research, Wako-shi, Saitama 351, Japan
(Received 27 October 1978)

The intensity distributions of F $K\alpha$ satellites produced by 84-MeV N^{4+} bombardment displayed a significant chemical effect. The dependence of the intensity distributions of several fluorides on the chemical environment is discussed in relation to the Pauling bond ionicity or covalency. A refilling of vacancies by ligand valence electrons prior to the x-ray emission accounted for the observed satellite distributions for the compounds used.

The use of enhanced $K\alpha$ satellites produced by heavy-ion impact has received much attention in recent years. Several investigations of change in intensity distributions of satellites have been performed on chemical compounds of F, Al, Si, S, and Cl.[1-5] To explain chemical effects, an L-shell vacancy refilling process through an interatomic transition has been postulated but the argument is still a matter of conjecture.

In the present Letter we report on measurements of the F $K\alpha$ x-ray satellites produced by 84-MeV N^{4+} impact on a series of fluorides, where intensity distributions vary to a large extent from one compound to another. With use of the observed relative intensities, an L-shell vacancy rearrangement probability and an L-shell width for a multiply ionized state were determined quantitatively for the first time. We found that the interatomic transition takes place only through a covalent component in the molecular orbital in the fluorides.

N^{4+} beams were accelerated by the cyclotron of the Institute of Physical and Chemical Research. An on-line Bragg spectrometer was equipped with a rubidium acid phthalate (010) flat crystal and employed a flow-mode proportional counter operated at 1 atm of P-10 and biased to 1900 V as the detecting element. Data were accumulated for fixed periods of charge integration. Evaporated thin films of NaF, Na_3AlF_6, AlF_3, NiF_2, and CuF_2 on Al backing (2 μm in thickness), and a sheet of Teflon, $(CF_2)_n$, without backing, all in 1–2-mg/cm^2 thickness which caused ~4-MeV energy loss of the beams, were used.

No enhancement of the F $K\alpha$ diagram line was observed even when the NaF target backed with thick Al foil, the Al backing being faced on downstream of the incident ions, or coated with Al layer on its surface, the Al layer being faced on upstream, was bombarded with N^{4+}. The spectra obtained in this experiment are then composed only of ion-induced x rays and free from F K x rays induced by secondary x rays and electrons. No correction was made for differences in self-absorption in the energy range from F K^1L^0 to K^1L^2 lines because energies of the absorption edge of F, for example, in NaF [~689 eV (Ref. 6)] and in AlF_3 [~692 eV (Ref. 6)] are higher than that of the F K^1L^2 line, where K^1L^n denotes a configuration with a single K vacancy and n L vacancies. Higher-order peaks than K^1L^2 were omitted from the evaluation of peak intensities, because their intensities even if modified by an absorption correction were estimated to be less than 5% of the total intensity. All the spectra were analyzed in terms of a least-squares peak-fitting procedure employing Gaussian functions. The observed relative intensities $y_n{}^X$ of the F $K\alpha$ spectra are listed in Table I. No distinct chemical shift of the satellite lines could be observed. The difference in the chemical character of these fluorides is, however, strongly reflected in spectral shapes, as shown in Fig. 1. Such a systematic change in intensity distributions relates to the Pauling bond ionicity or covalency.[7]

The F L shell forms a part of the valence band of the fluoride. The plasmon lifetime in solids[9] is, in general, much shorter than the single-K-vacancy radiative lifetime of the F atom[8] (2.4×10^{-13} sec). Prior to the F K-x-ray emission, the vacancies of the L shell produced by ion impact can then be transferred to the valence bands of neighboring atoms through molecular orbitals. Let us assume the vacancies in the F L shell to be filled, one by one, by the ligand valence electrons and also assume a probability of simultaneous multielectron transfer to be negligibly small. Then the probability for an L-shell-vacancy rearrangement by one electron $f_{n,n-1}$ is expressed as $\Gamma_L(K^1L^n)/[\Gamma_K(K^1L^n)+\Gamma_L(K^1L^n)]$ for a $K^1L^n \rightarrow K^1L^{n-1}$ transition where $\Gamma_L(K^1L^n)$ and $\Gamma_K(K^1L^n)$ denote L- and K-shell widths for a vacancy con-

TABLE I. Pauling bond ionicity, relative $K\alpha$ x-ray satellite intensities y_n^X, L-shell refilling probability f, ratio of the fluorescence yield ω_2/ω_0, and L-shell width Γ_L for several fluorides.

Compound	Ionicity[a]	y_n^X [b] $n=0$	$n=1$	$n=2$	f	ω_2/ω_0	Γ_L [d] (10^{-4}/a.u.)
NaF	0.91	0.382	0.412	0.206	-0.032 ± 0.03	1.222[c]	-2.3 ± 2.0
Na_3AlF_6	0.86	0.421	0.348	0.231	0.138 ± 0.010	1.68 ± 0.10	11.8 ± 1.2
AlF_3	0.79	0.466	0.306	0.228	0.267 ± 0.013	1.93 ± 0.10	26.9 ± 0.9
NiF_2	0.70	0.516	0.292	0.192	0.343 ± 0.017	1.73 ± 0.12	38.5 ± 1.2
CuF_2	0.66	0.531	0.278	0.191	0.381 ± 0.019	1.82 ± 0.12	45.4 ± 1.5
$(CF_2)_n$	0.43	0.574	0.242	0.183	0.477 ± 0.043	2.05 ± 0.21	67.3 ± 3.0

[a] The ionicity I is defined by Pauling to be $I = 1.0 - \exp[-0.25(x_A - x_B)^2]$ with x_N the electronegativity of element N (Ref. 7).

[b] The sum of the statistical errors for the intensities and those induced by the deconvolutions was at most 10% and typically much smaller.

[c] ω_2/ω_0 of Ne is used only for NaF.

[d] Γ_L is estimated using the theoretical value of $\Gamma_K(K^1L^0) = 73.8 \times 10^{-4}$/a.u. (Ref. 8).

figuration state of K^1L^n. Then the relative intensity of n^{th} satellite line y_n^X is expressed, through a cascading process,[10] as

$$y_n^X = (\omega_n/\tilde{\omega})(1 - f_{n,n-1})(y_n + f_{n+1,n}y_{n+1} + f_{n+2,n+1}f_{n+1,n}y_{n+2} + \cdots + f_{8,7}f_{7,6}\cdots f_{n+1,n}y_8), \tag{1}$$

where y_n, ω_n, and $\tilde{\omega}$ are a primary vacancy distribution and a fluorescence yield for K^1L^n, and an average fluorescence yield, respectively. Here the number of L-shell electrons in bonded F^- is to be 8 and $f_{n,n-1} = 0$ for $n = 0$. The difference in the chemical environment of F^- must then be reflected in the observed intensity distributions through $f_{n,n-1}$ and $\omega_n/\tilde{\omega}$. For small n we assume that $\Gamma_K(K^1L^n)$ and $\Gamma_L(K^1L^n)$ are not influenced by the L-shell vacancy configurations, and hence $\Gamma_K(K^1L^n)$, $\Gamma_L(K^1L^n)$, and $f_{n,n-1}$ can be replaced by Γ_K, Γ_L, and f, respectively, which are independent of n. Such an assumption is not unreasonable because in the exotic-atom experiment the L-shell refilling rates were not appreciably enhanced by the number of either L- or K-shell vacancies.[11] Then, in our experimental condition, i.e., $y_3^X \cong 0$, Eq. (1) can be reduced to the forms

$$y_0 = (1-f)^{-1}(\tilde{\omega}/\omega_0)[(1-f)y_0^X - f(\omega_0/\omega_1)y_1^X], \tag{2}$$

$$y_1 = (1-f)^{-1}(\tilde{\omega}/\omega_1)[y_1^X - f(\omega_1/\omega_2)y_2^X], \tag{3}$$

$$y_2 = (1-f)^{-1}(\tilde{\omega}/\omega_2)y_2^X, \tag{4}$$

and

$$y_0 y_2/y_1^2 = {}_8C_0\,{}_8C_2/{}_8C_1^2 = \tfrac{7}{16}. \tag{5}$$

The relation (5) is deduced from the assumption that the primary vacancy distribution is binomial,[12] i.e., $y_n = {}_8C_n\tilde{P}_L(0)^n[1-\tilde{P}_L(0)]^{8-n}$, where ${}_8C_n$ is a binomial coefficient and $\tilde{P}_L(0)$ is an average ionization probability at zero impact parameter. Here f can be determined by solving the quadratic equation (5) and $\tilde{P}_L(0)$ is also determined from the relation $y_1/y_2 = 8[1-\tilde{P}_L(0)]/28\tilde{P}_L(0)$ if ω_1/ω_0 and ω_2/ω_0 are known.

When the ionicity becomes unity the electron configuration of F^- is considered to be the same as that of a Ne atom. Then ω_n/ω_0 or F^- in NaF ($I = 0.91$) is now replaced approximately by that of the Ne atom. Using the ratios $\omega_1/\omega_0 = 1.055$ and $\omega_2/\omega_0 = 1.222$ determined experimentally for Ne,[13] we got $f = -0.032$ and $\tilde{P}_L(0) = 0.109$ for NaF. From the zero or almost zero probability of the L-vacancy rearrangement f for NaF we understand that no vacancy transfer occurs in highly ionic compounds.

For the fluoride with small ionicity where a degree of localization of a valence electron density on F^- is small and hence the wave function of the F L shell cannot be replaced by that of Ne atom, the situation is more complicated and Eqs.

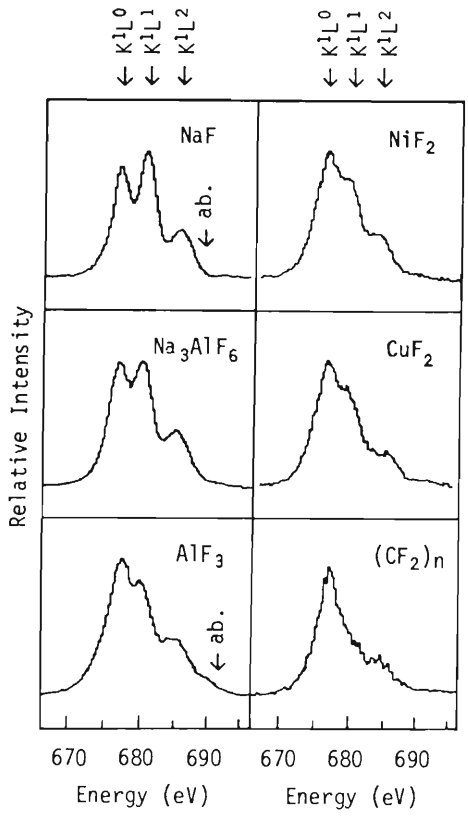

FIG. 1. F $K\alpha$ spectra of NaF, Na_3AlF_6, AlF_3, NiF_2, CuF_2, and Teflon $(CF_2)_n$ induced by 84-MeV N^{4+}. The arrows indicate the positions of the K absorption edges.

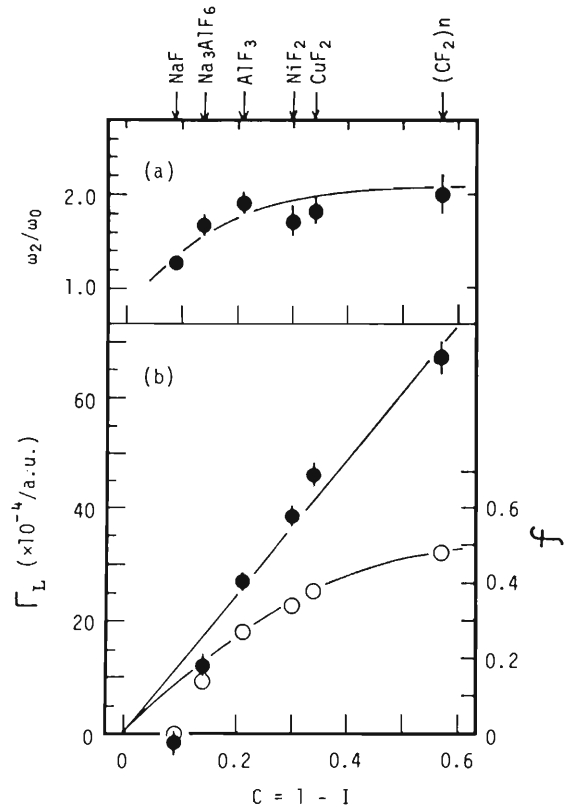

FIG. 2. The fluorescence yield ratio ω_2/ω_0, the L-shell refilling probability f, and the L-shell width Γ_L plotted as a function of the covalency C for all of the fluorides examined. (a) Variation of ω_2/ω_0 with the covalency. (b) Variation of Γ_L (closed circles) and f (open circles) with the covalency.

(2)–(5) cannot be used to evaluate f because ω_n/ω_0 for the fluoride deviates from that for the Ne atom. Such a deviation may be more significant for higher-order K^1L^n states but not for the K^1L^1 state. This is drawn from an analogy to the fact that the discrepancy between ω_n/ω_0, for the Ne atom, obtained with the statistical scaling procedure and with the exact Hartree-Fock-Slater calculation increases with n.[14] On the other hand, the primary vacancy distribution y_n is considered to be less sensitive[1] to the change in the chemical environment under the condition where the direct Coulomb ionization process is dominant. Then in the case of small $\tilde{P}_L(0)$ we can apply the same binomial distribution y_n, which is generated from $\tilde{P}_L(0) = 0.109$ obtained with NaF, and the same $\omega_1/\omega_0 = 1.055$ obtained with the Ne atom to the fluorides other than NaF. f and ω_2/ω_0 can now be determined by solving Eq. (1) if we make the ratios y_0^X/y_1^X for f and y_2^X/y_0^X for ω_2/ω_0 using terms up to y_3 (= 0.041), as listed in Table I. f and ω_2/ω_0 increase with the covalency ($C = 1 - I$) as shown in Figs. 2(a) and 2(b). As Γ_K is less sensitive than Γ_L to the change in the chemical environments we use the same Γ_K for all the fluorides. Γ_L is now estimated by using the theoretical value of $\Gamma_K(K^1L^0)$.[8] Here a linear relationship between Γ_L and C can be seen in Fig. 2(b). Such a trend will be discussed in view of the bonding nature of the compounds.

The molecular-orbital (MO) wave function of the valence band of a fluoride MF is written as $\Psi(\mathrm{MO}) = (1+\lambda^2)^{-1/2}(\lambda\Psi_{M:F} + \Psi_{M^+F^-})$, where $\Psi_{M:F}$ and $\Psi_{M^+F^-}$ are the wave functions associated with the covalent and ionic bonds, respectively. The covalency C is expressed as $\lambda^2/(1+\lambda^2)$ which is a measure of delocalization of the valence electrons. Γ_L relates to a degree of the spatial overlap of the initial and final states of $\Psi(\mathrm{MO})$. Then it can be deduced from the linear relationship between Γ_L and C that the vacancies produced in the F^- L shell transfer, only through the covalent character of $\Psi(\mathrm{MO})$, to the valence bands of the

neighboring atoms. Further consideration of change in ω_1/ω_0 for F compounds with different chemical environments may improve ω_2/ω_0 here obtained. Study of the dependence of ω_1/ω_0 and ω_2/ω_0 on the covalency is in progress.

The chemical effect reflected in the intensity distributions of the F $K\alpha$ x-ray satellites produced by N^{4+} bombardment was observed and first explained quantitatively by introducing the vacancy rearrangement process in the L shell or the valence band of F^-. Γ_L estimated from the L-vacancy rearrangement probability f is directly proportional to the covalency. The technique offers promise for determining the ionicity or covalency of the chemical compounds with valence L-shell electrons.

Helpful discussion with K. Ishii and M. Kamiya on the analysis and comments on the manuscript by J. T. McDonald and R. L. Watson are gratefully acknowledged.

[1]R. L. Watson, A. K. Leeper, B. I. Sonobe, T. Chiao, and F. E. Jenson, Phys. Rev. A 15, 914 (1977).

[2]J. A. Demarest and R. L. Watson, Phys. Rev. A 17, 1302 (1978).

[3]R. L. Kauffman, K. A. Jamison, T. J. Gray, and P. Richard, Phys. Rev. Lett. 36, 1074 (1976).

[4]C. F. Moare, D. L. Matthews, and H. H. Wolter, Phys. Lett. 54A, 407 (1975).

[5]F. Hopkins, A. Little, N. Cue, and V. Dutkiewicz, Phys. Rev. Lett. 37, 1100 (1976).

[6]Y. Hayashi, private communication.

[7]L. Pauling, *The Nature of the Chemical Bond* (Cornell Univ. Press, Ithaca, N. Y., 1960), 3rd ed.

[8]E. J. McGuire, Phys. Rev. 185, 1 (1969).

[9]R. A. Pollak, L. Ley, F. R. McFeely, S. P. Kowalczyk, and D. A. Shirley, J. Electron Spectrosc. 3, 381 (1974).

[10]R. L. Watson, F. E. Jensen, and T. Chiao, Phys. Rev. A 10, 1230 (1974).

[11]G. T. Condo, Phys. Rev. Lett. 37, 1649 (1976).

[12]J. H. McGuire and P. Richard, Phys. Rev. A 8, 1374 (1973).

[13]D. L. Matthews, B. M. Johnson, L. E. Smith, J. J. Mackey, and C. F. Moore, Phys. Lett. 48A, 93 (1974).

[14]C. P. Bhalla, N. O. Folland, and M. A. Hein, Phys. Rev. A 8, 649 (1973).

Reprinted from J. Phys. Soc. Jpn., 50, 3023–3031 (1981).

Atomic Replacement in Ordered Cu_3Au Alloy Irradiated with Protons, α-Particles and Carbon Ions from a Cyclotron

Hideo SAKAIRI, Eiichi YAGI, Akio KOYAMA
and Ryukiti R. HASIGUTI*

The Institute of Physical and Chemical Research, Wako, Saitama 351

(Received December 15, 1980)

The resistivity increase by charged particle irradiation at liquid helium temperature has been measured on ordered and disordered Cu_3Au alloys. Comparison of the resistivity increase rate among these alloys and Cu is made for the same damage energy density. The number of disordering replacements per Frenkel pair in ordered Cu_3Au is estimated to be 27. The Snyder-Neufeld integral equation on the damage function is solved under the condition including the effect of focusing replacements. By modification of the result a semiempirical damage function is obtained.

§1. Introduction

One of the fundamental problems of radiation damage in solids by energetic particles is a structure of collision cascade, which determines the number of displaced atoms and their spacial distributions. In a previous paper experimental results on electrical resistivity increase in pure Cu irradiated with charged particles at liquid helium temperature were presented, from which the number of displaced atoms was deduced and compared with the results of computer simulation.[1] (This paper will be referred to as the paper I hereafter.) In the present paper the atomic replacement in an irradiated order-disorder alloy Cu_3Au is studied experimentally and its role in collision cascade formation is discussed.

It has been pointed out that the order-disorder alloys play an important role in experimental approaches to the study of replacement events of atoms occurring in a collision cascade.[2] The order-disorder alloys are also considered to be useful in a study of radiation damage because an order-disorder reaction often causes a significant change in physical properties of the alloys.

Fundamental understanding of an irradiated state requires irradiation experiments at temperatures as low as possible, but most of early works on the order-disorder alloys were performed at room temperature, except a few at liquid nitrogen temperature.[3,4] As to the most widely studied order-disorder alloy, Cu_3Au, the results of irradiation experiments at liquid helium temperature were presented by two groups in 1973.[5,6] The one was carried out by electron irradiation and the other by neutron irradiation. As expected generally, radiation effects observed in the two experiments were largely different from each other, that is, a disordering effect in the ordered alloy was much smaller for the electron irradiation than for the neutron irradiation.

In the present study the Cu_3Au alloys were irradiated at liquid helium temperature with charged particles (p, α, and carbon ions) from a cyclotron of IPCR. Defect introduction rates were studied by measurement of electrical resistivity changes. The number of replaced atoms in a collision cascade was derived from the results and compared with those of the experiments with electrons and neutrons. The effect of atomic replacement chains on defect production in a collision cascade was discussed on a simple model.

§2. Experimental Procedure

2.1 Specimen preparation

The Cu_3Au alloy was prepared by smelting Cu and Au metals of 99.999% purity in a quartz tube. Content of Au in this alloy was 25.8 atomic percent, corresponding to $Cu_{2.97}Au_{1.03}$ alloy. It was processed to a foil of 30 μm thickness by repeating several times

* Present address: The Science University of Tokyo, Faculty of Engineering, Shinjuku-ku, Tokyo 162.

cold rolling and annealing. Specimens of bridge shape were cut from the foil and annealed at 800°C for 30 min in vacuum.

Heat treatment for ordering followed Cook and Cushing;[7] 30 min at 800°C in vacuum, furnace cooling to 350°C, 6 h at 350°C, 16 h at 340°C, 4 h at 330°C, 4 h at 320°C, 16 h at 300°C and furnace cooling to room temperature. Electrical resistivities of ordered specimens, measured by ordinary DC potentiometry, were 2.7 to 3.0 $\mu\Omega$cm at liquid nitrogen temperature. The experimentally obtained specific resistivity of a well ordered Cu_3Au alloy was reported to be about 2 $\mu\Omega$cm at liquid nitrogen temperature.[8] As electrical resistivity due to excess content of Au (0.8 at%) is estimated to be about 0.7 $\mu\Omega$cm from a relation between the resistivity and the composition of the Cu_3Au alloy given in the ref. 2, the specimens used in the present experiment can be regarded as fairly well ordered.

A program for preparation of disordered specimens was as follows: 30 min at 800°C in vacuum, furnace cooling to room temperature, 1 h at 500°C in an evacuated pyrex glass capsule and quenching into silicone oil. Their specific resistivity was 9.995 $\mu\Omega$cm at liquid nitrogen temperature. As it was reported to be about 10 $\mu\Omega$cm for a well disordered Cu_3Au alloy,[8] the specimens thus obtained can be regarded as nearly perfectly disordered.

2.2 *Irradiation*

Irradiation procedure was nearly the same as that in the paper I, therefore only an abbreviated description is given here. A foil specimen, thin enough for beam to pass through, was supported with GE-7031 varnish on a mica plate which was fixed on a copper plate 1 mm thick. For avoiding temperature increase by beam heating, this specimen holder has a window behind the specimen through which particles coming out from the specimen pass. The specimen holder was equipped in a liquid helium cryostat. An aluminum foil 40 μm thick was placed at a beam inlet of the cryostat for isolating the cryostat from a vacuum system of the cyclotron. Carbon ions, which were accelerated as C^{4+} in the cyclotron, were regarded to be C^{6+} after they passed through the aluminum foil as a result of charge stripping. Beam intensity was about 100 nA/cm^2 in proton and α-particle irradiations and about 50 nA/cm^2 in carbon ion irradiation. Temperature of the specimen during the irradiation was below 18 K, which was monitored with a Cu vs Au–2.1%Co thermocouple.

Average energies of the irradiating particles in the specimens were calculated by a following equation

$$\langle E\rangle=\frac{1}{d}\int_0^d E\,\mathrm{d}x=\frac{1}{d}\int_{E_{\mathrm{in}}}^{E_{\mathrm{out}}} E\frac{\mathrm{d}x}{\mathrm{d}E}\,\mathrm{d}E, \qquad (1)$$

where d is a thickness of the specimen. A range-energy relation for Cu_3Au was obtained by numerical integration of the reciprocal of stopping power, on the simple assumption that stopping cross sections are additive as

$$\frac{\mathrm{d}E}{\mathrm{d}x}(Cu_3Au)=\frac{3}{4}\frac{N(Cu_3Au)}{N(Cu)}\frac{\mathrm{d}E}{\mathrm{d}x}(Cu)+\frac{1}{4}\frac{N(Cu_3Au)}{N(Au)}\frac{\mathrm{d}E}{\mathrm{d}x}(Au). \qquad (2)$$

Here $\mathrm{d}E/\mathrm{d}x$ and N are the stopping power and the number of atoms in a unit volume, respectively, of the alloy or the metals indicated in parentheses. The range-energy relation for Cu used here was the same as in the paper I. For Au the relations for protons and α-particles were taken from the tables by Whaling[9] and of Northcliffe and Schilling.[10] Error of the range-energy relation obtained here is considered to amount to several per cent, which is comparable to the experimental error of ten per cent.

§3. Results

Some experimental curves on the resistivity increase with an irradiation dose are shown in Fig. 1. A linear relation was observed within a dose range covered in this experiment. Results of resistivity increase rate in all irradiation runs are collected in Table I. These data are related to damage energy, a definition and a calculation of which are described below.

Theoretical models present the number of displaced atoms in a collision cascade caused by a primary knocked-on atom (PKA), ν, generally as a function of E_1, kinetic energy of the PAK. It is often called as a damage function. An expected value of the number of displaced atoms produced by all cascades created by an incident particle with energy E can be expressed

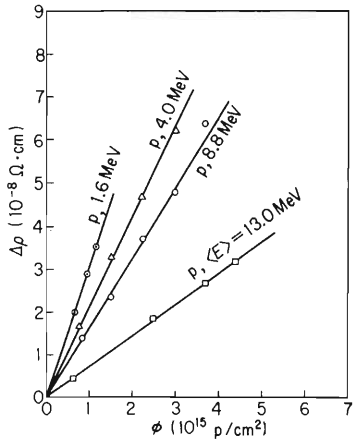

Fig. 1. Increase of electrical resistivity of ordered Cu_3Au alloys with increase in proton dose.

by this function as

$$N_d = N \int_{E_d}^{E_{p(max)}} \nu(E_1)\, d\sigma(E; E_p). \qquad (3)$$

Here $d\sigma(E; E_p)$ is a differential cross section of the primary collision transferring E_p and E_d is threshold energy for permanent displacement of atoms. The kinetic energy E_1 is $E_p - E_d$. The eq. (3) is based on a model with sharp threshold for analytical simplicity.

From most of the collision cascade models it was derived that $\nu(E_1)$ is approximately a linear function of E_1, except in the low energy region near displacement threshold and in the high energy region where electronic excitation dominates elastic scattering. Therefore N_d can be regarded in most cases to be nearly proportional to

$$\int_{E_d}^{E_{p(max)}} E_1\, d\sigma(E; E_p) = \int_{E_d}^{E_{p(max)}} (E_p - E_d)\, d\sigma(E; E_p). \qquad (4)$$

When E_1 exceeds the ionization threshold E_c, above which the cross section of electronic excitation is larger than that of elastic scattering, an effect of energy dissipation for ionization by PKA cannot be neglected in displaced atom production. For neutrons which create a wide uniform distribution of E_1, correction for this loss is essential. But for charged particles the cross section $d\sigma(E; E_p)$ is in proportion to E_p^{-2}, so it decreases rapidly with the increase in E_p and the effect of electronic excitation upon N_d is regarded to be small.

The ionization loss is taken into consideration approximately with the sharp ionization threshold model; (1) PKAs with E_1 above E_c dissipate all of their energy by electronic excitation only before their energy decreases to E_c and (2) PKAs with E_1 below E_c dissipate all of their energy only by elastic collision. Thompson suggested that a better correction is made by using $2E_c$ in place of E_c from the consideration that the contribution from the elastic collision in the energy range above E_c is not so small as to be entirely neglected.[11] In this paper, the damage energy density, S, was calculated according to this suggestion as

Table I. Initial rate of resistivity increase.

Irradiating particles	Specimen No.	E_{in} (MeV)	$\langle E \rangle$ (MeV)	$d\rho/d\phi$ (10^{-23} Ωcm/(particle/cm²))
		(a) Ordered Cu_3Au		
Protons	1	13.7	13.0	0.73
	2	13.7	13.0	0.85
	3	9.7	8.8	1.57
	4	5.4	4.0	2.1
	5	3.6	1.6	3.0
α-particles	6	38.5	37.0	5.1
	7	38.9	36.7	6.1
	8	20.5	17.8	12.4
C^{6+} ions	9	72.5	49.8	85
		(b) Disordered Cu_3Au		
α-particles	10	20.5	14.7	3.3
	11	20.5	14.5	3.1

$$S=N_{\mathrm{Cu}}\left\{\int_{E_d}^{2E_c^{\mathrm{Cu}}} E_1\,\mathrm{d}\sigma^{\mathrm{Cu}}(E;E_p)+\int_{2E_c^{\mathrm{Cu}}}^{E_p^{\mathrm{Cu}}(\max)} 2E_c^{\mathrm{Cu}}\,\mathrm{d}\sigma^{\mathrm{Cu}}(E;E_p)\right\}$$
$$+N_{\mathrm{Au}}\left\{\int_{E_d}^{2E_c^{\mathrm{Au}}} E_1\,\mathrm{d}\sigma^{\mathrm{Au}}(E;E_p)+\int_{2E_c^{\mathrm{Au}}}^{E_p^{\mathrm{Au}}(\max)} 2E_c^{\mathrm{Au}}\,\mathrm{d}\sigma^{\mathrm{Au}}(E;E_p)\right\}, \tag{5}$$

where $E_1=E_p-E_d$.

The calculation was made for the average energy of the irradiating particles in the specimens, because a drop in the particle energy in the thin foil specimens was not large. Only for the irradiation with carbon ions, however, an energy drop was very large (from 72.5 MeV to 19 MeV) due to the large stopping cross section. The cross-over of the energy losses by elastic collision and by electronic excitation occurs near the energy E_x above which the ionization occurs, so E_c can be equated with E_x.[11] According to the conventional expression for E_x,[12] values of E_c^{Cu} and E_c^{Au} are estimated to be 65 keV and 200 keV, respectively. The differential cross section was assumed to be that of the Rutherford scattering as in the paper I. The values of E_d of Cu and Au atoms in the Cu_3Au alloy were assumed to be the same as that in the pure copper i.e. 22 eV. Experimental values of $d\rho/d\phi$ are plotted against S in Fig. 2. The experimental points for ordered alloys fall on a linear curve corresponding to linear proportionality. For the comparison the results on Cu which were presented in the paper I are also included.

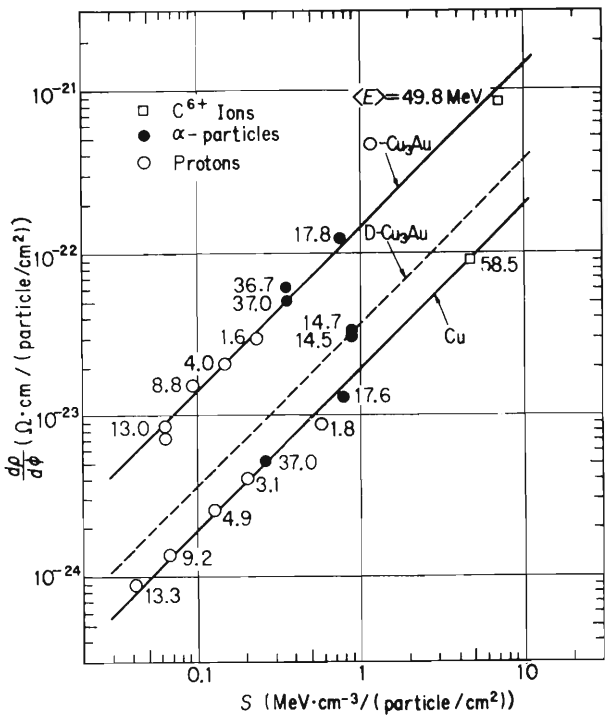

Fig. 2. Resistivity increase rate vs total damage energy in ordered Cu_3Au (O-Cu_3Au), disordered Cu_3Au (D-Cu_3Au) and Cu specimens. Figures affixed to each point indicate average energies of irradiating particles in specimens. The data on Cu were taken from the paper I. The calculation of S for Cu in the paper I was made with E_p in place of E_1 in the eq. (5). The replacement of E_p with E_1 made S decrease by about 10%, but it does not affect a linear relation between $d\rho/d\phi$ vs S.

§4. Discussions

4.1 The number of disordering replacement in ordered Cu_3Au

For the study of atomic replacement occurring in a collision cascade, it is necessary to suppress the thermal migration of Frenkel defects which may be accompanied by the atomic replacement. In general the liquid helium temperature is considered to be low enough for it. As to irradiation experiments on ordered alloys performed at that temperature there have been still a few. Kirk, Blewitt and Scott suggested by the analysis of a change of saturation magnetization of Ni_3Mn irradiated by thermal neutrons that a 450 eV recoil from the (n, γ) reaction produces about 130 replacements.[13] Takamura and Okuda measured an increase in electrical resistivity of Cu_3Au alloys irradiated with fast neutrons.[5] They estimated the ratio of the number of replacement to the number of displacement to be about 50. In the experiments by Becker *et al.* on Fe_3Ni with electrons the ratio was found to be about 2.[14] It is obvious that the disordering phenomena is closely related to the collision cascade.

On pure metals the number of displaced atoms, that is, the number of Frenkel pairs, n_F, can be deduced from the resistivity increase, $\Delta\rho$, and a known value of the resistivity due to a Frenkel pair, $\Delta\rho_F$. The number of replacement in alloys, n_R, can also be deduced from the resistivity increase of alloys on some assumptions, if a value of the resistivity increase due to a replacement, $\Delta\rho_R$, could be

known. Takamura and Okuda estimated the value of $\Delta\rho_R$ to be 0.4 $\mu\Omega$cm/%repl. in ordered Cu_3Au, with the formula by Becker *et al.*[14] on the relation between the change of the long range order parameter and the number of replacement in A_3B type fcc lattices. It must be noted that in their calculation the resistivity increase was averaged over all replacements, not for disordering replacements only.

Takamura and Okuda made the assumptions that

(1) the numbers of Frenkel pairs in the three kinds of specimens are the same for the same irradiation dose,

(2) the resistivity increase of the disordered alloy is entirely due to the Frenkel pairs,

(3) the resistivity due to a Frenkel pair in the ordered alloy is the same as that in the disordered alloy,

(4) for pure copper, $\Delta\rho_F = 2.5$ $\mu\Omega$cm/%F.P., and for ordered alloy $\Delta\rho_R = 0.4$ $\mu\Omega$cm/%repl. The ratio of n_R to n_F in ordered Cu_3Au alloys can be, then, calculated as

$$\frac{n_R}{n_F} = \frac{(\Delta\rho(\text{O-Cu}_3\text{Au}) - \Delta\rho(\text{D-Cu}_3\text{Au}))/\Delta\rho_R}{\Delta\rho(\text{Cu})/\Delta\rho_F}. \quad (6)$$

The resulted value was 50.

In our experiment the ratio of the resistivity increase of ordered Cu_3Au to that of Cu was almost constant for various irradiation runs, as seen in Fig. 2. The same situation can be also expected for disordered Cu_3Au. The ratios of the resistivity increase of alloys to that of Cu obtained for the same value of S are listed in Table II together with the results of neutron irradiation experiments. In the latter case the ratios obtained for the same neutron dose are listed.

Instead of the assumption (1) described above, we assumed that (1′) the numbers of Frenkel pairs in the three kinds of specimens are the same for the same value of the total damage energy density S. With this assumption and those (2) to (4) described above, the ratio of n_R to n_F was calculated to be 34. This value is about two thirds of the value obtained in the neutron irradiation experiments. If a more general assumption, $\Delta\rho = 2.0$ $\mu\Omega$cm/%F.P., is taken, the values of the ratio n_R/n_F decrease to 40 and 27 for the experiment by Takamura and Okuda and for the present one, respectively. The value obtained by the former will be made smaller if the comparison between Cu and Cu_3Au would be made in the same way as that in this paper, i.e., for the same S value.

Table II. The ratios of $d\rho/d\phi$ between Cu_3Au and Cu.

	Neutron irradiation[a]	Charged particle irradiation[b]
Ordered Cu_3Au	10.9	7.3
Disordered Cu_3Au	2.5	1.9
Cu	1	1

[a] for the same total dose (ref. 5).
[b] for the same S value (present authors).

Another study on this problem by Kirk *et al.* was made on Ni_3Mn irradiated with neutrons.[13] They suggested that a 450 eV recoil from (n, γ) reaction produced 132 replacements. They stated that the Kinchin-Pease-like analysis predicts the generation of 4 to 8 Frenkel pairs for that recoil, therefore, the ratio of the number of replacement to that of displacement falls within 16.5 to 33. Jenkins and Wilkens observed by TEM the images of disordered zones produced in ordered Cu_3Au by irradiation with 10 keV Cu^+ ions.[15] From an analysis of contrast profile of the images they estimated the ratio n_R/n_F to be at least of the order of 10, although the irradiation was made at room temperature and some annealing effects might be involved.

Thus it is considered to be a general feature in high energy cascades that the number of disordering replacement in alloys is larger than the number of displaced atoms by a factor of a few tens. It was about 30 in the present experiment on the Cu_3Au alloy.

4.2 *The role of focused replacement in collision cascade*

The damage function $\nu(E_1)$ was treated theoretically for the first time by Kinchin and Pease[16] and by Snyder and Neufeld.[17] Its approximate form below the ionization threshold, E_c, is

$$\nu(E_1) = \frac{E_1}{2E_d}, \quad (7)$$

except near the displacement threshold. The simple calculation of $\nu(E_1)$ with this formula gives a value about three or four times as large as the experimental ones.[1,18]

In the Kinchin-Pease and the Synder-Neufeld models, the stability of each Frenkel pairs was assumed to be independent of other pairs, while Beeler *et al.* found by computer simulation that the interaction of displaced atoms with other Frenkel pairs in the vicinity of themselves make them unstable and reduce the damage function.[19] This dynamic recombination effect was taken into account in the more elaborate simulation by Robinson-Torrens.[20] From the numerical results of the simulation they gave an approximate expression for the damage function, with which they calculated the number of displaced atoms in Cu irradiated with neutrons and showed that the calculated values are twice as large as the experimental ones. We made irradiation experiments on Cu with charged particles and calculated the number of displaced atoms with the damage function of Robinson and Torrens under the irradiation condition of our experiments. The results showed that calculated values are also twice as large as the experimental ones. The detailed discussion of this problem was given in the paper I.

Other hopeful mechanism to remove the discrepancy is the focused replacement. Once the focused replacement collision sequence occurs, the kinetic energy kept at the beginning of the sequence is mostly dissipated without producing any displaced atoms except at the end of the replacement chain. Therefore the large reduction of $\gamma(E_1)$ can be expected. If most of the replacement events occur without accompanying the displacement, it is required for several atoms to move coincidently along some closed circuit, which was examined as the self-diffusion mechanism in the early stage of the study of diffusion in solids.[21] As such circular replacement event without accompanying displacements is considered to be low energy event as compared with that accompanying the displacement, the frequency of occurence is expected to be larger in electron irradiation than in heavy particle irradiation. The experiment on Fe_3Ni with electrons by Becker *et al.* showed, however, that the ratio of the number of replacement to that of Frenkel pairs is only about 2.[14] Therefore most replacement events were supposed to be generated in the focused collision chain.

From the linear relation between $d\rho/d\phi$ and S in Fig. 2, the damage energy per Frenkel pair S/n_F can be derived. Taking $\Delta\rho_F=2.0$ $\mu\Omega$cm/%F.P., S/n_F was calculated to be 118 eV for pure copper. This value is $2.7(2E_d)$, which means that the number of displaced atoms calculated with Kinchin-Pease formula is 2.7 times as large as the value estimated from the present experiment. (It was $3.0(2E_d)$ in the paper I, in which S was calculated with E_p in place of E_1 in the eq. (5). This change from E_p to E_1 made S decrease by about 10%, but it does not affect a linear relation between $d\rho/d\phi$ vs S).

Here it is assumed that the number of replacements in Au is about the same as that in Cu_3Au. The damage energy per Frenkel pair (S/n_F) being 118 eV as calculated above, the energy loss per replacement is estimated to be about 3.5 eV ($=(118-E_d)/27$). In the ordered Cu_3Au, however, a half of $\langle 110\rangle$ close packed rows consist of alternate arrangement of Cu and Au atoms and the other half consist of Cu atoms only. The value 3.5 eV is obtained by averaging over the replacements on both the Cu rows and the Cu–Au rows. This value is large compared with those obtained by the computer simulation, about 2 eV for the Cu–Au replacements in Cu_3Au,[11] and about 2/3 eV for the Cu–Cu replacements in Cu.[22] The value of $S/n_F=118$ eV is considered to be overestimated because the electronic loss in low energy cascades and the contribution from $\langle 100\rangle$ focused replacements were neglected in the present analysis. It is, however, plausible that the value for Cu is smaller than that for Cu_3Au and, therefore, the ratio n_R/n_F in Cu is large compared with that in Cu_3Au. The ratio, 27, obtained from the results on Cu_3Au must be considered as a lower limit for that of Cu.

In the computer simulations, however, the focusing events seemed not to be given a major role in reducing the number of displaced atoms. Robinson and Torrens pointed out that the computer simulation of the collision cascade is unsatisfactory at present because it does not deal with a low energy collision event as a many body effect; that is, in order to make computer simulation on a large collision cascade, a large model crystal has to be used and then the two body collision approximation is adopted because of the limitation in computer capacity. Perhaps this may be the reason

why the large reduction of the damage function ascribable to the focusing effect was not observed in the computer simulation of a large collision cascade.[19,20] Thus, the occurrence of a few tens of replacement events per Frenkel pair, which was observed experimentally in ordered alloys, is considered to be the most strong support for the effect of the focused replacement in reducing the number of displaced atoms.

Analytical treatment of the cascade containing the focused replacement collision, however, is difficult and a few expressions have been proposed for the damage function containing the focusing effect. Thompson proposed to replace $2E_d$ in the Kinchin-Pease formula by E_f, which is the maximum energy initiating focusing replacement,[11] that is,

$$\nu(E_1)=\frac{E_1}{E_f}. \tag{8}$$

This replacement is, however, unable to reduce the calculated $\nu(E_1)$ value for Cu, because the value of E_f is about 40 eV (calculated theoretically)[22] or about 50 eV (estimated from sputtering experiments),[23] that is, the magnitude of E_f cannot exceed that of $2E_d$. There is another proposal to replace E_d, instead of $2E_d$, by E_f, which can make $\nu(E_1)$ decrease to about a half.[24] But these replacement procedures were not given a plausible theoretical basis.

Here the modification of $\nu(E_1)$ by the focusing effect will be examined. There are two extreme relations between the Frenkel pairs and the replacements; (1) most Frenkel pairs are generated without focused replacement chains and only a few pairs are produced as a result of very long replacement collision sequences; in this case the number of replacement collision sequences reaches to several hundreds; (2) most Frenkel pairs are produced at the end of focused replacement chains; in this case the number of replacements in a sequence remains a few tens. The case (2) seems to be more realistic because all available values of E_f in copper are not so large as to maintain a very long sequence. For simplicity it is assumed here that all Frenkel pairs are produced through focused replacement chains, that is, all recoil atoms which are transferred the energy lower than E_f can form a replacement chain. A mathematical expression in this situation is that the value of the damage function is 1 for the recoils with the kinetic energy between zero and E_f.

We start from the basic equation presented by Snyder and Neufeld,[17] that is,

$$\nu(E_1)=\int_0^{E_1}\nu(E_2)\frac{dE_2}{E_1}+\int_0^{E_1-E_d}\nu(E_1-E_2-E_d)\frac{dE_2}{E_1}, \tag{9}$$

where E_1 is a kinetic energy of PKA, i.e. $E_1=E_p-E_d$. The first integral in the right-hand side is ascribed to the PKA whose energy was reduced from E_1 to E_2 by the secondary collision and the second integral comes from the secondary knocked-on atom produced by that collision. According to the simplified model described above, the boundary condition was set as

$$\nu(E_1)=1 \quad \text{for } 0\le E_1\le E_f. \tag{10}$$

The eq. (9) can be solved analytically to be

$$\nu(E_1)=\ln\frac{E_1}{E_f}+1, \quad E_f<E_1<E_f+E_d. \tag{11}$$

In further energy region the equation must be solved numerically. An example of the results of calculation is given in Fig. 3. Such curves were obtained for various combinations of E_d and E_f. From these curves it was found that $\nu(E_1)\times(E_d+E_f)/E_1$ changes only between 0.9 and 1.0 for the acceptable values of E_d+E_f, as shown in Fig. 4. The damage function can then be expressed approximately as

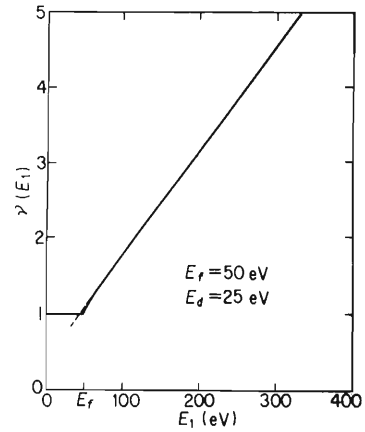

Fig. 3. An example of a damage function $\nu(E_1)$ on a collision cascade model, in which the focused replacement effect is taken into account. Values of E_d and E_f are taken as 25 eV and 50 eV, respectively.

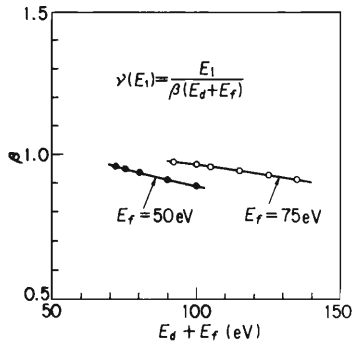

Fig. 4. The values of β in $\nu(E_1)=E_1/\{\beta(E_d+E_f)\}$, which is derived from eq. (9) in the region of large E_1, as a function of E_d+E_f.

$$\nu(E_1)\simeq\frac{E_1}{E_d+E_f}. \tag{12}$$

For $E_f=E_d$, this formula coincides with the Kinchin-Pease formula.

The damage energy per Frenkel pair S/n_F, which is the average of $E_1/\nu(E_1)$, is $2.7(2E_d)$ in the present study. For $E_f=2E_d$, $3E_d$ and $4E_d$, the values of $E_1/\nu(E_1)$ calculated with eq. (12) are $1.5(2E_d)$, $2.0(2E_d)$ and $2.5(2E_d)$, respectively. Though $E_f=4E_d$ can give good agreement between the calculation and the experiments, it seems rather large as compared with both theoretically calculated values and experimentally obtained values, i.e. $(2\sim3)E_d$. When $E_f=(2\sim3)E_d$, $E_1/\nu(E_1)$ is still smaller than the experimental value by the factor 1.5. Taking account that the effect of these events is emphasized excessively in the present model, it seems impossible to explain the experimental values only with the contribution of focused replacement events.

It can be suggested, however, that the eq. (12) is applicable as a semiempirical formula if other effects than focused replacement, *e.g.* the dynamic recombination effect as discussed in the paper I, could be included into the equation with a constant factor k as

$$\nu(E_1)=k\frac{E_1}{E_d+E_f}. \tag{13}$$

On a gold, a value of E_f for $\langle110\rangle$ focusing is 170 eV according to the sputtering experiment by Thompson,[25] which is about four times as large as that in Cu. Cooper *et al.* measured the damage rate for 12 MeV-deuterons on Cu, Ag and Au.[26] From their results on $d\rho/d\phi$, 3.8×10^{-24} Ωcm/(d/cm^2) for Au and 2.3×10^{-24} Ωcm/(d/cm^2) for Cu, the ratio of the Frenkel pair concentrations, c_F^{Au}/c_F^{Cu}, is derived to be 1.0 with the values of $\Delta\rho_F^{Au}=3.3$ $\mu\Omega$cm/%F.P.[27] and $\Delta\rho_F^{Cu}=2.0$ $\mu\Omega$cm/%F.P. The calculation with eqs. (3) and (13) with the sharp ionization threshold approximation is made under the irradiation condition of Cooper *et al.* The average energy of deuterons in their specimen is estimated to be 9.6 MeV in both Au and Cu. By using $E_f^{Au}=170$ eV, $E_d^{Au}=35$ eV,[28] $E_f^{Cu}=50$ eV and $E_d^{Cu}=22$ eV, the calculation leads to that $c_F^{Au}/c_F^{Cu}=0.95$. Thus the ratio of Frenkel pair concentration calculated with the eq. (13) agrees quite well with the experimental value by Cooper *et al.* in spite of the large difference in E_d+E_f values, i.e. 205 eV for Au and 72 eV for Cu. The value of constant factor k is determined to be 0.60 by the comparison of the calculated values of the formula eq. (13) with the results on Cu in our experiments,

$$\nu(E_1)=0.6\frac{E_1}{E_d+E_f}. \tag{14}$$

§5. Summary

(1) The resistivity increase by charged particle irradiation at liquid helium temperature was measured on ordered and disordered Cu_3Au alloys. The comparison of the resistivity increase rate among these alloys and Cu presented in the previous paper was made for the same damage energy density S, from which some physical quantities were derived.

(2) The number of disordering replacements per Frenkel pair in ordered Cu_3Au was estimated to be 27. Such large value indicates the importance of the focused replacement effect in collision cascade in the crystalline solids.

(3) The Snyder-Neufeld integral equation on the damage function was solved under a new boundary condition which includes the effect of focusing replacement. The resulted form of the damage function is

$$\nu(E_1)=\frac{E_1}{E_d+E_f}.$$

(4) As a semiempirical formula of the damage function,

$$\nu(E_1)=0.6\frac{E_1}{E_d+E_f},$$

was proposed. It was applied satisfactorily to

Au, E_f value of which is quite different from that of Cu.

Acknowledgement

The authors would like to express their appreciation to the members of the cyclotron laboratory of the Institute of Physical and Chemical Research. They are also indebted to the members of the user group of liquid helium in IPCR for their collaboration in operation and maintenance of a helium liquefier. They wish to acknowledge the assistance of Messrs. K. Rokutanda, T. Nakamura and H. Yokota in experiments.

References

1) H. Sakairi, E. Yagi, A. Koyama, T. Karasawa and R. R. Hasiguti: J. Phys. Soc. Jpn. **43** (1977) 999.
2) S. Siegel: Phys. Rev. **75** (1949) 1823.
3) J. A. Brinkman, C. E. Dixon and C. J. Meechan: Acta Met. **2** (1954) 38.
4) T. H. Blewitt and R. R. Coltman: Acta Met. **2** (1954) 549.
5) S. Takamura and S. Okuda: Rad. Effects **17** (1973) 151.
6) J. Gilbert, H. Herman and A. C. Damask: Rad. Effects **20** (1973) 37.
7) L. C. Cook and R. L. Cushing: Acta Met. **1** (1953) 549.
8) M. Hirabayashi and Y. Muto: Acta Met. **9** (1961) 497.
9) W. Whaling: *Handbuch der Physik*, ed. S. Flügge (Springer, Berlin, 1958) Vol. 34, p. 193.
10) L. C. Northcliffe and R. F. Schilling: Nuclear Data Tables **A7** (1970) 265.
11) M. W. Thompson: *Defects and Radiation Damage in Metals* (Cambridge Univ. Press, London, 1967) Chap. 5.
12) D. K. Holmes: *Radiation Damage in Solids*, ed. D. S. Billington (Academic Press, New York and London, 1962) p. 214.
13) M. A. Kirk, T. H. Blewitt and T. L. Scott: Phys. Rev. **B15** (1977) 2914.
14) D. Becker, F. Dworschak, C. Lehmann, K. T. Rie, H. Schuster, H. Wollenberger and J. Wurm: Phys. Status. Solidi. **30** (1968) 219.
15) M. L. Jenkins and M. Wilkens: Phil. Mag. **34** (1976) 1155.
16) G. H. Kinchin and R. S. Pease: Rep. Progr. Phys. **18** (1955) 1.
17) W. S. Snyder and J. Neufeld: Phys. Rev. **97** (1955) 1636.
18) D. K. Holmes: *The Interaction of Radiation with Solids*, ed. R. Strumane *et al.* (North-Holland, Amsterdam, 1964) p. 147.
19) J. R. Beeler, Jr.: Phys. Rev. **150** (1960) 470.
20) M. T. Robinson and I. M. Torrens: Phys. Rev. **B9** (1974) 5008.
21) A. Seeger: *Handbuch der Physik*, ed. S. Flügge (Springer-Verlag, Berlin, 1955) VII/I, p. 421.
22) J. B. Gibson, A. N. Goland, M. Milgram and G. H. Vineyard: Phys. Rev. **120** (1960) 1229.
23) B. W. Farmery and M. W. Thompson: Phil. Mag. **18** (1968) 415.
24) R. S. Nelson: *Ion Implantation*, ed. G. Dearnaley *et al.* (North-Holland, Amsterdam, 1973) p. 154.
25) M. W. Thompson: Phil. Mag. **18** (1968) 377.
26) H. G. Cooper, J. S. Koehler and J. W. Marx: Phys. Rev. **94** (1954) 496.
27) H. Wollenberger: *Vacancies and Interstitials in Metals*, ed. A. Seeger *et al.* (North-Holland, Amsterdam, 1970) p. 215.
28) W. Bauer and A. Sosin: Phys. Rev. **135** (1964) A521.

Reprinted from J. Phys. B: At. Mol. Phys., 15, 3759–3767 (1982).

X-rays from radiative electron capture induced by 110 MeV Ne ions

T Kambara, Y Awaya, A Hitachi†, M Kase, I Kohno and T Tonuma
Institute of Physical and Chemical Research, Hirosawa, Wako-shi, Saitama 351, Japan

Received 5 October 1981, in final form 15 June 1982

Abstract. Energy spectra of radiative electron capture (REC) x-rays have been studied for 110 MeV Ne ion bombardment on gaseous targets of H_2, He, CH_4, N_2, O_2 and Ne. A Si(Li) detector placed at 90° to the beam direction was used for the measurements. The width and peak energy of the REC peak are compared with the impulse approximation calculation and fair agreement is obtained.

The REC x-ray yield and the peak energy have been measured for the H_2 target as a function of the gas pressure and the results are discussed in relation to the charge equilibration process of the ions in the gas.

1. Introduction

When a projectile ion captures an electron from a target into its vacant orbit, a photon can be emitted in this transition with a certain probability. The energy of the photon from such a process, radiative electron capture (REC), is distributed near the sum of the kinetic energy of an electron with the velocity of the projectile and the electron binding energy of the captured orbit in the projectile ion. The REC x-rays from heavy-ion bombardment were first reported by Schnopper *et al* (1972) and many works have considered the REC process.

The profile of REC x-ray energy spectra relates to the momentum distribution of the electrons in the outer shell of the target atoms. Sohval *et al* (1976a) measured the width of the REC peak from the bombardment of oxygen ions on gaseous targets with atomic number $Z_T \leqslant 8$ and reported that it changes suddenly above $Z_T = 2$, reflecting the shell structure of the target atoms. They also compared the width with the impulse approximation and obtained good agreement.

In the present work, we used Ne ions as the projectile and various gases with $Z_T \leqslant 10$ as the targets. The energies of K x-rays from Ne^{9+} ions (hydrogen-like) are less than 1.4 keV and the K x-rays from the target atoms have lower energies, while the REC x-ray energy in the present case is about 4 keV. The absorption of the REC photons due to the target material and the detector window is small. Therefore it is easy to resolve the REC x-rays from the characteristic x-rays emitted from both collision partners and to reproduce the REC x-ray spectra from the experimental data.

The experimental set-up is described in § 2 and the processing of the data obtained is described in § 3 together with a discussion of the background x-rays. We have compared the REC peak energy and width with the impulse approximation, which is

described in § 4.1. The relation between the target density dependence of the REC spectrum and the charge equilibration processes in H_2 gas is discussed in § 4.2.

2. Experiments

A beam of 120 MeV Ne^{6+} ions from the IPCR cyclotron passed into a gas target cell which contained gases such as H_2, He, CH_4, N_2, O_2 and Ne. The gas cell was made of Al and had two windows with 7 μm thick Al foils for the beam entrance and exit, and one window with a 4 μm thick Mylar foil faced to a Si(Li) detector. The detector was placed at 90° to the beam direction. The length of the beam path between the entrance foil and the area viewed by the detector was about 7 cm.

The gas pressure was monitored by an alphatron gauge and could be raised to 120 Torr. The measurements for the He gas target were performed at pressures of 25 and 116 Torr and those for targets heavier than He were performed at pressures between 20 and 40 Torr. Additional measurements were performed for the H_2 target at various gas pressures between 9 and 120 Torr.

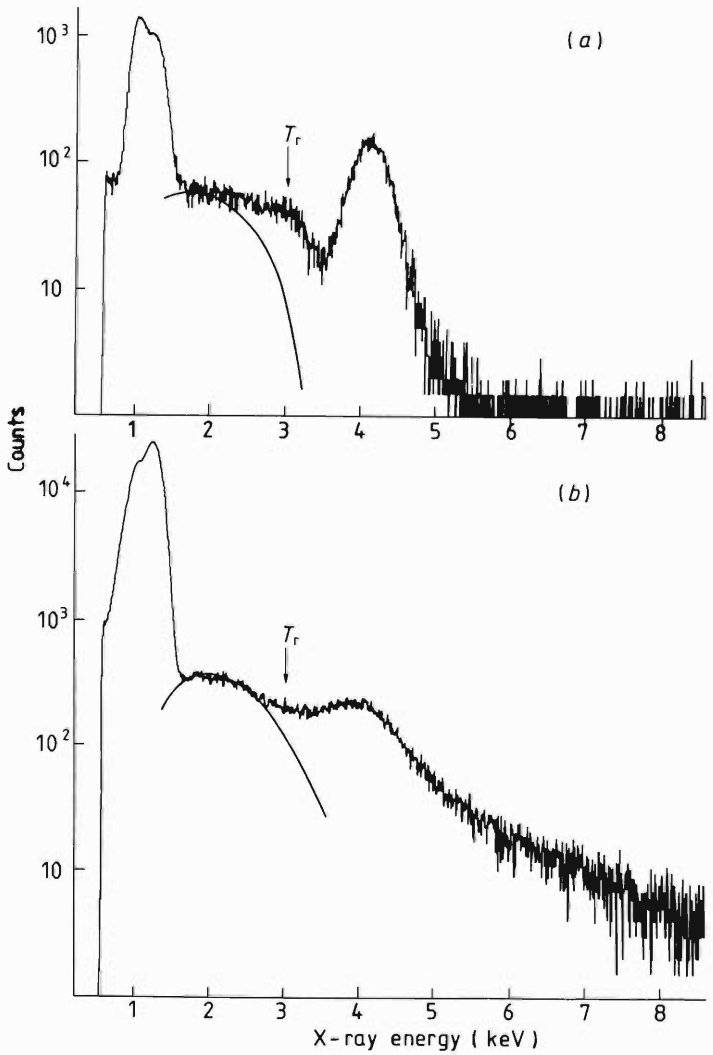

Figure 1. Spectra of x-rays from Ne ion bombardment on gas targets: (*a*) 120 Torr H_2 gas; (*b*) 40 Torr Ne gas. The full curves show the calculated results for the contribution from the quasi-free electron bremsstrahlung.

The energy loss of the ions in the beam entrance window foil reduced the beam energy by about 8.3 MeV (Northcliffe 1960). The energy loss in the target gas between the entrance window and the area viewed by the detector depends on the gas species and the pressure, and was about 1.8 MeV at maximum (Zieger 1980). The projectile velocity variation caused by the difference in energy loss in the different gases was within 1%.

Emitted x-rays passed through the Mylar foil and were detected by the Si(Li) detector with a 7.5 μm thick Be window. The space between the gas cell window and the detector window was evacuated to avoid additional photon absorption by air. The resolution of the Si(Li) detector was about 250 eV (FWHM) at 6.4 keV.

An x-ray spectrum measured for a H_2 gas target at 120 Torr is shown in figure 1(*a*) and for a Ne gas target at 40 Torr in figure 1(*b*). Two overlapping peaks at about 1.0 keV and 1.2 keV correspond to the K x-rays from Ne^{9+} ions in the beam. It was verified by high-resolution measurements with a crystal spectrometer that the 1.0 keV peak was due to the 2p–1s transition and the 1.2 keV peak was a superposition of the lines from the np–1s transitions ($n \geq 3$). A broader peak near 4 keV corresponds to the REC x-rays from the transition to the ground state of the Ne ions.

3. Background x-rays and processing of experimental data

In addition to the peaks due to the transitions in the projectile ions and the REC process, there is a continuous x-ray background in the spectra and its shape varies with the target gas species. The x-rays are considered to be due mainly to the following processes: (i) radiative transitions of the target electrons into a continuum state (quasi-free electron bremsstrahlung—QFEB) and (ii) secondary electron bremsstrahlung (SEB) (Jakubassa and Kleber 1975). The first process is predominant when the photon energy is less than $T_r = \frac{1}{2}mv_0^2$ where m is the electron mass and v_0 is the projectile velocity. The second process becomes more important when the photon energy is greater than T_r and smaller than $4T_r$, which represents the maximum energy of the SEB photons, and when the target atomic number Z_T becomes larger.

We calculated the x-ray emission cross section from the QFEB process using a formula based on the PWBA (Yamadera *et al* 1981). The cross section decreases strongly when the photon energy exceeds T_r, which is about 3 keV in our experiment. The steepness of the decline around T_r depends on the target species. The result of the calculation is shown by the full curves in figures 1(*a*) and (*b*), which are corrected for absorption in the materials between the target centre and the detector and are normalised to the experimental data.

According to some experiments and calculations (Folkmann *et al* 1974, Ishii *et al* 1976), the x-ray spectrum due to the SEB process decreases almost exponentially and the decline is less steep than that due to the QFEB process at photon energies less than $4T_r$.

In the case of the H_2 gas target, which is shown in figure 1(*a*), there seems to be little contribution from the SEB process. The background spectrum has a shoulder around 3 keV, the position of which is higher than that predicted by the calculation by about 0.5 keV. The origin of the difference between the data and the calculation is considered to be the REC process to the outer shell of the projectile ions (O-REC) (Sohval *et al* 1976b). In the case of the He target, the shoulder disappears, probably because it is hidden by the broader REC peak due to the transition to the K shell.

In the case of heavier targets, like the Ne target shown in figure 1(*b*), an exponentially decreasing background which is considered to be due to the SEB process is seen at energies greater than T_r and the yield increases for higher Z_T. The contribution of the QFEB process is observable as a broad shoulder below T_r and its position agrees with the result of the calculation. The contribution from the O-REC process is not observed clearly in the spectra.

The spectra obtained experimentally were corrected for photon absorption in the target gas, the Mylar foil window of the target cell and the Be foil window of the detector. The REC peak was fitted by a least-squares technique to a Gaussian curve with a background. The formula for the background for the H_2 target was chosen as the extrapolation of the steep decline of the QFEB and O-REC contributions in the lower-energy region. For targets heavier than H_2, an exponential curve corresponding to the contribution from the SEB process was chosen.

The absorption correction changes the calculated peak position and width by no more than 4 eV and 6% respectively. The peak width derived from the least-squares fit was corrected for instrumental broadening by using the linewidth in the calibration spectra. The peak energy was corrected for the beam energy loss in various gas species and for various pressures.

4. Results and discussion

4.1. Impulse approximation

We have calculated the peak energies and widths of the REC spectra by the impulse approximation (Kleber and Jakubassa 1975) with the approximate wavefunction given by Slater (1960) for the bound electrons of the target atoms. In the calculation, we assumed that (i) the projectile was Ne^{10+}, (ii) the target was of atomic particles (C for CH_4) and (iii) only the outermost shell electrons were captured by the K shell of the projectile. In the impulse approximation the REC cross section is given by

$$d^2\sigma/dE_x\, d\Omega = \int d\boldsymbol{p}_i (d\sigma_f/d\Omega)_{\boldsymbol{p}_i+\boldsymbol{p}_0} |\phi(p_i)|^2\, \delta(E_i - E_f) \tag{1}$$

where $d\Omega$ is the solid angle, E_x is the energy of the x-ray quanta, $\boldsymbol{p}_0 = m\boldsymbol{v}_0$ with the projectile ion velocity $\boldsymbol{v}_0$ and electron mass m, $\boldsymbol{p}_i$ is the momentum of the target electrons to be captured, the δ function guarantees energy conservation and $|\phi(\boldsymbol{p}_i)|^2$ is the momentum distribution of the target electrons. The capture cross section $d\sigma_f/d\Omega$ of free electrons by a bare nucleus with charge Ze at 90° is (Bethe and Salpeter 1977)

$$\frac{d\sigma_f}{d\Omega} = 1.09 \frac{\eta^6 \exp(-4\eta \tan^{-1}(1/\eta))}{(1+\eta^2)^2(1-\exp(-2\pi\eta))} \times 10^{-21}\ \text{cm}^2 \tag{2}$$

with $\eta = Ze^2/\hbar v$ where v is the relative velocity between the electron and the nucleus. The approximate wavefunction of Slater (1960) gives the momentum distribution as

$$|\phi(p_i)|^2 = 8p_s^5/\pi^2(p_i^2 + p_s^2)^4 \tag{3}$$

where $p_s = Z_{sc}me^2/\hbar n^*$ with screened nuclear charge Z_{sc} and effective principal quantum number n^*. Z_{sc} and n^* used in the calculation are listed in table 1 together with the average kinetic energy $p_s^2/2m$.

Table 1. Values for the parameters of the target electrons used in the impulse approxiation.

Target	H_2	He	CH_4	N_2	O_2	Ne
Z	1	2	6	7	8	10
n^*	1	1	2	2	2	2
Z_{sc}	1	1.7	3.25	3.9	4.55	5.85
$p_s^2/2m$ (eV)	13.6	19.5	35.9	51.9	70.4	117

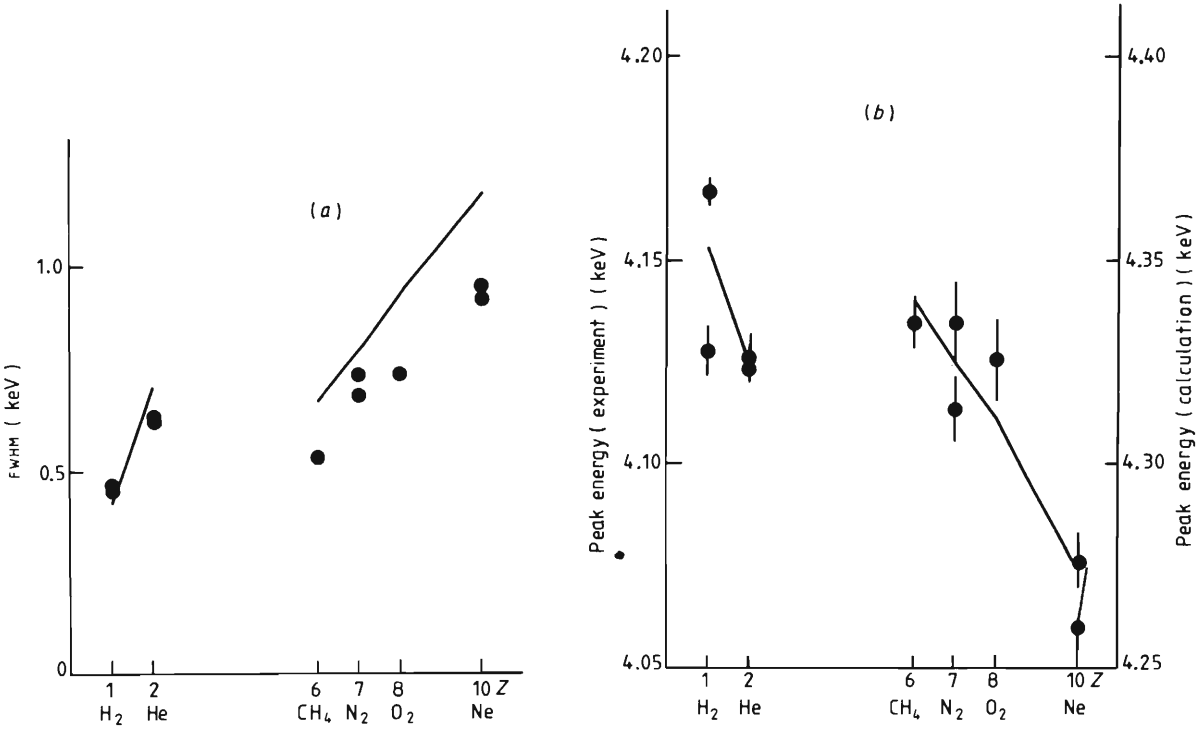

Figure 2. Dependence of REC peak width (*a*) and peak energy (*b*) on the target species. The full curves show the calculated results of the impulse approximation and the full circles are the experimental data. The error bars denote only the uncertainty in the least-squares fit.

The calculated and experimental results for the REC width and peak energy are shown in figure 2 as a function of the target atomic number Z_T.

Values of the width and peak energy lie on two lines in each figure, which correspond to the $n = 1$ shell for H_2 and He and the $n = 2$ shell for CH_4, N_2, O_2 and Ne. Concerning the widths, the agreement between the experiment and the calculation is good for the $n = 1$ shell, but the calculation predicts 10–20% larger values than experiment for the $n = 2$ shell. The result is consistent with the experimental data reported by Sohval *et al* (1976a) where the REC width tends to decrease for higher projectile velocity.

For the peak energies, the agreement is good as far as their relative values are concerned. The REC peak energy depends on the atomic number of the target because the free-electron capture cross section given in equation (2) increases for electrons with lower relative velocity. The REC cross section in equation (1) is larger for electrons with the same initial momentum direction in the target atoms and the projectile

than those with the opposite direction, so that the peak energy is shifted to a lower energy. The shift is greater for targets with higher average electron momentum.

For the targets heavier than He, a REC transition of an electron from the $n = 1$ shell of the target atoms is possible in addition to that from the $n = 2$ shell described above. According to the impulse approximation, however, the width of the REC peak due to the former process is three or four times broader than that from the latter and the REC cross section from the former is smaller than the latter. Therefore the contribution from the $n = 1$ shell of the target atoms to the x-ray spectrum is probably hidden in the background x-rays.

4.2. Gas pressure dependence

The peak energy of the REC spectrum for the H_2 target shown in figure 2(*b*) has two different values which correspond to different target gas pressures; it has a higher value at 120 Torr than at 14 Torr. We have investigated the REC spectrum for the H_2 target as a function of the gas pressure from 9 to 120 Torr, which corresponds to a target thickness from 2×10^{18} to 2.8×10^{19} molecules cm^{-2}. The measurement system and data processing are described in §§ 2 and 3, but the projectile energy was lower by a few MeV than in the other measurements. The peak energy of the REC spectrum is shown in figure 3(*a*) and the x-ray yield of the peak divided by the gas pressure is shown in figure 3(*b*) as a function of the gas pressure.

The REC peak shifts to higher energy by about 20 eV and the x-ray yield increases by about 20% when the gas pressure increases from 9 to 120 Torr. There seems to be no correlation between the width and the gas pressure and it is not shown in a figure.

We will explain these effects by the change of the charge-state distribution of the projectile ions with the change in gas pressure.

Fast heavy ions in H_2 gas are considered to have a different equilibrium charge-state distribution from those in heavier gases or solids. For example, Martin (1965) reported that for carbon ions of 4 MeV amu^{-1}, the equilibrium fraction of C^{6+} is more than 98% in H_2, 76% in N_2 and Ar and 85% in Ni foil. This is considered to be due to a very small electron capture cross section for fast ions in H_2 gas compared with the electron-loss cross section. The capture and loss processes are balanced at a higher fraction of the bare nucleus state in H_2 gas.

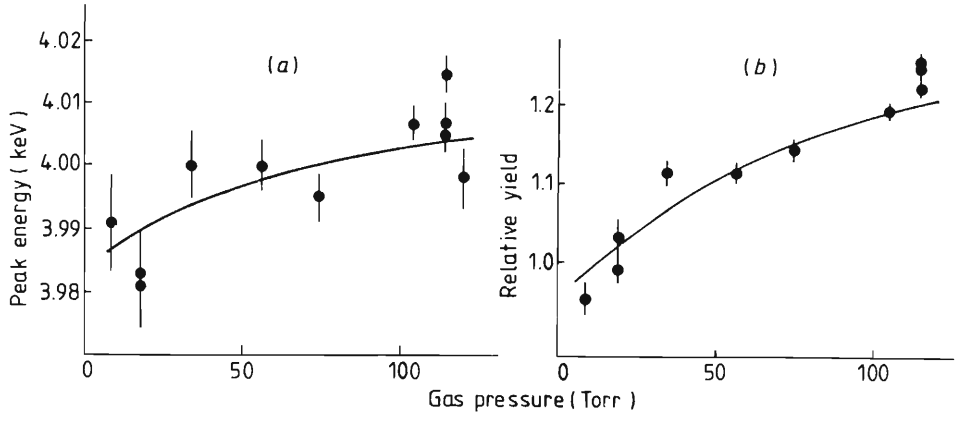

Figure 3. Dependence on REC peak energy (*a*) and REC yield divided by gas pressure (*b*) on the gas pressure for the H_2 target. The full curves show the calculated results based on the charge equilibration process of the ions in the gas.

In the present case, the Ne ions are at the equilibrium charge-state distribution in Al after they pass the entrance foil. When they are travelling in the H_2 gas, their charge-state distribution changes to that in H_2 gas. Consequently, the fraction of Ne^{10+} ions is considered to increase at higher pressure, which means a greater target thickness.

The change of the charge-state distribution affects the REC process as follows. For a Ne^{9+} ion whose K shell is already occupied by an electron, the REC cross section is smaller than that for a Ne^{10+} ion due both to the Pauli principle and to the reduction of the radiative transition probability caused by the screening of the nuclear charge of the ion. At the same time, the existence of an electron in the K shell of a Ne^{9+} ion reduces the binding energy of an additional electron by about 170 eV (Moore 1970) and the REC photon energy is reduced by the same amount. The REC peak consists of the x-rays from the transitions to the Ne^{9+} and Ne^{10+} ions in the beam. Therefore, the decrease in Ne^{9+} ions and the increase in Ne^{10+} ions in the beam lead to an increase in the total x-ray yield and an increase in the average energy of the photons.

We have estimated the above effects and have compared the result with the present data. If multiple electron transfer processes are negligible, the fraction of the charge state q of ions passing through gas of total thickness x (atoms cm^{-2}) is determined by the rate equation

$$df_q(x)/dx = \sigma_C^{q+1} f_{q+1}(x) + \sigma_L^{q-1} f_{q-1}(x) - (\sigma_C^q + \sigma_L^q) f_q(x) \tag{4}$$

where $f_q(x)$ is the fraction of ions with charge q, σ_L^q is the electron loss cross section and σ_C^q is the electron capture cross section of the ions. In our estimate, we neglected the contribution from charge states lower than 8+ and also neglected the electron capture cross section σ_C^q. Then the solution of equation (4) becomes

$$\begin{aligned} f_8 &= f_8^0 \exp(-\sigma_L^8 x) \\ f_9 &= f_9^0 \exp(-\sigma_L^9 x) + f_8^0 \frac{\sigma_L^8}{\sigma_L^8 - \sigma_L^9} (\exp(-\sigma_L^9 x) - \exp(-\sigma_L^8 x)) \\ f_{10} &= 1 - f_9 - f_8 \end{aligned} \tag{5}$$

where f_q^0 is the fraction of charge state q at the entrance foil.

The value of the electron loss cross section σ_L^9 was taken from the calculated result of Shirai *et al* (1977) based on the BEA model, which gives about 2.6×10^{-20} cm^2 for the cross section of the process $Ne^{9+} + H \rightarrow Ne^{10+} + H + e$. The cross section σ_L^8 was estimated by the same calculation assuming that $Z = 9$ and multiplying the result by two, the number of electrons in the ion. The initial charge-state fractions f_q^0 at the entrance foil were obtained from the experimental data on the equilibrium charge-state distribution for heavy ions in Al (Northcliffe 1963), which give 62% for f_{10}^0 and 35% for f_9^0.

The electron capture cross section was computed using the OBK model with a scaling factor (Eichler and Chan 1979), which gives about 1×10^{-22} cm^2 for the reaction $Ne^{10+} + H \rightarrow Ne^{9+} + H^+$. The capture cross section is smaller than the loss cross section by a factor of less than 10^{-2}, which permits the neglection of this process.

The ratio of the REC cross section for a Ne^{9+} ion to that for a Ne^{10+} ion was estimated as the ratio of the free-electron capture cross section in equation (2) by a

nucleus with $Z = 9$ to that with $Z = 10$ multiplied by 0.5, which is the ratio of the number of vacancies in the K shell. The result is about 0.35.

Using these values, the x-ray yield and the peak energy were calculated assuming that the REC spectrum consists of two Gaussian peaks separated by 170 eV corresponding to the transitions to Ne^{9+} and Ne^{10+} respectively. The results are shown by full curves in figures 3(*a*) and (*b*). The calculated peak energy in figure 3(*a*) must be lowered by about 250 eV to fit the experimental data. The agreement between the calculated results and the experimental data is good for both the x-ray yield and the relative peak energy shift. It is estimated that the change in the charge-state distribution affects the width of the REC peak by less than 4%, which is smaller than the uncertainty in the experimental data.

To represent the target thickness required to equilibrate the charge-state distribution of the ions in gas, we define a thickness x_0 which is equal to the reciprocal of the cross section σ_L^9. In the present case, where the path length of the ions in gas is about 7 cm, the thickness x_0 corresponds to a pressure of 80 Torr for the H_2 target.

The electron transfer cross sections for targets heavier than He are considered to be larger than 10^{-18} cm^2 (Macdonald *et al* 1972) and the thickness x_0 corresponds to pressure lower than 4 Torr under the present experimental conditions; consequently the ions reach charge equilibrium before they reach the area viewed by the detector. In addition, the equilibrium charge-state distributions in such gases are not very different from each other (Martin 1965). Therefore we conclude that the change-state equilibration process does not affect the REC x-ray spectra for such gases.

The pressure dependence which is seen in the H_2 target is also expected in the case of the He target, but the REC peak energy values at pressures of 25 and 116 Torr are very similar, as shown in figure 2(*b*). The cross section σ_L^9 for the He target is larger than that for H_2 because $Z_T = 2$ and the ions reach charge-state equilibrium at lower pressure. The difference between the charge-state distributions at the pressures mentioned above may be small, and the effect is probably within the uncertainty in the experimental data, which is about 10 eV for the peak energy.

5. Conclusion

The REC x-rays from Ne ion bombardment on gaseous targets with $Z_T \leqslant 10$ were measured and the data were compared with the impulse approximation. The peak width and energy reflect the shell structure of the target atoms.

The gas pressure dependence of the REC spectrum for the H_2 target was found to be related to the charge transfer process with the gas atoms. This effect can be used as a tool to study the charge-state equilibration process of fast heavy ions in a gas.

References

Bethe H A and Salpeter E E 1977 *Quantum Mechanics of One- and Two-Electron Atoms* (New York: Plenum) pp 320–2

Eichler J and Chan F T 1979 *Phys. Rev.* A **20** 104–12

Folkmann F, Caarde C, Huus T and Kemp K 1974 *Nucl. Instrum. Meth.* **116** 487–99

Ishii K, Morita S and Tawara H 1976 *Phys. Rev.* A **13** 131–8

Jakubassa D H and Kleber M 1975 *Z. Phys.* A **273** 29–35

Kleber M and Jakubassa D H 1975 *Nucl. Phys.* A **252** 152–62

Macdonald J R, Ferguson S M, Chiao T, Ellsworth L D and Savoy S A 1972 *Phys. Rev.* A **5** 1188–94
Martin F W 1965 *Phys. Rev.* **140** A75–86
Moore C E 1970 *Nat. Stand. Ref. Data Ser.* (Washington, DC: Nat. Bur. Stand.) **34** 1–8
Northcliffe L C 1960 *Phys. Rev.* **120** 1744–57
—— 1963 *Ann. Rev. Nucl. Sci.* **13** 67–102
Schnopper H W, Betz H D, Delvaille J P, Kalata K, Sohval A R, Jones K W and Wegner H E 1972 *Phys. Rev. Lett.* **29** 898–901
Shirai T, Iguchi K and Watanabe T 1977 *J. Phys. Soc. Japan* **42** 238–45
Slater J C 1960 *Quantum Theory of Atomic Structure* vol 1 (New York: McGraw-Hill) p 369
Sohval A R, Delvaille J P, Kalata K, Kirby-Docken K and Schnopper H W 1976a *J. Phys. B: At. Mol. Phys.* **9** L25–9
Sohval A R, Delvaille J P, Kalata K and Schnoper H W 1976b *J. Phys. B: At. Mol. Phys.* **9** L47–51
Yamadera A, Ishii K, Sera K, Sebata M and Morita S 1981 *Phys. Rev.* A **23** 24–33
Ziegler J F 1980 *The Stopping and Ranges of Ions in Matter* vol 5 (New York: Pergamon)

Reprinted from J. Phys. Chem., 86, 4726–4733 (1982).

Emission Mössbauer Studies of Carrier-Free Pentavalent Antimony-119 Ions Adsorbed on α-Fe_2O_3 and Cr_2O_3 Surfaces

T. Okada, S. Ambe, F. Ambe,* and H. Sekizawa

The Institute of Physical and Chemical Research, Wako-shi, Saitama, 351 Japan *(Received: May 19, 1982; In Final Form: July 30, 1982)*

Emission Mössbauer measurements of ^{119}Sn were made on carrier-free pentavalent ^{119}Sb ions hydrolytically adsorbed on surfaces of antiferromagnetic oxides, α-Fe_2O_3 and Cr_2O_3. From the broadening of emission spectra, the nuclei of $^{119}Sn^{4+}$ arising from the adsorbed $^{119}Sb^{5+}$ were shown to feel the supertransferred hyperfine fields from the magnetically ordered Fe^{3+} or Cr^{3+} ions of the substrates. This finding indicates that the $^{119}Sb^{5+}$ ions predominantly formed M^{3+}–O^{2-}–Sb^{5+} bonds with metal ions (M^{3+}) of the oxides. It is also concluded from the observations that there exist no "nonmagnetic layers" on surfaces of the substrates. Heat treatments of the oxides with adsorbed $^{119}Sb^{5+}$ increased the hyperfine magnetic fields on $^{119}Sn^{4+}$. The variation of hyperfine fields on $^{119}Sn^{4+}$ was interpreted in terms of various $^{119}Sn^{4+}$-ion locations in the surface layers.

Introduction

Hydrolytic adsorption of the so-called "carrier-free" metal ions onto surfaces attracted much attention of radiochemists in connection with radiocolloid formation.[1] This rather classical phenomenon is still very important as a basis of studying the effect of additives on catalytic activity of oxide surfaces,[2] because it provides surfaces with ideally dilute additives. Little is known yet, however, concerning the chemical states of the carrier-free metal ions adsorbed on the surfaces. Conventional tracer experiments do not tell us much about the chemical environment of the adsorbed ions, while the sensitivity of various physicochemical methods widely used in studies of adsorbed species[2-4] is not sufficient for such dilute ions.

Application of emission Mössbauer spectroscopy[5-8] to the problem is promising, because it provides us information on chemical states of carrier-free ions serving as the source of resonant γ-rays. In the case of hydrolyzed metal ions on oxide surfaces, however, neither isomer shifts nor quadrupole splittings derived from the emission spectra are expected to be informative enough to allow us the following judgments: (i) whether the hydrolyzed ions form clusters or not and (ii) whether the hydrolyzed ions are weakly adsorbed (by van der Waals force or by hydrogen bonding) or they form chemical bonds with the cations of the substrate through oxide ions. In the study of magnetic materials, Mössbauer nuclei in nominally diamagnetic ions such as $^{119}Sn^{4+}$ and $^{121}Sb^{5+}$ have often been utilized as valuable probes by virtue of their sensitiveness to the supertransferred hyperfine (hereafter abbreviated as STHF) magnetic fields coming from the magnetic environment.[9-14]

The present work aims to clarify the chemical states of dilute pentavalent antimony ions adsorbed on the surfaces of magnetic oxides as well as to elucidate the magnetic states of the surfaces by emission Mössbauer measurements of STHF magnetic fields.[15] Namely, emission Mössbauer spectroscopy of ^{119}Sn with ^{119}Sb as the source nuclide[16-19] has been applied to carrier-free pentavalent antimony ions adsorbed on the surfaces of corundum-type antiferromagnetic oxides, α-Fe_2O_3 and Cr_2O_3 (Néel temperatures: 963 and 303 K, respectively). In the measurements, Mössbauer analysis was made on the 23.9-keV γ-rays emitted by ^{119}Sn nuclei in the first excited state ($^{119}Sn^*$, half-life: 17.8 ns) arising from ^{119}Sb (half-life: 38.0 h) by the EC decay (Figure 1). The information furnished by the resonant γ-rays from $^{119}Sn^*$ can be utilized to determine the chemical state of ^{119}Sb before the EC decay, since the Mössbauer γ-ray is emitted immediately (25.7 ns on average) after the decay of ^{119}Sb. To describe this rather complicated situation more clearly, we denote the source nuclide as $^{119}Sb(\rightarrow{}^{119}Sn^*)$ or simply as $^{119}Sb(\rightarrow{}^{119}Sn)$ and the daughter as $^{119}Sn^*$ or $^{119}Sn(\leftarrow{}^{119}Sb)$, when necessary.

The chemical states of the $^{119}Sb^{5+}$ ions adsorbed on the oxide surfaces are reflected in the broadening of the emission spectra due to STHF interaction of $^{119}Sn^{*4+}(\leftarrow{}^{119}Sb^{5+})$ with the magnetic ions of the substrates. Variations of the STHF fields with heat treatments are interpreted on the basis of a simplified model, in which $^{119}Sn^{4+}$

(1) N. A. Bonner and M. Kahn in "Radioactivity Applied to Chemistry", A. C. Wahl and N. A. Bonner, Eds., Wiley, New York, 1951, Chapter 6.
(2) S. R. Morrison, "The Chemical Physics of Surfaces", Plenum Press, New York, 1977.
(3) K. Hachiya, M. Ashida, M. Sasaki, H. Kan, T. Inoue, and T. Yasunaga, *J. Phys. Chem.*, **83**, 1866 (1979).
(4) R. D. Astumian, M. Sasaki, T. Yasunaga, and Z. A. Schelly, *J. Phys. Chem.*, **85**, 3832 (1981).
(5) G. K. Wertheim in "The Electronic Structure of Point Defects", Part 1, S. Amelinckx, R. Gevers, and J. Nihoul, Eds., North-Holland Publishing Co., Amsterdam, 1971.
(6) J. M. Friedt and J. Danon, *Radiochim. Acta*, **17**, 173 (1972).
(7) G. Vogl, *J. Phys. (Paris)*, **35**, C6-165 (1974).
(8) P. P. Seregin, F. S. Nasredinov, and L. N. Vasilev, *Phys. Status Solidi A*, **45**, 11 (1978).
(9) I. S. Lyubutin and Yu. S. Vishnyakov, *Zh. Eksp. Teor. Fiz.*, **61**, 1962 (1971) (*Sov. Phys.—JETP (Engl. Transl.)*, **34**, 1045 (1972)).
(10) B. J. Evans and L. J. *Swartzendruber, Phys. Rev. B*, **6**, 223 (1972).
(11) H. Sekizawa, T. Okada, and F. Ambe, "Proceedings of the International Conference on Magnetism, ICM-73", Vol. 2, Nauka, Moscow, 1974, p 152.
(12) H. Sekizawa, T. Okada, and F. Ambe, *Physica*, **86-88B**, 963 (1977).
(13) T. Okada, H. Sekizawa, and T. Yamadaya, *J. Phys. (Paris)* **40**, C2-299 (1979).
(14) T. Okada and H. Sekizawa, *J. Magn. Magn. Mater.*, **15-18**, 649 (1980).
(15) Partly presented at the International Conference on the Applications of Mössbauer Effect, Jaipur, 1981. Abstract only, in the proceedings.
(16) F. Ambe, H. Shoji, S. Ambe, M. Takeda, and N. Saito, *Chem. Phys. Lett.*, **14**, 522 (1972).
(17) F. Ambe, S. Ambe, H. Shoji, and N. Saito, *J. Chem. Phys.*, **60**, 3773 (1974).
(18) F. Ambe and S. Ambe, *J. Chem. Phys.*, **73**, 2029 (1980).
(19) F. Ambe and S. Ambe, *J. Chem. Phys.*, **75**, 2463 (1981).

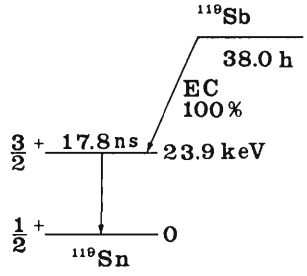

Figure 1. Decay scheme of the Mössbauer source nuclide ^{119}Sb.

ions locate at various sites in the surface layers of the oxides.

Experimental Section

Materials. The magnetic oxides used in the present work, α-Fe_2O_3 and Cr_2O_3, were high-purity lamellar powders with diameters of approximately 0.5 (α-Fe_2O_3) and 1 (Cr_2O_3) μm. The oxides were identified by powder X-ray diffraction and Mössbauer spectroscopy. Their surface areas were measured by the BET method.

Radiochemical Procedures. A tin plate was irradiated with about 1 C of 38-MeV α particles accelerated by the RIKEN cyclotron of our institute. The target containing ^{119m}Te (half-life: 4.68 days) produced by the Sn(α,-xn)^{119m}Te reactions was dissolved in aqua regia and the ^{119m}Te was separated chemically in metallic form with a small amount of tellurium carrier by reducing with Na_2SO_3 and $NH_2NH_2{\cdot}2HCl$. The daughter nuclide ^{119}Sb accumulated in the tellurium metal by the EC decay of ^{119m}Te was separated by dissolving the tellurium and reprecipitating it. The desired nuclide ^{119}Sb remaining in the solution was purified by anion exchange. This procedure was repeated every 2 or 3 days to obtain ^{119}Sb ions as a 0.5 mol dm^{-3} LiOH solution in a radiochemically pure and carrier-free (strictly speaking, no-carrier-added) state with a radiochemical yield of about 70%. The ^{119}Sb ions in the solution were oxidized to the pentavalent state by air bubbling. The pH of the solution was adjusted to 4.0 ± 0.2 for α-Fe_2O_3 and to 3.0 ± 0.2 for Cr_2O_3 with 0.5 mol dm^{-3} HCl.

About 30 mg of α-Fe_2O_3 or Cr_2O_3 powder was added to 40 cm^3 of the solution containing 0.1–1 mCi of $^{119}Sb^{5+}$ and the suspension was stirred at 23, 50, or 100 °C (see the Discussion section) to let the pentavalent ^{119}Sb ions be adsorbed onto the oxide surfaces. Within a few hours more than 90% of ^{119}Sb in the solution was adsorbed onto the suspended oxide. The oxide was filtered and washed thoroughly with distilled water and then dried at room temperature over fresh P_2O_5 under vacuum. The dried oxide with adsorbed ^{119}Sb was either subjected to emission Mössbauer measurement without further treatments ("as adsorbed" specimen) or heat-treated before measurement in air at various temperatures so as to obtain specimens with ^{119}Sb diffused into the surface layers of the oxide in different degrees.

Mössbauer Measurement. Emission Mössbauer spectra of ^{119}Sn arising from ^{119}Sb on the surfaces of the oxide specimens were recorded at various temperatures against a $BaSnO_3$ (0.9 mg of ^{119}Sn cm^{-2}) absorber kept at 296 K by means of a conventional spectrometer in the absorber-drive mode. The spectra obtained were analyzed with the FACOM 230-75 computer of our institute.

Results

α-Fe_2O_3–^{119}Sb. Emission Mössbauer spectra of the "as adsorbed" (A) and 2-h heat-treated (B–E) α-Fe_2O_3–^{119}Sb specimens taken at liquid-nitrogen temperature are shown in Figure 2. The temperatures of heat treatment were 200

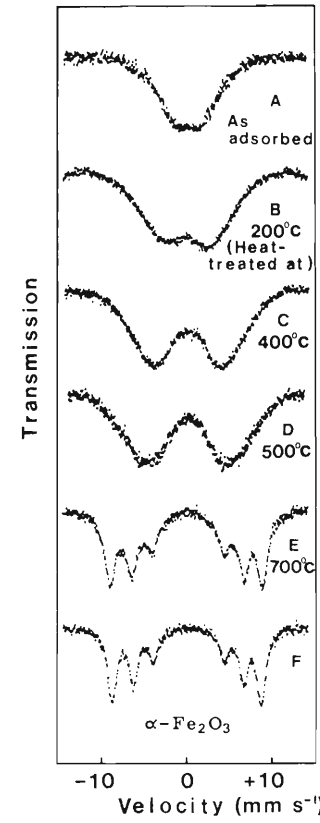

Figure 2. Emission Mössbauer spectra of the "as adsorbed" (A) and 2-h heat-treated (B–E) α-Fe_2O_3–$^{119}Sb^{5+}$ specimens taken at liquid-nitrogen temperature. The spectrum of a specimen prepared by coprecipitation is also shown for comparison (F). The isomer shift is given relative to $BaSnO_3$ at room temperature and the sign of relative velocity is defined as in usual absorption spectra.

(B), 400 (C), 500 (D), and 700 (E) °C. In Figure 2 is shown also the spectrum of a specimen (F) obtained by coprecipitating carrier-free $^{119}Sb^{5+}$ with Fe^{3+} from an aqueous solution with subsequent calcination in air at 700 °C for 2 h.

It can be seen from Figure 2A that even in the case of the "as adsorbed" specimen (A) the emission line is considerably broadened compared with that of diamagnetic $^{119}Sn^{4+}$ ions. It is noteworthy that any sharp central peak due to $^{119}Sn^{4+}$ in the absence of magnetic field (so-called "paramagnetic peak") was not observed in the spectrum. (The line width of emission lines from ordinary diamagnetic $^{119}Sn^{4+}$ ions in the absence of both magnetic hyperfine field and electric field gradient (EFG) is estimated to be about 1.0 mm s^{-1} when measured with the $BaSnO_3$ absorber used in the present work.[18]) With elevation of the temperature of heat treatment, the spectra become broader and finally a well-resolved six-line pattern appears, split due to the magnetic hyperfine fields (B–E). We attribute the origin of the broadening and splitting to the STHF magnetic interactions of the $^{119}Sn^{4+}$(←^{119}Sb) ions with the magnetically ordered Fe^{3+} ions of the α-Fe_2O_3 substrate.

The distributions of hyperfine field (H_{hf}) obtained by analyzing the spectra by means of the method of Hesse[20] are shown in Figure 3. The spectra were also analyzed by the method of Window[21] and the results were in good agreement with those by the method of Hesse. The distributions of H_{hf} obtained in room-temperature measure-

(20) J. Hesse and A. Rübartsch, *J. Phys. E*, 7, 526 (1974).
(21) B. Window, *J. Phys. E*, 4, 401 (1971).

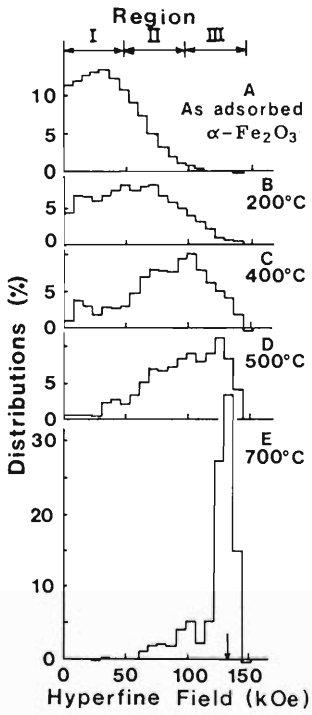

Figure 3. Distribution of the STHF magnetic fields on $^{119}Sn^{4+}$ arising from $^{119}Sb^{5+}$ of the "as adsorbed" (A) and 2-h heat-treated (B–E) α-Fe_2O_3 specimens derived from the spectra in Figure 2. The peak value of the coprecipitated specimen (F) is given with an arrow on the abscissa for E.

ments were similar in trend to those at liquid-nitrogen temperature. The similarity is consistent with the fact that the Néel temperature of α-Fe_2O_3 (963 K) is much higher than the above two temperatures of measurements.

From the values of isomer shift (0.3 ± 0.3 mm s^{-1} relative to $BaSnO_3$), it is certain that the ^{119}Sn ions resulting from the adsorbed $^{119}Sb^{5+}$ are tetravalent in all the α-Fe_2O_3 specimens. In the well-resolved six-line spectrum (Figure 2E), the sign of EFG conicides with that of the bulk specimen (F). In the other spectra (A–D), determination of the sign of EFG was hardly possible. The ratios of the adsorption area of the spectra at room temperature to that at liquid-nitrogen temperature were in the range of 0.7–0.8 in the coprecipitated (F), heat-treated (B–E), and even "as adsorbed" (A) specimens. This observation indicates that the adsorbed ^{119}Sb ions have unexpectedly high effective Debye temperatures.

As can be seen in Figure 3A, no noticeable peak was observed at $H_{hf} = 0$ in the hyperfine field distribution of nominally diamagnetic $^{119}Sn^{4+}(\leftarrow{}^{119}Sb)$ ions in the "as adsorbed" specimen. Detailed discussion will be given on this finding in the following section.

In order to analyze the effect of the heat treatments on the distribution of H_{hf}, the range of distributed H_{hf} was limited to the one extending from zero to $(H_{hf})_{max}$. The maximum value of H_{hf} was taken somewhat arbitrarily as a little above $(H_{hf})_{peak}$ of the bulk specimen with due regard to its distribution. This range of H_{hf} was then divided into three regions with equal width (Figure 3). The reasons for this procedure will be given in the Discussion section.

Variation of the weights of the three regions is plotted against the temperature of heat treatment in Figure 4. The weight of region I which is dominant before the heat treatment (A) decreases monotonically with the heating temperature. The weight of region II increases slowly to about 500 °C (B–D) and decreases abruptly above it. The

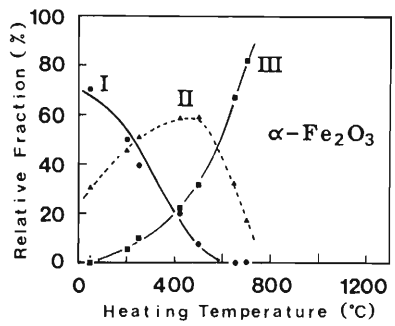

Figure 4. Variation of the weights of the three regions with the heating temperature in the field distribution given in Figure 3.

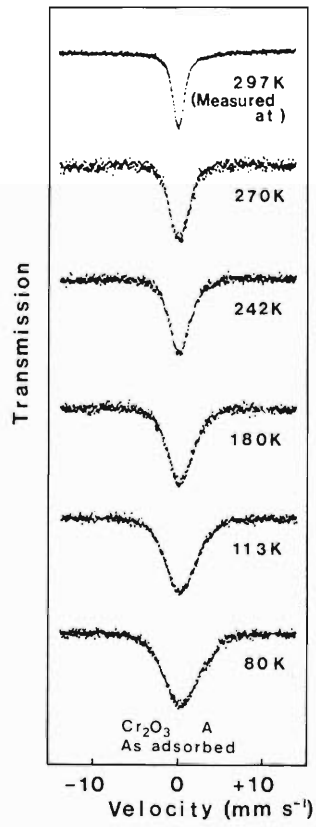

Figure 5. Emission Mössbauer spectra of the "as adsorbed" Cr_2O_3–$^{119}Sb^{5+}$ specimen (A) measured at different temperatures. The isomer shift is given as in Figure 2.

decrease in the weight of region II is accompanied by rapid increase in the weight of region III, which dominates at the heating temperature of 700 °C (E). The distribution of H_{hf} in specimen E is almost equal to that of the coprecipitated specimen F, which means that the adsorbed ^{119}Sb ions diffuse into the substrate deep enough by 2-h heat treatment at 700 °C so as to make the nuclei of $^{119}Sn^{4+}(\leftarrow{}^{119}Sb)$ feel the same hyperfine magnetic fields as those felt by the nuclei of $^{119}Sn^{4+}$ in the coprecipitated specimen. The variations of hyperfine field distribution with the heat treatments will be discussed later in terms of the STHF interactions on $^{119}Sn^{4+}$ ions in various sites of the surface structure of α-Fe_2O_3. The peak value of H_{hf} for the coprecipitated specimen (F) agrees well with the one obtained by absorption Mössbauer spectroscopy.[22]

(22) P. B. Fabritchnyi, A. M. Babechkin, and A. N. Nesmeianov, *J. Phys. Chem. Solids*, 32, 1701 (1971).

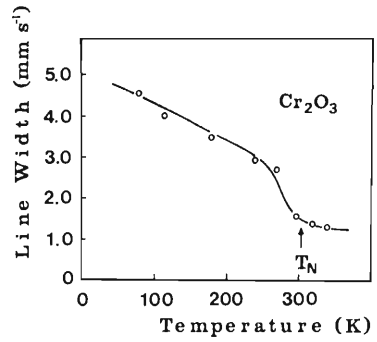

Figure 6. Variation of the full width at half-maximum of the emission line of the "as adsorbed" Cr_2O_3–$^{119}Sb^{5+}$ specimen (A) given in Figure 5 with the temperature of measurement. T_N is the Néel temperature of bulk Cr_2O_3.

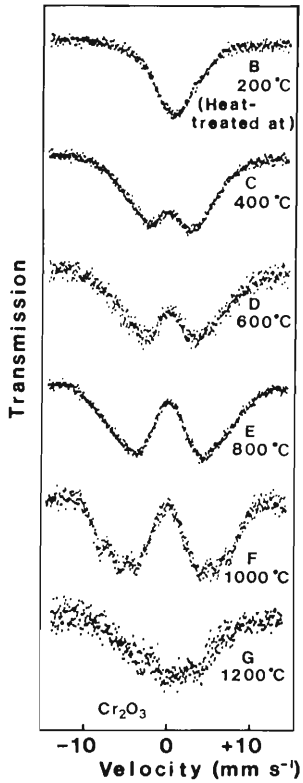

Figure 7. Emission Mössbauer spectra of the 2-h heat-treated Cr_2O_3–$^{119}Sb^{5+}$ specimens (B–G) taken at liquid-nitrogen temperature. The isomer shift is given as in Figure 2.

Cr_2O_3–^{119}Sb. Mössbauer emission spectra of the "as adsorbed" Cr_2O_3–^{119}Sb specimen (A) measured at various temperatures are shown in Figure 5. The spectra consist of an emission line of $^{119}Sn^{4+}$, whose width depends remarkably on the temperatures of measurements. In Figure 6, the apparent widths of the emission lines are plotted against the temperature of measurement. It can be seen in Figure 6 that above the Néel temperature of Cr_2O_3 the emission line has a width corresponding to ordinary diamagnetic $^{119}Sn^{4+}$ ions (about 1.3 mm s^{-1}), but it is considerably broadened below that temperature. Namely, the broadening occurs in parallel with the magnetic ordering of Cr^{3+} ions of the substrate. This observation can be regarded as decisive evidence for our view that the observed broadening is caused by the hyperfine interaction of the $^{119}Sn^{4+}$(←adsorbed ^{119}Sb) ions with the magnetically ordered Cr^{3+} ions of the Cr_2O_3 surfaces.

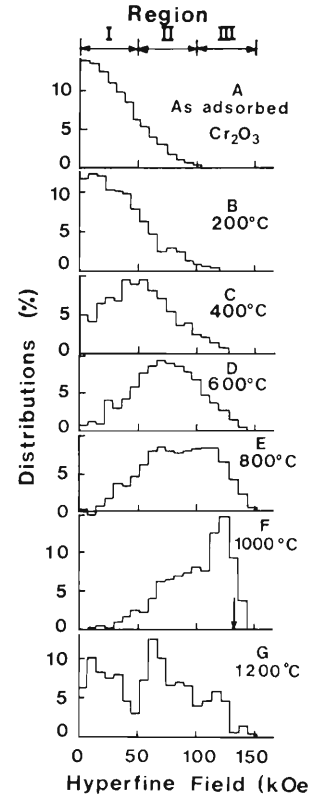

Figure 8. Distribution of the STHF magnetic fields on $^{119}Sn^{4+}$ arising from $^{119}Sb^{5+}$ of the "as adsorbed" (A) and 2-h heat-treated (B–G) Cr_2O_3 specimens derived from the spectra of Figures 5 (80 K) and 7. The value of the coprecipitated specimen (ref 23) is given with an arrow on the abscissa for F.

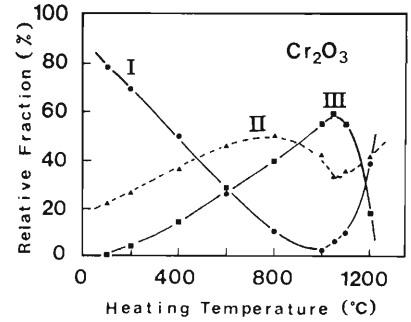

Figure 9. Variation of the weights of the three regions with the heating temperature in the field distribution given in Figure 8.

In Figure 7 are shown the emission spectra of the Cr_2O_3–^{119}Sb specimens heat-treated at 200 (B), 400 (C), 600 (D), 800 (E), 1000 (F), and 1200 (G) °C for 2 h (measured at liquid-nitrogen temperature). As can be seen from Figure 7, the effect of heat treatments on the Cr_2O_3 specimens is similar to that on the α-Fe_2O_3–^{119}Sb described above. In the present case of Cr_2O_3–^{119}Sb, however, remarkable decrease in H_{hf} was observed above around 1000 °C. This is ascribable to coagulation of $^{119}Sb^{5+}$ ions with diamagnetic impurities on the surfaces. The specimens heat-treated at 1200 °C (G) gave a much broadened and somewhat asymmetric structureless pattern (Figure 7). The asymmetry is considered to be due to $^{119}Sn^{2+}$ from $^{119}Sb^{3+}$ produced in the specimen by the heat treatment.

Analysis, by the method of Hesse, of the spectra of Cr_2O_3–^{119}Sb measured at liquid-nitrogen temperature gave the histograms of the H_{hf} distributions shown in Figure

8. The variation of the weights of the three regions in the distribution of the H_{hf} is plotted in Figure 9 against the temperatures of heat treatment as in the case of α-Fe_2O_3. The specimen heat-treated at 1000 °C (F) still has a fairly wide distribution of H_{hf}, but its peak value agrees roughly with the result of absorption measurement on a bulk specimen.[23]

Discussion

Supertransferred Hyperfine (STHF) Interaction. In magnetic oxides, metal ions have localized electron spin densities with associated magnetic moments. Although the magnetic metal ions are separated by large intervening oxide ions, they interact with each other through the superexchange interaction. The localized spin densities on the magnetic metal ions permeate the oxide ions and come to the neighboring magnetic ions to interact with the electron spins on them. The mechanism giving rise to the STHF magnetic field is fairly similar to the one for the superexchange. Although several possible schemes have been suggested, the dominant one is as follows.[10,24] When a diamagnetic cation ($^{119}Sn^{4+}$ in our case) substitutes a magnetic metal ion (Fe^{3+} or Cr^{3+} in our case) in the lattice of a magnetic oxide, the spin densities from the magnetic ions permeate the oxide ions surrounding the diamagnetic cation and are further "supertransferred" to the outer s orbitals of the diamagnetic cation. The spin-polarized (spin-unbalanced) s electrons contact the nucleus of the diamagnetic cation giving rise to the Fermi contact magnetic field. The hyperfine field can be observed as magnetic splitting in the Mössbauer spectrum of γ-rays emitted by such nuclei.

The crucial point of the STHF interaction in interpreting our Mössbauer results is that significant spin transfer occurs practically only to such diamagnetic cations that are bound through anions to ordered magnetic metal ions. If we assume a chain of ions, for example, $-Fe^{3+}-O^{2-}-Sn_a^{4+}-O^{2-}-Sn_b^{4+}-$, spin transfer from the Fe^{3+} ion to Sn_b^{4+} is by far smaller than that to Sn_a^{4+}.

Crystal and Magnetic Structures of α-Fe_2O_3 and Cr_2O_3. Both α-Fe_2O_3 and Cr_2O_3 have the corundum (α-Al_2O_3)-type crystal structure[25] (Figure 10). They are composed of layers of hexagonally close-packed oxide ions along the ⟨111⟩ axis with metal ions inserted between the neighboring oxide-ion layers. The metal ions, two-thirds in number against oxide ions, occupy the octahedral sites and make honeycomb lattice layers. Along the ⟨111⟩ direction, pairs of metal ions are spaced by single vacant ion sites. There are slight deviations in coordinates of the metal and oxide ions from the above simplified description. The lattice position of each metal ion is shifted slightly up- or downward in the ⟨111⟩ direction resulting in slight distortion of the (111) layers. We call these sites up and down sites seen from a certain ⟨111⟩ direction. These deviations lead as a whole to the rhombohedral structure with the space group $R\bar{3}c$.

α-Fe_2O_3 and Cr_2O_3 are antiferromagnetic with the Néel temperatures of 963[26] and 303 K, respectively. (The Néel temperatures of Cr_2O_3 in the literature show a considerable scattering[27] probably due to differences in processes of preparation and measurement. The value given above was obtained by heat capacity measurement on our Cr_2O_3 sample used for the present work.) In α-Fe_2O_3, the electron spins in each honeycomb layer are parallel to each other, and the neighboring layers are coupled antiferromagnetically.[28] In Cr_2O_3, the spins in each honeycomb layer constitute an antiferromagnetic arrangement, and the pairs of spins along the c axis are coupled again antiferromagnetically.[29] Weak ferromagnetic moment appears in α-Fe_2O_3 above 250 K,[30] but it is neglected in the following discussion because of its unimportance to the present work.

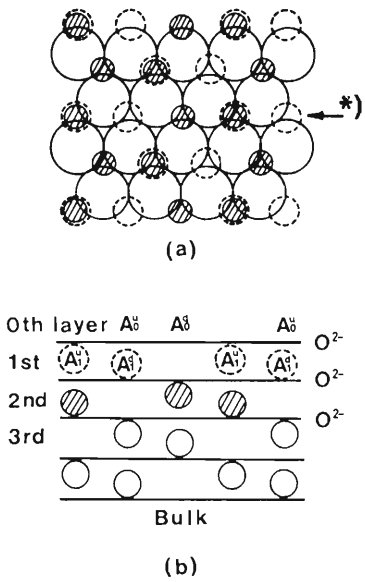

Figure 10. Schematic representation of the surface crystal structure of α-Fe_2O_3 and Cr_2O_3. Part b shows the metal-ion layers (circles) and oxide-ion layers (lines) along the ⟨111⟩ direction. Up- and downward shifts of the metal ions are exaggerated. A_0^d, A_0^u, A_1^d, and A_1^u are the possible sites for $^{119}Sb^{5+}$ ions (d: down; u: up). Part a shows the first (small broken circles) and the second (small shadowed circles) metal-ion layers and the oxide-ion layer in between (large circles) seen from the ⟨111⟩ direction. In the figures, surface protons are not shown. *) The arrow shows the position of the cross section given in part b.

Although various crystal planes can be observed on exposed surfaces of corundum-type crystals, (111) faces are most dominant in lamellar samples such as ours.[31] Therefore, we confine our attention to the (111) faces of the oxides in the following semiquantitative disucssion and the contribution of other faces is regarded as one of the causes of deviation from such idealized considerations. We denote the sequence of Fe^{3+}- or Cr^{3+}-ion layers by numbers along the ⟨111⟩ direction as shown in Figure 10.

Chemical Aspects of the Adsorption. The source nuclide ^{119}Sb used in the present work was in the no-carrier-added state and was also free from contamination of impurity antimony in the tin targets (2 ppm), since antimony had been elminated in the separation of the parent ^{119m}Te from target tin. Neutron activation analysis showed, however, that each α-Fe_2O_3–^{119}Sb and Cr_2O_3–^{119}Sb specimen (about 30 mg) contained 50–300 ng of antimony (1 mCi of ^{119}Sb weighs 1.44 ng). The majority of antimony found in the specimens is considered to originate in the

(23) P. B. Fabritchnyi and L. P. Fefilatiev, *Solid State Commun.*, 28, 513 (1978).
(24) R. E. Watson and A. J. Freeman in "Hyperfine Interactions", A. J. Freeman and R. B. Frankel, Eds., Academic Press, New York, 1967, p 90.
(25) R. W. G. Wyckoff, "Crystal Structures", Vol. 2, 2nd ed., Interscience-Wiley, New York, 1964, p 6.
(26) S. Freier, M. Greenshpan, P. Hillman, and H. Shechter, *Phys. Lett.*, 2, 191 (1962).
(27) T. R. McGuire, E. J. Scott, and F. H. Grannis, *Phys. Rev.*, 102, 1000 (1956).
(28) C. G. Shull, W. A. Strauser, and E. O. Wollan, *Phys. Rev.*, 83, 333 (1951).
(29) B. N. Brockhouse, *J. Chem. Phys.*, 21, 961 (1953).
(30) F. J. Morin, *Phys. Rev.*, 78, 819 (1950).
(31) E. S. Dana and W. E. Ford, "Mineralogy", Wiley, New York, 1932, p 483. Cited in ref 39.

chemical reagents employed. (The quantity of antimony in the oxide samples before the adsorption of ^{119}Sb was less than the detection limit of the activation analysis (about 3 ng).) Since the surface areas determined by the BET method were 27 $m^2\ g^{-1}$ for α-Fe_2O_3 and 6 $m^2\ g^{-1}$ for Cr_2O_3, the amount of antimony adsorbed is considered to have been much smaller than the capacity of the oxide samples in monolayer adsorption all over the surfaces. (It is estimated that about 2×10^{-4} m^2 of the oxide surfaces is required in monolayer adsorption of 300 ng of antimony.)

All the ^{119}Sb ions in the solution were oxidized to the pentavalent state before adsorption. The reason for this procedure is that the EC decay of ^{119}Sb in the trivalent state can lead to both divalent and tetravalent ^{119}Sn species[17] making the analysis of the spectra rather difficult. In the present measurements with pentavalent ^{119}Sb, no ^{119}Sn species other than tetravalent tin was observed in the spectra within the experimental uncertainties. (The only exception was Cr_2O_3–^{119}Sb specimen (G) heat-treated at 1200 °C.) By chemical analysis, the ^{119}Sb was found to be still in the pentavalent state when desorbed from the oxide surfaces with 1.5 mol dm^{-3} HCl.

It is well established that the surfaces of metal oxides exposed to an aqueous solution or water vapor are covered with a layer of amphoteric hydroxyl groups,[32-37] which are considerably resistive against desiccation and heating.[35,38-40] Since the adsorption of $^{119}Sb^{5+}$ onto the oxides was made in solutions with pH lower than the zero point of charge for the oxides (6.5–8.6 for α-Fe_2O_3[33] and 7.03 for Cr_2O_3[41]), the surfaces of the oxides are considered to have been positively charged in the course of adsorption. Dilute antimony ions in the pentavalent state were reported[42] to be hydrolyzed to form the complex ions, $[Sb(OH)_6]^-$ in the pH and concentration range comprising the conditions of our adsorption procedure. The adsorption of pentavalent ^{119}Sb onto α-Fe_2O_3 and Cr_2O_3 is considered, therefore, to be initiated by the electrostatic attraction between the negatively charged complex ions in the solution and the positively charged oxide surfaces. The adsorption was observed to proceed with measureable rates increasing with an increase in temperature.

Adsorption of pentavalent ^{119}Sb onto α-Fe_2O_3 was made at 23 °C in the case of the "as adsorbed" specimen and at 50 °C in the specimens for heat treatments. Boiling solutions of ^{119}Sb were used in the case of Cr_2O_3, for which the rate of adsorption was much smaller than for α-Fe_2O_3. Although the specimens were dehydrated under vacuum, their surfaces are considered to have been still covered with hydroxyl groups to some extent.

From the distributions of hyperfine fields on $^{119}Sn^{4+}$ in the "as adsorbed" α-Fe_2O_3 (Figure 3A) and Cr_2O_3 (Figure 8A) specimens, it can be seen that the great majority of $^{119}Sn^{4+}$(←$^{119}Sb^{5+}$) ions are interacting more or less with the magnetically ordered Fe^{3+} or Cr^{3+} ions of the substrates. As the distribution of hyperfine field extends down to $H_{hf} = 0$, minute contribution of components with $H_{hf} \approx 0$ is not necessarily ruled out. However, it is difficult to draw a definite conclusion concerning the existence of such components, because the distributions are much broadened due to various effects discussed later. Besides, in the region near $H_{hf} = 0$, a variety of factors neglected in our analysis (EFG, distribution in isomer shift, deviation from Lorentzian, etc.) might have made false contributions to the apparent distributions of the magnetic field. Anyhow, we can conclude from the observed distributions of hyperfine field that the $^{119}Sb^{5+}$ ions adsorbed on the oxide surfaces form, at least predominantly, M^{3+}–O^{2-}–Sb^{5+} bonds with the magnetic metal ions of the substrates. This argument is consistent with the unexpectedly high effective Debye temperature of the $^{119}Sn^{4+}$(←"as adsorbed" ^{119}Sb) mentioned already. Thus, for $^{119}Sb^{5+}$ ions on the "as adsorbed" specimens of α-Fe_2O_3 and Cr_2O_3, three-dimensional cluster formation and multilayer adsorption as well as adsorption by van der Waals force or by hydrogen bonding are excluded within the limit of experimental uncertainties independent of possible surface models to be adopted.

Model Considerations. In the idealized surface model of Figure 10 (surface protons are not shown in the figure), the $[^{119}Sb(OH)_6]^-$ ion is considered to settle on the surface with liberation of water molecules to form predominantly an extension of the close-packed oxide-ion lattice with the $^{119}Sb^{5+}$ ion occupying the octahedral site. From consideration of the electrostatic energy, it is certain that the configuration of three consecutive cations lined along the ⟨111⟩ axis should be avoided. The site just above a vacancy (A_0^d site in Figure 10) should have the lowest energy and accordingly the highest probability, and that above the down-site M^{3+} (A_0^u site) comes next. We denote these locations as the 0th layer. Heat treatment of the specimens is naturally expected to let the adsorbed $^{119}Sb^{5+}$ ions diffuse into the inner layers. The diffused $^{119}Sb^{5+}$ ions are considered to replace the Fe^{3+} or Cr^{3+} ions in each layer of the lattice. In the following discussion, contribution of surface protons to the STHF interaction is neglected because they are considered to play rather minor roles.

Paths of superexchange interaction between magnetic metal ions in a corundum-type lattice are well studied and classified in connection with mutual configurational relations between the ions.[43,44] We use the same notations as those in ref 44 for the paths of STHF interaction between the magnetic ions and the nominally diamagnetic impurity $^{119}Sn^{4+}$ ion. The notations Γ_a and Γ_b are the paths of STHF interaction on $^{119}Sn^{4+}$ from the magnetic metal ions situated in the nearest-neighbor layers and moreover in the nearest-neighbor ⟨111⟩ column, while Γ_c and Γ_d are those from the nearest-neighbor metal ions in the same plane and from the one in the same column, respectively. For the superexchange interactions, Γ_c and Γ_d are known to be much weaker compared with Γ_a and Γ_b, and the same argument holds for the STHF interaction. The interactions Γ_a and Γ_b can be assumed to be the same in magnitude, if we neglect the effect of the slight displacement of constituent ions of the lattice from the honeycomb plane (up and down sites). Therefore, in the following discussion we assume

$$\Gamma_a = \Gamma_b = \Gamma \qquad \Gamma_c = \Gamma_d = 0$$

(32) G. Blyholder and E. A. Richardson, *J. Phys. Chem.*, **66**, 2597 (1962).
(33) G. A. Parks and P. L. de Bruyn, *J. Phys. Chem.*, **66**, 967 (1962).
(34) G. A. Parks, *Chem. Rev.*, **65**, 177 (1965).
(35) J. B. Peri, *J. Phys. Chem.*, **69**, 211 (1965).
(36) R. J. Atkinson, A. M. Posner, and J. P. Quirk, *J. Phys. Chem.*, **71**, 550 (1967).
(37) E. McCafferty, V. Pravdic, and A. C. Zettlemoyer, *Trans. Faraday Soc.*, **66**, 1720 (1970).
(38) T. Morimoto, M. Nagao, and F. Tokuda, *J. Phys. Chem.*, **73**, 243 (1969).
(39) C. H. Rochester and S. A. Topham, *J. Chem. Soc., Faraday Trans. 1*, **75**, 1073 (1979).
(40) K. Morishige, S. Kittaka, S. Iwasaki, and T. Morimoto, *J. Phys. Chem.*, **85**, 570 (1981).
(41) S. N. Tewari and S. Ghosh, *Acad. Sci. India (Allahabad), Proc.*, **A21**, 29 (1952). Cited in ref 33.
(42) G. Jander and H. J. Ostmann, *Z. Anorg. Allg. Chem.*, **315**, 241 (1962).
(43) W. P. Osmond, *Proc. Phys. Soc., London*, **79**, 394 (1962).
(44) D. E. Cox, W. J. Takei, and G. Shirane, *J. Phys. Chem. Solids*, **24**, 405 (1963).

The mechanism giving rise to the STHF interaction Γ in α-Fe_2O_3 is as follows. Since the Fe^{3+} ions are in the octahedral site with a slight distortion, we can take the electronic state of the Fe^{3+} ions approximately as $(d\epsilon)^3(d\gamma)^2$. For oxide ions and Sn^{4+} ions, it is sufficent to take only the $p\sigma$ and 5s orbitals into account, respectively, as proposed by Osmond.[43] The overlap between $d\epsilon$ of Fe^{3+} and $p\sigma$ of O^{2-} as well as that between $p\sigma$ of O^{2-} and 5s of Sn^{4+} is fairly large in α-Fe_2O_3. This ensures the transfer of spin polarization through the path Fe^{3+} $(d\epsilon) \rightarrow O^{2-}(p\sigma) \rightarrow Sn^{4+}(5s)$.

In α-Fe_2O_3, all the Fe^{3+} ions transferring spin densities to an impurity Sn^{4+} ion through Γ are aligned parallel to each other and the magnetic field H_i acting on the nuclei of $^{119}Sn^{4+}(\leftarrow{}^{119}Sb^{5+})$ in the ith layer of the surface is just Γ for a single path multiplied by the number of paths. The STHF field for $^{119}Sn^{4+}$ in the 0th layer of α-Fe_2O_3 is thus

$$H_0 = 3\Gamma \ (A_0^u \text{ site}) \text{ or } 6\Gamma \ (A_0^d \text{ site})$$

depending on the location of $^{119}Sn^{4+}$ against the honeycomb arrangement of Fe^{3+} ions in the first layer (Figure 10).

When the diffusing $^{119}Sb^{5+}$ ions come down to the first layer, it is considered to be most probable that they occupy substitutionally the sites of Fe^{3+} ions as impurities. Then, we have

$$H_1 = 3\Gamma \ (A_1^u \text{ site}) \text{ or } 6\Gamma \ (A_1^d \text{ site})$$

Finally, when i becomes equal to or larger than 2, the environment of the diffusing $^{119}Sb^{5+}$ ions is exactly the same as the bulk state in our model and we get

$$H_{i\geq 2} = H_{\text{bulk}} = 9\Gamma$$

Now, we turn to the case of Cr_2O_3, in which the electronic state of Cr^{3+} is $(d\epsilon)^3(d\gamma)^0$ and the transfer through Γ', $d\epsilon \rightarrow p\sigma \rightarrow 5s$, occurs. There is an important difference in the magnetic interaction of $^{119}Sn^{4+}(\leftarrow{}^{119}Sb)$ with the magnetic Cr^{3+} ions of Cr_2O_3 compared to that with Fe^{3+} of α-Fe_2O_3. Because of spin structure of Cr_2O_3, the transferred fields cancel each other in some combinations. Consideration similar to that on α-Fe_2O_3 leads to the following values of the STHF fields:

$$H'_0 = 0 \ (A_0^d \text{ site}) \text{ or } 3\Gamma' \ (A_0^u \text{ site})$$

$$H'_1 = 0 \ (A_1^d \text{ site}) \text{ or } 3\Gamma' \ (A_1^u \text{ site})$$

$$H'_{i\geq 2} = H'_{\text{bulk}} = 3\Gamma'$$

The interaction Γ' is estimated to be approximately 3 times larger than Γ, since H_{bulk} for α-Fe_2O_3 and H'_{bulk} for Cr_2O_3 are comparable to each other as mentioned before.

We regard the uppermost values of regions I–III in Figures 3 and 8 as 3Γ, 6Γ, and 9Γ for α-Fe_2O_3 and as Γ', $2\Gamma'$, and $3\Gamma'$ for Cr_2O_3. This is the reason that we divided the distribution of the H_{hf} equally into the three regions. In case of Cr_2O_3, for which only 0 and $3\Gamma'$ appear in our idealized surface model, the division into three regions may appear rather arbitrary. However, for the purpose of comparison with the case of α-Fe_2O_3, we adopted the same way of division. Moreover, in real surfaces, where crystallographic imperfections such as steps and pits can play important roles in the adsorption, our procedure is still meaningful as discussed below.

Field Distributions and Magnetic State of the Oxide Surfaces. The broad and wide distributions of H_{hf} in Figures 3 and 8 are attributed firstly to the contribution of surfaces other than (111) and to crystallographic imperfections on the surfaces. The $^{119}Sn^{4+}$ ions on an edge of a step,[45] for example, should give H_{hf} deviated from that predicted by our idealized model. Partial deficits in the six M^{3+} ions in the first layer transferring spin densities to $^{119}Sn^{4+}$ in the A_0^d site of Figure 10 would give rise to decrease in the STHF field from 6Γ of the perfect surfaces to 5Γ, 4Γ, ... for α-Fe_2O_3, while to increase from 0 field to Γ', $2\Gamma'$, and $3\Gamma'$ for Cr_2O_3. Such imperfections on the surfaces can contribute as active sites considerably to the observed wide field distributions. In the case of Cr_2O_3, where our idealized model predicts all or nothing ($3\Gamma'$ or 0) for $^{119}Sn^{4+}$ in different sites, the contribution of such active sites is apparent.

The second possible origin of the distributions of H_{hf} is the approximations adopted in our idealized model. Especially, for the surface-layer sites of Cr_2O_3 with $H_{hf} = 0$ (A_0^d and A_1^d sites in Figure 10), the difference between Γ_a and Γ_b neglected in the above considerations ought to be properly estimated to give some contribution to the region of low H_{hf}. However, the observed distribution of H_{hf} for "as adsorbed" Cr_2O_3–^{119}Sb (Figure 8A) concentrated in the lower field region as compared with the one for "as adsorbed" α-Fe_2O_3–^{119}Sb (Figure 3A) can be explained on the basis of our model as follows: The STHF field for $^{119}Sn^{4+}$ in the energetically most favorable site of the 0th layer (A_0^d) is much smaller (null in our model) for Cr_2O_3 than that for α-fe_2O_3 (6Γ in our model).

Thirdly, metal vacancies and reduced metal ions (Fe^{2+}, for example), if any, near the surfaces would decrease or increase the H_{hf} on $^{119}Sn^{4+}$. In fact, substitution of Fe^{3+} or Cr^{3+} by $^{119}Sb^{5+}$ is likely to produce nearby cation vacancies or reduced metal ions in the substrate to preserve local charge balance of the lattice.

Aftereffects of the EC decay of ^{119}Sb to ^{119}Sn are the fourth possible origin of the broadening in the field distributions. Although the recoil energy of the decay is estimated to be smaller than the displacement energy in solids,[17] Coulomb repulsion following the Auger process can disturb the lattice locally,[46] bringing about decrease or increase in H_{hf} on $^{119}Sn^{4+}$.

Another possible mechanism giving rise to decrease in H_{hf} is the magnetically "dead" layers proposed for metals.[47,48] It assumes the existence of nonordered or weakly ordered spin layers due to the decrease in number of neighboring ions near the surfaces compared with the bulk state. Such layer or layers should exert no or decreased H_{hf} on the impurity $^{119}Sn^{4+}$.

As discussed above in relation to the chemical state of the adsorbed ^{119}Sb, each $^{119}Sn^{4+}$ ion in the "as adsorbed" α-Fe_2O_3 or Cr_2O_3 specimen feels more or less the STHF fields from the magnetic ions of the substrates. From these observations, we now come to the conclusion concerning the magnetic state of the surfaces that there exist no "nonmagnetic layers" on α-Fe_2O_3 and Cr_2O_3. Moreover, it can be concluded from the temperature dependence of the line width of the "as adsorbed" Cr_2O_3 specimen (Figure 6) that the Néel temperature of the first Cr^{3+} layer of Cr_2O_3 is essentially the same as that of bulk Cr_2O_3.

Effects of Heat Treatment. The effects of heat treatment on the distribution of H_{hf} (Figure 3 and 8) can be reasonably interpreted on the basis of the above idealized model. The shift of H_{hf} toward 9Γ or $3\Gamma'$ with increasing temperature of the heat treatments indicates clearly the diffusion process of $^{119}Sb^{5+}(\rightarrow{}^{119}Sn^{4+})$ from the outermost surfaces into the second and deeper layers of the sub-

(45) G. A. Somorjai, *Catal. Rev.*, 7, 87 (1972).
(46) J. H. O. Varley, *Nature (London)*, 174, 886 (1954).
(47) L. N. Liebermann, D. R. Fredkin, and H. B. Shore, *Phys. Rev. Lett.*, 22, 539 (1969).
(48) L. Liebermann, J. Clinton, D. M. Edwards, and J. Mathon, *Phys. Rev. Lett.*, 25, 232 (1970).

strates. It can be concluded from Figure 4 that diffusion of adsorbed $^{119}Sb^{5+}$ into the second and deeper layers of α-Fe_2O_3 requires 2-h heating at about 750 °C. By means of the conventional analyzing procedure[49] for one-dimensional bulk diffusion from a surface, the diffusion constant of $^{119}Sb^{5+}$ in the surface layers of α-Fe_2O_3 is estimated to be of the order of 10^{-15} cm^2 s^{-1} at 750 °C, whereas that of Fe^{3+} in bulk α-Fe_2O_3[50] extrapolated to 750 °C is 5×10^{-19} cm^2 s^{-1}. Thus, it seems that the diffusion of $^{119}Sb^{5+}$ in the surface layers of α-Fe_2O_3 along the normal direction is considerably faster than that of Fe^{3+} in bulk crystals of the oxide. Presumably, this difference is due to very defective structure of the surface layers.

Comparison of Figures 4 and 9 indicates that the diffusion of $^{119}Sb^{5+}$ into the bulk matrix of Cr_2O_3 is considerably more difficult than that into the bulk of α-Fe_2O_3. In Cr_2O_3, the weight of region III never arrives at 100% and heat treatments at higher temperatures induce coagulation of diamagnetic impurites including ^{119}Sb. These experimental results indicate that the replacement of M^{3+} ions in the lattice by $^{119}Sb^{5+}$ ions is much easier in α-Fe_2O_3 than that in Cr_2O_3, probably because the reduction of nearby M^{3+} ions to M^{2+} is much easier in the former matrix. The size of the ions is considered to be not essential in the present case of α-Fe_2O_3 and Cr_2O_3, since the ionic radii of Sb^{5+}, Fe^{3+}, and Cr^{3+} happen to be practically the same.

(49) C. D. Thurmond in "Methods of Experimental Physics", Vol. 6, Part A, L. Marton, Ed., Academic Press, New York, 1959, p 39.
(50) R. Lindner, *Z. Naturforsch. A*, 10, 1027 (1955).

Summary and Conclusion

By emission Mössbauer measurement of supertransferred hyperfine (STHF) magnetic fields on $^{119}Sn^{4+}$ ions produced by the EC decay of $^{119}Sb^{5+}$, it was shown that carrier-free pentavalent ^{119}Sb ions hydrolytically adsorbed on surfaces of antiferromagnetic α-Fe_2O_3 and Cr_2O_3 from aqueous solutions are predominantly bound with the metal ions of the substrates by the M^{3+}–O^{2-}–Sb^{5+} bonds (M = Fe or Cr). It was also shown that there exist no "nonmagnetic layers" on the surfaces of the oxides. From variation of the hyperfine fields by heat treatment of the α-Fe_2O_3–$^{119}Sb^{5+}$ specimens, the diffusion rate of Sb^{5+} ions into a few surface layers of the substrate was estimated with the aid of a simplified surface model.

Emission Mössbauer spectroscopy of STHF interactions has thus been shown to be a valuable technique in studying the chemical state of very dilute diamagnetic metal ions adsorbed on surfaces of magnetic oxides. It also provides useful information on the magnetic state of the surfaces as well as on diffusion of adsorbed ions into a few layers of the surfaces.

Acknowledgment. Cooperation of the staff of the RIKEN cyclotron in many irradiation runs is gratefully acknowledged.

Reprinted from Bull. Chem. Soc. Jpn., 43, 2745–2749 (1970).

Radiation Chemical Studies with Cyclotron Beams. II. The Radiolysis of an Aqueous Ferrous Ammonium Sulfate Solution with Carbon- and Nitrogen-Ion Radiations[1)]

Masashi IMAMURA, Masao MATSUI and Takashi KARASAWA

The Institute of Physical and Chemical Research, Yamato-machi, Saitama

(Received April 13, 1970)

The yield of ferric ions in the radiolysis of an aqueous ferrous ammonium sulfate solution has been determined in the very high LET (linear energy transfer) range. The radiations used were ions of carbon-12 and nitrogen-14, which were accelerated by means of the IPCR cyclotron and which had energies (E_s) of 31—77 MeV for C-ions and of 17—78 MeV for N-ions; the LET ranges for water were 24—46 eV/Å and 26—85 eV/Å respectively. From the plot of $G(Fe^{3+})E_s$ *vs.* E_s, the value for $G(Fe^{3+})$ at an infinite LET was found to be in the vicinity of 2.9. It has also been shown that there is a substantial difference in the instantaneous yield (G_i) between the two ion radiations of the same LET; this may be ascribed to the differences in the track structures of the heavy-ion radiations.

In most of the experimental work on the LET (linear energy transfer) effect in radiolysis, protons, deuterons, or helium ions have usually been used as radiation sources with a high LET.[1-8)] The maximum LET available in water, however, is approximately 7 eV/Å for protons and 25 eV/Å for helium ions. It is expected that a much higher LET can be obtained from fission fragments of ^{235}U (several hundred eV/Å), but they are attended with some inevitable experimental difficulties.

Schuler[9)] has used ^{12}C-ions accelerated with a HILAC and has made measurements of the yields for aqueous ferrous ammonium sulfate solutions; the energy of the C-ions was in the range of 54—102 MeV. Other heavy ions, such as ^{14}N- and ^{20}Ne-ions, have been used by Burns and his colleague for the radiolysis of liquid cyclohexane and benzene.[10)]

We have initiated radiolysis studies using heavy-ion radiations made available by the IPCR 160 cm cyclotron, which can accelerate several heavy ions at variable energies. While the previous paper[1)] of this series has reported the radiolysis of aqueous ferrous ammonium sulfate solutions with protons and helium ions, the present paper

1) Part I of this series: M. Matsui, H. Seki, T. Karasawa and M. Imamura, *J. Nucl. Sci. Tech.*, **7**, 97 (1970).

2) a) R. H. Schuler and A. O. Allen, *J. Amer. Chem. Soc.*, **77**, 507 (1955). b) R. H. Schuler and A. O. Allen, *ibid.*, **79**, 1565 (1957).

3) a) R. H. Schuler and N. F. Barr, *ibid.*, **78**, 5756 (1956). b) N. F. Barr and R. H. Schuler, *J. Phys. Chem.*, **63**, 808 (1959).

4) H. A. Schwarz, J. M. Caffrey, Jr., and G. Scholes, *J. Amer. Chem. Soc.*, **81**, 1801 (1959).

5) A. Appleby and H. A. Schwarz, *J. Phys. Chem.*, **73**, 1937 (1969).

6) A. R. Anderson and E. J. Hart, *Radiat. Res.*, **14**, 689 (1961).

7) G. L. Kochanny, Jr., A. Timnick, C. J. Hochanadel and C. D. Goodman, *ibid.*, **19**, 462 (1963).

8) For organic compounds, see, W. G. Burns and R. Barker, "Progress in Reaction Kinetics," Vol. 3, ed. by G. Porter, Pergamon Press, Oxford (1965), p. 303.

9) R. H. Schuler, *J. Phys. Chem.*, **71**, 3712 (1967).

10) a) W. G. Burns, W. R. Marsh and C. R. V. Reed, *Nature*, **218**, 867 (1968). b) W. G. Burns and C. R. V. Reed, *Chem. Commun.*, **1968**, 1468.

will concern the results with C- and N-ions, which had energies of 31—77 and 17—78 MeV respectively; a single result with 58 MeV ^{16}O-ions is also included.

By extrapolating the present results at very high LET's, one could obtain the value for $G(Fe^{3+})$ at an infinite LET and, therefore, the limiting yield of water decomposition, G_{-H_2O}. It has also been shown that there is a substantial difference in the instantaneous yield among C-, N-, and O-ions. This may be explained by the differences in the track structures of these heavy-ion radiations.

Experimental

The irradiation arrangement and experimental procedure were similar in outline to those described previously.[1] The ions accelerated in the cyclotron had a charge of +4.[11] The accelerated ions were withdrawn through a beam duct (10 m long) to a target. In the vicinity of the exit window of the duct, the ion beams were passed through a thin gold foil (2μ) and a small fraction of them were elastically scattered by it. The number of ions passing through the foil was thus monitored by counting the number of the scattered ions by a solid-state detector. Meanwhile, the beam currents of ions passing through the foil were determined with a Faraday cup. The number of ions collected in a Faraday cup was then calculated from the total charge, Q, and the average charge, $\langle z\rangle_f$, of ions collected in a Faraday cup after passing through the gold foil; the average charges of ions were obtained in a manner described below. As the number counted by the solid-state detector should be proportional to the number of ions collected in the Faraday cup, one can readily obtain the total number of ions deposited in the solution by assuming no loss of ions between the scattering foil and the solution. The ratio of the number of the scattered ions to that of the collected ions was determined before and after each run; the data were in agreement, within an error of 3%, for each run.

The incident energies of ions were obtained within an error of $\pm 2\%$ by $E_c(\mathrm{MeV}) = 0.107Af^2$, where A is the mass number of the ion and, f(MHz) the radio frequency of the cyclotron being operating. As the ion beams were passed through the scattering foil (2μ Au), the exit window (10μ Al), the air layer (10 mm), and the cell window (10μ mica), the incident energy, E_c, was reduced to E_s when the ions entered the solution. The initial energies of ions entering the solution, E_s, were estimated by the use of the range-energy relations given by Northcliffe.[12]

The principal difference between protons (or helium ions) and heavy ions is that the former can be regarded as charge-invariant over most of the energy region, while the latter can not. With an increase in the atomic number of the ion, there is an expansion of the velocity region in which charge variation is of importance. Northcliffe[13] summarized experimental equilibrium charge distribution data for several heavy ions. It seems that the data can be represented reasonably well by a single universal curve for each value of z/z' (z: atomic number; z': net charge). In the present experiment, the total thickness of absorbers was sufficient to allow the heavy ions to be charge-equilibrated before entering the solution. We have calculated the average charge of ions entering the solution, $\langle z\rangle_s$, by taking weighted means of each fraction of ions having a charge, z', in a charge-equilibrated monoenergetic beam. Table 1 lists the values of z' and $\langle z\rangle_s$ for each ion used in this experiment.

A ferrous ammonium sulfate solution (10^{-2} M $Fe(NH_4)_2(SO_4)_2$, 10^{-3} M NaCl, 0.8 N H_2SO_4) in triply-

Table 1. Average charges, initial LET's and overall yields for heavy ions

Ion	E_c*1	E_s*2	Fraction of ions having charge z' of					$\langle z\rangle_s$	Initial LET (eV/Å)	$G(Fe^{3+})$
			+4	+5	+6	+7	+8			
^{12}C	54.1	31.0	2	23	75	—	—	5.7_3	45.5	3.8_3
^{12}C	73.5	57.0	0	8	92	—	—	5.9_2	30.0	4.1_1
^{12}C	74.2	58.0	0	8	92	—	—	5.9_2	29.6	4.2_0
^{12}C	91.5	77.0	0	4	96	—	—	5.9_6	23.7	4.9_1
^{14}N	51.8	17.0*3	3	29	49	19	—	5.8_4	84.7	3.3_9
^{14}N	52.7	17.0	3	29	49	19	—	5.8_4	84.7	3.4_3
^{14}N	66.8	35.5	0	6	36	58	—	6.5_2	59.8	3.7_7
^{14}N	82.2	61.5	0	1	17	82	—	6.8_1	42.3	4.1_2
^{14}N	96.6	78.5	0	0	12	88	—	6.8_8	35.5	4.4_6
^{16}O	91.7	58.0	0	0	4	33	63	7.5_9	59.2	4.3_2

*1 The energy of ions accelerated in the cyclotron.
*2 The energy of ions entering the solution.
*3 A Ni (3μ) scattering foil was used.

11) Y. Miyazawa, T. Tonuma, I. Kohno, S. Nakajima, T. Inoue, A. Shimamura, K. Yoshida and T. Karasawa, *Japan J. Appl. Phys.*, **9**, 532 (1970).
12) L. C. Northcliffe, "Studies in Penetration of Charged Particles in Matter," Publication 1133, National Academy of Sciences-National Research Council, Washington, D. C. (1964), p. 173.
13) L. C. Northcliffe, *Ann. Rev. Nucl. Sci.*, **13**, 1 (1963).

distilled water was used under aerated conditions. The irradiation cells were the same as those used previously;[1] the aperture of the cell (10 mm in diameter) was glazed with mica (10 μ thick), the range of which was estimated to be 2.7 mg/cm^2. The solution was stirred during irradiation by means of a magnetic stirrer at a speed of 36 rps.

The oxidation yields of ferrous ions (the number of Fe^{3+} ions oxidized by 100 eV of energy deposited in the solution) were calculated by the equation:[1]

$$G(Fe^{3+}) = 0.96\times10^{7}\times\frac{DV}{\varepsilon d}\times\frac{\langle z\rangle_f}{E_sQ}$$

where: D: the optical density at 304 nm,
ε: the molar extinction coefficient of Fe^{3+} at 304 nm in M^{-1} cm^{-1},
d: the optical path-length for D-measurement in cm,
V: the volume of the irradiated solution in ml,
E_s: the initial energy of ions entering the solution in Mev,
Q: the total charge collected in a Faraday cup in nanocoulomb, and
$\langle z\rangle_f$: the average charge of ions collected in a Faraday cup.

The initial LET values for ions with an energy of E_s and a net charge of z' were calculated by the reduced Bethe equations:

$$-\frac{dE}{dx} = \frac{22.2z'^2}{E_s}\log(2.75E_s) \quad \text{for } C^{+z'}\text{-ions}$$

$$-\frac{dE}{dx} = \frac{25.9z'^2}{E_s}\log(2.36E_s) \quad \text{for } N^{+z'}\text{-ions}$$

where the mean excitation potential (I) is assumed to be 66 eV for water and where $-dE/dx$ is expressed in eV/Å when E_s is in MeV. The effective values of $-dE/dx$ for ions with an average charge of $\langle z\rangle_s$ were obtained by taking the weighted means of the value for each z'-value; they are summarized in Table 1.[14]

Results and Discussion

The oxidation yield of ferrous ions was found to be linearly dependent on the dose. Some typical examples are given in Fig. 1; Figure 1 also shows that the yield is independent of the beam current in the range of 0.1—3 nA;[15] above 5 nA the yield decreases.

The radiation chemical yields ($G(Fe^{3+})$) were calculated from the slopes of these linear yield-dose plots and are summarized in Table 1. Figure 2 shows the dependence of the observed $G(Fe^{3+})$ value on the initial LET's of ions. The yields obtained by Schuler[9] with C-ions, also plotted in Fig. 2, indicate good agreement with the present C-ion data. It does not seem, however, that the

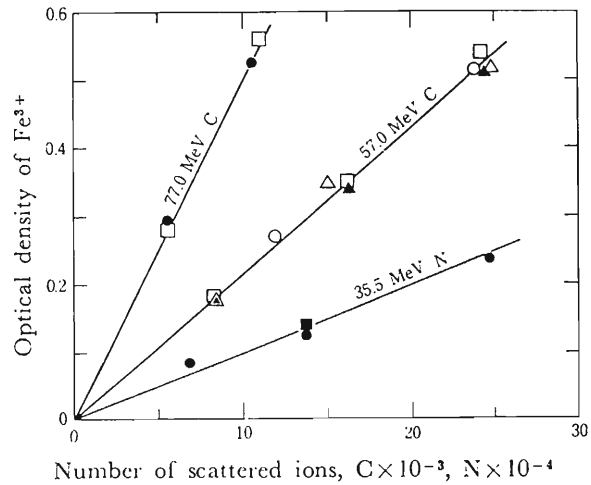

Fig. 1. Plots of Fe^{3+}-yield *vs.* number of ions scattered by a gold foil at various beam currents. The number of scattered ions is proportional to the total number of ions deposited in the solution. The optical densities (d=10 mm) were determined at 304 nm.
○, 0.1 nA; ●, 0.2 nA; □, 0.5 nA; ■, 0.7 nA; △, 1.5 nA; ▲, 3.0 nA

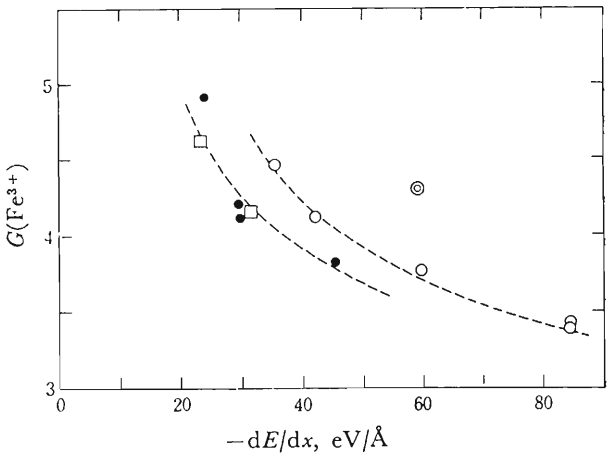

Fig. 2. A plot of the observed $G(Fe^{3+})$ *vs.* reciprocal LET. The initial LET values were calculated by the equations described in the text.
●, C-ions; ○, N-ions; □, C-ions by Schuler (Ref. 9); ◎, O-ions

data for the three ions are superimposable: the heavier the ion, the greater the yield. A similar discrepancy has also been observed between protons or deuterons and helium ions.[16] Furthermore, it seems that the yields at higher LET's can be extrapolated to a value lower than 3.6, which was assumed by Schuler and Allen[2b] to be a limiting yield at an infinite LET.

The $G(Fe^{3+})$-values have hitherto been determined by using accelerated protons, deuterons, and helium ions (LET as high as ~5 eV/Å) and

14) Table 1 also contains a single result with O-ions; the experimental procedure was quite similar to that for C- or N-ions. The initial LET for O-ions is given by $(-dE/dx)=(29.6\ z'^2/E_s)\log(2.06\ E_s)$.

15) The beam currents determined by the use of a Faraday cup.

16) A. O. Allen, "The Radiation Chemistry of Water and Aqueous Solutions," Van Nostrand, Princeton, N. J. (1961), p. 54.

the recoil particles from (n,α) reactions of Li and B (~25 eV/Å).[17] These results indicate that the $G(Fe^{3+})$ decreases as the LET of the radiation is increased. No experimental value of $G(Fe^{3+})$ at the LET's higher than the above value has been reported except for those by Schuler with C-ions (LET's as high as ~30 eV/Å) shown in Fig. 2.[9] The present results indicate that the $G(Fe^{3+})$ still decreases at LET's above 30 eV/Å.

The integrated yield of ferric ions produced by an ion with E_s is given by:

$$G(Fe^{3+}) \times E_s = \int_0^{E_s} G_i dE \qquad (E_s \text{ in } 100\,eV)$$

where G_i represents an instantaneous yield at a a given energy. In Fig. 3 the values of $G(Fe^{3+}) \times E_s$ for C-, N-, and O-ions are plotted as a function of E_s; the data of Schuler with C-ions[9] are also included. It seems that, in unexpected contrast to Fig. 2, all the data fit a universal curve, as is shown in Fig. 3. The instantaneous yields, G_i, for given values of E_s are readily obtained from the slopes at the corressponding points on this curve, *i.e.*,

$$G_i(Fe^{3+}) = \frac{d[G(Fe^{3+})E_s]}{dE_s}$$

The values of $G_i(Fe^{3+})$ thus obtained are plotted as a function of the reciprocal LET in Fig. 4 for C-, N-, and O-ions. The dotted line in Fig. 3 represests the tangent at an infinite LET, which gives $G_i(Fe^{3+})=2.9$.

As may be seen in Fig. 3, the data for C- and N-ions and probably for O-ions apparently fit a single universal curve within the limits of experimental error. This is presumably adventitious; the curves may not coincide with each other at higher E_s's. Figure 4 clearly indicates the existence of substantial differences in $G_i(Fe^{3+})$ among these ions at the same LET. These differences may be explained by assuming the different contribution of high-energy secondary electrons; the heavier ion ejects the more energetic secondary electrons. The net yield is, therefore, a combination of the yields for the "core" of the track and for the emergent secondary electrons. The higher yields of heavier ions can thus be understood by assuming the effective expansion of the heavy-ion tracks; such a model has been proposed by Mozumder *et al.*[18] A similar effect observed with deuterons and helium ions has been discussed in terms of the kinetics of secondary electron production.[19] Further experimental study on this effect due to the quality of heavy ions is in progress by using C-, N-, and O-ion radiations.

The oxidation yield of ferrous ions in an aerated aqueous solution is given by the equations:

$$G(Fe^{3+}) = G_{OH} + 3G_H + 2G_{H_2O_2}$$
$$= G_{-H_2O} + 3G_H = 2G_{H_2} + 4G_H$$

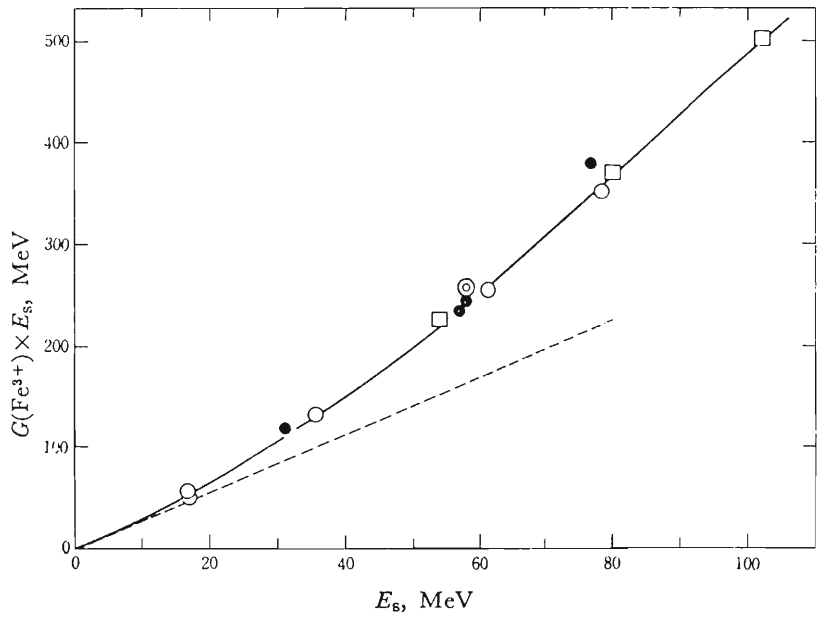

Fig. 3. A plot of the integrated yield of ferric ions *vs.* energy of the heavy ions entering the solution. The dotted line represents the limiting yield of $G(Fe^{3+})=2.9$ at an infinite LET.
●, C-ions; ○, N-ions; □, C-ions by Schuler (Ref. 9) ◎, O-ions

17) W. R. McDonell and E. J. Hart (*J. Amer. Chem. Soc.*, **76**, 2121 (1954)) have obtained $G(Fe^{3+})=5.2$ and 4.2 for $^6Li(n, \alpha)^3H$ and $^{10}B(n,\alpha)^7Li$ recoils and R. H. Schuler and N. F. Barr (Ref. 3a) 5.69 and 4.22, respectively.

18) a) A. Mozumder, A. Chatterjee and J. L. Magee, *Advan. Chem. Ser.*, **81**, 27 (1968). b) A. Mozumder, *Advan. Radiat. Chem.*, **1**, 1 (1969).

19) R. E. Faw and H. J. Donnert, *Nucl. Instr. Methods*, **58**, 307 (1968).

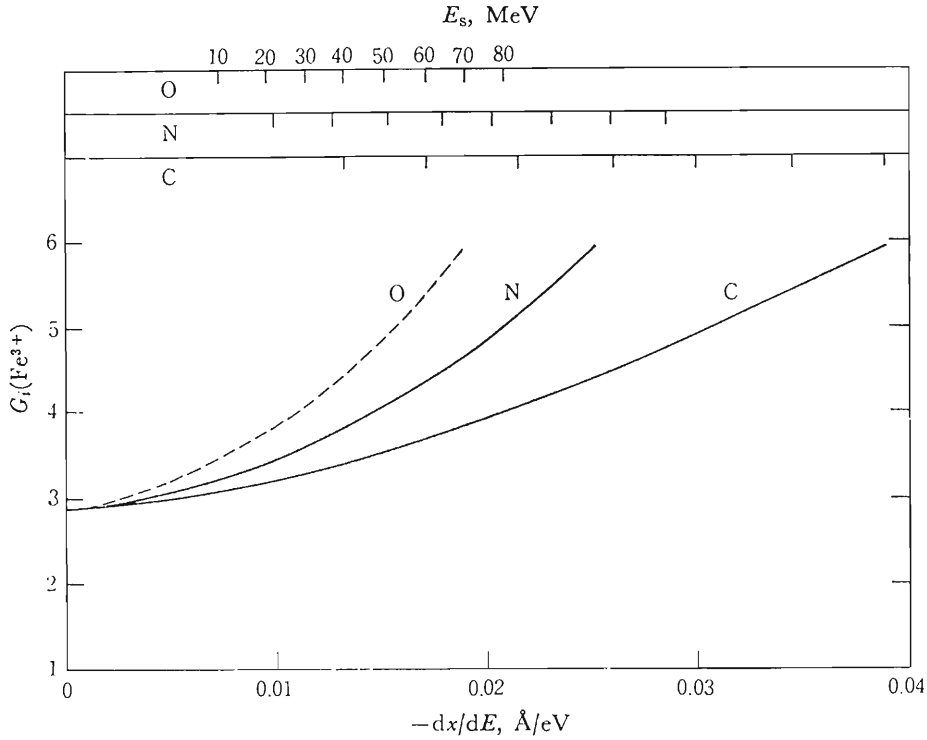

Fig. 4. Dependence on reciprocal LET of the instantaneous yields for C- and N-ions obtained from Fig. 3. Probable dependence for O-ions is also shown.

At an infinite LET, the free radical yields will vanish;[6,20] $G(Fe^{3+})$ will, therefore, approach G_{-H_2O} or $2G_{H_2}$. Schuler and Allen[2b] have assumed the limiting $G(Fe^{3+})=3.6$ from the values for G_{-H_2O} $(=3.6)$ or $2G_{H_2}(=3.4)$ in the radiolysis of an aqueous solution with $^{10}B(n,\alpha)^7Li$ recoil particles. As has been mentioned above, the present results gave the value of 2.9 for the limiting $G(Fe^{3+})$ at an infinite LET, which would mean $G_{-H_2O}\simeq 2.9$ according to the above argument.[21]

According to Allen,[22] the G_{-H_2O} for the 0.8 N H_2SO_4 solution decreases with an increase in the LET to about 3.6 at about 5 eV/Å; then it becomes constant in the higher LET range. In a neutral solution the G_{-H_2O} increases with an increase in LET above 5 eV/Å. However, Anderson and Hart,[6] who investigated the LET dependence of the initial yields from water using a formic acid solution saturated with oxygen, found that the value for G_{-H_2O} decreases with an increase in LET down to 2.4—2.6 for helium ions of about 10 MeV (LET ~5 eV/Å), and then increases slightly.

The present results indicate that the G_{-H_2O} in the 0.8 N H_2SO_4 solution seems substantially lower than the 3.6 estimated by Schuler and Allen.[2b] Although some discussions have been made concerning the value of G_{-H_2O} at very high LET's[21-24] and concerning the difference in that value between acid and neutral solutions,[6] more data should be accumulated in the higher LET region, and the variation in the value of G_{-H_2O} at LET's above 5 eV/Å is still open to question.

The authors wish to express their gratitude to the members of the cyclotron operation group, and also to Hiroshi Seki and Takahisa Imai for their experimental assistance.

20) A. Kuppermann, "Radiation Research 1966," ed. by G. Silini, North-Holland Publ. Co., Amsterdam (1967), p. 212.

21) In the high-LET tracks, some reactions between molecular products and free radicals may be taken into consideration. The most noteworthy reaction of them may be: $H_2O_2+OH\rightarrow H_2O+HO_2$ (*cf.* Ref. 16, p. 51). The formation of HO_2 in the α-ray tracks has been reported by Donaldson and Miller (*Trans. Faraday Soc.*, **52**, 652 (1956) and Appleby and Schwarz (Ref. 5). However, the rate constant of this reaction is not high (4.5×10^7 M^{-1} ses^{-1}, Schwarz, *J. Phys. Chem.*, **66**, 255 (1962)) and the yield has not been established. If this reaction is assumed to occur at all, the $G(Fe^{3+})$ is given, by assuming the material balance suggested by Allen (Ref. 16, p. 51(, by $G(Fe^{3+}(=G_{-H_2O}+G_{HO_2}$ at an infinite LET, yielding the value of G_{-H_2O} lower than 2.9.

22) A. O. Allen, Ref. 16, p. 58.

23) C. J. Hochanadel, "Comparative Effects of Radiation," ed. by M. Burton, J. S. Kirby-Smith and J. L. Magee, John Wiley & Sons, New York (1960), p. 151.

24) M. Anbar, "Fundamental Processes in Radiation Chemistry," ed. by P. Ausloos, Interscience, New York (1968), p. 651.

Radiochemistry, radiation chemistry, and radiation biology

Reprinted from Proc. 1st. World Cong. Nucl. Medicine, p. 17–19 (1974).

CYCLOTRON PRODUCTION OF MEDICAL-USE RADIOISOTOPES IN JAPAN.

Tadashi Nozaki. Institute of Physical and Chemical Research, Wako-shi, Saitama, Japan.

The cyclotron of the Institute of Physical and Chemical Research has been the sole cyclotron utilizable for the production of medical-use radioisotopes in Japan till now (March 1974). This machine is an ordinary type, variable energy, 160 cm cyclotron, capable of accelerating protons, deuterons, α-particles and ^{3}He-particles, up to energies of 18 MeV, 28 MeV, 45 MeV and 48 MeV, respectively, and also heavy particles, such as ^{12}C, ^{14}N and ^{16}O. It is for multi-purpose use, and consequently its machine time for radioisotope production has been quite limited. However, two medical cyclotrons are now under test operation in and near Tokyo, and shall become utilizable for isotope production by the summer of 1974. Up to present, we have produced ^{18}F, ^{28}Mg, ^{43}K, ^{52}Fe, ^{67}Ga, ^{111}In, ^{123}I, $^{197-197m}$Hg, etc., and supplied most kinds of them to hospitals. In this congress, our presentation will be focused on the following three subjects: (1) the yield of ^{18}F for various reactions, together with the comparison of them in view of the practical production purpose, (2) our technique of the production of ^{43}K, and (3) the yield of ^{28}Mg for various reactions , and the carrier-free separation of ^{28}Mg from an aluminium target.

We measured the excitation curves for the reactions of deuteron and ^{3}He-particle on neon to give ^{18}F and the thick target yield of ^{18}F for the reaction of triton on oxygen, up to the deuteron and triton energies of 24 MeV and the ^{3}He-particle energy of 42 MeV. The excitation curves for the ^{3}He- and α-particle reactions on oxygen to yield ^{18}F were also measured by the same experimental technique as was used in the neon reaction in order to compare the results with the already-reported curves. From the excitation curves, the thick target saturation activities were calculated in dps/μA, which is identical with the production rate. They are shown in Fig. 1. As for the accuracy of the present results, the absolute yield might involve up to 10 % uncertainty, but the relative value of the yield within each of the reactions as well as among them can be thought to be usually sure within an uncertainty range of 5 %.

In view of the practical production of ^{18}F, the following things were considered in addition to the yield: (1) impurities in the product, (2) the accessibility of the particle acceleration and ease of bombardment, and (3) the chemical and physical state of the target as well as of the product. The deuteron bombardment of neon thus is regarded as the most convenient method for the production of anhydrous ^{18}F for the labelling of organic compounds. The ^{3}He-bombardment of water, on the other hand, is a useful technique of producing ^{18}F for bone scanning. The bombardment under a maximum available energy is regarded as often unprofitable, because (1) the formation of radiochemical impurities generally increases with energy, (2) the total heat evolved is exactly proportional to the incident energy, and the rate of total radiation decomposition is approximately proportional to it, and (3) the thick target yield does not increase steeply with energy for energy regions far above the maximum of the excitation curve.

The yield curves of the ^{3}He reactions on oxygen and neon show that: in energy regions over 15 MeV, neon gives a much higher ^{18}F activity than oxygen; under 10 MeV, only oxygen yields a sufficiently high activity of ^{18}F. Thus, both anhydrous and aqueous ^{18}F can be simul-

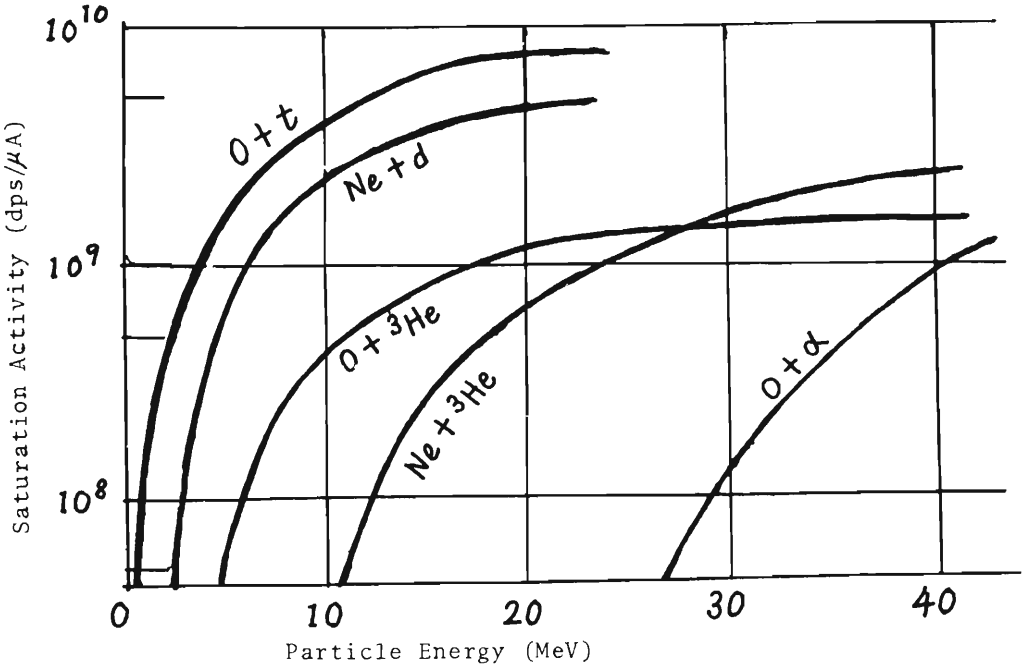

Fig. 1. Thick target yield of ^{18}F for various reactions.

taneously obtained in good yields by the following bombardment: ^{3}He-particles of an incident energy over 25 MeV is caused first to traverse a neon target with such a thickness as to reduce their energy to about 15 MeV and then to enter a water target through a thin separation foil.

Some of our works on the synthesis of ^{18}F-labelled compounds and the study of their behaviour in animals are presented in this congress by Dr. T. Ido.

In the ^{3}He-bombardment of water, titanium foil is usually used as the beam window. The foil after the bombardment contains fairly high activities, such as ^{48}Cr and ^{48}V. We measured the excitation curves for the formation of them. For the carrier-free separation of the ^{48}Cr, adsorption of the other elements on anion exchange resin from a dilute hydrofluoric acid solution has proved to be useful.

In the production of ^{43}K by the $^{40}Ar(\alpha,p)^{43}K$ reaction, we now use a stainless steel pipe (60 cm in length, 5 cm in diameter) as the gas target container, with its well polished inside surface being thinly coated with phosphoric acid. The coating is carried out by drenching the surface completely with a H_3PO_4-H_2O mixtre (1 vol : 1 vol) and keeping the pipe vertically on sheets of filter paper for more than 3 hours. The inside surface has been found to be thus covered with 50$\sim$100 mg of H_3PO_4. A slow stream of argon (2 l/min) is bombarded by α-particles in this pipe through an aluminum foil window; more than 80 % of the ^{43}K formed is adsorbed in this pipe.

After the bombardment, a round-bottom quartz flask containing water (50 ml) is attached to one end of the pipe and heated strongly by a direct flame. Steam generated in the flask condenses on the inside surface of the pipe, and carries the ^{43}K back to the flask together with the phosphoric acid. The solution is then passed through a small column of anion exchange resin in OH-form for the removal of the phosphoric acid, and the effluent is evaporated to a desired volume to give an aqueous solution of ^{43}K ready for i.v. injection. The overall yield of ^{43}K is estimated to be 60$\sim$70 %.

The excitation curves for the formation of ^{28}Mg by the reaction of triton and α-particle on magnesium and aluminium were measured up to a triton energy of 24 MeV and α-particle energy of 42 MeV. The thick target yield of ^{28}Mg calculated from the excitation curves are shown in Fig. 2 (for magnesium target of natural isotopic composition). It is obvious from Fig. 2 that the triton bombardment of aluminium is the best method of producing carrier-free ^{28}Mg, if a triton beam of a fairly high flux and energy be available. Also, aluminium is more convenient than magnesium for cyclotron bombardment with a maximum available flux. The reaction of $^{26}Mg(t,p)^{28}Mg$, on the other hand, gives the highest yield of ^{28}Mg in the incident energies of our experiment, though the product is not carrier-free. With a completly enriched ^{26}Mg target, a yield of about 0.15 mCi/μA·h can be obtained for an incident triton energy of 20 MeV. Since the triton bombardment is of quite limited accessibility at present, the use of the α-particle reactions should also be considered. We are going to produce carrier-free ^{28}Mg by the bombardment of aluminium with 75 MeV α-particles.

Since the bombarded targets always contain byproduct activities, such as ^{24}Na and ^{7}Be, some chemical treatment of the ^{28}Mg is required. The following process has proved to be useful for the carrier-free separation of ^{28}Mg from an aluminium target: (1) dissolution of the target in HCl, (2) addition of NaOH to the solution (to pH of 13), (3) treatment of the solution with a cellulose column, ^{28}Mg being adsorbed in the column while aluminium, ^{24}Na and most part of ^{7}Be passing through it, and (4) washing of the column with water, and elution of the ^{28}Mg with dilute HCl. The product can be further purified by repetition of Steps. 2, 3 and 4. ^{28}Mg of a sufficient purity has proved to be thus obtained with a yield over 90 %.

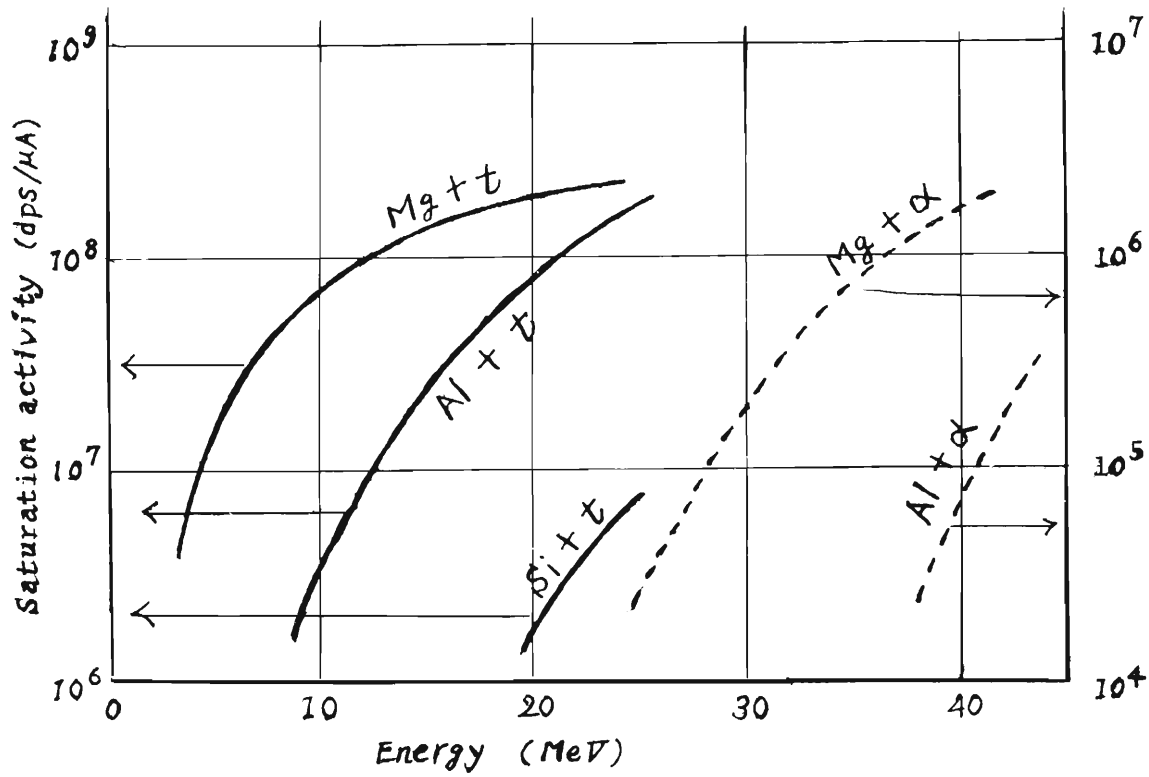

Fig. 2 Thick target yield of ^{28}Mg.

Reprinted from J. Chem. Phys., 60, 3773–3778 (1974).

Mössbauer emission spectra of ^{119}Sn after the EC decay of ^{119}Sb in metals, oxides, and chalcogenides of antimony and tellurium*

F. Ambe, S. Ambe, H. Shoji, and N. Saito

The Institute of Physical and Chemical Research, Wako-shi, Saitama 351, Japan
(Received 1 February 1974)

Mössbauer emission spectra of ^{119}Sn have been measured in metals, oxides, and chalcogenides of antimony and tellurium labeled with ^{119}Sb or ^{119m}Te. Sources of ^{119}Sb and ^{119m}Te metals gave an emission line in the Sn(0) region. In the emission spectra of $^{119}Sb_2O_3$ the species attributable to the Sn(II) state were dominant, while only the Sn(IV) species was found in the $^{119m}TeO_2$ samples. The $^{119}Sb_2S_3$ and $^{119}Sb_2Se_3$ gave two emission lines attributable to the Sn(II) and Sn(IV) states. The $^{119}Sb_2Te_3$ showed only an emission line in the Sn(II) region. These observations were discussed in terms of the aftereffect of the EC (electron capture) decays and the properties of the matrices.

I. INTRODUCTION

Mössbauer emission spectroscopy provides a useful way of studying the electronic state of defect atoms produced as a result of nuclear decay in solids. The technique has been extensively applied to investigations on ^{57}Fe after the EC (electron capture) decay of ^{57}Co as well as on ^{119}Sn after the IT (isomeric transition) of ^{119m}Sn.[1] Recent studies have shown that in case of compounds with radiation-sensitive ligands the oxidation state of ^{57}Fe or ^{119}Sn atoms is affected by the oxidizing or reducing species produced in local radiolysis of the ligands by conversion electrons and Auger electrons.[2–7] However, no mechanism of general validity for stabilization of defect charge states of ^{57}Fe has been established yet for compounds with simple rigid ligands, although parameters such as the concentration of lattice defects,[8] the ionic size,[9] or the lattice energy[10] have been suggested as the determining factors for selected compounds. On the other hand, no change in the valence state has been reported for ^{119}Sn after the IT in simple Sn(II) or Sn(IV) compounds.[11]

In view of these observations, it appeared of interest to study the electronic state of ^{119}Sn arising from ^{119}Sb, which decays by EC directly to the Mössbauer level of ^{119}Sn (Fig. 1). This system can be considered as a hybrid of the well-studied $^{57}Co \xrightarrow{EC} {}^{57}Fe$ and $^{119m}Sn \xrightarrow{IT} {}^{119}Sn$ systems regarding the type of the nuclear decay and the chemical element involved. Moreover, the system has a distinct feature in itself, that the daughter has no common stable oxidation states with the parent except for the metals. The ^{119}Sb has received little attention as a source nuclide for ^{119}Sn–Mössbauer spectroscopy[12] because its half life is much shorter than that of ^{119m}Sn.

We report here an investigation of the valence state of ^{119}Sn after the EC decay of ^{119}Sb in a variety of matrices. The Mössbauer emission spectra of ^{119}Sn arising from ^{119}Sb were measured in metal, trioxide, and chalcogenides of antimony. Studies were also made on ^{119}Sn produced by the successive EC decays of ^{119m}Te by way of ^{119}Sb (Fig. 1) in tellurium metal and dioxide. Preliminary results on some of the materials were already reported.[13]

II. EXPERIMENTAL

The 38.0 hr ^{119}Sb was produced by bombarding a tin plate of natural isotopic abundance with 15 MeV protons accelerated in the IPCR 160 cm cyclotron. The target was dissolved in concentrated HCl with the aid of concentrated HNO_3. The ^{119}Sb was separated from tin by isopropylether extraction from 9*M* HCl and purified by anion exchange procedures. The 4.7 day ^{119m}Te was produced similarly by 35 MeV α irradiation of tin. The nuclide was separated by precipitation as metal from 3*M* HCl with an appropriate amount of tellurium carrier and purified by anion exchange. Detailed description of the radiochemical procedures will be given elsewhere.

Metals and compounds of antimony and tellurium labeled with ^{119}Sb or ^{119m}Te were prepared, care being taken of the homogeneity of the bulk antimony or tellurium with the nuclides.

Antimony metal labeled with ^{119}Sb was prepared by reducing ^{119}Sb(III) in 6*M* HCl with Cr(II) and was purified by sublimation in vacuum (about 5×10^{-4} torr, and so forth) at 550 °C. ^{119m}Te-labeled tellurium metal was prepared by reduction of ^{119m}Te(IV) in 3*M* HCl with sodium sulfite and hydrazine hydrochloride followed by sublimation in vacuum at 430 °C. $^{119}Sb_2O_3$ was obtained by hydrolysis of a 3*M* HCl solution of ^{119}Sb(III) with NH_4OH. The precipitate was dehydrated at 120 °C under a reduced pressure and sublimed in vacuum at 500 °C. $^{119m}TeO_2$ was prepared by neutralizing an alkaline solution of ^{119m}Te(IV) with 2*M* acetic acid. The precipitate was dried at 120 °C in air. Amorphous $^{119}Sb_2S_3$ was precipitated by H_2S from a 3*M* HCl solution of ^{119}Sb(III) containing tartaric acid. The orange sulfide was converted into the crystalline black form by sublimation in vacuum at 500 °C. $^{119}Sb_2Se_3$ and $^{119}Sb_2Te_3$ were prepared by fusing a stoichiometric mixture of the ^{119}Sb-labeled antimony and selenium, or tellurium in argon. The deviation from the stoichiometry of the selenide and telluride samples is estimated to be of the order of 0.3%. The samples were identified by the Debye–Scherrer patterns and in some cases by the ^{121}Sb–Mössbauer absorption spectra. Their purity was checked by chemical analysis of the component elements. Absence of Sb(V) species in the $^{119}Sb_2O_3$ samples was further confirmed by a radiochemical technique utilizing

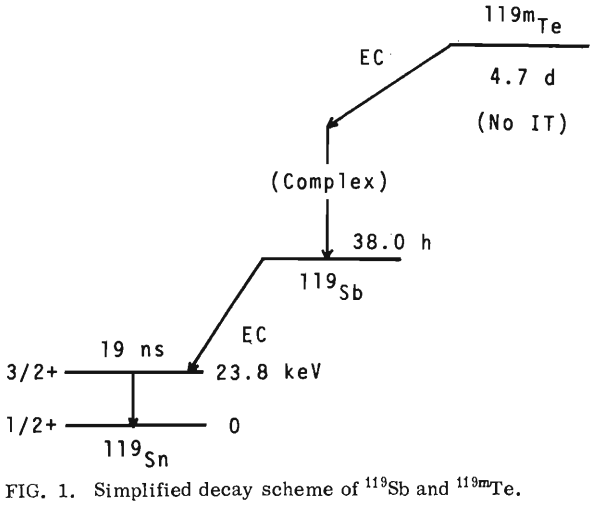

FIG. 1. Simplified decay scheme of ^{119}Sb and ^{119m}Te.

the ^{124}Sb (a by-product of the p-irradiation) in the samples as the tracer.

The sources were driven against an absorber by means of a Hitachi Mössbauer Spectrometer operated in the constant acceleration mode. The temperature of the sources was 78 ± 1 K. The absorber was $BaSnO_3$ (0.6 mg ^{119}Sn/cm^2) kept at 296 ± 2 K, which gave a single line absorption with a FWHM of 1.07 mm/sec against a $Ba^{119m}SnO_3$ source obtained from New England Nuclear. The 23.8 keV resonant γ rays were detected with a 2 mm NaI scintillator, the Sn K x rays being eliminated with an 80 μm Pd foil critical absorber. In case of the sources labeled with ^{119m}Te the measurement was carried out after the ^{119}Sb had attained a state of radiocative equilibrium with ^{119m}Te in the samples at liquid nitrogen temperature. The velocity calibration was based on the ^{57}Fe-magnetic hyperfine splitting[14] of an iron foil. The zero point of motion was determined from the absorption spectra of $BaSnO_3$ against the $Ba^{119m}SnO_3$ source assuming a zero isomer shift between them at the same temperature. The spectra obtained were least-squares fitted to single or sum of Lorentzians by means of FACOM 270-30 and 230-60 computers of this Institute.

III. EXPERIMENTAL RESULTS

Typical emission spectra obtained are shown in Figs. 2–4. Table I summarizes the Mössbauer hyperfine parameters derived from the spectra by least-squares fitting together with the valence assignment. The isomer shifts of the emission lines are given relative to $BaSnO_3$ at 296 ± 2 K, the sign being as in usual absorption spectroscopy. Table I also contains the parameters of the absorption lines of the corresponding tin compounds at liquid nitrogen temperature collected from the literature.[15–22]

The position and the relative intensity of the emission lines showed good reproducibility with reasonable fluctuations expected from the statistics and the stability of the spectrometer, while the line width often varied from sample to sample.

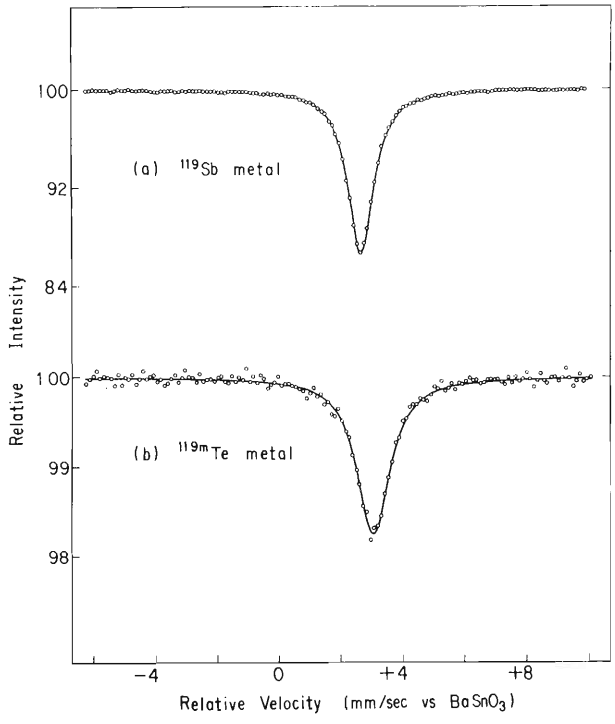

FIG. 2. ^{119}Sn-Mössbauer emission spectra of (a) ^{119}Sb metal and (b) ^{119m}Te metal at 78 ± 1 K against $BaSnO_3$ at 296 ± 2 K. (In the abscissa a velocity of approach is taken negative and in the ordinate the background is not corrected.)

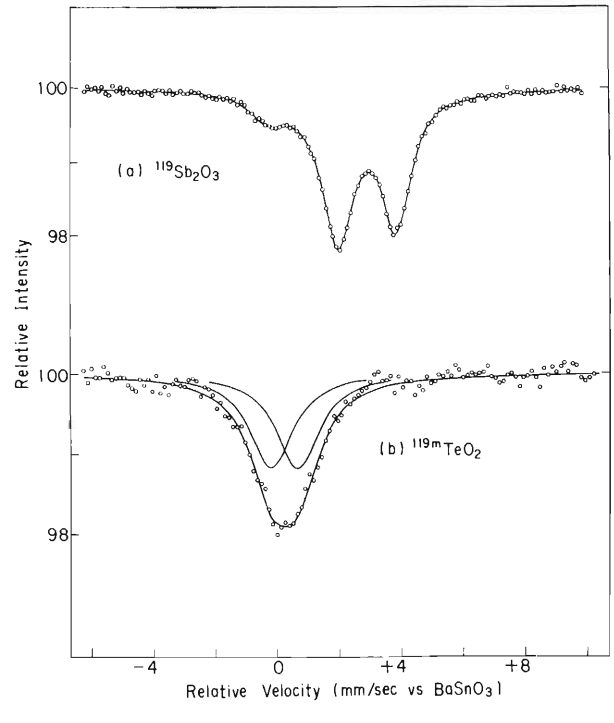

FIG. 3. ^{119}Sn-Mössbauer emission spectra of (a) $^{119}Sb_2O_3$ and (b) $^{119m}TeO_2$ at 78 ± 1 K against $BaSnO_3$ at 296 ± 2 K. (In the abscissa a velocity of approach is taken negative and in the ordinate the background is not corrected.)

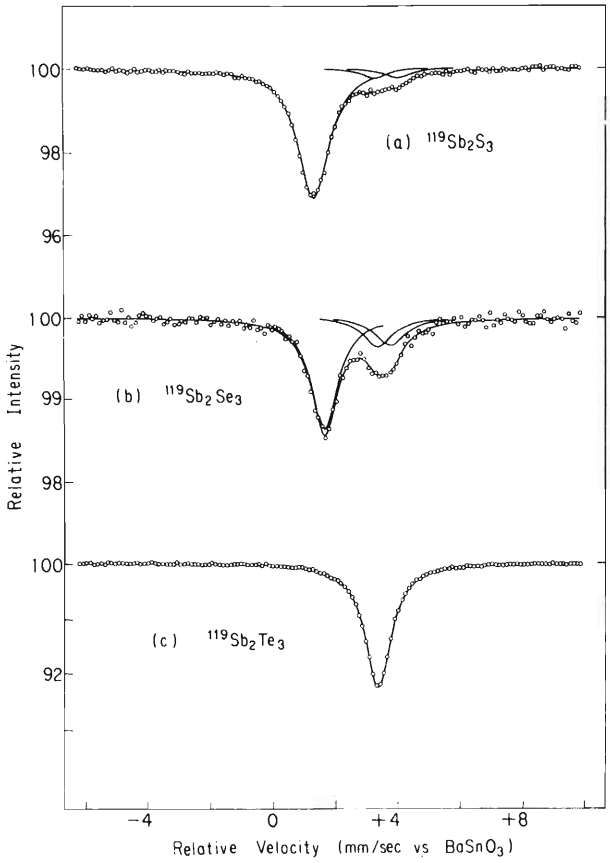

FIG. 4. ^{119}Sn-Mössbauer emission spectra of (a) $^{119}Sb_2S_3$, (b) $^{119}Sb_2Se_3$ and (c) $^{119}Sb_2Te_3$ at 78±1 K against $BaSnO_3$ at 296±2 K. (In the abscissa a velocity of approach is taken negative and in the ordinate the background is not corrected.)

A. ^{119}Sb and ^{119m}Te metals

The emission spectra of ^{119}Sn produced in rhombohedral antimony metal consisted of a single line with an isomer shift of 2.68 mm/sec [Fig. 2(a)]. The line can be attributed to a Sn(0) state as is expected from the high electric conductivity of the metal (9.6×10^4 ohm$^{-1}\cdot$cm^{-1} at liquid nitrogen temperature).[23]

The ^{119}Sn arising from the sequential EC decays of ^{119m}Te in semiconducting hexagonal tellurium gave also an emission line in the Sn(0) region as shown in Fig. 2(b). The isomer shift, 3.02 mm/sec, was slightly higher than that of ^{119}Sn in antimony, indicating a higher s-electron density at the nucleus of ^{119}Sn in the tellurium matrix than in antimony.

B. $^{119}Sb_2O_3$ and $^{119m}TeO_2$

The $^{119}Sb_2O_3$ samples obtained by sublimation in vacuum were in the cubic modification (senarmontite). A typical emission spectrum is shown in Fig. 3(a). It consists, at first glance, of a dominant doublet and a subsidiary peak close to the zero relative velocity. The former may be identified as a quadrupolar doublet of Sn(II) on the basis of the fact that its isomer shift and quadrupole splitting are close to those of the tetragonal or rhombic SnO (Table I). The latter peak can be attributed to the Sn(IV) state in a similar manner. However, computer decomposition of the spectra into three Lorentzians indicates that the apparent Sn(II) doublet is asymmetric both in area and in width.

Repetition of sublimation (up to four times) induced no significant change on the emission spectra of $^{119}Sb_2O_3$. In the $^{119}Sb_2O_3$ samples, which had not been sublimed, the relative intensity of the Sn(IV) peak was much larger, though the Sn(II) doublet was still dominant.

The $^{119m}TeO_2$ samples gave a broad emission line with an isomer shift close to zero [Fig. 3(b)]. The isomer shift, 0.19 mm/sec, is only slightly higher than the corresponding value for SnO_2 (Table I). The quadrupole splitting, computed on an assumption that the peak is an unresolved symmetric doublet of quadrupolar origin, amounts to about 0.9 mm/sec. No line was detected in the region of Sn(II) within the limit of the sensitivity of the measurement.

C. $^{119}Sb_2S_3$, $^{119}Sb_2Se_3$ and $^{119}Sb_2Te_3$

Antimony sulfide and selenide are semiconductors[24,25] crystallizing in an isomorphous orthorhombic structure. As can be seen in Fig. 4(a), the crystalline $^{119}Sb_2S_3$ samples sublimed in vacuum gave two emission peaks with isomer shifts of 1.34 and 3.7 mm/sec respectively, the former being much more intense than the latter. They are attributable to the Sn(IV) and Sn(II) states on the basis of the similarity of their isomer shifts with those of SnS_2 and SnS (Table I). The upper limit of the quadrupole splitting of the emission line corresponding to the Sn(II) state in the $^{119}Sb_2S_3$ was estimated to be about 0.6 mm/sec.

In the crystalline $^{119}Sb_2S_3$ samples prepared by heating amorphous $^{119}Sb_2S_3$ in an inert atmosphere (Henz method),[26] the intensity of the Sn(II) and Sn(IV) lines was almost equal,[13] and in the samples crystallized in dilute HCl the amplitude of the Sn(IV) line was much smaller than that of the Sn(II) line.

Two emission peaks were also observed for the $^{119}Sb_2Se_3$ samples [Fig. 4(b)]. The weaker line with an isomer shift of 3.57 mm/sec can be assigned to the Sn(II) ions surrounded by selenide ions. The quadrupole splitting of the Sn(II) peak was estimated to be about 0.5 mm/sec by least-squares fitting to a symmetric Lorentzian doublet. The other line may be identified as due to a tetravalent state of ^{119}Sn, though the isomer shift, 1.66 mm/sec, is somewhat higher than that of $SnSe_2$ reported by Baggio and Sonnino (Table I).[21]

Rhombohedral antimony telluride has a metallic conductivity amounting to 1.6×10^4 ohm$^{-1}\cdot$cm^{-1} at liquid nitrogen temperature.[27] The $^{119}Sb_2Te_3$ samples gave an emission line in the region of Sn(II) as shown in Fig. 4(c). No line attributable to Sn(IV) species was detected within the experimental error in contrast with the results on sulfide and selenide. The observed isomer shift, 3.39 mm/sec, is essentially identical to the value of SnTe (Table I).

TABLE I. Mössbauer parameters of the emission lines of ^{119}Sn in metals and compounds of antimony and tellurium labeled with ^{119}Sb or ^{119m}Te and those of the absorption lines of the corresponding metals and compounds of tin at liquid nitrogen temperature.

	Emission lines (this work)			Absorption lines (from the literature)			
Source materials	Isomer[a] shift (mm/sec)	Quadrupole splitting (mm/sec)	Assigned valence	Corresponding tin compounds	Isomer[b] shift (mm/sec)	Quadrupole splitting (mm/sec)	Ref.
^{119}Sb	2.68 ± 0.02		Sn(0)	α-Sn	2.00		15
				β-Sn	2.56	0.32	15, 16
$^{119}Sb_2O_3$	2.90 ± 0.03[c]	1.88 ± 0.03	Sn(II)	SnO[d]	2.71	1.45	17
	1.9 ± 0.1[c]		Sn(?)	SnO[e]	2.60	2.20	17
	−0.3 ± 0.1[c]		Sn(IV)	SnO_2	0.00	0.50	15,16
	2.89 ± 0.03[f]	1.62 ± 0.03	Sn(II)	(See above)			
	2.84 ± 0.03[f]	2.19 ± 0.03	Sn(II)	(See above)			
	−0.2 ± 0.1[f]		Sn(IV)	(See above)			
$^{119}Sb_2S_3$	3.7 ± 0.1	0.6 ± 0.2	Sn(II)	SnS	3.16	0.8	18
	1.34 ± 0.03		Sn(IV)	SnS_2	1.20		19
$^{119}Sb_2Se_3$	3.57 ± 0.03	0.5 ± 0.2	Sn(II)	SnSe	3.45	0.60	20
	1.66 ± 0.03		Sn(IV)	$SnSe_2$	1.27		21
$^{119}Sb_2Te_3$	3.39 ± 0.02		Sn(II)	SnTe	3.21		22
^{119m}Te	3.02 ± 0.02		Sn(0)	(See above)			
$^{119m}TeO_2$	0.19 ± 0.05	0.9 ± 0.3	Sn(IV)	(See above)			

[a]Relative to $BaSnO_3$ at 296 ± 2 K.
[b]Relative to $BaSnO_3$. Conversion of data was done with the values given in p. 374 of Ref. 15.
[c]Decomposition into two singlets and a doublet with the same width [Fig. 5(a)].
[d]Tetragonal.
[e]Rhombic.
[f]Decomposition into a singlet and a pair of doublets each with the same width [Fig. 5(b)].

IV. DISCUSSION

The EC decay converts ^{119}Sb into ^{119}Sn in the first excited level with emission of a neutrino, leaving a hole in an inner electron shell of the tin atom. The observed Mössbauer emission spectra represent the electronic state of the ^{119}Sn on a time scale of the mean life of the level (2.7×10^{-8} sec) after the decay. The Auger process following the EC decay is assumed to bring about buildup of a high positive charge on the atom, as has been demonstrated for a variety of gaseous systems by mass spectrometry.[28] In the solid, the charge is expected to be rapidly neutralized by the electrons from the surroundings. In metals the relaxation time of the multiple charge has been estimated to be less than 10^{-12} sec.[29] Delayed coincidence measurements on ^{57}Fe in a variety of insulators have also shown that charge relaxation goes to completion in time short compared to the life time of the Mössbauer level.[30,31] The recoil energy associated with the neutrino, Auger electrons and x rays following the EC decay of ^{119}Sb is estimated to be 1.4, 0.14 and 0.004 eV respectively. Since the recoil energy is much smaller than the threshold energy required to displace an atom from its normal lattice site (~25 eV),[32] the ^{119}Sn atoms are expected to occupy the site of antimony substitutionally after the EC decay of ^{119}Sb in antimony compounds, unless local radiolysis due to Auger electrons or a mechanism such that suggested by Varley[33] is working. In case of the source materials labeled with ^{119m}Te the possibility of displacement of the atom cannot be excluded, since the recoil energy due to the neutrino emission in the EC decay of ^{119m}Te to ^{119}Sb is estimated to be of the same order of magnitude (24 eV) as the displacement energy in solids.

Defect charge states created by nuclear decay in a crystal must be inevitably accompanied by a local disturbance of the lattice. The defect atoms may be associated with a charge compensating vacancies or trapped electrons and the configuration of ligands around them may be different from that of the corresponding normal compounds. However, the experimental results accumulated so far on a variety of Mössbauer nuclides allow us to conclude that the isomer shift of such defect atoms is still a good measure of the valence state of them. On the other hand, the quadrupole splitting is sometimes sensitive to defects created near the atoms.[34]

Hannaford and Wignall reported that a fraction of the ^{119}Sn produced by thermal neutron capture of ^{118}Sn in Mg_2SnO_4 was present as Sn(II) associated with a charge compensating oxygen vacancy.[35] However, the IT of ^{119m}Sn has been shown to induce no change in the valence state of ^{119}Sn in simple rigid compounds of Sn(II) or Sn(IV) such as oxides and halides,[11] which indicates a preferential stabilization of ^{119}Sn in the parent form in such compounds.

In the matrices studied in the present work, the ^{119}Sn atoms were found in the electronic states attributable to the Sn(0), Sn(II), and Sn(IV) states, the distribution depending on the properties of the matrices.

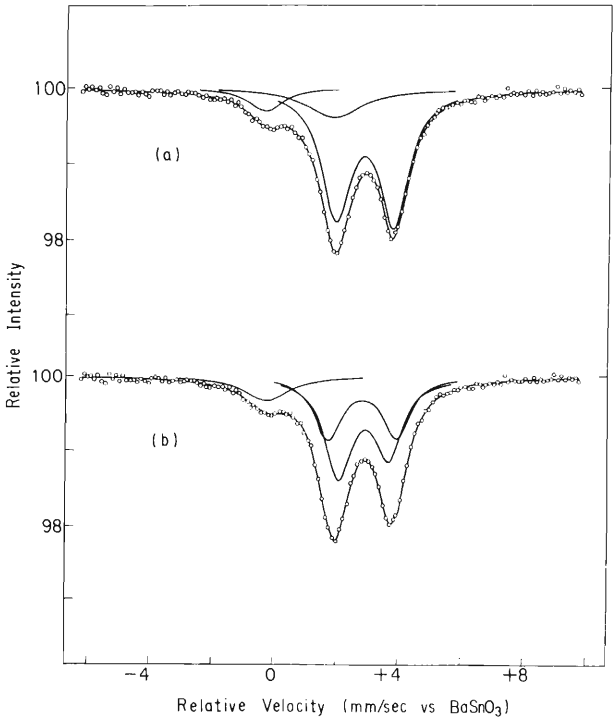

FIG. 5. Typical results of the computer fitting of the emission spectra of $^{119}Sb_2O_3$. (a) Decomposition into two singlets and a doublet with the same width. (b) Decomposition into a singlet and a pair of doublets each with the same width.

Since the ^{119}Sn atoms are stabilized as Sn(0) in antimony and tellurium metals, their emission spectra can be regarded to show the electronic structure of infinitely dilute tin atoms in the metals. The isomer shift of the emission line of ^{119}Sn in antimony, 2.68 mm/sec, is really in good agreement with the value obtained by extrapolating the data of absorption measurements on Sn–Sb solid solutions to Sn content of 0% (2.660 mm/sec from the data of Ruby *et al.*[36] and 2.66 mm/sec from those of Kuzmin *et al.*[37]). The observation that the isomer shift of the emission line of ^{119m}Te metal is higher than that of ^{119}Sb metal is qualitatively in accord with the results of absorption measurements on dilute solid solutions of tin in tellurium.[37] However, the isomer shift of the emission line of ^{119m}Te is somewhat smaller than that of the absorption line of tin in tellurium.

The emission spectra of $^{119}Sb_2O_3$ are the most complex of those observed in this work. As has been described above, the apparent doublet attributable tentatively to the Sn(II) state is asymmetric both in area and width. A quadrupole doublet of ^{119}Sn in isotropic powder samples can be asymmetric for two reasons as in the case of ^{57}Fe.[38] The first is the Goldanskii–Karyagin effect due to the anisotropy of the recoiless fraction, giving rise to asymmetry in peak area but not in width.[39,40] The second is the relaxation of paramagnetic ions causing fluctuating magnetic fields on the nuclei.[41,42] Since the Sn(II) ions are in the nonmagnetic $^1S_0$ state, the second reason above is excluded in the present case. Therefore, asymmetry in area, but not in width, may be expected for the Sn(II) state. Computer fitting of the observed doublet to a pair of Lorentzians with the same width, but not necessarily with the equal area, discloses a broad line with an isomer shift of 1.9 mm/sec [Fig. 5(a) and Table I]. The valence assignment of this fourth line is not straightforward on the basis of the Mössbauer data accumulated so far on tin compounds, though the isomer shift suggests covalent Sn(IV) species, metallic tin or an Sn(III) state. Alternately the doublet can be considered to be a superposition of two sets of doublets each with the same width, assuming two different sites of ^{119}Sn in the Sb_2O_3 lattice. A typical result of computer decomposition carried out on the assumption is shown in Fig. 5(b) and Table I.

The result that the ^{119}Sn atoms are distributed among two or more different chemical states after the EC decay of ^{119}Sb in Sb_2O_3 presents an interesting contrast with the observation on ^{121}Sb in SnO_2. It is well established that all the ^{121}Sb atoms are found in the Sb(V) state after the β^- decay of ^{121m}Sn in SnO_2 (one of the standard source forms of ^{121}Sb-Mössbauer absorption spectroscopy), which shows a preferential stabilization of ^{121}Sb in the isoelectronic state with the Sn atoms in the matrix. The complex behavior of the ^{119}Sn in Sb_2O_3 may be attributed to the disturbing effect of the EC decay followed by the Auger cascade, which is stronger than that of the β^- decay, and also to the rather complex structure of Sb_2O_3 compared with SnO_2.

In contrast with the case of $^{119}Sb_2O_3$, the emission spectrum of $^{119m}TeO_2$ was quite simple giving one broad peak attributable to the Sn(IV) state. The valence state of ^{119}Sb after the EC decay of ^{119m}Te in the TeO_2 matrix can not be determined by Mössbauer or other conventional physical techniques. However, a radiochemical method was applicable which consisted of dissolution of the samples and chemical separation of Sb(III) and Sb(V) species followed by radioactivity measurement of ^{119}Sb in each fraction. The result has shown that about sixty percent of ^{119}Sb was in the Sb(III) state and the rest in the Sb(V) state after the EC decay of ^{119m}Te in TeO_2.[43] To sum up, about sixty percent of the ^{119}Sb atoms were in the Sb(III) state with oxide ions as ligands after the EC decay of ^{119m}Te in the TeO_2 matrix, and they have been turned into ^{119}Sn in the tetravalent state by the second EC decay. This contrasts with the result on $^{119}Sb_2O_3$, in which the majority of ^{119}Sn was found in the Sn(II) state after the decay of ^{119}Sb(III) with oxide ion ligands. These observations suggest the importance of the valence state of the cations in the matrix in determining the final valence state of ^{119}Sn. The appearence of ^{119}Sn only as Sn(IV) in TeO_2 is in accord with the similarity of the crystal structures of TeO_2 and SnO_2 (rutile type) and the fact that the stabilization of ^{119}Sn in the Sn(IV) state requires no charge compensation in TeO_2 as in the case of the IT in $^{119m}SnO_2$.

In the series of antimony chalcogenides the effect of the ligands on the fate of ^{119}Sn is evident. $^{119}Sb_2S_3$ and $^{119}Sb_2Se_3$ give two emission lines attributable to the Sn(II) and Sn(IV) states respectively, the relative intensity of the Sn(II) line being larger in $^{119}Sb_2Se_3$ than in $^{119}Sb_2S_3$. In $^{119}Sb_2Te_3$ all the ^{119}Sn atoms appear as divalent tin.

These observations suggest the importance of the electronegativity of the ligand anions in determining the valence state of ^{119}Sn after the EC decay of ^{119}Sb. The ligands with higher electronegativity are considered to facilitate the formation of defect centers with trapped electrons and to increase, subsequently, the fraction of ^{119}Sn(IV). The finding that in $^{119}Sb_2Te_3$ all the ^{119}Sn atoms are in a lower valence state than the parent indicates that the final state of ^{119}Sn does not reflect the multiple charge state after the Auger cascade and is determined by the properties of the matrix alone. It can not be explained as the result of the stabilization of ions with smaller radius, since Sn(II) is larger than Sb(III) while Sn(IV) is smaller than Sb(III). The lower electronegativity of tellurium is considered to have excluded the stabilization of ^{119}Sn as Sn(IV) with telluride ions as ligands. In fact, no telluride of Sn(IV) seems to have been synthesized in ordinary macrochemistry. The result that only one ^{119}Sn species has been found in $^{119}Sb_2Te_3$ is also consistent with the relatively high electric conductivity of the matrix.

ACKNOWLEDGMENTS

We wish to thank Professor R. H. Herber for his interest and discussions. We are much grateful to Professor H. Sano for helpful suggestions and discussions. We are thankful to the staff of IPCR cyclotron for many irradiations, to Dr. M. Takeda for assistance in the early stage of the work, to Dr. T. Okada for preparation of barium stannate, to Y. Iimura for powder x ray pattern measurements, and also to the staff of the computation center of the Institute for many calculations.

*All correspondence concerning this paper is to be addressed to: Dr. Fumitoshi Ambe, The Institute of Physical and Chemical Research, Wako-shi, Saitama 351, Japan.

[1]G. K. Wertheim, In *The Electronic Structure of Point Defects*, edited by S. Amelinckx, R. Gevers, and J. Nihoul (North-Holland, Amsterdam, 1971), p.1.
[2]J. M. Friedt and J. P. Adloff, C. R. Acad. Sci. C 264, 1356 (1967).
[3]J. M. Friedt and J. P. Adloff, C. R. Acad. Sci. C 268, 1342 (1969).
[4]G. K. Wertheim and D. N. E. Buchanan, Chem. Phys. Lett. 3, 87 (1969).
[5]H. Sano and M. Kanno, Chem. Commun. 1969, 601 (1969).
[6]Y. Llabador and J. M. Friedt, Chem. Phys. Lett. 8, 592 (1971).
[7]E. Baggio-Saitovitch, J. M. Friedt, and J. Danon, J. Chem. Phys. 56, 1269 (1972).
[8]H. N. Ok and J. G. Mullen, Phys. Rev. 168, 550 (1968).
[9]G. K. Wertheim, H. J. Guggenheim, and D. N. E. Buchanan, J. Chem. Phys. 51, 1931 (1969).
[10]A. Cruset and J. M. Friedt, Phys. Status Solidi B 44, 633 (1971).
[11]R. H. Herber, *The Mössbauer Effect*, Proc. Symp. Faraday Soc. No. 1 (Chemical Society, London, 1967), p. 19 and 101.
[12]M. Yaqub and C. Hohenemser, Phys. Rev. 127, 2028 (1962).
[13]F. Ambe, H. Shoji, S. Ambe, M. Takeda, and N. Saito, Chem. Phys. Lett. 14, 522 (1972).
[14]A. H. Muir Jr., K. J. Ando, and H. M. Coogan, *Mössbauer Effect Data Index* 1958-1965 (Interscience, New York, 1966), p. 26.
[15]N. N. Greenwood and T. C. Gibb, *Mössbauer Spectroscopy* (Chapman and Hall, London, 1971), p. 371.
[16]K. P. Mitrofanov, M. V. Plotnikova, and V. S. Shpinel, Zh. Eksp. Teor. Fiz. 48, 791 (1965) [Sov. Phys.–JETP 21, 524 (1965)].
[17]C. G. Davies and J. D. Donaldson, J. Chem. Soc. A 1968, 946 (1968).
[18]J. D. Donaldson and B. J. Senior, J. Inorg. Nucl. Chem. 31, 881 (1969).
[19]M. Cordey-Hayes, J. Inorg. Nucl. Chem. 26, 915 (1964).
[20]B. I. Boltaks, S. I. Bondarevskii, P. P. Seregin, and V. T. Shipatov, Fiz. Tverd. Tela 11, 1839 (1969) [Sov. Phys.–Solid State 11, 1483 (1970)].
[21]E. M. Baggio and T. Sonnino, J. Chem. Phys. 52, 3786 (1970).
[22]J. D. Donaldson and B. J. Senior, J. Chem. Soc. A 1966, 1796 (1966).
[23]A. Eucken and G. Gehlhoff, Verh. Dtsch. Phys. Ges. 14, 169 (1912).
[24]S. Ibuki and S. Yoshimatsu, J. Phys. Soc. Japan 10, 549 (1955).
[25]B. T. Kolomiets, V. M. Lyubin, and D. V. Tarkhin, Fiz. Tverd. Tela 1, 899 (1959) [Sov. Phys.–Solid State 1, 819 (1959)].
[26]F. Henz, Z. Anorg. Chem. 37, 18 (1903).
[27]I. A. Smirnov, A. A. Andreev, and V. A. Kutasov, Fiz. Tverd. Tela 10, 1782 (1968) [Sov. Phys.–Solid State 10, 1403 (1968)].
[28]S. Wexler, Actions Chim. Biol. Radiat. 8, 107 (1965).
[29]H. Frauenfelder, in *Annual Review of Nuclear Science*, edited by J. G. Beckerley (Annual Reviews, Stanford, 1953), Vol. 2, p. 129.
[30]W. Triftshäuser and D. Schroeer, Phys. Rev. 187, 491 (1969).
[31]W. Triftshäuser and P. P. Craig, Phys. Rev. 162, 274 (1967).
[32]F. Seitz, in *Solid State Physics*, edited by F. Seitz and D. Turnbull (Academic, New York, 1956), Vol. 2, p. 305.
[33]J. H. O. Varley, Nature 174, 886 (1954).
[34]D. H. Lindley and P. G. Debrunner, Phys. Rev. 146, 199 (1966).
[35]P. Hannaford and J. W. G. Wignall, Phys. Status Solidi 35, 809 (1969).
[36]S. L. Ruby, H. Montgomery, and C. W. Kimball, Phys. Rev. B 1, 2948 (1970).
[37]R. N. Kuzmin, S. V. Nikitina and O. Kherkner, Moscow Univ. Bull. 3 24, 11 (1969).
[38]N. Thrane and G. Trumpy, Phys. Rev. B 1, 153 (1970).
[39]V. I. Goldanskii, G. M. Gorodinskii, S. V. Karyagin, L. A. Korytko, L. M. Krizhanskii, E. F. Makarov, I. P. Suzdalev, and V. V. Krapov, Dokl. Akad. Nauk SSSR 147, 127 (1962).
[40]S. V. Karyagin, Dokl. Akad. Nauk SSSR 148, 1102 (1963).
[41]M. Blume, Phys. Rev. Lett. 14, 96 (1965).
[42]M. Blume and J. A. Tjon, Phys. Rev. 165, 446 (1968).
[43]S. Ambe, F. Ambe and N. Saito, Radiochim. Acta 19, 121 (1973).

Reprinted from J. Radioanal. Chem., 19, 109–128 (1974).

BEHAVIOUR OF LIGHT IMPURITY ELEMENTS IN THE PRODUCTION OF SEMICONDUCTOR SILICON

T. NOZAKI,* Y. YATSURUGI,** N. AKIYAMA,**
Y. ENDO,** Y. MAKIDE*

**Institute of Physical and Chemical Research, Wako-shi, Saitama (Japan)*
***Komatsu Electronic Metals Co., Hiratsuka (Japan)*

Par l'emploi de l'analyse par activation aux particules chargées on mesure la concentration du carbone, de l'azote et de l'oxygène dans différentes qualités de silicium pour semi-conducteur. On détermine les solubilités de ces trois éléments dans le silicium solide et liquide au point de fusion. On dessine les courbes d'étalonnage pour la spectrométrie à infra-rouges du carbone et de l'oxygène dans le silicium. On montre que l'utilisation simultanée de l'analyse par activation et de la spectrométrie est efficace pour l'étude de l'état de dispersion des quantités minimes de carbone et d'oxygène dans du silicium de grande pureté. On a aussi étudié, à l'aide d'une nouvelle technique des radiotraceurs, l'évaporation des impuretés légeres du silicium en fusion. Le comportement du carbone, de l'azote et de l'oxygène dans la production du silicium pour semi-conducteur, a donc été éclairci.

Introduction

Commercial semiconductor silicon is today the purest substance in the world, and is a good example for showing the influence of trace impurities on the physical properties of the matrix. Much effort has been made in the trace analysis of semiconductor silicon, and recommended techniques for the determination of each of the impurities have been described.[1] As for the light-element impurities such as carbon, nitrogen and oxygen, however, reliable analytical methods have not as yet been fully developed, and consequently sufficient information about their concentration and behaviour is not available, though they are abundant in nature and are usually regarded as the final impurities in an extreme purification of any substance.

We have studied the behaviour of light-element impurities in the production of semiconductor silicon, especially in single-crystal formation, by the following three methods: (1) charged-particle activation analysis (for C, N and O), (2) infrared spectrophotometry calibrated by charged-particle activation analysis (for C and O), and (3) a special tracer technique (for Be, C, N, F, Na and P). Charged-particle activation analysis has proved to be the only useful method or the most reliable method for the determination of ppb levels of the impurities. The simultaneous use of several available methods, however, has been shown to be essential for our purpose. Some qualitative knowledge concerning the concentrations and behaviour of impurity elements, which can be guessed from their

properties and from the sample history, has been found to be very helpful in the present study.

We originally aimed at the following, and have achieved most of them: (1) to establish convenient procedures for activation analysis and infrared spectrophotometry, (2) to know the concentrations of carbon, nitrogen and oxygen in semiconductor silicon of various origins, (3) to obtain the phase diagrams of C–Si, N–Si and O–Si systems for extremely low carbon, nitrogen and oxygen concentration ranges, (4) to develop methods for the measurement of the distribution state of the trace impurities, and finally (5) to get reliable knowledge on the behaviour of the impurities in the production and in the thermal annealing of single-crystals of semiconductor silicon in order to make a contribution to future improvements in the semiconductor industry. In the course of these studies, it was always taken into account that many of the principles, methods and techniques used should be adaptable to the study of other high-purity matrices in general, with slight modifications. We have already reported some parts of the present studies[2-6] and will publish other results in the near future.[7-10]

In this communication, the following two units are used for the impurity concentration: (1) ppm (wt. ppm) or ppb, and (2) atom/cm^3 (number of impurity atoms per cm^3 of the matrix). For carbon, nitrogen and oxygen in silicon, 1 ppm = $1.15 \cdot 10^{17}$, $0.99 \cdot 10^{17}$ and $0.87 \cdot 10^{17}$ atom/cm^3, respectively.

Sample preparation

Semiconductor silicons of various origins and specifications were collected as samples. Many of them were prepared by the trichlorosilane process, and some by the monosilane process. Elementary silicon in various stages of the monosilane process in Komatsu Electronic Metals Co. was also taken to be analyzed.

Crude silicon used in both processes is produced by the reduction of SiO_2 with carbon (coke) at a temperature considerably higher than the melting point of silicon. It is thus natural that the crude silicon contains an appreciable amount of carbon. This silicon is converted either into trichlorosilane ($SiHCl_3$) or into monosilane (SiH_4), which is purified by fractional distillation and then decomposed into polycrystals of semiconductor-grade silicon. From the properties of carbon-hydrogen, carbon-chlorine or carbon-chlorine-hydrogen compounds, carbon in crude silicon can be suspected not to be removed easily in either of the processes. The monosilane process can be regarded as giving a purer product that the trichlorosilane process, because the number of volatile metal hydrides is less than the number of volatile metal chlorides. For nitrogen, however, the product of the monosilane process should be considered more seriously, because the SiH_4 is generated by the reaction of NH_4Cl on Mg_2Si in liquid ammonia.

The polycrystalline silicon is then made single-crystalline by float-zone melting or by

Czochralski's method. The float-zone melting is usually carried out in argon, but sometimes in vacuum. In Czochralski's process, the silicon is fused in a silica crucible heated with a graphite resistor, and a single-crystalline silicon rod is pulled up from the melt. The single-crystal is then sliced, polished, and often doped with some substance at an elevated temperature to give an elemental unit of a semiconductor device of desired electronic properties.

Commercial semiconductor silicon does not usually contain enough carbon, nitrogen or oxygen for the reliable measurement of their solubilities and equilibrium distribution coefficients. The following techniques were used for doping with (1) carbon, (2) nitrogen and (3) oxygen.

(1) Various quantities of carbon in aqueous suspension (Aquadag) were painted uniformly on silicon rods, and molten zones were passed through them. Then, in several parts of one of the resultant rods, molten zones were passed with various travelling velocities to give a sample from which distribution coefficient measurements were made. All the zone meltings were carried out in vacuum, and the sample was not exposed to air in the intervals between the zone meltings. In addition, Czochralski crystals were pulled from pyrolytic graphite crucible.

(2) A silicon rod was cut into two hemi-cylinders, and a sufficient quantity of Si_3N_4 powder was sandwiched between them. Molten zones were then passed in several parts of the sandwich, in argon containing nitrogen, with various travelling velocities. Additionally, pure silicon and Si_3N_4 in an evacuated quartz ampoule were kept just above the melting point of silicon, and then cooled suddenly to give granular silicon as the sample for the measurement of nitrogen solubility in liquid silicon.

(3) The results of KAISER and BRESLIN concerning oxygen doping[1] were used. In an atmosphere of argon containing about 10 torr of oxygen, molten zones were passed in several parts of a silicon rod with various travelling velocities. This gave the sample for the measurement of the solid solubility of oxygen in silicon. Molten zones saturated with oxygen were also cooled suddenly for the measurement of the solubility in liquid silicon.

Silicon samples containing appreciable amounts of carbon or oxygen were heat-treated over 1100 °C for the examination of the change in the dispersion state of the impurities.

Further, ^{11}C-containing silicon was prepared by two methods: (1) the proton-bombardment of boron-doped silicon, and (2) the fusion of pure silicon in an atmosphere containing ^{11}CO obtained by the proton-bombardment of B_2O_3 in a helium stream. In the latter method, the ^{11}C can be either entirely dissolved substitutionally or partly coagulated as SiC by the control of the quantity of non-radioactive carbon carrier.

Charged-particle activation analysis

We reported on the method of charged-particle activation analysis in the last Modern Trends of Activation Analysis (N. B. S., U. S. A., 1968), and also described it in Ref.[2] Since 1968, the technique has been improved only slightly, but the precision and accu-

racy have been examined more closely, and many more samples have been analyzed (slightly over 200 samples for carbon, about 200 samples for oxygen, and about 60 samples for nitrogen). In this communication, the analytical method is described briefly, the precision and accuracy are discussed, and the analytical results are shown.

Table 1

Activation reactions

Element	Carbon	Nitrogen	Oxygen
Reaction adopted	$^{12}C(^{3}He,\alpha)^{11}C$	$^{14}N(p,\alpha)^{11}C$	$^{16}O(^{3}He,p)^{18}F$ $^{16}O(^{3}He,n)^{18}Ne \rightarrow {}^{18}F$
Interference reactions	$^{9}Be(^{3}He,n)^{11}C$ [Exoth.]	$^{11}B(p,n)^{11}C$ [3.1]	$^{19}F(^{3}He,\alpha)^{18}F$ [Exoth.]
	^{10}B $(^{3}He,d)^{11}C$ [Exoth.]	$^{12}C(p,d)^{11}C$ [18.0]	$^{20}Ne(^{3}He,\alpha p)^{18}F$ [3.1]
	^{14}N $(^{3}He,\alpha d)^{11}C$ [10.2]		$^{20}Ne(^{3}He,\alpha n)^{18}Ne \rightarrow {}^{18}F$ [9.1]
	^{16}O $(^{3}He,2\alpha)^{11}C$ [6.3]		$^{23}Na(^{3}He,2\alpha)^{18}F$ [0.4]
	^{28}Si $(^{3}He,^{20}Ne)^{11}C$ [11.3]		^{27}Al $(^{3}He,3\alpha)^{18}F$ [11.6]
			^{29}Si $(^{3}He,^{14}N)^{18}F$ [11.8]
			^{30}Si $(^{3}He,^{15}N)^{18}F$ [11.5]
Selected energy of bombardment	15 MeV	12 MeV	15 MeV

Note: The figures in square brackets indicate the threshold energy in MeV.

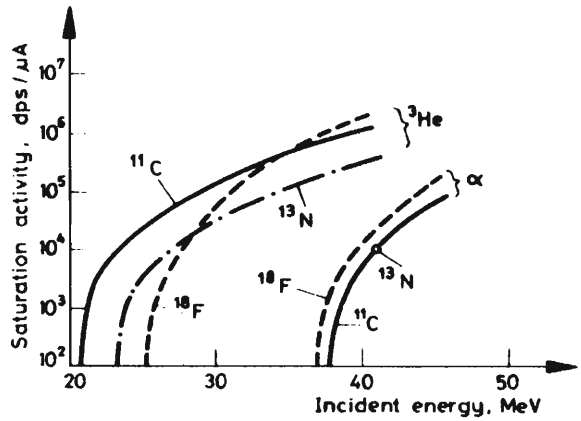

Fig. 1. Thick-target saturation activities for ^{3}He and α-particle reactions on silicon

Method of the analysis

Table 1 shows the nuclear reactions employed in our analyses, and the possible interference reactions with their threshold energies. The Table also gives convenient incident particle energies, which were selected in view of the excitation curves of the adopted reactions, the ranges of the charged particles, and some information about the interference reactions. Fig. 1 shows the thick-target yields for the formation of ^{11}C, ^{13}N and ^{18}F from the matrix silicon itself. These reactions give rise to the most serious interference, when the selection of the incident particle energy is inconvenient. More detailed discussions about the interferences are given in Ref.[2]

The sample disks were bombarded (1–8 μA, usually for 20 min) in a beam duct of the 160-cm variable-energy cyclotron of the Institute of Physical and Chemical Research, behind an aluminium foil, which prevented additional surface contaminations by ^{11}C and ^{18}F formed from residual gases in the cyclotron. The beam current was measured with a current recorder and a current integrator. The surface of the sample (20–25 μm in thickness) was then removed by etching with HF–HNO_3. As activation standards for carbon, nitrogen and oxygen, disks of graphite, nylon and silica were used. They were covered with aluminium foils having thicknesses equivalent to the sample surface to be removed by the etching, and bombarded with lower fluxes and for shorter durations (0.1–0.3 μA, 10–50 sec).

^{11}C in the bombarded sample was separated by the following technique. Two polyethylene bottles were connected to make a closed system. In one of them a solution of NaOH, $KMnO_4$ and carrier Na_2CO_3 was placed, and in the other the sample was decomposed with a mixture of HF, HNO_3 and KIO_4. When the sample was dissolved, the alkaline solution was caused to flow into the acid solution to give an alkaline mixture, which was then treated with H_2SO_4 for the evolution of $^{11}CO_2$. This was converted into $BaCO_3$ precipitate for the activity measurement. The carrier recovery was determined by acid-alkali titration.

^{18}F in the sample was sometimes measured non-destructively but usually after chemical separation. The sample was powdered and dissolved in a NaOH solution containing carrier NaF. $HClO_4$ was added to the solution, and the fluorine was distilled and converted into PbFCl precipitate for the activity measurement. For the carrier recovery measurement,the PbFCl was dissolved in HNO_3, and the chlorine was titrated with a standard $Hg(NO_3)_2$ solution.

The separated ^{11}C and ^{18}F had such high radiochemical purities that their activities were measured satisfactorily with a simple scintillation counter.

Sensitivity, precision and accuracy

As low as a few ppb of carbon and oxygen, and slightly less than 1 ppb of nitrogen can be determined by the present method. The lowest concentration ever found has been 10±6 ppb for carbon, 4±6 ppb for oxygen, and 1.0±0.4 ppb for nitrogen, where the figures after the sign ± are the counting standard errors.

In order to estimate the precision in the carbon analysis, two silicon rods containing uniformly different concentrations of carbon were analyzed. The results for each five runs were 62 ppb and 2.28 ppm, with relative standard deviations of 15% and 4%, respectively. Oxygen was found to be determined with the same or slightly better precision as carbon.

In the examination of the accuracy in the activation analysis, possible errors in the chemical separation and in the charged-particle beam measurement should be considered. The chemical process for ^{11}C was checked by the use of the ^{11}C-containing silicon. After the chemical treatment of 15 samples, it was found that the carbon content obtained by our method should be corrected by a factor of 1.03. By the measurement of ^{18}F activity formed in samples of high oxygen contents, first non-destructively and then after the chemical separation, it was shown that our results of the separation-involving method for oxygen should be corrected by a factor of 1.19 ± 0.03. This correction is due to (1) the loss of the sample in the pulverization, (2) the coprecipitation of some $PbCl_2$ with the PbFCl, and (3) the self-absorption of the annihilation radiation in the PbFCl. The second can be regarded as the main cause. In ordinary chemical analysis for fluorine involving the precipitation of PbFCl, the coprecipitation of $PbCl_2$ seems to counterbalance the incompleteness of the precipitation of fluorine.

The accuracy of the charged-particle beam measurement (beam integrator reading) cannot be estimated easily. The error in it, however, is not regarded as serious, because only the ratio of the integrator reading for the sample to that for the activation standard is needed and because well-reproducible results were obtained for bombardments under different beam intensities and in different cyclotron machine times.

Oxygen was also analyzed by the $^{16}O(\alpha,pn)^{18}F$ reaction for the ascertainment of the ^3He analysis. It was found that when the following are fulfilled in the α-particle analysis, good agreement is shown in the results of the two analyses: (1) the incident particle energy is not over 35 MeV, (2) the original sample surface is not rough, and (3) at least 25 μm of the surface is removed uniformly.

Concentrations of carbon, nitrogen and oxygen in semiconductor silicon

Table 2 shows the carbon and oxygen contents of various kinds of commercial semiconductor silicon produced by modern industrial techniques. In general, the carbon and oxygen contents of single-crystal silicon appear to depend more significantly on the conditions in the single-crystal formation than on the chemical purification method. The

Table 2

Carbon and oxygen contents of commercial semiconductor silicon

	Carbon content, 10^{17} atom/cm^3	Oxygen content, 10^{17} atom/cm^3
Polycrystal	0.20 ~ 0.50 [0.82]*	0.80 ~ 3.0 [0.04]*
Single-crystal		
FZ in argon	0.080 ~ 0.35	0.05 ~ 0.20
FZ in vacuum	0.030 ~ 0.40	0.010 ~ 0.030
CZ in argon	0.30 ~ 3.0	2.0 ~ 10
Dislocation-frree FZ	0.40, 0.13, 0.016, 0.30	0.013, 0.019, 0.026, 0.10

* The figures in brackets are exceptional values.

Table 3

Change of carbon content in an industrial process

	Carbon content, 10^{17} atom/cm^3	Oxygen content, 10^{17} atom/cm^3
Crude	>40	10
Polycrystal	0.20 ~0.25	0.80 ~ 0.85
FZ in argon*		
(Single pass)	0.15	0.06
FZ in vacuum*		
Single pass	0.03	0.03
Three passes	0.02	0.015
CZ in argon*	1.0	4

*Middle portion of the rod.

carbon and oxygen contents of dislocation-free samples show no obvious difference from ordinary float-zone silicon. The high carbon and oxygen contents of the Czochralski crystals can be explained as contaminations from the graphite heating devices and silica crucible used in the process.

Table 3 shows the change of the carbon and oxygen contents in the course of the production of single-crystal silicon. The polycrystalline silicon as the raw material for all

the single-crystals was produced by the monosilane process in Komatsu Electronic Metals Co., and its carbon and oxygen contents were very uniform and constant.

Single-crystals with the lowest carbon and oxygen contents were obtained by float-zone melting in vacuum. After multiple zone passes, the concentrations were found to be reduced, attaining values which seem to be determined by several conditions in the process. For example, in order to reduce the carbon content below about $5 \cdot 10^{15}$ atom/cm^3, special care should be taken to prevent the back-diffusion of vacuum-pump oil. Silicon crystals after float-zone melting in argon were found to contain varying quantities of carbon and oxygen, although the concentrations were always lower than the polycrystal content. The purity of the argon is probably the critical factor in determining the impurity content.

The nitrogen content of commercial silicon single-crystals was always found to be less than $1 \cdot 10^{15}$ atom/cm^3 and usually in the range of $1-5 \cdot 10^{14}$ atom/cm^3, regardless of the method of chemical purification of the silicon.

Solubility and equilibrium distribution coefficient

Carbon

When molten zones were passed through the carbon-covered silicon rods, silicon carbide powder appeared on the surface of the melts; the larger the quantity of the carbon, the sooner the appearance of the particles. The resultant carbon distribution in one of the samples is shown in Fig. 2. The carbon concentration just prior to the appearance of silicon carbide was always found to be $(3.5 \pm 0.4) \cdot 10^{17}$ atom/cm^3, regardless of the quantity of carbon painted on the rod. This is explained clearly by the phase rule. When three condensed phases, e. g. solid silicon, liquid silicon and silicon carbide, coexist in equilibrium in a

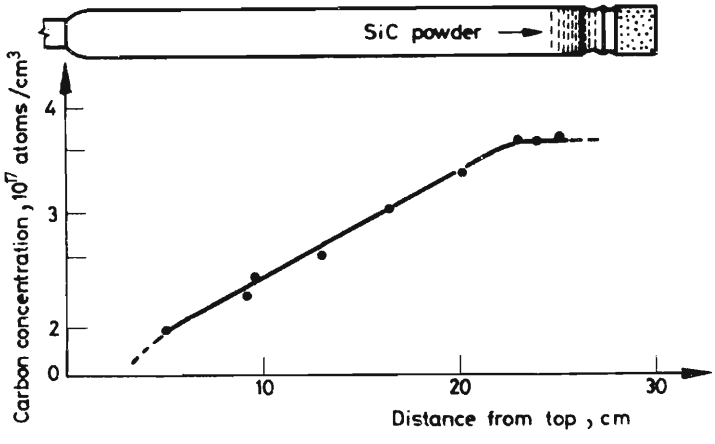

Fig. 2. Carbon distribution after a single zone pass through a carbon-painted silicon rod

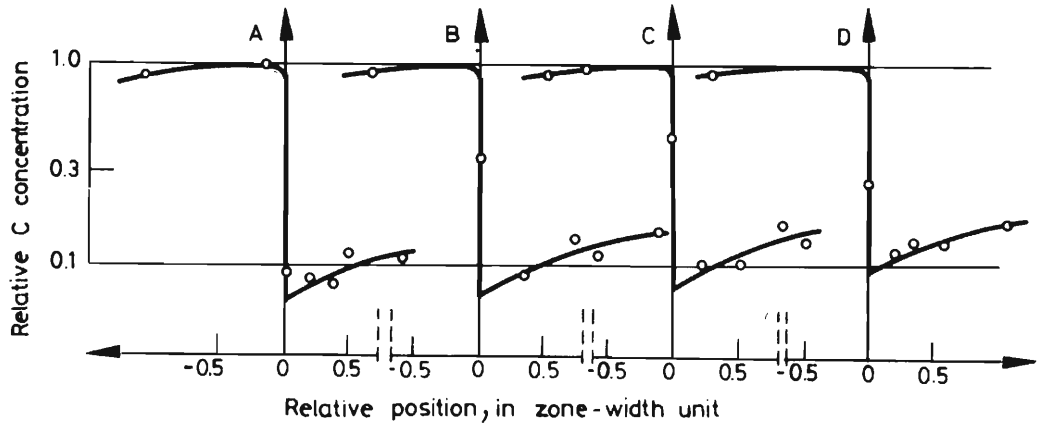

Fig. 3. Carbon distribution for various zone velocities. Zone travelling velocity: A–0.4 mm/min; B–0.8 mm/min; C–1.2 mm/min; D–1.6 mm/min

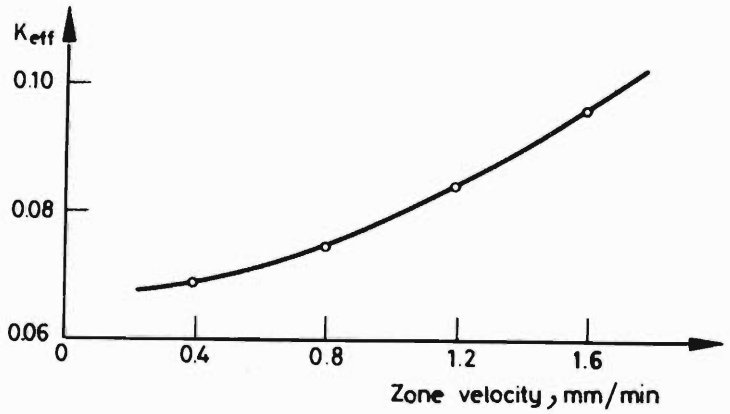

Fig.4. K_{eff} vs. zone velocity

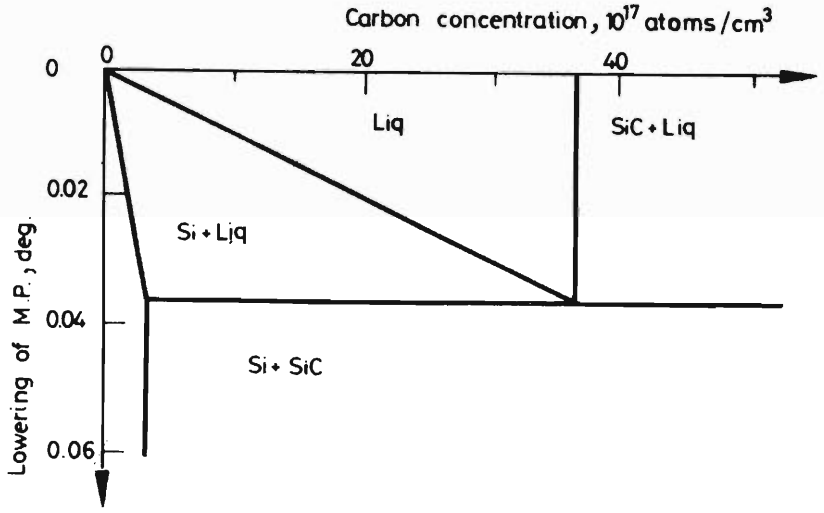

Fig. 5. Phase diagram of C–Si system at extremely low carbon concentrations

two-component system, e. g. silicon and carbon, the compositon of each phase should be uniquely determined. Therefore, $(3.5 \pm 0.4) \cdot 10^{17}$ atom/cm^3 is the observed value for the solubility of carbon in solid silicon at its melting point. Approximately the same carbon content was also exhibited by Czochralski crystals from a graphite crucible.

The equilibrium distribution coefficient of carbon between solid and liquid silicon was obtained by the following method. Fig. 3 shows the carbon distribution after single zone passes with various velocities. From these distributions, the effective distribution coefficients (denoted as K_{eff} in Fig. 4 are obtained in relation to the zone velocities, as shown in Fig. 4. By extrapolating the curve in Fig. 4 to zero velocity, the equilibrium distribution coefficient is obtained as 0.07 ± 0.01.

From the above information, the phase diagram of the C–Si system in the extremely low carbon concentration range can be drawn (see Fig. 5). The lowering of the melting point was calculated via the formula: $T = RT_m^2 X/\Delta H$, where R is the gas constant, T_m is the melting point of silicon, X is the mole fraction of the impurity, and ΔH is the molar heat of fusion of silicon.

Nitrogen

For the sample prepared by the zone melting of the Si_3N_4-inserted silicon rod, the nitrogen concentration was found to be almost constant thoughout its entire portion except the tail end. As is obvious from the preparation method, the molten zone was always saturated with nitrogen. The solid silicon after the zone melting, however, could contain a higher concentration of nitrogen than its solubility in solid silicon at the melting point, because the solid-liquid boundary might be dendritic and thus the growing solid phase would capture a small fraction of the liquid phase. In fact, the nitrogen concentration was found to depend on the zone-travelling velocity, as shown in Fig. 6. The solid solubility at the melting point, therefore, would be given as the nitrogen concentration for an infinitely low zone velocity. This can be obtained as about $(4.5 \pm 1.0) \cdot 10^{15}$ atom/cm^3

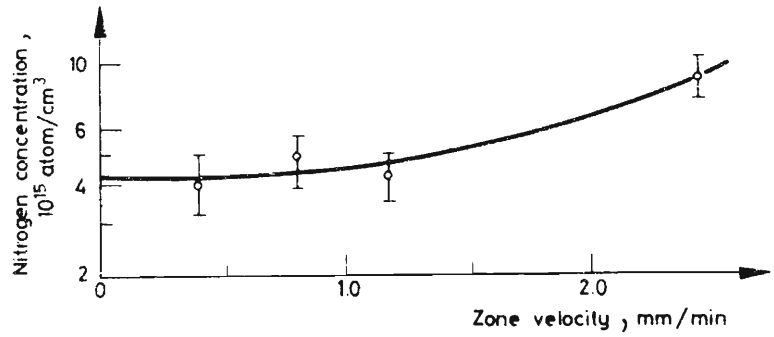

Fig. 6. Nitrogen concentration after single zone passes through a Si_3N_4-inserted silicon rod with various travelling velocities

by the extrapolation of the curve in Fig. 6 to zero velocity. The nitrogen solubility in liquid silicon at the melting point was found to be about $6 \cdot 10^{18}$ atom/cm^3 by the use of the suddenly solidified samples. The equilibrium distribution coefficient, therefore, which is the ratio of the solubility in solid silicon to that in liquid silicon, was determined as about $7 \cdot 10^{-4}$.

Oxygen

By similar methods as used in nitrogen, the solubilities of oxygen in solid silicon and liquid silicon were obtained as $(3.1 \pm 0.5) \cdot 10^{18}$ atom/cm^3 and $(2.2 \pm 0.3) \cdot 10^{18}$ atom/cm^3, respectively, at the melting point. The equilibrium distribution coefficient is thus 1.4 ± 0.3. Hence, oxygen in silicon is an inverse impurity (an impurity which is segregated towards the top in zone melting) and its phase diagram is of a different type from that of the C–Si system.

Table 4 summarizes the determined solubilities and equilibrium distribution coefficients.

Table 4

Solubilities (10^{17} atom/cm^3) at the melting point of silicon and equilibrium distribution coefficients

Element		C	N	O
Solubility	in solid Si	3	0.045	31
	in liquid Si	40	60	22
Equilibrium distribution coefficient		0.07 ± 0.01	$7 \cdot 10^{-4}$	1.4 ± 0.3

Infrared spectrophotometry

Although charged-particle activation analysis is indispensable for the study of light element impurities in ultra-pure substances, it is quite limited in accessibility. For the determination of carbon and oxygen in semiconductor silicon and germanium, infrared absorptiometry is also useful. Infrared spectrophotometry is non-destructive, and is much simpler, much more easily accessible and usually more precise than activation analysis.

Th is method, further, is convenient for the fine distribution measurement of the two elements. Activation analysis is less suitable for this purpose, because bombardment by a fine charged-particle beam with a high total flux often damages the sample by heat evolution within its limited part. Infrared spectrophotometry, however, can be applied only to single-crystal samples which show no birefringence and are free from any notable amount of electrically-active impurities.

For quantitative spectrophotometric determination, a calibration curve is needed. The curve now used for carbon in semiconductor silicon was suggested by NEWMAN and WILLIS[12] who used ^{14}C-doped crystals to know the carbon concentration. The curve for oxygen which has been adopted in the ASTM manual was originally constructed by KAISER and KECK by the use of vacuum fusion.[13] We used various silicon crystals already analyzed for carbon and oxygen by charged-particle activation in order to obtain more reliable calibration curves.

After close examination of the measurement conditions in the spectrophotometry, the transmittance was measured at 602 cm^{-1} and 1108 cm^{-1} for the determination of carbon and oxygen, respectively, at room temperature. As the reference of the spectrophotometry, extremely pure silicon was used, which was known by activation to contain 20 ± 10 ppb of carbon and 10 ± 6 ppb of oxygen.

Fig. 7 shows our calibration curve together with the earlier curve. The former gives carbon concentrations lower by a factor of about 0.7 than does the latter. This can be explained as follows: as NEWMAN and WILLIS themselves noted, their crystals contained such amounts of oxygen as to give an infrared absorption band due to C–O bonding, and

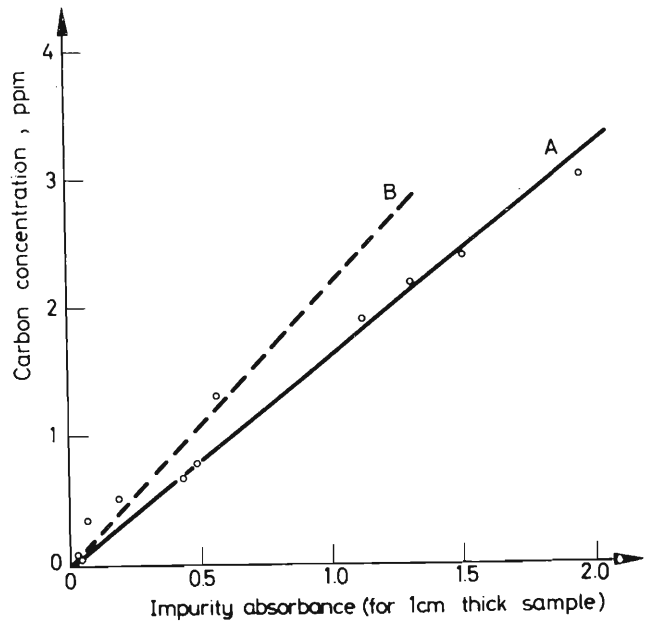

Fig. 7. Calibration curve for the infrared spectrophotometry of carbon in silicon. Curve A–present calibration curve;Curve B–calibration curve by NEWMAN and WILLIS

thus part of the carbon did not take part in the absorption at the measurement wavenumber.

Care should be taken regarding the fact that the present spectrophotometry is sensitive only to the substitutionally dissolved carbon. When the carbon concentration is over the solubility in solid silicon at the melting point, SiC precipitates may be included in the sample. An increase in the transmittance was observed when samples containing a few ppm of carbon were kept over 1200 °C for many days, without any notable decrease of the total carbon concentrations determined by activation. Further, as is seen in Fig. 7, some samples with low carbon contents gave experimental plots lying above the straight line of the calibration curve. Infrared spectrophotometry, therefore, may not give a reliable value for the carbon content when this is under 0.5 ppm. The nature of this infrared-insensitive carbon has not yet been made clear.

Fig. 8 shows our calibration curve for oxygen in its low concentration range, together with the curve in the ASTM manual. Since no reference silicon is used in the ASTM method, its calibration curve does not pass through the origin. The two curves in Fig. 8, however, are almost parallel and give almost the same oxygen concentration. The surface oxygen has proved to be insensitive to the present spectrophotometry.

For the higher oxygen concentration range, most of the observed plots have been found to be located over the straight line of our calibration curve in Fig. 8. This suggests the presence of oxygen insensitive to the present spectrophotometry when the total oxygen concentration is higher than several ppm. Oxygen in such concentrations in silicon is known to associate fairly rapidly at elevated temperatures. In practical processes of single-crystal formation, the crystal is not cooled rapidly after being solidified, and thus oxygen in it can associate to some extent.

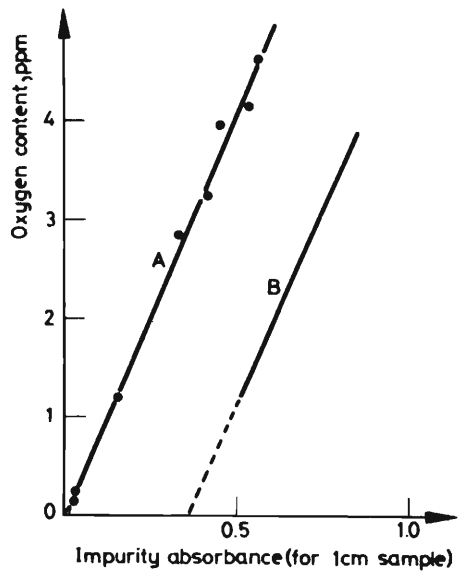

Fig. 8. Calibration curve for the infrared spectrophotometry of oxygen in silicon. Curve A—present calibration curve;, Curve B—calibration curve in the ASTM manual

The detection limit of the spectrophotometry at room temperature reaches down to 50 ppb for carbon and 30 ppb for oxygen in the infrared-sensitive states, provided that sufficiently pure silicon already analyzed by activation is used as the reference. For a 500 ppb level, the relative error can be regarded as about 10% for both carbon and oxygen.

Dispersion state of the impurity

By the use of the ^{11}C-containing silicon, the chemical behaviour of carbon in the dissolution and the fusion of the matrix was examined. The results are shown in Figs 9 and 10. It is obvious from Fig. 9 that the substitutional carbon is oxidized almost quantitatively either by dissolution in $HF-HNO_3-KIO_4$ and succeeding $KMnO_4$ treatment, or by fusion

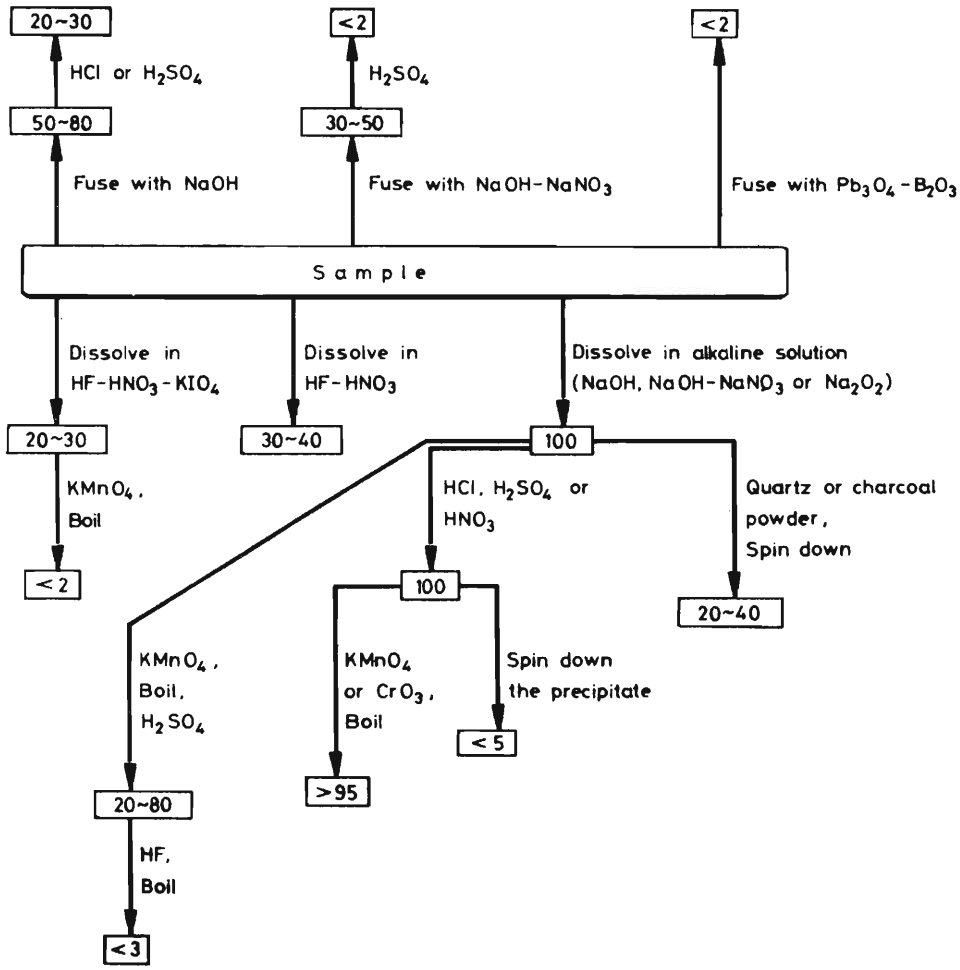

Fig. 9. Behaviour of substitutionally dissolved carbon in the dissolution and the fusion of matrix silicon. Fraction of the ^{11}C remaining in the reaction mixture, %.

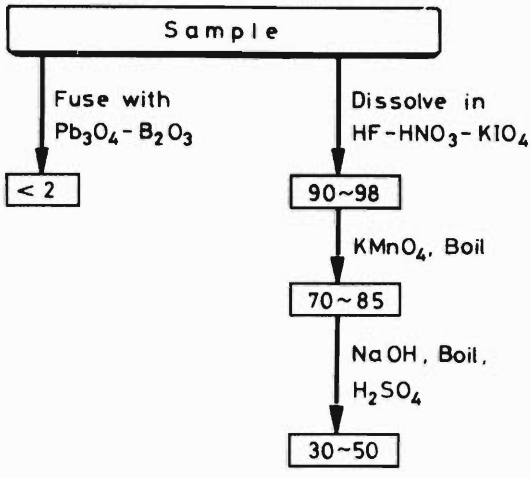

Fig. 10. Behaviour of coagulated carbon in the dissolution and the fusion of matrix silicon. Fraction of the ^{11}C remaining in the reaction mixture, %.

Table 5

Sensitivities of the three methods to the different physical states of carbon

Method		Homogeneously dispersed carbon	Coagulated carbon
Activation analysis	$Pb_3O_4 - B_2O_3$ fusion	+	+
	$HF-HNO_3-KIO_4-KMnO_4$ dissolution	+	±
Infrared spectrophotometry		+	—

with $Pb_3O_4 - B_2O_3$. Hence, these can be used for the separation of ^{11}C in the activation analysis of carbon. For the coagulated carbon, however, the two methods give different information, as is obvious from Fig. 10.

Table 5 shows the three methods useful for the determination of carbon in silicon. The fraction of the coagulated carbon sensitive to the second method of Table 5 depends on the state of the coagulates, namely their grain size and the perfectness of their crystal structure. By the use of the three methods or two of them, therefore, it is possible to get information about the physical state of carbon in silicon, though high accuracy is often needed in the determinations. Table 6 shows some results of the three methods.

Table 6

Results of carbon analysis by the three methods (ppm)

Sample	Activation with Pb_3O_4-B_2O_3 fusion	Activation with HF-HNO_3-KIO_4 dissolution	Infrared spectrophotometry
A) Crude silicon	36	18	
B) Crude silicon	140	100	
C) As-grown single-crystal		7.0 ± 0.8	6.8
D) After heat--treatment of C	6.8	6.3 ± 0.8	2.3
E) As-grown single-crystal		2.8 ± 0.3	2.8
F) After heat--treatment of E		2.7 ± 0.3	1.3

Special tracer technique

As is obvious from Fig. 1, the bombardment of silicon by ^{3}He particles with an energy over 40 MeV gives fairly high activities of ^{11}C, ^{13}N and ^{18}F from the matrix silicon itself. ^{7}Be, ^{22}Na, ^{24}Na and ^{32}P have also been found to form simultaneously. The radionuclides thus formed in silicon are especially useful for the study of the evaporation of light impurity elements from a silicon melt. The bombarded silicon sample placed in a quartz plate or on a semiconductor silicon rod was fused by radio-frequency heating in vacuum or in a helium stream, and the resultant distribution of the radiotracers was measured.

The results can be summarized as follows: (1) the ease of the escape of the impurity elements decreased in the order: $F \geqslant N \geqslant Na > P \geqslant Be \gg C$; (2) only ^{11}C was found in the evolved gas, no $^{13}N_2$ was detected; and (3) the sublimate deposited on the vessel wall near the melt contained a considerable proportion of ^{11}C and nearly all of the other elements which had escaped from the melt. After fusion for 3 min, the ^{18}F disappeared almost quantitatively from the sample and less than 10% of the ^{22}Na and ^{24}Na remained. Under the same conditions, about 60% of the ^{32}P and 70% of the ^{7}Be remained.

For carbon, the chemical form of the evolved ^{11}C and the rate of the evolution into the helium stream were also examined. The results show: (4) a part of the ^{11}C escaped almost instantaneously when the sample was fused; (5) in fusion on a semiconductor silicon rod, no further escape was observed, while in fusion in a quartz dish the escape continued until most of the ^{11}C disappeared from the melt; (6) in vacuum almost no gaseous ^{11}C activity

was found but the sublimate contained a notable ^{11}C activity, while in helium a large proportion of the ^{11}C evolved was detected as ^{11}CO; and (7) no marked differences due to the original bulk contents of carbon and oxygen were observed when samples containing up to 3 ppm of carbon or 6 ppm of oxygen were used.

Fig. 11 shows the continuous evolution of the gaseous ^{11}C activity into a helium stream; the silicon sample containing about 50 ppb of both carbon and oxygen was fused on semiconductor silicon, and after a few minutes the melt was brought into contact with a quartz tube wall. The reaction of a ppb level of carbon with a trace quantity of oxygen is obvious. It is thus clear that carbon can escape only as CO from molten semiconductor silicon. The instantaneous escape of part of the ^{11}C can be attributed to the surface oxygen.

This special tracer technique, which is characterized by the tracer-incorporation method, can be applied to other matrices, such as high-purity aluminium. This technique has enabled us to trace as low as 10^{-11} g of carbon. The results described above offer some information valuable in guessing the concentration of interference elements in practical samples of activation analysis for light elements.

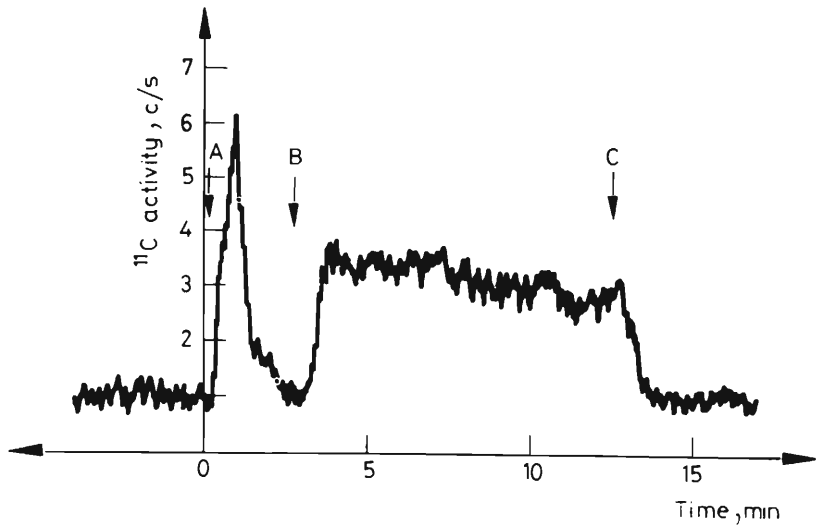

Fig. 11. Evolution of gaseous ^{11}C from a silicon melt. A – melting of the silicon sample; B – contact of the melt with quartz; C – solidification of the melt

Behaviour of carbon, nitrogen and oxygen

The behaviour of carbon, nitrogen and oxygen in the production of semiconductor silicon has been made fairly clear by our results.

A considerable amount of carbon is present in crude silicon, but most of it is removed in the chemical purification process. In the single-crystal formation by zone melting, car-

bon is segregated with an equilibrium distribution coefficient of 0.07 ± 0.01. In the Czochralski process carbon is often incorporated into the melt from the atmosphere, which contains some CO formed on the surface of the graphite heating device. Carbon does not evaporate from a silicon melt when all oxygen sources are absent.

Carbon with a concentration higher than $3 \cdot 10^{17}$ atom/cm^3, which is almost the solid solubility at the melting point, is often coagulated as SiC. In the solidification of the eutectic C–Si mixture,however, it is quite natural for carbon to behave differently from the one component of an ordinary binary alloy due to the following phenomena: (1) silicon carbide will not usually precipitate immediately when the liquid phase has become supersaturated; and (2) silicon carbide appearing on the solid-liquid boundary can be removed to the liquid-gas surface, leaving only the solid silicon rather than the solid eutectic mixture.

According to whether the removal of the silicon carbide and the supersaturation of the liquid phase take place or not, varying types of resultant carbon distribution are possible after a single zone pass of a silicon rod with a relatively high original carbon content. This is shown in Fig. 12. The original carbon content is about $15 \cdot 10^{17}$ atom/cm^3, and the liquid phase has become saturated at Location B. The carbon levels at C, I and D should be equal to the original carbon content. In practice, distributions corresponding to the partial removal of the silicon carbide probably occur more frequently than those in Fig. 12. From these considerations, carbon contents of silicon single-crystals exceeding the solubility at the melting point can be explained. Such high carbon concentrations were sometimes found in old silicon crystals, but rarely in modern products.

Nitrogen evaporates readily from molten silicon, and is highly segregated with an equilibrium distribution coefficient of about $7 \cdot 10^{-4}$. The nitrogen content of semiconductor

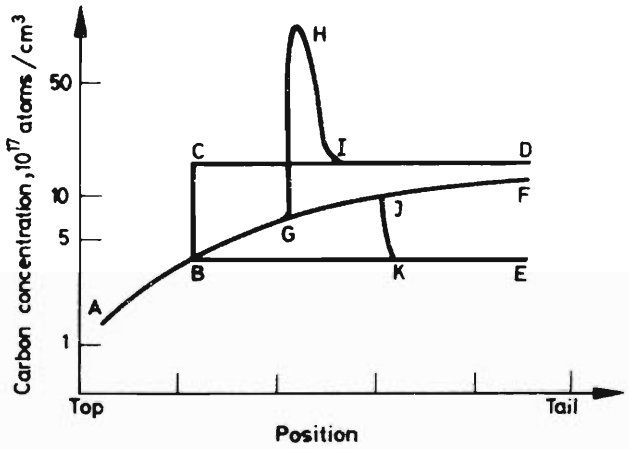

Fig. 12. Various possible carbon distributions after a single zone pass. ABCID, no supersaturation of the liquid phase and no removal of the silicon carbide; ABKE, no supersaturation but complete removal; ABGJF, supersaturation throughout; ABGHID, supersaturation up to G and then no removal; ABGJKE,, supersaturation up to J and then complete removal

silicon is, in fact, always very low. From the measurement of the electrical properties of nitrogen-doped silicon, nitrogen was found not to be ionized. Hence, no special care is usually required for nitrogen in the production of semiconductor silicon.

Oxygen is not removed by segregation because its equilibrium distribution coefficient is slightly larger than unity, but it easily evaporates from a silicon melt as SiO. It can be incorporated into a silicon melt from an atmosphere containing O_2 or CO. In the Czochralski process, oxygen enters the melt from the silica crucible. Oxygen in solid silicon is often in associated states, when its total concentration is over several ppm. The association proceeds fairly rapidly at temperatures near the melting point.

Semiconductor silicon containing less than 20 ppb of carbon and 10 ppb of oxygen can be obtained by the following process: (1) a single zone pass of a semiconductor silicon rod loaded with a small quantity of high-purity SiO_2, and (2) a few zone passes of the resultant silicon rod in a vacuum carefully made free from any carbon source. The study of the equilibrium and kinetics between carbon and oxygen in a silicon melt with CO in the ambient atmosphere is now under way.

Future study

We intend to begin the following studies in the near future: (1) effect of carbon and oxygen on th properties of semiconductor silicon, and (2) charged-particle activation analysis for surface impurities of semiconductor silicon.

*

The authors would like to express their thanks to the Cyclotron Group of the Institute of Physical and Chemical Research for their bombardment services, and to members of the Komatsu Electronic Metals Co. for their aid in the sample preparation and in the analytical practice.

References

1. E.g., J.P. CALI, Trace Analysis of Semiconductor Materials. Pergamon, Oxford, 1964.
2. T. NOZAKI, Y. YATSURUGI, N. AKIYAMA, J. Radioanal. Chem., 4 (1970) 87.
3. T. NOZAKI, Y. YATSURUGI, N. AKIYAMA, J. Electrochem. Soc., 117 (1970) 117.
4. T. NOZAKI, Y. MAKIDE, Y. YATSURUGI, N. AKIYAMA, Y. ENDO, Int J. Appl. Radiat. Isotopes, 22 (1971) 607.
5. T. NOZAKI, Y. MAKIDE, Y. YATSURUGI, Y. ENDO, N. AKIYAMA, Bull. Chem. Soc. Japan, in the press.
6. Y. ENDO, Y. YATSURUGI, N. AKIYAMA, T. NOZAKI, submitted to Anal. Chem.

7. Y. YATSURUGI, Y. ENDO, N. AKIYAMA, T. NOZAKI, to be published.
8. Y. YATSURUGI, N. AKIYAMA, Y. ENDO, T. NOZAKI, to be published.
9. N. AKIYAMA, Y. YATSURUGI, Y. ENDO, T. NOZAKI, to be published.
10. T. NOZAKI, Y. YATSURUGI, N. AKIYAMA, Y. ENDO, to be published.
11. W. KAISER, J. BRESLIN, J. Appl. Phys., 29. (1958) 1292.
12. R. C. NEWMAN, J. B. WILLIS, J. Phys. Chem. Solids, 26 (1965) 373.
13. W. KAISER, P. H. KECK, J. Appl. Phys., 28 (1957) 882.

Reprinted from J. Radiat. Res., 16, 99–112 (1975).

Inactivation of Bacterial Cells by Cyclotron Beam

YATAGAI, F.,*,** TAKAHASHI, T.** and MATSUYAMA, A.**

*Department of Applied Physics, School of Science and Engineering, Waseda University, Tokyo, Japan

**The Institute of Physical and Chemical Research, Saitama-ken 351, Japan

(Received December 9, 1974; Revised version received January 31, 1975)

B. subtilis spores, *E. coli* B_{s-1} and *E. coli* B/r were bombarded with α-particles and heavy ions of carbon, nitrogen and oxygen accelerated in the IPCR Cyclotron. The RBE versus LET_∞ curve for *B. subtilis* spores showed a maximum peak at ~120 keV/μm, while those for *E. coli* B_{s-1} and *E. coli* B/r declined without any maximum as LET_∞ values increased. In the region of α-particles, the effective inactivation cross section (S_{eff}) for these three strains increased with increasing LET_∞, and the rates of increase in S_{eff} in the LET region from ~30 to ~150 keV/μm were 15.0, 1.5 and 2.5 times for *B. subtilis* spores, *E. coli* B_{s-1} and *E. coli* B/r, respectively. In the case of *B. subtilis* spores, S_{eff} values for heavy ions were almost independent of their energies, but the other two strains showed a considerable dependence upon beam energy. The charcteristic LET dependence of S_{eff} observed in this study was fairly well explained by the target theory based on microdose concept.

INTRODUCTION

LET dependence of lethal and genetic effects on bacterial and yeast cells, which are the larger and more complex biological systems as compared with dry enzymes and phages, have been studied with several species such as *E. coli*,[1~7] *S. flexneri*,[6,7] *M. radiodurans*,[8] *B. subtilis* spores,[7,9,10] *B. megaterium* spores[11] and diploid strains of *S. cerevisiae*.[12~14] In these studies,[1~14] the basic mechanism of inactivation of bacterial cells has been explained by the target theory assuming that DNA would be the cellular principal target. However, the problem of the contribution of δ-rays in bacterial cells has been by-passed or insufficiently referred to. It appears that there are considerable difficulties in establishing the satisfactory model on inactivation of bacterial cells by charged-particle bombardment, since the physical state of the bacterial-target containing DNA strand is more complex as compared with enzyme molecules and most bacteria are endowed with DNA-repair capacity.

In order to overcome these difficulties, microdose concept was introduced by Rossi[15] and Oda *et al.*,[16] and they tried to interpret the radiation effects on biological systems by much more detailed information on spatial energy distribution in irradiated materials.

* 谷田貝文夫： 早稲田大学理工学部応用物理学科，東京都新宿区西大久保 4–170 〒160
** 高橋 旦，松山 晃： 理化学研究所，埼玉県和光市広沢 2–1 〒351

In a series of our studies on LET effects dealing bacterial cells, *B. subtilis* spores, *E. coli* B_{s-1} and *E. coli* B/r were bombarded by various cyclotron beams, and lethal effects of these charged particles were determined. General features for *B. subtilis* spores were similar to those obtained by Howard Franders[7] and Powers *et al.*,[11] and results for *E. coli* B_{s-1} and B/r were also similar to those obtained by Inch and Haynes.[17] In our experiments, the more detailed determinations were made for different kinds of ion beams and their energies, so that detailed discussion on the δ-ray effect of heavy ions could be made. In the present paper, observed LET effects of charged particles on bacterial cells mentioned above and an analysis of these effcts by utilizing the target theory based on microdose concept proposed by Oda *et al.*[16] and Numakunai *et al.*[18] will be described.

MATERIALS AND METHODS

(1) Bacteriological Procedure

Spores of *B. subtilis* 168 thy^- ind^- leu^- (MY2Y1U2) which was kindly provided by Prof. H. Yoshikawa of Kanazawa University, were prepared by the same procedure described previously.[10] The spores were suspended in sterile distilled water ($\sim 10^9$ spores/m*l*) and stored at 4°C until the use. For the preparation of cell suspensions of *E. coli* B_{s-1} and B/r, an inoculum from a nutrient agar slant was grown to saturation at 37°C with shaking in a minimal medium (2 g NH_4Cl, 15 g $Na_2HPO_4 \cdot 12\,H_2O$, 3 g KH_2PO_4, 3 g NaCl, 0.25 g $MgSO_4 \cdot 7\,H_2O$, 0.01 g $CaCl_2$, 0.054 mg $FeCl_3$, 2 g glucose and 1000 m*l* H_2O: pH 7.0). A 2~3 m*l* portion of this culture was transferred into 100 m*l* of the fresh minimal medium and incubated at 37°C with shaking. After 3~4 hours, log-phase cells were chilled, harvested by centrifugation, washed twice with 0.067 M phosphate buffer and resuspended in the same buffer at a concentration of $\sim 10^8$ cells/m*l*. After irradiation, survivals were determined by visible-colony counting method using Schaeffer's agar plates for *B. subtilis* spores and meat extract-peptone agar plates for *E. coli*. Electron microscopy was also carried out to determine the geometry of the bacteria by direct observation of the whole bacteria as well as the thin sectioning.[19]

(2) Irradiation

Bacterial cells were bombarded with α-particles and heavy ions of carbon, nitrogen and oxygen accelerated in the IPCR Cyclotron which is variable-energy type of the machine.[20] They were also irradiated with gamma rays from 12 kCi ^{60}Co at a dose rate of about 6.5~6.8 krad/min for comparison. Cyclotron-beam irradiation was carried out by the track-segment method,[21~23] experimental arrangement and procedure of which were already described.[10] A monolayer of bacterial cells was prepared on a membrane filter using the cell suspensions mentioned above and exposed to cyclotron beams under mechanical shaking for the dose uniformity. Dosimetry was performed by the nuclear electronic method as previously described.[24] The absorbed dose, D, in krad was calculated according to the following formula:

$$D=0.174\times\frac{LQ}{Z^{*}_{sc}}$$

where L is the LET value at a position of the sample in keV/μm, Q is the charge input in nC and Z^{*}_{sc} is the effective charge number of ionizing particles[25] immediately after traversing a scattering foil.

RESULTS

All survival curves of *B. subtilis* spores and *E. coli* B_{s-1} and B/r determined for α-particles and heavy particles of C-ions, N-ions, and O-ions as well as ^{60}Co γ-rays were of an exponential type as shown in Fig. 1. In the case of exponential survival curve, S_{eff} is calculated by the relation $N/N_0=\exp(-S_{eff}\phi)$, where N/N_0 is the surviving fraction for a given particle fluence ϕ. The 37% dose, D_{37}, is given by the relation $D_{37}=L\phi_{37}$, where ϕ_{37} is corresponding fluence and LET_∞ the unrestricted LET of the bombarding particles.

The relationship between relative biological effectiveness (RBE) and LET_∞ is shown in Fig. 2, where RBE is represented by the reciprocal of 37% dose, $1/D_{37}$. In the case of *B. subtilis* spores, as LET_∞ increased, RBE remarkably increased in the region of α-particles, followed by a decrease in the heavy-ion region (Fig. 2(a)). Although the accurate determination can not be made under the present experimental condition, the RBE peak seems to be obtained at ~120 keV/μm. This value, 120 keV/μm, is fairly well consistent with the value for *B. subtilis* spores, 100 keV/

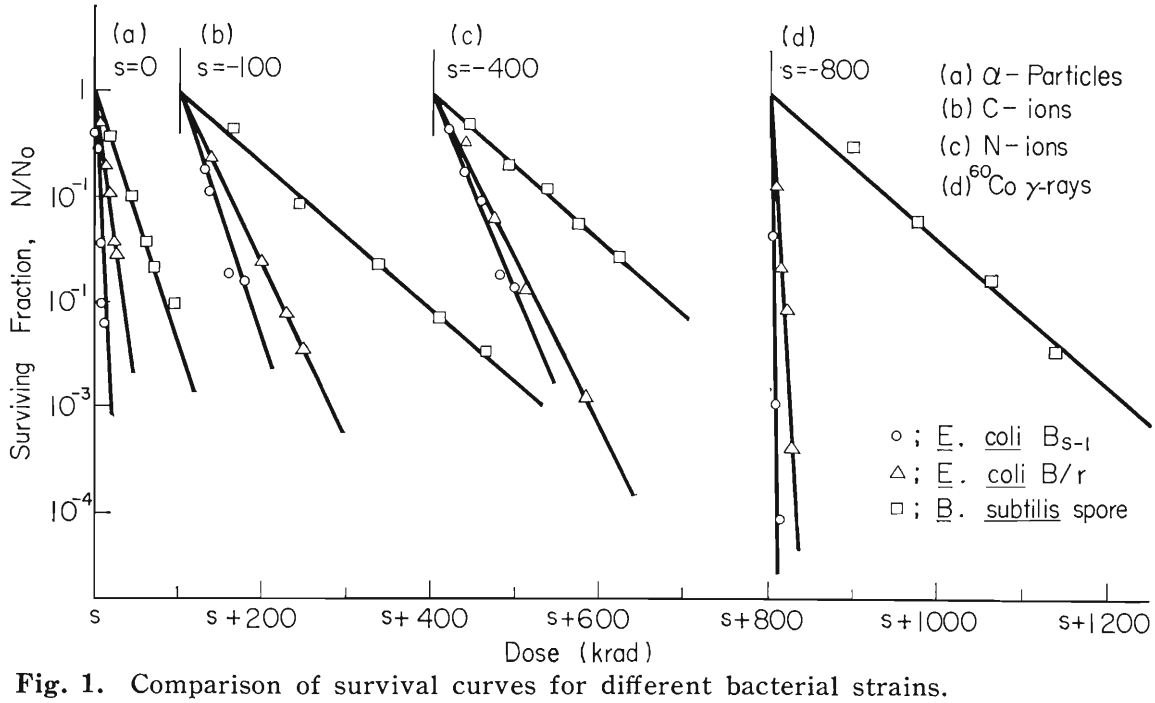

Fig. 1. Comparison of survival curves for different bacterial strains.
(a) α-particles: 0.795 MeV/amu for *B. subtilis* spores, 1.32 MeV/amu for *E. coli* B_{s-1} and 1.01 MeV/amu for *E. coli* B/r; (b) C-ions: 0.889 MeV/amu for *B. subtilis* spores and 1.03 MeV/amu for *E. coli* B_{s-1} and B/r; (c) N-ions: 1.23 MeV/amu for *B. subtilis* spores and 1.03 MeV/amu for *E. coli* B_{s-1} and B/r; (d) ^{60}Co γ-rays.

μm, reported by Howard-Flanders,[7] and the similar RBE peak has been observed with Transforming DNA,[26] Human kidney cells[27,28] and Haploid yeast.[12] However, the RBE-LET curves for *E. coli* B_{s-1} and *E. coli* B/r simply declined with increasing LET over the whole range of LET determined (Fig. 2 (b) and (c)), and this observation is also consistent with the results obtained by Brustad[3] and Haynes.[4,17]

The $1/D_{37}$ value for ^{60}Co γ-rays was found to be 0.0157 for *B. subtilis* spores, 0.794 for *E. coli* B_{s-1} and 0.274 $(krad)^{-1}$ for *E. coli* B/r, as shown in Fig. 2. On the other hand, the $1/D_{37}$ values at 1120 keV/μm, which was the highest value of LET_∞ in our experiments given by N-ions, were found to be 0.033 and 0.026 $(krad)^{-1}$ for *E. coli* B_{s-1} and *E. coli* B/r, respectively. The difference in $1/D_{37}$ value between *E.*

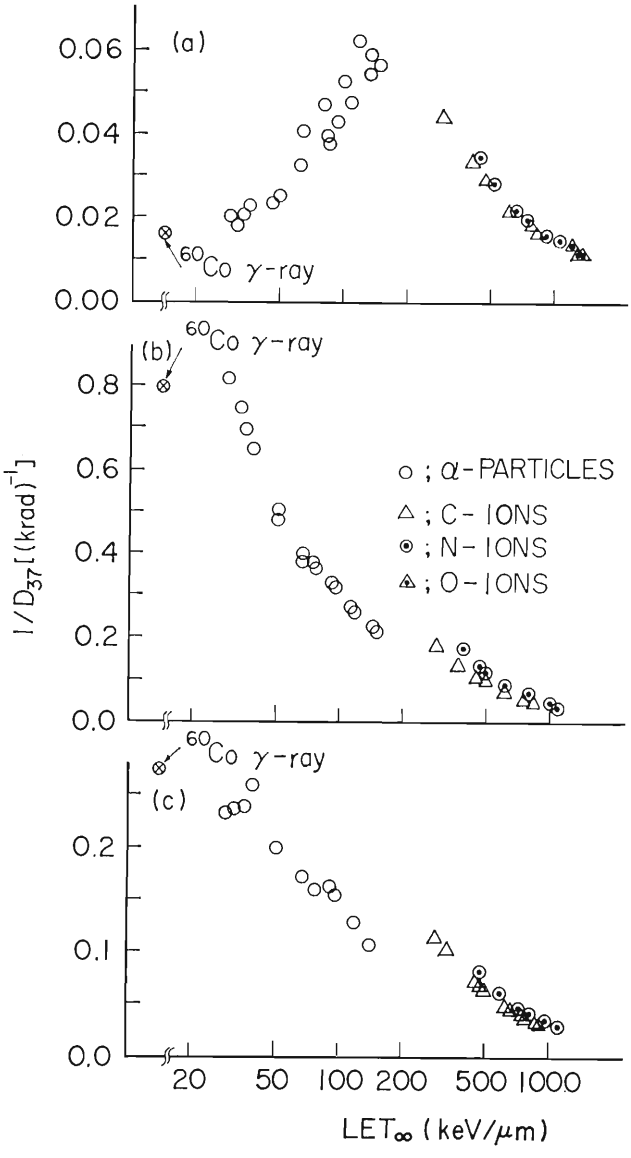

Fig. 2. Relation between LET_∞ and RBE $(1/D_{37})$.
(a) *B. subtilis* spores; (b) *E. coli* B_{s-1}; (c) *E. coli* B/r.

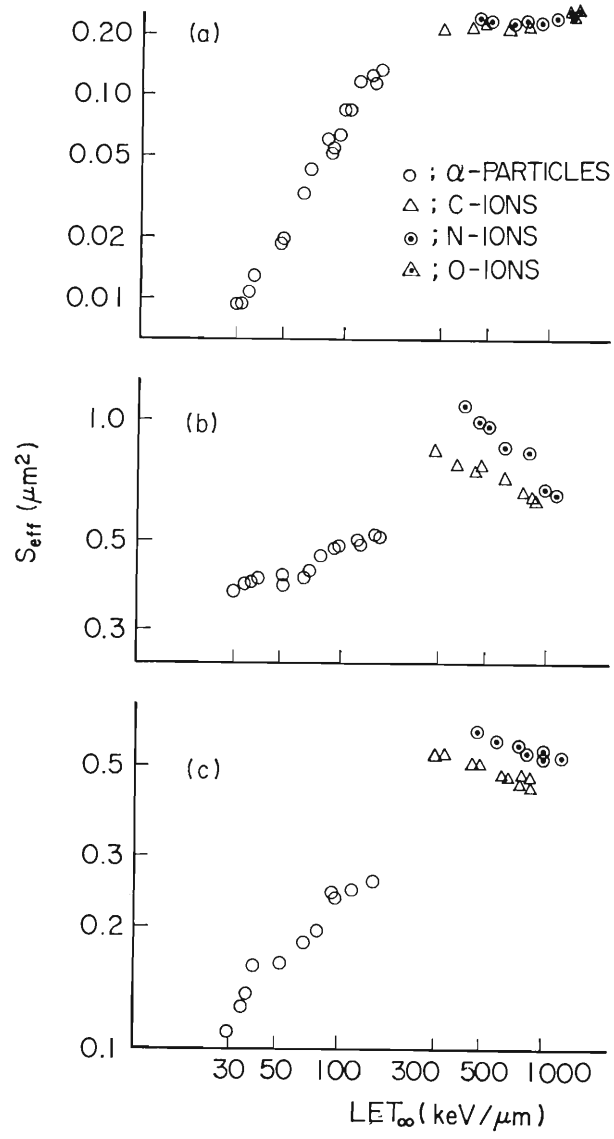

Fig. 3. Relation between LET_∞ and the effective inactivation cross section, S_{eff}.
(a) *B. subtilis* spores; (b) *E. coli* B_{s-1}; (c) *E. coli* B/r.

coli B_{s-1} and *E. coli* B/r declined as the LET of the bombarding particles increased. This fact seems to be compatible with the results obtained with the same bacteria by heavy ions from HILAC at Barkeley.[4,17]

Figure 3 shows the LET dependence of S_{eff} for these bacterial strains.

B. subtilis spores: S_{eff} for *B. subtilis* spores remarkably increased (0.00929~0.136 μm^2) with increasing LET_∞ in the range of α-particles, 30~150 keV/μm, but it was not reached at a plateau within this LET_∞ range of α-particles (Fig. 3(a)). In the LET range of heavy ions, the S_{eff} values at the same LET_∞ obtained by different kinds of heavy ions increased with the atomic number of bombarding particles, that is, in the order of C-, N- and O-ions. However, almost no LET dependence of S_{eff} for each kind of heavy particles was observed, and the mean values of S_{eff} for C-, N- and O-ions were found to be 0.220, 0.233 and 0.256 μm^2, respectively and all these values were much greater than the maximum S_{eff} value in the α-particle region, 0.136 μm^2.

E. coli B_{s-1}: S_{eff} for *E. coli* B_{s-1} increased (0.379~0.521 μm^2) with increasing LET_∞ within the range of α-particles (Fig. 3(b)). Such an increase of S_{eff} was very small as compared with that for *B. subtilis* spores, and the S_{eff} values for α-particles of higher LETs seem to be almost approached to a plateau. Similarly to the case of *B. subtilis* spores, all values of S_{eff} in the LET range of heavy ions were greater than those in the range of α-particles (0.52 μm^2 or less), and bombarding particles of the larger atomic number gave the greater S_{eff} values at the same LET. The LET dependence of S_{eff} was observed for each kind of heavy particles, for example the S_{eff} for N-ions decreased from 1.09 to 0.660 μm^2 in accordance with the increase of LET_∞ from 393 to 1120 keV/μm. This tendency of LET dependence was not observed with *B. subtilis* spores, and it seems to be attributed to the contribution of δ-rays from heavy-ion tracks.

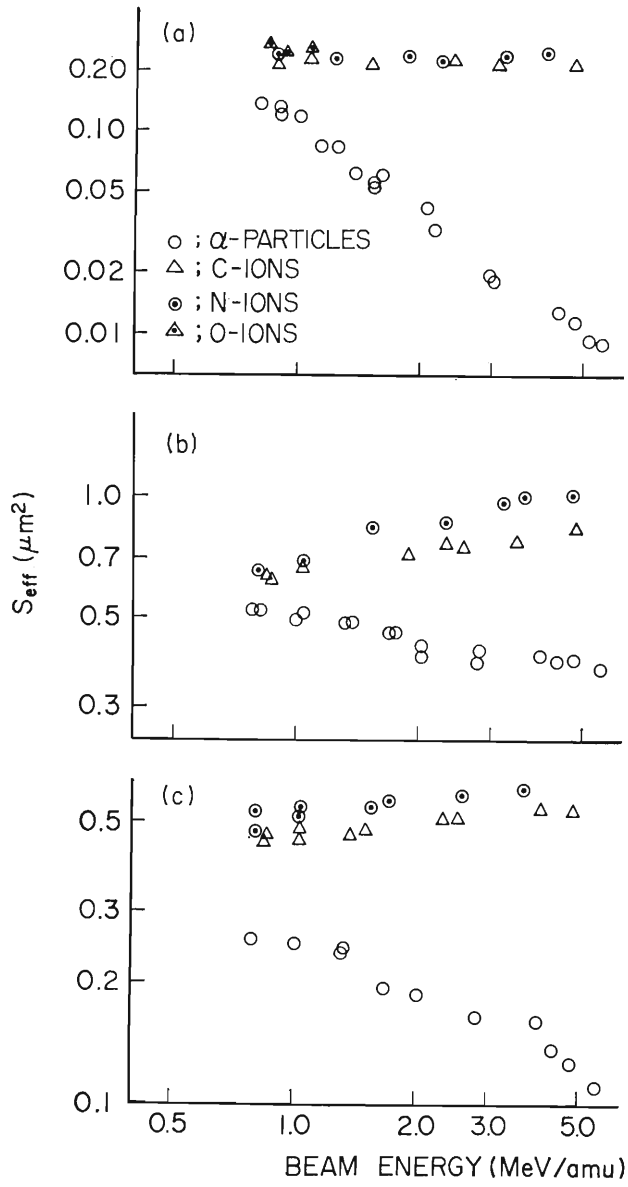

Fig. 4. Relation between the beam energy and the effective inactivation cross section, S_{eff}.
(a) *B. subtilis* spores; (b) *E. coli* B_{s-1}; (c) *E. coli* B/r.

E. coli B/r: S_{eff} for *E. coli* B/r increased (0.110~0.258 μm^2) with increasing LET in the range of α-particles (Fig. 3 (c)). This increase of S_{eff} was greater than that of *E. coli* B_{s-1}, but much smaller than that of *B. subtilis* spores. Moreover, the LET dependence of S_{eff} in higher LET region of α-particles also seems to be similar to that of *E. coli* B_{s-1} rather than to that of *B. subtilis* spores. Similarly to the cases of *B. subtilis* spores and *E. coli* B_{s-1}, S_{eff} values of *E. coli* B/r for heavy ions were found to be greater than the maximum value in the α-particle region, 0.258 μm^2 and showed the increase with increasing the atomic number of bombarding particles at the same LET_∞ in the heavy-ion region. The LET dependence of S_{eff} in the heavy-ion region was observed similarly to that of *E. coli* B_{s-1}, for example S_{eff} for N-ions decreased from 0.612 to 0.504 μm^2 with the increase of LET_∞ from 475 to 1120 keV/μm. Such a tendency of LET dependence of S_{eff} in the high-LET region appears very similar to that of *E. coli* B_{s-1}, although the contribution of δ-ray effect is somewhat smaller in *E. coli* B/r than *E. coli* B_{s-1}.

Energy dependence of S_{eff} for each charged particles was also shown in Fig. 4. The S_{eff} values of *B. subtilis* spores for heavy ions were scarcely found to be depependent on the energy of the bombarding particles, while that values for *E. coli* B_{s-1} and B/r increased with increasing beam energy. This figure also demonstrates the distinct difference in S_{eff} between α-particles and heavy ions in the low-energy region less than 1.0 MeV/amu where the δ-ray contribution may be considered relatively small.

The characteristic features of LET dependence of lethal effect on three bacterial strains mentioned above are summarized in Table 1.

DISCUSSION

Powers *et al.*[11] reported the LET dependence of inactivation of *B. megaterium* spores bombarded with stripped atoms accelerated in the heavy-ion linear accelerator (HILAC). Their determination was made under the experimental condition that the spatial energy distribution by δ-rays were the same for different accelerated ions. They interpreted the relation between S_{eff} and LET by the following functional form:

$$S_{eff}=S_{\alpha\infty}[1-\exp(-\alpha L_\infty)]+S_{\beta\infty}[1-\exp(-\beta L_\infty{}^2)] \quad (1)$$

Table 1. Comparison of the lethal effects of charged particles on different bacterial strains.

Strains	RBE-LET curve	Increment of S_{eff} in the LET region of α-particles (50~150 keV/μm)	S_{eff} for N-ions of~0.8 MeV/amu (1100 keV/μm)	Energy dependence of S_{eff} in the heavy-ion region
B. subtilis spore	RBE peak (120 keV/μm)	0.00929 → 0.136 μm^2 (~15.0 times)	0.224 μm^2	—
E. coli B/r	No RBE peak	0.110 → 0.258 μm^2 (~2.5 times)	0.492 μm^2	+
E. coli B_{s-1}	No RBE peak	0.379 → 0.521 μm^2 (~1.5 times)	0.660 μm^2	++

An interpretation of this expression is that single ionization events act on one set of molecules with overall limitting cross section of $S_{\alpha\infty}$ and double ionization events on another set of molecules with another limitting cross section $S_{\beta\infty}$. These two components in formula (1) represent that there are clearly two different primary mechanism, effective at low and at high LET, respectively. According to Powers *et al.*,[11] type A event may alter in some way one of the strands of double-strand DNA; this can lead sometimes to death, and type B events may simultaneously affect both strands of DNA (e. g. double-strand scission); when this occurs in the absence of repair mechanism, the effect would be usually lethal.

The data on *B. subtilis* spores in this study were obtained by the determination method different from that of Powers *et al.*[11] Nevertheless, their method of the data analysis seems to be valid for our data on the spore inactivation, since the δ-ray contribution to the inactivation was observed very small in the previous study.[10] Using the non-linear minimization program for computer, the limitting cross-section $S_{\alpha\infty}$, $S_{\beta\infty}$ and the inactivation constants α, β were calculated from our experimental data. Values of best-fit parameters are given in Table 2, with the values on *B. megaterium* spores reported by Powers *et al.*[11] for comparison, and Fig. 5 shows the best-fit curve to the experimental data. As can be seen in this figure, the theoretical curve agrees fairly well with the experimental data. Table 2 reveals the fact that the inactivation mechanism B for *B. subtilis* spore is very similar to that for *B. megaterium* spores, but the contribution of mechanism A for the inactivation of *B. subtilis* spores is significantly greater than that for *B. megaterium* spores. Powers *et al.* also mentioned that the value of $(S_{\alpha\infty}+S_{\beta\infty})$ in Table 2 corresponds to the projected area of the whole region without spore coat. The value 0.268 μm^2 for $(S_{\alpha\infty}+S_{\beta\infty})$ in our results is somewhat smaller than the projected area of about 0.32 μm^2, but much greater than than the projected area of the spore core ($\sim$0.12 μm^2). These values were determined by the electron microscopy. This fact suggests that very high-LET particles are lethal on their traversal not only through the nuclear region of the spore, that is spore core, but also through some other parts.

However, it seems to be impossible to apply their analytical method for the experimental results much affected by δ-rays, especially our data on *E. coli* B_{s-1} and *E. coli* B/r, since they have by-passed the δ-ray problem, as they have described in their paper.[11]

Table 2. Values of best-fit parameters in formula (1) determined by the method of non-linear minimization. The values for *B. megaterium* spores are reported by Powers *et al.*[13]

Strains	$S_{\alpha\infty}+S_{\beta\infty}$ (μm^2)	$S_{\alpha\infty}$ (μm^2)	$S_{\beta\infty}$ (μm^2)	α (μm/keV)	β (μm/keV)
B. subtilis spore	0.268	0.0559	0.212	4.67×10^{-4}	4.35×10^{-5}
B. megaterium spore	0.184	0.0045	0.1795	$6.35\times10^{2-}$	4.56×10^{-5}

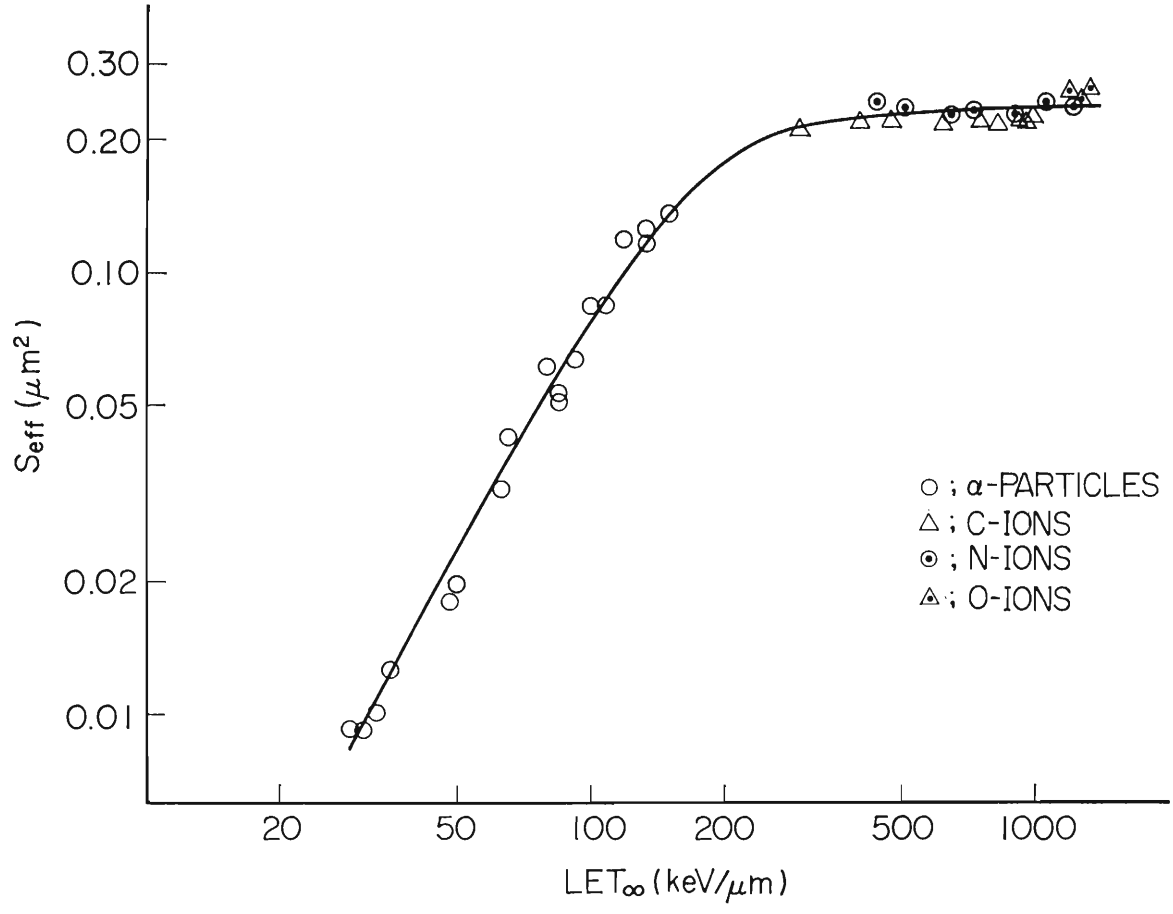

Fig. 5. A theoretical curve calculated from formula (1) was fitted with experimental data of S_{eff} for *B. subtilis* spores (see text).

LET dependence of S_{eff} can be analyzed by essentially the same method as Pollard, Guild, Hutchinson and Setlow,[29] Barendsen[28] and Oda,[16] which is based on the idea that a given number of j_0 or more ionizations must be produced within a length of particle track ι, in order to cause one lethal-hit. Therfore, the following formula (2) is derived from the assumption that the energy dissipated by high-energy δ-rays at a considerable distance from the track core of the particle may not contribute to the bacterial inactivation:

$$S_{eff}=S_0\left(1-\sum_{j=0}^{j_0-1}g_j\right), \tag{2}$$

where S_0 is the stationary level of S_{eff}, and g_j is the probability that an incident particle gives j ionizations within a critical length ι. The probability g_j is given by the Poisson distribution as follows,

$$g_j=\frac{(\iota L_{core}/W)^j}{j!}\exp\ (-\iota L_{core}/W),$$

where L_{core} is the track core LET and W the mean energy per primary activation, then $(\iota L_{core}/W)$ is the average number of ions or primary products produced within a critical length ι.

In the previous report,[10] it was indicated that formula (2) well explained the

LET dependence of S_{eff} for *B. subtilis* spore in the region of α-particles. However, it is easily expected that formula (2) would encounter the difficulty in the account for LET dependence of S_{eff} if it is affected by δ-rays, especially in the high-LET region of heavy ions. In order to interpret the experimental results mentioned above, it seems to be necessary to distinguish the cell inactivation due to the track core effect of particles from that due to the effect of δ-rays.

An attempt was made to analyze the present experimental data by the target theory based on microdose concept proposed by Oda *et al.*[16] and Numakunai *et al.*[18] According to their theory, effects of δ-rays are estimated by considering secondary electrons having energies greater than a certain cutoff value. In the case of exponential survival curve, the following expression for effective inactivation cross section (S_{eff}) is given by them,

$$S_{eff}=S_0(1+\alpha Z_{eff}^2)\left(1-\sum_{j=0}^{j_0-1} f_j\right), \tag{3}$$

where S_0 is the geometrical cross section of the target and Z_{eff} the effective charge for heavy charged particles as passing through the bacterial cell or target. As in formula (2), f_j means the probability to produce j primary ionizations in the target when charged particles pass through the target, and at least a certain number of primary ionization j_0 must take place in the target to produce one lethal-hit. Since there are two kinds of radiation fields, primary ions and δ-rays, f_j must be obtained by the sum of f_j for heavy ions and f_j for δ-rays. In accordance with their theory, we defined an approximate function f_j as follows:

$$f_j=[\bar{\phi}_p P(E_p, j)+\bar{\phi}_\delta P(\bar{E}_\delta, j)]/\bar{\phi}_t \tag{4}$$

Although the second term in formula (4) must be essentially integrated for all the secondary electrons having various energies, the mean energy of the secondary electrons was used in this study to make the calculation easier. This function f_j has parameters such as primary energies of heavy ions, E_p, cutoff energies, η, and other parameters which will be described below. Particle flux, $\bar{\phi}_t$ was calculated as the sum of that for primary ions, $\bar{\phi}_p$, and that for δ-rays, $\bar{\phi}_\delta$, $\bar{\phi}_t=\bar{\phi}_p+\bar{\phi}_\delta$, where $\bar{\phi}_p=\int\phi_p(E)\,dE$ and $\bar{\phi}_\delta=\int\phi_\delta(E)\,dE$. The relation between $\bar{\phi}_p$ and $\bar{\phi}_\delta$ is represented by $\bar{\phi}_\delta=\bar{\phi}_p\,\alpha\,Z_{eff}^2$, where "$\alpha$" is a numerical factor and corresponds to the total flux of δ-rays produced by unit flux density of heavy ions with $Z_{eff}=1$, and given by the formula, $\int_\eta^{E_\delta^{max}}\phi_\delta(E)dE=\bar{\phi}_\delta=\alpha$, where E_δ^{amx} is the maximum energy of δ-rays. Then $\bar{\phi}_t$ is expressed as $\bar{\phi}_t=\bar{\phi}_p(1+\alpha Z_{eff}^2)$, and this expression is used in formula (3) by the reason described above. In general P(E, j) represents the probability to produce j primary ionizations within a critical length ι of track of particle with energy E, and is given by the following Poisson distribution:

$$P(E, j)=\frac{[\iota L_\iota(E, \eta)/W]^j}{j!}\exp[-\iota L_\iota(E, \eta)/W] \tag{5}$$

$P(E_p, j)$ and $P(\bar{E}_\delta, j)$ in formula (4) correspond to P(E, j) for primary charged particles and that for δ-rays, respectively. In the estimation of $P(E_p, j)$, $L_\iota(E_p, \eta)$ in formula (5) means the track core LET of the charged particle, while in the case of

Table 3. Values of $\bar{E}_\delta$ used in the calculation.

η(keV)	$\bar{E}_\delta$ (keV)				
	E_p=1.0 MeV/amu	E_p=2.0 MeV/amu	E_p=3.0 MeV/amu	E_p=4.0 MeV/amu	E_p=6.0 MeV/amu
0.125	0.500	1.00	1.41	1.68	2.38
0.250	0.707	1.19	1.68	2.00	2.83
0.500	0.841	1.41	2.00	2.38	3.36
1.000	1.34	2.00	2.49	3.00	4.00

$P(\bar{E}_\delta, \eta)$ means the local LET of the secondary electrons ejected from the track of heavy ions as δ-rays. The values of $\bar{E}_\delta$ is defined as the mean energy of secondary electrons and obtained by the distribution of $\phi_\delta(E)$. Values of $\bar{E}_\delta$ used in the calculation were shown in Table 3. On account of the technical problem of calculation by computer, parameter k is defined as follows: $k=\iota/W$.

To fit formula (3) with our experimental data, it is necessary to determine four parameters: S_0, k, η and j_0. Accordingly, calculation was proceeded by fixing two of them, η and j_0, and then the best-fit values of S_0 and k for a certain set of the two fixed parameters were estimated by the least-square method, and such calculation was repeated for the other sets of η (0.125, 0.250, 0.500 and 1.00 keV) and j_0 (1, 2 and 3). To judge the goodness of fit, the values of χ^2 were computed for each fit, with χ^2 defined as:

$$\chi^2=\sum_i\left[\frac{y_i-y(x_i)}{y_i}\right]^2. \qquad (6)$$

The method of least squares is built on the hypothesis that the optimum description of a set of data is one which minimize the weighted sum of squares of deviations of the data y_i from the fitting function $y(x_i)$ as expressed in formula (6). In formula (6), y_i is the S_{eff} value observed for x_i or an LET_∞, and $y(x_i)$ is the theoretical one derived from formula (3). This χ^2 test gave the best-fit parameters as summarized in Table 4, and the best-fit curves with these parameters are shown in Fig. 6.

According to the definition of formula (3), the parameter S_0 must express the target size. However, the value of S_0, 0.215 μm^2, obtained with *B. subtilis* spores, is inconsistent not only with ~0.12 μm^2 for the spore core but also with ~0.32 μm^2 for the whole region without spore coat. Moreover, the S_0 values, 0.421 and 0.353 μm^2, found for *E. coli* B_{s-1} and *E. coli* B/r, respectively, are much smaller than the

Table 4. Values of best-fit parameters in formula (3) determined by the least-square method.

Strains	S_0 (μm^2)	k (μm/keV)	j_0	η (keV)	χ^2
B. subtilis spore	0.215 ± 0.00981	0.0149 ± 0.00059	2	0.5	0.310
E. coli B_{s-1}	0.421 ± 0.0141	0.0311 ± 0.00123	1	1.0	0.694
E. coli B/r	0.353 ± 0.0136	0.0127 ± 0.00117	1	1.0	0.222

projected area of nuclear region for both strains ($\sim$1.1 μm^2) from electron micrographs. This result suggests the fact that S_0 reflects not only the target size but also the repair capacity of target molecules as discussed by Haynes[4] and Burch[6]. It can be concluded that there might be any targets other than DNA molecules in the case of *B. subtilis* spores but not in the case of *E. coli*. As far as *B. subtilis* spores are concerned, this conclusion is consistent with that previously obtained by the method of Powers.

Assuming an average energy (W) of 35 eV required for one primary product,[28] critical length ι was estimated by the best-fit value of k ($=\iota/W$). The values of ι were found to be 0.52, 1.1 and 0.44 nm for *B. subtilis* spores, *E. coli* B_{s-1} and *E. coli* B/r, respectively. Using the best-fit parameters j_0 and ι in Table 4, inactivation mechanism may be expressed as follows: in the case of *B. subtilis* spores, at least two ionizations within a critical length 0.52 nm are required for producing one-lethal hit, while in the case of *E. coli* B_{s-1} and *E. coli* B/r, it is sufficient for inactivation to occur one ionization within a critical length 1.1 and 0.44 nm, respectively. It is found that ionizations more closely spaced within the critical length are required for *B. subtilis* spores than for the other two strains. The values of cutoff energy η shown in Table 4 also seem to reflect the target size.

Figure 6 shows a fairly good agreement of the theoretical curves with the experimental data, but some inconsistency is also observed in the LET region of heavy ions, especially in the case of *E. coli*. Whether there is any other effects

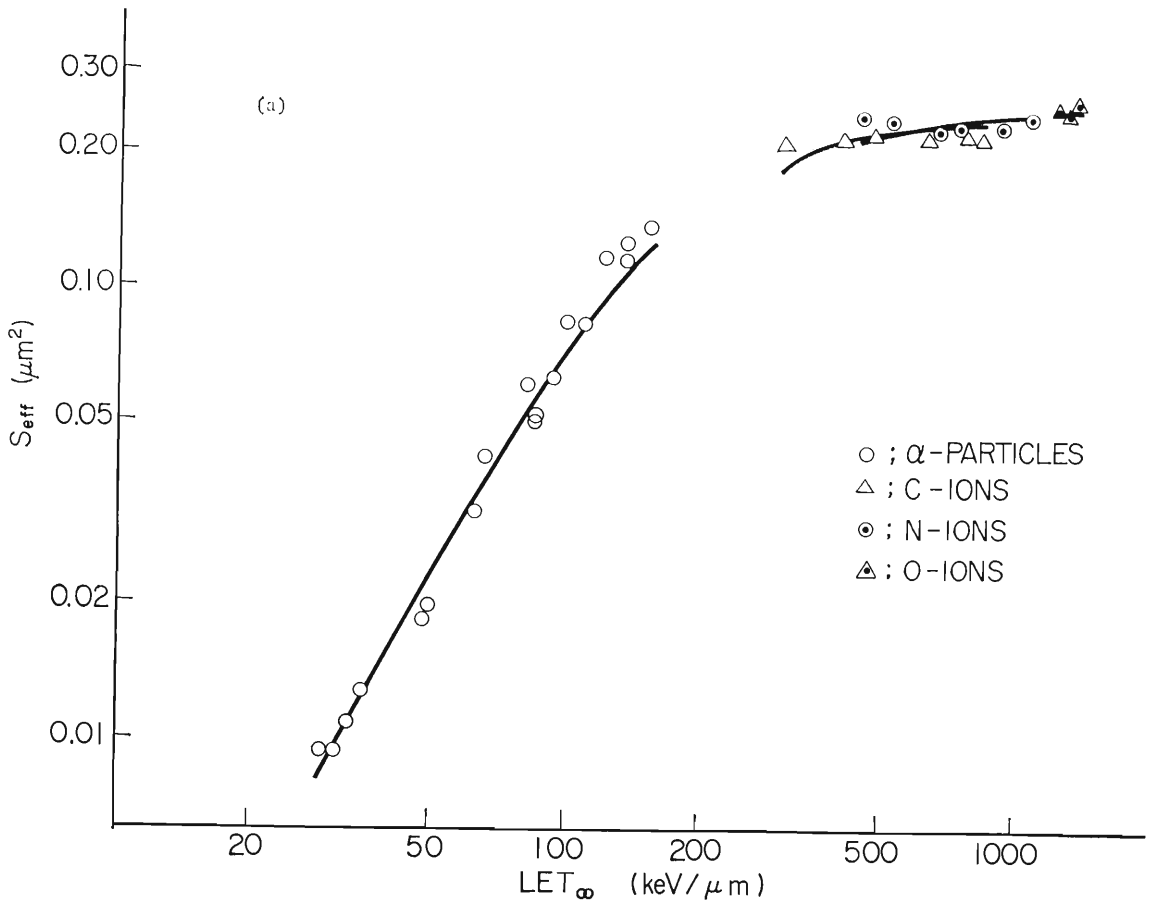

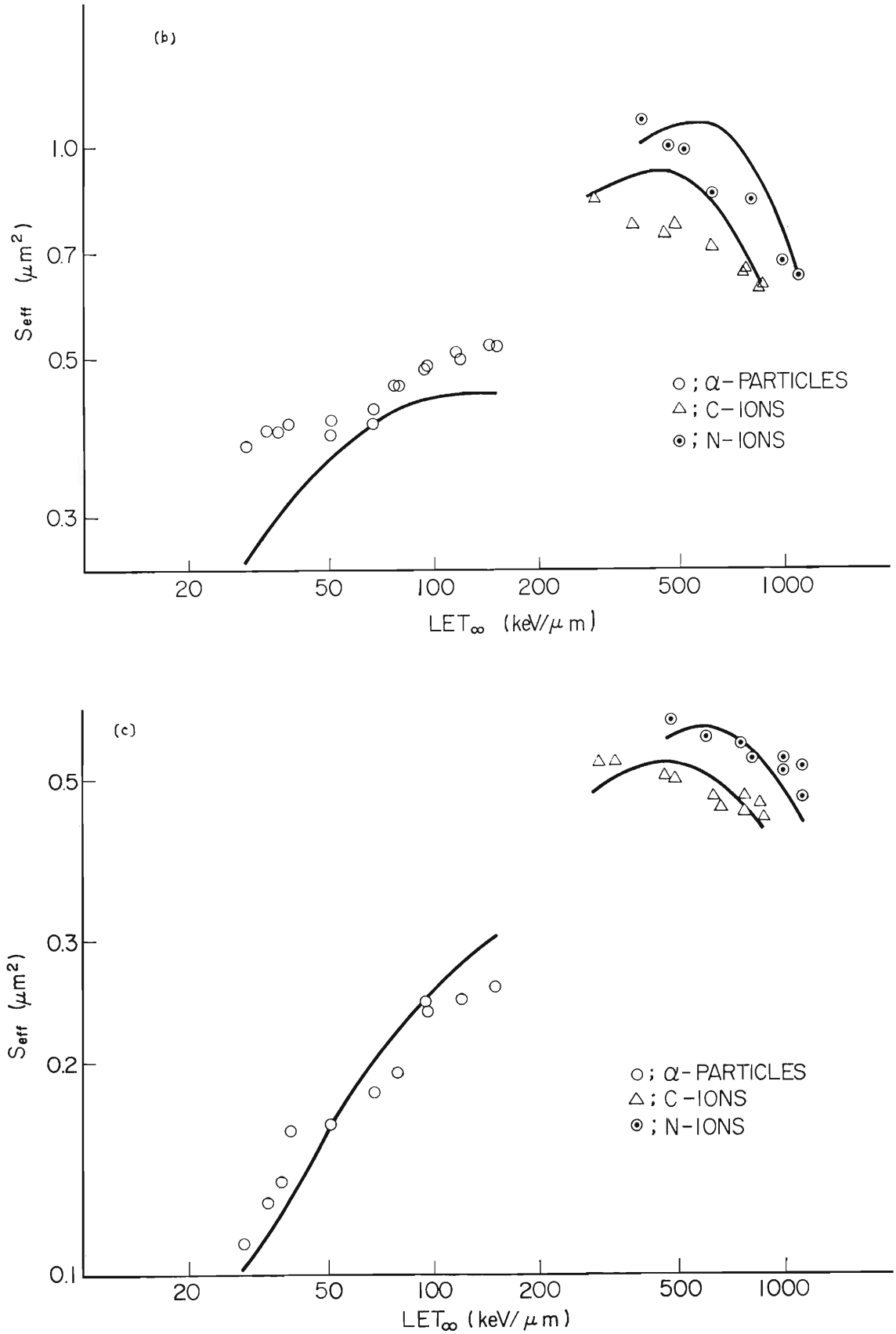

Fig. 6. Theoretical curves for each kind of charged particles calculated from formula (3) were fitted with experimental data of S_{eff} (see text). (a) *B. subtilis* spores; (b) *E. coli* B_{s-1}; (c) *E. coli B*/r.

given by high-LET heavy ions[30,31] is now under study.

ACKNOWLEDGEMENT

The authors indebted to Prof. H. Yoshikawa of Kanazawa University for the strain of *B. subtilis* spore and to Mr. H. Miyamoto of Tokyo Medical and Dental University for the electron microscopy. They also wish to express their appreciation for the cooperation and interest shown by Dr. H. Kamitsubo and the stuff of the IPCR Cyclotron Laboratory and Dr. T. Katou of Radiation Laboratory; without their kind help this study could not have been completed. This work was supported by research grants from the Science and Technology Agency and Ministry of Education of Japan.

REFERENCES

1. Matsuyama, A., Takahashi, T. and Yatagai, F. (1973) Inactivation of bacterial cells by charged particles. *IPCR Cyclotron Progr. Rept.*, **7**, 117–121.
2. Deering, R. A. (1963) Mutation and killing of *Escherichia coli* WP-2 by accelerated heavy ions and other radiations. *Radiat. Res.*, **19**, 169–178.
3. Brustad, T. (1961) Molecular and cellular effects of fast charged particles. *Radiat. Res.*, **15**, 139–158.
4. Haynes, R. H. (1966) The interpretation of microbial inactivation and recovery phenomena. *Radiat. Res.*, Suppl. **6**, 1–29.
5. Munson, R. J., Neary, G. J., Bridges, B. A. and Preston, R. J. (1967) The sensitivity of *Escherichia coli* to ionizing particles of different LETs. *Int. J. Radiat. Biol.*, **13**, 205–224.
6. Burch P. R. J. (1969) Charged particle tracks in solids and liquids. Proc. of 2nd L. H. Gray Conf., Chambridge. The Institute of Physics and The Physical Society Conference Series., 8, 127–139.
7. Howard-Franders, P. (1958) Physical and Chemical mechanism in the injury of cells by ionizing radiations. *Adv. Biol. Phys.*, **6**, 553–603.
8. Dewey, D. L. (1969) The survival of *Micrococcus radiodurans* irradiated at high LET and the effect of acridine orange. *Int. J. Radiat. Biol.*, **16**, 583–592.
9. Donnelian, J. E. and Morowitz, H. J. (1957) The irradiation of dry spores of *Bacillus subtilis* with charged particles. *Radiat. Res.*, **7**, 71–78.
10. Yatagai, F., Takahashi, T., Kitajima, Y. and Matsuyama, A. (1974) Inactivation of bacterial spores by charged particles. *J. Radiat. Res.*, **15**, 90–95.
11. Powers, E. L., Lyman, J. T. and Tobias, C. A. (1968) Somo effects of accelerated charged particles on bacterial spore. *Int. J. Radiat. Biol.*, **4**, 313–330.
12. Manney, T. R., Brustad, T. and Tobias, C. A. (1963) Effects of glycerol and of anoxia on the radiosensitivity of haploid yeasts to densely ionizing particles. *Radiat. Res.*, **18**, 374–388.
13. Mortimer, R., Brustad, T. and Cormack, D. V. (1965) Influence of linear energy transfer (LET) and oxygen tension on the effectiveness of ionizing radiations for induction of mutations and lethality in *Saccharomyces cerevisiae*, *Radiat. Res.*, **26**, 465–482.
14. Nakai, S. and Mortimer, R. (1967) Induction of different classes of genetic effects in Yeast using heavy ions. *Radiat. Res.*, Suppl. **7**, 172–181.
15. Rossi, H. H. (1967) Energy distribution in the absorption of radiation. *Adv. Biol. Med. Phys.*, **11**, 27–85.
16. Oda, N., Numakunai, T. and Ohtani, S. (1971) Analysis of dose-effect relationships based

on microdose concept. Biophysical Aspects of Radiation Quality. IAEA-SM 145/47, Vienna, pp. 99–117.
17. Inch, W. R. and Haynes, R. H. (1966) Non-repairability of densely ionizing radiation damage in *E. coli*. *Radiat. Res.* **27,** 545.
18. Numakunai, T., Ohtani, S., Kawai, K. and Oda. N. (1969) Calculation of primary energy transfer and effective inactivation cross section of biological targets for heavy charged particles based on microdose concept. *JAERI* 1179.
19. Kellenberger, E., Ryter, A. and Sechaud, J. (1958) Electron microscope study of DNA-containing plasma. Vegetative and mature phage DNA as compared with normal bacterial nucleoids in different physiological states. *J. Biophys. Biochem. Cytol.*, **4,** 671–678.
20. Matsuyama, A., Karasawa, T., Kitayama, S. and Takeshita, R. (1969) The LET effects on bacterial cells. *IPCR Cyclotron Progr. Rept.*, **3,** 101–103.
21. Barendsen, G. W. and Walter, H. M. D. (1963) Effects of different ionizing radiations on human cells in tissue culture. II Experiments with cyclotron-accerated alpha-particles and deuterons. *Radiat, Res.*, **18,** 106–119.
22. Todd, P. W., Lyman, J. T. and Armar, R. A. (1968) Dosimetry and apparatus for heavy ion irradiation of mammalian cells *in vitro*. *Radiat. Res.* **34,** 1–23.
23. Todd, P. W. and Schroy, C. B. (1971) Spatial distribution of biological effect in a 3.9 GeV nitrogen ion beam. *Science*, **174,** 1127–1128.
24. Karasawa, T., Seki, H., Imamura, M., Matsuyama, A. and Matsui, M. (1970) Studies of radiation chemistry and biology with IPCR 160 cm Cyclotron. The uses of cyclotron in chemistry, metallurgy and biology (edited by C. B. Amphlett). Butterworths, London. pp. 76–119.
25. Northcliffe, L. C. and Schilling, R. F. (1970) Range and stopping power tables for heavy ions. *Nuclear Data Tables*, **A 7,** 233–463; Northcliffe, L. C. (1963) Passage of heavy ions through matter. *Annual Review of Nuclear Science*, **13,** 67–102.
26. Hutchinson, F. (1965) The inactivation of DNA and other biological molecules by ionizing radiation, in Cellular Radiation Biology, williams and Wilkins Company, Boltimore, pp. 86.
27. Todd, p. (1965) Reversible and irreversible effects of ionizing radiations on the reproductive capacity of cultured human cells. *Med. Coll. Virginia Quart.* **1,** 2–14.
28. Barendsen, G. W. (1964) Impairment of the proliferative capcity of human cells in culture by α-particles with differing linear-energy transfer. *Int. J. Radiat. Biol.*, 8, 453–466.
29. Pollard, E. C., Guild, W. R., Hutchinson, F. and Setlow, R. B. (1955) The direct action of ionizing radiation on enzymes and antigens. *Prog. Biophys. Chem.*, **5,** 72–108.
30. Kondo, S. (1961) Linear energy transfer and relative biological effectiveness. *Butsuri, Monthly Review Journal Published by the Physical Society of Japan (in Japanese)*, **16,** 584–586.
31. Chatterjee, A. and Tobias, C. A. (1974) Applications of a high LET track model. *Radiat. Res.*, **59,** 297.

Reprinted from Phys. Lett., 67A, 159–161 (1978).

EMISSION SPECTRA OF EXCITONS CREATED IN A SINGLE CRYSTAL OF KBr BY IRRADIATION OF HEAVY IONS AT 4.2 K

Kazuie KIMURA and Masashi IMAMURA
The Institute of Physical and Chemical Research, Wako, Saitama 351, Japan

Received 22 March 1978

An intensity ratio of the σ- to π-emission higher than that in X-irradiation was observed for a heavy-ion irradiated single crystal of KBr at 4.2 K. The result was interpreted in terms of the interaction of free excitons at higher energy states.

Although energetic heavy ions are currently in increasing use in solid-state physics and radiation chemistry, experimental information regarding the primary physicochemical processes in irradiated matter is still scarce; several theories published so far [1] are not so elaborate for predicting actual processes either. Measurement of the emission spectra from the electronic excited states in irradiated matter may be one of the useful experimental approaches to this end. A KBr crystal was chosen in the present study because spectral assignments for the excitons and color centers formed in alkali halides by X-, electron-, and photo-irradiation are well established.

He-, C-, and N-ions of 8 MeV per nucleon from the cyclotron at the Institute of Physical and Chemical Research were used and, for pulse irradiation, they were chopped into 40 μs pulses with a repetition of 416 s^{-1}. The beam current was mostly between 0.1 and 1 nA, and between 0.1 and 100 nA for experiments of dose rate effects. Emission spectra were measured under (1) stationary irradiation and under (2) pulse irradiation followed by strobe measurements to obtain the time-resolved spectra. In the former, a photo-multiplier (Hamamatsu R758) and Optical Multichannel Analyser (OMA; Princeton applied research) were used; in the latter, the gate of the OMA was synchronized with each pulse and the aperture time of the gate was 3 μs. The photomultiplier, a grating monochromator (Ritsu MC-25N) and filters were calibrated using an NBS standard lamp. A single crystal of KBr obtained from Harshaw Chemical Co. was cleaved into thin plates (10 × 10 × 1 mm^3). The crystal was cooled to 4.2 K using a cryostat (Oxford Instruments, CF-240).

Emission spectra with peaks at 280 and 512 nm were observed for KBr irradiated with C-ions at 4.2 K (fig. 1). They may be assigned to the emission due to σ- and π-excitons which are self-trapped excitons known in X- and electron-irradiated KBr [2,3]. An additional peak other than the σ- and π-emissions, reported by Ukai et al. for RbI irradiated at 77 K [4] could not be recognized under the present experimental conditions. The intensity ratio of the σ-

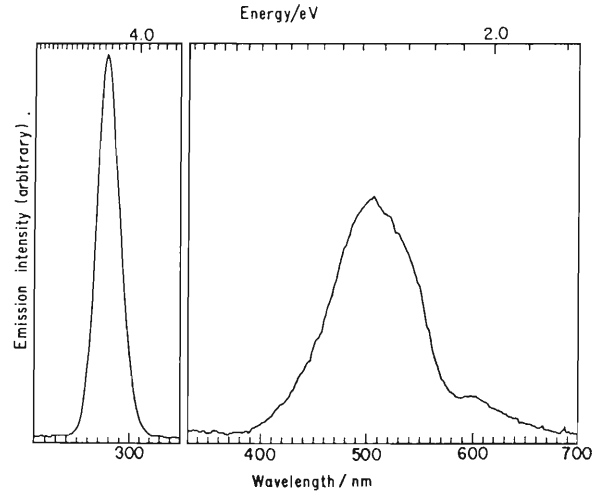

Fig. 1. Emission spectrum of KBr at 4.2 K under irradiation of 85 MeV, 1 nA C-ions. Intensity scale of the right-hand spectrum is expanded 5 times.

to π-emission (I_σ/I_π) was found to be 10–12 which is 5–6 times higher than 2, as reported in electron-irradiation [5]. Self-absorption at the absorption edge of the F-center (peak at 600 nm) was negligibly small since the emission spectra were measured in the region where the optical density at 512 nm was less than 0.05. The effect of temperature increase caused by irradiation does not account for the high value of I_σ/I_π, since I_σ is known to decrease faster than I_π with increasing temperature. In addition, the currents (1 nA) employed were not so high to raise the temperature of the sample significantly. Consequently, the possible mechanisms that may be responsible for the higher value of I_σ/I_π are: (1) a larger probability of radiationless annihilation of the π-excitons, (2) a larger probability of radiative decay of the σ-excitons, and (3) preferential formation of the σ-excitons.

Both I_σ and I_π increased linearly with increasing dose in the low dose range, but in the higher dose range they decreased with increasing dose; the rate of the decrease was larger for I_σ than for I_π. Plots of I_σ/I_π versus doses, in the irradiation with He-, C-, and N-ions, are shown in fig. 2. Fig. 2 shows a distinct LET effect for I_σ/I_π: 2 for X-rays, 5.8 for He-ions, 10 for C-ions, and 15 for N-ions. It is also shown in fig. 2 that the value of I_σ/I_π in heavy-ion irradiation is almost constant for doses less than 3000 nC, above this value they decrease. This fact indicates that the σ-excitons are deactivated easily by the color centers such as H, H′, and F, more than the π-excitons. Therefore, the value of I_σ/I_π in heavy-ion irradiation cannot be interpreted in terms of annihilation of the π-excitons by the centers which may be formed densely by heavy-ion irradiation.

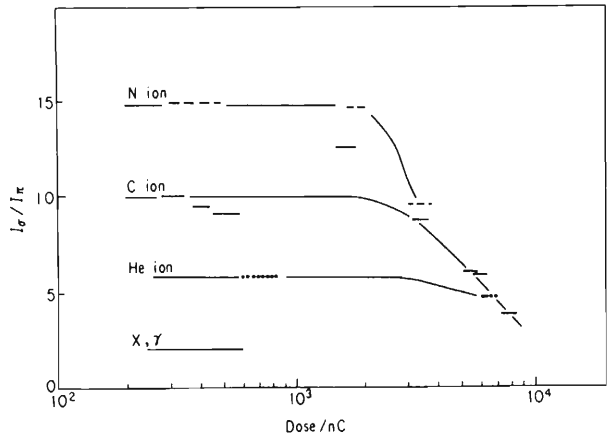

Fig. 2. Dose dependence of I_σ/I_π.

Dense excitation by heavy-ion irradiation would cause interaction between excitons, resulting in a shorter lifetime of the exciton. This interaction may occur to the π-exciton, since its lifetime (0.1 ms at 4.2 K) [5] is much longer than that of the σ (1–5 ns at 5 K) [7]. The time-resolved spectra of the π-emission were measured at 0, 1.5×10^{-4}, 3.0×10^{-4}, and 1.32×10^{-3} s after the heavy-ion pulses (fig. 3) and a decay curve was obtained by plotting peak intensities, as shown in fig. 4. Although the decay curve appears non-linear, this is consistent with the result of Karasawa and Hirai [6] who found that the decay curve consists of a fast and a slow component. The lifetime of the fast component, 0.2 ms in the present experiment, cannot be regarded as being shorter than the value reported by Pooley and Runciman [5] for the electron pulse radiolysis of KBr, 0.1 ms at 4.2 K and Karasawa and Hirai [6] for photoirradiation using an N_2-laser, 20 μs at 4.2 K. This result leads to the conclusion that the lifetime of the π-exciton is not decreased. Since both σ- and π-excitons in alkali halides are self-trapped, collisional interaction between them is not likely to take place. If there is interaction, the excitons may either decay radiatively as known in semiconductors or form excitonic molecules which decay with strong characteristic emissions; neither is the case. Process (2) should be also ruled out because of the self-trapping of

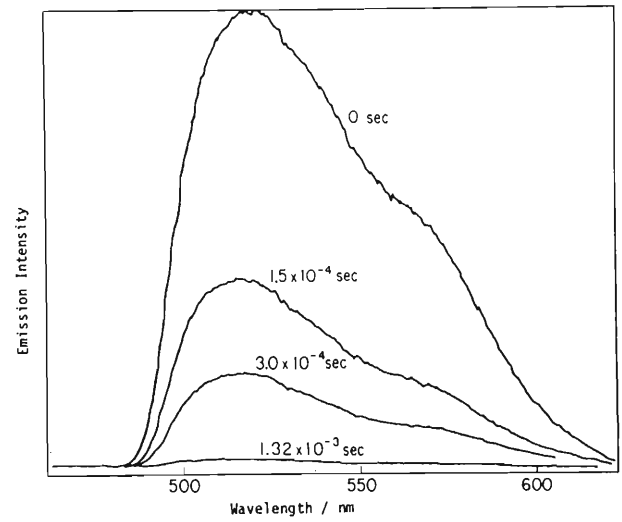

Fig. 3. Time-resolved π-emission spectra of a KBr single crystal irradiated with 85 MeV C-ions at 4.2 K.

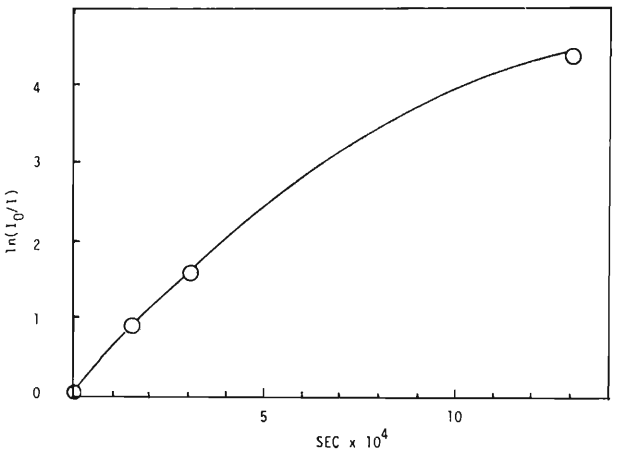

Fig. 4. Decay of π-emission.

the σ-excitons. Process (3) is, therefore, most plausible.

Recently, Nishimura [8] and Hayashi et al. [9] reported that free excitons exist for a short time in a photo-irradiated single crystal of KI before relaxing into the self-trapped state. In heavy-ion irradiation, the free excitons formed densely in the vicinity of the tracks collide with each other, so that the σ- and π-excitons may be formed in a ratio that differs from the case of the spontaneous intersystem crossing in X-, electron-, and photo-irradiation.

The authors are grateful for helpful discussions with Professor N. Itoh, Professor M. Hirai, and Dr. Karasawa. They would also like to acknowledge technical assistance of Mr. H. Endo and the operation group of the cyclotron.

References

[1] Reviewed by U. Fano, Ann. Rev. Nucl. Sci. 13 (1963) 1; C. Crispin and G.N. Fowler, Rev. Mod. Phys. 42 (1970) 42.
[2] N. Itoh, J. Physique Colloq. 37 (1976) C7–27.
[3] M. Hirai, Intern. Conf. on Color centers in ionic crystals (Sendai, 1974) Abstract D36.
[4] T. Ukai, N. Matsunami, K. Morita and N. Itoh, Phys. Lett. 56A (1976) 127.
[5] D. Pooley and W.A. Runciman, J. Phys. C3 (1970) 1815.
[6] T. Krasawa and M. Hirai, J. Phys. Soc. Japan 40 (1976) 755, 769.
[7] I.M. Blair, D. Pooley and D. Smith, AERE-R6906 (1971).
[8] H. Nishimura, J. Phys. Soc. Japan 43 (1977) 157.
[9] T. Hayashi, T. Ohata and S. Koshino, J. Phys. Soc. Japan 42 (1977) 1647.

Reprinted from Int. J. Appl. Radiat. Isotopes, 25, 393–399 (1974).

Yield of ^{18}F for Various Reactions from Oxygen and Neon

TADASHI NOZAKI, M. IWAMOTO and T. IDO*
Institute of Physical and Chemical Research, Wako-shi, Saitama, Japan

(*Received* 20 *December* 1973; *in revised form* 8 *March* 1974)

The excitation curves for the reactions of deuteron and ^3He-particle on neon to give ^{18}F and the thick target yield of ^{18}F for the reaction of triton on oxygen were measured up to the deuteron and triton energies of 24 MeV and the ^3He-particle energy of 42 MeV. These three reactions, together with the reactions of ^3He- and α-particle on oxygen, were then compared with a view to the practical production of ^{18}F in various useful states. The ^3He-bombardment of a target system consisting of neon and water separated by a thin foil has proved to provide, simultaneously, anhydrous ^{18}F and aqueous ^{18}F, both in good yields. The triton bombardment can be regarded as the most valuable method for the activation analysis of trace oxygen.

RENDEMENT DE ^{18}F POUR DIFFERENTES REACTIONS D'OXYGENE ET DE NEON

Les courbes d'excitation pour les réactions du deuteron et du ^3He sur le néon pour rendre du ^{18}F, ainsi que le rendement de cible épaisse de ^{18}F pour la réaction du triton sur l'oxygène, furent mesurés pour les énergies de deuteron et de triton jusqu'à 24 MeV et pour l'énergie de ^3He jusqu'à 42 MeV. Ensuite ces trois réactions ainsi que les réactions de ^3He et de la particule α sur l'oxygène furent comparées ensemble avec le but de la production praticable du ^{18}F en différentes formes utiles. Il s'est trouvé que le bombardement avec du ^3He d'une cible formée de néon et d'eau séparés par une mince feuille produit simultanément de bons rendements de ^{18}F anhydrique et de ^{18}F aqueux. Le bombardement aux tritons peut être considéré comme la méthode la plus importante pour l'analyse par activation de traces d'oxygène.

ВЫХОД ^{18}F ДЛЯ РАЗЛИЧНЫХ РЕАКЦИЙ ОТ КИСЛОРОДА И НЕОНА

Кривые возбуждения для реакций дейтрона и частицы ^3He на неон для получения ^{18}F и выход толстой мишени ^{18}F для реакции тритона на кислород измерены до энергий дейтрона и тритона в 24 Мэв и при энергии частицы ^3He в 42 Мэв. Эти три реакции вместе с реакциями частиц ^3He и α на цислород были сравнены в целях практического производства ^{18}F в различных полезных состояниях. В случае системы мишени, состоящей из неона и воцы, разделенных посредством тонкой фольги, бомбардировка частицами ^3He обеспечит одновременно хороший выход и безводного и водного ^{18}F. Возможно считать бомбардировка тритонами самым ценным методом активационного анализа следов кислорода.

^{18}F-AUSBEUTE FÜR VERSCHIEDENE REAKTIONEN VON SAUERSTOFF UND NEON

Die Anregungskurven für die Reaktionen von Deuteron und ^3He-Teilchen auf Neon zur Abgabe von ^{18}F und die ^{18}F-Ausbeute einer dicken Treffplatte für die Reaktion von Triton auf Sauerstoff wurden gemessen bis zu Deuteron- und Triton-Energien von 24 MeV und der ^3He-Teilchenenergie von 42 MeV. Diese drei Reaktionen, zusammen mit den Reaktionen des ^3He- und Alpha-Teilchen auf Sauerstoff wurden dann vergleichen vom Gesichtspunkt der praktischen Herstellung von ^{18}F in verschiedenen nützlichen Zuständen. Die ^3He-Beschiessung eines Zielsystems, das aus Neon und Wasser mit einer dünnen Trennfolie bestand, hat gleichzeitig wasserfreies ^{18}F und wässriges ^{18}F, beides in guten Ausbeuten, geliefert. Die Triton-Beschiessung kann als die wertvollste Methode zur Aktivierungsanalyse von Sauerstoffspuren betrachtet werden.

* Present address: National Institute of Radiological Sciences, Anakawa, Chiba, Japan (280).

1. INTRODUCTION

^{18}F IS REGARDED as one of the most important radionuclides in nuclear medicine, and various nuclear reactions induced by cyclotron bombardment have been used or considered useful for its production.[1–4] The yield curves for some of the reactions, however, have not as yet been clearly established. We measured the excitation curves for the reactions of deuterons and ^{3}He-particles on neon to give ^{18}F and the thick target yield of ^{18}F for the reaction of triton on oxygen, up to the deuteron and triton energies of 24 MeV and the ^{3}He-particle energy of 42 MeV. The excitation curves for the ^{3}He- and α-particle reactions on oxygen to yield ^{18}F were also measured by the same experimental technique as was used in the neon reactions in order to compare the results with the previously-reported curves.

In this paper, the yield curves are shown, and the reactions are compared in view of the practical production of ^{18}F in various useful physical and chemical states. Table 1 shows the Q-values and threshold energies for the predominate ^{18}F-yielding reactions from the target elements of natural isotopic compositions (^{16}O, 99·759%; ^{17}O, 0·037%; ^{18}O, 0·204%. ^{20}Ne, 90·92%; ^{21}Ne, 0·257%; ^{22}Ne, 8·82%.).

2. EXPERIMENTAL

2.1 *Target preparation and bombardment*

Cylinders (exactly 25 mm in height, 60 mm in inner diameter, 2 mm in wall thickness) were cut out from copper pipes, and two side tubes for gas introduction (10 mm in diameter, 30 mm in length) were connected in an air-tight fashion to each cylinder. Aluminium foils of a known thickness (about 3·5 mg/cm^2) were adhesive-stuck so as to be airtight to both its brims to make its base surfaces. Containers of the target gas 25 mm thick were thus prepared.

A number of these containers were connected in series with short rubber tubes. For filling with neon, the containers were put in a desiccator, which was first evacuated completely and then filled with neon to exactly 1 atm. The desiccator was opened, and the rubber tubes were quickly pinch-cocked to shut up the neon in each container separately. For filling with oxygen, oxygen was streamed through the connected containers for a sufficient time.

For bombardment, from 5 to 15 of these containers were closely lined up on an electrical insulator and set in an external beam path of the cyclotron of the Institute of Physical and Chemical Research (160 cm, variable energy, ordinary-type cyclotron). A thin aluminium foil was placed just before the first container to protect it from contamination by radio nuclides recoiling from outside. Also, aluminium foils of convenient thicknesses were often inserted between the containers in order to lower the beam energy and to facilitate the monotoring of activities formed in the foil aluminium itself. A titanium foil 20 μm thick) for the beam-extraction window was set at the end of the beam duct, which was electrically insulated from the cyclotron itself but connected to the target containers for the beam-current reading.

The target assembly was then placed close to the extraction window and bombarded with a charged particle beam (0·3–1 μA, 5–15 min), with the beam current being measured by an integrator. The entire shape of the excitation curve was surveyed in the first bombardment; its details were examined in subsequent bombardments with varying incident energies.

Stacks of Mylar foils (3·3 mg/cm^2 thick) were

TABLE 1. Q-value and threshold energy

Bombardment	Predominate reaction	Q-value (MeV)	Threshold energy (MeV)
O + t	$^{16}O(t, n)^{18}F$	+1·270	0
O + ^{3}He	$^{16}O(^3He, p)^{18}F$	+2·003	0
	$^{16}O(^3He, n)^{18}Ne \rightarrow {}^{18}F$	−3·196	3·795
O + α	$^{16}O(\alpha, pn)^{18}F$	−18·544	23·180
	$^{16}O(\alpha, 2n)^{18}Ne \rightarrow {}^{18}F$	−23·773	29·716
Ne + d	$^{20}Ne(d, \alpha)^{18}F$	+2·796	0
Ne + ^{3}He	$^{20}Ne(^3He, \alpha p)^{18}F$	−2·697	3·102
	$^{20}Ne(^3He, \alpha n)^{18}Ne \rightarrow {}^{18}F$	−7·296	9·115

also used as oxygen targets in order to compare the excitation curve obtained by the use of the present gas target with that obtained by the use of an ordinary stacked-foil target. The stacks were bombarded with ^{3}He-beams of various incident energies with lower fluxes (5–10 nA).

For the measurement of the thick target yield of the triton reaction, silica disks (300 μm thick, 30 mm in diameter) were used. Two sets of their piles were bombarded with triton beams (1 μA) of different incident energies. We have had no further chance to bombard with tritons.

2.2 *Activity measurement and data treatment*

A NaI scintillator (3 in. × 3 in.) with a 100-channel analyzer was usually used for the activity measurement. One base surface of the bombarded gas container was placed on a glass plate set about 30 cm upward from the scintillator. The other base surface was covered by a glass plate for the complete annihilation of the positrons.

The γ-ray spectrum was measured, with the front surface of the container first set towards the lower side and then inverted to the upper side. The measurements were usually repeated several times at about 1-hr intervals, but when the spectrum or decay curve showed the presence of an interference activity, it was continued further with longer intervals. In some cases, the insides of the target containers were washed with a dilute acid for the elution of the entire activities, which were then measured.

A standard ^{22}Na source was used for the determination of the counting efficiency. In order to examine the effect of the distribution of the activity within the container on the counting efficiency, the standard source was set at several positions and its activity was measured.

The spectra thus obtained were treated by Covell's method, and the decay curves were analyzed to give the ^{18}F activities. The reported range-energy relationships were used for the calculation of: (1) the beam energy at each position of the target assembly, and (2) the thick target yields from the obtained excitation curves.

3. RESULTS AND DISCUSSION

3.1 *Excitation curves and thick target yields*

The excitation curves are shown in Figs. 1 and 2. Figures 3–5 show the thick target yields as saturation activities in dps/μA, which are identical with the production rates.

In the ^{3}He-particle reaction of oxygen, the present excitation curves agree with the results

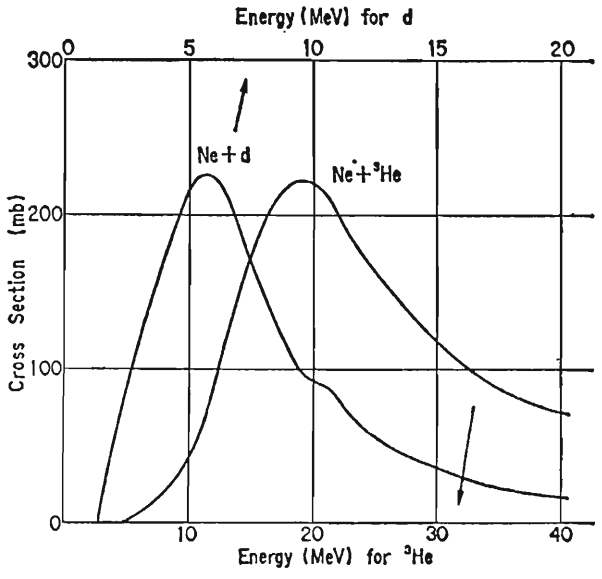

FIG. 1. Excitation curves for the reactions of deuteron and ^{3}He-particle on neon to give ^{18}F.

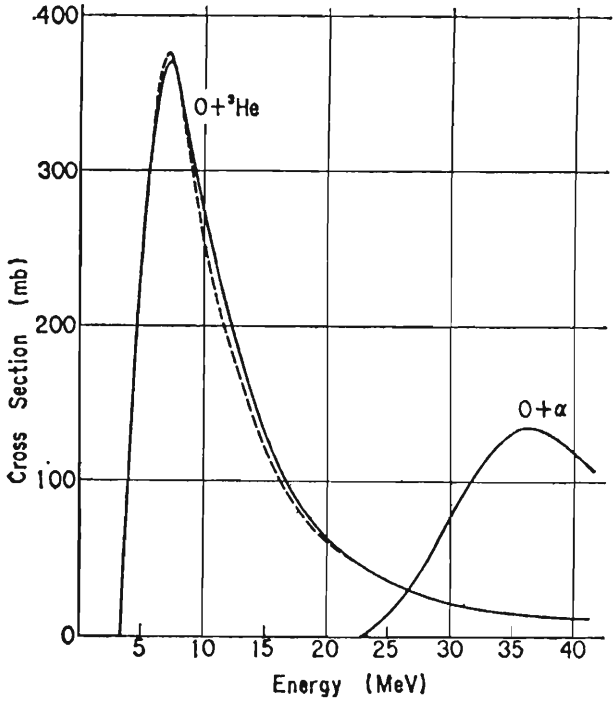

FIG. 2. Excitation curves for the reactions of ^{3}He-particle and α-particle on oxygen to give ^{18}F. —measured by the gas target; – – – measured by the stacked foil target.

of MARKOWITZ *et al.*,[5] though some apparent broadening of the peak is observed in the curve obtained by the gas target. This broadening is probably due to the larger thickness of the target. For the α-particle reaction of oxygen, noticeable discrepancies are found between the present curve and the curves we reported

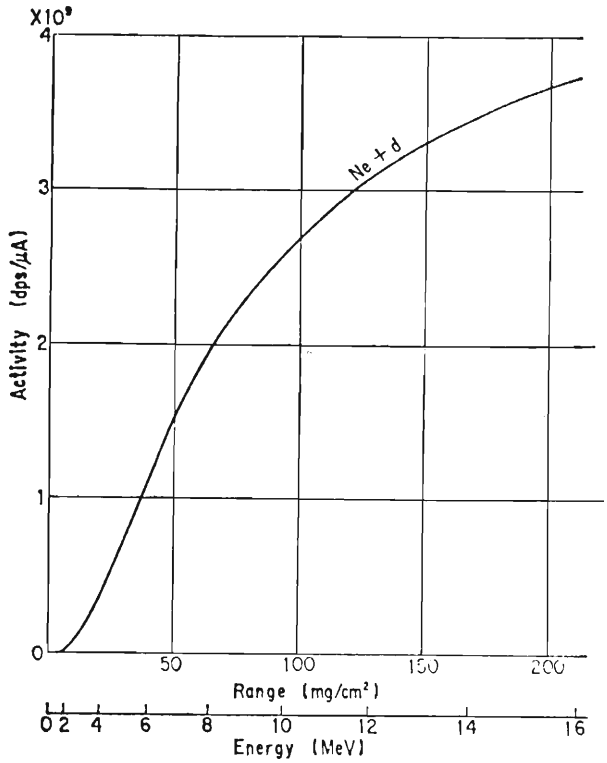

FIG. 3. Thick target saturation activity for the reaction of deuteron on neon to give ^{18}F.

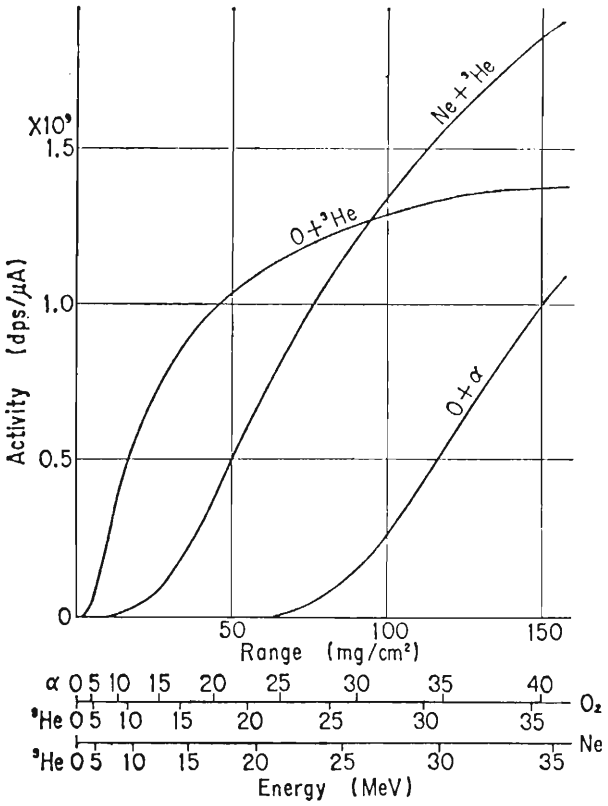

FIG. 4. Thick target saturation activities for the reactions of ^{3}He-particle on oxygen, ^{3}He-particle on neon, and α-particle on oxygen to give ^{18}F.

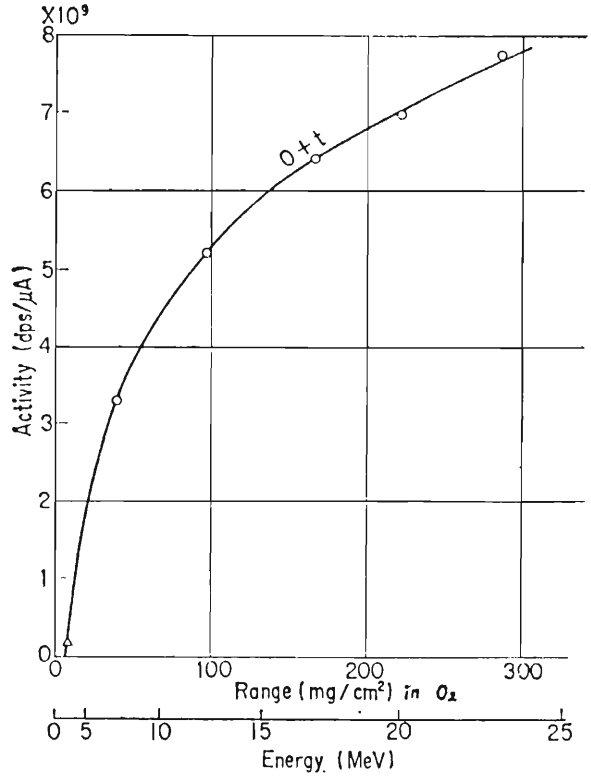

FIG. 5. Thick target saturation activity for the reaction of triton on oxygen to give ^{18}F.

previously.[2,6] The discrepancies can be regarded as due to experimental faults in our previous measurement, e.g. the use of a Na_2CO_3 target which gives ^{18}F also by the $^{23}Na(\alpha, 2\alpha n)$ ^{18}F reaction. Actually, the present curves agree with the results of several workers.[7]

As for the accuracy of the present curves, the absolute cross section might involve up to a 10 per cent uncertainty. However, the relative value of the thick target yield within each of the reactions as well as among them can be thought to be sure within an uncertainty range of 5 per cent, except in energy regions notably below the maximum of the excitation curve.

3.2 *Consideration of practical* ^{18}F *production*

In the practical production of ^{18}F, the following things should be considered in addition to the yield: (1) radiochemical impurities in the product, (2) the accessibility of the particle acceleration and ease of bombardment, and (3) the chemical and physical state of the target as well as of the product. The bombardment under a maximum available energy is

regarded as often unprofitable because: (1) the formation of radiochemical impurities generally increases with energy, (2) the total heat evolved is exactly proportional to the incident energy, and the rate of total radiation decomposition is approximately proportional to it, and (3) the thick target yield does not increase steeply with the energy for energy regions far above the maximum of the excitation curve.

3.3 *Impurities in the product*

In order to use the ^{18}F product for bone scanning, its radiochemical purity should be severely controlled. However, when it is used for the synthesis of ^{18}F-labelled compounds, usually the impurity activities are not incorporated in the product; thus, their presence is permissible.

The possible by-products of the present reactions with half-lives longer than 5 min are ^{3}H, ^{7}Be, ^{10}Be, ^{11}C, ^{14}C, ^{13}N, ^{22}Na and ^{24}Na, the last two being formed only from neon. No notable activities of ^{3}H, ^{10}Be and ^{14}C can occur, however, because of their long lives. The contamination of the ^{18}F with moderate quantities of ^{11}C and ^{13}N is permissible, unless the ^{18}F is measured soon after the bombardment, because of their short lives. In the bombardment of an oxygen target, however, the high yields of the following reactions should be taken into account: (1) $^{16}O(^{3}He, 2\alpha)^{11}C$ for ^{3}He energies over 20 MeV,[8] and (2) $^{16}O(^{3}He, \alpha)^{15}O$ for lower ^{3}He energies (half-life of ^{15}O, 2 min). A triton-bombarded target is naturally contaminated seriously with ^{3}H.

The formation of ^{7}Be by the ^{3}He reactions on oxygen and neon is known; the cross sections have been shown to be from a few to several milli-barns at a ^{3}He energy of 25 MeV.[9] A notable contamination of the ^{18}F with ^{7}Be is thus regarded as inevitable for an incident ^{3}He energy over 15 MeV. The deuteron-bombarded neon does not contain ^{7}Be when the incident energy is under 10·75 MeV, which is the threshold energy of the $^{20}Ne(d, ^{15}N)^{7}Be$ reaction. The threshold energy of the $^{16}O(t, ^{12}B)^{7}Be$ reaction is also as high as 22·47 MeV. The α-particle bombardment of oxygen is thought to give less ^{7}Be than the ^{3}He-particle bombardment, because only in the latter can there be some contribution of the pick-up reaction in which the incident ^{3}He-particle picks up an α-particle cluster in the target nucleus to form ^{7}Be.[10]

From neon, ^{22}Na is formed by the reactions of $^{20}Ne(^{3}He, p)^{22}Na$, $^{22}Ne(d, 2n)^{22}Na$, etc. A noticeable ^{22}Na activity was actually found in neon bombarded with 25 MeV ^{3}He-particles, but the bombardment with 9 MeV deuterons gave a much lower ^{22}Na activity. Among the present bombardments, only the reaction of $^{22}Ne(^{3}He, p)^{24}Na$ gives ^{24}Na. Since the Q-value of this reaction is as positively high as +8·04 MeV, no high activity of ^{24}Na can be formed in ^{3}He energy ranges over 15 MeV.

Beside the radio-impurities formed from the target element itself, contamination with radionuclides recoiled from the beam-window foil of the target container should be considered. It is well known that the higher the energy and mass of the incident particle, the higher the recoiled-out fraction from a foil of a given thickness. In the practical ^{3}He-bombardment of water, titanium foil is often used because of its high corrosion resistivity in oxidizing solutions, though the product is unavoidably contaminated with ^{48}V, ^{48}Cr, etc.

3.4 *Accessibility and ease of particle acceleration*

Deuterons of 10 MeV energy can usually be obtained with more ease and with a higher flux than α-particles of 40 MeV energy by the use of an ordinary-type cyclotron. With compact AVF cyclotrons now commercially available, deuterons and ^{3}He-particles can be accelerated up to or over the required energy for the present purpose, but the maximum α-particle energy is deficient. The triton acceleration is not easily accessible because of the possible hazard due to tritium contamination.

3.5 *Ease of bombardment*

As can easily be understood from Figs. 1–4, the spatial distribution of ^{18}F just formed in the target gas of a given pressure and temperature possesses a peak whose width is the narrowest for the reaction of O + ^{3}He, slightly broader for the three reactions of Ne + ^{3}He, Ne + d, and O + t, and the broadest for the reaction of O + α. It is clear that the narrower the distribution, the smaller the required target

size, and thus the easier the bombardment technique.

In the practical bombardment of a gas target with a maximum available flux, the possible rupture of beam-extraction foil often makes the most serious problem. The principal cause of the rupture is usually the heat evolved in the foil, with additional effects of the chemical reaction of the foil with gases in contact and radiation damage. It is thus clear that the rupture possibility is higher (1) in the ^{3}He- and α-bombardments than in the deuteron and triton bombardments, and (2) for a lower particle energy than for a higher energy under a given beam flux; also it is higher in the absence of an efficient cooling of the window than in its presence.

The ^{3}He-bombardment of oxygen gas is the least favorable in view of the foil rupture, but the ^{3}He-bombardment of water has been widely used for the production of ^{18}F for bone scanning. We have experienced no rupture of titanium beam-extraction foils of various thicknesses in contact with target water for ^{3}He-beams of 30 μA flux and 18 MeV energy.

3.6 *Target and product*

Since neon is an expensive gas, it should be bombarded in a closed container or in a closed circulation system. Oxygen can be bombarded in various chemical and physical states. In the bombardment of O_2 and H_2O, however, oxidizing products, such as O_3 and H_2O_2 are formed, and they often attack the inside wall of the bombardment vessel.

The ^{18}F formed in Ne and O_2 is easily adsorbed on many substances. According to our experience, the adsorption could be made almost quantitative in the initial stage of bombardment, but became less and less complete as the bombardment proceeded. The adsorbability depended, of course, on the nature and surface conditions of the adsorbent, but was found to be slightly higher from neon than from oxygen. The ^{18}F adsorbed on glass, plastics, and noble metals can be eluted by liquids or some fluorine-containing gases, though an almost quantitative elution is usually difficult.

Many ^{18}F-containing solid fluorinating agents, such as KF, SbF_3, and $NaBF_4$ can be prepared conveniently by the bombardment of neon slightly compressed in a closed container, with its inside wall covered by a thin layer of the agents, under efficient external cooling. Labelled gaseous fluorinating agents, such as F_2, BF_3 and NOF, can be prepared by the bombardment of neon containing them or by the elution of the adsorbed ^{18}F with them diluted in an inert gas or solvent.

The solid fluorinating agent thus obtained contains ^{18}F only in the superficial layers of its grains. When the fluorination reaction is conducted in a partial solution of this agent, as is usual in halogen-interchange fluorination, the superficial layers react before the inner parts. Thus, the ^{18}F can be concentrated in the small fraction of the product formed in the beginning stage of the reaction. An example is shown in Fig. 6; ethyl monochloroacetate (0·10 mol) and $K^{18}F$ prepared as above (0·21 mol) were heated in acetamide to give ethyl monofluoroacetate, which was continuously separated from the mixture by a simple fractional distillation.

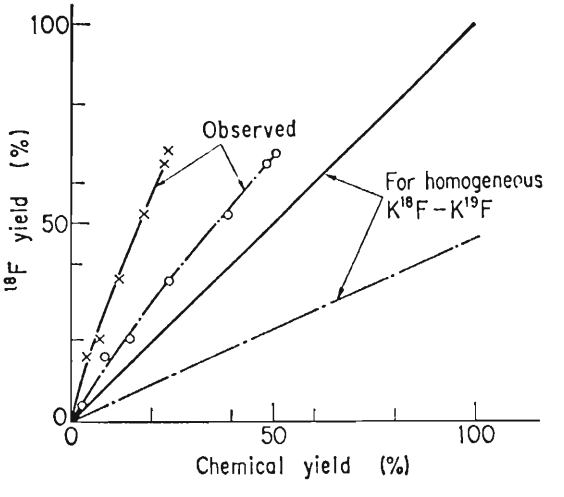

FIG. 6. ^{18}F-yield vs. chemical yield for the reaction of

$$K^{18}F + CH_2ClCO_2Et \rightarrow CH_2{}^{18}FCO_2Et.$$

— × — : yield based on KF;
— — — ○ — — —: yield based on CH_2ClCO_2Et.
Observed: Experimental result in the use of KF containing ^{18}F only in superficial layers of its grains.
For homogeneous $K^{18}F$–$K^{19}F$: Theoretical relationship for a homogeneous solid solution of $K^{18}F$ in $K^{19}F$.

The direct labelling of organic compounds by the ^{18}F formed in neon has been reported;[11] we also have used this technique with some success. However, the possible radiation decomposition of the compounds by scattered charged particles and secondary photons should be taken into account in the design of the experimental arrangement.

3.7 *Usefulness of each bombardment*

As has been described above, the deuteron bombardment of neon is the most convenient method of producing anhydrous ^{18}F for the labelling of organic compounds. The ^{3}He-bombardment of water, on the other hand, is a useful technique of producing ^{18}F for bone scanning.

The excitation curves of the ^{3}He reactions in Figs. 1 and 2 show that in energy regions over 15 MeV, neon gives a much higher ^{18}F activity than oxygen; under 10 MeV, only oxygen offers a sufficiently high yield of ^{18}F. Thus, both anhydrous and aqueous ^{18}F can be simultaneously obtained in good yields by the following bombardment: ^{3}He-particles of an incident energy over 25 MeV are caused first to traverse a neon target of such a thickness as to reduce their energy to about 15 MeV and then to enter a water target through a thin separation foil. We have actually used this technique with some success, but further efforts to develop beam-window foils more durable to higher flux bombardments, as well as to improve the cooling techniques, are now being made. A thick foil or a foil with a high atomic number is not convenient because of the scattering of incident particles.

The triton bombardment is not practical for routine ^{18}F production because of the limitation of triton acceleration and because of the contamination of product with tritium. The triton reaction, on the other hand, is believed to be more suitable for the activation analysis of trace oxygen than the ^{3}He- or α-particle reaction, because fewer elements can interfere and because the triton has a longer range, which makes easier the surface-contamination removal after the bombardment.[12] The threshold energies of the triton reactions on F, Na, and Al to give ^{18}F are all higher than 12 MeV. The reaction of $^{20}Ne(t, \alpha n)^{18}F$, with its threshold energy of 3·98 MeV, is probably the sole interference reaction in the oxygen determination.

Acknowledgements—The authors are indebted to the Cyclotron Group of our institute for their services in the cyclotron bombardment. Also, we appreciate very much the collaboration of Dr. MICHIAKI FURUKAWA, Dr. SANSHIRO KUME and Dr. RIKI SEKI in the triton experiment.

REFERENCES

1. CLARK J. C. and SILVESTER D. J. *Int. J. appl. Radiat. Isotopes* **17,** 151 (1966).
2. NOZAKI T., TANAKA Y., SHIMAMURA A. and KARASAWA T. *Int. J. appl. Radiat. Isotopes* **19,** 27 (1968).
3. FOWLER J. S., FINN R. D., LAMBRECHT R. M. and WOLF A. P. *J. nucl. Med.* **14,** 63 (1973).
4. CLARK J. C., GOULDING R. W., ROMAN M. and PALMER A. J. *Radiochem. Radioanal. Letts* **14,** 101 (1973).
5. MARKOWITZ S. S. and MAHONY J. D. *Analyt. Chem.* **34,** 329 (1962).
6. FURUKAWA M. and TANAKA S. *J. phys. Soc. Japan* **16,** 129 (1961).
7. RAUTENBACH W. L., STEYN J., RICHARDS D. and SMITH H. J. *Uses of Cyclotrons in Chemistry, Metallurgy and Biology* (Edited by C. B. AMPHLET), p. 365. Butterworths, London (1970).
8. KRASNOV N. N., DIMITRIYEV P. P., DIMITRIYEVA S. P., KONSTANTINOV I. O. and MOLIN G. A. *Uses of Cyclotrons in Chemistry, Metallurgy and Biology* (Edited by C. B. AMPHLET), p. 341. Butterworths, London (1970).
9. MIKUMO T., SEKI R., TAGISHI Y., FURUKAWA M. and YAMAGUCHI H. *Phys. Letts* **23,** 586 (1966).
10. DETRAY C., DUHM H. H. and HAFNER H. *Nucl. Phys.* **A147,** 488 (1970).
11. LEBOSITZ E., RICHARDS P. and BARANOSKY J. *Int. J. appl. Radiat. Isotopes* **23,** 392 (1972).
12. NOZAKI T., YATSURUGI Y. and AKIYAMA N. *J. radioanal. Chem.* **4,** 87 (1970).

Reprinted from Radiat. Res., 77, 250–258 (1979).

Inactivation of Phage ϕX 174 by Accelerated Ions

Enhanced δ-Ray Effect by Air Layer in Front of the Samples

FUMIO YATAGAI, SHIGERU KITAYAMA, AND AKIRA MATSUYAMA

The Institute of Physical and Chemical Research, Saitama-ken 351, Japan

YATAGAI, F., KITAYAMA, S., AND MATSUYAMA, A. Inactivation of Phage ϕX 174 by Accelerated Ions. Enhanced δ-Ray Effect by Air Layer in Front of the Samples. *Radiat. Res.* **77**, 250–258 (1979).

Different inactivation rates of phage ϕX 174 were observed between two irradiation methods for charged particles. In method EA, phage particles were spread on a thin film and exposed to air during irradiation. In method CF, the phage sample was covered with a thin polycarbonate film to eliminate the effect of secondary electrons ejected from air in front of the sample. The apparent inactivation efficiency of primary particles determined by method EA was found to be higher than that found by method CF in the case of both α-particles and nitrogen ions. The observed increase in inactivation can be explained by the dispersed energy loss of secondary electrons produced in air as compared with those produced in polycarbonate.

INTRODUCTION

Various effects of high-LET radiations on biological materials, such as phages and bacterial and mammalian cells, in air have been investigated in thin layers in order to avoid a substantial change of LET while the particles pass through the samples. Investigators have taken advantage of this track-segment irradiation method (*1*) to obtain more detailed information on the LET dependence of biological effects. Such studies have demonstrated the oxygen effect (*2*, *3*), but the effect of δ rays ejected from environmental gases in front of samples has rarely been discussed. While charged particles are passing through the air layer in front of the samples, secondary electrons with appreciably long ranges in air will be ejected from the track core. Some fraction of them is likely to strike the biological samples, even if they are far from the track core. Such a δ-ray effect should be more easily detected by using a biological system that shows one-hit kinetics.

In the present paper, we are presenting the inactivation rates of phage ϕX 174 obtained with charged particles under two different irradiation conditions. The observed difference due to the air-layer effect will also be discussed from the viewpoint of the δ-ray effect.

MATERIALS AND METHODS

1. Phage Sample

Bacteriophage ϕX 174, which contains single-stranded circular DNA, was grown and purified by essentially the same procedure as that described by Sinsheimer (*4*). The purified phage was suspended in sodium borate buffer and stored below 5°C until use. Stock solutions of the phage were diluted 100-fold with TPG–CA medium (0.5 g NaCl, 8.0 g KCl, 1.1 g NH_4Cl, 0.8 g sodium pyruvate, 1.0 g KH_2PO_4, 12.1 g tris(hydroxymethyl)aminomethane, and 2.7 g casamino acids in 950 ml H_2O; pH 7.4) just before use. A 10-μl aliquot of the suspension was spread on a polycarbonate film (Nucleopore) 8 mm in diameter, 5 μm in thickness, and 0.03 μm in pore size. The polycarbonate film was placed on a paper pad containing TPG–CA medium to protect the phage against drying during irradiation. Survivors of ϕX 174 after irradiation were determined as plaque-forming units on a lawn of *Escherichia coli* C cells.

2. Irradiation Conditions for Phage Samples

The phage was bombarded with α-particles or N-ions in air at room temperature ($\sim$20°C) using two different methods for irradiation as shown in Fig. 1. Figure 1a shows the method in which the sample spread on polycarbonate film is covered with a film of the same material to eliminate the effect of δ rays that would be ejected from air in front of the sample (method CF). In the other method (EA) the sample on polycarbonate film is exposed to air during irradiation [Fig. 1b] with a polycarbonate film of the same type placed about 2 mm ahead of the sample so that the entrance energy of ions at the surface of the sample was equal to that in the CF method.

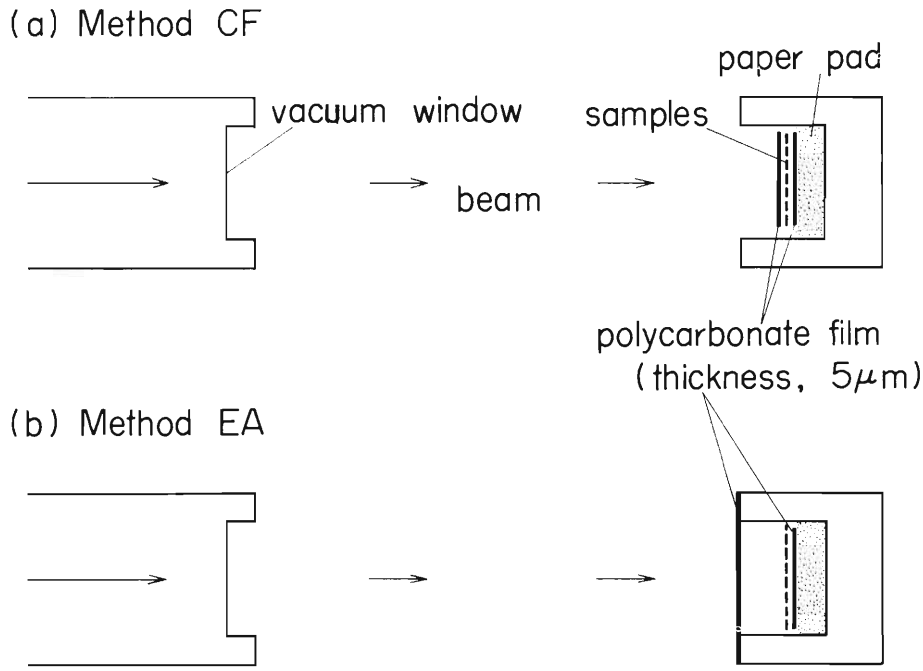

FIG. 1. A schematic diagram for cyclotron-beam irradiation of phage ϕX 174 (see text). (a) In method CF, the sample is spread on a polycarbonate film and is covered with a film of the same type. (b) In method EA, the sample is exposed to air during irradiation.

Since the highest energy of secondary electrons in this experiment is approximately 10 keV and the range of electrons is below about 2.5 μm in water, the secondary electrons ejected from the air just in front of the sample cannot pass through the 5-μm-thick polycarbonate film. Therefore, method CF can be considered as a good approximation to the irradiation of biological samples in water.

Unirradiated samples were also mounted in the holder during irradiation under the same condition as irradiated samples. Approximately the same number of phages was recovered from the unirradiated films with the two methods.

3. Irradiation and Dosimetry

Alpha particles and nitrogen ions were accelerated by the IPCR cyclotron. Before reaching the sample on the polycarbonate film, each ion beam passed through collimators, a scattering foil for dosimetry, an aluminum vacuum window, an air gap, and an absorber foil. The absorber foil was placed about 7 mm ahead of the sample in the air gap (not shown in Fig. 1).

As shown in Table I, the entrance energy of the ions at the surface of sample was adjusted by changing the initial energy of the accelerated particles and the thickness of the aluminum absorber. Beam energy and LET values in Table I were calculated from range–energy tables given by Northcliffe and Schilling (*5*). From these calculations, the difference in beam energy between the two methods due to the different positions of polycarbonate film was found to be negligible. Since the pores in polycarbonate film occupy only 0.4% of the whole area and may be filled with water, the effect of pores on beam energy or LET at the site of sample was neglected.

As the size of a main-beam spot (2 mm square) is smaller than the film (8 mm in diameter) on which the ϕX 174 was spread, the sample was moved across the beam axis in both the horizontal and vertical directions to be uniformly irradiated. Photographic paper was used to check the beam alignment and dose uniformity. The particle fluence was determined by replacing the sample with a Faraday cup according to the method of Kochanny *et al.* (*6*). The flux of charged particles was regulated in order to finish the irradiation of each sample within 1 to 5 min. Detailed procedures for the cyclotron-beam irradiation and dosimetry have been described (*7*).

TABLE I

Beam Energy and LET Values for Different Experimental Conditions Used

Experiment	*Particle*	E_i[a] (*MeV/amu*)	*Scattering foil* (*thickness, μm*)	*Vacuum window* (*thickness, μm*)	*Thickness of air gap* (*mm*)	*Aluminum absorber* (*thickness, μm*)	E_t[b] (*MeV/amu*)	LET_∞[c] (*keV/μm*)
I	α	4.0	Ni (3)	Al (25)	43	+ (50)	1.23	34
II	α	5.5	Au (2)	Al (25)	45	—	4.62	110
III	N-Ion	5.5	Au (2)	Al (15)	37	+ (15)	1.38	850
IV	N-Ion	6.8	Au (2)	Al (15)	37	—	4.65	400

[a] E_i: Initial energy of the accelerated ions.
[b] E_t: Beam energy at the site of target.
[c] LET_∞: Value of LET_∞ at the site of target.

Phage ϕX 174 was also irradiated with γ rays at a dose rate of about 11 krad/min. Gamma irradiations were performed using methods similar to those in the case of accelerated particles and also by using an aqueous phage suspension bubbled with air.

RESULTS AND DISCUSSION

As shown in Fig. 2, the survival curve of ϕX 174 following γ irradiation in aqueous solution bubbled with air was exponential with a D_{37} of about 120 krad. This result was consistent with that of Freifelder (*8*).

The phage ϕX 174 spread on a polycarbonate film was also irradiated with γ rays using the two different methods, CF and EA. As can be seen in Fig. 2, there was no substantial difference in the inactivation rates obtained with these two methods, and the rates were also similar to that of the suspension described above. Thus, method CF can be considered as irradiation under aerobic conditions.

Survival curves obtained for irradiation with α-particles and N-ions are shown in Fig. 3. These curves indicate some deviation from first-order or one-hit kinetics toward a decrease in inactivation rate at higher fluences of primary

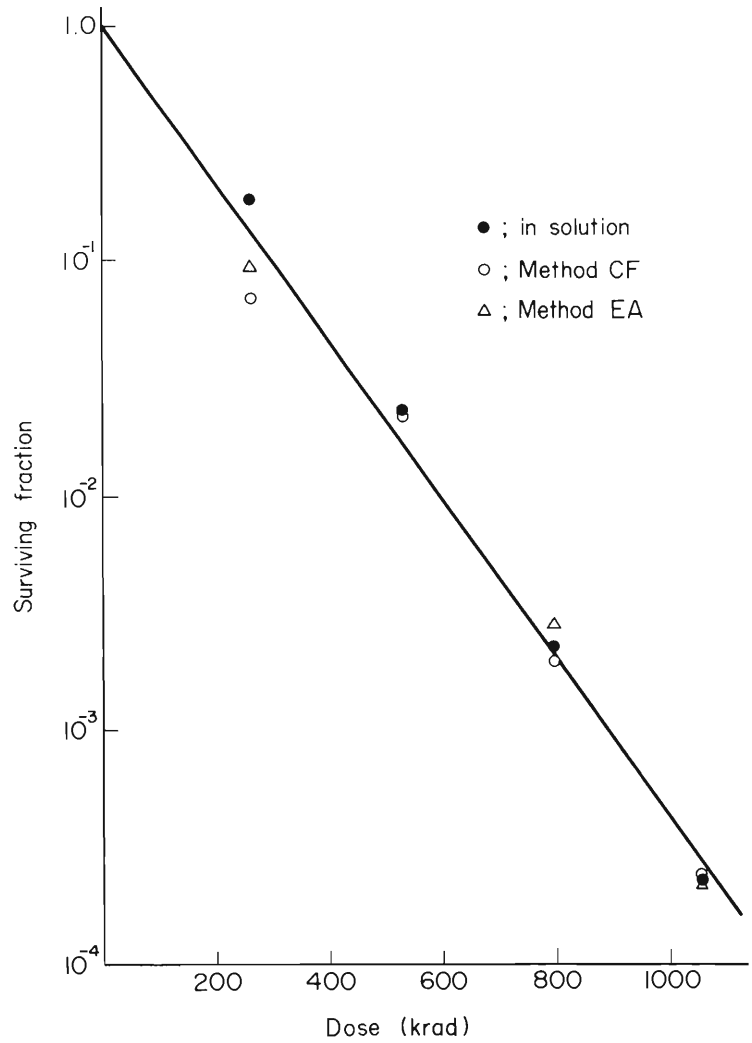

FIG. 2. Survival curve of ϕX 174 for ^{60}Co γ-ray irradiation (see text).

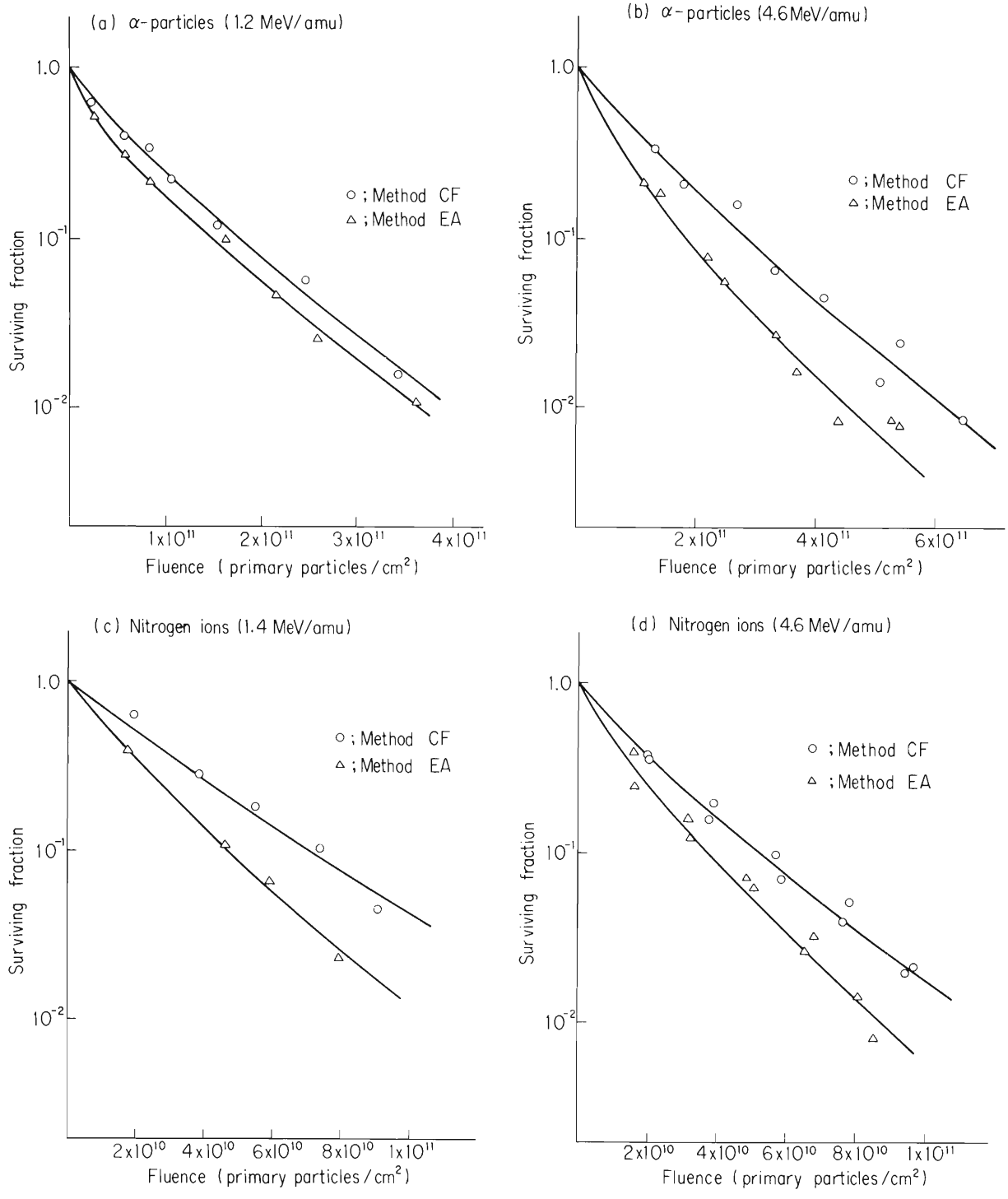

FIG. 3. Survival curves of ϕX 174 obtained by the two different methods for cyclotron-beam irradiation; (a) α-particles of 1.2 MeV/amu (L_∞ = 110 keV/μm), (b) α-particles of 4.6 MeV/amu (L_∞ = 34 keV/μm), (c) N-ions of 1.4 MeV/amu (L_∞ = 850 keV/μm), and (d) N-ions of 4.6 MeV/amu (L_∞ = 400 keV/μm) (see text).

particles. As can be seen in Fig. 3, this tendency is more pronounced in the curves obtained with method EA than in those obtained with method CF. A similar tendency has been observed with heavy-ion irradiation of ϕX 174 (9) and of coliphage λ and its DNA (*10*). Although such nonlinearity cannot be fully explained at present, it may be due to spatially inhomogeneous deposition of energy and/or some other effects caused by the irradiation conditions (*10*).

TABLE II

Apparent Inactivation Efficiency of Primary Particles and Estimation of the Contribution of the δ-Ray Effect

Particle beam energy (MeV/amu)	*α-Particle 4.6*	*α-Particle 1.2*	*N-Ion 4.6*	*N-Ion 1.4*
F_{10}^{CF} (primary particles/cm²)	2.76×10^{11}	1.81×10^{11}	5.28×10^{10}	7.15×10^{10}
F_{10}^{EA} (primary particles/cm²)	1.84×10^{11}	1.45×10^{11}	3.78×10^{10}	4.77×10^{10}
Enhancement ratio (F_{10}^{CF}/F_{10}^{EA})	1.50	1.25	1.40	1.50
S^{CF} (cm²)	8.36×10^{-12}	1.28×10^{-11}	4.37×10^{-11}	3.22×10^{-11}
S^{EA} (cm²)	1.25×10^{-11}	1.59×10^{-11}	6.10×10^{-11}	4.82×10^{-11}
$(S^{CF} - S_0{}^a)/S_0{}^a$	3.92	6.53	24.7	17.9
$(S^{EA} - S_0{}^a)/S_0{}^a$	6.36	8.35	34.9	27.3

[a] S_0: Geometrical cross section of the DNA in the phage, calculated from the physical-chemical molecular weight as a sphere of density 1.7 g/cm³ containing the viral DNA (*9*).

The apparent inactivation efficiency (AIE) of primary particles was estimated from the primary-particle fluence required for 10% survival, F_{10} (Table II). The enhancement ratios of AIE due to the air-layer effect, F_{10}^{CF}/F_{10}^{EA}, fell in the range 1.24 to 1.50, as shown in Table II. From these ratios, the apparent lethal effect of primary particles on φX 174 is found to be higher with method EA than with method CF in the case of both α-particles and N-ions.

An inactivation cross section, S (S^{CF} and S^{EA}), was calculated from F_{37} ($=0.434 \times F_{10}$) to estimate the contribution of δ rays to the inactivation of phage. Assuming that phage must be inactivated by a traversal of one high-LET particle track through the geometrical cross section, S_0, of DNA in the phage, values of $(S - S_0)/S_0$ may reflect the contribution of δ rays to the inactivation. These calculated values of $(S - S_0)/S_0$ show an increase in δ-ray effect with increasing atomic number of the primary particle, as expected (Table II). It can also be considered from Table II that δ rays produced under the irradiation condition EA contribute to the inactivation more efficiently than those produced under condition CF (Table II).

Secondary electrons should be ejected while the primary particles pass through the phage or through the water which could be supplied by the wet pad behind the film even in method EA. However, the phage size and the water layer thickness would be small enough so one might neglect the contribution of such δ rays for the phage inactivation in method EA. Therefore, the inactivation efficiency of δ rays ejected in air in front of the sample was compared with that of δ rays ejected in the covering film to estimate the enhanced δ-ray effect due to the presence of air (Fig. 4).

Figure 4 shows a schematic view of the cases in which secondary electrons are ejected by a N-ion (4.65 MeV/amu) from air or polycarbonate film in front of the sample under condition EA or condition CF, respectively. This scheme is

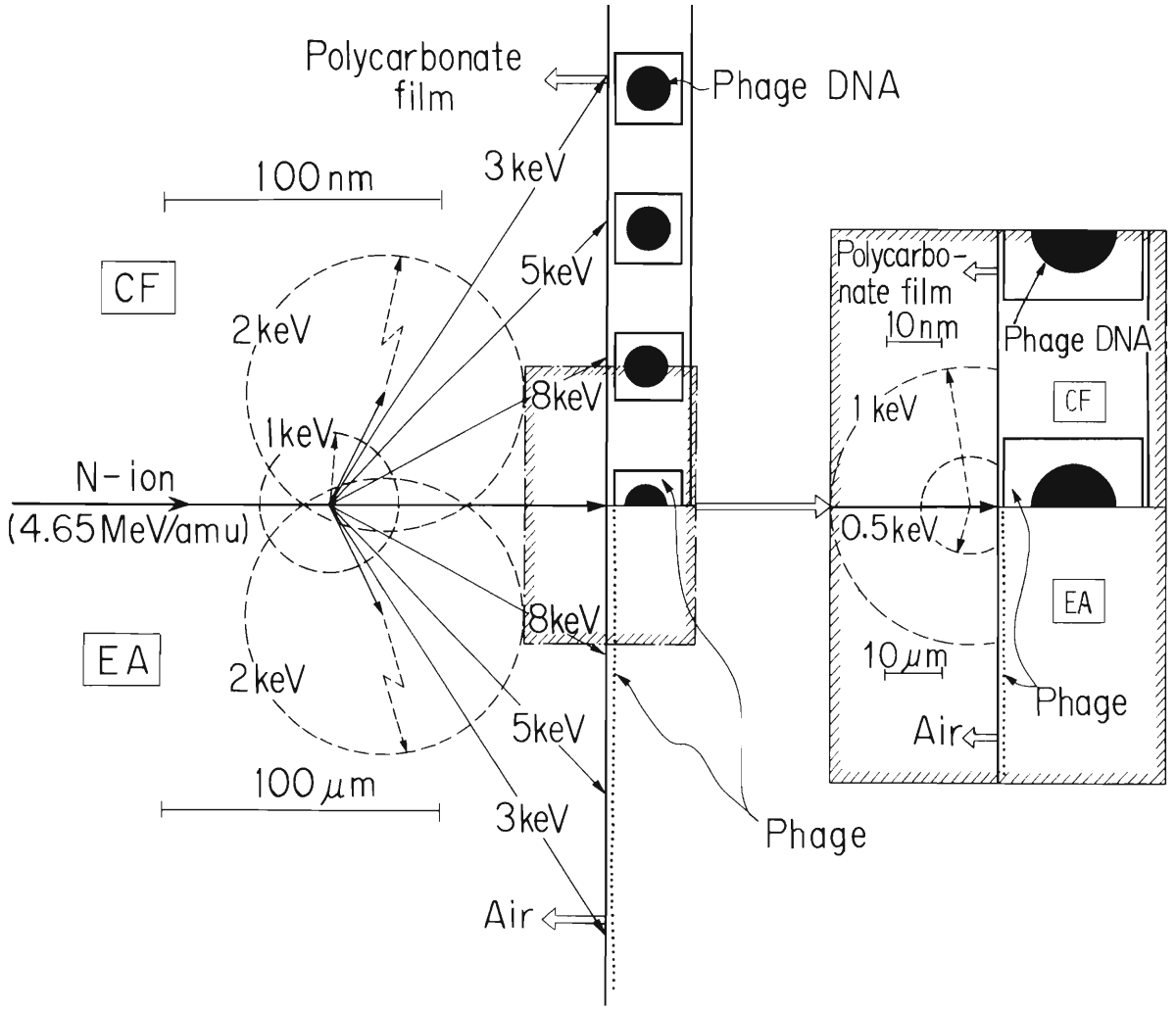

FIG. 4. A Schematic view of a N-ion track (4.65 MeV/amu) projected in a plane perpendicular to the track axis. Secondary electrons with a various energies are assumed to be ejected from a point ahead of the sample, although this is not actually the case. As an example, in the polycarbonate film the point is chosen 0.1 μm in front of the sample (method CF), which corresponds to 0.1 mm in front of the sample in air (method EA). For convenience in comparing the δ-ray effect between the two methods, both methods are shown in the same figure, on different scales (1000 times greater for CF than EA). Methods CF and EA are represented above and below the track axis, respectively. Inset: The special case of relatively low-energy electrons produced at a point extremely close to the sample, for example, 5 nm and 5 μm away in method CF and EA, respectively.

based on the Rutherford Scattering Law, which governs the production of secondary electrons due to knock-on collisions. According to this theory, the spectrum and angular distribution of secondary electrons were considered to be the same for those ejected in air and in polycarbonate (Fig. 4). An angle θ of ejection for an electron with energy ϵ was estimated from the formula, $\cos\theta = (\epsilon/\epsilon_{max})^{\frac{1}{2}}$, which is given by the theory. ϵ_{max} is the maximum energy transfered to an electron, and the calculated value is 10.3 keV in the case of Fig. 4.

In this scheme, it was assumed that secondary electrons having energy greater than 1.6 keV penetrate in an approximately straight path. The length of this straight path was calculated from Bethe stopping-power theory. Instead of range,

mean-square penetration $\langle r^2 \rangle^{\frac{1}{2}}$ was estimated for secondary electrons with energy lower than 1.6 keV because of their diffusive motion (*11*, *12*). Both range and $\langle r^2 \rangle^{\frac{1}{2}}$ of electron in air were also assumed to be 1000 times greater than those in polycarbonate (water) owing to the difference in density between air and the film.

The energy of secondary electrons produced varies up to about 10 keV, and the electron with higher energy is ejected with smaller angle, as illustrated in Fig. 4. A secondary electron ejected in air with a certain energy can hit the phages, even if they are too far from the particle track for an electron ejected in the film with the same energy to strike them. Thus, more of the energy deposited by δ rays is deposited in phage particles in method EA than in method CF.

However, secondary electrons having energies of 3 or 5 keV when ejected in air (method EA) or in the film (method CF) can hit with almost the same efficiency because their ranges are greater than the diameter of a phage even in the case of method CF. Figure 4 also illustrates the case of low-energy secondary electrons which might have an important role in the enhanced δ-ray effect. The mean-square penetration of an electron with energy of 500 eV is shorter than the diameter of a phage under the conditions of method CF, while it is still longer than the target diameter under the conditions of EA. Therefore, the inactivation efficiency of these low-energy electrons would be much higher with method EA than with method CF. Even under the conditions of method EA, an electron with still lower energy would not reach any phage particles other than those traversed by primary particle tracks.

Although this theoretical analysis is difficult to present in more quantitative detail, the observed enhancement of inactivation rate can be explained partially, if not completely, by the δ-ray effect as shown in the above scheme.

ACKNOWLEDGMENTS

The authors are deeply indebted to Dr. Takahashi, Radiation Laboratory, for aid and advice in dosimetric procedures. They also wish to express their appreciation for operation of the cyclotron and interest shown by Professor Kamitsubo and the staff of IPCR Cyclotron Laboratory. This work was supported by research grants from the Science and Technology Agency and Ministry of Education of Japan.

RECEIVED: August 10, 1978

REFERENCES

1. G. W. BARENDSEN, Impairment of the proliferative capacity of human cells in culture by α-particles with differing linear-energy transfer. *Int. J. Radiat. Biol.* **8**, 453–466 (1964).
2. G. J. NEARY, V. F. W. SIMPSON-GILDEMEISTER, and A. R. PEACOCKE, The influence of radiation quality and oxygen on strand breakage in dry DNA. *Int. J. Radiat. Biol.* **18**, 25–40 (1970).
3. E. L. POWERS, J. T. LYMAN, and C. A. TOBIAS, Some effects of accelerated charged particles on bacterial spores. *Int. J. Radiat. Biol.* **14**, 313–330 (1968).
4. R. L. SINSHEIMER, Single-stranded DNA. In *Procedures in Nucleic Acid Research* (G. L. Cantoni and D. R. Davie, Ed.), pp. 569–571. Harper & Row, New York, 1966.
5. L. C. NORTHCLIFFE and R. F. SCHILLING, Range and stopping power tables for heavy ions. *Nucl. Data Tables A* **7**, 233–463 (1970).

6. G. L. KOCHANNY, JR., A. TIMNICK, C. J. HOCHANADEL, and C. D. GOODMAN, Radiation chemistry studies of water as related to the initial linear energy transfer of 11-MeV to 23-MeV protons. *Radiat. Res.* **19**, 462–473 (1963).
7. F. YATAGAI, T. TAKAHASHI, Y. KITAJIMA, and A. MATSUYAMA, Inactivation of bacterial spores by charged particles *J. Radiat. Res.* **15**, 90–95 (1974).
8. D. FREIFELDER, S. T. DONTA, and R. GOLDSTEIN, X-Ray inactivation of bacteriophages: Role of O_2-dependent damage in single- and double-strand DNA phages. *Virology* **50**, 516–519 (1972).
9. P. E. SCHAMBRA and F. HUTCHINSON, The action of fast heavy ions on biological material. II. Effects on Tl and ϕX-174 bacteriophage and double-strand and single-strand DNA. *Radiat. Res.* **23**, 514–526 (1964).
10. S. E. BRESLER, V. L. KALININ, YU. T. KOPYLOVA, A. S. KRIVISKY, V. N. RYBCHIN, and V. N. SHELEGEDIN, Study of genetic effects of high energy radiations with different ionizing capacities on extra-cellular phages. *Mutat. Res.* **29**, 1–20 (1975).
11. A. CHATTERJEE, H. D. MACCABEE, and C. A. TOBIAS, Radial cutoff LET and radial cutoff dose calculations for heavy charged particles in water. *Radiat. Res.* **54**, 479–494 (1973).
12. A. MOZUMDER, Stopping, scattering and penetration of low-energy electrons in water. In *Proceedings of the 3rd Tihany Symposium on Radiation Chemistry, 1971* (J. Dobo and P. Hedvig, Eds.), Vol. II, pp. 1123–1132. Akademia Kiado, Budapest, 1972.

Reprinted from Adv. Space Res., 3, 95–104 (1983).

EFFECT OF HEAVY IONS ON BACTERIAL SPORES

Tan Takahashi, Fumio Yatagai and Shigeru Kitayama

The Institute of Physical and Chemical Research, Wako-shi, Saitama 351, Japan

ABSTRACT

Inactivation of B. subtilis spores has been studied using accelerated He, C, N, O and Ne ions. The energy dependence of the inactivation cross sections for heavy ions was very weak and the mean cross sections for carbon ions (0.6 - 4.7 MeV/amu), nitrogen ions (0.6 - 4.1 MeV/amu), oxygen ions (0.8 - 1.1 MeV/amu), and neon ions (2.2 - 3.7 MeV/amu) were found to be about 0.22, 0.23, 0.26, and 0.33 μm^2, respectively. Analysis was carried out along lines similar to Katz's target theory but the parameters were chosen so that they have an experimental basis.

INTRODUCTION

Inactivation of B. subtilis spores by heavy ions has been studied by several investigators, and new progress has recently been made by Schäfer, Facius, Baltschukat and Bücker[1] and by Horneck and Bücker[2] who use heavy ions ranging from carbon to uranium for the inactivation of the spores. In earlier papers [3,4] we analyzed our data by the track segment method [5,6,7], by Powers, Lyman and Tobias's theory [8] and by Oda's theory [9]. In recent papers [10], we attempted to apply Katz's theory [11,12]. Katz's theory seems to explain fairly well the inactivation cross sections of E. coli B/r but it is difficult to reconcile with the experimental survival curve of B. subtilis spores for gamma-rays if the theory is used in its original form. In this paper, we attempt to modify Katz's theory to get a more realistic idea on the inactivation processes. For instance, in analyzing our data and inactivation cross sections for the very heavy ions studied by Schäfer et al.[1], the area of "sensitive element" πa^2 in Katz's theory is chosen so that it corresponds to the spore core area, as will be described below. Experiments using Ne ions are also made and preliminary results are shown.

MATERIALS AND METHODS

Biological samples. Spores of Bacillus subtilis 168 requiring thymine, indole, and leucine for growth were purified by the treatment with lysozyme and sodium dodecylsulfate (SDS) [13]. The purified spores were suspended in sterile distilled water and stored below 5°C until use. For charged particle irradiation, a 20 µl aliquot of the spore suspension (10^9 spores/ml in M/15 phosphate buffer, pH 7.0) was spread on a membrane filter (Millipore filter type HA) 8 mm in diameter, which had been placed on a wet paper pad [3]. After irradiation, the surviving fraction of the spores were measured by a visible colony counting method using Schaefer's agar plates [3].

Irradiation conditions. He, C, N, O, and Ne ions were accelerated by the IPCR cyclotron. Before reaching the sample on the membrane filter, each ion beam passed through collimators, slits, a scattering foil, an aluminum vacuum window, an air gap, and an absorber foil. The absorber foil was placed about 7 mm ahead of the sample in the air gap. The entrance energy of the ions at the surface of the sample was adjusted by changing the initial energy of the accelerated particles and the thickness of the aluminum absorber [14]. The LET_∞ values were obtained from the range-energy tables given by Northcliffe and Schilling [15].

As the size of a main beam spot (2 mm square) is smaller than the area of the filter (8 mm in diameter) on which the samples to be irradiated were spread in a thin layer, the filter was moved in a plane perpendicular to the beam axis so as to be uniformly irradiated [14]. A new apparatus, which became available only recently, was used for irradiation with Ne ions. This apparatus permitted us to irradiate samples by the beam elastically scattered by a Au foil (thickness, 2µm) at a small angle (2° 45') with respect to the beam axis [16]. The sample filter mounted on a holder faced the vacuum window and could be rotated to obtain

uniform irradiation because of the fact that the relative intensity of the scattered beam decreases with increasing scattering angle. In both irradiation systems, solid state detectors and a Faraday Cup were used for the determination of particle fluence according to the method of Kochanny et al. [17]. Gamma irradiations were performed using an aqueous suspension of spore (10^7 spores/ml in M/15 phosphate buffer, pH 7.0) under bubbling with air.

DOSE AROUND THE TRAJECTORY OF AN ION

Katz's Dose D_{KZ}. Among several formulae given by Katz, we adopt here the simplest formula for the dose [11] deposited by secondary electrons, $D_{KZ}(x)$ where x is the distance from the path of an ion:

$$D_{KZ} = \frac{CZ^{*2}}{2\pi x\beta^2}\left(\frac{1}{x} - \frac{1}{X_m}\right). \tag{1}$$

Here, C is a constant (C = 0.85 keV/μm for water), Z*e is the effective charge of an ion, βc is the speed of the ion (c is the speed of light) and X_m is the range of the delta electrons having maximum kinetic energy. The effective charge is given by

$$Z^* = Z[1 - \exp(-125\beta Z^{-2/3})] \tag{2}$$

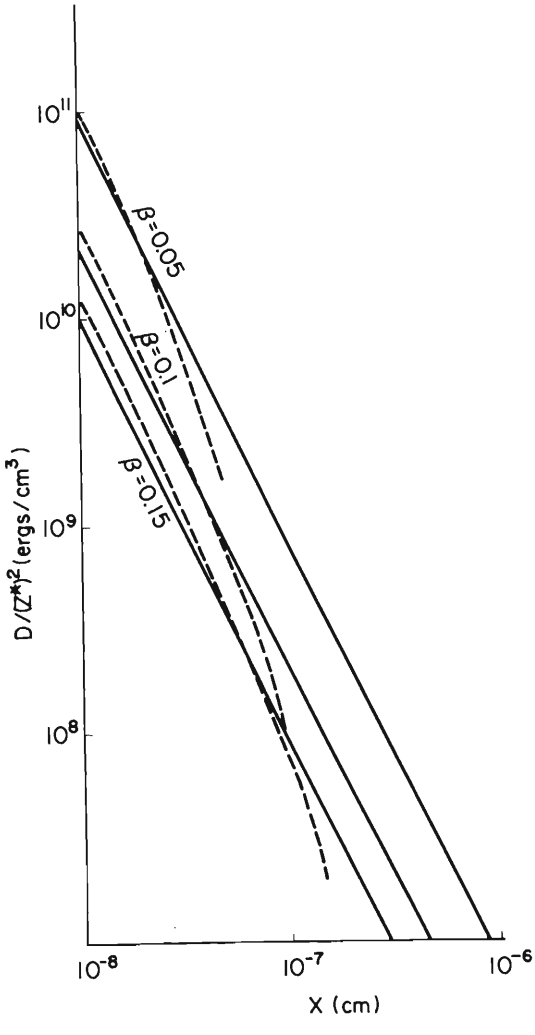

Fig.1 Solid lines are Katz's doses from Eq.(1) and dotted lines are Ahlen's prompt doses from Eq.(4) for β = 0.05, 0.1 and 0.15.

where Ze is the nuclear charge of the projectile. The range of the maximum energy delta electrons is given by

$$X_m = k\omega_{max} = k(2mc^2\beta^2\gamma^2), \tag{3}$$

where k is a constant (k = 10 μg/cm²keV for water) and $\gamma = (1 - \beta^2)^{-1/2}$. According to Ahlen [18] Equation (1) is in good agreement with nuclear emulsion experiments for $Z \lesssim 26$ and $\beta \lesssim 0.8$.

Katz-Ahlen's Dose D_{KA}. Since Katz's dose takes into account only close collisions, we tried to incorporate the dose due to distant collisions. According to Ahlen [18], the distant collision dose or the prompt primary dose is given as

$$D_p(x) = \frac{2NZ^{*2}e^4}{m\beta^2c^2x^2} \sum_{E_k} f_k[\xi_k^2K_1^2(\xi_k) + \gamma^{-2}\xi_k^2K_0^2(\xi_k)], \tag{4}$$

where N is the number of electrons per unit volume, ξ_k is given as $\omega_k x/\gamma\beta c$, $E_k = h\omega_k/2\pi$ is the k th excited energy level, K_0 and K_1 are the modified Bessel functions of order 0 and 1 respectively, and f_s is the oscillator strength divided by the number of electrons in a molecule. We adopted the f_s values for water given in table 2 of Ref. 19. As shown in Fig.1, $D_p(x)$ is larger than $D_{KZ}(x)$ for x smaller than several Ångstroms. In our

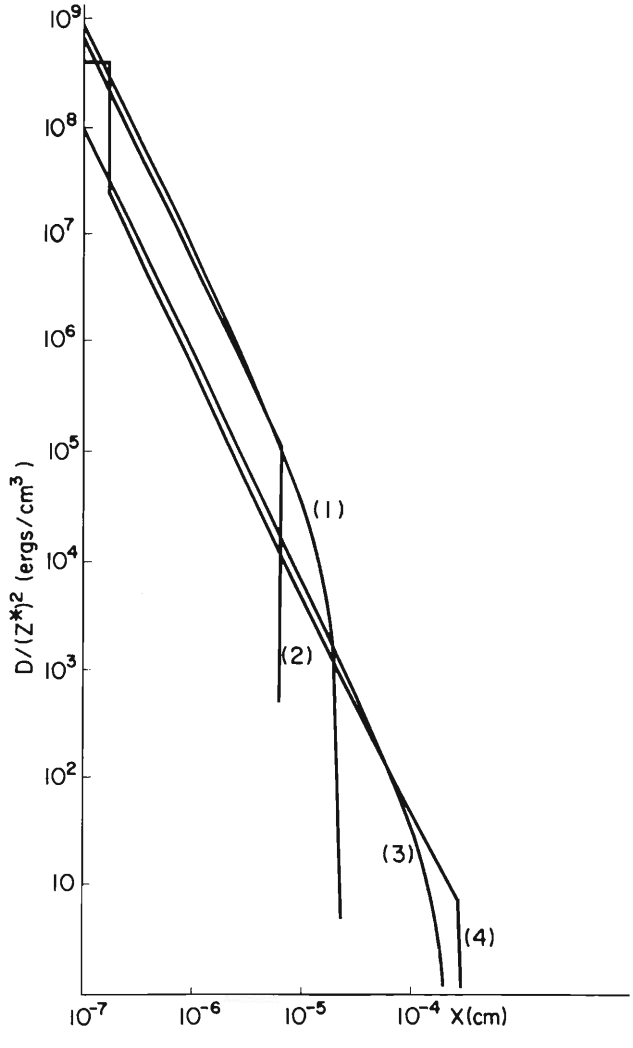

Fig.2 1) Katz's dose for β = 0.05; 2) Chatterjee and Schaefer's dose for β = 0.05; 3) Katz's dose for β = 0.15; 4) Chatterjee and Schaefer's dose for β = 0.15.

calculation, Katz-Ahlen's dose $D_{KA}(x)$ is defined as follows:

$$D_{KA}(x) = D_p(x) \quad \text{for regions where } D_p(x) > D_{KZ}(x) \tag{5}$$

and

$$D_{KA}(x) = D_{KZ}(x) \quad \text{for regions where } D_p(x) < D_{KZ}(x). \tag{5'}$$

D_p joins smoothly with D_{KZ} as shown in Fig.1.

Chatterjee and Schaefer's Dose D_{CS}. Chatterjee and Schaefer [20] give the following expressions for water:

$$D_{CS}(x) = \frac{LET_\infty}{2\pi r_c^2} + \frac{LET_\infty}{4\pi r_c^2 \ln(e^{1/2} r_p/r_c)}, \qquad x < r_c$$

$$D_{CS}(x) = \frac{LET_\infty}{2\pi x^2 \ln(e^{1/2} r_p/r_c)}, \qquad x > r_c \tag{6}$$

where r_c and r_p are the core and penumbral radii, respectively;

$$r_p = (0.768T - 1.925T^{1/2} + 1.257)\ \mu m,$$
$$r_c = 0.0116\beta\ \mu m, \tag{6'}$$

and T is the ion energy in MeV/amu. D_{CS} and D_{KZ} are shown in Fig.2 for comparison.

ANALYSIS OF INACTIVATION CROSS SECTIONS

In this paper, we assume one sensitive element in a cell and equate its radius to that of the spore core determined by electron microscopy. According to our observations, the core area is 0.2 - 0.3 μm^2, whereas DNA regions were about 0.12 μm^2. We adopt here the value 0.22 μm^2 following Schäfer et al.[1], instead of 0.12 μm^2, because in the course of analysis we found that the value 0.22 μm^2 explains experimental results better than the value 0.30 μm^2 or 0.12 μm^2. Furthermore, the value 0.22 μm^2 is in good agreement with the sensitive area (0.215 μm^2) obtained from our heavy ion data [4] by use of Oda's theory[9]. If we assume the whole spore core is a sensitive element and is a short cylinder of radius a, whose axis is parallel to and at a distance r from the path of an ion, the mean absorbed dose by the element $\bar{D}(r)$ is calculated [21] as follows:

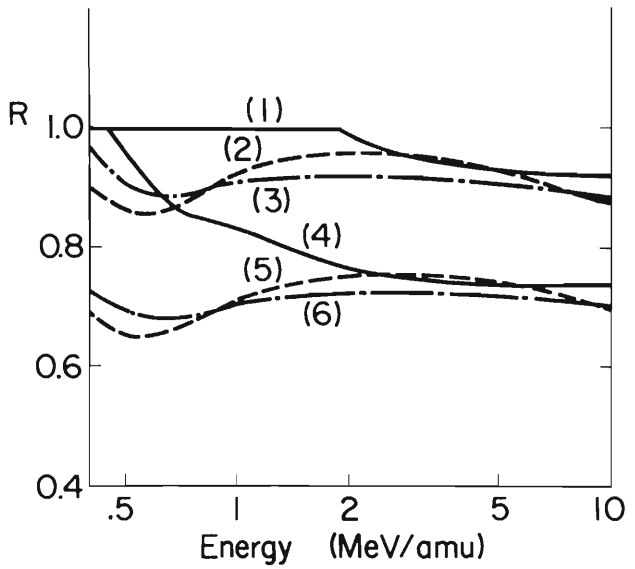

Fig.3 Ratio R given by Eq.(9). 1) R for D_{KA}, Z = 92; 2) R for D_{KA}, Z = 2; 3) R for D_{KA}, Z = 7; 4) R for D_{KZ}, Z = 92; 5) R for D_{KZ}, Z = 2; 6) R for D_{kz}, Z = 7.

$$\bar{D}(r) = (\pi a^2)^{-1}[\pi r_1^2 D(r_1) + \int_{x=r_1}^{x=a-r} 2\pi x D(x)dx + \int_{x=a-r}^{x=a+r} 2x\theta D(x)dx], \quad r < a$$

$$\bar{D}(r) = (\pi a^2)^{-1}\int_{x=r-a}^{x=r+a} 2x\theta D(x)dx, \quad r > a \tag{7}$$

where θ is given by

$$\theta = \arccos[(r^2 + x^2 - a^2)/2rx]. \tag{8}$$

Here, the constant r_1 was chosen to be a/1000 for Katz's dose D_{KZ}, 1 Å for Katz-Ahlen's dose D_{KA} and r_c for Chatterjee-Schaefer's dose D_{CS}. Since the value a/1000 or 1 Å is rather arbitrarily chosen, we calculated the ratio

$$R = [\pi r_1^2 D(r_1) + \int_{x=r_1}^{\infty} D(x)dx]/LET_\infty \tag{9}$$

for $D_{KZ}(x)$ and $D_{KA}(x)$ as shown in Fig.3. For $D_{CS}(x)$, the ratio is known to be unity. The LET_∞ value was taken from Ref.15. We adjusted r_1 so that R does not exceed 1.0 for the U ion in the case of D_{KA}. Such adjustment does not give rise to any appreciable change for the calculated result of inactivation cross sections.

The inactivation probability and cross sections are estimated by modifying Katz's target theory. By using equations (7) and (8), the inactivation probability is given as

$$P = [1 - \exp(-\bar{D}(r)/E_0)]^m, \tag{10}$$

if the sensitive element has m targets in it. E_0 is a dose at which there is an average of one hit per target. The inactivation cross section is given by

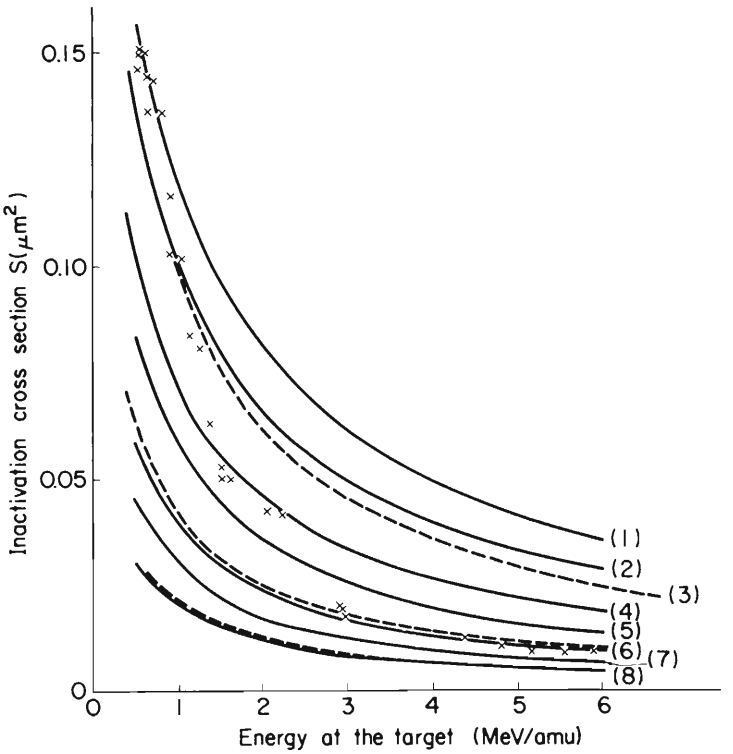

Fig.4 Inactivation cross sections of Bacillus subtilis as a function of He ion energy. x:Experimental; 1)-8):Theoretical curves (Eq.11 or Eq.13) for πa^2= 0.22 μm^2. 1) E_0= 8 krad, D_{KZ}; 2) E_0= 10 krad, D_{KZ}; 3) E_{in}= 10 krad, E_δ= 63.5 krad, D_{KZ}; 4) E_0= 15 krad, D_{KZ}; 5) E_0= 20 krad, D_{KZ}; 6) E_0= 30 krad, D_{KZ} & D_{KA}(dotted litne); 7) E_0= 40 krad, D_{KZ}; 8) E_0= 63.5 krad, D_{KZ} & D_{KA}(dotted line).

$$S = \int_0^{\infty} 2\pi r P dr. \tag{11}$$

Katz et al.[12] adopted m=4 and a = 5.8 x 10^{-6}cm, but the multitarget model is not consistent with the exponential survival curve observed for B. subtilis spores irradiated with gamma-rays [10]. Furthermore, the meaning of a adopted by Katz et al. is not clear. We restrict m to be unity and πa^2 was chosen to be equal to the area of the spore core, 0.22 μm^2, although the area is not well known yet (see discussion at beginning of the section).

To analyze He ion data, equations (10) and (11) were used for an energy range 63.5 krad $\geq E_0 \geq$ 8 krad, setting m = 1 (Figs.4 and 5). The dose D_{KA} yields several percent higher inactivation cross sections than D_{KZ}. D_{CS} gives the highest cross sections.

Instead of using equations (10) and (11), we used the following equations for heavy ions in order to separate out the effect of delta-rays:

$$P_{in} = 1 - \exp(-\bar{D}(r)/E_{in}), \qquad r < a \tag{12}$$

$$P_{\delta} = 1 - \exp(-\bar{D}(r)/E_{\delta}), \qquad r > a \tag{12'}$$

and

$$S = \int_0^{a} 2\pi r P_{in} dr + \int_a^{\infty} 2\pi r P_{\delta} dr. \tag{13}$$

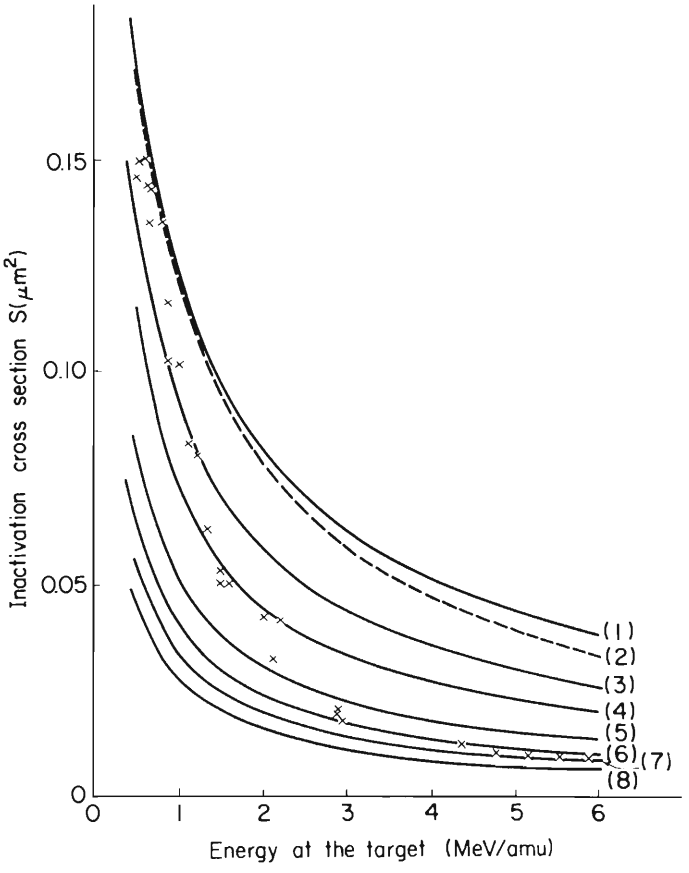

Fig.5 Inactivation cross sections of Bacillus subtilis as a function of He ion energy. x:Experimental; 1)-8):Theoretical curves for πa^2= 0.22 μm^2 calculated by D_{CS}. 1) E_0= 10 krad; 2) E_{in}= 10 krad, E_{δ}= 63.5 krad; 3) E_0= 15 krad; 4) E_0= 20 krad; 5) E_0= 30 krad; 6) E_0= 40 krad; 7) E_0= 50 krad; 8) E_0= 63.5 krad.

Here, P_{in} is the probability that the spore is inactivated when the ion impinges upon and goes through the spore core, and E_{in} is a parameter as will be discussed below. P_δ is the probability of inactivation when the ion passes by the spore core and the trajectories of its delta electrons come into the spore core. E_δ is the 37% survival dose for delta electrons. Since the exact value of the 37% survival dose for delta electrons is not known, an E_δ value was fixed at D_{37}^{γ} = 63.5 krad, and only the E_{in} value was decreased from 63.5 krad. No change in the calculated inactivation cross sections, S, was found for U ions, assuming E_{in} values ranging from 63.5 krad to 8 krad (Fig.6). The E_{in} value is limited by the experimental inactivation cross sections for He ions. If E_{in} is lower than 8-10 krad, the calculated S yields larger cross sections than the experimental cross sections for He ions of the lowest energies (Figs.4 and 5). The best fit E_{in} value was found to be 8-10 krad for N ions (Figs.6 and 8). Therefore, E_{in} value of 8-10 krad explains the experimental data of N ions and low energy He ions.

The E_δ value was heretofore fixed to be 63.5 krad, but it may be smaller than this value. According to Howard-Flanders [6] the LET distribution for delta electrons is similar to 10 MeV/amu He ions. As shown in Figs.4 and 5, cross sections for 5-6 MeV/amu He ions are found to be well represented by the curve E_0 = 30 krad for D_{KZ} and D_{KA}, and 40 krad for D_{CS}. These values are thought to be lower limits for delta electrons because 10 MeV/amu He ions would give higher E_0 value than 5-6 MeV/amu He ions. Therefore, we examined this possibility by fixing the E_δ value to be 30 krad for D_{KZ} and D_{KA}, and 40 krad for D_{CS}(Figs.7 and 8). For U ions no change was found for E_{in} values in the range 8 krad $\leq E_{in} \leq E_\delta$. For Xe ions, the situation was the same as for U ions. The best fit E_{in} value was 8-10 krad for N ions as in the case of E_δ = 63.5 krad. For He ions, S is found to be mainly determined by the E_{in} value. For instance, if E_{in} is fixed to be 10 krad, an increase in E_δ from 10 to 63.5 krad yields a cross section about 20% lower at

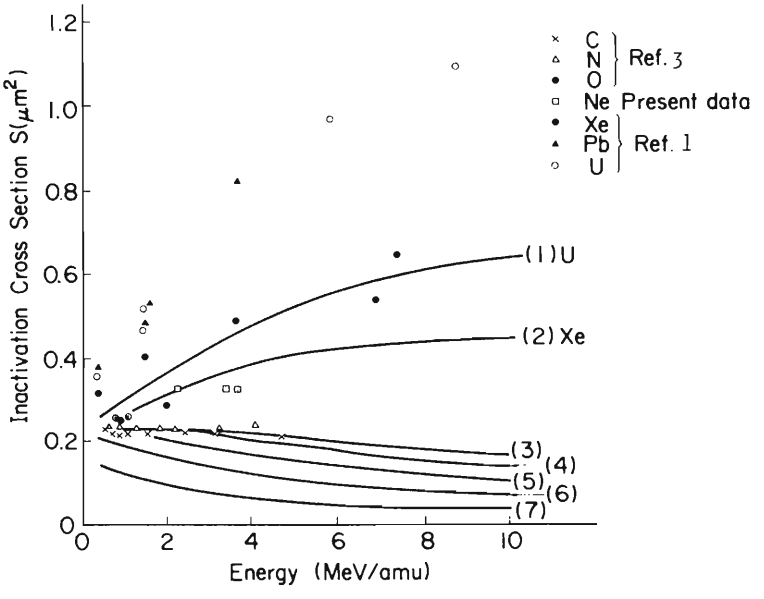

Fig.6 Experimental and theoretical inactivation cross sections.
1)-7): Theoretical curves from Eqs. (12), (12') & (13), by using D_{KZ}. E_δ was fixed to be 63.5 krad. Almost the same result was obtained for D_{KA}. 1)-2) E_{in} = 8-63.5 krad; 3) N ion, E_{in} = 8 krad; 4) N ion, E_{in} = 10 krad; 5) N ion, E_{in} = 15 krad; 6) N ion, E_{in} = 25 krad; 7) N ion, E_{in}= 63.5 krad.

6 MeV/amu, but this lower value is still higher than the experimental cross sections (Figs.4 and 5). In these calculations, we choose πa^2 value of 0.22 μm^2. For a πa^2 value of 0.30 μm^2, the allowable range of E_δ is the same, but a difficulty arises in interpreting the plateau-like region of N and C ions. The situation is much worse for a core area of 0.12 μm^2.

COMMENTS ON THE INACTIVATION MECHANISM

As seen in Fig.4 or Fig.5, the theoretical curves for E_0 = 30 krad or 40 krad seem to account for the experimental inactivation cross sections for 4-6 MeV/amu He ions. The experimental cross sections for lower energy He ions correspond to lower E_0 values. This fact seems to be explainable by the decrease in repairability with increasing LET as shown by Horneck [22]. The RBE peak also appears at about 150 keV/μm which corresponds to about 0.8 MeV/amu He ions (Fig.9). The track segment method as discussed in an earlier paper [3] could account for this region qualitatively. For spores inactivated by He ions, more than 7 or 8 "primary ionizations" are required for producing a lethal hit within a track segment of 30 Å [3,6]. The "primary ionizations" would produce, e.g., OH free radicals whose diffusion lengths are known to be about 90 Å [23].

For U ions, the calculated inactivation cross sections based on E_δ = 63.5 krad (upper limit), and E_δ = 30 krad (lower limit for D_{KZ} and D_{KA}) or 40 krad (lower limit for D_{CS}) are all below the experimental cross sections given by Schäfer et al.[1](Figs.6 - 8). It is easily shown from equation (4) or Fig.1, that most atoms or molecules would be excited or ionized at $x \leq 10$ Å for $Z^* = 33$, $\beta = 0.1$ (D_P(10 Å) $\simeq 10^{11}$ ergs/g). Such densely excited or ionized species may react with each other [24] and cause thermal spike effects [1,5,25] which give rise to augmentation of inactivation cross sections[1] or derangement of biological systems [26]. For $Z^* = 10$, $\beta = 0.1$, the region in which most atoms are excited or ionized is limited to $x \leq 5$ Å. The plateau-like region for C, N and Ne ions may correspond to this case. The higher experimental inactivation cross sections observed for Ne ions (Fig.8) relative to calculated cross sections may be due to long range effects but the experimental values may have rather large uncertainties because a new irradiation unit was recently introduced and its calibration for Ne ions is not sufficiently complete.

As given in equation (12), an E_{in} value corresponds to a 37% survival dose when the nucleus of the ion hit the spore core. The E_{in} value of 8-10 krad found for N ions and low energy

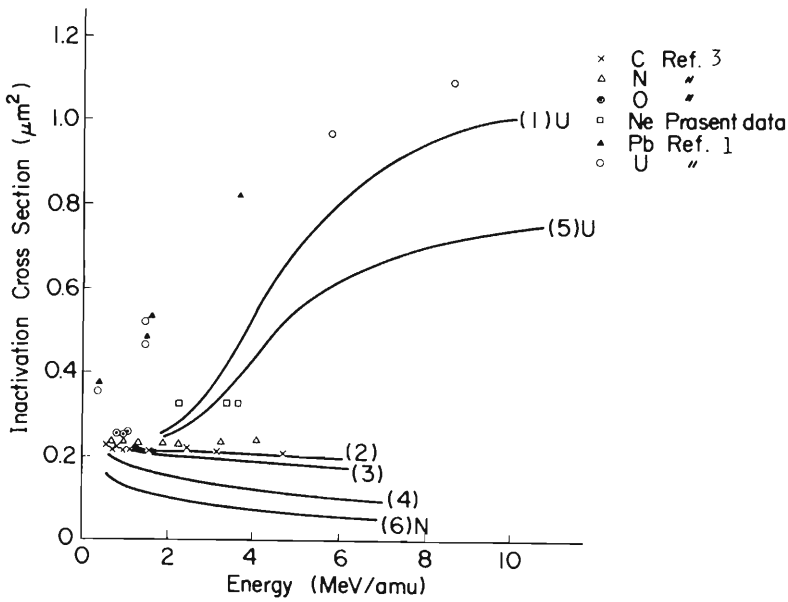

Fig.7 Experimental and theoretical inactivation cross sections.
1)-7): Theoretical curves from Eqs. (12), (12') & (13), by using D_{CS}. 1) E_δ = 40 krad, E_{in} = 10-40 krad; 2) N ion, E_δ = 40 krad, E_{in} = 10 krad; 3) N ion, E_δ = 40 krad, E_{in} = 15 krad; 4) N ion, $E_\delta = E_{in}$ = 40 krad; 5) E_δ = 63.5 krad, E_{in} = 10-63.5 krad; 6) N ion, $E_\delta = E_{in}$ = 63.5 krad.

He ions (LET > 150 keV/μm) are lower than the lowest D_{37}^{γ} for repair deficient strains (24 krad) reported by Sadaie and Kada [27]. The low E_{in} value may be explained by the fact that dose $\bar{D}(r)$ is averaged over the whole spore core. Therefore, the ratio E_{in}/D_{37}^{γ} might give some information about the area damaged by the ion core.

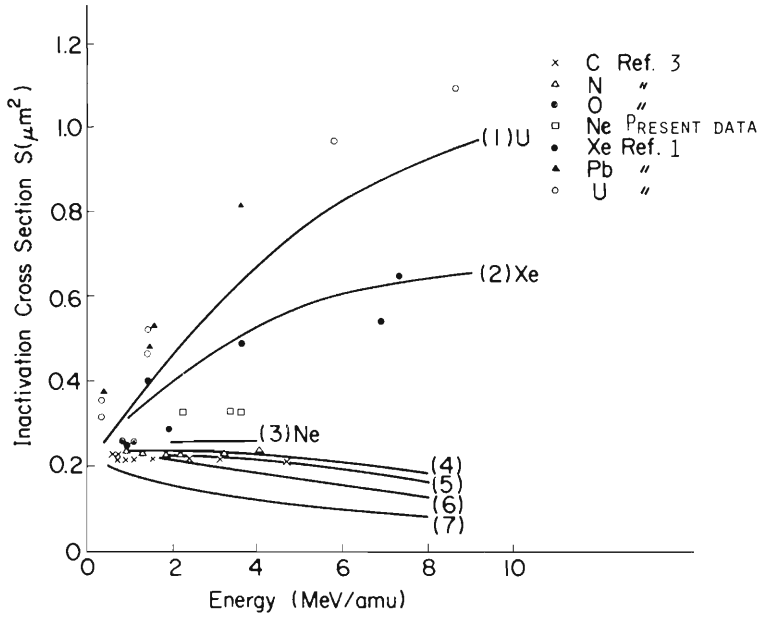

Fig.8 Experimental and theoretical inactivation cross sections.
1)-7): Theoretical curves from Eqs.(12), (12') & (13), by using D_{KZ}. E_{δ} was fixed to be 30 krad. Almost the same result was obtained for D_{KA}. 1)-2) E_{in} = 8-30 krad; 3) E_{in} = 8 krad; 4) N ion, E_{in} = 8 krad; 5) N ion, E_{in} = 10 krad; 6) N ion, E_{in} = 15 krad; 7) N ion, E_{in} = 30 krad.

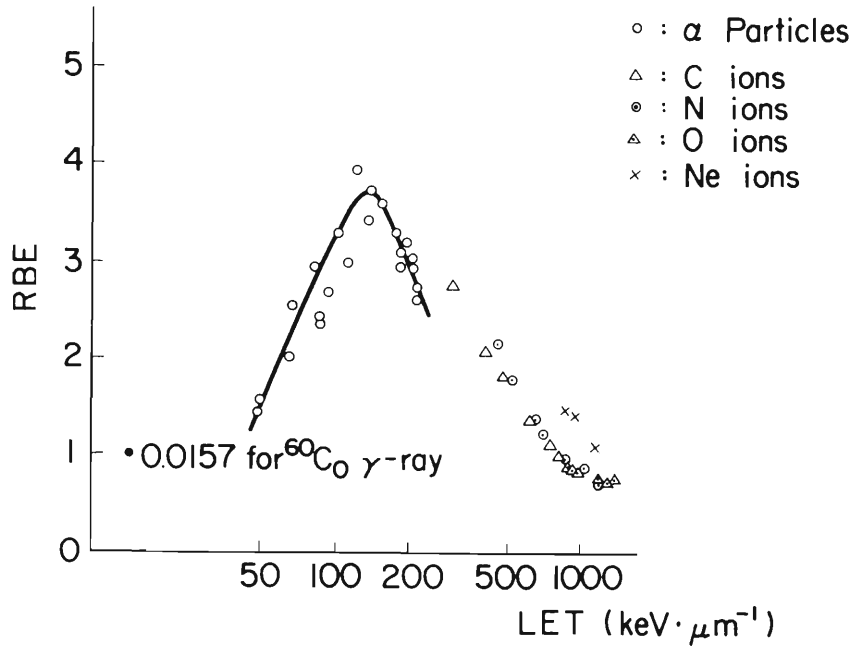

Fig.9 Relation between LET_{∞} and RBE ($1/D_{37}^{\gamma}$ = 0.0157 $krad^{-1}$).

REFERENCES

1. M. Schäfer, R. Facius, K. Baltschukat and H. Bücker, 7th Symposium on Microdosimetry (1980).
2. G. Horneck and H. Bücker, Spore Radiology Meeting, Tokyo (1979); G. Horneck and H. Bücker, Int. J. Radiat. Biol.37, 558 (1980).
3. F. Yatagai, T. Takahashi, Y. Kitajima and A. Matsuyama, J. Radiat. Res. 15, 90 (1974).
4. F. Yatagai, T. Takahashi and A. Matsuyama, J. Radiat. Res. 16, 99 (1975).
5. S. Kondo, Hoshasen Idengaku (in Japanese), Shokabo, Tokyo (1964).
6. P. Howard-Flanders, Adv. Biol. Phys. 6, 553 (1958).
7. G. W. Barendsen, Int. J. Radiat. Biol. 8, 453 (1964).
8. E. L. Powers, J. T. Lyman and C. A. Tobias, Int. J. Radiat. Biol. 4, 313 (1968).
9. N. Oda, IAEA-SM-145/47, Vienna (1971) p.99.
10. F. Yatagai, T. Takahashi and A. Matsuyama, Spore Radiology Meeting, Tokyo (1979); F. Yatagai, T. Takahashi and A. Matsuyama, Int. J. Radiat. Biol. 37, 558 (1980).
11. J. J. Butts and R. Katz, Radiat. Res. 30, 855 (1967).
12. R. Katz, B. Ackerson, M. Homayoonfer and S. C. Sharma, Radiat. Res. 47, 402 (1971); R. Katz, 9th Int. Conf. Solid State Nuclear Track Detectors (1976).
13. H. Yoshikawa, Proc. Natl. Acad. Sci. (U.S.A.) 53, 1476 (1965).
14. F. Yatagai, S. Kitayama and A. Matsuyama, Radiat. Res. 77, 250 (1979).
15. L. C. Northcliffe and R. F. Schilling, Nucl. Data Tables A7, 233 (1970).
16. F. Yatagai and A. Matsuyama, IPCR Cyclotron Progr. Rept. 13, 118 (1979).
17. G. L. Jr. Kochanny, A. Timnick, C. J. Hockanadel and C. D. Goodman, Radiat. Res. 19, 462 (1963).
18. S. P. Ahlen, Rev. Mod. Phys. 52, 121 (1980).
19. K. H. Tan, C. E. Brion, Ph. E. Van der Leeuw and M. J. Van der Wiel, Chem. Phys. 29, 299 (1978).
20. A. Chatterjee and H. J. Schaefer, Radiat. Environ. Biophys. 13, 215 (1976).
21. T. Takahashi, F. Yatagai and A. Matsuyama, Sci. Pap. Inst. Phys. Chem. Res. 74, 51 (1980).
22. G. Horneck, 1st Int. Conf. on Cell and Molecular Biology in Space, Toledo (1978).
23. R. Roots and S. Okada, Radiat. Res. 64, 306 (1975).
24. A. Hitachi, T. Takahashi, T. Hamada, E. Shibamura, A. Nakamoto, N. Funayama, K. Masuda and T. Doke, Phys. Rev. B23, 4779 (1981).
25. M. Matsui and M. Imamura, IPCR Cyclotron Progr. Rep. 5, 93 (1971); M. Matsui and Imamura, Bull. Chem. Soc. Japan 47, 1113 (1974).
26. C. A. Tobias, A. Chatterjee, M. J. Malachowski, E. A. Blakely and T. L. Hayes, 6th Int. Congress Radiat. Res., C-SY-3-1, Tokyo (1979).
27. Y. Sadaie and T. Kada, Mutation Res. 17, 138 (1973).

Reprinted from Int. J. Radiat. Biol., 45, 21–26 (1984).

Differential recovery from potentially lethal damage in normal human lung fibroblasts after irradiation with ^{60}Co γ-rays and accelerated N-ion beam

TADAO OHNO†, TETSUJI NISHIMURA‡§,
KAZUSHIRO NAKANO‡, and ICHIRO KANEKO‡¶

National Institute of Radiological Sciences, 4–9–1, Anagawa, Chibashi 260 and ‡The Institute of Physical and Chemical Research, 2–1, Hirosawa, Wakoshi, Saitama 351, Japan

(*Received 5 May 1983; revision received 11 August 1983; accepted 16 August 1983*)

PLD recovery after irradiation with accelerated N-ion was examined and compared with that after irradiation with ^{60}Co γ-rays in normal human lung fibroblasts (IMR-90). No shoulder region was observed in the survival curve of the cells after N-ion irradiation. Ratios of D_0 values before and after a 6-hour incubation in plateau phase were 1·1 and 1·8 for N-ion irradiation and γ-ray irradiation, respectively. The results show that recovery after irradiation with high-LET radiation is slow and much less than after low-LET irradiation.

Indexing terms: PLD repair, human fibroblasts, heavy ions, N-ion beam.

1. Introduction

Irradiation with high-LET charged particles may lead to effective therapy for solid malignant tumours. Although there have been many investigations on tumour cell inactivation after high LET irradiation, there are conflicting data on the extent of recovery from potentially lethal damage (PLD) in normal human cells after irradiation with high-LET particles.

Early investigators (Shipley *et al.* 1975, Hall and Kraljevic 1976, Gragg *et al.* 1977) reported that tumour cells showed little if any recovery from PLD after irradiation with neutrons. In contrast, EMT-6 cell in plateau phase did show a substantial recovery from PLD after neutron irradiation (Rasey *et al.* 1978). The EMT-6 cells also showed virtually no difference in recovery from PLD after irradiation with ^{60}Co γ-rays or Bragg peak helium ions (Guichard *et al.* 1977). Brain tumour cells recovered to an almost identical extent from PLD *in situ* after irradiation with BEVALAC accelerated carbon ions or 220 kVp X-rays (Wheeler *et al.* 1980).

We therefore tested whether or not normal human lung fibroblasts in the plateau phase show differences in recovery from PLD after irradiation with IPCR cyclotron-accelerated N-ion beam or ^{60}Co γ-rays.

† Visiting researcher of the Institute of Physical and Chemical Research.

§ Present address: Institute of Public Health, 4–6–1, Shirokanedai, Minato-ku, Tokyo 108, Japan.

¶ To whom requests for reprints should be addressed.

2. Materials and methods

2.1. *Cell culture and colony formation*

Normal human lung fibroblasts (IMR-90) were maintained as described (Ohno 1979) in TOM-H medium (an improved MEM for human cells) containing 10 per cent foetal bovine serum (FBS). The cells were used when they had undergone between 28 and 39 population doublings since the establishment of the culture. More than 7 days before irradiation, the cells were seeded onto 25-mm round cover glasses. The cover glasses were fixed with silicon grease in 35-mm glass Petri dishes. One hundred thousand cells suspended in 0·3 ml of the medium were placed on each cover glass and incubated overnight and 2 ml of the medium were then added to the dish. The dish was kept for 1 to 2 weeks in a humidified CO_2-incubator until the cells had reached saturation on the cover glass. During this period, the medium was changed every 3 to 4 days. Medium changing was carried out very gently to avoid any detachment of the cells from the cover glass. Generally, growth of the fibroblasts was restricted to the cover glass. If any detached colonies were found on the Petri-dish surface, these dishes were discarded.

After irradiation with the N-ion beam or ^{60}Co γ-rays (see below) or after incubation for PLD repair, cells were removed with trypsinization and mixed with feeder IMR-90 cells (Cox and Masson 1974). These feeder IMR-90 cells were prepared by irradiating IMR-90 cells with 5·5 Gy of ^{60}Co γ-rays just before the mixing. The mixed cells suspended in 8 ml of the medium were seeded into a 60-mm plastic culture dish. The total number of cells seeded into each dish was adjusted at $2{\cdot}5 \times 10^4$. After 14 days incubation, the cells were fixed with 10 per cent formalin in Dulbecco's phosphate buffered saline (PBS) and stained with 0·1 per cent crystal violet. Cell aggregates consisting of over 50 cells were considered to be colonies. Plating efficiencies were between 20 and 30 per cent in the different experiments.

2.2. *Irradiation procedures*

IMR-90 cells cultured on 25-mm cover glasses were washed once with PBS and covered with a 30-mm polycarbonate membrane filter (Nucleopore, with a pore size of 0·2 μm and a thickness of 5 μm) moistened with phosphate buffered saline. Each 35-mm glass dish was then wrapped with sterilized polyester film (Diafoil, Mitsubishi Kasei Co. Ltd., with a thickness of 5 μm) to maintain moisture and sterility and was then placed on an irradiation apparatus attached to the IPCR cyclotron, as illustrated in figure 1. Details of the irradiation method are described elsewhere (Yamawaki *et al.* 1976, Yatagai and Matsuyama 1979). Briefly, the 95 MeV ^{14}N-ion beam was scattered once with a 2 μm gold foil and led to the open air through a 5 μm thick aluminium window. Cover glasses were positioned vertically 1 cm from the window and 0·92 mm nearer to the window than the Bragg peak of the specific ionization curve (Takahashi, personal communication). Taking account of the presence of the membrane filter and polyester film, the LET of the N ions at this position is 392 keV/μm and the dose rate is 0·6 Gy/min. The holders of the 35-mm glass dish were rotated at a constant speed of 100 r.p.m. during the irradiation. Four cover glasses were irradiated at once at room temperature.

For comparison, other IMR-90 cells were also irradiated with ^{60}Co γ-rays at a dose rate 1 Gy/min.

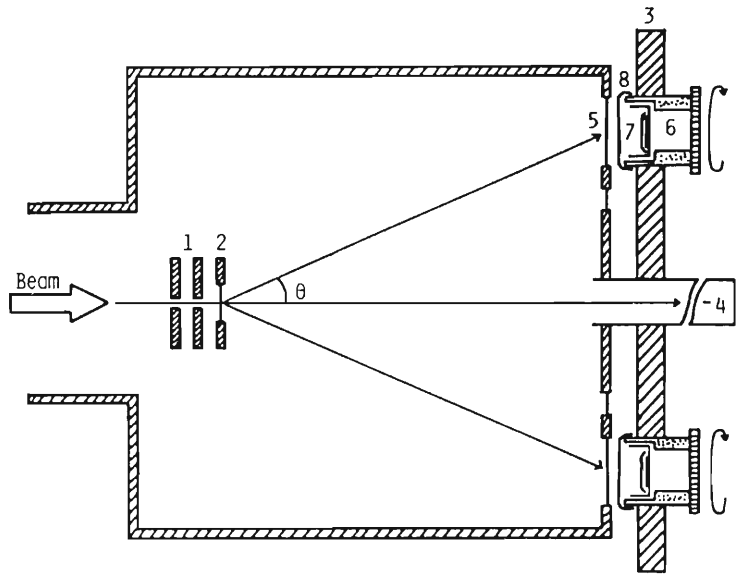

Figure 1. Illustration of the apparatus for the N-ion irradiation. The horizontal beam passed through the slit (1) and was scattered by a gold foil (2). The cells were mounted on cover glasses which were fixed in holders (6). 3, sample wheel; 4, Faraday cup; 5, aluminium window; 7, 5-μm thick Nucleopore membrane filter (pore size, 0·2 μm); 8, polyester film. $\theta = 6° 00'$.

3. Results

Survival curves after irradiation with ^{60}Co γ-rays or the N-ion beam are given in figures 2 (*a*) and (*b*). No shoulder region was observed after the N-ion irradiation. The r.b.e. calculated from the D_0 ratio after γ-ray and N-ion irradiation and immediate plating was 1·6.

When the cells were incubated for 6 hours before replating, recovery from PLD was found in those cells irradiated with the γ-rays (figure 2 (*a*)). The ratio of D_0 values before and after incubation was 1·8. For the cells irradiated with the N-ion beam and incubated for 6 hours before replating, a slight increase in the surviving fraction was observed. This increase was consistent if one compared dishes paired before and after the 6 hour incubation at each radiation dose on the same batch of cells, although, since variations of the surviving fraction between different N-ion doses were relatively large, statistically significant differences between the two curves were not found ($0·05 < P < 0·1$) in the results of the particular experiment shown in figure 2 (b) when the *t*-test was applied to variations of the inclination of the two lines. Other parameters derived from these figures are summarized in the table.

Figure 3 shows the time-course of increasing survival after irradiation. Survival increased by 8·7-fold and 1·6-fold by 6 hours after irradiation with 5·2 Gy of ^{60}CO γ-rays and 2·4 Gy of the N-ion beam, respectively. Both of these increases were statistically significant ($P < 0·05$). In another set of experiments, similar slight increases of survival were observed in the N-ion irradiated cells after the 6-hour incubation. This increase was also statistically significant ($P < 0·05$). Initial rates of recovery were apparently different for the two radiations (figure 3). The time of half maximum recovery from PLD was 1·3 hours and 3·1 hours after irradiation with γ-rays or with the N-ion beam, respectively. Additional recovery from PLD was not evident later than 6 hours after the irradiation with the N-ion beam.

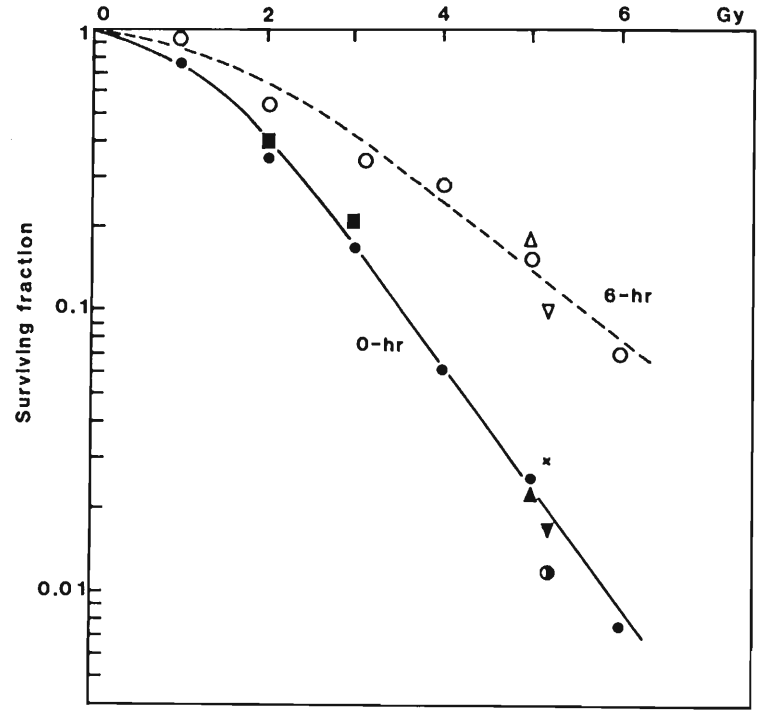

(*a*)

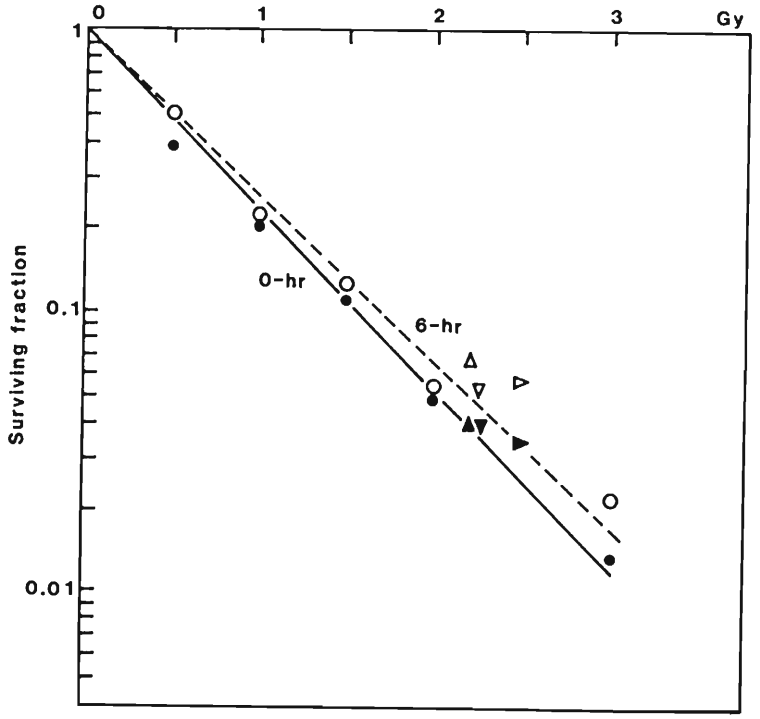

(*b*)

Figure 2. Radiosensitivities of IMR-90 cells to (*a*) ^{60}Co γ-rays and (*b*) N-ion before and after a 6 hour incubation. Each point represents the mean of three dishes. Closed symbols, before the 6 hour incubation; open symbols, after the 6 hour incubation. Different symbols correspond to different experiments. The solid- and broken-lines in (*a*) and (*b*) are fitted to a particular experiment (● and ○) carried out at the same time on the same batch of the cells. Note the scale of the abscissa in (*b*) is half of that in (*a*).

Parameters of radiation sensitivity of IMR-90 cells calculated from the data shown in figure 2.

Incubation (hours) before replating	^{60}Co		N-ions	
	0	6	0	6
D_0 (rad)	104	183	67	73
n	2·7	2·0	1	1
Ratio of D_0	1·8		1·1	

Values were calculated by the least-squares method from the linear part of the curves consisting of at least four different radiation doses.

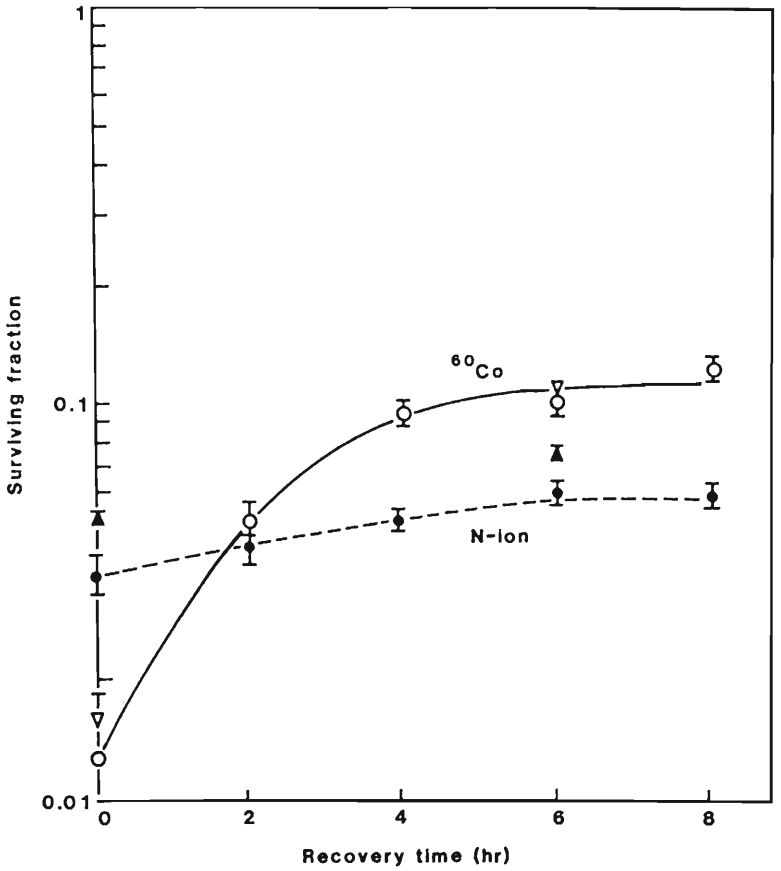

Figure 3. Time course of recovery from potentially lethal damage after irradiation with ^{60}Co γ-rays and N-ion in IMR-90 cells. The doses of radiation were for γ-rays 5·2 Gy (open symbols), and for N-ion irradiation 2·2 Gy (closed triangles) and 2·4 Gy (closed circles), respectively. Vertical bars represent the standard deviation of the mean of four dishes.

4. Discussion

Cox and Masson (1980) showed that normal human fibroblasts have a broad distribution of X-ray sensitivities with a D_0 range of 98–160 rad. The γ-ray sensitivity of IMR-90 cells was within this range. The dose-modifying factor of PLD repair after γ-ray irradiation (figure 2) was slightly larger than that reported by these investigators. Deschavanne *et al.* (1980) showed that a quadratic model was well

suited for fitting the survival curves of normal human fibroblasts. We therefore calculated values of α and β from the data shown in figure 2. Except for the β value for the 0 hours, γ-ray curve, which was $6{\cdot}71 \times 10^{-6}$ rad^{-2}, other values were within the range found by Deschavanne *et al.* (1980).

The r.b.e. based on D_0 between N-ion and γ-irradiation was comparable to the results of Cox *et al.* (1977) who reported that the r.b.e. of N-ions at 470 keV/μm was 1·7 when compared with 250 kVp X-rays. Our results on the rate of recovery from PLD after γ-ray irradiation were similar to the recovery at long time periods reported by Malcolm and Little (1980) and by Cox *et al.* (1981). Our data are therefore comparable to those given by other investigators.

Although we did not observe statistically significant recovery from PLD after the N-ion irradiation in the experiments shown in figure 2 (*b*), the tendency of slight recovery from PLD was suggested. This was confirmed in the experiments shown in figure 3. The data suggest that recovery from PLD after N-ion irradiation is very slow and much less than after low LET radiation. These findings should be taken in consideration in radiation therapy with high-LET particles.

Acknowledgments

This work was supported in part by a grant-in-aid from the Ministry of Education, Science and Culture of Japan. We thank Dr. T. Takahashi for advice on the dose of N-ion beam.

References

Cox, R., and Masson, W. K., 1974, *Int. J. Radiat. Biol.*, **26,** 193; 1980, *Ibid.*, **38,** 575.

Cox, R., Masson, W. K., Weichselbaum, R. R., Nove, J., and Little, J. B., 1981, *Int. J. Radiat. Biol.*, **39,** 357.

Cox, R., Thacker, J., Goodhead, D. T., and Munson, R. J., 1977, *Nature, Lond.*, **267,** 425.

Deschavanne, P. J., Fertil, B., Malaise, E. P., and Lachet, B., 1980, *Int. J. Radiat. Biol.*, **38,** 167.

Gragg, R. L., Humphrey, R. M., and Meyn, R. E., 1977, *Radiat. Res.*, **71,** 461.

Guichard, M., Lachet, B., and Malaise, E. P., 1977, *Radiat, Res.*, **71,** 413.

Hall, E. J., and Kraljevic, U., 1976, *Radiology*, **121,** 731.

Malcolm, A. W., and Little, J. B., 1980, *Int. J. Radiat. Biol.*, **38,** 439.

Ohno, T., 1979, *Mech. Ageing Dev.*, **11,** 179.

Rasey, J. S., Nelson, N. J., and Carpenter, R. E., 1978, *Int. J. Radiat. Oncol. Biol. Phys.*, **4,** 1023.

Shipley, W. U., Stanley, J. A., Courtenay, V. D., and Field, S. B., 1975, *Cancer Res.*, **35,** 932.

Wheeler, K. T., Deen, D. F., and Leith, J. T., 1980, *Int. J. Radiat. Biol.*, **37,** 225.

Yamawaki, Y., Yatagai, F., Kaneko, I., Sakamoto, K., Okada, S., and Matsuyama, A., 1976, *IPCR Cyclotron Prog. Rep.*, **10,** 36.

Yatagai, F., and Matsuyama, A., 1979, *IPCR Cyclotron Prog. Rep.*, **13,** 118.

List of Publications

1. Accelerator development and accelerator physics

1) Y. Chiba, M. Odera, and T. Fujisawa: "The Radio Frequency System of the I.P.C.R. 1.6m Cyclotron (I). Cavity Resonator", Reports I.P.C.R., (in Japanese), 40, 67 (1964).
2) T. Karasawa, S. Motonaga, Y. Miyazawa, N. Nakanishi, M. Hemmi, and H. Kumagai: "A B-Constant Magnet Pole Design", Proc. Int. Symp. Magnet Technology, p. 472 (1965).
3) M. Hemmi, T. Karasawa, and S. Motonaga: "A Simple and Convenient Method for Field Mapping by Differential Usage of Hall Generators", Proc. Int. Symp. Magnet Technology, p. 472 (1965).
4) I. Kohno, T. Tonuma, and S. Nakajima: "Multiply Charged Heavy Ion source", J. Vac. Soc. Japan, 10, 26 (1966).
5) T. Tonuma, S. Nakajima, and I. Kohno: "^{3}He Gas Circulation System for the Ion Source of the RIKEN Cyclotron with the Results of its Test by Gas Analysis", J. Vac. Soc. Japan, 10, 228 (1966).
6) T. Fujisawa, M. Odera, Y. Chiba, and O. Terajima: "Measurement of the Resonant Frequency and Q-Value of the Model Cavity Resonator of I.P.C.R. 1.6m Cyclotron", Reports I.P.C.R., (in Japanese), 42, 27 (1966).
7) N. Nakanishi and K. Matsuda: "Design of Nuclear Reaction Particle Analyzer", Nucl. Instr. Methods, 57, 245 (1967).
8) T. Fujisawa, M. Odera, and Y. Chiba: "The Radio Frequency System of the I.P.C.R. 1.6m Cyclotron (II). Oscillator Tube and Resonator Coupling Circuit", Reports I.P.C.R., (in Japanese), 44, 1 (1968).
9) M.Odera, Y. Miyazawa, T. Tonuma, M. Hemmi, and O. Terajima: "Design and Performance of a Focusing Magnetic Channel for a Variable Energy Multiparticle Cyclotron", Nucl. Instr. Methods, 65, 247 (1968).
10) I. Kohno, T. Tonuma, Y. Miyazawa, S. Nakajima, T. Inoue, A Shimamura, and T. Karasawa: "A Multicharged Heavy Ion Source for the IPCR Cyclotron", Nucl. Instr. Methods, 66, 283 (1968).
11) N. Nakanishi, S. Motonaga, Y. Miyazawa, and T. Karasawa: "On Circular Trimming Coils Mounted on Magnet Pole Faces", Japan. J. Appl. Phys., 8, 1229 (1969).
12) Y. Miyazawa, T. Tonuma, I. Kohno, S. Nakajima, T. Inoue, A. Shimamura, K. Yoshida, and T. Karasawa: "Acceleration of Multicharged Heavy Ions in IPCR (Riken) Ordinary 160cm Cyclotron", Japan. J. Appl. Phys., 9, 532 (1970).
13) T. Tonuma, Y. Miyazawa, T. Karasawa, and I. Kohno: "Charge Exchange of Carbon and Nitrogen Ions in Nitrogen Gas", Japan. J. Appl. Phys., 9, 1306 (1970).
14) I. Kohno, S. Nakajima, T. Tonuma, and M. Odera: "Elastic Scattering of Carbon and Nitrongen Ions", J. Phys. Soc. Japan, 30, 910 (1971).
15) Y. Miyazawa, I. Kohno, T. Tonuma, T. Inoue, A Shimamura, and S. Nakajima: "A Source for Multiply-charged Ions and Acceleration of C, N and O Ions by IPCR Cyclontron", IEEE Trans. Nucl. Sci., NS-19, 105 (1972).
16) I. Kohno, Y. Miyazawa, T. Tonuma, T. Inoue, A. Shimamura, and S. Nakajima: "Production of Multiply-charged Ions of Ne, Ar, Kr and Xe by the Electron-bombarded Hot Cathode Ion Source of IPCR", IEEE Trans, Nucl. Sci., NS-19, 109 (1972).

17) S. Yamaji: "The Coupled-Channel Born-Approximation Calculation of the Reaction ^{100}Mo (t,p) ^{102}Mo", J. Phys. Soc. Japan, 34, 298 (1973).
18) C. Gil, K. Nishiyama, T. Nomura, T. Yamazaki, and K. Miyano: "A New Short-Lived Isomer in ^{114}Sb", J. Phys. Soc. Japan, 34, 874 (1973).
19) S. Takeda, S. Yamaji, K. Matsuda, I. Kohno, N. Nakanishi, Y. Awaya, and S. Kusuno: "^{100}Mo (t,p) ^{102}Mo Reaction at 15.8 MeV", J. Phys. Soc. Japan, 34, 1115 (1973).
20) M. Odera, Y. Chiba, T. Fujisawa, Y. Miyazawa, and O. Terajima: "The Radiofrequency System of the IPCR (RIKEN) Variable Energy Multi-Particle Cyclotron", Sci. Papers I.P.C.R., 67, 90 (1973).
21) I. Kohno: "Elastic and Inelastic Scatterings of ^{14}N and ^{12}C Projectiles by ^{12}C, ^{27}Al, ^{28}Si, and ^{58}Ni", Sci. Papers I.P.C.R., 68, 38 (1974).
22) T. Motobayashi, I. Kohno, K. Katori, M. Yoshie, T. Ooi, and H. Kamitsubo: "Anomalous Angular Distribution in the Transition to the Sy_2 State in ^{17}O", Phys. Rev. Lett., 36, 391 (1976).
23) T. Mikumo, I. Kohno, K. Katori, T. Motobayashi, S. Nakajima, M. Yoshie, and H. Kamitsubo: "Systematics of Optimum Q Values in Multinucleon Transfer Reactions Induced by Heavy Ions", Phys. Rev., C14, 1458 (1976).
24) T. Ooi, T. Motobayashi, K. Katori, and I. Kohno: "Detection and Identification of ^{8}Be Nuclei with a Position Sensitive Detector and Counter Telescope", Reports I.P.C.R., (in Japanese), 52, 145 (1976).
25) T. Kammuri: "On the Importance of the Sequential Transfer Process in the Two-Nucleon Transfer between Heavy Ions", Nucl. Phys., A259, 343 (1976).
26) I. Kohno, K. Katori, T. Mikumo, T. Motobayashi, S. Nakajima, M. Yoshie, and H. Kamitsubo: "Single-and Multi-Nucleon Transfer Reactions Induced by ^{14}N and ^{12}C on fb-Shell Nuclei", J. Phys. Soc. Japan, 42, 1 (1977).
27) H. Nakajima, S. Kohara, T. Kageyama, and I. Kohno: "Production of C, N, O, and Ne Ions by Pulsed Ion Source and Acceleration of These Ions in the Cyclotron", Reports I.P.C.R., (in Japanese), 53, 132 (1977).
28) H. Takebe, K. Ogiwara, and I. Kohno: "Measurements of the Turn-Separation and ν_z of the Ion Beam in the IPCR 160 cm Cyclotron", Reports I.P.C.R., (in Japanese), 54, 77 (1978).
29) T. Kammuri, T. Motobayashi, I. Kohno, S. Nakajima, M. Yoshie, K. Katori, T. Mikumo, and H. Kamitsubo: "Effects of Recoil and Sequential Transfer on the ^{12}C (^{14}N, ^{12}C)^{14}N Reaction", J. Phys. G.: Nucl. Phys., 4, L94 (1978).
30) M. Yanokura, I. Kohno, H. Nakahara, and K. Yanakoshi: "Heavy Ion Identification System by Using a Gas Proportional Telescope", Oyo Buturi, 49, 1095 (1980).
31) H. Kamitsubo: "Heavy Ion Reaction-Quasi Elastic and Deep Inelastic Collision", Butsuri, 35, 981 (1980).
32) H. Kudo, Y. Nagame, H. Nakahara, K. Miyano, and I. Kohno: "Correlation between Angular Anisotropy and Fragment Mass in 15 MeV Proton-Induced Fission of ^{232}Th", Phys. Rev. C, 25, 909 (1982).
33) H. Kudo, H. Muramatsu, H. Nakahara, K. Miyano, and I. Kohno: "Fission Fragment Yields in the Fission of ^{232}Th by Protons of Energies 8 to 22 MeV", Phys. Rev. C, 25, 3011 (1982).

34) Y. Nagame, H. Nakahara, K. Sueki, H. Kudo, M. Yanokura, and I. Kohno: "Studies on Strongly Damped Components in Relatively Light Heavy Ion Reaction Systems", Z. Phys. A-Atoms Nuclei, 317, 31 (1984).

35) I. Kohno, K. Ogiwara, S. Fujita, K. Ikegami, T. Kageyama, S. Kohara, and H. Takebe: "RIKEN 160 cm Cyclotron", Proc. 11th Int. Conf. Cyclotrons and Their Applications, Tokyo, Oct. 1986, p. 46 (1987).

2. Nuclear physics and nuclear instrumentation

1) N. Nakanishi and K. Matsuda: "Design of Nuclear Reaction Particle Analyzer", Nucl. Instr. Methods, 57, 245 (1967).
2) K. Matsuda, N. Nakanishi, S. Takeda, and T. Wada: "Cross Sections of the ^{12}C (^{3}He, p) ^{14}N Reaction", J. Phys. Soc. Japan, 25, 1207 (1968).
3) H. Kamitsubo, T. Wada, T. Fujisawa, and M. Igarashi: "Large-Angle Scattering of ^{3}He Particles by ^{58}Ni", Phys. Letters, 28B, 408 (1969).
4) Y. Awaya, K. Matsuda, N. Nakanishi, S. Takeda, and T. Wada: "The ^{91}Zr (p, p') Reaction at 14.52 MeV", J. Phys. Soc. Japan, 27, 1087 (1969).
5) S. Yamaji and S. Yoshida: "Calculation of the Heavy Particle Stripping Process in the Reaction ^{11}B(d, n)^{12}C", Progr. Theor. Phys.,44, 125 (1970).
6) S. Kobayashi, S. Motonaga, Y. Chiba, K. Katori, A. Stricker, T. Fujisawa, and T. Wada: "Spin Flip in the Inelastic Scattering of Protons from ^{12}C at Energies around 13.1 MeV Resonance", J. Phys. Soc. Japan, 29, 1 (1970).
7) S. Nagamiya, T. Katou, T. Nomura, and T. Yamazaki: "Effective Spin and Orbital Magnetism of the Proton Studies from the Magnetic Moments of the 8^+ States of ^{90}Zr and ^{92}Mo", Phys. Letters, 33B, 574 (1970).
8) T. Yamazaki, T. Nomura, T. Katou, T. Inamura, A. Hashizume, and Y. Tendow: "Core Polarization Effect on the Magnetic Moment of the $(h^2_{9/2})$ 8^+ State of ^{210}Po", Phys. Rev. Letters, 24, 317 (1970).
9) T. Yamazaki, T. Nomura, S. Nagamiya, and T. Katou: "Aromalous Orbital Magnetism of Proton Deduced from the Magnetic Moment of the 11^- State of ^{210}Po", Phys. Rev. Letters, 25, 547 (1970).
10) N. Nakanishi, Y. Chiba, Y. Awaya, and K. Matsuda: "Elastic Scattering of ^{3}He Particles on Ca at Five Incident Energies between 18.8 and 39.3 MeV", Nucl. Phys., A140, 417 (1970).
11) S. Nagamiya, T. Nomura, and T. Yamazaki: "Stroboscopic Determination of the Magnetic Moment of the 8^+ Isomeric State of ^{208}Po", Nucl. Phys., A159, 653 (1970).
12) S. Nagamiya, T. Katou, T. Nomura, and T. Yamazaki: "Magnetic Moments of the 8^+ Isomeric States of ^{90}Zr and ^{92}Mo", J. Phys. Soc. Japan, 31, 319 (1971).
13) T. Nomura, T. Yamazaki, S. Nagamiya, and T. Katou: "Magnetic Moment of the Lowest 6^+ State in ^{42}Ca and Effects of the Deformed States", Phys. Rev. Letters., 27, 523 (1971).
14) S. Nagamiya and T. Yamazaki: "Evidence of Anomalous Orbital Magnetism of the Nucleon and the Mesonic Exchange Effect", Phys. Rev., C4, 1961 (1971).
15) T. Inamura, A. Hashizume, T. Katou, and Y. Tendow: "Identification of Neutron Deficient Isotopes ^{100}Ag and ^{104}In", J. Phys. Soc. Japan, 30, 884 (1971).
16) I. Kohno, S. Nakajima, T. Tonuma, and M. Odera: "Elastic Scattering of Carbon and Nitrogen Ions", J. Phys. Soc. Japan, 30, 910 (1971).
17) T. Yamazaki and S. Nagamiya: "Unstable Nuclear Magnetic Probes", Solid State Phys., (in Japanese), 6, 323 (1971).
18) T. Yamazaki: "Nuclear Magnetic Moment", Buturi, (in Japanese), 26, 637 (1971).
19) S. Yamaji: "The Manual of the Code for the Form Factor Computation of the Two-Nucleon Transfer Reaction", Sci. Papers I.P.C.R., 65, Nos. 3-4, 79 (1971).

20) T. Nomura and T. Yamazaki: "Effective Magnetic Moment and E2 Polarization Charge in $f_{7/2}$ Nuclei", 'The Structure of the $lf_{7/2}$, Nuclei', ed. R.A. Ricci (Editrice Compositori, Bologna, 1971), p. 437.

21) S. Nagamiya and T. Inamura: "Isomeric States in Neutron-Deficient Po-Isotopes (A = 200 ~ 203) Studied by (HI, xnγ) Reactions", Nucl. Phys., A182, 84 (1972).

22) T. Nomura, T. Yamazaki, S. Nagamiya, and T. Katou: "Magnetic Moment of the Lowest 6^+ State in ^{42}Ca", J. Phys. Soc. Japan, 33, 286 (1972).

23) T. Nomura, K. Hiruta, T. Inamura, and M. Odera: "In-Beam Alpha Spectroscopy of N = 128 Isotones, Lifetimes of ^{216}Ra and a New Isotope ^{217}Ac", Phys. Lett., 40B, 543 (1972).

24) J.I. Fujita, S. Yamaji, and M. Hirata: "Effects of Exchange Currents on Orbital g-Factor and E1 Sum Rule", J. Phys. Soc. Japan, 33, 541 (1972).

25) T. Kammuri, S. Kusuno, and S. Yamaji: "The Use of the Angular Momentum Projection Technique in Two-Nucleon Transfer Reactions on Deformed Nuclei", Phys. Lett., 39B, 327 (1972).

26) K. Matsuda, Y. Awaya, N. Nakanishi, and S. Takeda: "Elastic and Inelastic Scattering of Alpha-Particles from Even Mass Molybdenum Isotopes", J. Phys. Soc. Japan, 33, 298 (1972).

27) Y.Awaya, K. Matsuda, T. Wada, N. Nakanishi, S. Takeda, and S. Yamaji: "Inelastic Scattering of Protons from ^{100}Mo and ^{98}Mo", J. Phys. Soc. Japan, 33, 881 (1972).

28) Y. Abe and N. Takigawa: "Stability and Persistency of α Cluster Structures", Prog. Theor. Phys. Suppl., 52, (1972).

29) T. Inamura, Y. Tendow, S. Nagamiya, and A. Hashizume: "Excited Levels in ^{190}Hg and 24.5 ns Isomer", J. Phys. Soc. Japan, 32, 1163 (1972).

30) T. Inamura: "Search for Shape Isomers in Neutron Deficient Even Xe and Ba Isotopes in the Nanosecond Time Range", Sci. Papers I.P.C.R., 66, 141 (1972).

31) S. Nagamiya: "Study of the Effective Spin and Orbital Magnetic Moments of Nucleons", Sci. Papers I.P.C.R., 66, 39 (1972).

32) K. Hiruta, T. Nomura, T. Inamura, and M. Odera: "Alpha Decay of ^{218}Th, a New Isotope", Phys. Lett., 45B, 244 (1973).

33) Y. Yamazaki, S. Nagamiya, T. Nomura, K. Nakai, and T. Yamazaki: "Magnetic Moment of a Core-Excited Isomeric State in ^{210}Po", Phys. Lett., 44B, 440 (1973).

34) T. Suzuki and C. Hinohara: "The Splitting of the Isospin and Spin-Isospin Dipole Resonances in ^{12}C", Nucl. Phys., A204, 289 (1973).

35) C. L. Lin, S. Yamaji, and H. Yoshida: "Finite-Range Calculation of Two-Nucleon Transfer Reaction", Nucl. Phys., A209, 135 (1973).

36) S. Nagamiya, Y. Yamazaki, O. Hashimoto, T. Nomura, K. Nakai, and T. Yamazaki: "Magnetic Moments of the $[\pi h^2_{9/2}]$ 8^+ States in Po Isotopes and of the $[(\pi h^9_{9/2})$ $8^+ \otimes \nu\ p_{1/2}]$ 17/2-State in ^{209}Po", Nucl. Phys., A211, 381 (1973).

37) T. Nomura, K. Hiruta, T. Inamura, and M. Odera: "Ground State Alpha Decays of N = 128 Isotones; ^{216}Ra, ^{217}Ac and ^{218}Th", Nucl. Phys., A217, 253 (1973).

38) T. Nomura and K. Hiruta: "A Method of Measuring Alpha Decays in the Nanosecond Range", Nucl. Instr., 108, 61 (1973).

39) T. Fujisawa, S. Yamaji, K. Matsuda, S. Motonaga, F. Yoshida, H. Sakaguchi, and K. Masui: "The Elastic and Inelastic Scattering of ^{3}He from ^{12}C at 24.0, 29.2, 34.7 and 39.6 MeV", J. Phys. Soc. Japan, 34, 5 (1973).

40) S. Yamaji: "The Coupled-Channel Born-Approximation Calculation of the Reaction ^{100}Mo(t,p)^{102}Mo", J. Phys. Soc. Japan, 34, 298 (1973).

41) C. Gil, K. Nishiyama, T. Nomura, T. Yamazaki, and K. Miyano : "A New Short-Lived Isomer in ^{114}Sb", J. Phys. Soc. Japan, 34, 874 (1973).

42) S. Takeda, S. Yamaji, K. Matsuda, I.Kohno, N. Nakanishi, Y. Awaya, and S. Kusuno : "^{100}Mo(t,p)^{102}Mo Reaction at 15.8 MeV", J. Phys. Soc. Japan, 34, 1115 (1973).

43) O. Hashimoto, T. Nomura, T. Yamazaki, K. Miyano, and M. Ishihara : "Magnetic Moment of the $8^{+}[(\nu g_{9/2})^{-2}]$ State in ^{86}Sr", J. Phys. Soc. Japan, 34, Suppl. 259 (1973).

44) O. Hashimoto, A. Sumi, T. Nomura, S. Nagamiya, K. Nakai, and T. Yamazaki : "The g Factor of the 7^{+} Isomeric State in ^{202}Tl", J. Phys. Soc. Japan, 34, Suppl. 269 (1973).

45) S. Nagamiya, Y. Yamazaki, O. Hashimoto, T. Nomura, K. Nakai, and T. Yamazaki : "Magnetic Moments of High-Spin Isomeric States in Po Isotopes", J. Phys. Soc. Japan, 34, Suppl. 283 (1973).

46) Y. Yamazaki, S. Nagamiya, T. Nomura, K. Nakai, and T. Yamazaki : "Magnetic Moment of a Core-Excited Isomeric State in ^{210}Po", J. Phys. Soc. Japan, 34, Suppl. 286 (1973).

47) T. Nomura : "On the Violation of the Additivity of the $lf_{7/2}$ Neutron Moments", J. Phys. Soc. Japan, 34, Suppl. 331 (1973).

48) T. Nomura : "Magnetic Moments of the $lf_{7/2}$ Nuclei", J. Phys. Soc. Japan, 34, Suppl. 619 (1973).

49) O. Hashimoto, T. Nomura, T. Yamazaki, K. Miyano, and M. Ishihara : "The g-Factor of the 8^{+} State in ^{86}Sr", J. Phys. Soc. Japan, 35, 337 (1973).

50) T. Suzuki: "New Giant Resonances", Nucl. Phys., A217, 182 (1973).

51) T. Suzuki: "Momentum Transfer Dependence of the Effective Charge for Electroexcitation", Phys. Rev., C8, 2111 (1973).

52) I. Kohno: "Elastic and Inelastic Scatterings of ^{14}N and ^{12}C Projectiles by ^{12}C, ^{27}Al, ^{28}Si, and ^{58}Ni", Sci. Papers I.P.C.R., 68, 38 (1974).

53) T. Wada and S. Yamaji: "Automatic Search Code for Coupled-Channel Calculation", Sci. Papers I.P.C.R., 68, 65 (1974).

54) A. Iwamoto, S. Suekane, S. Yamaji, and K. Harada: "Asymmetric Fission of ^{236}U", Progr. Theor. Phys., 51, 1617 (1974).

55) A. Hashizume, H. Kumagai, Y. Tendow, and T. Katou: "A Mechanical Beam Chopper System for the Measurement of Half-Lives in the Millisecond Region", Nucl. Instr. Meth., 119, 209 (1974).

56) O. Hashimoto, A. Sumi, T. Nomura, S. Nagamiya, K. Nakai, T. Yamazaki, and K. Miyano: "Measurement of the g-Factor of the 0.57 ms 7^{+} State in ^{202}Tl", Nucl. Phys., A218, 180 (1974).

57) T. Takemasa:"Finite-Range Calculation of Two-Neutron Transfer Reactions on Rate-Earth Nuclei", Nucl. Phys., A220, 31 (1974).

58) T. Suzuki: "Sum Rule Approach for Nuclear Vibrations and Effects of Core Polarization", Nucl. Phys., A220, 569 (1974).

59) T. Suzuki and C. Hinohara: "Sum Rules and Nonexchange Force", Phys. Rev., C9, 1186 (1974).

60) T. Nomura, K. Hiruta, M. Yoshie, and O. Hashimoto: "Alpha-Decay of ^{215}Fr", Phys. Rev., C9, 1168 (1974).

61) S. Yamaji, T. Fujisawa, H. Kamitsubo, K. Matsuda, S. Motonaga, F. Yoshida, H. Sakaguchi, and K. Masui: "The Multi-Step Process in the ^{12}C(^{3}He, α)^{11}C Reaction", J. Phys. Soc. Japan, 37, 1191 (1974).

62) T. Takemasa: "Full Finite-Range Calculation for Heavy Ion Two Nucleon Transfer Reactions", Phys. Lett., 55B, 28 (1975).

63) T. Nomura, K. Hiruta, M. Yoshie, H. Ikezoe, T. Fukuda, and O. Hashimoto: "In-beam α- and γ-ray Spectroscopy for ^{216}Ra", Phys. Lett., 58B, 273 (1975).

64) T. Motobayashi, I. Yamane, Y. Nogami, N. Takahashi, M. Hara, K. Sagara, M. Katoh, H. Yamashita, and B. Imanishi: "Full Recoil Analysis of the Elastic Scattering of ^{16}O on ^{19}F by the Core-Exchange Model", Phys. Lett., 59B, 421 (1975).

65) W. Kutschera, B. A. Brown, H. Ikezoe, G. D. Sprouse, Y. Yamazaki, Y. Yoshida, T. Nomura, and H. Ohnuma: "Lifetimes of the 6^+ States in ^{42}Ti and ^{46}Ca and E2 Effective Charges in $(lf_{7/2})^{\pm 2}$Nuclei", Phys. Rev., C12, 813 (1975).

66) H. Ohnuma, S. Takeda, N. Nakanishi, S. Yamada, M. Sekiguchi, and H. Toyama: "Study of the ^{58}Ni(d,t)^{57}Ni Reaction at 24 MeV", J. Phys. Soc. Japan, 38, 1557 (1975).

67) S. Kusuno and T. Wada: "Microscopic Theory for Proton, Deutron, Helion, and Alpha Scattering from Collective Levels in Doubly Even Spherical Nuclei", Sci. Papers I.P.C.R., 69, 147 (1975).

68) M. Yoshie and I. Kohno : "Studies of ^{14}N, ^{12}C, and ^{11}B Induced Reactions on ^{90}Zr and $^{92\text{-}100}$Mo at Energies above the Coulomb Barrier", Sci. Papers I.P.C.R., 69, 63 (1975).

69) I. Kohno : "Elastic and Inelastic Scattering of ^{14}N and ^{12}C Projectiles by ^{12}C and ^{28}Si", J. Phys. Soc. Japan, 38, 945 (1975).

70) T. Motobayashi, I. Kohno, K. Katori, M. Yoshie, T. Ooi, and H. Kamitsubo: "Anomalous Angular Distribution in the Transition to the Sy_2 State in ^{17}O", Phys. Rev. Lett., 36, 391 (1976).

71) T. Mikumo, I. Kohno, K. Katori, T. Motobayashi, S. Nakajima, M. Yoshie, and H. Kamitsubo: "Systematics of Optimum Q Values in Multinucleon Transfer Ractions Induced by Heavy Ions", Phys. Rev., C14, 1458 (1976).

72) T. Ooi, T. Motobayashi, K. Katori, and I. Kohno: "Detection and Identification of ^{8}Be Nuclei with a Position Sensitive Detector and Counter Telescope", Reports I.P.C.R., (in Japanese), 52, 145 (1976).

73) B. Imanishi and K. I. Kubo: "Multi-Step Core-Exchange Analysis of ^{16}O + ^{18}O Scattering with the Full-Recoil Calculation", Phys. Rev. Lett., 36, 132 (1976).

74) T. Kammuri: "On the Importance of the Sequential Transfer Process in the Two-Nucleon Transfer between Heavy Ions", Nucl. Phys., A259, 343 (1976).

75) A. Iwamoto, S. Yamaji, S. Suekane, and K. Harada: "Potential Energy Surfaces for the Fission of the Actinide Nuclei", Prog. Thoer. Phys., 55, 115 (1976).

76) T. Inamura, M. Ishihara, T. Fukuda, T. Shimoda, and K. Hiruta: "Gamma-Rays from an Incomplete Fusion Reaction Induced by 95 MeV ^{14}N", Phys. Lett., 68B, 51 (1977).

77) K. Sugimoto, N. Takahashi, A. Mizobuchi, Y. Nojiri, T. Minamisono, M. Ishihara, K. Tanaka, and H. Kamitsubo: "Spin Polarization of ^{12}B in the Heavy-Ion Reaction $^{100}Mo(^{14}N, ^{12}B)^{102}Ru$", Phys. Rev. Lett., 39, 323 (1977).

78) F. G. Resmini, F. Soga, and H. Kamitsubo: "Possibility of Quasimolecular Bands in ^{28}Si", Phys. Rev., C15, 2241 (1977).

79) I. Kohno, K. Katori, T. Mikumo, T. Motobayashi, S. Nakajima, M. Yoshie, and H. Kamitsubo: "Single-and Multi-Nucleon Transfer Reactions Induced by ^{14}N and ^{12}C on fb-Shell Nuclei", J. Phys. Soc. Japan, 42, 1 (1977).

80) K. Koyama, N. Nakanishi, S. Takeda, S. Yamada, H. Sakaguchi, M. Nakamura, S. Takeuchi, and H. Ohnuma: "(^{3}He, d) Stripping to Bound and Unbound States in ^{29}P", J. Phys. Soc. Japan, 43, 755 (1977).

81) Y. Horikawa, T. Hoshino, and A. Arima: "Core Polarization Effects on the Coulomb Form Factor", Nucl. Phys., A278, 297 (1977).

82) T. Kammuri, T. Motobayashi, I. Kohno, S. Nakajima, M. Yoshie, K. Katori, T. Mikumo, and H. Kamitsubo: "Effects of Recoil and Sequential Transfer on the $^{12}C(^{14}N, ^{12}C)^{14}N$ Reaction", J. Phys. G.: Nucl. Phys., 4, L94 (1978).

83) F. Soga, J. Schimizu, N. Takahashi, K. Takimoto, R. Wada, T. Fujisawa, T. Wada, and H. Kamitsubo: "Study of the Quasimolecular Resonance by the ^{24}Mg $(\alpha,\gamma)^{12}C$, ^{16}O Reactions", J. Phys. Soc. Japan, 44, Suppl., 644 (1978).

84) Y. Toba, H. Sakaguchi, A. Goto, F. Ohtani, N. Nakanishi, N. Kishida, M. Yasue, and T. Hasegawa: "Proton Inelastic Scattering on $^{28,29,30}Si$ and Blocking Effect in the Core-Excitation of ^{29}Si", J. Phys. Soc. Japan, 45, 367 (1978).

85) H. Amakawa, S. Yamaji, A. Mori, and K. Yazaki: "Two-Step Process in Proton Inelastic Scattering", Phys. Lett., 76B, 157 (1978).

86) K. I. Kubo and H. Amakawa: "Energy Dependence of Two-Step (p, t) Cross Sections", Phys. Rev., C17, 1271 (1978).

87) F. Soga, J. Schimizu, H. Kamitsubo, N. Takahashi, K. Takimoto, R. Wada, T. Fujisawa, and T. Wada: "Intermediate Structures in $^{12}C + ^{16}O$ System through α-induced Reactions on ^{24}Mg", Phys. Rev., C18, 2457 (1978).

88) T. Nomura, H. Utsunomiya, T. Motobayashi, T. Inamura, and M. Yanokura: "Statistical Analysis of Preequilibrium α-Particle Spectra and Possible Local Heating", Phys. Rev. Lett., 40, 694 (1978).

89) T. Tamura, T. Udagawa, and H. Amakawa: "Reformulation of DWBA Form Factor for Heavy Ion Transfer Reactions", Prog. Theor. Phys., 60, 1238 (1978).

90) K. Sato, A. Iwamoto, K. Harada, S. Yamaji, and S. Yoshida: "Microscopic Calculation of Friction in Heavy Ion Reaction Using Linear Response Theory", Z. Physik A, 288, 383 (1978).

91) H. Amakawa, S. Yamaji, A. Mori, and K. Yazaki: "Adiabatic Treatment of Elastic Deuteron-Nucleus Scattering", Phys. Lett., 82B, 13 (1979).

92) H. Amakawa and K. Yazaki: "Adiabatic Treatment of Deuteron Breakup on a Nucleus", Phys. Lett., 87B, 159 (1979).

93) T. Nomura, H. Utsunomiya, T. Inamura, T. Motobayashi, and T. Sugitate: "Energy Relaxation during the Fusion Process Probed by Preequilibrium α Emission in Heavy-Ion Reactions", J. Phys. Soc. Japan, 46, 335 (1979).

94) N. Kishida and H. Ohnuma: "Exact Finite-Range DWBA and Adiabatic-Deuteron-Breakup Calculations Including the Deuteron D-state for the ^{58}Ni(p,d)^{57}Ni Reaction at 52 MeV", J. Phys. Soc. Japan, 46, 1375 (1979).

95) K. Sato, S. Yamaji, K. Harada, and S. Yoshida: "A Numerical Analysis of the Heavy-Ion Reaction Based on the Linear Response Theory", Z. Physik, A290, 149 (1979).

96) H. Amakawa and K. I. Kubo: "Analyzing Power of Two-Step ($\vec{p}$,t) Reaction Leading to the Unnatural-Parity State", Phys. Rev., C19, 2403 (1979).

97) S. Yamaji: "Analysis of Heavy-Ion Reactions Based on the Linear Response Theory", Sci. Papers I.P.C.R., 73, 19 (1979).

98) J. Fujita and M. Ichimura: "Mesonic Effects in Photonuclear Sum Rules", Meson in Nuclei, (eds. M. Rho and D.H. Wilkinson), North-Holland Pub. Co., Amsterdam, 2, 627 (1979).

99) T. Inamura, T. Kojima, T. Nomura, T. Sugitate, and H. Utsunomiya: "Multiplicity of Gamma Rays Following Fast Alpha-Particle Emission in the 95-MeV ^{14}N + ^{159}Tb Reaction", Phys. Lett., B84, 71 (1979).

100) T. Motobayashi, I. Kohno, T. Ooi and S. Nakajima : "α – Transfer Reactions between Light Nuclei", Nucl. Phys., A331, 193 (1979).

101) M. Yanokura, I. Kohno, H. Nakahara, and K. Yanakoshi: "Heavy Ion Identification System by Using a Gas Proportional Telescope", Oyo Butsuri (in Japanese), 49, 1095 (1980).

102) H. Ohnuma, T. Kubo, N. Kishida, T. Hasegawa, N. Ueda, T. Fujisawa, T. Wada, K. Iwatani, and T. Suehiro: "Vector Analyzing Power and Polarization Measurements for the ^{116}Sn(d,p)^{117}Sn Reaction and Deuteron D-State Effects", Phys. Lett., 97B, 192 (1980).

103) H. Kamitsubo: "Heavy Ion Reaction - Quasi Elastic and Deep Inelastic Collision", Butsuri (in Japanese), 35, 981 (1980).

104) M. Ichimura, E. Takada, T. Yamaya, and K. Nagatani: "Reaction Mechanism of ^{12}C(^{16}O,α): ^{12}C Transfer to Nuclear Molecular Resonances", Phys. Lett., 101B, 31 (1981).

105) H. Utsunomiya, T. Nomura, M. Ishihara, T. Sugitate, K. Ieki, and S. Kohmoto: "Angular-Momentum Transfer and Alignment Following Preequilibrium α-Particle Emission in the Reaction ^{209}Bi + ^{14}N", Phys. Lett., 105B, 135 (1981).

106) S. Yamaji, A. Iwamoto, K. Harada, and S. Yoshida: "Microscopic Calculation of the Mass Diffusion Coefficient Using Linear Response Theory", Phys. Lett., 106B, 443 (1981).

107) Y. Gono, K. Hiruta, T. Nomura, M. Ishihara, H. Utsunomiya, T. Sugitate, and K. Ieki: "In-Beam α- and γ-Ray Spectroscopy for ^{214}Rn", J. Phys. Soc. Japan, 50, 377 (1981).

108) T. Fujisawa, N. Kishida, T. Kubo, T.Wada, Y. Toba, T. Hasegawa, M. Sekiguchi, N. Ueda, M. Yasue, F. Soga, H. Kamitsubo, M. Nakamura, K. Hatanaka, Y. Wakuta, T. Tanaka, and A. Nagao: "Analyzing Power-Polarization Inequality in the Inelastic Scattering of Protons on ^{12}C for Incident Energies from 22.0 to 29.0 MeV", J. Phys. Soc. Japan, 50, 3198 (1981).

109) H. Amakawa, A. Mori, H. Nishioka, K. Yazaki, and S. Yamaji: "Adiabatic Approximation for Deuteron Breakup Effect", Phys. Rev. C, 23, 583 (1981).

110) A. Ichimura and M. Ichimura: "Coupled Channel Analysis for the Anomaly of the (^{18}O, ^{18}O*) Reaction", Prog. Theoret. Phys., 66, 913 (1981).

111) M. Yanokura, H. Nakahara, and I. Kohno: "Isotopic Dependence of the Strongly Damped Events in the 115 MeV Nitrogen Induced Reactions on Nickel", J. Phys. Soc. Japan, 50, 369 (1981).

112) H. Kudo, Y. Nagame, H. Nakahara, K. Miyano, and I. Kohno: "Correlation between Angular Anisotropy and Fragment Mass in 15 MeV Proton-Induced Fission of ^{232}Th", Phys. Rev. C, 25, 909 (1982).

113) H. Kudo, H. Muramatsu, H. Nakahara, K. Miyano, and I. Kohno: "Fission Fragment Yields in the Fission of ^{232}Th by Protons of Energies 8 to 22 MeV", Phys. Rev. C, 25, 3011 (1982).

114) S. Kohmoto, M. Ishihara, H. Kamitsubo, T. Nomura, Y. Gono, H. Utsunomiya, T. Sugitate, and K. Ieki: "Final-State Interaction and Time Information in ^{14}N-induced Reactions Studied by α-α Correlations", Phys. Lett., 114B, 107 (1982).

115) T. Inamura and M. Wakai: "Calculation of Gamma-Ray Multiplicity Moments Associated with Massive-Transfer Reactions", J. Phys. Soc. Japan, 51, 1 (1982).

116) M. Tohyama: "Proton Particle – Neutron Quasiparticle Calculations of the Isobaric Analog Resonances of the Tin Isotopes", Prog. Theor. Phys., 68, L317 (1982).

117) T. Sugitate, T. Nomura, M. Ishihara, Y. Gono, H. Utsunomiya, K. Ieki, and S. Kohmoto: "Polarization of Preequilibrium Proton Emission in the ^{93}Nb + ^{14}N Reaction", Nucl. Phys., A388, 402 (1982).

118) M. Ishihara: "Direct Reaction with Heavy Ions", Nucl. Phys., A400, 153C (1983).

119) Y. Itoh, Y. Gono, T. Kubo, M. Sugawara, and T. Nomura: "Excited States in ^{216}Ra", Nucl. Phys., A410, 156 (1983).

120) T. Fujisawa: "Analyzing Power-Polarization Inequality in the Inelastic Scattering of Protons on ^{12}C for Incident Energies from 22.0 to 29.0 MeV", Sci. Papers I.P.C.R., 77, 113(1983).

121) M. Tohyama and S. Yamaji: "Effects of Two Particle-Two Hole Excitations on the Mass Distribution in Ion-Ion Collisions", Phys. Lett., 123B, 16 (1983).

122) S. Yamaji and A. Iwamoto: "Friction Coefficients for Deep Inelastic Heavy-Ion Collisions", Z. Phys. A-Atoms and Nuclei, 313, 161 (1983).

123) H. Muramatsu, T. Miura, H. Nakahara, M. Fujioka, E. Tanaka, and A. Hashizume: "Calibration of the Isomer Shift of ^{119}Sn from Internal Conversion Measurements", Hyp. Int., 15/16, 269 (1983).

124) K. Ieki: "Study of Spin Polarization of Residual Nuclei in Heavy-Ion Induced Reactions by Gamma-ray Circular Polarization Measurement", Reports I.P.C.R., (in Japanese), 59, 20 (1983).

125) S. Yamaji and M. Tohymama: "Effects of Two Particle-Two Hole Excitations of the Mass Distribution in the ^{16}O + ^{40}Ca Reaction at E_{Lab} = 157.3 MeV", Phys. Lett., 147B, 399 (1984).

126) M. Sugawara, Y. Gono, and Y. Itoh: "In Beam γ-Ray Study of ^{217}Ra", J. Phys. Soc. Jpn., 53, 2956 (1984).

127) Y. Nagame, H. Nakahara, K. Sueki, H. Kudo, M. Yanokura, and I. Kohno: "Studies on Strongly Damped Components in Relatively Light Heavy Ion Reaction Systems", Z. Phys. A-Atoms Nuclei, 317, 31 (1984).

128) K. Asahi, M. Ishihara, H. Kamitsubo, N. Takahashi, Y. Nojiri, T. Minamisono, A. Mizobuchi, and K. Sugimoto: "Measurement of Ejectile Spin Polarization in Heavy Ion Reactions via β Decay Asymmetry", Nucl. Instrum. Methods, 220, 389 (1984).

129) T. Nomura and T. Sugitate: "Energetic Light-Particle Emission and Its Polarization in Heavy-Ion Reactions", Butsuri, (in Japanese), 39, 261 (1984).

130) H. Muramatsu, T. Miura, H. Nakahara, M. Fujioka, E. Tanaka, and A. Hashizume: "Determination of the Change of Nuclear Radius of the ^{119}Sn Mossbauer Transition by Internal Conversion", Hyp. Int., 20, 305 (1984).

131) J. Kasagi, T. Murakami, and T. Inamura: "Use of Charge Integration ADC's with Pulse Shape Discriminators for Neutron-Gamma Discrimination", Nucl. Instrum. Methods A, 236, 426 (1985).

132) T. Murakami, J. Kasagi, H. Harada, and T. Inamura: "Performance of a Neutron Multiplicity Filter Composed of Six Liquid Scintillation Detectors", Nucl. Instrum. Methods A, 241, 172 (1985).

133) M. Sugawara, Y. Gono, Y. Ishikawa, M. Fukuda, and I. Fujiwara: "In-Beam γ-Ray Study of ^{212}Po", Nucl. Phys. A, 443, 461 (1985).

134) K. Ieki, M. Ishihara, T. Inamura, S. Kohmoto, H. Utsunomiya, K. Sueki, and H. Kudo: "Spin Polarization of Residual Nuclei in (^{14}N, α) Reactions at 115 MeV", Phys. Lett. B, 150, 83 (1985).

135) N. Yoshida and A. Arima: "Aligned Bands in Ge Isotopes in the Interacting Boson Model", Phys. Lett. B, 164, 231 (1985).

136) N. Yoshinaga: "Intrinsic States in the sdg Interacting Boson Model", Nucl. Phys. A, 456, 21 (1986).

137) Y. Gono, T. Kohno, M. Sugawara, Y. Ishikawa, and M. Fukuda: "Collective Vibrations in ^{218}Ra", Nucl. Phys. A, 459, 427 (1986).

138) T. Murakami, J. Kasagi, H. Tachibanaki, K. Yoshida, Y. Shibata, T. Nakagawa, M. Ogihara, S. M. Lee, T. Kubo, and T. Motobayashi: "Properties of BaF_2 Scintillators in Charged Particle Detection", Nucl. Instrum. Methods A, 253, 163 (1986).

139) T. Otsuka and N. Yoshinaga: "Fermion-Boson Mapping for Deformed Nuclei", Phys. Lett, B, 168, 1 (1986).

140) J. Kasagi, H. Harada, T. Murakami, K. Yoshida, H. Tachibanaki, and T. Inamura: "Enhanced E2 Transitions between 9^- and 8^- States in ^{110}Sn and ^{112}Sn", Phys. Lett. B, 176, 307 (1986).

141) T. Kohno, M. Adachi, S. Fukuda, M. Taya, M. Fukuda, H. Taketani, Y. Gono, M. Sugawara, and Y. Ishikawa: "Level Structure and Electromagnetic Properties in ^{212}Ra", Phys. Rev. C, 33, 392 (1986).

142) N. Yoshinaga, A. Akiyama, and A. Arima: "The sdg Interacting Boson Model Applied to ^{168}Er", Phys. Rev. Lett., 56, 1116 (1986).

143) K. Ikeda, S. Yoshida, and S. Yamaji: "Application of Time-Dependent Mean-Field Theory to Heavy Ion Collisions: Simple Example of an S-Matrix Calculation for Elastic Scattering", Z. Phys. A-Atomic Nuclei, 323, 285 (1986).

144) T. Inamura: "Massive Transfer in Heavy Ion Reactions," Heavy Ions in Nuclear Physics, Hardwood Academic Publishers, New York, p. 1 (1986).

145) H. Harada, T. Murakami, K. Yoshida, J. Kasagi, T. Inamura, and T. Kubo: "Intruder Deformed Bands in ^{110}Sn and ^{112}Sn", Phys. Lett. B, 207, 17 (1988).

146) Y. Hatsukawa, T. Ohtsuki, K. Sueki, H. Nakahara, I. Kohno, M. Magara, N. Shinohara, and D.C. Hoffman: "Alpha Decay Properties of Light Einsteinium Isotopes", Nucl. Phys., A500, 90 (1989).

3. Atomic and solid-state physics

1) H. Sekizawa, T. Okada, S. Okamoto, and F. Ambe: "Mössbauer Effect of ^{61}Ni in Spinel Type Magnetic Oxides", J. de Phys., 32, C1-326 (1971).
2) T. Tonuma, I. Kohno, Y. Miyazawa, F. Yoshida, T. Karasawa, T. Takahashi, and S. Konno: "Charge Changing of Energetic Heavy Ions in Gases", J. Phys. Soc. Japan, 34, 148 (1973).
3) N. Shiotani, T. Okada, H. Sekizawa, T. Mizoguchi, and T. Karasawa: "Positron Annihilation in Ferromagnetic Nickel", J. Phys. Soc. Japan, 35, 456 (1973).
4) K. Matsumoto, T. Kataoka, H. Kamei, M. Terasawa, T. Karasawa, J. Sakairi, and E. Yagi: "Embrittlement of Austenitic Stainless Steels Irradiated with α-Particles", Trans. Iron and Steel Inst. Japan, 14, 118 (1974).
5) N. Shiotani, T. Okada, T. Mizoguchi, and H. Sekizawa: "Angular Distribution of Positron Annihilation Radiation in Vanadium and Niobium-Experiment", J. Phys. Soc. Japan, 38, 423 (1975).
6) H. Shiraishi, H. Sakairi, E. Yagi, T. Karasawa, R. R. Hasiguti, and R. Watanabe: "Growth Process of Helium Bubbles in Aluminum", Nippon Kinzoku Gakkaishi, (in Japanese), 39, 233 (1975).
7) Y. Awaya, K. Izumo, T. Hamada, M. Okano, T. Takahashi, A. Hashizume, Y. Tendow, and T. Katou: "K and L X Rays Induced by 5-MeV/amu α-Particle and Nitrogen-ion Bombardment of Ten Target Elements Ranging from Cr to Bi", Phys. Rev., A, 13, 992 (1976).
8) H. Tawara. Y. Awaya, Y. Tendow, T. Katou, M. Akiba, and T. Tonuma: "Ar-K-Shell Ionization by High Energy Carbon Ion Impact", Phys. Lett., 59A, 14 (1976).
9) Y. Awaya and K. Izumo: "X-rays Induced by Swift Heavy Ion Bombardment", Oyo Butsuri, (in Japanese), 45, 905 (1976).
10) A. Koyama, E. Yagi, and H. Sakairi: "Secondary Electron Emission from Ni and Al by High-Energy Proton and α-Particle Bombardment", Japan. J. Appl. Phys., 5, 1811 (1976).
11) H. Shiraishi, H. Sakairi, E. Yagi, T. Karasawa, R. R. Hasiguti, and R. Watanabe: "Growth Process of Helium Bubbles in Aluminum", Trans. Japan Inst. Metals, 17, 749 (1976).
12) H. Sakairi, E. Yagi, A. Koyama, T. Karasawa, and R. R. Hasiguti: "Cyclotron Irradiation of Cu_3Au Alloys at Low Temperatures", Proc. Intern. Conf. Fundamental Aspects of Radiation Damage in Metals, Gatlinburg, 1975, USERDA, p. 643 (1976).
13) Y. Awaya, M. Akiba, T. Katou, H. Kumagai, Y. Tendow, K. Izumo, T. Takahashi, A. Hashizume, M. Okano, and T. Hamada: "The Kα and Kβ X-Ray Spectra of Al, Ti, Cr, Fe, and Ni Induced by 84 MeV Nitrogen Ions", Phys. Lett., 61A, 111 (1977).
14) H. Tawara, Y. Awaya, Y. Tendow, T. Katou, M. Akiba, and T. Tonuma: "The Innershell Ionization of Ar K-shell Electrons by High Energy Carbon Ions", Studies of Atomic Collisions and Related Topics in Japan (Progr. Report), No. 3, p. 56 (1977).
15) Y. Awaya, T. Hamada, M. Okano, A. Hashizume, T. Takahashi, K. Izumo, Y. Tendow, H. Kumagai, T. Katou, and M. Akiba: "K X-Rays of Al, Ti, Cr, Fe, and Ni Induced by Nitrogen Ions", Studies of Atomic Collisions and Related Topics in Japan (Progr. Report), No. 3, p. 57 (1977).

16) H. Kumagai, Y. Awaya, Y. Tendow, T. Katou, and M. Akiba: "A Step Scan Controll and a Data Accumulating System of an On-line Bragg Crystal Spectrometer", Reports I.P.C.R., (in Japanese), 53, 153 (1977).

17) T. Watanabe, H. Tawara, and Y. Awaya: "By Using Heavy Ions as Projectile", Butsuri, (in Japanese), 32, 306 (1977).

18) E. Yagi, A. Koyama, H. Sakairi, and R. R. Hasiguti: "Defect Structures of Slightly Reduced Semiconducting Rutile as Observed by the Channelling Method", Rad. Effec. in Semiconduc. 1976, The Inst. of Phys., London, p. 485 (1977).

19) E. Yagi, A Koyama, H. Sakairi, and R. R. Hasiguti: "Investigation of Ti Interstitials in Slightly Reduced Rutile (TiO_2) by Means of Channeling Method", J. Phys. Soc. Japan, 42, 939 (1977).

20) H. Sakairi, E. Yagi, A. Koyama, T. Karasawa, and R. R. Hasiguti: "Atomic Displacement in Copper Irradiated with Protons, α-Particles and Carbon Ions from a Cyclotron", J. Phys. Soc. Japan, 43, 999 (1977).

21) K. Matsumoto, T. Kataoka, M. Terasawa, M. Shimada, S. Nakahigashi, H. Sakairi, and E. Yagi: "Embrittlement of Austenitic Stainless Steel Irradiated with α-Particles", J. Nucl. Materials, 67, 97 (1977).

22) A. Koyama: "Contribution of Directly Excited Electrons to the Secondary Electron Emission from Al by High Energy Proton or α-Particle Bombardment", Japan J. Appl. Phys., 16, 431 (1977).

23) N. Shiotani, T. Okada, H. Sekizawa, S. Wakoh, and Y. Kubo: "Angular Correlation of Positron Annihilation Radiation in Chrominum and Molybdenum", J. Phys. Soc. Japan, 43, 1229 (1977).

24) T. Takahashi: "Spatial Distribution of Ionization Energy Deposited about the Path of a Heavy Ion — Application to Target Theory", Tech. Rep. Res. React. Inst., Kyoto Univ., (in Japanese), KURRI-TR-174, p. 24 (1978).

25) A. Koyama: "Secondary Electron Emission from Al by High Speed Proton or α-Particle Bombardment (Calculation)", Ionizing Radiation, (in Japanese), 5, 17 (1978).

26) Y. Awaya and H. Kumagai: "An On-line X-ray Crystal Spectrometer of IPCR", Ionizing Radiation, (in Japanese), 5, 74 (1978).

27) N. Shiotani, T. Okada, H. Sekizawa, A. Nakamoto, H. Murakami, and K. Mori: "A Two Dimensional Position Sensitive γ Ray Detector for Angular Correlation Measurements", Proc. 5th Intern. Conf. Positron Annihilation, The Japan Institute of Metals, Sendai, p. 267 (1979).

28) N. Shiotani, T. Okada, N. Sakai, H. Sekizawa, and S. Wakoh: "Angular Correlation of Positron Annihilation Radiation and Compton Profiles in Magnesium", Proc, 5th Intern. Conf. Positron Annihilation, The Japan Institute of Metals, Sendai, p. 669 (1979).

29) K. Hinode, S. Tanigawa, M. Doyama, K. Shiraishi, and N. Shiotani: "Positron Lifetime Study of Gas Bubbles", Proc. 5th Intern. Conf. Positron Annihilation, The Japan Institute of Metals, Sendai, p. 733 (1979).

30) N. Owada, H. Kumakura, K. Hinode, S. Tanigawa, M. Doyama, S. Okuda, and N. Shiotani: "The Annealing Study of ^3He and Neutron Irradiated Platinum by Means of Positron Annihilation", Proc. 5th Intern. Conf. Positron Annihilation, The Japan Institute of Metals, Sendai, p. 775 (1979).

31) S. Tanigawa, K. Hinode, R. Nagai, M. Doyama, and N. Shiotani: "Effect of Doping and Thermal Vacancies on Positron Annihilation in Semiconductors", Appl. Phys., 18, 81 (1979).

32) M. Uda, H. Endo, K. Maeda, Y. Awaya, M. Kobayashi, Y. Sasa, H. Kumagai, and T. Tonuma: "Bonding Effect on F Kα Satellite Structure Produced by 84 MeV N^{4+}", Phys. Rev Lett., 42, 1257 (1979).

33) T. Tonuma, Y. Awaya, T. Kambara, H. Kumagai, I. Kohno, and S. Özkök: "Argon Kα X-ray Satellites Produced by Impact of Nitrogen Ions in the 4.7 — 7.8 MeV/amu Energy Range", Phys. Rev., A20, 989 (1979).

34) T. Takahashi, Y. Awaya, T. Tonuma, H. Kumagai, K. Izumo, A. Hashizume, S. Uchiyama, and A. Hitachi: "Energy Straggling of C and He Ions in Metal Foils", Nucl. Instr. Meth., 166, 587 (1979).

35) Y. Awaya, K. Izumo, T. Katou, H. Kumagai, T. Tonuma, Y. Tendow, T. Takahashi, A. Hashizume, and T. Hamada: "The L X-rays Following Multiple Inner-Shell Ionization", Atomic Collision Research in Japan, 5, 81 (1979).

36) M. Uda, K. Maeda, H Endo, Y. Sasa, and M. Kobayashi: "Chemical Effect on Ion-Induced L X-Ray Spectra of Transition Elements", Proc. Intern. Conf. X-Ray Processes and Inner-Shell Ionization, Plenum Pub. Co., New York (1980).

37) Y. Awaya: "Systematics of Multiple Ionization in Heavy Ion Collisions", Electronic and Atomic Collisions, North-Holland Pub. Co., Amsterdam, p. 325 (1980).

38) Y. Awaya, T. Katou, H. Kumagai, T. Tonuma, Y. Tendow, K. Izumo, A. Hashizume, T. Takahashi, and T. Hamada: "Ratio of Single K-Shell Ionization Cross Section to Double K-Shell Ionization Cross Section in Heavy-Ion-Atom Collision", Phys. Lett., 75A, 478 (1980).

39) H. Endo, M. Uda, and K. Maeda: "Influence of the Chemical Bond on the Intensities of F Kα X-Ray Satellites Produced by Electron and Photon Impacts", Phys. Rev. A, 22, 1436 (1980).

40) T. Tonuma, Y. Awaya, T. Kambara, H. Kumagai, M. Kase, A. Yagishita, and I. Kohno: "Krypton Kβ/Kα Intensity Ratios for 6 MeV/amu Ion Bombardment", Atomic Collision Research in Japan, 6, 86 (1980).

41) T. Kambara, Y. Awaya, A. Hitachi, M. Kase, I. Kohno, and T. Tonuma: "X-Rays from 110 MeV Ne Ions Passing through Gaseous Targets", Atomic Collision Research in Japan, 6, 91 (1980).

42) H. Fukushima and N. Shiotani: "Positron Annihilation in Amorphous Alloys", Solid State Phys., (in Japanese), 15, 475 (1980).

43) T. Tonuma, A. Yagishita, M. Kase, T. Kambara, Y. Awaya, and I. Kohno: "Multiple Ionization of Gas Targets by Ion Bombardment", Atomic Collision Research in Japan, No. 7, p. 76 (1981).

44) T. Kambara, Y. Awaya, A. Hitachi, M. Kase, I. Kohno, and T. Tonuma: "X-Rays from Radiative Electron Capture Induced 110-MeV Ne-Ions", Atomic Collision Research in Japan, No. 7, p. 78 (1981).

45) E. Yagi, A. Koyama, H. Sakairi, M. Iwaki, and R. R. Hasiguti: "Lattice Location of Ni Atoms Implanted into Al Crystals as Investigated by Means of Channeling Method", J. Phys. Soc. Japan, 50, 873 (1981).

46) H. Sakairi, E. Yagi, A. Koyama, and R. R. Hasiguti: "Atomic Replacement in Ordered Cu_3Au Alloy Irradiated with Protons, α-Particles and Carbon Ions from a Cyclotron", J. Phys. Soc. Japan, 50, 3023 (1981).

47) M. Uda, H. Endo, K. Maeda, Y. Sasa, and M. Kobayashi: "Chemical Effect on F Kα X-ray Satellites Produced by 6 MeV/amu P, α and C^{4+}", Z. Phys. A – Atom and Nuclei, 300, 1 (1981).

48) T. Tonuma, Y. Awaya, T. Kambara, H. Kumagai, M. Kase, A. Yagishita, and I Kohno: "Krypton Kβ/Kα Intensity Ratios for 6 MeV/amu Ion Bombardment", Inner-Shell and X-ray Physics of atoms and Solids, Prenum Press, New York and London, p. 153 (1981).

49) Y. Awaya, A. Hitachi, T. Kambara, M. Kase, H. Kumagai, T. Tonuma, and A. Yagishita: "A Broad Range X-Ray Crystal Spectrometer and Angular Distributions of X-Rays Following Multiple Inner-Shell Ionization", Atomic Collision Res. in Japan Progr. Rep., No. 8, p. 99 (1982).

50) T. Kambara, Y. Awaya, M. Kase, A. Hitachi, T. Tonuma, and I. Kohno: "Target Gas Pressure Dependence of K X-Rays from 110 MeV Ne Ions", Atomic Collision Res. in Japan Progr. Rep., No. 8, p. 321 (1982).

51) A. Koyama, T. Shikata, H. Sakairi, and E. Yagi: "Secondary Electron Emission from Metal targets under Heavy Ion Bombardment", Jpn. J. Appl. Phys., 21, 586 (1982).

52) A. Koyama, T. Shikata, H. Sakairi, and E. Yagi: "Dependence of Secondary Electron Emission Coefficients on Z_1 in Metal Targets under Bombardment with Bare Projectiles", Jpn. J. Appl. Phys., 21, 1216 (1982).

53) T. Kambara, Y. Awaya, A. Hitachi, M. Kase, I. Kohno, and T. Tonuma: "X-Rays from Radiative Electron Capture Induced by 110 MeV Ne Ions", J. Phys. B: At. Mol. Phys., 15, 3759 (1982).

54) A. Hitachi, H. Kumagai, and Y. Awaya: "Broad Range X-Ray Crystal Spectrometer", Nucl. Instr. Methods, 195, 631 (1982).

55) T. Okada, S. Ambe, F. Ambe, and H. Sekizawa: "Emission Mössbauer Studies of Carrier-Free Pentavalent Antimony-119 Ions Adsorbed on α-Fe_2O_3 and Cr_2O_3", J. Phys. Chem., 86, 4726 (1982).

56) H. Endo and M. Uda: "Atomic Number Dependence of L-Shell Vacancy Rearrangement Probabilities on Kα X-ray Satellites Induced by 6 MeV/amu N^{4+} Impacts", Z. Phys. A, 306, 187 (1982).

57) Y. Awaya, H. Kumagai, and A. Hitachi: "Position Sensitive Proportional Counter for X-ray Measurements", The Handbook of Atomic Collisions-Techniques-, Study Group of Fundamental Atomic Process, (in Japanese), p. 74 (1982).

58) K. Ishii, M. Sebata, M. Kamiya, A. Kuwako, S. Morita, Y. Awaya, and T. Tonuma: "K-Shell Vacant Production in Light-Element with α-Particles and N^{7+} Ions of 5,6, and 7 MeV/amu", J. Phys. Soc, Japan, 51, 4021 (1982).

59) H. Sakairi, E. Yagi, A. Koyama, and R. R. Hasiguti: "The Damage Function Based on the Focusing Model", Point Defects and Defect Interactions in Metals, Univ. of Tokyo Press, Tokyo, p. 818 (1982).

60) T. Kambara, Y. Awaya, M. Kase, A. Hitachi, T. Tonuma, and I. Kohno: "Collisional Quenching of Hydrogen-Like Ne-Ions with Kinetic Energy of 5.5 MeV/amu", Atomic Collision Res. in Japan, No. 9, p. 91 (1983).

61) T. Takahashi, Y. Awaya, T. Tonuma, H. Kumagai, K. Izumo, M. Nishida, A. Hitachi, A. Hashizume, S. Uchiyama, and T. Doke: "Stopping Power of Ni, Ag, Au, and Pb for ~ 7 MeV/nucleon α Particles and Carbon Ions. Z_1^3 Deviation from the Bethe Formula", Phys. Rev. A, 27, 1360 (1983).

62) T. Kambara: "Radiative Electron Capture in Heavy Ion-Atom Collisions", Butsuri, 38, 376 (1983).

63) M. Uda, H. Endo, K. Maeda, Y. Sasa, K. Fujima, and K. Fuwa: "Application of Ion Induced X-Ray Emission Spectroscopy to Chemistry", Proc. 2nd Symp. on Ion Beam Technology, Hosei Univ., p. 129 (1983).

64) T. Kambara: "Collisional Quenching of np States of 110 MeV H-Like Ne Ions in Gaseous Targets", J. Phys. B: At. Mol. Phys., 17, 1599 (1984).

65) K. Asai, F. Ambe, S. Ambe, and H. Sekizawa: "TDPAC of γ-Rays Emitted from ^{111}Cd ($\leftarrow^{111}$In) in α-Fe_2O_3", J. Phys. Soc. Jpn., 53, 4109 (1984).

66) K. Fukai, K. Shiraishi, E. Yagi, S. Hamada, and T. Sawai:"Measurement of Mean Projected Range for Argon- and Nitrogen-ions Irradiated in Stainless Steels", J. At. Energy Soc. Jpn. (in Japanese), 26, 974 (1984).

67) M. Uda, A. Koyama, K. Maeda, and Y. Sasa: "Valence Electron Rearrangement Prior to X-Ray or Auger Emission", Proc. Int. Conf. on X-Ray and Inner-Shell Processes in Atoms, Molecules and Solids (ed. by A. Meisel and J. Finster), Leipzig, p. 307 (1984).

68) K. Hino, N. Toshima, I. Shimamura, and T. Watanabe: "Theory of Radiative Electron Capture I: Nonrelativistic Treatment of Theoretical Paradox", Atomic Collision Res. in Japan-Prog. Rep., No. 11, p. 53 (1985).

69) K. Hino and T. Watanabe: "Theory of Radiative Electron Capture II: Relativistic (Semi-Covariant) Treatment", Atomic Collision Res. in Japan-Prog. Rep., No. 11, p. 57 (1985).

70) N. Sakai and H. Sekizawa: "A New Technique of Mössbauer Spectroscopy without Using Doppler Modulation", J. Phys. Soc. Jpn., 54, 474 (1985).

71) K. Asai, T. Okada, and H. Sekizawa: "TDPAC of γ-rays Emitted from ^{111}Cd ($\leftarrow^{111}$In) in Fe_3O_4", J. Phys. Soc. Jpn., 54, 4321 (1985).

72) I. Tanaka, S. Nasu, F. E. Fujita, F. Ambe, S. Ambe, and T. Okada: "^{119}Sb Mössbauer Study on Quenched-in Vacancies in Gold", J. Phys. F: Met Phys., 16, L151 (1986).

73) F. Ambe, K. Asai, S. Ambe, T. Okada, and H. Sekizawa: "Comparative Mössbauer and TDPAC Studies on the After-Effects of the EC Decays of ^{119}Sb and ^{111}In in α-Fe_2O_3", Hyperfine Interact., 29, 1197 (1986).

74) N. Sakai and H. Sekizawa: Observation of Mössbauer Spectrum without Utilizing Doppler Motion", Hyperfine Interact., 29, 1521 (1986).

75) M. Uda: "Chemical Effects in Characteristic X-Rays Emitted from Multiply Ionized Sates", Atomic and Nuclear Heavy Ion Interactions Brasov Int. School 1984, Central Institute of Physics Bucharest Romania, p. 293 (1986).

76) Y. Higashiguchi, Y. Suzuki, E. Yagi, M. Narui, and H. Kayano: "Effect of Helium on the Deformation Mode for Ti-7.5 Al Alloy", J. Nucl. Mater., 149, 328 (1987).

77) K. Asai, F. Ambe, S. Ambe, T. Okada, and H. Sekizawa: "An Investigation on the After-Effects of ^{111}In($\rightarrow^{111}$Cd) EC Decay in α-Fe_2O_3", Hyperfine Interact., 34, 277 (1987).

78) K. Asai, T. Okada, and H. Sekizawa: "Super-transferred Hyperfine Magnetic Fields at ^{111}Cd ($\leftarrow^{111}$In) in Ferrimagnetic Oxides with the Spinel Structure", Hyperfine Interact., 34, 435 (1987).

79) T. Kambara, Y. Awaya, M. Kase, H. Kumagai, H. Shibata, and T. Tonuma: "REC X-Rays for ^{3}He and ^{4}He Targets", J. Phys. Soc. Jpn., 56, 1907 (1987).

80) E. Yagi, H. Sakairi, A. Koyama, and R. R. Hasiguti: "Recovery and Reverse Annealing of Proton- and α-Particle-Irrradiated Cu_3Au at Low Temperatures", (Extended Abstract), Proc. 3rd Sino-Jpn. Symp. Metal Physics and Physical Metallurgy, Shanghai Iron and Steel Res. Inst., Shanghai, p. 1 (1988).

81) E. Yagi, H. Sakairi, A. Koyama, and R. R. Hasiguti: "Isochronal Annealing of Proton- or α-Particle-Irradiated Cu_3Au at Low Temperatures", Phys. Rev. B, 38, 3189 (1988).

82) K. Hino and T. Watanabe: "Radiative Electron Capture Processes in the Relativistic Incident Energy Region", Butsuri, (in Japanese), 43, 759 (1988).

83) K. Shiraishi, K. Fukai, and E. Yagi: "Damage Profiles in a Stainless Steel Irradiated with Ar- and N-ions", J. Nucl. Mater., (1990). (in press)

4. Radiochemistry, radiation chemistry, and radiation biology

1) T. Nozaki, Y. Tanaka, A. Shimamura, and T. Karasawa: "The Preparation of Anhydrous HF^{18}", Int. J. Appl. Radiat. Isotopes, 19, 27 (1968).
2) M. Inarida and A. Shimamura: "Separation of Carrier-free ^{206}Bi from the ^{206}Pb Target", Radioisotopes, 18, 19 (1969).
3) F. Ambe, S. Ambe, M. Takeda, H. H. Wei, K. Ohki, and N. Saito: "Radiochemical Preparation of ^{61}Cu-Copper Single Line Source for the Measurement of the Mössbauer Effect in ^{61}Ni", Radiochem. Radioanal. Letters, 1, 341 (1969).
4) M. Inarida and A Shimamura: "Separation of Carrier-free ^{76}As from the ^{78}Se Target", Radiochem. Radioanal. Letters, 2, 87 (1969).
5) S. Ambe, N. Shiotani, T. Okada, and T. Karasawa: "Preparation of RI Sources by the IPCR Cyclotron for the Study of Solid Physics, (I)", Reports I.P.C.R., (in Japanese), 46, 15 (1970).
6) S. Kitayama, K. Igarashi, T. Karasawa, and A. Matsuyama: "LET Effects in Micrococcus radiodurans Irradiated with Alpha Particles in the Liquid Phase", Agr. Biol. Chem., 34, 1346 (1970).
7) M. Imamura, M. Matsui, and T. Karasawa: "Radiation Chemical Studies with Cyclotron Beams. II. The Radiolysis of an Aqueous Ferrous Ammonium Sulfate Solution with Carbon- and Nitrogen-Ion Radiations", Bull. Chem. Soc. Japan, 43, 2745 (1970).
8) M. Matsui, H. Seki, T. Karasawa, and M. Imamura: "Radiation Chemical Studies with Cyclotron Beams. I. Fricke Solutions", J. Nucl. Sci. Tech., 7, 97 (1970).
9) F. Ambe and N. Saito: "Chemical Effects of Neutron-Induced Nuclear Reactions in Halates and Related Compounds III, The (n, γ) and (n, 2n) Reactions in Iodates", Radiochim. Acta, 13, 105 (1970).
10) T. Nozaki, Y. Yatsurugi, and N. Akiyama: "Concentration and Behavior of Carbon in Semiconductor Silicon", J. Electrochem. Soc., 117, 1566 (1970).
11) T. Nozaki, Y. Yatsurugi, and N. Akiyama: "Charged Particle Activation Analysis for Carbon, Nitrogen and Oxygen in Semiconductor Silicon", J. Radioanal. Chem., 4, 87 (1970).
12) M. Aratani and N. Saito: "Characterization and Discussion of Charge Spectrometer by Means of Ion Beam Experiment", Radioisotopes, 19, 22 (1970).
13) M. Aratani and N. Saito: "Mass Spectroscopic Studies on the Mechanism of Ionization of Atoms Formed as a Result of Radioactive Decay Process. I", Mass Spectros., 18, 906 (1970).
14) T. Karasawa, H. Seki, M. Imamura, A. Matsuyama, and M. Matsui: "Studies of Radiation Chemistry and Biology with the IPCR 160cm Cyclotron", The Use of Cyclotrons in Chemistry, Metallurgy and Biology, Ed. C. B. Amphlett, Butterworths (London), p. 76 (1970).
15) M. Aratani and N. Saito: "The Mass Spectrometry Using Radioisotopes as an Ion Source", Mass Spectros., 19, 195 (1971).
16) T. Nozaki, Y. Makide, Y. Yatsurugi, N. Akiyama, and Y. Endo: "A New Radio-Tracer Technique for the Evaporation Study of Light Elements from Molten Silicon", Int. J. Appl. Radiat. Isotopes, 22, 607 (1971).
17) F. Ambe, H. Shoji, S. Ambe, M. Takeda, and N. Saito: "A Mössbauer Study of the Valence State of ^{119}Sn after EC Decay of ^{119}Sb in Antimony, Sb_2Te_3 and Sb_2S_3", Chem. Phys. Lett., 14, 522 (1972).

18) T. Nozaki, Y. Makide, Y. Yatsurugi, Y. Endo, and N. Akiyama: "Chemical Behavior of Carbon in High-purity Silicon in the Dissolution and Fusion of the Matrix", Bull. Chem. Soc. Japan, 45, 2776 (1972).
19) Y. Endo, Y. Yatsurugi, N. Akiyama, and T. Nozaki: "Infrared Spectrophotometry for Carbon in Silicon as Calibrated by Charged Particle Activation", Anal. Chem., 44, 2258 (1972).
20) F. Akiha, T. Aburai, T. Nozaki, and Y. Murakami: "Yield of ^{52}Fe for the Reactions of ^{3}He and α on Chromium", Radiochim. Acta, 18, 108 (1972).
21) F. Suhadi, S. Kitayama. Y. Okazawa, and A. Matsuyama: "Isolation and Some Radiobiological Properties of Mutants of Micrococcus radiodurans Sensitive to Ionizing Radiations", Radiat. Res., 49, 197 (1972).
22) A. Matsuyama, T. Takahashi, T. Karasawa, and F. Yatagai: "Biomedical Application of Heavy Ionizing Particle", Tokyo J. Medical Sci., 80, 126 (1972).
23) F. Ambe and S. Ambe: "Mössbauer Spectroscopic Verification of Two Different States of Impurity ^{119}Sn Atoms in Sb_2Te_3", Phys. Lett., 43A, 399 (1973).
24) F. Ambe, S. Ambe, and H. Shoji: "Preparation of ^{119}Sb for Mössbauer Spectroscopy of ^{119}Sn", Radiochem. Radioanal. Lett., 15, 349 (1973).
25) N. Akiyama, Y. Yatsurugi, Y. Endo, Z. Imayoshi, and T. Nozaki: "Lowering of Breakdown Voltage of Semiconductor Silicon Due to the Precipitation of Impurity Carbon" Appl. Phys. Lett., 22, 630 (1973).
26) Y. Yatsurugi, N. Akiyama, Y. Endo, and T. Nozaki: "Concentration, Solubility, and Equilibrium Distribution Coefficient of Nitrogen and Oxygen in Semiconductor Silicon", J. Electrochem. Soc., 120, 975 (1973).
27) F. Ambe and S. Ambe: "Chemical Effects of Neutron-Induced Nuclear Reactions in Halates and Related Compounds IV. The (n, γ) and (n, 2n) Reactions in Chlorates", Radiochim. Acta, 19, 42 (1973).
28) S. Ambe, F. Ambe, and N. Saito: "The Oxidation States of ^{119}Sb after the EC Decay of ^{119m}Te in TeO_2 and H_6TeO_6", Radiochim. Acta, 19, 121 (1973).
29) S. Ambe and F. Ambe: "A Mössbauer Study of the Oxidation State of ^{119}Sn after the Successive EC Decays of ^{119m}Te in Telluric Acid", Radiochim. Acta, 20, 141(1973).
30) M. Matsui and M. Imamura: "Radiation Chemical Studies with Cyclotron Beams. III. The Heavy-Ion Radiolysis of Liquid Aliphatic Ketones", Bull. Chem. Soc. Japan, 47, 1113 (1974).
31) T. Nozaki, Y. Yatsurugi, N. Akiyama, Y. Endo, and Y. Makide: "Behaviour of Light Impurity Elements in the Production of Semiconductor Silicon", J. Radioanal. Chem., 19, 109 (1974).
32) M. Suehiro, M. Aratani, and N. Saito: "Ionization Caused by Beta Emitters", Mass Spectroscopy, 22, 183 (1974).
33) F. Ambe, S. Ambe, H. Shoji, and N. Saito: "Mössbauer Emission Spectra of ^{119}Sn after the EC Decay of ^{119}Sb in Metals, Oxides and Chalcogenides of Antimony and Tellurium", J. Chem. Phys., 60, 3773 (1974).
34) F. Yatagai, T. Takahashi, Y. Kitajima, and A. Matsuyama: "Inactivation of Bacterial Spores by Charged Particles", J. Rad. Res., 15, 90 (1974).
35) K. Igarashi, F. Yatagai, T. Takahashi, and A. Matsuyama: "LET Dependence of DNA Single-Strand Scission in E. coli B_{S-1} by Charged Particles", J. Rad. Res., 15, 148 (1974).

36) A. Matsuyama, T. Takahashi, and F. Yatagai: "Biological and Medical Studies on Heavy Ion Effects", J. Atomic Energy Soc. Japan, 16, 24 (1974).

37) F. Ambe and S. Ambe: "A Mössbauer Study of the Valence States of ^{119}Sn after the EC Decay of ^{119}Sb in Antimony and Tellurium Iodides", Bull. Chem. Soc. Japan, 47, 2875 (1974).

38) T. Nozaki, M. Iwamoto, and T. Ido: "Yield of ^{18}F for Various Reactions from Oxygen and Neon", Intern. J. Appl. Radiat. Isotopes, 25, 339 (1974).

39) S. Ambe and F. Ambe: "Mössbauer Emission Spectrum of ^{119}Sn in ^{119}Sb (OH) (C_2O_4)", Inorg. Nucl. Chem. Lett., 11, 139 (1975).

40) K. Kimura, M. Ogawa, M. Matsui, T. Karasawa, M. Imamura, Y. Tabata, and K. Oshima: "ESR Study of the Spatial Distribution of Radicals Trapped in the Heavy Ion-Irradiated n-Eicosane Single Crystal", J. Chem. Phys., 63, 1797 (1975).

41) S. Ambe and F. Ambe: "Mössbauer Emission Spectrum of ^{121}Sb after the B^- Decay of ^{121m}Sn in SnS_2: Nuclear Decay Synthesis of Antimony (V) Sulfide", J. Chem. Phys., 63, 4077 (1975).

42) T. Nozaki, M. Furukawa, S. Kume, and R. Seki: "Production of ^{28}Mg by Triton and α-Particle Induced Reactions", Intern. J. Appl. Radiat. Isotopes, 26, 17 (1975).

43) F. Yatagai, T. Takahashi, and A. Matsuyama: "Inactivation of Bacterial Cells by Cyclotron Beam", J. Radiat. Res., 16, 99 (1975).

44) M. Matsui and M. Imamura: "Radiation Chemical Studies with Cyclotron Beams. IV. The Effect of Water in the Heavy-Ion Radiolysis of Liquid Acetone", Bull. Chem. Soc. Japan, 48, 2346 (1975).

45) F. Ambe and S. Ambe: "A ^{119}Sn Mössbauer Emission Study of Recoil ^{119}Sb Atoms after Proton Reactions in SnTe", Chem. Phys. Lett., 39, 294 (1976).

46) F. Ambe and S. Ambe: "Defect ^{119}Sn Atoms after Nuclear Decays and Reaction in SnSb and SnTe", J. Physique, 37, C6-923 (1976).

47) T. Nozaki, Y. Yatsurugi, and Y. Endo: "Charged Particle Activation Analysis. Studies on Carbon, Nitrogen and Oxygen Mainly in Semiconductor Silicon", J. Radioanal. Chem., 32, 43 (1976).

48) T. Nozaki, K. Fukushi, and T. Irie: "Some Radiohalogen Derivatives of Cholesterol", J. Labelled Comp., 13, 226 (1977).

49) Y. Harata, M. Matsui, and M. Imamura: "Radiation-Induced Chain Isomerization of cis-2-Butene in Benzene Solution", Chem. Lett., 1977, 199.

50) S. Kitayama, K. Shiratori, F. Yatagai, and A. Matsuyama: "Enhanced Lethal Effect of Various Agents on M. Radiodurans by Postincubation at Nonpermissive Temperature", Agr. Biol. Chem., 41, 2297 (1977).

51) F. Yatagai and A. Matsuyama: "LET-Dependent Radiosensitivity of Escherichia coli K-12 rec and uvr Mutants", Radiat. Res., 71, 259 (1977).

52) M. Matsui and M. Imamura: "The Radiolysis of Binary Mixtures of Tetrahydrofuran with Benzene, Thiophene, Pyridine, and Nitrobenzene", Bull. Chem. Soc. Japan, 51, 2191 (1978).

53) K. Kimura and M. Imamura: "Emission Spectra of Excitons Created in a Single Crystal of KBr by Irradiation of Heavy Ions at 4.2 K", Phys. Lett., 67A, 159 (1978).

54) F. Yatagai, S. Kitayama, and A. Matsuyama: "Inactivation of Phage φX 174 by Accelerated Ions. Enhanced δ-ray Effect by Air Layer in Front of the Samples", Radiat. Res., 77, 250 (1979).

55) T. Nozaki, M. Iwamoto, and Y. Itoh: "Production of ^{77}Br by Various Nuclear Reactions", Int. J. Appl. Radiat. Isotopes, 30, 79 (1979).

56) T. Nozaki, Y. Itoh, and K. Ogawa: "Yield of ^{73}Se for Various Reactions and Its Chemical Processing", Int. J. Appl. Radiat. Isotopes, 30, 595 (1979).

57) T. Nozaki, M. Iwamoto, K. Usami, K. Mukai, and A. Hiraiwa: "Helium-3 Activation Analysis of Oxygen in Silicon Nitride Films on silicon Wafers", J. Radioanal. Chem., 52, 449 (1979).

58) F. Ambe and S. Ambe: "Mössbauer Emission Studies of Defect ^{119}Sn, ^{119}Sb, and ^{119m}Te Atoms after Nuclear Decays and Reactions in SnSb, SnTe, and Sb_2Te_3", J. Chem. Phys., 73, 2029 (1980).

59) F. Yatagai, T. Takahashi, and A. Matsuyama: "Effect of Heavy Ions on Bacterial Spores", Int. J. Radiat. Biol., 37, 558 (1980).

60) T. Takahashi, F. Yatagai, and A Matsuyama: "Possible Long Range Effects in the Inactivation of Bacterial Cells by Heavy Ions", Sci. Papers I.P.C.R., 74, 51 (1980).

61) K. Kimura, K. Mochizuki, T. Fujisawa, and M. Imamura: "Measuremet of the Decay and Time-Resolved Spectra of the Emission from σ-Excitons in KBr in the Nano Second Range, Produced by Heavy-Ion Irradiation", Phys. Letters, 78A, 108 (1980).

62) T. Nozaki, T. Karasawa, M. Io, K. Imamura, S. Iida, and H. Yoshida: "Present Status in the Use of the Prototype Baby Cyclotron", J. Label. Comp. & Radiopharm., 18, 181 (1981).

63) T. Nozaki and M. Iwamoto: "Some Fundamental Data Concerning the Formation of Low Z. Radionuclides", J. Label. Comp. & Radiopharm., 18, 230 (1981).

64) T. Nozaki and M. Iwamoto: "Yield of ^{14}O for the Reactions ^{14}N(p, n)^{14}O, ^{12}C(^{3}He, n)^{14}O and ^{12}C(α, 2n)^{14}O", Radiochim. Acta, 29, 57 (1981).

65) H. Muramatsu, H. Nakahara, and M. Yanokura: "Production of ^{119m}Sn by Alpha Particle Bombardment of ^{116}Cd and Its Carrier-free Separation", J. Inorg. Nucl. Chem., 43, 1727 (1981).

66) F. Ambe and S. Ambe: "A Site Distribution of Dilute ^{119}Sb and ^{119m}Te on Solidification of SnTe and SnSb by Mössbauer Emission Spectroscopy of ^{119}Sn", J. Chem. Phys., 75, 2463 (1981).

67) Y. Itoh and T. Nozaki: "Oxygen Depth Profiling by Activation with the ^{16}O(^{3}He, p)^{18}F Reaction", J. Radioanal. Chem., 70, 329 (1982).

68) T. Nozaki: "Chemical Separation of ^{18}F as KBF_4 in Oxygen Analysis by the ^{16}O(^{3}He, p) ^{18}F Reaction", J. Radioanal. Chem., 72, 527 (1982).

69) H. Emori, M. Umehara, M. Takeya, K. Nomura, Y. Terai, and T. Nozaki: "Determination of Oxygen in GaAs by ^{3}He Activation Analysis", Gallium Arsenide and Related Compounds 1981, Inst. Phys., Bristol, p. 47 (1982).

70) M. Iwamoto, T. Nozaki, Y. Takahashi, and K. Usami: "Distribution of Forward Recoil Range of ^{18}F Formed by Various Nuclear Reactions", Radiochim. Acta, 30, 73 (1982).

71) K. Maeda and M. Uda: "Computer Programs for Quantitative Analysis by PIXE-(I)", Reports I.P.C.R., (in Japanese), 58, 96 (1982).

72) T. Takahashi, F. Yatagai, K. Aoki, and S. Yamanaka: "Track Structure Theories and Inactivation Cross Sections of Bacterial Spores for Heavy Ions", Ionizing Radiat., 9, 24 (1982).

73) T. Irie, K. Fukushi, O. Inoue, T. Yamasaki, T. Ido, and T. Nozaki: "Preparation of ^{18}F-labeled 6- and 2-fluoro-9-benzylpurine as a Potential Brain-scanning Agent", Int. J. Appl. Radiat. Isotopes, 33, 633 (1982).

74) Y. Itoh and T. Nozaki: "Oxygen Depth Profiling in Heat-treated Silicon as Measured by Charged Particle Activation Analysis", TG SSD 81-115～130 IECE of Japan (1982).
75) F. Yatagai, T. Takahashi, and S. Kitayama: "W-Reactivation and W-Mutagenesis in Phage φX 174", Adv. Space Res., 3, No.8, 65 (1983).
76) T. Takahashi, F. Yatagai, and S. Kitayama: "Effect of Heavy Ions on Bacterial Spores", Adv. Space Res., 3, No. 8, 95 (1983).
77) Y. Nagame, M. Watanabe, H. Kudo, K. Sueki, H. Nakahara, and I. Kohno: "Recoil Studies in the Reaction Induced by 115 MeV ^{14}N on ^{62}Ni", Radiochim. Acta, 33, 127 (1983).
78) K. Kimura and J. Hormes: "Roles of the Rydberg Transitions in Fast Excitation Transfer Studied in Cyclohexane and n-Heptane Using Synchrotron Radiation", J. Chem. Phys., 79, 2756 (1983).
79) I. Kaneko: "Current Topics in Potentially Lethal Damage Repair Research", Tissue Culture, 9, 328 (1983).
80) A. Akanuma, F. Yatagai, K. Igarashi, K. Usuba, and T. Irifune: "Mouse Skin Reactions to 40 MeV Helium Ion Irradiation", Radiological Medicine (Hoshasenka), 1, 243 (1983).
81) K. Maeda, Y. Sasa, Y. Yokode, M. Maeda, M. Kobayashi, K. Fujima, and M. Uda: "Several Applications of PIXE Analysis", Proc. 2nd Symp. on Ion Beam Technology, Hosei Univ., p. 157 (1983).
82) T. Ohno, T. Nishimura, K. Nakano, and I. Kaneko: "Differential Recovery from Potentially Lethal Damage in Normal Human Lung Fibroblasts after Irradiation with ^{60}Co γ-Rays and Accelerated N-Ion Beam", Int. J. Radiat. Biol., 45, 21 (1984).
83) T. Takahashi, F. Yatagai, T. Katayama, M. Inada, and S. Konno: "Track Structure Theories and Their Application for Inactivation Cross Sections of Bacterial Cells", J. Radiat. Res., 25, 21 (1984).
84) M. Nakamura, Y. Mochizuki, K. Usami, Y. Itoh, and T. Nozaki: "Infrared Absorption Spectra and Compositions of Evaporated Silicon Oxides (SiO_x)", Solid State Comm., 50, 1079 (1984).
85) M. Yuasa, Y. Ogata, H. Nishide, E. Tsuchida, M. Iwamoto, and T. Nozaki: "Determination of Chemically Bound Oxygen by ^{15}O-O Tracer Method. Application to Hemoglobin- and Synthetic Heme-Bound Oxygen", Chem. Lett., 1984, 1889.
86) S. Ambe: "Separation of Trace Elements, In(III), Sn(IV), Sb(V) and Te(IV) by Adsorption on Activated Carbon and Graphite", J. Radioanal. Nucl. Chem. Articles, 81, 77 (1984).
87) M. Nakamura, Y. Mochizuki, K. Usami, Y. Itoh, and T. Nozaki: "Infrared Absorption Spectra and Compositions of Evaporated Silicon Oxides (SiO_x)", Solid State Commun., 50, 1079 (1984).
88) Y. Itoh, T. Nozaki, T. Masui, and T. Abe: "Calibration Curve for Infrared Spectrophotometry of Nitrogen in Silicon", Appl. Phys. Lett., 47, 488(1985).
89) K. Kimura: "Large Yield of Photoemission Near Maximum Stopping Power in the Track of N-ion Impinged Helium Gas; Possibility of Cluster Formation of Excimers in Liquid Helium", Hoshasen (Ion. Radiat.) (in Japanese), 11, 94 (1985).
90) T. Takahashi, K. Eguchi, T. Katayama, and I. Kaneko: "Recent Topics on Biological Heavy-Ion Action and the Track Structure", Hoshasen (Ion. Radiat.) (in Japanese), 11, 122 (1985).
91) Y. Itoh and T. Nozaki: "Solubility and Diffusion Coefficient of Oxygen in Silicon", Jpn. J. Appl. Phys., 24, 279 (1985).

92) T. Nozaki, Y. Itoh, Y. Ohkubo, T. Kimura, and H. Fukushima: "Simultaneous Charged Particle Activation Analysis of Carbon and Boron in Gallium Arsenide", Jpn. J. Appl. Phys., 24, 801 (1985).

93) Y. Sugita, H. Kawata, S. Nakamichi, T. Okabe, T. Watanabe, S. Yoshikawa, Y. Itoh, and T. Nozaki: "Measurement of the Out-Diffusion Profile of Oxygen in Silicon", Jpn. J. Appl. Phys., 24, 1302 (1985).

94) M. Nakamura, Y. Mochizuki, K. Usami, Y. Itoh, and T. Nozaki: "Infrared, Raman, and X-Ray Diffraction Studies of Silicon Oxide Films Formed from SiH_4 and N_2O Chemical Vapor Deposition", J. Electrochem. Soc.: Solid-State Sci. Technol., 132, 482 (1985).

95) K. Kimura: "Spectral Measurements along the Path of N Ions Impinged into Dense He Gas (400 Torr, 5.2K). I. Emission Spectra and Decay Measurements", J. Chem. Phys., 84, 2002 (1986).

96) K. Kimura: "Spectral Measurements along the Path of N Ions Impinged into Dense Helium Gas (400 Torr and 5.2 K). II. Excimer Reactions Dependent on Stopping Power and Large Emission Yields near the Termination of the Track", J. Chem. Phys., 84, 2010 (1986).

97) K. Kimura: "Electronic Excitation at High-Density by Heavy-Ion Irradiation", Radiat. Chem., (in Japanese), 42, 2 (1986).

98) K. Kimura: "Clustering of Helium-Excimer under the High-Density Electronic Excitation by Heavy Ion Irradiation", Ioniz. Radiat., (in Japanese), 12, No. 3, 32 (1986).

99) I. Kohno, M. Yanokura, S. Motonaga, H. Kamitsubo, M. Yatsuhashi, T. Suematsu, and H. Kobayashi: "Effects on the Fast Neutron Irradiation on Cable Materials", IEEE Trans. Nucl. Sci., NS-33, Vol. 1, 77 (1986).

100) F. Ambe, S. Ambe, T. Okada, and H. Sekizawa: "In Situ Mössbauer Studies of Metal Oxide/Aqueous Solution Interfaces with Adsorbed Co-57 and Sb-119 Ions", Geochemical Processes at Mineral Surfaces, Am. Chem. Soc., Washington, D. C., p. 403 (1986).

101) T. Nozaki, Y. Itoh, T. Masui, and T. Abe: "Behavior of Oxygen in the Crystal Formation and Heat Treatment of Silicon Heavily Doped with Antimony", Appl. Phys., 59, 2562 (1986).

102) A. Kira, M. Imamura, and M. Matsui: "Trapped Electron Yield in Ethanol Glasses at 80K Irradiated with High-LET Ion Beams", Radiat. Phys. Chem., 27, 425 (1986).

103) T. Nozaki, Y. Itoh, S. Hayashi, and Q. Qiu: "Utilization of Deuterium and ^{15}N as Activable Tracers in Solid State Sciences", J. Radioanal. Nucl. Chem., 112 (1), 47 (1987).

104) H. Fukushima, T. Kimura, H. Hamaguchi, T. Nozaki, Y. Itoh, and Y. Ohkubo: "Routine Determination of Light Elements by Charged-Particle Activation Analysis", J. Radioanal. Nucl. Chem., 112 (2), 415 (1987).

105) T. Nozaki: "Charged Particle Activation Analysis of Light Impurity Elements in Semiconductor Materials", Proc. 11th Int. Conf. Cyclotrons and Their Applications, Tokyo, Oct. 1986, p. 579 (1987).

106) I. Kaneko, K. Eguchi-Kasai, T. Takahashi, T. Kosaka, and K. Nakano: "Beamport and Irradiation Chamber of the RIKEN Cyclotron for Biological Samples", 11th Int. Conf. Cyclotrons and Their Applications, Tokyo, Oct. 1986, p. 633 (1987).

107) K. Eguchi-Kasai, T. Kosaka, I. Kaneko, T. Takahashi, A. Maruhashi, and K. Nakano: "Cell Death and DNA Lesion Caused by Accelerated Charged Particles", 11th Int. Conf. Cyclotrons and Their Applications, Tokyo, Oct. 1986, p. 667 (1987).

108) T. Seguchi, T. Sasuga, W. Kawakami, M. Hagiwara, I. Kohno, and H. Kamitsubo: "Proton Irradiation Effects on Organic Polymers", Proc. 11th Int. Conf. Cyclotrons and Their Applications, Tokyo, Oct. 1986, p. 669 (1987).

109) T. Takahashi, F. Yatagai, T. Katayama, S. Konno, K. Takahashi, Y. Takayanagi, K. Nakano, and I. Kaneko: "Calculation of Dose around the Trajectory of an Ion and Interpretation of Inactivation Cross Sections of Microorganisms", J. Radiat. Res., 28, 71 (1987).

110) K. Eguchi-Kasai, T. Kosaka, I. Kaneko, T. Takahashi, A. Maruhashi, and K. Nakano: "Induction of Non-Repairable DNA Strand Breaks by N-ion Beams", J. Radiat. Res., 28, 213 (1987).

111) S. Ambe: "Adsorption Kinetics of Sb(V) Ions onto α-Fe_2O_3 Surfaces from an Aqueous Solutions", Langmuir, 3, 489 (1987).

112) K. Kimura: "Roles of Electronic Excited States in Irradiation Effect of Heavy Ion", Radiat. Chem., (in Japanese), 44, 42 (1987).

113) K. Eguchi, T. Inada, M. Yaguchi, S. Satoh, and I. Kaneko: "Induction and Repair of DNA Lesions in Cultured Human Melanoma Cells Exposed to a Nitrogen-Ion Beam", Int. J. Radiat. Biol., 52, 115 (1987).

114) T. Takahashi, K. Eguchi, A. Hashizume, and T. Inada: "Data Requirements in Heavy Ion Radiotherapy — Considerations on Available Physical Quantities —", Proc. Advisory Group Meeting on Nuclear and Atomic Data for Radiotherapy and Related Radiobiology, IAEA Panel Proc. Ser. STI/PUB/741, p. 367 (1987).

115) I. Kaneko: "Basic Researches for Cancer Therapy with Heavy Charged Particles — DNA Lesions and Their Repair in Human Melanoma Cells", Rep. Mochida Mem. Found. Med. Pharm. Res., 3, 241 (1987).

116) T. Takahashi, F. Yatagai, T. Katayama, T. Doke, and H. Ohashi: "The Inactivation of Microorganisms by Different Heavy Ions", Proc. 1986 Int. Symp. Biological Sciences in Space (eds. S. Watanabe et al.), MYU Research, Tokyo, p. 365 (1987).

117) T. Takahashi, F. Yatagai, T. Katayama, S. Konno, K. Nakano, I. Kaneko, and T. Kasuya: "Position Determination by Laser Marks of Biological Samples Placed on a Plastic Track Detector and Inactivation of B. Subtilis Spores by a Single Heavy Ion", Jpn. J. Appl. Phys., 27, 2181 (1988).

118) H. Sunaga, T. Agematsu, R. Tanaka, K. Yoshida, and I. Kohno: "Dosimetry by a Cellulose Triacetate Film Dosimeter in Proton-Beam Irradiation", Radioisotopes, (in Japanese), 37, 84 (1988).

119) T. Takahashi, T. Katayama, F. Yatagai, S. Konno, I. Kaneko, T. Kasuya, T. Doke, and H. Ohashi: "The Inactivation of Bacterial Spores by a Single Heavy Ion and Preparation for Experiments in a Spacecraft", J. Radiat. Res., 29, 37 (1988).

120) T. Takahashi, F. Yatagai, T. Katayama, and I. Kaneko: "Biological Effects of HZE Particles in Cosmic Rays and Experimental Programme", Space Environ. Monit., (in Japanese), 5, 115 (1988).

121) S. Ambe, T. Okada, F. Ambe, I. Tanaka, S. Nasu, and F. E. Fujita: "In and Ex Situ Emission Mössbaur Spectra of No-Carrier-Added ^{119}Sb Electrodeposited on Gold", J. Electrochem. Soc., 135, 949 (1988).

122) K. Maeda, Y. Sasa, M. Maeda, H. Yusuyama, and M. Uda: "Application of PIXE to Biological Materials in Daily Life", Proc. 12th Int. Symp. Hosei Univ., p. 453 (1988).

123) K. Kimura, T. Kataoka, T. Azuma, Y. Aoki, Y. Ito, and Y. Tabata: "New Emission Bands at High Density Excitation of Dense Gas and Liquid of Helium Irradiated by N-Ions", Phys. Lett. A, 133, 91 (1988).

124) Y. Kobayashi, M. Katada, H. Sano, T. Okada, K. Asai, N. Sakai, S. Ambe, and F. Ambe: "Mössbauer Spectroscopic Studies of Ruthenium Trichlorides", Hyperfine Interact., 41, 487 (1988).

125) M. Suehiro, F. Yokoi, T. Nozaki, and M. Iwamoto: "No-carrier-added Radiobromination Via the Gattermann Reaction", J. Labelled Compd. & Radiopharm., 24, 1143 (1988).

126) T. Nozaki, Y. Itoh, and Q. Qiu: "Dissolution of Hydrogen and Nitrogen in Silicon", J. Radioanal. Chem., 124, 341 (1988).

127) I. Kaneko, K. Eguchi-Kasai, T. Kosaka, K. Nakano, A. Maruhashi, and T. Takahashi: "DNA-Lesion and Cell Death by α-Particles and Nitrogen Ions", Adv. Space Res., 9, 73 (1989).

128) S. Ambe: "Adsorption of No-Carrier-Added ^{119}Sb(V) Ions onto Metal Oxide and Hydroxide Surfaces from Aqueous Solutions", Radiochim. Acta, 46, 145 (1989).

129) S. Ambe, T. Okada, and F. Ambe: "Mössbauer and Tracer Studies of Metal Oxide/Aqueous Solution Interface", Proc. Int. Symp. Advanced Nuclear Energy Research — Near-Future Chemistry in Nuclear Energy Field —, p. 407 (1989).

130) T. Takahashi, T. Kosaka, K. Kasai, K. Nakano, F. Yatagai, and I. Kaneko: "Recent Topics on the Effect of High LET Radiation on Microorganisms and Cultured Mammalian Cells", Radiation, (in Japanese), 16, 146 (1989).

131) Y. Kobayashi, M. Katada, H. Sano, T. Okada, K. Asai, and F. Ambe: "^{99}Ru and ^{57}Fe Mössbauer Spectroscopy of a Ruthenium Alloy, $RuFe_2Si$", J. Radioanal. Nucl. Chem. Lett., 136, 387 (1989).

132) Y. Itoh, Y. Kadota, T. Nozaki, H. Fukushima, and K. Takeda: "CPAA Study on Carbon, Boron and Oxygen in LEC-GaAs", Jpn. J. Appl. Phys., 28, 210 (1989).

133) Y. Itoh, Y. Sugita, and T. Nozaki: "Effect of Carbon and Oxygen Precipitation on Gold Diffusion in Silicon", Jpn. J. Appl. Phys., 28, 290 (1989).

134) K. Kimura: "Effects of High Density Excitation by Heavy Ion Irradiation", Ion. Radiat., 16, 131 (1989).

Postface

The 160 cm Cyclotron, the first beam from which was obtained in October 1966, was shut down on the 30th of April in 1990. The Cyclotron, the first heavy-ion accelerator in Japan, produced many pioneering and distinguished studies in various fields. The present supplement is edited, on this occasion, to leave records on the Cyclotron.

Editors are indebted to F. Ambe, H. Azeyanagi, A. Hashizume, F. Higo, M. Imamura, A. Matsuyama, T. Nozaki, H. Sekizawa, K. Shinohara, T. Takahashi, Y. Tendow, E. Yagi, F. Yatagai for their generous help in preparation of the publication.

November 1990
(Y. Awaya)

Illustration: Y. Tendow

RIKEN Accelerator Progress Report

理化学研究所加速器年次報告 Supplement (1990)

印　刷　平成2年 (1990) 11月25日
発　行　平成2年 (1990) 11月30日
発行者　理化学研究所
代表者　小田　稔
〒351-01　埼玉県和光市広沢2番1号
電話 (0484) 62－1111
編集者　理化学研究所加速器研究施設運営委員会
印刷所　勝美印刷株式会社
〒112　東京都文京区小石川1丁目3番7号

定価 5,000円
(消費税別)

理化学研究所

埼玉県　和光市　広沢